Solidification and characterization of aluminum-magnesium-lithium alloy

Kozina, Franjo

University of Zagreb

Faculty of Metallurgy

Franjo Kozina

SOLIDIFICATION AND CHARACTERIZATION OF ALUMINIUM-MAGNESIUM-LITHIUM ALLOY

DOCTORAL DISSERTATION

Supervisors:
Zdenka Zovko Brodarac, Professor
Mitja Petrič, Assistant professor

Sisak, 2024

University of Zagreb

Metalurški fakultet

Franjo Kozina

SKRUĆIVANJE I KARAKTERIZACIJA ALUMINIJ-MAGNEZIJ-LITIJ LEGURE

DOKTORSKI RAD

Mentori:
prof. dr. sc. Zdenka Zovko Brodarac
doc. dr. sc. Mitja Petrič

Sisak, 2024

BIBLIOGRAPHY DATA

UDK:	669.017.13(043)
Keywords:	aluminum-magnesium-lithium alloy, chemical composition, thermodynamic parameters, solidification sequence, intermetallic phases, mechanical properties
Scientific area	TECHNICAL SCIENCES
Scientific field:	Metallurgy
Institution:	Faculty of Mechanical Engineering and Naval Architecture
Thesis supervisors:	prof.dr.sc. Zdenka Zovko Brodarac doc.dr.sc. Mitja Petrič
Number of pages:	380
Number of figures:	126
Number of tables:	43
Number of references:	359
Date of examination	February 29, 2024.
Thesis defence commission:	

Prof.dr.sc. Natalija Dolić, University of Zagreb - chairman of defence commission
Prof.dr.sc. Branko Bauer, University of Zagreb – member
Prof.dr.sc. Jožef Medved, University of Ljubljana – member
Prof.dr.sc. Primož Mrvar, University of Ljubljana – member
Prof.dr.sc. Franc Zupanič – University of Maribor – external member

Archive:	University of Zagreb Faculty of Mechanical Engineering and Naval Architecture

TABLE OF CONTENTS

ACKNOWLEDGEMENT

Za vrijeme izrade ovoga rada pomogli su mi brojni profesori i kolege, te obitelj i prijatelji. Njihova pomoć i potpora nisu samo doprinijeli ovom istraživanju već i mom znanstvenom, stručnom, društvenom i duševnom napretku.

Ponajprije se zahvaljujem mentorima prof.dr.sc. Zdenki Zovko Brodarac i doc.dr.sc. Mitji Petriču na uloženom trudu te brojnim razgovorima, raspravama, savjetima i konstruktivnim kritikama. Trebalo je imati strpljenja nebrojeno puta postaviti pitanje „I? Kad se branimo?...više“ Iako pitanje „što je bilo prije kokoš ili jaje“ nismo formirali kao hipotezu, pokazalo se ključnim u tumačenju rezultata i znanstvenog doprinosa istraživanja.

Zahvaljujem prof.dr.sc. Nataliji Dolić, prof.dr.sc. Branku Baueru, prof.dr.sc. Jožefu Medvedu, prof.dr.sc. Primožu Mrvaru te prof.dr.sc. Francu Zupaniču, članovima Povjerenstva za ocjenu i obranu doktorskog rada koji su ukazavši na nedostatke doprinijeli kvaliteti ovoga rada.

Zahvaljujem se kolegici Sandri Brajčinović te kolegama Nevenu Kolingeru, Blažu Leskovaru, Andreju Penku, Tilenu Balašku i Martinu Lamutu čije su mi znanje i stručnost omogućili da bolje upoznam svojstva ove legure.

Na kraju, zahvaljujem svojim roditeljima Milki i Davoru na velikoj podršci i strpljenju tijekom cjelokupnog školovanja. Pitam se jeste li bili svjesni što činite kad ste mi „predložili“ da upišem Metalurški fakultet. Veliko hvala prijateljici Barbari Tubić Bulat koja nije propustila priliku voditi evidenciju ali se i nasmijati svakoj izokrenutoj riječi. Brojne kolege su svratile u sobu 9 pitati čemu se sad smijemo. Puno hvala prijateljima Draganu i Slađani na podršci i cjeloživotnom prijateljstvu. Ispričavam se ako ste o metalurgiji i aluminijskim legurama naučili više no što ste htjeli.

SUMMARY

The continuous development of innovative materials with improved functional properties is needed to meet the demands of modern transport industry. Given that previous research did not cover aluminum (Al) alloys with combined additions of magnesium (Mg) and lithium (Li), a contemporary approach in design and synthesis of an Al-Mg-Li alloy was applied. The research was performed under the basic assumption that the solidification sequence and microstructure development can be affected by the chemical composition, thermodynamic parameters, and processing parameters. A proper correlation of these parameters should result in an alloy with improved properties in the as-cast condition.

The chemical composition was selected based on the literature review and the application of thermodynamic calculations of equilibrium and non-equilibrium solidification sequence, while sample synthesis comprehended the use of four different experimental setups to minimize the loss of Li and Mg. During casting the simple thermal analysis was used to estimate the solidification rate and changes in the material's temperature with respect to the cooling time. Further insight into the impact of heating and cooling rates on phase transformation was obtained using simultaneous thermal analysis. The macrostructure and microstructure of the synthesized alloys were identified using different techniques of metallographic analysis. The potential improvements in functional properties of synthesized alloys were estimated through density measurements, compression testing, hardness measurements at macro-, micro-, and nano- scale as well as through the assessment of the microstructure stability in corrosive environment.

The characterisation of alloys' physical properties confirmed the influence of Li and Mg additions on density. The lowest density of 2.27 g/cm^3 was obtained in the alloy containing highest amounts of Li (2.58 wt.%) and Mg (2.57 wt.%), while the highest density of 2.49 g/cm^3 was calculated for the sample containing lowest amount of Mg (0.38 wt.%).

The characterization of mechanical properties indicated higher hardness measurements and compression properties for the samples in as-cast with respect to the solutionized condition indicating beneficial influence of intermetallic phases on alloys' properties. The deviation was noted during nanoindentation measurements. Surface penetration measurements indicated higher hardness and modulus values for samples in solutionized

condition. This confirmed that modulus is an intrinsic proportion of the alloy typically attributed to electron redistribution between the Al-Li bounds in the α_{Al} solid solution.

The application of chemical and electrochemical degradation testing indicated higher microstructure stability of the sample in as-cast condition compared to the solutionized sample. While degradation of the as-cast sample degradation progressed by dissolution of the Al_8Mg_5 (β) and Al_2LiMg (T) phases located between the branches of the α_{Al} dendritic network, the solutionized sample degraded through the grain boundary and α_{Al} grain involvement. The remnant of the AlLi (δ) phase inside the α_{Al} grains resulted in cavity formation and sample surface layering. Furthermore, dealloying of α_{Al} solid solution through Li^+ and Mg^{2+} cation loss weakening the hardening effect of solutionizing resulting in lower microhardness values.

The contemporary approach to design and synthesis allowed for Al-Mg-Li alloy solidification sequence to be amended:

- Li/Mg > 1:

  $\alpha_{Al} \rightarrow Al_3Li$ (δ') $\rightarrow$ AlLi (δ) $\rightarrow$ (Al_8Mg_5 (β) + Al_2LiMg (T)) $\rightarrow$ Al_8Mg_5 (β)

- Li/Mg ≤ 1:

  - $\alpha_{Al} \rightarrow Al_3Li$ (δ') $\rightarrow Al_2LiMg$ (T) $\rightarrow$ (Al_8Mg_5 (β) + Al_2LiMg (T) $\rightarrow$ Al_8Mg_5 (β)

It was proven that regardless of the Li/Mg ratio, the Al_3Li phase (δ') will serve as a precursor but also as one of the hardening phases.

Keywords:

Aluminum-magnesium-lithium alloy, chemical composition, thermodynamic parameters, solidification sequence, intermetallic phases, mechanical properties

PROŠIRENI SAŽETAK

Iako su dosadašnja istraživanja pokazala da svaki dodani 1,0 mas% litija (Li) smanjuje gustoću za 3,0 %, povećava modul elastičnosti za 6,0 % te specifičnu čvrstoću za 5,0 %, taj povoljan učinak na svojstva legura aluminija (Al) smatra se izuzetkom koji dokazuje pravilo legiranja. U slučaju kada se želi poboljšati neko svojstvo, u ovom slučaju modul elastičnosti, aluminiju se dodaju legirajući elementi s višim modulom elastičnosti u odnosu na modul elastičnosti metalne osnove aluminija (α_{Al}). S obzirom na to da je Li alkalni metal niske točke taljenja (165,85 °C) te maksimalnog modula elastičnosti od svega 5,2 GPa, taj atipični učinak na mehanička svojstva pripisuje se raspodjeli elektrona pri vezi između atoma Al-Li te izdvajanju intermetalnih faza tijekom skrućivanja. Skrućivanje i precipitacija intermetalnih faza posljedica je smanjene topljivosti Li u metalnoj osnovi α_{Al} koja se smanjuje s 4,0 mas% pri eutektičkoj temperaturi (603,0 °C) na 1,0 mas% pri temperaturi od 100,0 °C. Osnovni očvršćujući interetalni spoj u Al-Li legurama je metastabilna Al_3Li (δ') faza koja skrućuje koherentno s metalnom osnovom α_{Al}. Preferirano izdvajanje Al_3Li (δ') faze može se postići dodatkom magnezija (Mg). Smanjujući topljivost Li u metalnoj osnovi α_{Al} i djelomično zamjenjujući atome Li u rešetci Al_3Li (δ') faze, Mg povećava njen volumni udio. Pored skrućivanja metastabilne Al_3Li (δ') faze, Al-Mg-Li legirajući sustav podrazumijeva precipitaciju Al_2LiMg (T), $Al_{12}Mg_{17}$ (γ) i Al_8Mg_5 (β) faza ovisno o Li/Mg omjeru. Iako će preferirano izdvajanje faza ovisiti o kemijskom sastavu, termodinamički parametri poput brzine hlađenja i pothlađenja će utjecati na mehanizam nukleacije intermetalnih faza te slijed skrućivanja. Skrućivanje metalne osnove α_{Al} te skrućivanje i precipitacija faza odvijaju se pri brzinama hlađenja od 2,0 °C/s do 12,0 °C/s. Pri višim brzinama hlađenja nastaje prezasićena čvrsta otopina (SSS) α_{Al} dok se pri nižim brzinama potiskuje izdvajanje tercijarne faze. Zbog visoke reaktivnosti litija s atmosferom peći i vatrostalnim materijalima, potrebno je obratiti pažnju na procesne parametre tijekom taljenja i lijevanja Al-Mg-Li legure. S obzirom na to da ne postoji vatrostalni materijal koji je istovremeno kompatibilan s Li i Mg, potrebno je prilagoditi procesne parametre tako da se izbjegne dugo vrijeme zadržavanja taline nakon dodatka legirajućih elemenata te smanji mogućnost erozije lonca i kontaminacija taline. Pri odabiru odgovarajućeg materijala za izradu kalupa, dizajn kalupa i vrijeme lijevanja utječu potrebno je uzeti u obzir visoku sklonost Al-Mg-Li legura k volumnom stezanju, pojavi poroznosti uslijed stezanja pri skrućivanju te toplih pukotina. Ljevačke greške koje se javljaju

kao rezultat loše odabranih procesnih parametara negativno utječu na razvoj mikrostrukture i mehanička svojstva legure.

Na temelju ranije navedenog, može se zaključiti da je redizajniranjem kemijskog sastava aluminijskih legura dodatkom Li i Mg moguće ostvariti poboljšanje mehaničkih svojstava uz istovremeno smanjenje gustoće. Ključ postizanja navedenih poboljšanja krije se u poznavanju utjecaja kemijskog sastava te termodinamičkih i procesnih parametra na razvoj mikrostrukture tijekom skrućivanja Al-Mg-Li legura. Za razliku od intermetalnih faza koje se izdvajaju tijekom skrućivanja i termo-mehaničke obrade aluminij-silicij (Si)-bakar (Cu) i Al-Si-Mg legura, metastabilna Al_3Li faza ostaje sferična i koherentna s metalnom osnovom α_{Al} pri znatno višim temperaturama te dugom vremenu zadržavanja omogućujući uklanjanje zaostalih naprezanja te postizanje visoke čvrstoće i specifičnih mehaničkih svojstava. Niska osjetljivost na povišene temperature, visoka specifična čvrstoća i modul elastičnosti kao i mogućnost dodatnog smanjenja mase kao posljedice smanjenja gustoće čine aluminij-magnezij-litij legure iznimno interesantnima s potencijalom primjene u automobilskoj, zrakoplovnoj i svemirskoj industriji.

Cilj istraživanja i motivacija

Jedino stalan razvoj inovativnih materijala s poboljšanim funkcionalnim svojstvima može udovoljiti zahtjevima suvremene transportne industrije za sigurnijim, bržim, učinkovitijim, isplativijim i ekološki prihvatljivim vozilima. S obzirom na to da dosadašnja istraživanja nisu obuhvatila Al legure s kombiniranim dodacima Mg i Li, očekuje se suvremeni pristup u dizajniranju i sintezi Al-Mg-Li legure s poboljšanim svojstvima već u lijevanom stanju. Poboljšana svojstva u lijevanom stanju bit će rezultat korelacije kemijskog sastava, termodinamičkih parametara, procesnih parametra kao i razvoja mikrostrukture tijekom skrućivanja.

Hipoteze rada

Kako bi se ispunio cilj istraživanja, formulirane su sljedeće hipoteze:

- *Dodatak Mg i Li pridonijet će smanjenju gustoće legure.*
- *Dodatak Mg i Li utjecat će na razvoj očvršćujućih intermetalnih faza te povoljno utjecati na mehanička svojstva Al-Mg-Li legure.*

- *Korelacija kemijskog sastava, termodinamičkih i procesnih parametara omogućit će određivanje slijeda skrućivanja Al-Mg-Li legure.*

Formulirane hipoteze pretpostavljaju da će poboljšana svojstava legure Al-Mg-Li proizaći iz razvoja mikrostrukture tijekom skrućivanja, pri čemu će kemijski sastav, termodinamički parametri i procesni parametri izravno utjecati na slijed skrućivanja te odrediti vrstu, veličinu, volumni udio i raspodjelu intermetalnih faza.

Struktura rada

Kako bi se dokazale formulirane hipoteze potrebno je provesti istraživanje. Zbog bolje sljedivosti, istraživanje je podijeljeno u nekoliko etapa:

1. Dizajniranje i prilagodba kemijskog sastava bazirati će se na pregledu dosadašnjih istraživanja te termodinamičkom proračunu ravnotežnih i neravnotežnih dijagrama stanja primjenom Thermo-Calc programskog paketa. S obzirom na to da su i Li i Mg reaktivni metali, motivacija za odabir kemijskog sastava bazirati će se na poboljšanju mehaničkih svojstava minimalnim dodatkom legirajućih elementa.
2. Sinteza Al-Mg-Li legure provesti će se u indukcijskoj peći pod laboratorijskim uvjetima. Kako bi se smanjili gubitci Li i Mg potrebno je pomno odabrati procesne parametre poput atmosfere peći, vatrostalnog materijala, materijala za izradu kalupa te temperature dodatka legirajućih elemenata i lijevanja.
3. Primjena jednostavne toplinske analize tijekom lijevanja i skrućivanja omogućit će procjenu brzine skrućivanja kao i identifikaciju promjene u temperaturi materijala s vremenom hlađenja.
4. Nakon sinteze analizirat će se kemijski sastav dobivene legure. Usporedbom rezultata kemijskog sastava s dodatkom legirajućih elemenata, procijenit će se njihov gubitak tijekom taljenja i skrućivanja.
5. Primjenom simultane toplinske analize (STA) procijenit će se utjecaj različitih brzina zagrijavanja i hlađenja na tijek skrućivanja. Temperatura taljenja, latentna toplina taljenja, temperatura faznih transformacija, temperatura i energija faznih precipitacija odredit će se primjenom diferencijalne pretražne kalorimetrije (DSC) pri brzinama zagrijavanja i hlađenja od 2,0, 10,0, 20,0, 30,0, 40,0 i 50,0 K/s.
6. U svrhu određivanja mehaničkih svojstava uzoraka koristit će se tlačno ispitivanje te mjerenje tvrdoće na makro-, mikro- i nano- razini.

7. Analiza makrostrukture i mikrostrukture uzoraka primjenom svjetlosne i elektronske mikroskopije kao i difrakcije X-zraka biti će provedena nakon standardne metalografske pripreme brušenjem i poliranjem.
8. Procjena stabilnosti mikrostrukture u korozivnom mediju obuhvatit će primjenu kemijskih i elektrokemijskih metoda ispitivanja. U obje metode koristit će se vodena otopina natrij klorida, kalij klorida i dušične kiseline s početnom pH vrijednosti od 0.4 (EXCO otopina). Procjena osjetljivosti mikrostrukture raslojavanju provesti će se izlaganjem uzorka korozivnoj otopini u trajanju od 5, 24, 48, 72 h. Metode elektrokemijske korozije omogućit će određivanje korozijskog potencijala (E_{corr}), gustoće struje pri koroziji (i_c), anodnog nagiba (B_a), katodnog nagiba (B_c) te brzine korozije (v_{corr}).

Rezultati i diskusija

Rezultati analize kemijskog sastava ukazali su na uspješnu sintezu uzoraka uz korištenje zaštitne atmosfere Ar i vakuuma. Najkraće vrijeme zadržavanja taline nakon legiranja postignuto je tijekom sinteze u vakuumu. Značajniji gubitak legirajućih elemenata rezultat je dodatnih operacija kao što su duže vrijeme potrebno za izjednačavanje tlaka u vakuumskoj komori i gubitak zaštitne atmosfere kao posljedica lijevanja dva zasebna uzorka. Neadekvatan izbor premaza lončića uzrokovao je reakciju talina/lonac i kontaminaciju taline.

Rezultati proračuna gustoće ukazali su na utjecaj kemijskog sastava na fizikalna svojstva sintetiziranih uzoraka. Najmanja gustoća izračunata je za uzorak s najvećim udjelom Li (2,58 mas%) i Mg (2.57 mas%), dok je najveća gustoća izračunata za uzorak s najmanjim udjelom Mg (0,38 mas%). Primijećeno je smanjenje u gustoći što je omjer Li/Mg bliži 1. Usporedbom rezultata gustoće kao funkcije debljine presjeka, uočeno je slično ponašanje između svih uzoraka osim uzorka sintetiziranom pod vakuumom. Ovo odstupanje proizlazi iz plinske poroznosti uočene tijekom vizualnog pregleda. Manja gustoća središnjeg dijela (ø 20,0 mm) svih uzoraka ukazuje na segregaciju Li i Mg tijekom skrućivanja, dok povećanje gustoće gornjih dijelova (ø 30,0 mm) ukazuje na gubitak legirajućih elemenata uslijed oksidacije.

Rezultati termodinamičkog proračuna pomoću Thermo-Calc programskog paketa ukazali su na pojavu sljedećih faza: čvrsta otopina α_{Al}, faze AlLi (δ), Al_2LiMg (T), Al_8Mg_5 (β) i Al_3Mg_2. Proširenje kemijskog sastava elementima nečistoća (Fe, Si, Mn) ukazalo je na dodatno stvaranje $Al_{13}Fe_4$, AlLiSi i Mg_2Si. Utjecaj omjera Li/Mg na ravnotežni slijed

skrućivanja AlLi (δ) i Al_2LiMg (T) faza procijenjen je primjenom proračuna ravnotežnog faznog dijagrama i proračuna jednoosnih faznih ravnoteža (eng. *one axis equilibrium diagram*). Proračun neravnotežnog slijeda skrućivanja ukazao je na to kako sastav poslijednje skrućujuće faze neće ovisiti samo o omjeru Li/Mg već i interakciji između Li i Mg. Dok Li pokazuje veću tendenciju prema segregaciji na granici kruta/tekuća faza, Mg ima tendenciju stvaranja čvrste otopine α_{Al}.

Primjena jednostavne toplinske analize tijekom skrućivanja Al-0,38Mg-2,16Li legure ukazala je na nedostatak karakterističnih pikova povezanih sa skrućivanjem pojedinih faza. Obrada krivulje hlađenja i prve derivacije krivulje hlađenja, omogućila je identifikaciju temperature nukleacije, temperature likvidusa, eutektoida i solidusa. Rezultati jednostavne toplinske analize također su ukazali na nisko podhlađenje kao posljedicu skrućivanja metastabilne faze pri povišenim temperaturama.

Primjena diferencijalne pretražne kalorimetrije (DSC) omogućila je identifikaciju karakterističnih temperatura kao što su temperatura likvidusa (T_L), temperatura solidusa (T_S) te temperature reakcija u tekućem i čvrstom stanju. Ispitivanje pri različitim brzinama zagrijavanja i hlađenja ukazalo je na proširenje intervala skrućivanja kao posljedicu povećanja entalpije i pomicanja maksimuma pikova prema višim temperaturama. Primjena DSC metode omogućila je identifikaciju karakterističnih temperatura i korelaciju slijeda skrućivanja Al-Li-Mg legura u ovisnosti o Li/Mg omjeru. Korelacijom rezultata DSC analize s rezultatima termodinamičkih proračuna i podacima dostupnim u literaturi, dobiveni su sljedovi skrućivanja koji značajno odstupaju od rezultata Thermo-Calc proračuna. Najveća razlika uočena u sva tri tipa omjera odnosi se na skrućivanje metastabilne Al_3Li (δ') faze na temperaturi primarne kristalizacije i Al_8Mg_5 (β) na eutektičkoj temperaturi. U uzorku s povećanim udjelom nečistoća uočena je razlika u raspodjeli visokotemperaturne ($Al_{13}Fe_4$) i eutektičke (Mg_2Si, β-Al_5FeSi) faze te faze niskog tališta (Al_3Mg_2).

Makrostruktura uzoraka je tipična za skrućivanje legure s vidljivim zonama smrznutih, stubčastih i jednakoosnih kristala. Dodatkom cjepiva u potpunosti je uklonjena kristalografska tekstura. Debljina kristalografske teksture smanjuje se sa smanjenjem omjera Li/Mg. To je posljedica utjecaja Mg na topljivost Li u metalnoj osnovi α_{Al} te obogaćenja interdendritnog područja Li i nukleacije intermetalnih faza. Korištenje svjetlosne mikroskopije omogućilo je identifikaciju α_{Al} dendritne mreže, AlLi (δ), Al_2LiMg (T), (Al_8Mg_5 (β) + Al_2LiMg (T)) i Al_8Mg_5 (β) intermetalnih faza. Uočene intermetalne faze pokazuju tendenciju skrućivanja i precipitacije

u interdendritnom području. Jedino odstupanje pokazuje AlLi (δ) faza čije se skrućivanje temelji na prethodnom izdvajanju metastabilne Al_3Li (δ') faze. Ta faza skrućuje unutar dendritne mreže α_{Al} te po granicama zrna. Slijed skrućivanja u interdendritnom području identificiran je korištenjem pretražne elektronske mikroskopije (SEM) i energetske disperzivne spektroskopije (EDS). Prva faza koja skrućuje u interdendritnom području je Al_2LiMg (T) nakon čega slijedi skrućivanje dvofaznog (Al_8Mg_5 (β) + Al_2LiMg (T)) područja i sekundarnog eutektika Al_8Mg_5 (β). Ova pretpostavka je u skladu s rezultatima termodinamičkog modeliranja slijeda skrućivanja i podacima dostupnim u literaturi. Rezultati SEM i EDS analize ukazali su na skrućivanje intermetalnih faza na bazi Fe u uzorcima s povišenim sadržajem nečistoća. Na temelju njihovog kemijskog sastava, morfologije i položaja u mikrostrukturi, faze su identificirane kao $Al_{13}Fe_4$.

Rezultati difrakcije rendgenskih zraka (XRD) ukazali su na razvoj Al_2LiMg (T) i Al_3Li (δ') intermetalnih faza u metalnoj osnovi α_{Al} za sva tri uzorka (Li/Mg = 0,88, Li/Mg = 1,0 i Li/Mg = 5,68). U uzorku s Li/Mg = 5,68 omjerom dodatno je detektirana AlLi (δ) faza. Skrućivanje i zadržavanje metastabilne Al_3Li (δ') faze pri svim omjerima važno je za postizanje dobrih mehaničkih svojstava.

Provedbom transmisijske elektronske mikroskopije (TEM) i difrakcijske analize odabranog područja (SAD) identificirane su Al_3Li (δ’), AlLi (δ) i (Al_8Mg_5 (β) + Al_2LiMg (T)) intermetalne faze. U uzorku s povišenim sadržajem Fe i Si dodatno je identificirana $Al_{13}Fe_4$ faza.

Rezultati tlačnog ispitivanja ukazali su na smanjenje tlačnih svojstava, prvenstveno tlačne čvrstoće i granice tlačenja uslijed toplinske obrade otapajućim žarenjem. Usporedbom utjecaja Li/Mg omjera na uzorke u lijevanom i toplinski obrađenom stanuje, može se zaključiti da intermetalne faze imaju pozitivan utjecaj na tlačna svojstva uzoraka u lijevanom stanju. To se uglavnom odnosi na granicu tlačenja i tlačnu čvrstoću lijevanih uzoraka s Li/Mg = 0,90 i Li/Mg = 0,93 što ukazuje na raniji početak plastične deformacije kao i smanjenje površine uzorka. Rezultati metalografske analize provedene na uzorcima nakon tlačnog ispitivanja ukazuju na tri tipična ponašanja:

1. nejednaku deformaciju i bačvasti učinak,
2. stvaranje intergranularnog loma,
3. nastanak ravnina klizanja i linija toka materijala.

Formiranje linija toka materijala povezano je s nedostatkom precipitata i slobodnim kretanjem dislokacija. Formiranje intergranularnog loma inicirano je interakcijom između dislokacija i precipitata AlLi (δ) faze, dok je stvaranje ravnina klizanja posljedica prisutnosti intermetalnih faza na bazi Fe.

Mjerenja tvrdoće ukazala su na ovisnost tvrdoće o Li/Mg omjeru i dodatku Ti5B1 cjepiva. Posljedično, najveća tvrdoća izmjerena je u uzorcima s Li/Mg = 1,0 i Li/Mg = 0,90 koji sadrže AlTi5B1 cjepivo. Dodatno, povećanje tvrdoće s povećanjem specifičnog presjeka uzorka otkriveno je u svim uzorcima osim uzorka 1 gdje je najniža vrijednost tvrdoće izmjerena u središnjem dijelu uzorka (ø 20,0 mm) što ukazuje na utjecaj veličine i morfologije zrna na tvrdoću. Više vrijednosti mikrotvrdoće izmjerene su u interdendritnom području svih analiziranih uzoraka, čime se ukazuje na povoljan utjecaj intermetalnih faza, prvenstveno Al_8Mg_5 (β) i (Al_8Mg_5 (β) + Al_2LiMg (T)), na tvrdoću uzoraka. Najveće vrijednosti mikrotvrdoće metalne osnove α_{Al} i interdendritnog područja izmjerene su u uzorku s Li/Mg = 1,0 i dodatkom cjepiva. Ako se uzme u obzir povećanje vrijednosti mikrotvrdoće obaju područja, može se zaključiti da je Li/Mg = 1,0 optimalan za presjek ø 30,0 mm, dok je omjer Li/Mg = 0,93 optimalan za presjeke ø 10,0 mm i ø 20,0 mm.

Rezultati mjerenja nanoutiskivanjem ukazali su na veće vrijednosti tvrdoće i modula elastičnosti za toplinski obrađene uzorke. Postizanje viših vrijednosti modula elastičnosti u toplinski obrađenim uzorcima potvrđuje da je to unutarnje svojstvo legure koji se obično pripisuje preraspodjeli elektrona između Al-Li atoma u α_{Al} čvrstoj otopini. Ovi se rezultati razlikuju od rezultata dosadašnjih istraživanja koja pripisuju povećanje modula elastičnosti razvoju intermetalnih faza. Štoviše, smanjenje modula elastičnosti toplinski obrađenog uzorka s povećanjem sadržaja Li iznad 1,93 mas% odstupa od podataka dostupnih u literaturi prema kojima svaki dodani 1,0 % Li povećava modul elastičnosti za 6,0 % za dodatke do 4,2 mas.% Li.

Elektrokemijsko i kemijsko ispitivanje provedeno je na uzorcima legure Al-2,18Mg-1,92Li u lijevanom i toplinski obrađenom stanju kako bi se procijenilo njezino ponašanje u korozivnom okruženju i otpornost na degradaciju. Rezultati elektrokemijskog ispitivanja, uglavnom Tafelove polarizacijske krivulje, pokazali su negativniji korozijski potencijal, veću gustoću struje, anodni nagib, katodni nagib i brzinu korozije za toplinski obrađen uzorak. Dok je u lijevanom uzorku degradacija napredovala otapanjem faza Al_8Mg_5 (β) i Al_2LiMg (T) smještenih u interdendritnom području primarnog α_{Al}, toplinski obrađen uzorak degradirao je

interkristalno i transkristalno. Zaostala AlLi (δ) faza unutar zrna α_{Al} uzrokovala je stvaranje šupljina i raslojavanje površine uzorka. Rezultati ispitivanja kemijske degradacije ukazali su na smanjenje mase uzoraka u lijevanom i toplinski obrađenom stanju. Gubitak mase se povećavao s povećanjem vremena izlaganja, sve do razdoblja od 72 h. Najveća brzina korozije za oba stanja izračunata je za vrijeme izloženosti od 5 h. Smanjenje brzine korozije posljedica je povećanja pH vrijednosti otopine. Rezultati ICP-MS analize otopine nakon izlaganja uzorka ukazuju na odvijanje brzih anodnih i katodnih reakcija koje dovode do razgradnje čvrste otopine α_{Al} otpuštanjem kationa Li^+, Mg^{2+} i Al^{3+}.

U svrhu procjene utjecaja degradacije na mehanička svojstva uzoraka izmjerena je mikrostvrdoća na uzorcima nakon izlaganja. Niže vrijednosti mikrotvrdoće izmjerene su u elektrokemijski ispitanim uzorcima. Vrijednosti mikrotvrdoće uzoraka u lijevanom stanju ostaju nepromijenjene s povećanjem vremena izlaganja. Mikrotvrdoća toplinski obrađenih uzoraka smanjuje se s povećanjem vremena izlaganja kao posljedica otapanja čvrste otopine α_{Al} te gubitak Li^+ i Mg^{2+} kationa.

Zaključak

Ova disertacija imala je za cilj dizajnirati i sintetizirati Al-Mg-Li leguru s poboljšanim mehaničkim svojstvima u lijevanom stanju utvrđivanjem utjecaja kemijskog sastava, termodinamičkih i procesnih parametara na slijed skrućivanja i razvoj mikrostrukture. Primjena različitih tehnika karakterizacije kemijskog sastava, termodinamičkog ponašanja, razvoja mikrostrukture, kao i mehaničkih i korozijskih svojstava omogućila je testiranje i vrednovanje hipoteza postavljenih na početku ovog rada. Potvrđivanje postavljenih hipoteza i bolje razumijevanje slijeda skrućivanja postignuto je korelacijom navedenih parametara.

Ključne riječi:

Aluminij-magnezij-litij legura, kemijski sastav, termodinamički parametri, slijed skrućivanja, intermetalne faze, mehanička svojstva

NOMENCLATURE

Symbol	Unit	Description
$(\alpha_{Al} + \beta_{Si})$	-	two solid phases aluminum (face-centred cubic structure) and silicon (diamond cubic structure) cooperatively forming from the liquid at the eutectic point of 12.2 ± 0.1 at% Si and 577 ± 1°C
(ΔT_C)	K	supercooling due to the interface curvature or Gibbs-Thomson effect
(ΔT_D)	K	supercooling below the eutectic temperature due to the local deviation from the eutectic composition
(ΔT_K)	K	interface attachment kinetic supercooling that is usually neglected when compared to the other contributions
A_{SL}	m	solid/liquid interface area
A_{SL}	m^2	the solid/liquid area
A_{SM}	m^2	the solid/mold area
C^*	mol/m^3	the number of atoms needed to reach the critical size of the clusters
C_0	mol/m^3	atoms per unit volume in liquid phase
C_1	mol/m^3	atoms per unit volume in contact with heterogeneous nucleation sites
C_L	mol	the solute concentration of liquid in equilibrium with solid
C_L'	mol/m^2s^1	concentration gradient at the interface
C_S	mol	the solute concentration of solid in equilibrium with liquid

Symbol	Unit	Description
G_1	J/mol	Gibbs free energy
G_V^L	J/m^3	free energy per unit volume of liquid
G_V^S	J/m^3	free energy per unit volume of solid
L_V	J/m^3	latent heat of fusion per unit volume
L_V	J/m^3	latent heat of fusion per unit volume
L_t	J/mol	latent heat of fusion
N_0	-	density of nucleating sites
N_{het}	1/(m^{3}s)	volume rate of heterogeneous nucleation
N_{hom}	1/(m^{3}s)	volume rate of the homogeneous nucleation
T'	K/m	the temperature gradient (dT/dx) of solid and liquid phase
T_1	K	liquidus temperature for the bulk composition X_0.
T_3	K	Solidus temperature for the bulk composition X_0.
T_∞	K	temperature of the supercooled liquid far from the dendrite
T_L'	K	temperature gradient at the tip of hemispherical cap
T_M	K	melting temperature
T_i	K	interface temperature at tip of hemispherical cap
V^*	m^3	the volume of a critical nucleus (sphere or cap)
V_L	m^3	volume of the remaining liquid
V_S	m^3	the volume of spherical cap
V_s	m^3	volume of the solid sphere

Symbol	Unit	Description
X_0	mol%	initial composition of hypothetical single-phase alloy
X_E	mol%	eutectic composition of hypothetical single-phase alloy
X_L	mol%	mole fractions of solute element in the liquid phase
X_S	mol%	mole fractions of solute element in the solid phase
f_0	atoms/m^3	frequency of homogeneous nucleation
f_1	atoms/m^3	frequency of heterogeneous nucleation
f_s	%	volume fraction of solid
k_1	-	material constant used to calculate angular velocity of continuous growth
k_2	-	material constant used to calculate the velocity disk-shape layer growth
k_3	-	material constant used to calculate angular velocity of dislocation growth
n_1	-	number of atoms
n_{r0}	-	total number of atoms in the system
r^*	m	critical nucleus size necessary for efficient nucleation
r_{max}	m	maximum radius of the spherical particle
ΔG^*_{het}	J/mol^3	energy barrier of the heterogeneous nucleation
ΔG^*_{hom}	J/mol^3	energy barrier of the homogeneous nucleation
ΔG^a	J/mol^3	the activation energy barrier for continuous growth
ΔG_r	J/mol^3	the excess free energy associated with the cluster

Symbol	Unit	Description
ΔH_F	J/(mol·K)	the entropy of fusion (or latent heat of fusion)
ΔT_N	K	Critical undercooling for nucleation
ΔT_c	K	difference between the interface temperature (T_i) and the temperature of the supercooled liquid far from the dendrite (T_∞)
ΔT_r	K	undercooling occurring at the curved interface of the dendrite
γ_{ML}	J/mol^2	the mold/liquid interface energy
γ_{SL}	J/mol^2	solid/liquid interface energy
γ_{SM}	J/mol^2	the solid/mold interface energy
a	-	Jackson's factor
AA	-	Aluminum Association (Washington, DC) provides global standards, industry statistics and expert knowledge to member companies and policy makers nationwide to advance aluminum as the sustainable metal
$Al_3(Li_xZr_{1-x})$	-	the intermetallic compound that forms when β phase absorbs up to 1.3 at% of Li. The similarity in the structure type and lattice parameters, enables heterogeneous nucleation of δ' phase on the $Al_3(LixZr_{1-x})$ and formation of bull's eye structure during aging
APB	-	anti-phase boundary separates two domains of the same ordered phase resulting from symmetry breaking that occurs during ordering process

Symbol	Unit	Description
B_a	mV/dec	anode slope is defined as a drop in the corrosion potential due to the isolation effect of corrosion products on the electrode surface
B_c	mV/dec	cathode slope refers to the drop in the corrosion potential as a consequence of the changes in the electrolyte surrounding the electrode
CALPHAD	-	CALculation of PHAse Diagrams enables calculation of phase diagrams by assessing the thermodynamic parameters of all the phases present in the system
CRSS	-	critical resolved shear stress is the component of shear stress necessary to initiate slip in a grain
DSC	-	differential scanning calorimetry is a thermal analysis technique in which the heat flow into or out of a sample is measured as a function of temperature or time, while the sample is exposed to a controlled temperature program enabling the evaluation of materials properties
E	Pa	Young modulus or the modulus of elasticity quantifies the relationship between tensile stress (force per unit area) and axial strain (proportional deformation) in the linear elastic region of a material.
E_{corr}	mV	corrosion potential is the potential at which the rate of cathodic reactions and the rate of anodic dissolution of the electrode equalizes resulting in the zero current flow in the electrode
EDS	-	energy-dispersive spectroscopy

Symbol	Unit	Description
EXCO	-	test method for exfoliation corrosion susceptibility in 7XXX, 2XXX, and Aluminum-Lithium Alloys
fcc	-	face-centred cubic unit cell structure consists of atoms arranged in a cube where each corner of the cube has a fraction of an atom with six additional full atoms positioned at the centre of each cube face
G	Pa	the shear modulus or the modulus of rigidity is defined as a ratio of shear stress/displacement per unit sample length (shear strain)
GHG	-	in the Earth's atmosphere greenhouse gas consist of water vapor, carbon dioxide, methane, nitrous oxide, and ozone that absorb and emit radiant energy within the thermal infrared range
GP or GPB	-	Guinier - Preston - Bagaryatsky zones are intermetallic compounds serving as the precursors for the Al_2CuMg (S) phase precipitation in Al-Cu-Mg system
I/M	-	ingot metallurgy
i_c	$\mu A/cm^2$	a corrosion current is the current produced in an electrochemical cell while corrosion is occurring
ICP-MS	-	Inductively coupled plasma mass spectrometry
K	W/mK	thermal conductivity
$KAl(SO_4)_2 \cdot 12H_2O$	-	aluminum potassium sulphate dodecahydrate
L	-	the liquid phase
LME	-	liquid metal embrittlement

Symbol	Unit	Description
MASTMAASIS	-	cyclic acidified salt fog test
P/M	-	powder metallurgy
PFZ	-	the precipitation free zones are areas of low precipitation frequency usually formed near the grain boundaries
Q	-	the main thermodynamically stable intermetallic compound in Al-Si-Cu-Mg system with $Al_5Cu_2Mg_8Si_6$ stoichiometry
r	m	radius of the spherical particle
RSP	-	rapid solidification processing
S	-	the intermetallic compound with Al_2CuMg stoichiometry solidifying in Al-Cu-Mg-Si system during peritectic reaction at 497 °C
S'	-	the semi-coherent intermetallic compound with Al_2CuMg stoichiometry and crystal structure identical to equilibrium S phase
$S(\theta)$	-	shape factor
SAD	-	selected area (electron) diffraction
SCC	-	stress corrosion cracking is the fracture induced by the combined influence of tensile stress and a corrosive environment
SEM	-	scanning electron microscope
SF	-	stacking fault are local regions of incorrect stacking of crystal planes associated with the presence of partial dislocations
SSS	-	supersaturated solid solution

Symbol	Unit	Description
STA	-	simple thermal analysis
T	-	the intermetallic compound with Al_6CuMg_4 stoichiometry that solidifies during peritectic reaction at 470 °C temperature
T	-	the intermetallic compound with $Al_2Mg_3Zn_3$ or $(Al_{32}(Mg,Zn)_{49}$ stoichiometry precipitating from the α_{Al} saturated solid solution in Al-Mg-Zn systems containing above 5.49 wt% Mg
T	-	the intermetallic compound with Al_2LiMg stoichiometry solidifying at peritectic temperature of 536 °C and 19.4 at% Li in Al-Li-Mg system
T_1	-	the intermetallic compound with Al_2CuLi stoichiometry that solidifies at the peritectic temperature of 470 °C in Al-Cu-Mg system
T_2	-	the intermetallic compound with Al_6CuLi_3 stoichiometry
TCC	-	Thermo-Calc Calculations
TEM	-	transmission electron microscopy
T_m	K	equilibrium melting temperature
ν	-	Poisson's ratio measures the deformation in the material in a direction perpendicular to the direction of the applied force
ν_{corr}	mm/year	corrosion rate is the speed at which any metal or alloy deteriorate in a specific environment

Symbol	Unit	Description
W	-	the intermetallic compound with $Al_xCu_4Mg_5Si_4$ stoichiometry solidifying at peritectic temperature of 529 °C in Al-Si-Cu-Mg system
$XAl(SO_4)\cdot 12H_2O$	-	*alum* compound where X is a monovalent cation such as potassium (K+) or ammonium (NH4+))
α_{Al}	-	the solid solution of aluminum
α_{Al}'	-	the Zn enriched α_{Al} solid solution in binary Al-Zn solidifying during eutectic reaction at 381 °C
α-Al_8Fe_2Si	-	also denoted as $Al_{12}Fe_3Si_2$, $Al_{7.4}Fe_2Si$, α(AlFeSi) and c(AlFeSi) is the intermetallic compound with hexagonal lattice existing in the homogeneity range between 30.0 % and 33.0 % Fe and 6.0 % to 12.0 % Si in Al-Si-Fe system
β	-	the intermetallic compound with Al_8Mg_5 stoichiometry solidifying in Al-Li-Mg system at 450 °C and 34 at% of Li
β	-	in the Al-Mg system represents the stable eutectic phase with Al_8Mg_5 stoichiometry and maximum composition range between 38.5 at% and 40.3 at% Mg solidifying at 450 °C
β'	-	the intermetallic compound wit Mg_2Si stoichiometry and complex face-centre cubic lattice
β'	-	in Al-Mg system represents metastable phase with Widmannsttäten structure observed after aging at 150 °C
β'	-	the intermetallic compound with Al_3Zr stoichiometry that enables recrystallization control and prevents texture development

Symbol	Unit	Description
β"	-	metastable needle-like phase, also known as GP-II zones, forming through the transformation of spherical GP zones at approximately 180 °C and 260 °C in Al-Mg system
β_0	-	the precursor to the β phase precipitation with the same stoichiometry of Al_3Zr but with $L1_2$ structure
β-Al_5FeSi	-	the intermetallic compound with monolithic lattice existing in the homogeneity range of 25.0 % to 30.0 % Fe and 12.0 % to 15.0 % Si. This compound is also known as $Al_9Fe_2Si_2$, β(AlFeSi), and m(AlFeSi)
β_{Si}	-	the solid solution of silicone
β_{Zn}	-	the solid solution of Zn in binary Al-Zn alloys solidifying during eutectic reaction at 381 °C
γ	-	the intermetallic compound with $Al_{12}Mg_{17}$ stoichiometry and an α_{Mn} type of cubic lattice solidifying at peritectic temperature of 483 °C and 27.7 at% Mg
γ-Al_3FeSi	-	also denoted as γ(AlFeSi) has a monolithic structure with parameters a=1.78 nm, b=1.025 nm, c=0.890 nm, and β= 132 °
δ	-	the intermetallic compound with AlLi stoichiometry and cubic B32 structure solidifying at eutectic temperature of 600 °C and 28.5 at% of Li
δ'	-	the metastable intermetallic compound with Al_3Li stoichiometry and $L1_2$ lattice ordering that nucleates and grows on spherical particles with a small misfit and low interfacial energy with respect to the α_{Al} matrix
ΔG_V	J/m^3	free energy per volume unit

Symbol	Unit	Description
δ-Al_4FeSi_2	-	the intermetallic compound with tetragonal lattice existing in the homogeneity range narrower compared to the α-Al_8Fe_2Si and β-Al_5FeSi
ΔT	K	undercooling below equilibrium melting temperature
θ	-	in Al-Cu system represents the eutectic compound with Al_2Cu stoichiometry and tetragonal lattice structure that solidifies at temperature of 520 °C
θ'	-	the metastable intermetallic compound with Al_2Cu stoichiometry and tetragonally distorted structure that precipitates at the temperatures of ≈ 150 °C
θ''	-	the metastable intermetallic compound with Al_3Cu stoichiometry and face centred tetragonal structure that precipitates from supersaturated solid solution of α_{Al}
λ	-	the intermetallic compound with $Al_5Cu_2Mg_8Si_5$ stoichiometry precipitating homogeneously in the α_{Al} matrix increasing the age hardening capability of Al-Si-Cu alloys
Ω	-	the intermetallic compound with $Al_2(Cu,Ag)(Li,Mg)$ stoichiometry that forms when Ag atoms substituting Cu atomic positions and Mg atoms substituting Li atomic positions in T1 precipitates
ω-Al_7Cu_2Fe	-	intermetallic phase also denoted as β(FeCu) containing 36.2 % Cu and 16.2 % Fe and tetragonal syngony lattice
D	cm^2s^{-1}	diffusivity in the liquid
k	m^2kg/s^2K	Boltzmann's constant

Symbol	Unit	Description
v	°C/s	solid growth rate
ΔT_i	K	the undercooling of the interface below the equilibrium melting temperature T_m
θ	°	wetting angle of the embryo
ξ	-	the orientation factor defined as the ration between the number of nearest neighbours for a growth unit at the solid/liquid interface of the crystal (η) and the coordination number (v),

LIST OF FIGURES

LIST OF TABLES

1. INTRODUCTION

Paulo Coelho, "The Alchemist", 1988

"Lead will play its role until the world has no further need for lead; and then lead will have to turn itself into gold. That's what alchemists do. They show that, when we strive to become better than we are, everything around us becomes better, too."

The metallurgical production is one of the major factors influencing the world's economy development. In addition to its fundamental definition, the modern metallurgy comprehends far broader range of phenomenon, processes and experiences enabling research and development of innovative alloys with improved properties, products for special applications, technological development as well as quality and efficiency increase. To the present moment, metallurgy as a specific field of technical sciences is burdened with design, development, and characterization of everyday materials with mundane applications as well as alloys with high safety-critical requirements for specific utilization in transportation industry, particularly automotive, aviation and aerospace.

Since its emergence in the mid-20th century, the modern transportation industry has a key role in the globalization process connecting people, business, goods, and markets. This high mobility represents a growing demand for more secure, fast, efficient, cost-effective and environment friendly vehicles. In order to fulfil the required performance demands, the development of innovative alloys with improved properties is needed [1]. As an innovative material, aluminium (Al) and its alloys have been slowly introduced to the automotive industry for over two hundred years increasing the vehicles performances and enabling improvements in fuel economy and gas emissions through the weight reduction [2]. The Al alloys have played an essential role in aviation industry since the first flight in 1903 when the Al alloy containing 8.0 wt% copper (Cu) was used to produce engine crankcase of the Wright Flyer [3]. Later, in 1969 the essentially same Al alloy containing 6.3 wt% Cu was utilized in the production of shuttle boosters facilitating man's first walk on the Moon. Today both, aviation and aerospace industry gravitate towards the production of lightweight components with increased strength, improved elevated temperature sensitivity and corrosion resistance. This improvement in material properties will reduce the number of components and lower the vehicles manufacturing cost [4].

The vehicle production in transportation industry comprehends the use of both cast and wrought Al alloys. The cast Al alloys containing silicone (Si) as a principal alloying element are most frequently used in the automotive industry. The 3xx.x series of Al alloy are characterized by excellent castability, crack resistance and good technological properties enabling its utilization in the production of high-performance engine parts, transmissions, suspension parts and wheels [5]. Copper and magnesium (Mg) represent two important alloying elements that have been added to Al-Si alloys in order to improve corrosion resistance and obtain higher strength to density ratio [6]. High strength and good tensile properties are the result of microstructure development involving solidification and precipitation of complex intermetallic phases such as Mg_2Si (β'), Al_8Mg_5 (β), Al_2Cu (θ), Al_3Cu (θ''), Al_2CuMg (S), $Al_xCu_4Mg_5Si_4$ (W), $Al_5Cu_2Mg_8Si_5$ (λ) and $Al_5Cu_2Mg_8Si_6$ (Q) [7]. Although, subsequent solution hardening and artificial aging influence microstructure development and improve mechanical properties, the Al-Si-Cu, Al-Si-Mg and Al-Si-Cu-Mg alloys remain sensitive to elevated temperatures due to the phase dissolution or coarsening [8]. The wrought Al alloys of 2xxx and 7xxx series are used in the aviation and aerospace industry to produce fuselage, stringers, bulkheads, skin, rivets, and extruded sections. In 2xxx series of Al alloys Cu is principal alloying element often combined with Mg to improv toughness and damage tolerance. However, the complex microstructure development involving competitive solidification of stable Al_2Cu (θ), Mg_2Si (β'), Al_2CuMg (S), Al_6CuMg_4 (T) and metastable Guinier - Preston - Bagaryatsky (GPB) zones, θ'', semi-coherent Al_2CuMg (S') phases [9] can negatively affect yield strength, fracture toughness, weldability, elevated temperature sensitivity and corrosion resistance [10]. In 7xxx series of Al alloys the highest strength and specific strength are a consequence of combined addition of zinc (Zn), Cu and Mg enabling precipitation of Al_2CuMg (S) and $Al_2Mg_3Zn_3$ or $Al_{32}(Mg,Zn)_{49}$ (T) [11] phase during heat treatment [12]. The quench sensitivity introduces high residual stress, limits the effect of solution hardening, and enables coarsening of the intermetallic phases. The coarse Al_2CuMg (S) and $Al_{32}(Mg,Zn)_{49}$ (T) phase have negative impact on toughness, cross-section strength and stress corrosion cracking (SCC) [13].

The sensitivity to elevated temperatures, low stiffness, and modulus of elasticity as well as additional weight savings indicate the need for chemical composition redesign. Further weight savings, improved modulus of elasticity, stiffness, fracture toughness as well as fatigue crack growth resistance are facilitated through Li additions. Each 1.0 wt% of Li added decreases the density of an alloy by 3.0 %, increase modulus of elasticity by 6.0 % and stiffness by 5.0 % for the additions up to 4.2 wt% Li. However, increasing the Li content above 1.3 wt% will result in yield and tensile strength decrease, respectively [14]. The increase in Al-Li alloy's modulus

of elasticity is an exception to the general rule of alloying [15]. Usually, in Al alloys this is accomplished by the addition of elements with modulus of elasticity greater than Al matrix (α_{Al}). Since Li is alkaline metal with low melting point of 165.85 °C and maximum modulus of elasticity of 5.2 GPa [16], this atypical behaviour is attributed to electron redistribution between the Al-Li bounds in the α_{Al} solid solution and to the elastic modulus of intermetallic precipitates [17].

The mechanical property improvement is a result of microstructure development during solidification and processing. Chemical composition, thermodynamic parameters and processing parameters directly influence on solidification sequence and determine type, size, volume fraction and distribution of the precipitates.

The solid solubility of Li in α_{Al} solid solution reaches up to 4.0 wt% at the eutectic temperature of 603.0 °C and decreases to < 1.0 wt% at 100.0 °C enabling solidification of strengthening precipitates. The primary strengthening precipitate in Al-Li alloys is the metastable Al_3Li (δ') phase. With maximum solvus temperature between 300.0 °C and 350.0 °C at 4.0 wt% Li, the Al_3Li (δ') phase precipitates coherent to the α_{Al} matrix causing the order hardening. When compared to the intermetallic precipitates in 2xxx and 7xxx series of Al alloys, the Al_3Li (δ') phase stays spherical and coherent with α_{Al} matrix at significantly high temperatures and long exposure time enabling residual stress removal and increase in stiffness and strength [18]. The preferred precipitation of the metastable (Al_3Li) δ' phase in Al-Li alloys can be achieved with Mg additions. By reducing the solid solubility of Li in α_{Al} solid solution and partially substituting Li in the Al_3Li (δ') phase lattice, Mg additions increase the volume fraction of Al_3Li (δ') phase. The microstructure development in Al-Li-Mg alloys involves solidification of metastable Al_3Li (δ'), stable AlLi (δ), Al_2LiMg (T), $Al_{12}Mg_{17}$ (γ) and β phases depending on Li/Mg ratio. In the alloys containing high Li/Mg ratio solidification sequence begins with the eutectic reaction involving solidification of α_{Al} matrix and Al_3Li (δ') phase, followed by solidification of stable AlLi (δ) phase. During peritectic reaction between metastable Al_3Li (δ') phase and bulked liquid, stable AlLi (δ) phase solidifies at the α_{Al} grain boundaries. On the other hand, in the alloys containing low Li/Mg ratio, the peritectic reaction leads to the solidification of ternary Al_2LiMg (T) phase at the high angle grain boundaries. Consequently, dissolution of Al_3Li (δ') phase leads to the precipitation free zone (PFZ) formation near the α_{Al} grain boundaries. Solidification of the AlLi (δ) and Al_2LiMg (T) phase increase the volume fraction of the grain boundary precipitates. By increasing the plasticity and stress around the grain boundaries, both PFZ and high-volume fraction of grain boundary precipitates contribute to the formation of cracks at the grain boundaries [19]. The volume

fraction of the grain boundary precipitates is further incised by the solidification of $Al_{12}Mg_{17}$ (γ) and Al_8Mg_5 (β) phase. The $Al_{12}Mg_{17}$ (γ) phase solidifies at the α_{Al} grain boundaries during peritectic reaction between Al_2LiMg (T) phase and Mg bulked liquid restricting the grain boundary movement and preventing excessive grain growth [20]. At the end of solidification sequence, bulking of the liquid with Mg culminates in the solidification of Al_8Mg_5 (β) phase. Since it is a brittle particle with irregular morphology, it has no beneficial influence on the mechanical properties of an alloy [21]. Due to the high solid solubility of Mg (17.3 wt% Mg), the α_{Al} solid solution stays enriched in Mg causing the solid solution strengthening [19].

At the liquidus temperature, solidification sequence initiates as a change in the Gibbs free energy that is proportional to the undercooling and heat of fusion. For the given chemical composition, the undercooling necessary for the suppression of the heterogeneous nucleation can be influenced by cooling rate. Increase in the cooling rate results in higher degree of undercooling leading to the microstructure refinement and improvement in material properties [22]. In the Al-Li-Mg alloys cooling rates higher than 2.0 °C/s result in the solidification of bulked α_{Al} solid solution and low frequency of precipitates. Between cooling rates of 2.0 °C/s and 12.0 °C/s solidification sequence comprehends solidification of α_{Al} solid solution and Al_3Li (δ'), AlLi (δ), Al_2LiMg (T), $Al_{12}Mg_{17}$ (γ) and Al_8Mg_5 (β) phases. The cooling rate above 12.0 °C/s supress the solidification of Al_2LiMg (T) phase [23].

Due to the high reactivity of molten Li with atmosphere and refractory materials, the processing parameters during Al-Li-Mg alloy's production and casting need to be carefully considered. Lithium most commonly reacts with atmospheric gasses such as oxygen (O_2), nitrogen (N_2) and hydrogen (H_2) to form lithium oxide (Li_2O), lithium nitride (Li_3N) and lithium hydride (LiH). The high mobility and small atomic fraction of Li atoms will result in the early formation of Li-based compounds despite higher thermodynamic stability of magnesium oxide (MgO) [24]. Since there is no crucible material compatible with both Al and Li, it is necessary to adopt processing parameters to avoid long holding times after alloying in order to reduce the crucible attacks and melt contamination [25]. During casting, the Al-Li-Mg alloys exhibit high volume shrinkage, high susceptibility to gasses, shrinkage porosities, hot tearing and hot cracking [26]. In turn, these casting defects, formed as a result of poorly selected processing parameters, have a negative impact on the microstructure development and mechanical properties of the produced alloy [27].

As indicated, the redesign the Al alloy's chemical composition with the combined additions of Mg and Li represents an opportunity to improve mechanical properties while reducing the density of an alloy. By establishing the influence of chemical composition,

thermodynamic and processing parameters on microstructure development, the solidification sequence and its influence on mechanical properties will be understood.

1.1. Research aims and motivation

Since the global market for transportation industry continuously sets requirements for more secure, fast, efficient, cost-effective and environment friendly vehicles, the innovative materials with improved properties are needed. Since the recent investigations did not cover Al alloy with combined Mg and Li additions, a contemporary approach in design and production of light-weight Al-Mg-Li alloy with improved properties is expected. The improved properties in as-cast condition will result from the correlation between chemical composition, thermodynamic parameters, processing parameters and microstructure development during solidification.

1.2. Hypotheses

To fulfil the research aims the following hypotheses were formulated:

- *The addition of Mg and Li will contribute to the density reduction of the alloy.*
- *The addition of Mg and Li will affect the development of strengthening intermetallic phase and improve mechanical properties of the Al-Mg-Li alloy.*
- *Correlation of chemical composition, thermodynamic and processing parameters will enable determination of Al-Mg-Li alloy solidification sequence.*

The formulated hypotheses assume that the improvements in the Al-Mg-Li alloy properties will result from the microstructure development during solidification and processing. The chemical composition, thermodynamic parameters and processing parameters will directly influence solidification sequence and determine type, size, volume fraction and distribution of the precipitates.

The modification of chemical composition through the additions of low-density Mg (1.738 g/cm^3) and Li (0.534 g/cm^3) will enable density reduction of the alloy. For each wt% of Li added, the density decrease of 3.0 % will be expected. In addition to the density reduction, Li will enable order hardening through the metastable Al_3Li (δ') phase solidification. Besides solid solution strengthening, the Mg will have less direct influence on the mechanical properties improvement by reducing the solid solubility of Li in α_{Al} solid solution and replacing Li in the

Al_3Li (δ') phase lattice. The cooling rate, as the most important thermodynamic parameter will affect the microstructure refinement and solidification of phases. It is necessary to choose an appropriately high cooling rate to ensure sufficient undercooling to suppress the heterogeneous nucleation and Mg solid solution strengthening, but not high enough to prevent solidification of strengthening precipitates. Properly selected processing parameters will enable maximum absorption of alloying elements in the melt and prevent the casting defect.

Thus, correlation of chemical composition, thermodynamic and processing parameters will enable determination of Al-Mg-Li alloy microstructure development during solidification.

1.3. Research structure

To prove formulated hypotheses, the research study is conducted. For better traceability, the research is divided into several phases:

1. The design and modification of chemical composition will be based on the literature review and the calculation of equilibrium and non-equilibrium phase diagrams (CALPHAD) using Thermo-Calc software support (TCC). Since Li and Mg are reactive elements, the motivation for choosing the chemical composition will be based on the mechanical properties' improvement with the minimum alloying additions placing the targeted chemical composition in the Al-rich corner of the Al-Mg-Li ternary diagram.
2. The synthesis of the Al-Mg-Li alloy will be carried out in a laboratory induction melting furnace. To minimize the loss of Li and Mg, the processing parameters, such as furnace atmosphere, refractory materials, mould materials, alloying and casting temperature will be considered carefully.
3. During casting the simple thermal analysis will be used to estimate the solidification rate and changes in the material's temperature with respect to the cooling time.
4. The chemical composition will be analysed after synthesis. The loss of Li and Mg will be estimated by comparing the results of chemical analysis with the alloying additions.
5. To estimate the influence of heating and cooling rates on the solidification sequence and phase transformation a simultaneous thermal analysis (STA) will be performed. The melting temperature, latent melting heat, phase transformation temperature, and precipitation energy will be determined using differential scanning calorimetry (DSC) at heating and cooling rates of 2.0, 10.0, 20.0, 30.0, 40.0, 50.0 Ks^{-1}.

6. To determine the mechanical properties of the samples, compression testing and hardness measurements at macro-, micro-, and nano- scale will be used.
7. After standard metallographic preparation, the macrostructure and microstructure of the synthesized alloys will be identified using metallographic analysis. The identification of different microstructural constituents will comprehend the use of light and electron microscopy as well as X-ray diffraction.
8. Assessment of the microstructure stability in corrosive environment will comprehend the application of chemical and electrochemical corrosion testing methods. The solution of sodium chloride (NaCl), potassium nitrate (KNO_3), concentrated nitric acid (HNO_3) and distilled water with apparent pH value of 0.4 will be used in both methods. The sensitivity of microstructure to exfoliation corrosion will be assessed by exposing the samples to corrosive solution for 5, 24, 48, and 72 h. The electrochemical methods will be used to determine the corrosion potential (E_{corr}), corrosion current density (i_c), anode slope (B_a), cathode slope (B_c), and corrosion rate (v_{corr}).

Summarizing the results of individual research phases will enable design, synthesis and characterization of the microstructure and mechanical properties of the innovative Al-Mg-Li alloy.

1.4. Expected scientific contribution

The expected scientific contribution is to design and synthesise light-weight Al-Mg-Li alloy with improved mechanical properties in as-cast condition by establishing the influence of chemical composition, thermodynamic and processing parameters on the solidification sequence and microstructure development.

2. LITERATURE REVIEW

Considering that Al rarely occurs in nature in its native form (Al°), it is one of the newest metals to be discovered and utilized by mankind. Because of its chemical reactivity, Al° can only be found and preserved as a minor component in strongly reductive atmospheres, such as low oxygen cores of volcanoes and in ocean sediments. However, Al compounds constitute more than 270 different minerals [28], some of which have been used by the early human civilizations. The Roman scientist Pliny the Elder in his work the Natural History (lat. *Naturalis Historia*) tells the story of 1st century craftsman presenting a diner plate made of an unknown metal to the Roman Emperor Tiberius. The goldsmith boasted that only he and the gods knew how to obtain this metal from the common clay. Besides being one of the Rome's greatest generals, Tiberius was also a financial expert who knew the potential danger this new metal posed to his amassed fortune. So, instead of giving the goldsmith expected regard, Tiberius ordered his beheading [29]. Although this story is most likely a legend, it implies the possibility that other metals besides Cu, Pb, Sn and Hg may have been reduce in ancient times. Furthermore, Pliny the Elder in the book 35 *An account of paintings and colours*, chapter 52 *Alumen and the several varieties of it, thirty-eight remedies* mentions the military application of Al containing compounds. The Greek nobleman Archelaus was the grates general that served under the king Mithridates VI of Pontus in northern Anatolia. Archelaus used the Al based chemical compound *alum* ($X\mathrm{Al(SO_4)\cdot 12H_2O}$, where X is a monovalent cation such as potassium (K^+) or ammonium (NH_4^+)) during the First Mithridatic War against the Roman general Lucius Cornelius Sulla Felix [30]. The Archelaus realised that *alum* based solution can be used to treat wood in order to make it partially flame resistant [31]. While Archelaus used it to protect his wooden towers, the Roman general Sulla used the same solution to protect the fleet from Archelaus attempts to set it on fire using metallic mirrors [32]. The First Mithridatic War ended in Orchomenus where Sulla, using the terrains natural defences defeated Archelaus's more superior army [33]. The metallurgical application of alum is described in book 33 *On the natural history of metals*, chapter 20 *The methods of gilding*, where its use in Cu gilding is mentioned. According to the recipe, Cu is firstly well hammered, subjected to fire, and then cooled with a mixture of salt, vinegar, and *alum*. After it is cleansed of all extraneous substances using heat, Cu is prepared to receive the gold leaf using amalgam of pumice, *alum*, and quicksilver. Moreover, Pliny the Elder states that *alum* is as effective in purifying Cu as led (Pb) is in purifying Ag [34]. In addition to its technical application, *alum* was also used by tanners (lat. *alutarii*) to produce a special type of soft white leather (lat. *aluta*) [35]. In his

pharmacopeia entitled On medical material (lat. *De materia medica*), the Roman surgeon Dioscorides mentioned the use of aluminum potassium sulphate dodecahydrate ($KAl(SO_4)_2 \cdot 12H_2O$) as a haemostatic, in offensive odours prevention and in reduction of swelling [36]. The $KAl(SO_4)_2 \cdot 12H_2O$ of pharmaceutical quality was produced from aluminate ($KAl_3(SO_4)_2(OH)_6$) using extractive metallurgy. The roasting of the aluminate in a kiln was followed by lixiviation during which the roasted mass was sprinkled or immersed in water allowing for $KAl(SO_4)_2$ to be dissolved. The crystallization of $KAl(SO_4)_2 \cdot 12H_2O$ was achieved through the evaporation of saturated aqueous solution [37].

The detailed description of *alum* containing raw material mining and extractive metallurgy was described by Georgius Agricola in his catalogue entitled On the Nature of Metals (*lat. De re metallica*). In this catalogue, giving the state of the art of mining, refining, and smelting, the *alum* production is described in 12th book along with the salt, soda, vitriol, sulfur, bitumen, and glass. The *alum*, referred to as an astringent and sharp solidified juice (lat. *succi contracti*), was acquired from aluminous water, or a solution containing "*kind of earth*", rocks, pyrites and other minerals using hydrometallurgy (Figure 2.1 a) or pyrometallurgy (Figure 2.1 b). At the beginning of hydrometallurgical process, the raw material is placed into the wooden tanks (Figure 2.1 a, A) and mixed with water and urine. After the solution is mixed and stirred for several days (Figure 2.1 a, B), the plugs (Figure 2.1 a, C) are taken out and the solution is drawn into a wooden trough (Figure 2.1 a, D). This *alum*-rich solution is transported into a reservoir (Figure 2.1 a, E) and diluted with water and urine. After soaking the reservoirs are emptied through a launder (Figure 2.1 a, F) into a small led cauldron (Figure 2.1 a, G). The solution is boiled until a grate water portion evaporates. The obtained solution is full of meal consisting of fatty and aluminous matter as well as asbestos and gypsum impurities. Afterwards, the obtained solution can be cooled in a wooden tub (Figure 2.1 a, H) or purified by running through the vats. The purification of the cooled solution containing alum is performed by running the solution through the vats containing twigs that enable crystallization of *alum* (Figure 2.1 a, I). At the end of the hydrometallurgical process, the small transparent white cubes of *alum* are placed in the hot rooms to dry. The pyrometallurgical process comprehends the roasting of aluminous rocks in the furnace (Figure 2.1 b, A) until they become red in colour and desulfurize. After roasting and cooling, the desulfurized rocks are conveyed into an open space (Figure 2.1 b, B) to be sprinkled with water for four days. After moisturising for a given time, the *alum*-containing rocks begun to crumble (Figure 2.1 b, C). The obtained material is transported using deep ladles (Figure 2.1 b, D) into a copper cauldron (Figure 2.1 b, E) containing boiling water. After the solution is sufficiently purified and ready to congeal, it is ladled trough the launders

(Figure 2.1 b, F) into the trough (Figure 2.1 b, G). In wooden trough the solution congeals and condenses into the *alum* [38]. The obtained *alum* was extensively used for leather tawing and in colouring [39].

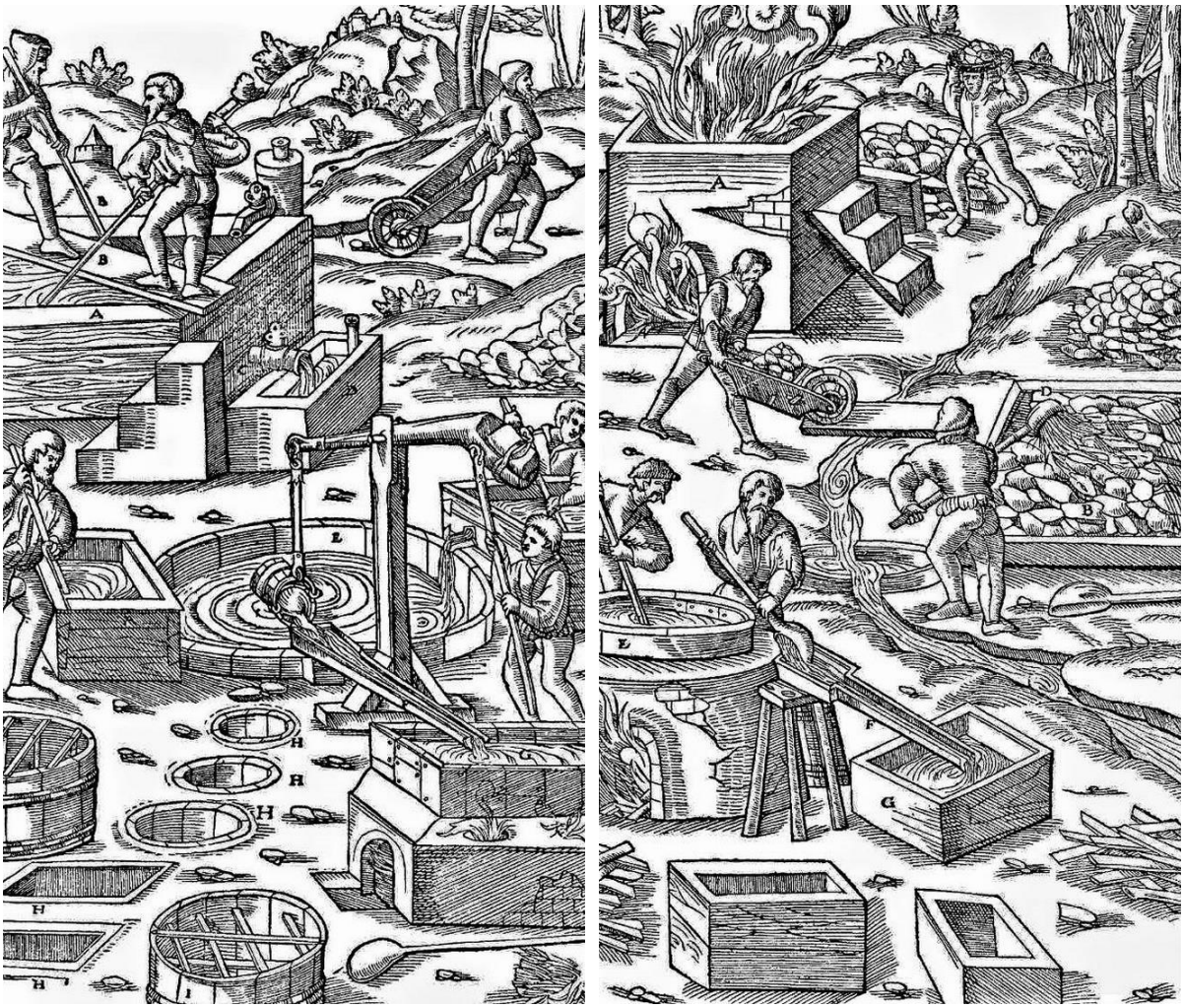

A – tanks, B – stirring poles, C – plug, D – trough, E – reservoir, F – launder, G – lead cauldron, H – wooden tubs sunk into the earth, I – vats in which twigs are fixed

a)

A – furnace, B – enclosed space, C – aluminous rock, D – deep ladle, E – caldron, F – launder, G - troughs

b)

Figure 2.1. The *alum* extraction process by a) hydrometallurgy, b) pyrometallurgy [38]

The search for metallic Al initiated with the Lavoisier's assumption that alumina (Al_2O_3) is a compound of metal with a strong affinity for oxygen and Volta's invention of battery. The first attempt to synthesize pure Al were made in 1807 by Berzelius and Humphry Davy. Berzelius attempted to extract Al, boron (B) and Si from aluminum fluoride (AlF_3) using potassium amalgam (KHg_2). Unfortunately, his attempt was not successfully due to the hight solubility of Al in caustic potassium produced during electrolysis [40]. Even though Al was first synthesized from alumina Humphry Davy named it after *alum*, this "*precious*" and "*bitter*"

white mineral. By introducing the molten compounds to an electric arch, Davy successfully produced pure K, sodium (Na), calcium (Ca), strontium (Sr), barium (Ba) and Mg. However, Davy was not able to synthesize pure Al. Instead, he synthesized Al-Fe alloy through electrochemical reactions in fluid alumina followed by carbon based reduction [41].

The Al was first synthesized by Hans Christian Ørsted during the reaction involving potassium amalgam (KHg_2) containing 1.5 % K and anhydrous aluminum chloride ($AlCl_3$). Firstly, Ørsted prepared $AlCl_3$ by passing a flow of chlorine (Cl) over a mixture of charcoal and alumina preheated to redness. The obtained $AlCl_3$ was mixed and heated with KHg_2 producing potassium chloride (KCl) and aluminum amalgam (Al(Hg)). Distillation of Al(Hg) in inert atmosphere produced "*a lump of metal which in colour and lustre somewhat resembles tin*". However, the synthesized "*gray mass*" contained impurities of materials used in its production [42]. At the end of his experiment, Ørsted reported:

"*Moreover the author has found, both in the amalgam and the aluminum, remarkable properties which do not permit him to regard the experiment as complete, but show promising prospects of important results*" [43].

By repeating the Ørsted's experiment and reheating the synthesized mass, Fridrich Wöehler was able to identify the present impurities as mostly K-based [44]. Since he was not able to produce pure Al by relaying on the previous methods, Wöehler was forced to find a new approach to Al synthesis. This new plan was based on decomposition of $AlCl_3$ using K and stability of Al in water. After adding the excess amount of hot potassium carbonate (K_2CO_3) to a boiling hot solution of *alumina*, Wöehler was able to precipitate aluminum hydroxide ($Al(OH)_3$). The $Al(OH)_3$ precipitates were rinsed in water, dried and mixed with powder charcoal, sugar and oil into a thick paste. Upon heating this paste in the closed crucible and introducing dry Cl gas, Wöehler produced $AlCl_3$. Since the $AlCl_3$ decomposition is too volatile for glass crucible, Wöehler used platinum (Pt) crucible and crucible cover. Although only gentle heat was applied to start the process, the exothermic reaction caused significant heat release and enabled crucible attacks. After cooling, the crucible was plunged into water allowing for the metallic Al to be separated as a gray powder. The obtained Al powder contained K, Pt and $AlCl_3$ impurities. Wöehler was able to first characterize the powder's properties and successfully melt it to a coherent metallic mass no larger than a pinhead. Since his process was not suitable for large scale production, Al remained more expensive then gold [42].

The large amount of pure Al was first produced when Henri-Etienne Sainte-Claire Deville became interested in the possibility of obtaining a lower aluminum oxide by reducing $AlCl_3$ with metallic K. He was not able to obtain the aluminum oxide but did produce a blend of $AlCl_3 \cdot KCl$ with voluminous globules of a "*brilliant white metal*". The metal was "*inalterable*" by air, resistant to potassium nitrate (KNO_3), S, nitric acid (HNO_3) and hydrogen sulphide (H_2S) [45]. After the initial success in Al synthesis, Sainte-Claire Deville set a goal to develop an industrial process for Al reduction. He was able to replace K with less expensive Na and develop a process to reduce Al from less volatile solution of aluminum chloride and sodium chloride ($AlCl_3 \cdot NaCl$) salts. Later, Sainte-Claire Deville used the same $AlCl_3 \cdot NaCl$ salt to obtain the metallic Al by electrolysis. Although Deville's method enabled reduction of 200 metric tons of Al [46], synthesized metal was primarily used for jewellery and in ornamental purposes. Disillusioned by its luxurious application, Sainte-Claire Deville stated:

"*There is nothing harder than to make people use a new metal. Luxury items and ornaments cannot be the only sphere of its application. I hope the time will come when aluminium will serve to satisfy the daily needs*" [47].

Further doubts about the Al applicability arouse in 1884 when it was chosen to complete the Washington monument. Although the largest Al billet with hight of 20.34 cm and weight of 2.83 kg was successfully cast for this purpose, the clients led by Thomas Lincoln Casey concluded that Al was not a practical metal for widespread use just yet, pointing out the difficulty in getting even 100-ounc sample (2.83 kg). Casey finished his report with words:

"*would seem to imply that Aluminium cannot yet be manufactured at such rates as to make it a commercial success*" [48].

It is important to emphasize that the source of Casey's frustration was not Al nor its use in the production of monument's cap, but its manufacturer William Frishmuth. Although Frishmuth was hired because of his previous work on Al purification using Na vapours, his business conduct proved to be highly questionable. After he was able to cast the billet (Figure 2.2. a), he displayed it in the Tiffany's jewellery store in New York City without permission. During its display, the cap was analysed by the professor F. I. Ricardo Seaven, who determined that it was not made from pure Al but from Al alloy containing 1.70 wt% Fe and 0.55 wt% Si. Unswayed by the purity of his creation, Frishmuth increased price from initial $100 to $225 and found a new purpose for the Al leftover from casting. By placing the advertisement in the

journal Scientific American, he offered watch charms from pure Al for 75 cents, Al alloy charms for 20 cents or gilded Al alloy charms for 20 cents. Even after the top of the Monument was tipped (Figure 2.2 b), Frishmuth was not prepared to part from his work but offered to provide lightning-rod. Frustrated by his previous behaviour, Casey rejected his proposal hiring Joseph Neumann. Unfortunately, Frishmuth's involvement did not stop there. In an attempt to reveal his secrets, two of Frishmuths assistants were apprehended, one of whom was convicted for stealing chemicals worth $2.50 [48].

a) **b)** **c)**

Figure 2.2. The first Al castings: a) The Washington Monument cap with lightning-rode, b) The toping of the Monument's tip [48]**, c) The crown jewels of Aluminum Company of America** [49]

Ironically, less than two years after the Washington Monument was topped, the process for making Al cheap and commercially available was discovered.

The time of Al widespread application came with the discovery of more cost-effective electrolytic method. The electrolytic reduction of Al was discovered by Charles Hall and Paul Héroult, independently and simultaneously. Charles Martin Hall found that melting temperature of alumina (2050.0 °C) could be lowered by adding cryolite (Na_3AlF_6). He assumed that passing electric current through the mixture of alumina and cryolite could lead to metallic Al reduction. His assumption was confirmed on 23rd of February 1886 when Al was first electrolysed. His first Al in form of the buttons was electrolyzed in the woodshed using home-made battery. The Al buttons are still treasured by the Aluminium Company of America and referred to as crown jewels (Figure 2.2 c). Paul Louis Toussaint Héroult was second to electrolyse Al from the same electrolyte mixture on April 23rd 1886 [50]. Apart from the differences in the electrode number and Al electrolysis cells design (Figure 2.2), the main difference is that Héroult preferred aluminum bronze over pure Al. Since his first experiments resulted in Al absorption on Cu cathode surface and increase in metal coalescence, Héroult became aware that it was easier to

produce aluminum bronze. However, to remain competitive to Hall, Héroult had to introduce changes in the pot lining and electrode pitch decreasing the current efficiency [51].

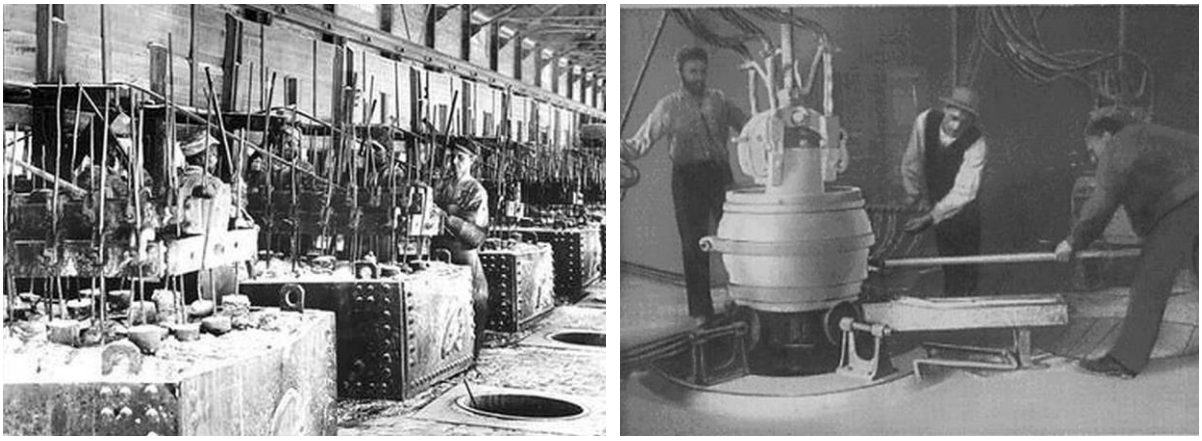

a) **b)**

Figure 2.3. The industrial application of: a) Hall cell containing 64 electrodes installed in 1901, b) Héroult's cell installed in 1889 [52]

Even though Hall and Héroult met only once in 1911 [52], the process for electrolytical production of primary Al bears both their names. The industrial scale application of Hall-Héroult process was enabled by the developments in electrical current supply and alumina production. The Bayer process boosted yield and practicality of Hall-Héroult method by producing alumina from bauxite ($Al_2O_3 \cdot Fe_2O_3 \cdot SiO_2 \cdot TiO_2$) more efficiently [46]. Since 1919 the increase in pot productivity, reduction of specific energy consumption, reduction in environmental impact as well as decrease in investment and productivity cost were achieved through:

- Invention of Søderberg anode,
- Introduction of pot computer control,
- Pot feeding of alumina,
- Polyvalent pot tending machines,
- Pot hooding and gas dry scrubbing [53],
- Mathematical modelling of pot thermo-electrical fields and magnetohydrodynamics [54].

Despite technological and process improvements the industrial production of primary Al still requires 14.21 MWh/tonne energy intensity and accounts for approximately 3.5 % of direct global greenhouse gas emissions (GHG) in the industrial sector [55]. The environment impact of primary Al production originates from electricity use, anode consumption and anode

effect. Electrolytic reduction is facilitated using fossil coal in the form of carbon anodes which are consumed during process resulting in carbon dioxide CO_2 and carbon monoxide (CO) emissions [56]. If the amount of Al_2O_3 in electrolyte is insufficient, the anode effect leads to the emissions of tetrafluoromethane (CF_4) and hexafluoroethane (C_2F_6) [57]. To minimize the anode/electrolyte interaction and reduce the impact of primary Al production on the environment, attempts were made to develop alternatives to primary Al production, such as:

- Inert anodes,
- Wettable cathodes,
- Carbothermic reduction of alumina,
- Aluminum chloride process [50].

Today, only the inert anode research is still active, and it is based on finding a suitable anode material with sufficient chemical and electrochemical stability in the electrolyte. The concept of dimensionally stable anodes was first suggested by Hall in his patent:

"*When formed of carbon, the electrode C is gradually consumed, and must therefore be renewed from time to time but when formed of copper an oxide coating is formed over the surface of the electrode from further destruction by the action of the oxygen but does not interfere materially with the conducting qualities of the electrode*" [50].

The potential anode material must have low solubility and reactivity in the electrolyte and show good chemical resistance to anodically produced hot oxygen gas. Additionally, it should be physically stable at the working temperatures, mechanically robust and resistant to thermal shocks. The development of inert anodes is associated with cost reduction, environmental friendliness and improved occupational health issues [58]. For now, only two types of materials with acceptable functional properties were developed:

- The *cermet* conducting electrodes containing nickel nanoferrites ($NiFe_2O_4$), nickel (II) oxide (NiO), Cu and silver (Ag),
- The metal anodes containing Ni, Fe and Cu [59].

Both types of anodes were subjected to the large-scale trials by retrofitting the conventional cell design, and have reported problems with anode wear, anode purity and oxidation at anode/electrolyte interface [60]. The commercial aspects of inert anodes have not yet been

proven and number of engineering problems remain to be solved, including the necessity for new cell design [61].

Despite high energy consumption and GHG emissions, more Al is produced today than all other nonferrous metals combined. The total annual world production of primary Al in 2019 was 63 657 · 10^3 t, while 1 327 351 · 10^3 t of primary Al was produced from 1973 till today [62]. In addition to the primary Al production, 32 877 · 10^3 t of secondary Al was recycled in 2019 [63]. In comparison to the other high-volume production metals, such as Cu, Zn, and Mg, Al has the largest energy difference between the primary and secondary production. Production of secondary Al through recycling allows for 95.0 % energy reduction and emits only 5.0 % of the GHG compared to primary Al reduction [64]. By producing 1 t of secondary Al, the 8.0 t of bauxite, 14 000 kWh of energy, 6300 l of oil and 7.6 m^3 of landfill are saved. The chemical composition is the main challenge in production of secondary Al. Since Al scrap consists of different types of Al alloys, it is difficult to obtain targeted chemical composition and control the impurity content. The Al alloys with high content of alloying elements are produced by downgrading the low-alloyed Al scrap. The downgrading is most frequently applied in the production of secondary cast Al alloys containing up to 20.0 wt% of alloying elements. To reduce the content of alloying elements below 10.0 wt% and produce secondary wrought Al alloys, the molten scrap is diluted by adding primary Al [65]. Although, downgrading and diluting enable control of chemical composition and reduce the impurity content, they also decrease recycling potential of Al scrap [66]. Nevertheless, secondary Al production continuously increases due to its economic and environmental advantages. The innovations in recycling process are focused on increasing the recycling potential of Al scrap and extending the melting capacity to span different types of scrap quality [67].

Although Al is a light metal, it is heavily demanded for both commercial and industrial use. The utilization of Al and its alloys originates from excellent physical, mechanical and tribological properties enabling its use for electrical, construction, automotive, marine, railway, aircraft, and aerospace applications. Due to its good electrical conductivity, Al is used in electrical industry as a cost-effective replacement for Cu in products such as electric cables and bus conductors [68]. The first significant application of Al alloys in civil engineering emerged in the first half of 20th century when they were used in reconstruction of railway bridge in Pittsburgh and New York City (Figure 2.4 a). Despite good combination of relatively high strength to weight ratio, increased durability and good formability, application of Al alloys in civil engineering and construction began late. The reasons for such a late development of Al as a construction material were ignorance of its properties, relatively complex design procedure,

and inability to apply pre-existing design methods and norms. Today, most impactful economic benefits of Al use are attained through construction of large span roof systems, structures located in inaccessible places, special structures difficult to maintain, structures exposed to aggressive environments, structures with movable parts and in refurbishment of historic buildings [69].

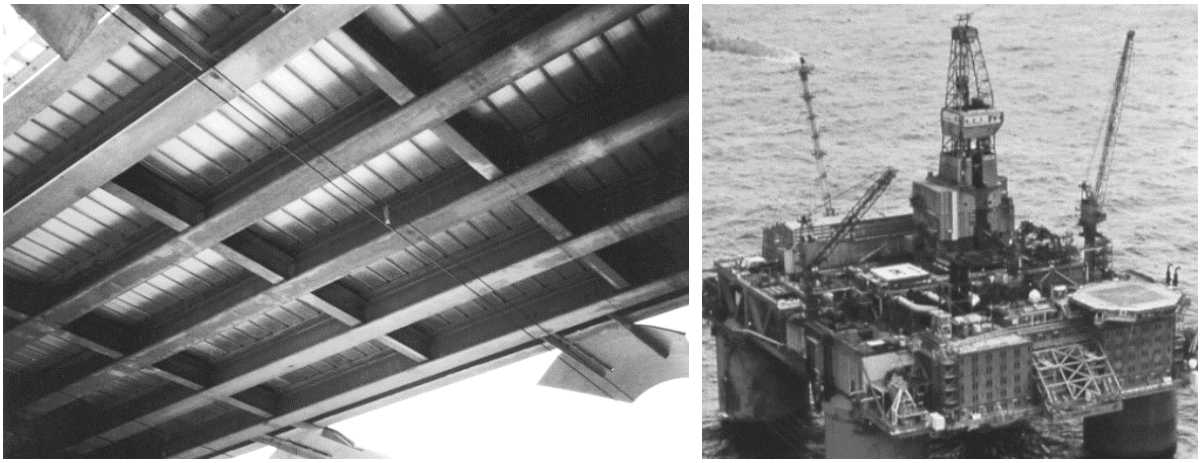

a) **b)**

Figure 2.4. The use of: a) Al-Si-Mg alloy in the production of replacement bridge decks, b) Al-Mg alloys in the superstructures of offshore oil rigs [68]

Utilization of Al alloys in marine, petroleum, and chemical industry stems from excellent combination of strength, corrosion resistance and weldability. While the resistance to seawater attacks enables their application in boats, ships, and offshore stations (Figure 2.4. b), in chemical industry Al alloys are used to contain very corrosive fluids [68]. In 2021, the global transportation sector accounted for an estimated 25.5 million tons of Al, representing 27.0 % of the total global usage. An additional increase in demand of 1.2 million tons is expected in 2022 [70]. This high demand is a consequence of the strategy for fuel economy improvements and GHG emission control based on the material substitution. In the automotive industry Al alloys have been used in the production of engine, transmission (Figure 2.5 a) and suspension parts, as well as in body structure components and panels (Figure 2.5 b) [71]. The main characteristics enabling the use of Al alloys for powertrain applications are good castability and thermal conductivity, while good formability and weldability potentiate additional weight reduction of the vehicle body structure [72]. The railway application comprehends the use of Al alloys in manufacturing of complete car-bodies and their ancillary structures (Figure 2.5). Recently, with the popularity of lightweight design concept for railway vehicles as well as the requirements for simplified construction and maintenance, large integral thin plates and hollow complex thin wall profiles have been developed successfully [73].

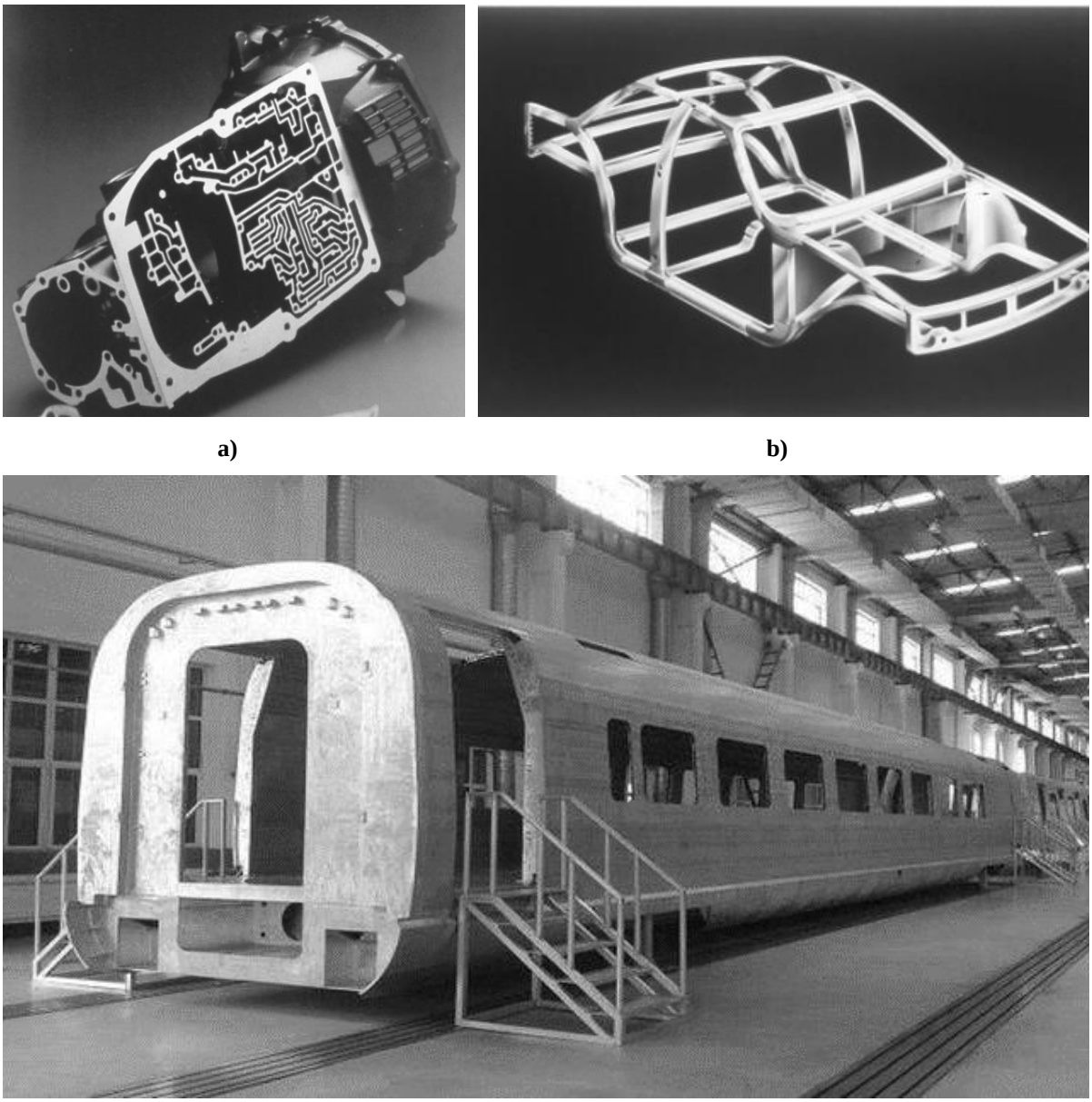

a) **b)**

c)

Figure 2.5. The automotive application of: a) Al-Si-Cu alloy in gearbox casting, b) Al-Mg-Si alloy used for extruded parts of body frame (Audi A-8) [68]**, c) Al-Mg and Al-Zn alloys in the production of high speed train body** [73]

In the air transportation Al alloys have been used as a primary airframe material since 1920s. Due to their low density and susceptibility to heat treat, Al alloys are used to produce primary and secondary structures with high specific properties. While the primary structure carries flight, ground, or pressurization loads and whose failure would reduce the aircraft's structural integrity, the loss of secondary structure would affect the operation of the aircraft, but it would not lead to its loss. Historically, wrought products were used in primary structures, while both cast and wrought products were utilized in the production of secondary structures [74]. Aluminum alloys for aircraft structures are high-strength Al-Cu-Mg alloys (Figure 2.6 a),

and ultra-high strength Al-Zn-Mg-Cu alloys. The development of new aircraft materials, comprehending Al-Li alloys, rapidly solidified Al alloys, and Al matrix composite materials initiated in the 1980s reducing the utilization of Al-Cu-Mg and Al-Zn-Mg-Cu alloys in military aircraft production [75].

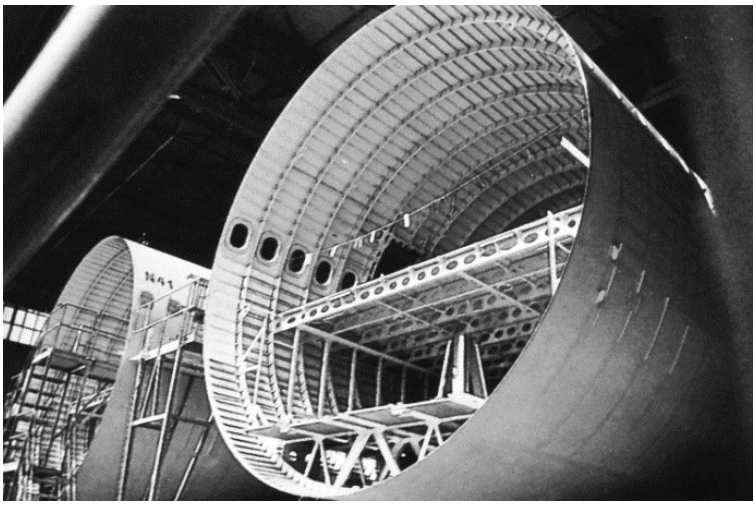

a)

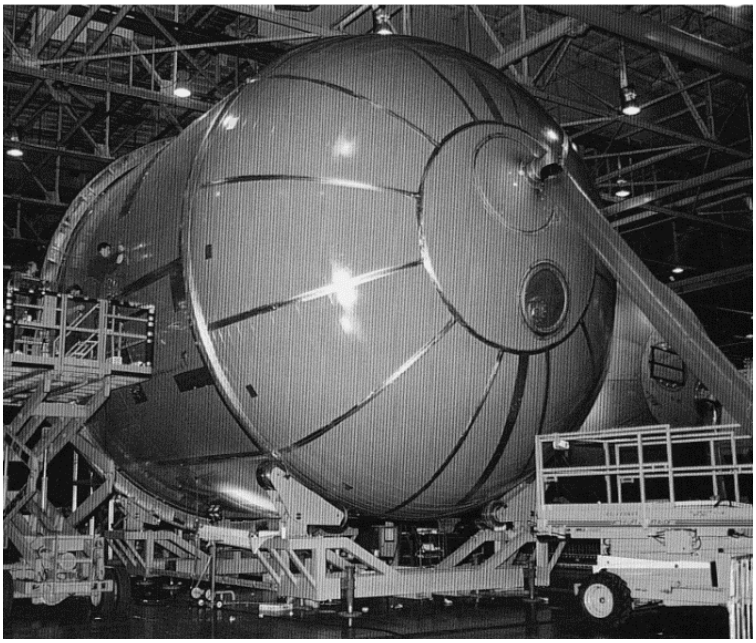

b)

Figure 2.6. The use of Al-Cu-Mg alloy extrusions and plate sin production of: a) aircraft internal structure, b) fuel tanks of the Space Shuttle [68]

The performance characteristic of advanced aerospace and space vehicles are critically dependant on the successful development of structural materials characterised by low density, high strength, high stiffness, and improved temperature resistant. Furthermore, with the emergence of new high-performance alloys, efforts have also been focussed on the adjustment

of processing methods to ensure their sufficient utilization in aerospace components. The requirement to identify both structurally efficient and cost affordable materials has never been a more critical issue in the aerospace industry [76]. Since majority of the airframe structure are fabricated from Al-based alloys, considerable attention has been paid to obtain additional weight and cost savings through the development and progressive application of high strength Al-Zn-Mg-Cu alloys (Figure 2.6 b), high damage tolerant Al-Cu-Mg and Al-Mg-Si alloys, as well as elevated temperature Al alloys, Al matrix composite materials and low-density Al-Li alloys [77].

The potential use of Al alloys for aerospace applications are best described by great French novelist, poet, and playwright Jules Verne in his book From the Earth to the Moon:

"*Aluminum is at once as white as silver, as incredible as gold, as tenacious as iron, as fusible as copper, and as light as glass. It is easily worked; it is widely spread in nature, alumina forming the bases of most rocks; it is three times lighter than iron; in short, it seems to have been created expressly to furnish material for our projectile!*" (Jules Vern, 1865).

2.1. The classification and properties of pure aluminum and its alloys

The physical and chemical properties of Al primarily depend on its purity. Primary Al is produced in variety of designations, typically in the range of 99.0 % to better than 99.99 % [78]. Although there is no specified nomenclature for the degrees of purity, the generally accepted classification is given in Table 2.1.

Table 2.1. The classification of primary produced Al by purity [79]

Grade of purity[1]	Designation
< 99.5	alloy or scrap
99.5 – 99.9	commercial purity
99.9 – 99.99	high purity
> 99.99	super purity

The purity of Al is limited by the number of impurities present in the raw materials. The Al of commercial purity (Table 2.1) is obtained by electrolytical reduction of Al_2O_3. In order to reach high purity, the Al of commercial purity needs to be refined. The number of methods for Al refining is restricted by its high boiling point. The Three-layer process and Segregation process are most frequently used to produce Al of 99.9 % - 99.99 % purity. The purification and layer separation in Three-layer process is assured by the difference in layer density. The Fractional crystallization and Unidirectional solidification process are two types of Segregation refining processes based on crystallization and separation of purified Al from the molten Al [80]. The Zone refining process combines both Three - layer and Segregation process to electrodeposit Al of super purity (Table 2.1) [81]. Despite the height of purity of differently designated Al, the greater variety of impurities with different proportions are present. In the Al of commercial purity, the main impurities are Fe (0.03 % Fe) and Si (0.05 % Si) with traces of gallium (Ga), vanadium (V), Ti, Cu, Na, Mn, Ni and Zn. In high purity Al, Fe remains the main impurity with the amount of Zn, Cu, Mg and Na exceeding the amount of Si impurities. In the Al of super purity, chromium (Cr), Mn, Ti and V are dominant impurities [79]. Aluminum of super purity is susceptible to "*soft errors*" associated with α-particle emission when used as a conductor for ultra-large-scale integrated circuits. The α-particle emission is a consequence of uranium (U) and thorium (Th) impurities [82].

[1] The purity of Al is calculated by deducing from 100.0 the sum of the analysed impurities. However, usually in practice, the impurities with the content lower than 0.005 % or 0.001 % are not reported but can impact the properties of the metal with higher purity designations.

2.1.1. The properties of pure aluminum

Aluminum is the chemical element of the third group in the periodic table of elements. The atomic number of Al is 13, values of the atomic weight are 26.9815 g/mol based on ^{12}C and 26.98974 g/mol based on ^{16}O. The Al has eight isotopes from which the naturally occurring ^{27}Al is the only one stable [83]. The physical properties of Al depend on its purity, as indicated in Table 2.2.

Table 2.2. Physical properties of Al with respect to purity [84]

Property	Purity, %				
	99.000	99.500	99.800	99.990	99.999
Melting point, °C	657.0	-	-	660.2	-
Boiling point, °C	-	-	-	2480.0	-
Latent heat of fusion, kJ/kg	389.37	-	-	396.07	-
Specific heat at 100°C, J/(kg · K)	0.2297	-	-	0.2226	-
Density at 20°C, g/cm^3	-	2.71	2.71	2.70	2.7
Electrical resistivity at 20°C, μΩ · cm	2.87	2.8	2.74	2.68	2.63
Temperature coefficient of resistivity	0.0040	0.0041	0.0042	0.0042	-
Coefficient of thermal exposure · 10^6	23.50	23.50	23.5	23.86	-
Thermal conductivity, W/(m · K)	0.54	0.55	0.56	0.57	-
Reflectivity, %	-	86.0	89.0	90.0	-

Aluminum crystallizes in the face-centered cubic (fcc) lattice. The fcc lattice is stable from -269.15 °C to the melting point. Theoretical density of solid Al calculated based on lattice parameters is 2.698 g/cm^3. The density of molten 99.99 % Al increases from 2.304 g/cm^3 at 899.8 °C to 2.368 at 659.85 g/cm^3. The solid 99.99 % Al has a density of 2.71 g/cm^3. The density of liquid and solid Al is reduced with the increase in purity (Table 2.2). The melting point of Al is between 657.0 °C for 99.00 % Al and 660.2 °C for 99.99 % Al. Aluminum has a high boiling point of 2480.0 °C (Table 2.2). The entropy of fusion varies from 389.37 kJ/kg to 396.07 kJ/kg with specific heat at 100.0 °C between 0.229 J/(kg · K) and 0.223 J/(kg · K) (Table 2.2). The impurities have strongest influence on electrical resistivity and thermal conductivity. The electrical resistivity increases from 2.63 μΩ · cm for Al of 99.999 % purity to 2.87 μΩ · cm for Al of 99.00 % purity, while thermal conductivity reduces from 0.57 W/(m · K) for 99.990 % Al to 0.54 W/(m · K) for 99.00 % Al (Table 2.2) [84]. The electrical resistivity and

thermal conductivity are highly affected by the impurity content at the temperatures < -173.15 °C. The effect of the grain size on the electrical resistivity is negligible [85].

Since Al has an odd number of valence electrons (3 electrons), it is paramagnetic. The magnetic susceptibility of Al varies with temperature, impurity content and degree of deformation. The increase in temperature reduces the magnetic susceptibility. The presence of Fe and Mn impurities increases the magnetic susceptibility of Al. The presence of other impurities has negative effect on paramagnetic properties of Al [86]. Although, the impact of deformation on paramagnetic properties is not completely clear, the 5.0 % to 15.0 % decrease in susceptibility at 50.0 % deformation is reported [84].

The reflectivity of smooth Al surface to light is more than 90.0 % for wavelengths between 0.9 μm to 12.0 μm. At the wavelengths < 0.2 μm the reflectivity of smooth Al surface drops below 70.0 % [87]. The reflectivity of Al surface significantly reduces with the roughness. The sandblasted Al surface exhibits 15.0 % to 25.0 % of the polished surface reflectivity. The highest reflectivity is obtained by vapor deposition which produces very smooth surface. The rough finish of the surface can increase emissivity of Al by 20.0 % to 30.0 %. The emissivity increases further with the increase in temperature [88].

Although Al is one of the most reactive commonly used metal, it is stable in many oxidizing environments. The high stability of Al originates from continuous film of Al oxide forming on the surface exposed to oxygen, water, or other oxidants. The thickness of oxide film depends on temperature, time, and the presence of water vapor. While two-layer films generally form in humid environments [89], The oxide films with more complex structure can form at the higher temperatures and in the Al alloys. Under those conditions the growth of oxide layer no longer depends solely on time [90]. Aluminum of 99.95 % purity is resistant to the attacks of most acids but can be dissolved by *aqua regia* (1 nitric acid (HNO_3): 3 chloride acid (HCl)). The protective oxide film rapidly dissolves in alkaline solutions producing alkali metal aluminates and hydrogen (H_2). The Al is amphoteric and can react with mineral acids to form soluble salts and release H_2 [91].

Molten Al reduces many oxygen containing compounds and is used in thermite reactions to produce pure metals and Al_2O_3 [92]. However, molten Al reacts explosively with water and should not come in contact with the moist tools or moist containers [93].

The mechanical properties of Al depend on purity and applied heat treatment. The increase in Al purity decreases it's mechanical properties. The modulus of rigidity (*G)*, Young modulus (*E*) and Poisson ratio (*v*) of super pure Al (*E*=69.0 – 72.0 GPa, *G*= 25.0 – 26.5 GPa, *v*= 0.31) are lower compared to the Al of commercial purity (*E*=70.0 – 72.5 GPa, *G*= 27.0 –

28.0 GPa, ν= 0.31 – 0.33) [84]. Increase in impurity content increases the tensile strength, hardness, and fatigue resistance of Al [79]. The beneficial influence of impurities on mechanical properties is connected to the grain growth and microstructure refinement during solidification and processing through the mechanisms of dynamic recovery and recrystallization [94].

2.1.2. The classification and properties of aluminum alloys

The designation system and Al alloy nomenclature are not internationally standardized. The most frequently used are Aluminum Association (AA) alloy nomenclature and temper systems. In the AA designation system, the alloy nomenclature consists of four digits, as indicated in Figure 2.7.

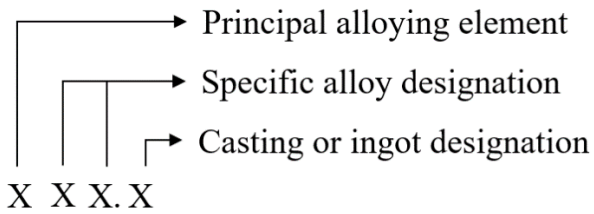

a)

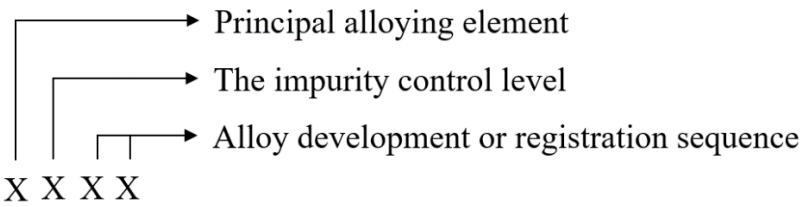

b)

Figure 2.7. The Al alloy designation system according to the AA: a) cast Al alloys, b) wrought Al alloys [95]

As indicated by Figure 2.7, Al alloys are divided into two major categories:

- Cast Al alloys,
- Wrought Al alloys.

According to the AA, cast Al alloys are designated using four numeric digits with a period between the third and fourth digit (Figure 2.7 a). The first digit in cast Al alloy designation defines the principal alloying element or elements. Depending on the first digit, the second and third digit can either indicate the level of purity or arbitrarily identify individual alloy in the group. The forth digit indicates the form of a final product [96].

The AA designation for wrought Al alloys consists of four digits without a period between the digits (Figure 2.7 b). The first digit defines the principal alloying element or elements. The level of impurity control necessary to obtain required properties is indicated by the second digit. The third and fourth digit are used to establish the purity of used Al raw material or indicate the alloy development sequence [95].

The division of Al alloys into two major categories and AA designation for individual composition series within the major categories is given in Figure 2.8.

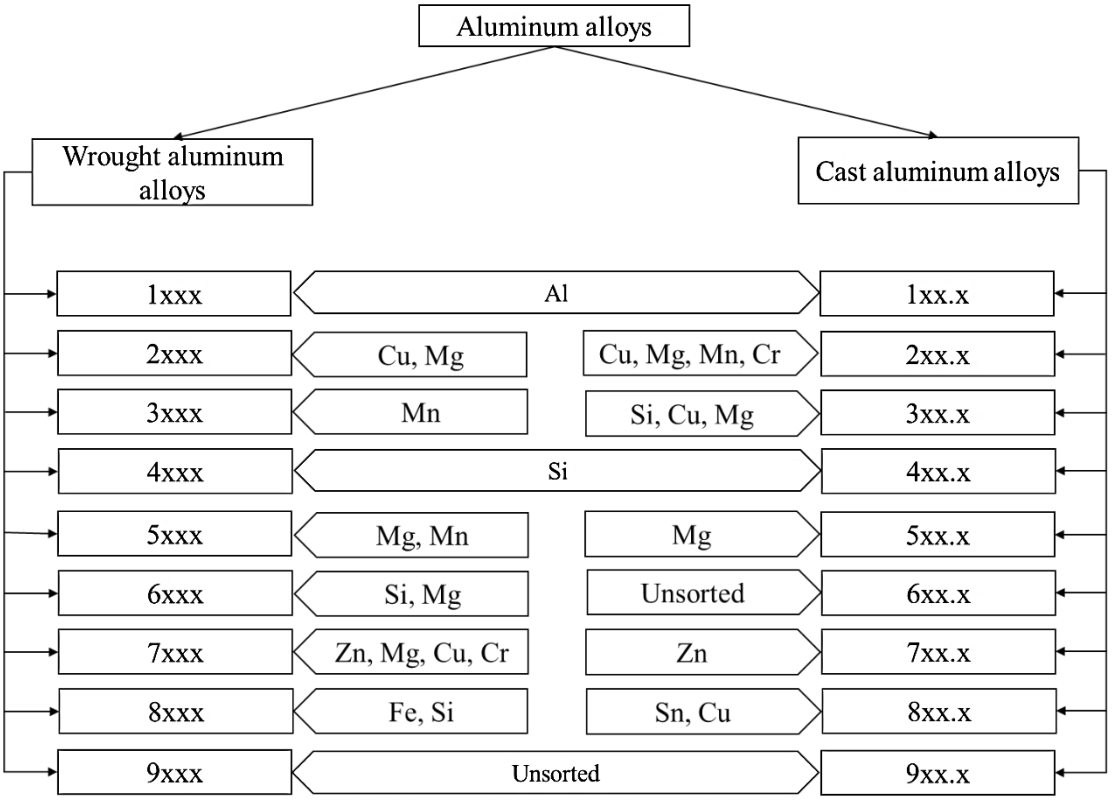

Figure 2.8. The division of Al alloys into two major categories with indicated composition series according to the AA designation system [83, 84]

The cast and wrought Al alloys are distinguished based on chemical composition, microstructure, and processing characteristics. The cast Al alloys contain between 4.0 wt% and 15.0 wt% alloying element additions [97], while the wrought Al alloys contain between 0.1 wt% and 5.0 wt% of alloying element additions [98].

In addition to being divided into cast and wrought, Al alloys can be further divided into heat treatable and non-heat treatable. The classification of Al alloys based on the metallurgical condition is given in Figure 2.9.

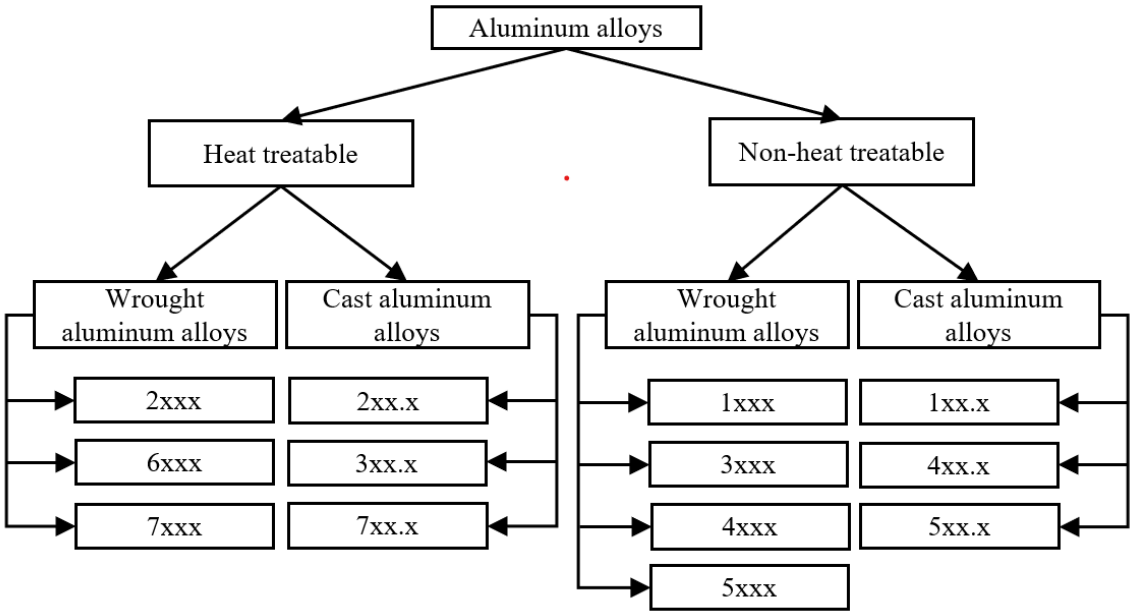

Figure 2.9. The classification of Al alloys based on the metallurgical condition [99]

As indicated in Figure 2.9, both wrought and cast Al alloys containing Cu, Mg, Si, and Zn are considered to be heat treatable. The heat treatment of Al alloys is normally performed to modify the microstructure and controllably influence their functional properties. Since Al-based alloy systems are characterized by the lack of allotropic transformations during heating or cooling, the microstructure modification is most frequently obtained through precipitation hardening or aging. The heat treatable Al alloys exhibit a temperature-dependent solid solubility of the alloying elements, meaning that their solid solubility decreases with decrease in temperature [100]. Those alloying elements are added in concentrations that exceed their equilibrium solid solubility in α_{Al} matrix at room and moderately high temperatures [101]. Although, this condition is met by most of the binary Al alloys, the major heat-treatable Al alloying systems include:

- Al-Cu system with strengthening obtained from Al_2Cu (θ) phase,
- Al-Cu-Mg system where Mg intensifies Al_2Cu (θ) phase precipitation,
- Al-Mg-Si system strengthened through the precipitation of Mg_2Si (β') phase,
- Al-Zn-Mg system strengthened by Zn_2Mg phase precipitation,
- Al-Zn-Mg-Cu system [102].

Aluminum alloy temper designation system according to AA is illustrated by Figure 2.10.

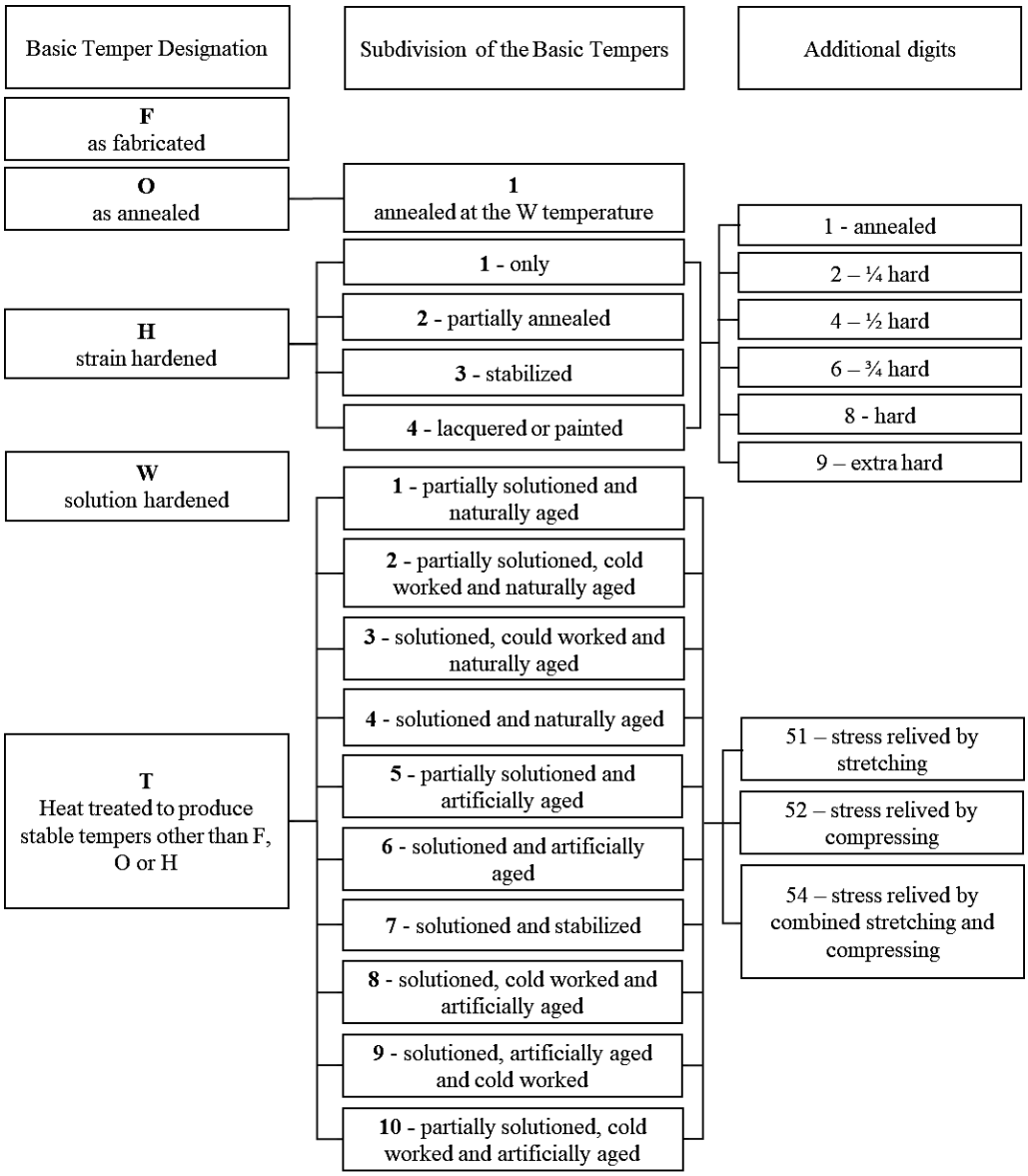

Figure 2.10. The Al alloy temper designation system according to AA [102]

According to the AA designation system, the alloy designation is followed by the temper designation. These two designations are separated by hyphen. The first character in the temper designation is a capital letter referring to the general class of the treatment. The basic temper designations are (Figure 2.10):

- *As fabricated* (F) that applies to the wrought or cast products made by shaping processes that have no special control over thermal conditions.
- *Annealed* (O) frequently referring to the wrought products that are annealed to obtain the lower strength tempers to increase subsequent workability.
- *Strain hardened* (H) is applied to the products with increased strength through the strain hardening treatment with or without additional treatments to reduce strength.

- *Solution heat treated* (W) alloys age spontaneously after solutionizing treatment and require additional designation to indicate the period of natural aging.
- *Thermally treated* (T) to produce stable tempers other than F, O or H applies to the products that are thermally treated with or without supplementary strain hardening.

The O, H and T general classes of the heat treatment are additionally subdivided to indicate specific combination of basic operations (Figure 2.10). For the products designated as strain hardened additional operations mainly refer to the pending heat treatment, while subdivision of the T treated product equally comprehends heat treatment and shaping operations [95].

2.1.2.1. Cast aluminum alloys

The cast Al alloys are the most versatile of all commonly produced Al alloys and generally have the highest castability ratings. They are characterized by:

- Good fluidity for filling thin sections of casting geometry,
- Lower melting point compared to the other metals and alloys,
- Shorter casting cycle due to the rapid heat transfer from the molten alloy to the mold,
- Many Al alloys are relatively free from hot cracking and hot tearing tendencies,
- Chemical stability,
- Good as cast surface finish [96].

The Al castings are usually produced by pressure die casting, permanent mold, green sand, dry sand, investment, and plaster casting. They are also routinely cast using vacuum, low-pressure, centrifugal, as well as pattern-related casting processes such as lost foam [96].

The cast Al alloy series designated as 1xx.x represents the unalloyed Al with strictly controlled purity used for electrical applications, in rotor casting and manufacturing (Figure 2.8) [97].

The highest strength properties are obtained in the 2xx.x series of alloys (Figure 2.8). These alloys contain 4.0 wt% to 6.0 % Cu, 0.25 wt% to 0.35 wt% Mg and in some cases 0.25 wt% to 0.35 wt% Mn or Cr and 0.7 wt% silver (Ag) [103]. The 2xx.x alloys containing up to 2.0 wt% Mg and additions of Mn, Ni, V and/or Zr are primarily used at elevated temperatures between 150.0 °C and 320.0 °C [104]. To obtain high ductility and strength, the 2xx.x alloys require high impurity control, special casting design and foundry technology. The high ductility

is obtained in the alloys containing less than 0.15 wt% Fe impurities [105]. The inadequate gating system can reduce castability, enable shrinkage porosities and have a negative impact on mechanical properties [106].

The 3xx.x series of alloys contains Si, Mg, Cu, and supplementary additions of beryllium (Be) or nickel (Ni) (Figure 2.8). Generally, 3xx.x series of alloy is divided into Al-Si-Mg, Al-Si-Cu, or Al-Si-Cu-Mg types. To obtain high fluidity, reduce hot cracking and minimize shrinkage porosity, the 3xx.x series contains between 9.0 wt% and 13.0 wt% Si. Both, the additions of Cu (up to 4.5 wt%) and Mg (from 0.3 wt% to 1.0 wt%) increase strength and hardness through solid solution and precipitation hardening [103]. The Al-Si-Cu-Mg alloys with 0.30 wt% to 1.02 wt% Ni additions have high fatigue life and strength properties at elevated temperatures [107].

The 4xx.x series of Al alloys is based on binary Al-Si system and contains between 5.0 wt% to 12.0 wt% Si (Figure 2.4). The Al-Si alloys have moderate strength, high ductility and impact resistance [97]. The binary Al-Mg alloys in the 5xx.x series are single phase alloys with moderate to high strength and toughness (Figure 2.8). Producing the Al-Mg alloy with high purity enables high corrosion resistance especially to seawater and marine atmosphere. These alloys have good machinability and are suitable for welded assemblies [108].

The 7xx.x series of Al alloys contains the additions of Zn (Figure 2.8). The Al-Zn alloys have good finishing characteristics, good general corrosion properties, and capability of developing high strength properties through natural aging. The peak strength of Al-Zn alloys is achieved after 20 to 30 days of natural aging at the room temperature [109]. However, the application of 7xx.x alloy series is limited by their low fluidity and tendency towards hot cracking [110].

The 8xx.x series of Al alloys contains approximately 6.0 wt% tin (Sn) with small additions of Cu and Ni for strengthening (Figure 2.8.). They were developed for bearing applications due to the Sn lubricity impartment. The reduced castability of 8xx.x alloys is a consequence of high tendency towards hot cracking [97].

The 6xx.x and 9xx.x series of Al alloys are unsorted (Figure 2.8.).

2.1.2.2. The wrought aluminum alloys

Compared to the cast, wrought Al alloys contain reduced proportion of alloying components and are less susceptible to the defects during the production process. This type of Al alloys is appreciated for its good weldability, corrosion resistance, strength, and ductility.

The 1xxx series of wrought Al alloys comprehends Al of commercial to super purity (Figure 2.8) with tensile strength in the range of 69.0 MPa to 186.0 MPa. These alloys are mostly used for electrical applications [97].

In the 2xxx series Cu is the principal alloying element often combined with Mg as a secondary addition. The Al-Cu alloys have high stiffness and strength at elevated temperatures, so they are most frequently used in transportation industry. The Al-Cu alloys have pour corrosion resistance and are prone to intergranular corrosion cracking [111].

The 3xxx series of Al alloys is based on binary Al-Mn system containing up to 1.25 wt% Mn (Figure 2.8). The higher Mn additions are avoided because in combination with Fe impurities they can lead to the embrittlement. The 3xxx alloys are used as general-purpose alloys for moderate strength applications and good workability requirements [97].

In 4xxx series of Al alloys Si is principal alloying element (Figure 2.8). Silicone is added in sufficient quantities (between 3.0 wt% and 13.5 wt%) to lower melting regime and avoid brittleness. The 4xxx series of alloys is frequently used as welding wire and brazing alloy for joining Al alloys with higher melting point [108].

The 5xxx series of Al alloys comprehends Al-Mg and Al-Mg-Mn types of alloys (Figure 2.8). Compared to Mn, Mg is more effective as alloying element and can be added in higher quantities [103]. The 5xxx series of Al alloys has moderate to high strength, good welding characteristics and good resistance to corrosion in marine environments. However, limitations should be placed on the amount of cold work and the safe operating temperatures for the alloys containing over 3.5 wt% Mg [112].

The 6xxx series of Al alloys represent the ternary Al-Si-Mg system (Figure 2.8). The 6xxx alloys possess medium strength, good formability, weldability, machinability, and corrosion resistance [103].

In the 7xxx series of Al alloys the Zn in the amounts of 1.0 wt% to 8.0 wt% is principal alloying element. The strength improvements are obtained by adding small amounts Mg, Cu, Cr, or scandium (Sc) (Figure 2.8). The Al-Zn alloys are utilized in the production of airframe structures, transportation equipment and other highly stressed parts [103]. However, 7xxx alloys can be susceptible to the stress corrosion cracking [113].

The 8xxx series of Al alloys constitute a wide range of chemical compositions (Figure 2.8). The adequate alloying system is chosen based on the required properties. When improved thermal stability at elevated temperatures is needed the Al-Fe-Ce system is used. The same performances can be achieved by combined additions of Fe, V and Si [113].

The 9xxx series of Al alloys remains unsorted (Figure 2.8).

2.1.2.3. The non-heat treatable aluminum alloys

The properties of non-heat treatable Al alloys originate from solid solution strengthening, second phase precipitation, dispersoid precipitation, and strain hardening.

2.1.2.3.1. Solid solution strengthening

As indicated in Figure 2.11, the solid solution strengthening occurs when there is a difference in atomic radii between the atoms of matrix and solute element (alloying element). Based on the atom radii, the solute element atoms can occupy interstitial or substitutional sites (Figure 2.11). The solute element atoms with atomic radii up to 57 % of the matrix atom radii reside in the interstitial spaces (Figure 2.11 a), while the substitutional spaces are occupied by solute element atoms with atomic radii of ± 15 % matrix atom radii (Figure 2.11 b and c) [114]. The similarity in atom radii, valence, electronegativity, and chemical bonding type are factors influencing solid solution formation. The relationship between these factors is described by Hume – Rothery rules [115]:

- If the atomic size of solute element atom differs by more than 15 % from matrix atom, the solid solution is unstable,
- The larger the difference in electronegativity between the solute and matrix atom, the stronger is the tendency to form compounds/precipitates rather than solid solution,
- To form a stable solid solution, the solute element atoms need to have lower valency compared to the matrix atoms.

The valence electron concentration and the atomic size factor are most important in solid solution formation and stability [116].

The increase in the material's strength through the interaction between solute element atoms and matrix atoms can be explained by three mechanisms [117]:

- The mechanism of elastic interactions,
- The mechanism of modulus misfit [118],
- The dislocation anchoring mechanism.

The elastic interaction is a consequence of the size misfit between the solute atom and the atoms of matrix creating a strain field around the solute atom (Figure 2.11). The modulus misfit mechanism comprehends difference in bounding force between the solute atom and matrix atoms resulting in variations in local hardness. The solute atom increases the initial yield stress and reduces dislocation recovery rate resulting in higher dislocation density, work hardening and different dislocation structures (Figure 2.11) [118].

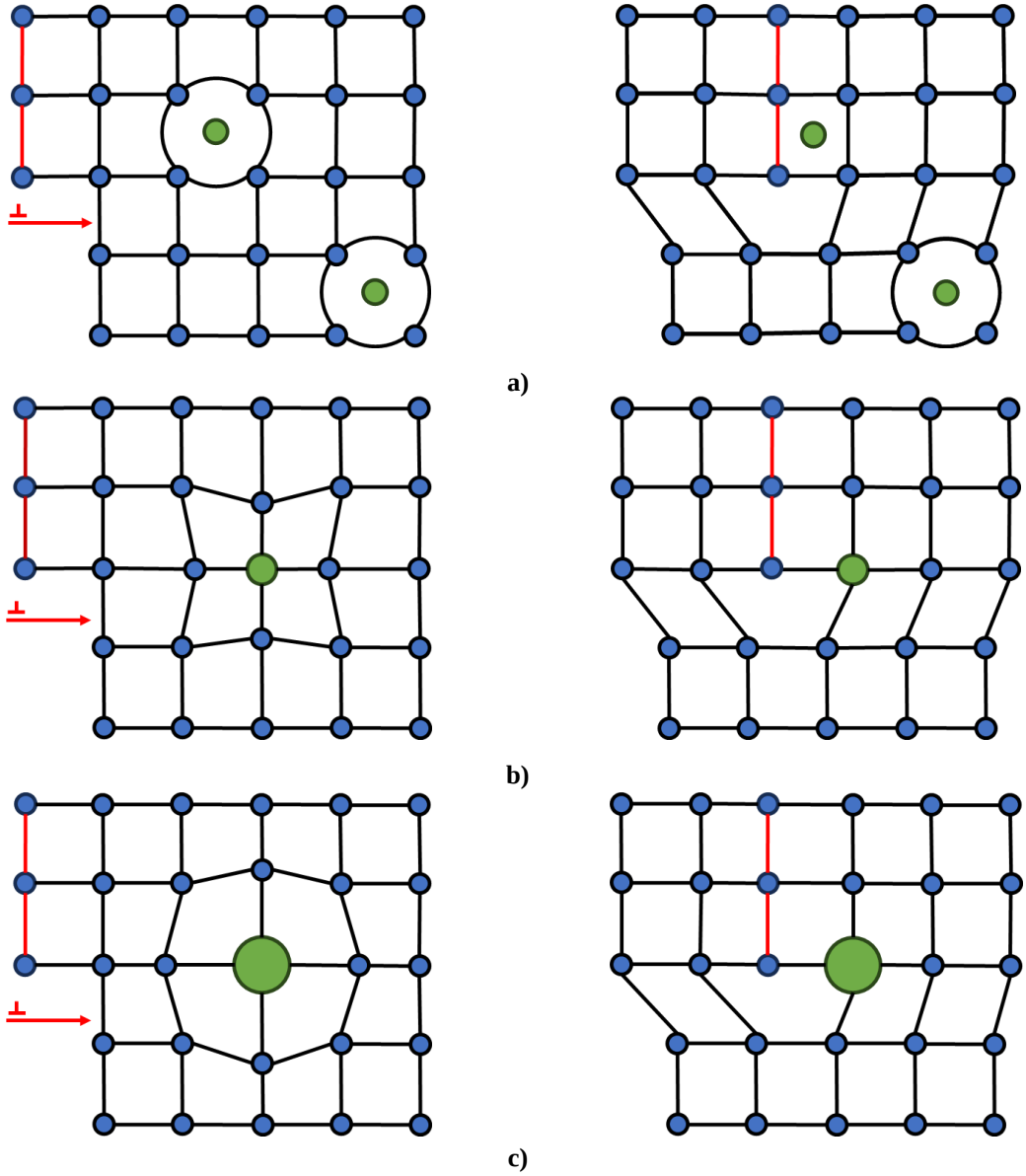

Figure 2.11. The solid solution strengthening and interaction between dislocations and solute element: a) occupying interstitial sites, b) with smaller atomic radii compared to matrix atom occupying substitutional space, c) with larger atomic radii compared to matrix atom occupying substitutional space [117]

To find atomic sites more suitable for their radii, solute elements tend to segregate around dislocations. The segregation of solute elements decreases the strain and anchors the dislocations [117]. A strengthening effect of solute elements occurs when lattice strain field

impede the dislocation movement (Figure 2.11) [119]. Since the solute element atom has different size and shear modulus compared to matrix atom, it imposes additional strain field on the surrounding matrix. The imposed strain field restricts dislocation motion through the solute lattice. In order to overcome solute stress field, additional stress must be applied (Figure 2.11). This additional stress represents the solid solution strengthening [114].

2.1.2.3.2. Strengthening through the second phase precipitation

The second phase precipitates solidify when element or combination of elements with lower solid solubility in matrix are added [120]. The volume fraction of second phase precipitates increases during solidification or processing influencing strength and hardness [121]. Since the precipitates promote strengthening by impeding the motion of dislocations, the additional stress is needed to enable the dislocations to shear or avoid precipitates by looping and extruding [114]. The degree of precipitation strengthening depends on [122]:

- Alloying system,
- The volume fraction of the precipitates,
- Size of the precipitates,
- Interaction between the precipitates and dislocations.

The precipitation strengthening is extensively used in ferrous systems for aging of low carbon steel, microalloyed steel, and in martensite tempering [123]. Since the structure refinement in non-ferrous alloying systems is restricted by the absence of allotropic modifications, the second phase precipitation represents the most important hardening mechanism, especially in wrought 2xxx, 4xxx and cast 2xx.x, 4xx.x alloying systems [124].
During precipitation, the size and volume fraction of second phase precipitates increase simultaneously till equilibrium fraction is achieved. Afterword, only the particle size increases through mechanisms of growth and coarsening [123]. During that, the solute elements are obtained from surrounding matrix or by dissolution of the smaller particles. The main difference is in the formation of transition phase and diffusion field behavior. The transition phase forms prior to the solidification of stable phase and serves as source of solute elements during growth and coarsening. Due to the increase in the number of nucleation sites and their saturation with solute elements, the distance of diffusion field is reduced during growth. On the other hand, the distance of diffusion field increases during coarsening due to dissolution and decrease in the particle number [125].

The interaction between the second phase precipitates and dislocations depends on their size and coherency. The smaller precipitates (< 10.0 nm) coherent with matrix tend to be sheared by dislocations, while larger particles (> 50.0 nm) with incoherent interfaces are by-passed by the formation of Orowan loops [124] or by dislocation cross-slip to the other crystallographic planes [126]. The interaction between coherent second phase precipitate and dislocation are illustrated in Figure 2.12. Shearing of second phase precipitates by dislocations can result in ledge (Figure 2.12 a) or anti-phase boundary formation (APB) (Figure 2.12 b). The ledges represent an additional precipitate/matrix interface formed when dislocation enters (Figure 2.12 a, during shearing) and exits (Figure 2.12 a, after shearing) the precipitate. Since the newly formed interface possesses surface energy, additional stress is required to shear the precipitate. This additional stress is known as chemical strengthening [127]. The influence of chemical strengthening on alloy properties depends on the size of precipitates. In alloys with smaller size of precipitates chemical strengthening has a beneficial influence on mechanical properties, while in the alloys with larger precipitates it can cause material softening. This negative impact on mechanical properties originates from additional increase in surface area that changes the interaction between the precipitates and dislocations from shearing to looping [128].

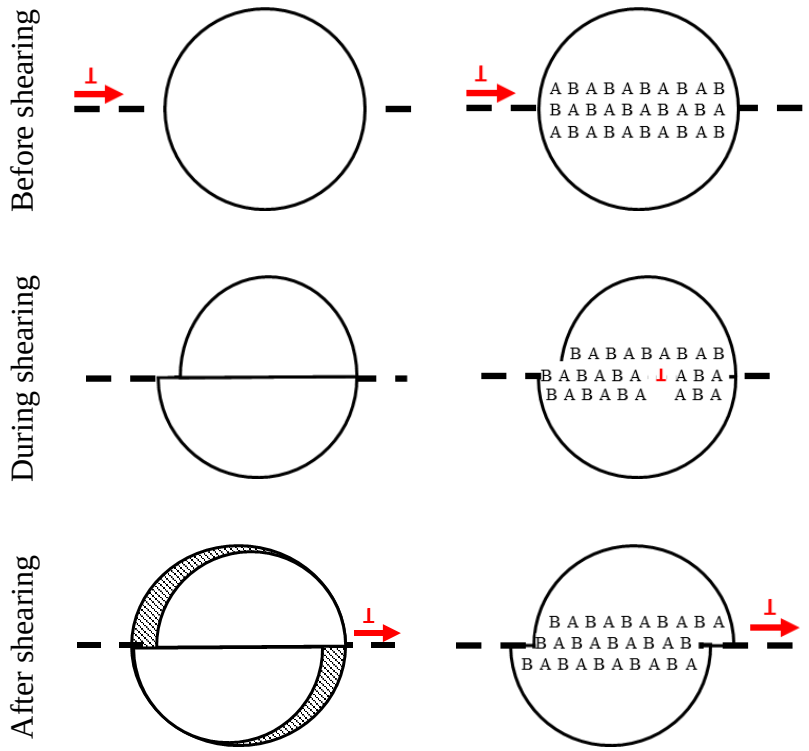

Figure 2.12. Interaction between coherent second phase precipitates and dislocations with formation of: a) ledges, b) Anti-phase boundaries [114]

The order strengthening occurs when a dislocation shears the coherent precipitate and creates an APB on the slip plane of the second phase precipitate (Figure 2.12 b). The APB energy per unit area on the slip plane, represents the force per unit length resisting the motion of the dislocation as it shears the precipitate [128]. As indicated by Figure 2.12 b, the slip in the precipitate is accompanied by the formation of an APB (A-A and B-B bonds) across the slip plane. After dislocation exits the precipitate, the APB surface occupies the whole slip plane area of the precipitate and increases its energy. To reduce APB surface energy and restore the order, additional dislocations are required (Figure 2.12 b, after shearing). So, it is characteristic for dislocations in ordered strengthened alloys to travel in groups. The number of dislocations in a group is determined by the number of dislocations required to reduce surface energy and restore order in the precipitates. This group of dislocations is referred to as superdislocation [114]. However, to lower the energy, superdislocation will often be dissociated into superpartials and bonded by stacking faults (SF) and APB. The area between two dislocation partials has a different structure and is called the SF. The materials with low SF energy have widely spaced partial dislocations, while high SF energy results in closely spaced partial dislocations [129]. If the SF energy is higher in the second phase precipitates compared to the matrix, dislocations will avoid passing through the precipitates as a result of stacking fault hardening [130]. Since the energy of dislocation is a function of the lattice shear modulus, the change in energy is associated with the interaction between dislocations and second phase precipitates that have different shear modulus compared to the matrix. There are two types of interaction regimes pending on whether the dislocation is inside or outside the particle. However, since the force is highest when dislocation enters the precipitate, this type of interaction is the most relevant for estimating the maximum increase in critical resolved shear stress (CRSS) due to modulus hardening [129]. The CRSS is the component of shear stress necessary to initiate slip in a plane that is not perpendicular nor parallel to the stress axis. The CRSS is material property and represents the value of shear stress at which yielding of the grain occurs [131].

Precipitation strengthening by dislocation looping occurs when precipitates pin two segments of the same dislocation, as indicated in Figure 2.13. Since the non-coherent second phase precipitates cannot be sheared (Figure 2.13 a), dislocation is forced by the applied stress to loop around the precipitates (Figure 2.13 b) and bypass them (Figure 2.13 d). After dislocation is extruded between two precipitates it reaches semi-circular configuration (Figure 2.13 c) and escapes leaving a dislocation loop around the precipitates called Orowan loop (Figure 2.13 d) [132]. In alloying systems containing both coherent and incoherent precipitates,

the total strengthening contribution is the minimum of both contributions because the easier mechanism will be used by dislocations [133].

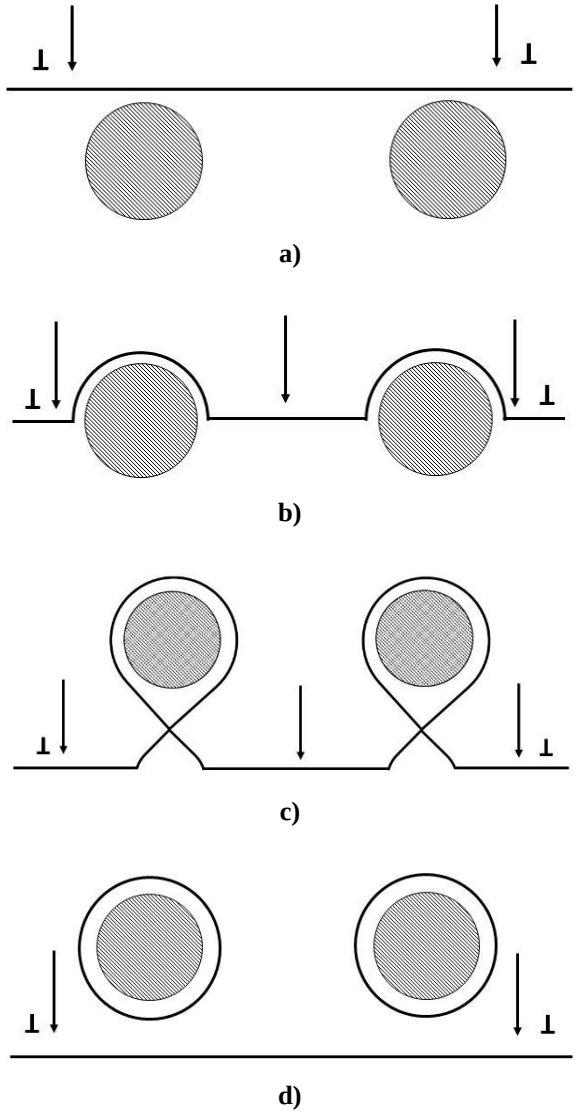

Figure 2.13. Dislocation looping between two precipitates with indicated: a) approaching situation, b) sub-critical situation, c) critical situation, d) escape situation [117]

In practice, it is necessary to obtain precipitates with radii slightly above the optimum value to avoid formation of local softening regions with stress concentration [115].

2.1.2.3.3. Dispersoid particle hardening

The dispersoid particles are complex intermetallic compounds often used in cast and wrought Al alloys to control grain growth and recrystallization. The grain size and distribution are important factors influencing mechanical properties and performance of an alloy. The coarse grains with large grain size exhibit low strength properties but have high ductility and

toughness. Decreasing the grain size increases yield strength, fracture toughness, and wear resistance at the expense of ductility and elongation. However, at the critical grain size material softening can occur. This decrease in material properties is a consequence of grain refinement saturation leading to grain coarsening, boundary sliding and changes in interactions between grain boundaries and dislocations [134]. Grain size reduction increases the alloy properties through the increase in grain boundary area. The grain boundaries have a major influence on alloy properties and failure mechanisms. The failure influencing factors, mainly crack nucleation and propagation, are directly affected by grain boundary geometry [135] that can either facilitate slip transfer between the grains or resist the slip movement [136]. The intergranular crack propagation is enabled by low angle grain boundaries and twin boundaries, while high angle grain boundaries induce high ductility and toughness. High and low angle grain boundaries differ in atomic misorientation angle, as indicated by Figure 2.14.

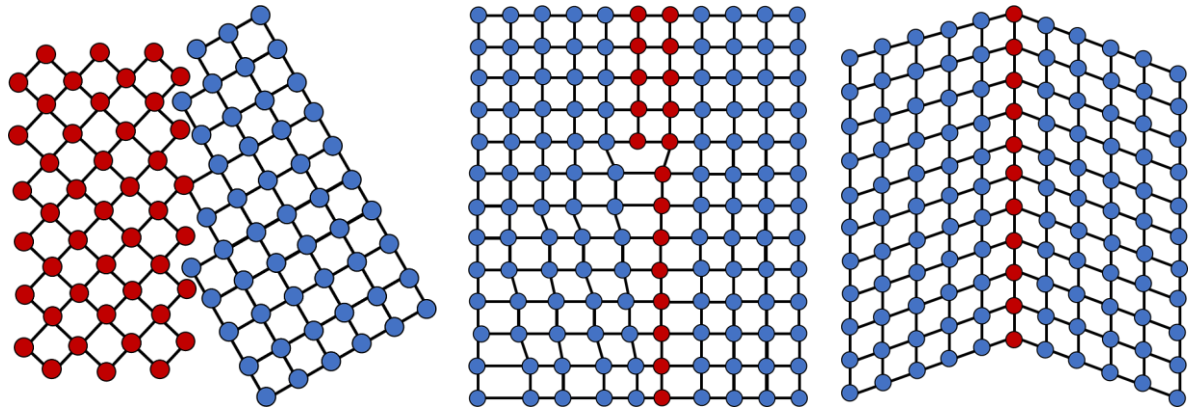

Figure 2.14. The grain boundary geometry: a) High angle grain boundary, b) Low angle grain boundary, c) twin grain boundary [137]

If the atomic misorientation angle between two grains is > 15°, it is a high angle grain boundary (Figure 2.14 a). The high angle grain boundaries are generated through accumulated stress and help to retard slip band formation and dislocation movements. Low angle grain boundaries are induced during plastic deformation and characterized by high strain hardening, low ductility, and low toughness. The low strengthening effect of low angle grain boundaries is caused by grain boundary sliding. Since, low angle grain boundaries have low grain rotation and misorientation (Figure 2.14 b), they cannot effectively resist dislocation movement between the grains [137]. Twinning is usually a consequence of coordinated movement of a large number of atoms in a crystal by shearing (Figure 2.14 c). The major factors influencing twining are plastic deformation, SF energy, and grain size [138]. The narrow region of atomic mismatch in twins induces dislocation pileups. The twin grains provide high strength and thermal stability

at elevated temperatures by hindering crack propagation. However, it has been indicated that cracks usually initiate at twin boundaries due to the high concentration of dislocations [139]. The grain boundary strengthening or strengthening by reduction of the grain size origins from dislocation pileups at the grain boundaries (Figure 2.15).

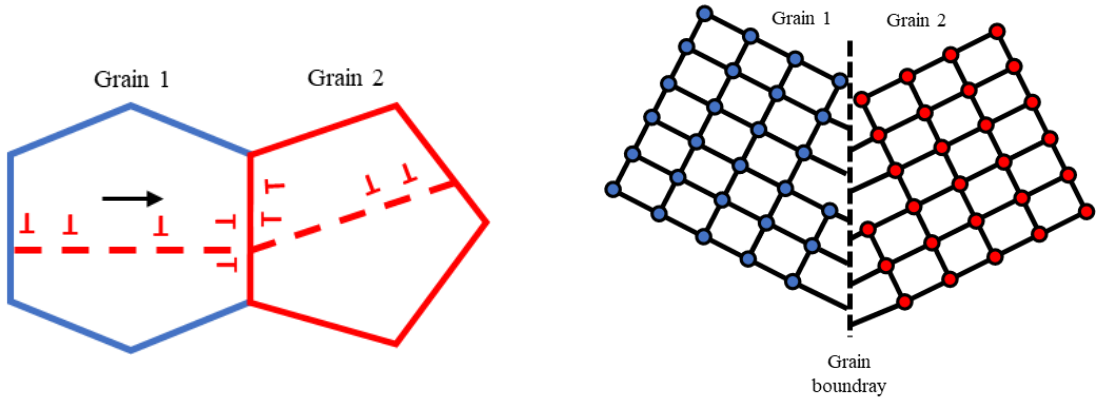

a) **b)**

Figure 2.15. The grain boundary strengthening between grains 1 and 2 through: a) dislocation pileup, b) atomic misorientation [137]

Grain boundaries are dense arrangement of tangled dislocations that contribute to stored strain energy. Under external loads dislocation movement and segregation results in plastic deformation and failure. Rupture and reformation of interatomic bonds are the fundamental mechanisms for dislocation movement [140]. Existing dislocations interact and move on the same slip plain in different directions. Material yielding is first initiated from a single grain by emitting a dislocation loop. This dislocation loop moves to the grain boundary that resists further movement and results in dislocation pileup (Figure 2.15 a, grain 1). If the number of dislocations piled up at the grain boundary is larger than required, the slip in adjacent grains will occur immediately (Figure 2.15 a, grain 2). The stress concentration induced in other grains starts plastic deformation and failure of whole material [137]. However, the failure will occur only when dislocation movement has started in sufficient number of grains.

In wrought Al alloys the dispersoid particles are used to control grain growth during ingot reheating and rolling. The precipitation of dispersoid particles is enabled by the rapid solidification during ingot casting. High cooling rate enables formation of solid solution with concentrations of alloying elements exceeding their equilibrium solubility. During reheating of the as-cast ingot for wrought processing, the supersaturated solid solution is dissolved as dispersoid particle precipitate in solid state. Unlike second phase precipitates, dispersoid particles have no direct effect on mechanical properties [141]. Their beneficial effect is manifested through grain growth and recrystallization control [142]. Due to their stability at

elevated temperatures dispersoid particles can act as nucleation sites for precipitation of second phase particles [143].

The dispersoid particles in cast Al alloys have direct influence on mechanical properties. Since the application of precipitation hardened cast Al alloys at elevated temperatures (> 200.0 °C) is limited due to the excessive coarsening of precipitates [144], the incoherent dispersoid particles provide increase in yield strength and reduce tendency towards intergranular embrittlement for fully aged alloys [145]. However, to achieve high strength levels, the dispersoid particles with very small radii need to be evenly distributed. Even distribution of fine dispersoid particles in matrix is a complex and expensive process [129].

2.1.2.3.4. The work hardening

The work or strain hardening is obtained through mechanical processing often combined with annealing for property development [103]. The strain hardening is the strengthening mechanism based on dislocation generation, multiplication, movement, and annihilation [137]. Increase in stress during mechanical processing enables Frank-Read configuration and spiral configuration to generate new dislocations and increase their density [146]. Multiplication of dislocations and increase in density creates the forest of dislocations that impedes their movement (Figure 2.16). Dislocations in material represent obstacles for movement of other dislocations by creating kinks or jogs (Figure 2.16). The annihilation of dislocations will occur if two opposite edge dislocations move on the same slip plane [115]. The increase in yield strength, hardness, tensile strength, and resistance to crack nucleation are obtained through the interaction between moving dislocations and forest of dislocations as well as dislocation annihilation. However, the material embrittlement lowers the crack growth resistance [119].

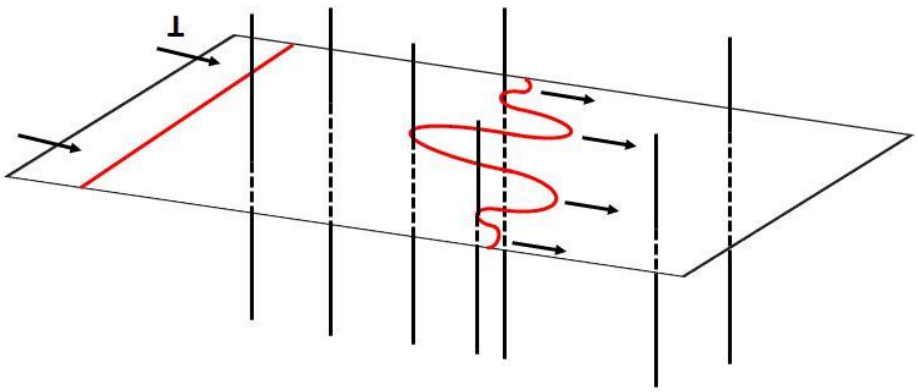

Figure 2.16. The forest of dislocations impeding the movement of dislocation on a slip plane [144]

The 1xx.x and 5xx.x series of non-heat treatable cast aluminum alloys are strengthened by one or more mechanisms and used in the as-cast condition. The solid solution strengthening in cast Al-Mg alloys containing between 10.0 wt% to 40.0 wt% Mg originates from high solid solubility of Mg in α_{Al} matrix (17.0 wt% [147]) as well as a large difference in the atomic size between Mg (150.0 pm [148]) and Al (125.0 pm [149]) atoms [150]. However, the solid solution hardening is utilized to increase ductility in Al alloys with higher Mg content. The poor ductility is primarily attributed to the solidification of course Al_8Mg_5 (β) phase during the eutectic reaction [21]. The solidification of eutectic β phase in the hypoeutectic Al-Mg alloys is a consequence of liquid phase bulking [151].

The 1xxx, 3xxx and 5xxx are non-heat treatable wrought Al alloys strengthening by solid solution strengthening and cold working [127]. The Al-Mn alloys are hardened through the mechanisms of work and dispersoid hardening. The dispersed particles precipitate during homogenization from supersaturated solid solution of Mn in the α_{Al} matrix. The α-Al(MnFe)Si and Al_6(MnFe) are dispersoid particles that can precipitate in the 3xxx alloys depending on the Si content, homogenization temperature and time. While α-Al(MnFe)Si dispersoid particles precipitate at higher Si levels, the Al_6(MnFe) stable dispersoid precipitates at lower Si additions and increased homogenization temperature and time, respectively [152]. In the 5xxx alloys the Mg additions decrease SF energy and increase the work hardening rate by suppressing dynamic recovery and affect the grain refinement during severe plastic deformation through the accumulation of high density of dislocations [150].

2.1.2.4. The heat treatable aluminum alloys

The heat treatment of cast and wrought Al alloys is intended to modify the structure of an alloy, and controllably influence its physical and mechanical properties to meet specific engineering criteria, such as:

- Increase in hardness,
- Improvement of machinability,
- Wear resistance improvement,
- Strength increase,
- Achievement of mechanical properties specific for a particular material condition,
- Stabilization of mechanical and physical properties,
- Dimensional stability insurances,

- Alteration of electrical conductivity,
- Alteration of corrosion resistance,
- Residual stress relieve.

To achieve any of the criteria annealing, solutionizing, quenching or aging can be utilized.

2.1.2.4.1. Annealing

Annealing is employed to provide alloys with dimensional and physical stability as well as the lowest level of residual stress. The cast Al alloys are annealed to obtain dimensional stability and increase ductility, while annealing of wrought Al alloys assures the lowest strength level. Besides annealing temperature, the efficiency of residual stress reduction is dependent on cooling rate. To prevent stress reintroduction, the alloys are typically cooled from the annealing temperature in the furnace or in still air [96].

2.1.2.4.2. Quenching

Quenching enables the highest possible degree of the solution hardening with the lowest level of induced residual stress and the lowest impact on dimensional stability and distortion. Rapid cooling from solution temperature is critical to obtain metastable, supersaturated solid solution state (SSS) [153]. Lower cooling rates result in slower temperature drop and a rapid precipitation of coarse particles with no beneficial influence on mechanical properties. The cast Al alloys are less sensitive to the lower cooling rates due to coarse structures and longer diffusion times. Even dough quenching has been accomplished in oil, salt and organic baths, the water quenching is most frequently used [154]. The obtained properties significantly depend on the temperature of the quenching medium. The lower temperatures of quenching medium assure higher strength, corrosion, and stress-corrosion resistance but result in higher residual stress and distortion. The obtained combination of properties and degree of distortion of quenched material depend on the heat extraction uniformity. The uniform quenching improves strength, hardness, and ductility [96].

2.1.2.4.3. Solutionizing

The solutionizing heat treatment increase the alloy properties through dissolution of soluble phases and matrix enrichment [154]. The soluble phases form during solidification and processing. The solution heat treatment consists of holding the alloy at a sufficiently high

temperature for a long enough time to obtain maximum amount of soluble elements in matrix to achieve homogeneous solid solution [155]. The degree of solution hardening is determined by the solutionizing temperature. The temperature affects diffusion rates that directly influence the degree of solution. The solid-state diffusion is a function of time at the given temperature. Course microstructure associated with slow solidification rates and high temperature thermo-mechanical processing, require longer soaking times to attain satisfying degree of solution [96]. As indicated in previous chapter, the solid solution hardening is a result of an interaction between the mobile dislocations and the solute atoms.

To reduce dislocation density the wrought Al alloys are often processed in solutionized condition [97]. The solutionizing heat treatment is unstable and applicable only to alloys that strengthen naturally at room temperature over a duration of months or years. Solution heat treatment is followed by natural or artificial aging [156].

2.1.2.4.4. Natural or artificial aging

Natural or artificial aging follows solution heat treatment and quenching enabling Al alloys to achieve wide range of properties. During natural aging, the properties of some Al alloys change at the room temperature as a function of time. Natural aging is a consequence of Guinier-Preston zone (GP) formation within the lattice structure. The GP zones are coherent particles that precipitate from metastable solid solution below the critical temperature that is defined with respect to metastable solvus line of the alloying system [157]. The hardening effect arises from complex interactions between dislocations and GP zones. Depending on dislocation characteristics, orientation between GP zones and dislocations, random particle distribution as well as the critical resolved shear stress (CRSS), interaction between GP zones and dislocations can result in particle shearing or Orowans' loop formation [158].

The process of hardening can be accelerated by artificial aging at temperatures from 90.0 °C to 260.0 °C depending on the chemical composition and desired properties. During artificial aging, the atoms of solute element diffuse from metastable supersaturated solid solution to high energy sites such as dislocations, dislocation tangles, and vacancies [96]. The microstructure development during artificial aging is influenced by [101]:

- Critical temperature,
- Excess vacancies,
- Formation of precipitation free zones (PFZ) at the grain boundaries,
- Double aging treatments,

- Sensitivity to changes in heat treatment.

The phase diagram for the hypothetical A-B system indicating β phase solvus and GP solvus for the concentration (a) is shown in Figure 2.17 a. The influence of equilibrium and excess vacancies on critical temperature is given in Figure 2.17 b.

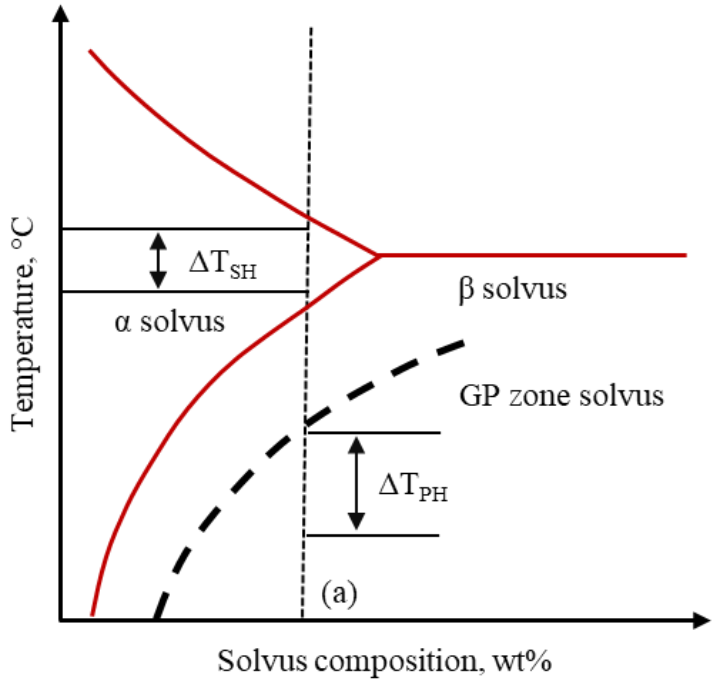

a)

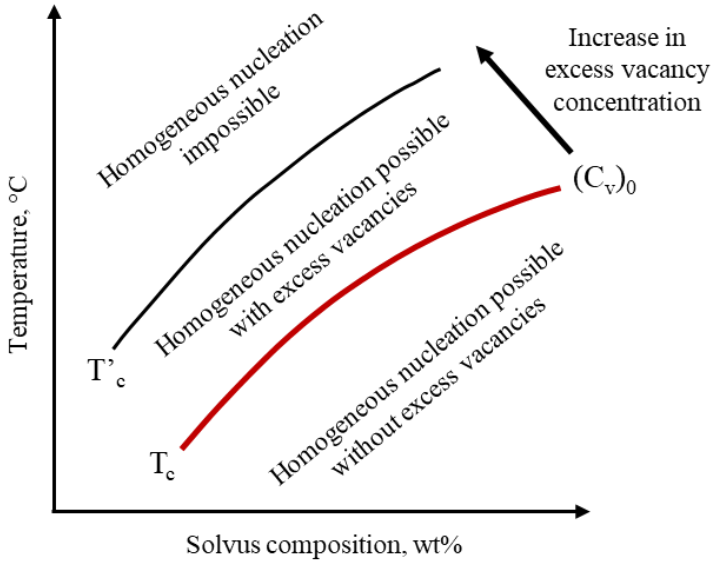

b)

Figure 2.17. The phase diagram for hypothetical A-B system indicating: a) temperature range for solution hardening (ΔT_{SH}) and precipitation hardening (ΔT_{PH}), b) influence of equilibrium (T_C) and excess (T'_C) vacancies on phase nucleation temperature [101]

The critical temperature is defined by the metastable solvus line of the equilibrium diagram. Since the supersaturated solid solution is metastable with respect to GP zones, the selected aging temperature will impact its decomposition and microstructure development (Figure 2.17 a). If the aging temperatures are above the critical, GP zones will not form. At the temperatures below critical, GP zones precipitate as clusters before precipitation of transitional and final structure. The critical temperature is influenced by the vacancy concentration (Figure 2.17 b). Since the vacancies can accelerate the formation of clusters during quenching or act as nucleation sties for precipitation of new phases, increasing the vacancy concentration increases the critical temperature [101].

The PFZ formation has a deleterious effect on Al alloy properties. Due to the lack of precipitates, the PFZ are softer compared to the surrounding matrix and lead to strain localization and fracturing. In the solute depleted PFZs the coarse grain boundary precipitates enable further crack propagation and evolution of low energy layering fracture. Furthermore, the PFZ can increase the susceptibility of age hardened Al alloys to stress corrosion cracking (SCC) [159]. The precipitation free zone can be minimized by lowering the aging temperature. Decreasing the aging temperature increases supersaturation and decreases diffusion rate. Consequently, the age hardening is performed twice. First, the alloys are aged at lower temperatures to increase the density of precipitates and minimize the formation of PFZ. Afterwards, aging is performed at higher temperatures to accelerate the growth of precipitates. This allows for the desired strength levels to be obtained in minimum amount of aging time [101].

The 2xxx, 6xxx and 7xxx wrought Al alloy series are utilized in heat treated condition. The content of alloying elements is in the limits of mutual solid solubility at the temperatures below the eutectic. The heat treatment of wrought Al alloys is used to achieve specific properties needed for further processing or final service applications [160].

The 2xx.x, 3xx.x and 7xx.x series of cast Al alloys are used in heat treated condition. Since some of the 2xx.x and all the 3xx.x series of Al alloys contain amounts of soluble elements that exceed solid solubility limits, the heat treatment will not affect the microstructure development but the phase morphology [161]. In addition to the morphology changes, the heat treatment of cast Al alloys minimizes or eliminates microsegregations and residual stress caused by solidification or quenching, alters morphology of insoluble phases and reduces susceptibility to corrosion [162].

2.2. The influence of alloying elements and impurities on aluminum alloy microstructure and properties

The utilization of Al alloys in different areas of manufacturing and technology is enabled by good combination of mechanical, physical and tribological properties. The high strength and wear resistance, high specific strength and stiffness, high temperature stability, controlled thermal exposure coefficient and improved damping capabilities are significantly affected by chemical composition. The alloying element or combination of alloying elements in conjunction with thermodynamic and processing parameters influence microstructure and substructure development determining the specific properties of an alloy.

The classification of alloying elements is illustrated in Figure 2.18.

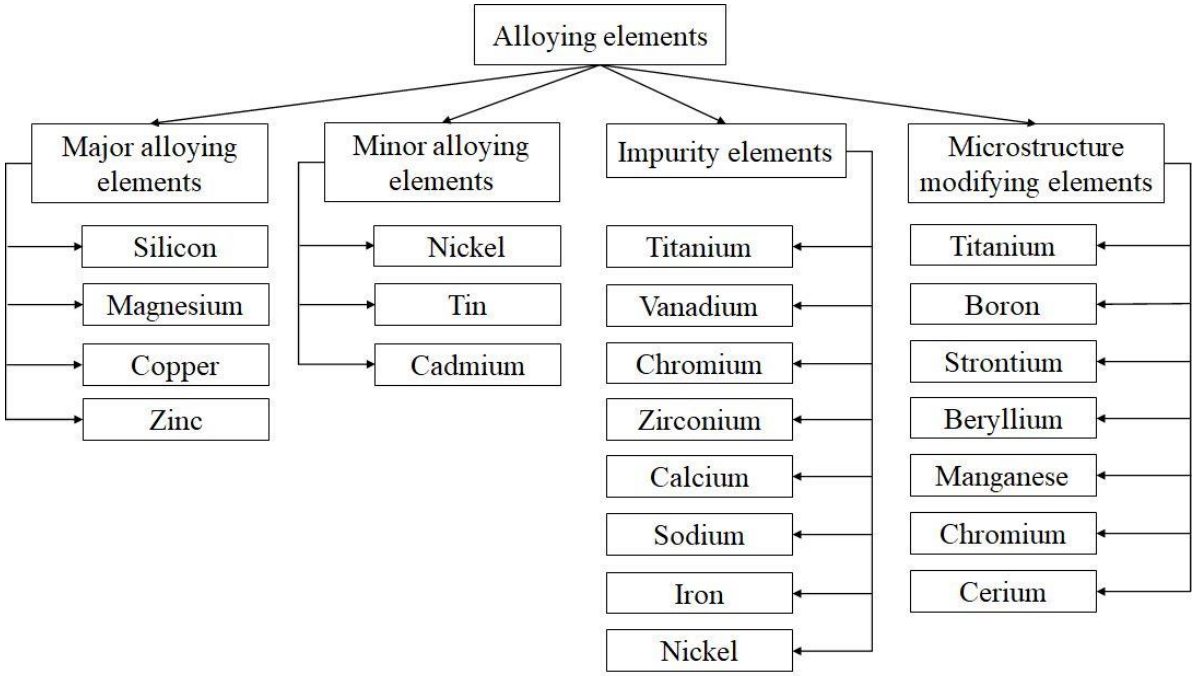

Figure 2.18. The classification of alloying elements based on their effect on Al alloy microstructure development and properties [85]

Silicone, Mg, Cu, and Zn are major alloying elements (Figure 2.18) added to Al alloys in the amounts necessary to define their microstructure and functional properties. Compared to other types of alloying elements, major alloying elements are characterized by higher solid solubility in α_{Al} matrix. Additionally, most industrially used Al alloys contain one or more alloying elements referred to as minor alloying elements or ancillary elements (Figure 2.18). Depending on whether the reaction between Al and these elements is of an eutectic or peritectic nature, their addition can lead to the formation of excess intermetallic phases or a solid solution

[163]. The impurity elements (Figure 2.18) in Al alloys can be present as inclusions or dissolved elements that originate from used raw materials or master alloys, melting unit refractory materials, and melting operations. The utilization of Al scrap accounts for the accumulation of impurities in secondary Al alloys providing a significant, long-term composition barrier in achieving energy and cost savings [164]. The microstructure modifying elements (Figure 2.18), such as Ti, B, Sr, Be, Mg, Cr and Ce, have direct influence on the final microstructure development by affecting the nucleation and growth dynamics of Al-major alloying element or Al-impurity element reactions [165]. Based on alloy composition series and required properties, the alloying elements can be classified differently, as indicated in Figure 2.18.

2.2.1. The major alloying elements

The major alloying elements are added to Al alloys in the amounts necessary to define their microstructure and properties. Since the solid solubility of Mg, Si, Cu and Zn exceeds 1.0 wt%, they are classified as major alloying elements. Contrary, the solid solubility of other alloying elements in Al is lower than 0.1 wt%. The schematic representation of the Al-major alloying element binary eutectic diagram is represented by Figure 2.19 with corresponding parameters indicated in Table 2.3.

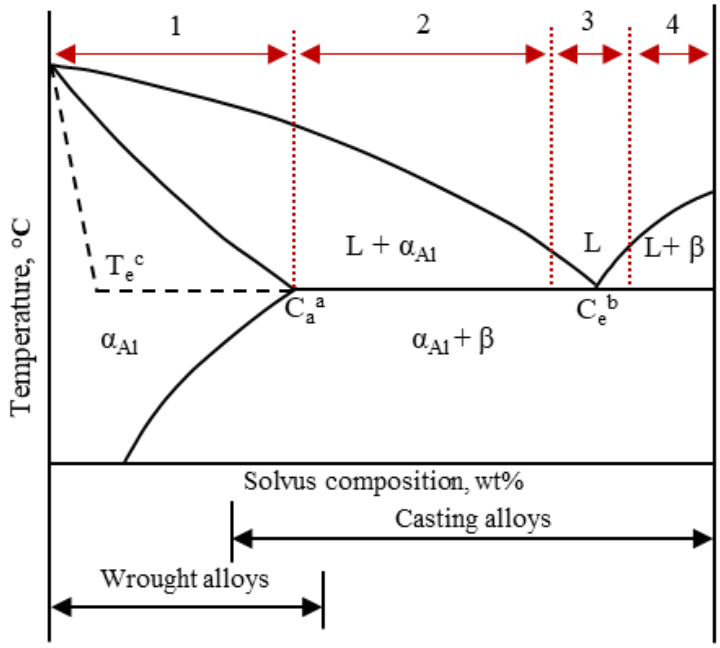

Figure 2.19. The schematic representation of the Al-major alloying element binary phase diagram of eutectic type with indicated classification of Al alloys in as cast condition [163]

According to the Figure 2.19 all industrially utilized Al alloys in as-cast condition can be classified as:

- Solid solution type alloys characterized by non-equilibrium eutectic reaction that can be nullified by solutionizing heat treatment and artificial aging (Figure 2.19, area 1),
- Hypoeutectic alloys that contain two principal microstructure constituents (Figure 2.19, area 2),
- Eutectic alloys with eutectic phase as principal microstructure constituent (Figure 2.19, area 3),
- Hypereutectic alloys with primary crystals of excessive phase (Figure 2.19, area 4).

The classification is applicable to the alloys whit microstructure that can be roughly described by the marked areas in corresponding binary phase diagram (Figure 2.19). However, this type of microstructural classification can be influenced by the presence of other types of alloying elements [163].

Table 2.3. The corresponding parameters for the Al-major alloying element binary eutectic phase diagram [163]

Major alloying element	C_a[a]		C_e[b]		T_e[C]	Phase in equilibrium with α_{Al}
	wt%	at%	wt%	at%	(°C)	
Cu	5.7	2.5	33.2	17.5	547.0	θ (Al_2Cu)
Mg	17.4	18.5	35	36.0	450.0	β (Al_8Mg_5)
Zn	82.0	49.3	94.9	75.0	382.0	primary β_{Zn}
Si	1.65	1.59	12.0	12.0	577.0	primary β_{Si}

C_a[a] Solubility limit at eutectic temperature
C_e[b] Concentration at eutectic point
T_e[c] Solidification temperature of binary eutectic

The main goal of major alloying element additions is to increase strength. The strengthening effect is achieved through solid solution strengthening and aging. The 5xxx and 5xx.x series of alloys containing from 0.5 to 10.0 wt% Mg are strengthened by solutionizing. These alloys often contain microstructure modifying elements such as Cr and Mn. Silicone and Cu are major alloying elements with lower solid solubility in α_{Al} that form second phase precipitates (Table 2.3) [103]. Although the solid solubility of Zn in α_{Al} is 0.85 at% at room temperature [166], its solid solution strengthening effect is minor due to the small atomic radii mismatch factor. Besides strengthening, major alloying elements can influence castability [163]. The castability is the property of an alloy to be cast into a given shape using a given process without the formation of casting defects. The castability is defined by fluidity,

macrosegregations, hot tearing and porosities. It will determine if the alloy can have an industrial application or not [167].

2.2.1.1. Silicon

As a major alloying element Si is used in the majority of cast Al alloys to influence casting characteristics. Addition of Si improves fluidity, resistance to hot tearing, solidification shrinkage and feeding. Higher heat of fusion of Si (50.2 kJ/mol [168]) compared to Al (10.7 kJ/mol [168]) improves fluidity enabling feeding of thin wall castings and production of more intricate casting designs. By expanding during solidification Si prevents formation of solidification shrinkage and hot tearing. High thermal conductivity and low thermal expansion coefficient of Al-Si alloys result from supersaturated solid solution (SSS) formation and precipitation of secondary phases [169]. The schematic representation of Al-Si phase diagram with indicated most frequently used Al-Si alloys is given in Figure 2.20.

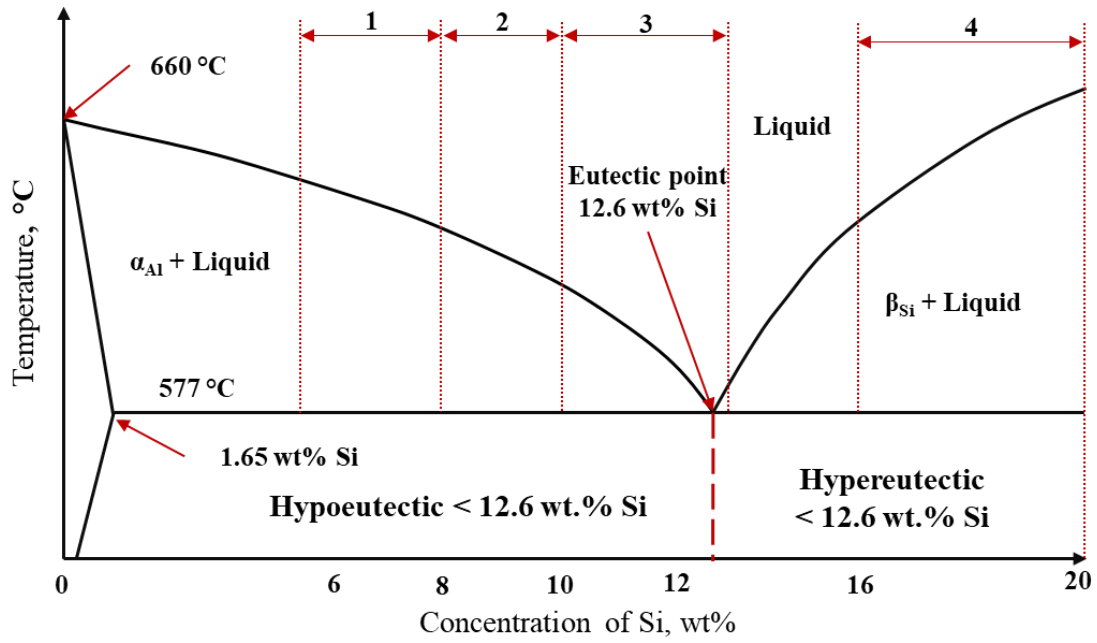

Figure 2.20. Binary Al-Si diagram with indicated frequently used alloys: 1) Hypoeutectic sand and gravity die casting alloys, 2) Hypoeutectic high pressure die casting alloys, 3) Eutectic and near-eutectic alloys: pistons, high-pressure die casting, sand, gravity die casting, 4) Hypereutectic wear-resistant alloys [170]

Based on the Si content (Figure 2.20), binary Al-Si alloys can be classified as [170]:

- Hypoeutectic alloys containing < 12.0 wt% Si,
- Near eutectic alloys containing 12.0 - 13.0 wt% Si,
- Hypereutectic alloys containing 14.0 - 25.0 wt% Si.

The microstructure development of hypoeutectic Al-Si alloy comprehends formation of primary α_{Al} dendritic network from the liquid (L) followed by solidification of eutectic (α_{Al} +β_{Si}) phase. Solidification of eutectic (α_{Al} +β_{Si}) phase in hypoeutectic alloys is a consequence of reduced solid solubility of Si in α_{Al} matrix as well as non-equilibrium solidification conditions. The solid solubility of Si is maximum 1.5 at% at the eutectic temperature of 577.0 °C (Table 2.3.), and decreases to 0.05 at% at 300.0 °C. The solid solubility of Al in Si is at about 0.04 at% [171]. The solidification of near eutectic Al-Si alloys involves solidification of eutectic (α_{Al} +β_{Si}) phase, while the microstructure development of Al-Si alloys with hypereutectic composition initiates with solidification of primary β_{Si} followed by the eutectic (α_{Al} +β_{Si}) phase formation. The solidification of Al-Si alloys containing up to 12.0 wt% Si is characterized by increased solidification time and decreased liquidus temperature. Increasing the Si content above 12.0 wt% increases the liquidus temperature [172]. Besides Si content, the microstructure development and coarsening depend on the cooling rate. At the higher cooling rates the eutectic temperature is depressed and the eutectic point is shifted towards higher Si content. This behavior is explained by the presence of asymmetric coupled zone. Since Si is a nonmetal that grows anisotropically, it requires a higher undercooling compared to the non-faceted α_{Al} phase [173]. The irregular Al-Si eutectic system can grow with a variety of morphologies such as: tin plate or corrugated crystal morphology, irregular plate-like eutectic β_{Si} structure [174], irregular fiber morphology with rounded cross-sections [175].

The microstructure development and eutectic β_{Si} phase morphology are further influenced by superheat of the bulk liquid, undercooling, and the presence of other major alloying elements, microstructure modifiers and impurities [176]. The tensile strength of Al-Si alloys slightly increases with an increase in Si content from 3.0 wt% to 8.0 wt%. The maximum tensile strength values are obtained in the 8.0 wt% Si to 15.0 wt% Si composition range. The increase in tensile strength is related to the preferred solidification of eutectic (α_{Al} +β_{Si}) and primary β_{Si} phase. Further increase in Si content leads to the eutectic (α_{Al} +β_{Si}) coarsening and transition of primary β_{Si} phase from fine star-like to massive plate-like morphology. The microstructure coarsening is followed by decrease in tensile strength, ductility and elongation [177].

2.2.1.2. Magnesium

The Al-Mg alloys are single-phase binary alloys with moderate to high strength and toughness, work hardening characteristics, good corrosion resistance and weldability [96]. The

5xxx series of Al alloys contains from 1.0 wt% to 5.0 wt% Mg while 5xx.x cast Al alloys contain between 5.0 wt% and 10.0 wt% Mg. Both wrought and cast Al-Mg alloys are used without precipitation hardening treatment. The Al alloys with Mg content ≥ 10.0 wt% are utilized after solution heat treatment [178]. The maximum solid solubility of Mg in α_{Al} matrix reduces from 18.5 at% at the eutectic temperature of 450.0 °C (Table 2.3) to 1.4 at% Mg at room temperature [179] having a high solid solution strengthening effect [163]. As a stable eutectic phase with a maximum composition range between 38.5 at% and 40.3 at% Mg, the Al_8Mg_5 (β) solidifies from liquid (L) at the eutectic temperature. Due to the similarities in Mg content between L (38.0 at% Mg) and β phase (38.5 at% Mg) the congruent melting point is registered at 451.0 °C [180]. The solidification of eutectic β phase is preceded by solidification of metastable phases as indicated by the equation (1) [181].

$$SSS \rightarrow \text{GP zones} \rightarrow \beta'' \ (Al_3Mg) \rightarrow \beta' \left(Al_8Mg_5\right) \rightarrow Al_8Mg_5(\beta) \quad (1)$$

The metastable Guinier-Preston (GP) zones with $L1_2$ superstructure and stoichiometry of 25.0 at% Mg can precipitate from supersaturated solid solution (SSS) containing 16.0 at% Mg at 110.0 °C or at 80.0 °C from SSS containing 13.0 at% Mg, respectively [180]. The metastable needle-like (Al_3Mg) β'' phases [182], also known as GP-II zones, can form through the transformation of spherical GP zones at approximately 180.0 °C and 260.0 °C [183]. The transformation of needle-like Al_3Mg (β') zone structure to Widmannsttäten Al_8Mg_5 (β') structure was observed at 150.0 °C. The Al_3Mg (β') phase needle-like morphology is obtained during isothermal aging at 150.0 °C. The transformation of metastable Al_3Mg (β') phase to stable Al_8Mg_5 (β) phase is obtained during artificial aging at 150.0 °C with extensive holding time [181]. The coarse eutectic Al_8Mg_5 (β) phase solidifies between the branches of α_{Al} dendritic network and at the α_{Al} grain boundaries forming a continuous network [184]. As a hard and brittle precipitate, Al_8Mg_5 (β) phase has no beneficial influence on mechanical properties [185]. The mechanical properties, electrical and thermal conductivity are further impacted by Al_8Mg_5 (β) phase martensitic transformation from complex fcc structure to the structure of lower symmetry. The martensitic transformation occurs at 240.0 °C for 37.5 at% Mg and at 10.0 °C for 39.7 at% Mg, respectively [180]. In Al-Si and Al-Si-Cu alloys Mg is used to increase strength, hardness and ductility through the solid solution strengthening and transformation of Al_3Mg (β') phase. To achieve the suitable combination of mechanical properties the cast components are subjected to solid solution strengthening and artificial aging. The solution heat treatment is used to influence the eutectic ($\alpha_{Al} + \beta_{Si}$) morphology and enrich

α_{Al} matrix by dissolving coarse eutectic Al_8Mg_5 (β) phase. The precipitation hardening is achieved by precipitation of Al_3Mg (β') phase during artificial aging from SSS [186].

2.2.1.3. Copper

The Al and Cu single-phase eutectic system is formed in the composition range between 0.0 and 53.0 wt% Cu. The eutectic Al_2Cu (θ) phase solidifies at 520.0 °C from the liquid (L) containing 33.2 wt% Cu (Table 2.3). The mechanical properties of Al-Cu alloys are determined by the growth, morphology, size and distribution of eutectic Al_2Cu (θ) phase has a significant effect on the mechanical properties [187]. The Al_2Cu (θ) phase often appears as a part of two-phase heterogeneous structure (α_{Al} + Al_2Cu (θ)) usually designated as eutectic constituent. Its lamellar morphology is a consequence of heterogeneous and epitaxial nucleation of α_{Al} on previously solidified Al_2Cu (θ) phase. The morphology of eutectic (α_{Al} + Al_2Cu (θ)), the spaces between the primary phases (lamellas of α_{Al} and Al_2Cu (θ)) and the appearance of degenerated eutectic (α_{Al} + Al_2Cu (θ)) morphology are influenced by chemical composition, cooling rate [188] and the presence of other intermetallic phases [189]. At the intermediate temperatures, the metastable transitional phases can precipitate from SSS, as indicated by Figure 2.21.

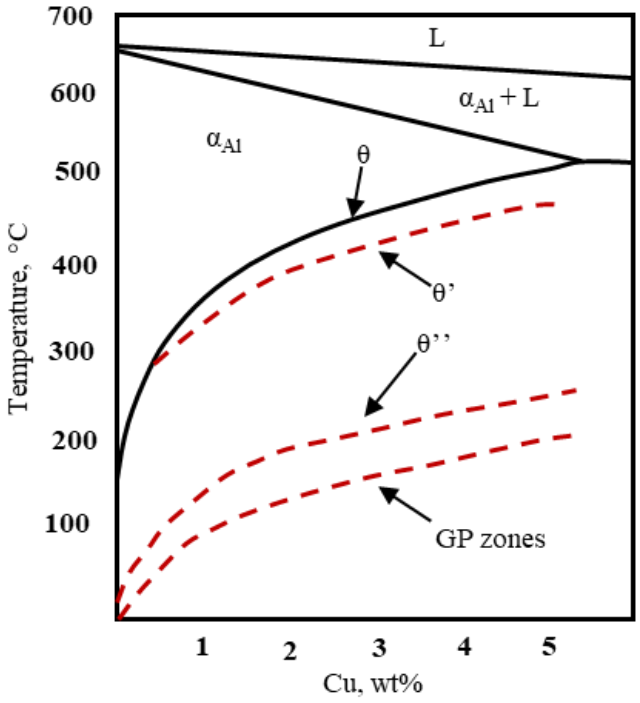

Figure 2.21. The binary Al-Cu phase diagram with indicated metastable phase formation [190]

The precipitation sequence comprehending metastable phase formation is shown by the equation (2):

$$SSS \rightarrow GP\ zones \rightarrow Al_3Cu(\theta'') \rightarrow Al_2Cu(\theta') \rightarrow Al_2Cu(\theta) \quad (2)$$

In the temperature range from room temperature to 150.0 °C the coherent Cu-rich Guinier-Preston zones precipitate from the supersaturated solid solution (SSS) (Figure 2.21). The GP zones are only one layer tick and have a highly strained coherent phase boundary with the α_{Al} matrix. The Al_3Cu (θ'') phase (also known as GP-II) has a fcc superlattice structure coherent with α_{Al} matrix and precipitates between 80.0 °C to 200.0 °C (Figure 2.21) [184]. Although both, GP zones and Al_3Cu (θ'') phase have plate-like morphology, the Al_3Cu (θ'') phase has larger particle size. The increase in Al_3Cu (θ'') phase particle size is connected to the increase in Cu layer number. While GP zones consist of Cu monolayer along {100} direction, in Al_2Cu (θ') zones two layers of Cu are separated by three plates of Al, respectively. Due to the influence of interfacial energy at GP/θ''/α_{Al} matrix interface, the equilibrium Cu content of the layers is 100.0 % [191]. The partially coherent Al_2Cu (θ') phase precipitates at approximately 250.0 °C [184]. In the Al-Cu system, the Al_2Cu (θ') phase is one of the most common and effective strengthening precipitate. Its strengthening potential originates from plate-like morphology with high aspect ratio [192]. This significant difference between the thickness (1.0 - 10.0 nm) and length (0.1 - 1.0 μm) establishes two different crystallographic orientations [193]:

- Coherent one on the broad side of the particle,
- Semi-coherent around the particle's rim.

Since it in part determines the height of the nucleation energy barrier and density of nuclei, the interfacial energy determines the size and distribution of the Al_2Cu (θ') particles. The transformation of Al_2Cu (θ') phase to Al_2Cu (θ) phase is followed by decrease in hardness [194]. The incoherent equilibrium Al_2Cu (θ) phase precipitates at the temperatures above 300.0 °C [184]. The precipitation of Al_2Cu (θ) phase is a consequence of high Cu content and over-ageing. Due to its coarse morphology Al_2Cu (θ) phase decreases the ductility of an alloy by acting as void/crack initiation site or enabling the preferred crack propagation direction. Additionally, coarse particles consume the large amount of Cu from SSS preventing the precipitation of strengthening phases during artificial aging. The negative effect of Al_2Cu (θ) phase can be neutralized through the solutionizing or cold plastic deformation processing [195].

2.2.1.4. Zink

Zink has the highest solid solubility in Al. The solubility of Zn in α_{Al} increases from 2.2 at% at 110.0 °C, to 16.5 at% at the eutectoid temperature of 277.0 °C. At the temperatures above eutectoid the solvus curve lies on the Zn-side of the fcc miscibility gape increasing the Zn content to 59.0 at%. At the eutectic temperature of 381.0 °C the amount of Zn increases to 67.0 at% (Table 2.3) [196]. Due to the atomic mismatch of only 7.0 % between the atoms of Al (with atomic radius of 0.143 nm) and Zn (with atomic radius of 0.134 nm) the formation of intermetallic phases in binary Al-Zn alloys is not expected [166]. Instead, the α_{Al} solid solution has extended composition range, interrupted by fcc miscibility gap. The solidification sequence comprehends the eutectic reaction at 381.0 °C resulting in the solidification of Zn enriched (α_{Al}') and solid solution of Zn (β_{Zn}), and the eutectoid reaction at 277.0 °C leading to the precipitation of α_{Al} and β_{Zn} from α_{Al}' [196]. The fcc miscibility gap refers to the spinodal decomposition of supersaturated solid solution (SSS) into the α_{Al} and Zn enriched α_{Al}' at the critical point of 351.0 °C [197]. The spinodal decomposition is driven by the changes in chemical composition, rather than nucleation. Although, formation of stable phases is not recognized in binary Al-Zn alloys, the metastable Guinier-Preston (GP) zones and distorted plate-like GP zones were identified as transitional phases for precipitation of α_{Al}' and β_{Zn} during heat treatment of hypoeutectic Al-Zn alloys [198]. The metastable phase formation during aging of Al-Zn alloys depend on the Zn content, homogenization temperature, quenching rate and processing [196].

Since the additions of Zn exert a very minor solid solution strengthening because of the small atomic radii mismatch factor, no significant improvement of mechanical properties can be obtained. However, with combined additions of Cu and Mg the high strength alloys can be produced. These alloys need to be artificially aged to assure the stability of mechanical properties. Precipitation hardening at lower temperatures reduces the corrosion stability [97].

2.2.2. The minor alloying elements

In addition to the major alloying elements, most industrial Al alloys contain one or more alloying elements that are usually considered as minor or ancillary. The concentration of minor alloying elements is typically in the order of 0.001 wt% to 0.01 wt%. The interaction between Al and minor alloying elements results in the formation of eutectic (Figure 2.19) or peritectic type of diagrams (Figure 2.22). The elements of eutectic type have low solid solubility

in α_{Al} (maximum ≈ 0.01 - 0.03 %) and do not form supersaturated solid solution (SSS) even after relatively rapid solidification. Their addition causes formation of excess phases that often reduces formability and corrosion resistance. The solid solubility of peritectic type elements in α_{Al} matrix is ≈ 0.1 wt% with tendency to increase significantly during non-equilibrium solidification. Under these conditions, the solubility of the peritectic type elements can increase significantly as a consequence of the Al corner transformation into the cigar-shape phase diagram (Figure 2.22) [163].

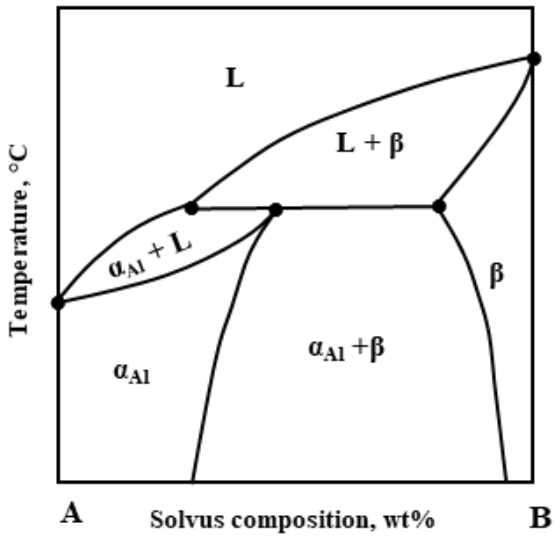

Figure 2.22. The schematic representation of the Al-minor alloying element (β) binary phase diagram of peritectic type [163]

2.2.2.1. Nickel

The solid solubility of Ni in Al does not exceed 0.04 at%. At the additions higher than its solid solubility, Ni is present as insoluble intermetallic precipitate of $AlNi_3$, AlNi, Al_3Ni_2, Al_3Ni, Al_3Ni_5 and Al_4Ni_3 types [199]. High strength properties of binary Al-Ni alloys and their stability at elevated temperatures is caused by solidification of $AlNi_3$ phase with $L1_2$ structure that remains coherent with α_{Al} matrix at elevated temperatures [200]. In high purity Al alloys, Ni has beneficial influence on strength properties, but reduces ductility. The Ni additions to Al-Cu and Al-Si alloys improve hardness and strength at elevated temperatures and reduce coefficient of thermal expansion [103]. The beneficial influence of Ni on the mechanical properties of the Al-Cu-(Ni) and Al-Si-(Ni) alloys originates from the solidification of eutectic (α_{Al} + Al_3Ni) phase [201], and precipitation of Al_3Ni_2, Al_3CuNi phase [202].

2.2.2.2. Tin

The Al-Sn based alloys, also known as "*soft tribological alloys*" contain up to 25.0 wt% Sn [103]. The Al alloys containing Sn are frequently used in transportation as sliding bearing materials for supporting the reciprocating rotation of the crankshaft in internal combustion engines owing to its excellent friction and wear properties. The excellent tribological properties are obtained when soft Sn-rich phase solidifies homogeneously distributed in α_{Al} matrix promoting the formation of protective surface film [203]. However, the Al-Sn alloys conventionally produced by casting cannot satisfy the high loud requirements. Lower strength and hardness originate from near-continuous large Sn zone formation around the Al grains weakening the interface bounding [204]. The mechanical properties can be improved through additional alloying or processing. The modification of chemical composition comprehends the addition of Si, Cu, Mg [205], while processing modification includes stir casting, rapid solidification, physical vapor deposition, severe plastic deformation and powder metallurgy [206]. In the amounts of 0.03 wt% Sn increases response of wrought Al alloys to artificial aging impacting strength and hardness. If the small additions of Mg are present, the artificial aging characteristics are reduced due to the precipitation of noncoherent secondary Mg_2Sn phase [207]. As little as 0.01 wt% Sn in commercial pure Al will cause surface darkening during annealing and increase the corrosion susceptibility. The segregation of Sn can be reduced by the small additions of Cu. The Al-Zn alloys with small additions of Sn can be used as sacrificial anodes in salt water environment [103].

2.2.2.3. Cadmium

As a low-melting minor alloying element Cd has a limited application in Al alloys. At the additions up to 0.3 wt% Cd may be added to Al-Cu alloys to increase strength and corrosion resistance by accelerating the age hardening. The accelerated hardening kinetics and increase in peak hardness during aging are achieved through the Cd interaction with vacancies and changes in Guinier-Preston (GP) zone formation [208]. Consequently, the amount of strengthening precipitates, mainly Al_2Cu (θ'), increases [209]. The additions of 0.1 wt% Cd to the Al-Zn-Mg alloys reduces aging time and improves free-cutting characteristics. The machinability of Al alloys can be improved by the addition of 0.1 wt% Cd. The use of Cd as an alloying element is limited due to its oral toxicity [103].

2.2.3. The impurity elements

Impurity elements are introduced to Al alloys during melting and processing. The used raw materials and melting unit refractory materials are considered to be major sources of impurity elements in the production of primary Al [210]. The significant amount of impurity elements represents the obstacle in the utilization of secondary Al and Al alloys [211]. The impurities can have a detrimental effect on the Al production process and alloy properties, as indicated by Table 2.4.

Table 2.4. The effect of impurity elements on Al production process and Al alloy properties [212]

Impurity elements	Effect on production process and Al alloy properties
Titanium Vanadium Chromium Zirconium	Negatively impact electrical conductivity Reduce cold working properties
Calcium Sodium	Contaminate electrolyte in the Hall-Héroult process Cause fabrication defects and hot cracks in cast Al alloys
Iron Nickel	Act as stress raiser and points of week coherence Reduce corrosion resistance

2.2.3.1. The titanium, zirconium, vanadium, and chromium impurities

The electrical conductivity and cold working properties of Al and Al alloys deteriorate with the presence of transition metal impurities such as Ti, Zr, V and Cr. In the Al of commercial purity produced by Hall-Héroult process these impurities originate from raw (bauxite, pitch, and petroleum coke) and cell materials (carbon cathodes, linings, furnaces, ladles, and launders linings) that meet molten Al during different stages of treatment and processing. The impact of transition metal impurities on the electrical resistivity is given in Table 2.5.

Table 2.5. The solubility of transitional metal impurity and their effect on the electrical conductivity of aluminum [213]

Element	Maximum solid solubility in α_{Al} matrix, wt%	Average increase in resistivity, $\mu\Omega \cdot cm$	
		In solid solution	As precipitate
Vanadium	0.50	3.58	0.28
Zirconium	0.28	1.74	0.044
Titanium	1.00	2.88	0.12
Chromium	0.77	4.00	0.18

The electrical resistivity presented in Table 2.5 indicates that transition metal impurities have more pronounced effect on the conductivity when they are dissolved in the α_{Al} solid solution [214]. This increase in electrical resistivity of impurity enriched α_{Al} solid solution is a consequence of the electron scattering due to discontinuities in the atomic crystal structure referring to the thermal vibrations, solutes, and crystal defects [215]. Vanadium and Cr have the most significant impact on the electrical resistivity increasing it by the factor of 10 to 20 when present in the α_{Al} solid solution (Table 2.5) [214]. The negative impact of transition metal impurities can be mitigated through the addition of Al-B master alloy during melt treatment and processing. In this process the transition metal impurities react with AlB_2 and AlB_{12} particles present in the Al-B master alloy to form stable solid zirconium diboride (ZrB_2), vanadium diboride (VB_2), titanium diboride (TiB_2), and chromium diboride (CrB_2). Since these solid borides are heavier compared to molten Al, they can be effectively separated using gravity settling [216].

2.2.3.2. The calcium and sodium impurities

Both Ca and Na contaminate electrolyte in Hall-Héroult process of primary Al production. The excess Ca originates from sponge coke treatment. Despite its beneficial influence on lowering the operating temperature and reducing the fraction of hard crust, excess Ca has a negative impact on specific gravity of the electrolyte. By reducing the density-based separation between liquid bath and liquid metal, Ca leads to the back-reactions and increases impurity content. Furthermore, calcium fluoride (CaF_2) carries Ca from the electrolyte into the newly produced anode, where it increase CO_2 reactivity and contributes to the higher amounts of anode dusting in reduction cells [217]. The major sources of Na in reduction cells are calcinated petroleum coke, smelter-grade alumina produced by refiners, aluminum fluoride (AlF_3) and sodium carbonate or soda ash (Na_2CO_3). Sodium limits pot life and affects energy consumption by depositing into the cathodes and leading to the cathode swelling, cracking, and damaging. Sodium primarily enters anodes with butts that have not been thoroughly cleaned during the brief period when anodes come into contact with liquid metal or are not electroactive [218]. Primary Al siphoned from reduction cells typically contains between 0.005 % and 0.02 % Na. Elevated Na content in primary Al poses a risk to the holding furnace refractory linings by chemical attack. The sodium concentrations over 0.0006 wt% can lead to the billet surface defects in 6xxx series of Al alloys. Above 0.0002 wt% concentration, Na can cause 5xxx series slabs to suffer edge cracking during rolling [217].

2.2.3.3. The nickel impurities

Although, there is no chemical composition limit specifically referring to the Ni content, the amount of Ni impurities in the commonly utilized Al alloys should not exceed 0.05 wt% for unspecified other elements. The issue of the increasing content of Ni impurities originates from the use of green coke in the anode production process [219]. The negative impact of Ni impurities on ductility and corrosion resistance is achieved through its interaction with Fe and precipitation of AlFe(Si)-based intermetallic compounds on the grain boundaries. The type of precipitated intermetallic compounds depends on Ni impurity content and metallurgical condition. The Al_m(Fe, Mn) and Al_6(Fe,Mn) are dominant Fe-based intermetallic compounds precipitating during solidification of the alloys containing 0.015 %, 0.02 % and 0.05 % Ni [163]. In the homogenized microstructure of the alloy containing 0.015 % Ni, the Al_6(Fe,Mn), Al_3Fe and α-Al_8Fe_2Si can be found. Increasing the Ni impurity content to 0.05 % reduces the number of intermetallic phases in the homogenized condition to Al_3Fe and α-Al_8Fe_2Si. The solutionizing heat treatment and artificial aging (T6) lead to the precipitation of α-Al_8Fe_2Si, β-Al_5FeSi and π-AlFeSi phases in the alloys containing ≥ 0.02 % Ni. The preferred precipitation of β-Al_5FeSi is expected in the alloys with Ni impurity content < 0.02 % in T6 condition. Even though, it is possible to achieve more compact morphology of AlFe(Si) precipitates using heat treatment, their presence has a negative impact on ductility and corrosion resistance [210].

2.2.3.4. The iron impurities

As a major impurity element in cast Al alloys, Fe is frequently acquired at the levels of 0.4 wt% to 0.8 wt% during melting and casting [220]. Although the presence of Fe prevents die soldering in high pressure die castings, the excess amount of iron negatively affects the mechanical properties of Al-Si, Al-Si-Cu and Al-Si-Mg cast alloys [221]. To prevent soldering effect and produce defect-free castings without short end-of-life, the Fe must be maintained at or slightly above its saturation point in the liquid Al. Despite its high solubility in liquid Al, Fe has a low solubility in α_{Al} aluminum solid solution of 0.052 wt%. As a result, Fe tends to form intermetallic compounds of various types [222]. Taking into account phase transformation and solidification in liquid and solid state, the Al_3Fe, α-Al_8Fe_2Si, β-Al_5FeSi, γ-Al_3FeSi and δ-Al_4FeSi_2 are five main Fe-rich intermetallic phases that can be encountered in Al-Si, Al-Si-Cu and Al-Si-Mg alloys. The δ-Al_4FeSi_2 phase solidifies in aluminum alloys with silicone content

of 14.0 wt%, while γ- Al_3FeSi phase is present in alloys with high Si (12.5 wt%) and Fe (7.5 wt%) content [223]. The thermodynamic stability of α-Al_8Fe_2Si phase is only achieved in high purity Al-Fe-Si alloys. The presence of other alloying elements, such as Mg, Cr and V, introduce changes into the lattice of α-Al_8Fe_2Si phase originating from substitution of Fe with other alloying elements as well as a mutual substitution of Si and Al atoms [224]. The β-Al_5FeSi intermetallic phase solidifies during pre-eutectic reaction in liquid/solid range. The brittle β-Al_5FeSi intermetallic phase has needle-like or plate-like morphology. This type of morphology acts as a crack initiator negatively affecting mechanical properties and castability [225]. Poor castability increases the content of shrinkage porosities. The β-Al_5FeSi intermetallic phase increases the porosity content by blocking dendritic flow and therefore acting as a nucleation site. Also, β-Al_5FeSi intermetallic phase enables growth of large Al-Si eutectic grains. Neutralizing negative effect of β-Al_5FeSi intermetallic phase comprehends modification of its needle-like morphology to more compact Chinese script morphology. This is achieved by adding soluble microstructure modifying elements such as Mn, Cr, Be or Sr [226].

2.2.4. The microstructure modifying elements

The microstructure modification of Al alloy comprehends the addition of:

- Ti, B, Zr, Mo, Sn, Cr to refine the grain size,
- Sr, Na, Ca, Ba to impact the eutectic β_{Si} morphology,
- Mn, Cr, Be, Sr to transform the β-Al_5FeSi phase needle-like morphology.

2.2.4.1. Microstructure modification through the grain refinement

Grain refinement is a microstructure modification technique that simultaneously improves soundness, strength, and ductility of metallic materials. The Hall-Petch relation theoretically explains the increase in strength at room temperature caused by grain refinement (Equation 3).

$$\sigma_y = \sigma_0 + k_y \cdot d^{-\frac{1}{2}} \tag{3}$$

where σ_y is the yield strength, σ_0 is a material constant referring to the starting stress for dislocation movement, k_y is the strengthening coefficient specific to the observed material and d is the average grain diameter [227].

In its initial formation Hall-Petch relation was used to express the dependency of the lower yield in Fe and to calculate the dependency of fracture stress on the gran size. Later, it was used to estimate the effect of the grain size on yield strength, yield stress and hardness of other polycrystalline materials and alloys. The Equation 3 indicates yield strength of polycrystalline materials as a result of two basic factors [228]:

- The flow stress of the grain interior (σ_0),
- The resistance to dislocation movement caused by the presence of the grain boundaries ($k_y \cdot d^{-\frac{1}{2}}$).

The common explanation of Hall-Petch relation originates from dislocation pileup theory. In this theory the grain boundary represents an obstacle for dislocation movement. Dislocation emitted from a source, moves along the same slip plane, and propagates towards the grain boundary. Once the leading dislocation is stopped by an obstacle, the trailing dislocation is retarded by mutual repulsion. As dislocation pileup forms, the force exerted on the grain boundary eventually exceeds its strength causing the polycrystalline material to yield [229]. Since material yielding and crack nucleation are influenced by the type of grain boundaries (previously described in 2.1.2.3. The non-heat treatable aluminum alloys), the Hall-Petch relation needs to be modified to include gran boundary geometry (Equation 4):

$$\sigma_f = \sigma_0 + k_2 \cdot D_B^{-\frac{1}{2}} \tag{4}$$

where D_B is grain boundary spacing and k_2 is a constant related to the grain boundary angle [228].

The empirical values of Equations 3 and 4 have led to the extensive research and development to increase yield strength of polycrystalline materials by refining their grain size [230].

The grain refinement of Al alloys has primarily been aimed at improving the soundness of cast Al alloys. Although many new techniques, such as the electromagnetic vibrational method and rapid solidification have been developed, adding grain refiners as nucleates (or inoculants) remains the most common method of refining the grain structure of Al alloys during solidification [231]. The addition of inoculants containing potent nuclei particles promotes formation of fine equiaxed microstructure by deliberately suppressing the growth of columnar

and twin columnar grains. The large grain castings have poor castability and mechanical properties compared to the fine equiaxed grain castings.

The most commonly used commercial master alloys are based on the Al-Ti-B and Al-Ti-C [227] systems. These master alloys are added at levels that result in the Ti concentrations below peritectic composition of 0.15 wt% Ti (Figure 2.23). While Al_3Ti represents the nucleant at the hyperperitectic Ti concentrations, the grain refining mechanism occurring at the hypoperitectic compositions remains unclear (Figure 2.23) [231].

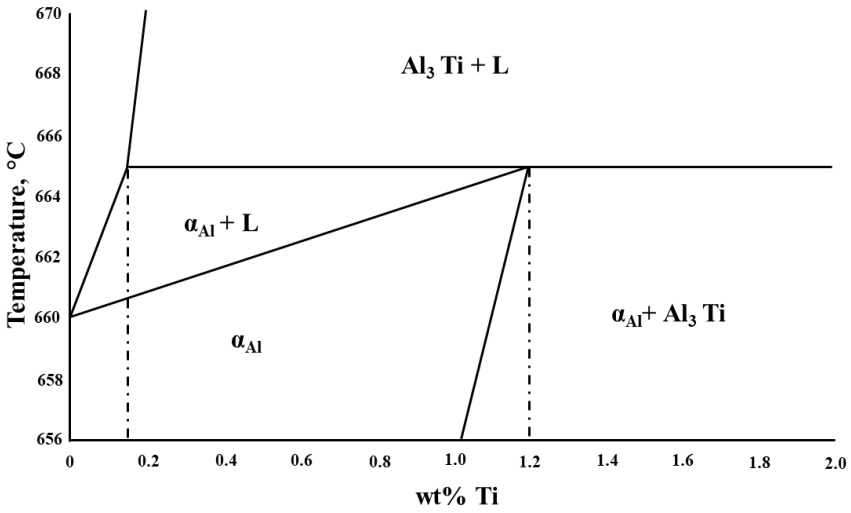

Figure 2.23. The Al rich corner of Al-Ti diagram with indicated peritectic concentration of 0.15 wt.% Ti [232]

Furthermore, it is believed that other solute elements like Zr, Mo, Sn and Cr can also produce effective grain refinement in Al alloys [214]. The grain refining paradigms and theories based on nucleation and solute element effects are summarized in Table 2.6.

The nucleation paradigm indicates that greater number of nucleation sites will result in finer grain size and comprehends the nucleation particle theories and phase diagram theories. The two strands of nucleation paradigm theories are related to two types of particles present in the Al-Ti-B master alloys. The particle theories or boride theories suggest that nucleation occurs on the borides from the master alloy, while phase diagram theories comprehend the nucleation on Al_3Ti properitectic phase particles. The theories developed to satisfy the nucleation paradigm are (Table 2.6):

- Other particle theory,
- The peritectic hulk theory,
- The hypernucleation theory,
- The duplex nucleation theory.

Since Al_3Ti is a much better nucleant compared to the TiB_2, the other particle theory assumes that the addition of B decreases the dissolution rate of aluminides (Table 2.6). This has been proposed to occur by the sheathing of the aluminides by borides [232]. However, further investigations have suggested that the addition of B has little or no effect on dissolution behavior of the aluminides [233]. This assumption led to the development of the high-energy plane theory based on the preferred nucleation on the high-energy planes that are present on the surface of duplex particles. This theory could only be possible for hyperperitectic concentrations (Figure 2.23) due to the quick dissolution of aluminides at the lower additions of Ti [234].

Table 2.6. The summery of grain refining paradigms and theories [214, 219]

Paradigm	Theory	Nucleating substrate	Effect of solute on grain refining performance
Nucleation	The other particle	Occurs on TiB_2, AlB_2, $(Al,Ti)B_2$, TiC	Nucleation of other type of particles such as borides [235]
	The peritectic hulk	Occurs on the Ti rich boride shell	Ti is present in the boride shell after Al_3Ti dissolution at the peritectic concentrations
	Hypernucleation	Peritectic reaction on borides	The Ti segregation provides suitable interface for nucleation of α_{Al}
	Duplex nucleation	Occurs on Al_3Ti that is formed on TiB_2 particles	The segregating Ti forms Al_3Ti on the surface of TiB_2 that is used to nucleate α_{Al}
Solute		Borides or other particles	The presence of solute elements causes constitutional undercooling in the solidification front affecting the subsequent nucleation behavior.

The peritectic hulk theory assumes that the dissolution of aluminides is slowed by the boride shell formation (Table 2.6.). Consequently, diffusion needs to proceed through the boride shell leaving a cell of liquid with approximately peritectic composition. Afterwards, the peritectic reaction initiates the formation of α_{Al} grains [232]. This theory does not seem possible because Al_3Ti particles still dissolve quickly at high temperatures, even with borides present in the master alloy [236]. This theory was further challenged after it was experimentally determined that the number of re-melting and re-solidification did not affect the grain refinement efficiency. If the peritectic hulk mechanism was occurring, the decrease in the grain refinement efficiency would be expected as a consequence of Ti diffusion from the bulk liquid [237].

The atomic size of the solute elements is a key factor in the hypernucleation theory (Table 2.6). The solute elements segregate to the melt/inoculant interface creating the stable pseudocrystals at the temperatures above principal liquidus of the melt. Immediately below the liquidus temperature these pseudocrystals allow α_{Al} to nucleate and grow without undercooling [232]. From a thermodynamic point of view, the hypernucleation theory does not seem probable because the chemical potential and the activity gradient are constant under equilibrium conditions [238].

The duplex nucleation theory is the most recent and the most attractive of all the nucleation paradigms and it is based on the formation of surface layer around the TiB_2 particles. At both hyperperitectic and hypoperitectic concentrations of Ti, the surface layer was identified as Al_3Ti. While the formation of surface layer in the alloys with hyperperitectic composition is connected to the excess Ti additions, the formation of surface layer for the hypoperitectic composition is still unclear. Earlier versions of duplex nucleation theory were based on the assumption that the role of the borides is to enable peritectic nucleation through the shift in the peritectic composition [232]. Later, the peritectic nucleation was linked to the establishment of the local equilibrium near the borides because of the Ti segregation gradient. Unfortunately, the establishment of the local equilibrium near the borides was refuted by the results of temperature measurements, which indicated that the nucleation and growth temperature of the hypoperitectic alloying system correspond to the Al-Ti liquidus line rather than the temperature of peritectic reaction. Moreover, the existence of Ti segregation gradient was never confirmed [237].

Although various theories of the nucleation paradigm have not fully explained the origin and role of Al_3Ti, they have indicated that borides directly or indirectly act as the nucleation sites [232].

The shift from nucleation to solute paradigm occurred because it was realized that grain refinement could not be explained without the influence of segregating elements on constitutional undercooling and dendrite growth. This was especially evident in trying to understand grain refinement of cast Al alloys in isolation from chemical composition. The solute paradigm proposes that segregating elements such as Ti, Si, Zr, Mo, Sn, and columbium (Cb) influence grain growth rate and produce undercooling needed for TiB_2 to become a suitable nucleant for α_{Al}. By restricting the grain growth rate, solute elements provide longer time for nucleation to occur enabling spontaneous and unidirectional solidification. The constitutional undercooling activates the nuclei in front of the solidification interface preventing further grain growth. This explains why it is necessary to have both nuclei particles and

segregating elements in order to achieve successful grain refinement. Since there are no segregating elements in pure Al, one of the requirements for effective grain refinements is not met. But when solute elements are present, borides become an effective nucleus due to the constitutional undercooling. On the other hand, the aluminides are considered to be good nucleants whit or without solute being present, because the Al_3Ti will begin to dissolve at liquidus temperature producing the solute Ti needed for effective grain refinement [232].

Figures 2.24 a to d show the impact of TiB_2 addition on the grain refinement of 99.97 % pure Al, while Figure 2.24 e illustrates the impact of 0.01 % solute Ti on grain refinement of Al containing 0.03 wt% TiB_2.

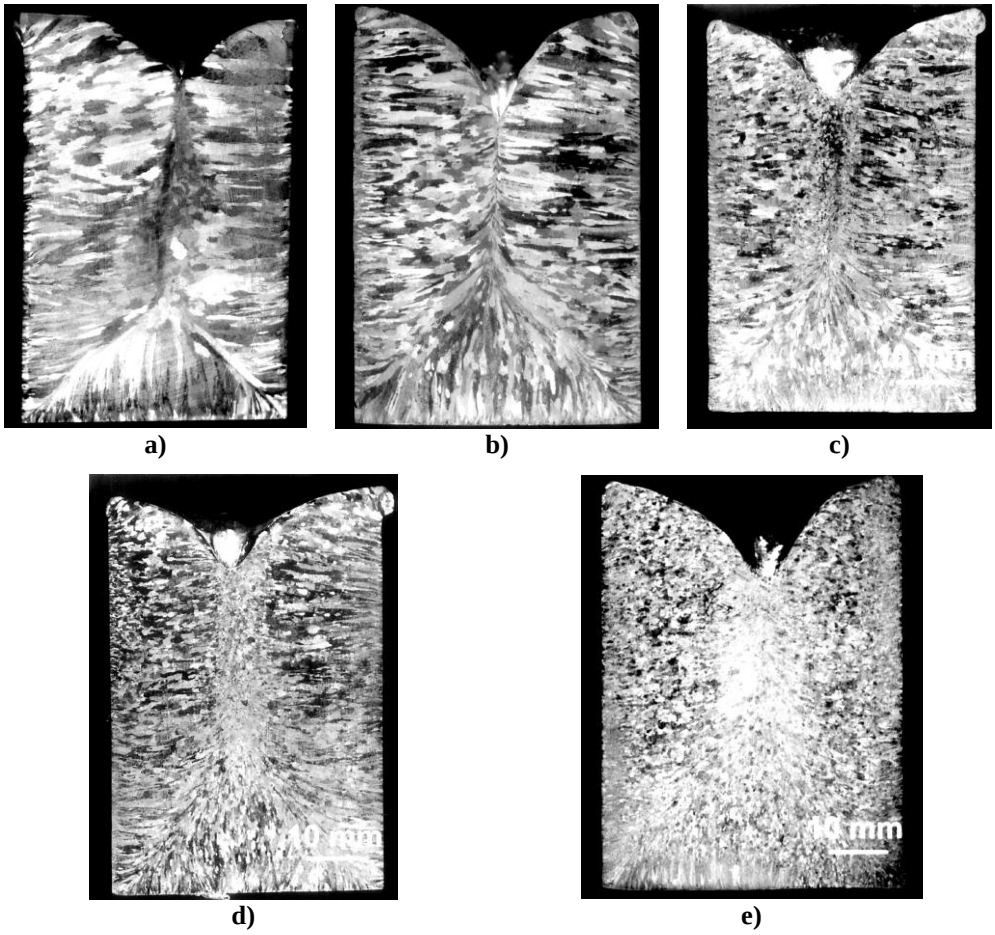

Figure 2.24. The macrostructure of the cast Al ingot containing: a) 0 wt% AlB_2, b) 0.03 wt% AlB_2, c) 0.06 wt% AlB_2, d) 0.12 wt% AlB_2 e) 0.03 wt% AlB_2 and 0.01 % solute Ti [239]

Although the typical macrostructure for permanent mold casting contains three zones of crystals with different morphologies, the zone of columnar crystals is predominant for castings containing 0.0 wt% AlB_2 and 0.03 wt% AlB_2 (Figure 2.24 a and b). The zone of equiaxed crystals in the center of the casting appears after the addition of 0.06 wt% AlB_2 and 0.12 wt% AlB_2 (Figure 2.24 c and d). By adding a small amount of solute Ti to Al containing

0.03 wt.% AlB_2, the significant reduction in grain size is observed. Besides that, the addition of solute Ti resulted in the solidification of the fully equiaxed macrostructure (Figure 2.24 e). Although it has been theoretically determined that the addition of AlB_2 to pure Al will not affect the grain size reduction [232], the results of macrostructure analysis presented in Figure 2.24 indicate that the grain refinement of columnar zone crystals has occurred. It is assumed that the grain refinement is a consequence of the accelerated nucleation along the mold walls due to the addition of AlB_2. However, the transformation from columnar to equiaxed macrostructure was achieved after the solute element addition, indicating that it has more pronounced effect. The solute Ti significantly reduces grain size even when no AlB_2 nucleants are present. To obtain the maximum grain refinement without the presence of AlB_2 particles, the addition of 0.06 wt% Ti is necessary. Contrarily, the addition of 0.02 wt% Ti is sufficient for maximum grain refinement effect [239].

During solidification, the segregating power of the element is described by the growth restricting factor. This factor is a measure of the growth restricting effect of solute element at the solid/liquid interface of the new grains as they grow into the melt [240]. The typical values of growth restricting factor for common alloying elements are given in Table 2.7.

Table 2.7. The growth restricting factor for solute elements in Al alloys [240]

Element	Growth restricting factor	Maximum concentration, wt%	Reaction type
Titanium	245.6	0.2	Peritectic
Zirconium	6.8	0.1	Peritectic
Molybdenum	7.5	0.1	Peritectic
Chromium	3.5	6.0	Peritectic
Magnesium	3.0	3.4	Peritectic
Iron	2.9	1.8	Peritectic
Tantalum	105	0.1	Peritectic
Niobium	13.3	0.2	Peritectic
Vanadium	10.0	0.1	Peritectic

Based on the values of growth restricting factors indicated in Table 2.7 there are several alloying elements that can be used for grain refinement. Even though Zr, V, Ta and Nb have high grain growth restricting factor and can impart a certain level of grain refinement in Al alloys, they have been neglected since they are less effective and more expensive compared to Ti (Table 2.7) [241].

Although many theories have been proposed, none of them can fully elucidate all the observations from experiments and practice. Generally, it is accepted that the presence of both potent nucleant particles and sufficient amount of solutes is essential for effective grain

refinement. Despite common recondition of these two essentials, the details of the grain refinement mechanisms are still ambiguous. One of the major problems is determination of the exact factors that control the efficiency of grain refinement [237].

2.2.4.2. The modification of eutectic ($\alpha_{Al} + \beta_{Si}$) morphology

Modification of eutectic (α_{Al}+β_{Si}) phase morphology is extensively performed during treatment of Al-Si based foundry alloys. This modification leads to a structural transformation of the eutectic β_{Si} phase from a course plate (Figure 2.25 a and b) to a fine fibrous morphology (Figure 2.25 c and d). Since mechanical properties of Al-Si castings strongly depend on the form, size, and distribution of the eutectic β_{Si} phase, this structural transformation results in improved mechanical properties, particularly ductility, tensile strength, and elongation. Improvement in mechanical properties is related to a lower aspect ratio and particle size of modified eutectic β_{Si} phase [242]. While larger and longer particles present in unmodified structure are prone to rapid cracking at lower strains (Figure 2.25 e), the high sphericity of modified eutectic β_{Si} phase reduces interface debonding and plastic deformation of α_{Al} matrix, directly influencing fracture surface geometry (Figure 2.25 f) [243].

The fine fibrous morphology can be obtained with chemical modification, rapid cooling rate or heat treatment [244]. Although Na and Sr are most frequently used in practice, chemical modification can be performed through the addition of alkaline, alkaline earth and rare earth metals. The first element that was extensively studied as a modifier was Na. Even though Na is a very effective modifying element, its utilization is hampered by the high vapor pressure and a tendency to fade. Since it is difficult to predict the efficiency of added Na, the utilization of Sr in the industrial practice began. Strontium is generally added in the form of Al-Sr master alloy with no fading effect during melt processing and solidification [245]. The refinement of large eutectic β_{Si} plates can also be achieved with the addition of Ca. Compared to Na and Sr, Ca has a weaker effect on the microstructure modification and requires larger additions to completely modify eutectic β_{Si} phase [233]. Furthermore, the efficiency of Ca modification depends on the cooling rate. The refinement of plate-like eutectic β_{Si} phase is obtained in the alloys solidifying with lower cooling rates, while higher cooling rates are required to achieve fine fibrous morphology [246]. The effect of Ba on microstructure modification is similar to that of Ca and requires higher additions. The additions of Ba below 0.89 g/kg cause partial modification or refinement of the eutectic β_{Si} phase with plate-like morphology [247]. From all rare earth elements, only Eu can transform eutectic β_{Si} phase

morphology from plate-like to fiber, while other elements led to the refinement of eutectic β_{Si} plates. The alloys modified by Eu additions are characterized by high density of crystallographic defects in eutectic β_{Si}, formation of pre-eutectic and eutectic Al_2Si_2Eu intermetallic phase, improved ultimate tensile strength and elongation [248].

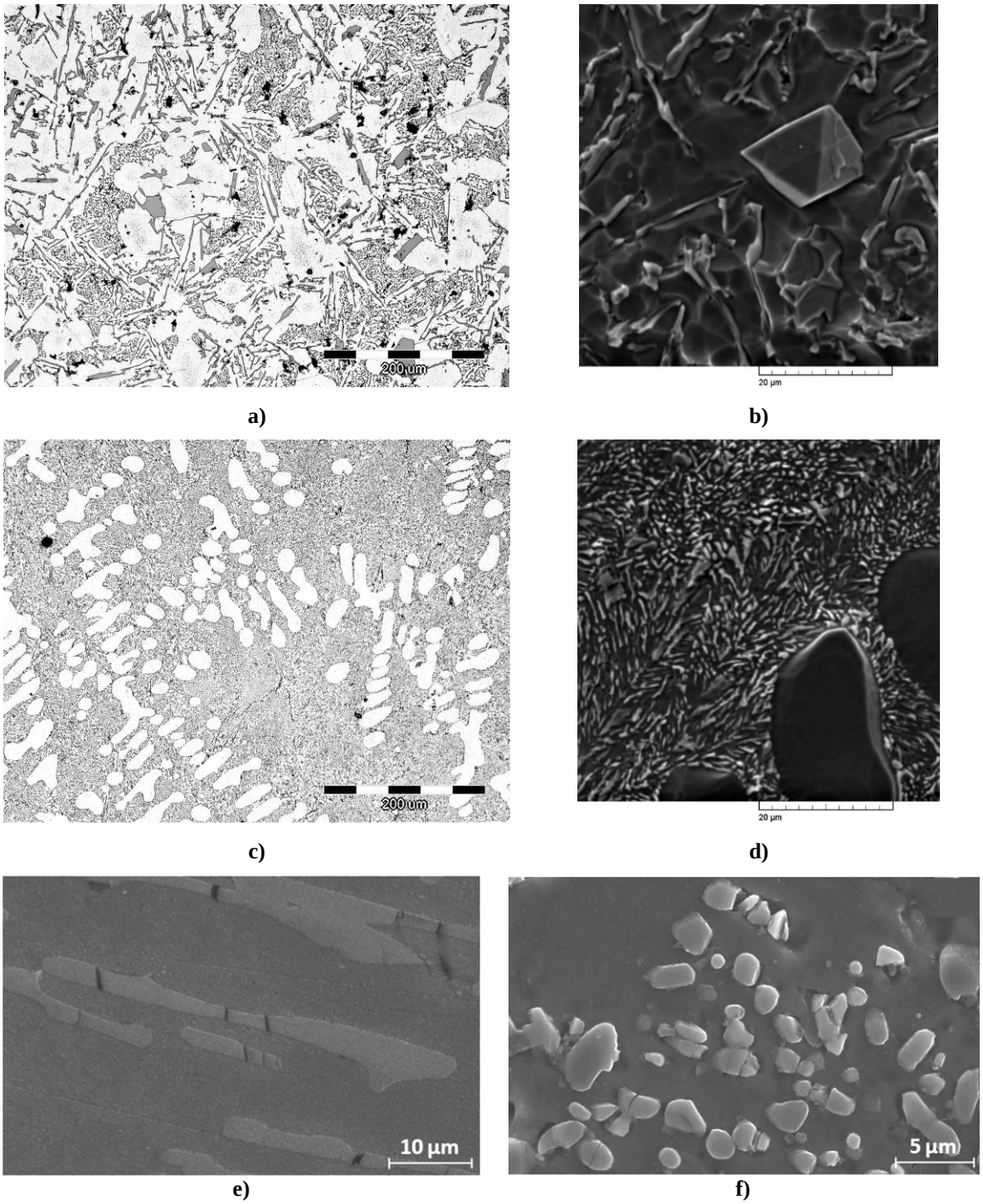

a) **b)** **c)** **d)** **e)** **f)**

Figure 2.25. Comparison between unmodified and modified microstructure: a) optical micrograph of unmodified microstructure, b) scanning electron image of unmodified microstructure, c) optical micrograph of modified microstructure, d) scanning electron image of modified microstructure [246]**, e) fracture surface of unmodified eutectic β_{Si} phase, f) fracture surface of modified β_{Si} phase** [243]

The modification of eutectic (α_{Al}+β_{Si}) through the additions of Na or Sr can be explained by their effect on β_{Si} phase nucleation and growth. The nucleation of eutectic β_{Si} phase is affected by poisoning of AlP particles responsible for heterogeneous nucleation mechanism, and formation of Na_2P, Sr_3P_2 or Al_2Si_2Sr particles [249]. Due to the poisoning effect, relatively few eutectic grains nucleate, and nucleation occurs independently of the surrounding dendrites. The impurity induced twining and restricted growth theory are two most established growth models for eutectic modification. During impurity induced twining, modifier is atomically adsorbed at the growth surfaces of eutectic β_{Si} phase facilitating the formation of new twins and locally enabling growth in many different directions. The restricted growth theory assumes that the modifier retards eutectic β_{Si} phase growth by being selectively adsorbed at growing surfaces. The accumulation of the modifier element at the solidification front limits the diffusion process and increases the undercooling and growth of the eutectic (α_{Al}+β_{Si}). Instead of growing fast as a plate in a few selected directions, modified β_{Si} phase grows isotropic in different directions [250].

An increase in the amount, size and distribution of gas and shrinkage porosity is considered to be a side effect of the addition of the microstructure modifying elements. Increased porosity levels in modified Al-Si alloys lead to low elongation, loss of tensile strength or poor fatigue strength. The increased porosity levels in modified alloys originate from:

- Increased hydrogen solubility in liquid phase (L),
- Lower surface tension and higher viscosity of the liquid (L),
- Heterogeneous nucleation of pores on the oxides and intermetallic compounds containing modifying elements [251].

Change in the solidification sequence caused by the modification of eutectic (α_{Al}+β_{Si}) phase morphology leads to the redistribution of porosities. In the unmodified alloy, the high number and small size of the eutectic grains will allow a good permeability of the liquid until the last stage of solidification. Although very small pools may form, porosity will mainly concentrate at the center of the casting. In contrast, the dramatic decrease in the number and increase in the size of the eutectic grains in the modified alloys, cause the isolation of well distributed relatively large pools of liquid resulting in the shrinkage porosities [252].

The porosities in hypoeutectic and eutectic alloys are impacted by the amount of Si. Higher content of Si decreases the volume fraction of primary α_{Al} dendrites and ensures longer feeding time. The combination of casting design together with the feeding efficiency defined

by the solidification sequence and the Si content, influences the amount of porosity in the alloys. Based on this knowledge, casting design can be used to ensure directional solidification towards the feeder to prevent porosity formation and increase casting soundness [253].

2.2.4.3. The modification of β-Al_5FeSi needle-like morphology

Neutralizing negative effect of β-Al_5FeSi intermetallic phase comprehends modification of its needle-like morphology to less deleterious form of Chinese script. Neutralizing effect is achieved by adding microstructure modifying elements such as Mn, Cr, Be or Sr [254]. The invariant equilibrium reactions in Al-rich corner of the Al-Fe-Mn-Si phase diagram are indicated in Table 2.8.

Table 2.8. The invariant equilibrium reactions in AL-rich corner of Al-Fe-Mn-Si phase diagram [255]

Reaction	Composition of the liquid (L), wt.%			Temperature, °C
	Fe	Mn	Si	
$L + Al_3Fe + Al_6(FeMn) \rightarrow \alpha_{Al} + \alpha\text{-}Al_{15}(FeMn)_3Si$	2.0	0.3	1.7	648.0
$L + Al_3Fe \rightarrow \alpha_{Al} + \alpha\text{-}Al_{15}(FeMn)_3Si + \alpha\text{-}Al_8Fe_2Si$	2.0-2.5	< 0.2	3.0-5.0	627.0-632.0
$L + \alpha\text{-}Al_8Fe_2Si \rightarrow \alpha_{Al} + \beta\text{-}Al_5FeSi + \alpha\text{-}Al_{15}(FeMn)_3Si$	1.0-2.0	0.1-0.5	5.0-10.0	597.0-607.0
$L + \beta\text{-}Al_5FeSi \rightarrow \alpha_{Al} + \beta_{Si} + \alpha\text{-}Al_{15}(FeMn)_3Si$	0.6	0.2	11.7	575.0

Manganese is the most frequently used microstructure modifying element that promotes precipitation of α-$Al_{15}(FeMn)_3Si_2$ phase with Chinese script morphology during peritectic reaction [256]. In the Al-Fe-Mn-Si alloying systems the solidification of α_{Al} dendritic network and α-$Al_{15}(FeMn)_3Si_2$ phase are the first reactions to occur. Their solidification is a result of peritectic reaction between liquid (L), Al_3Fe and $Al_6(FeMn)$ phases at 648.0 °C (Table 2.8). This peritectic reaction is continuous till the end of liquid state reactions. In the temperature range from 627.0 °C to 632.0 °C, primary α-Al_8Fe_2Si phase begins to solidify. The solidification of primary α-Al_8Fe_2Si enables peritectic reaction, in the temperature range from 597.0 °C to 607.0 °C and solidification of β-Al_5FeSi with needle-like morphology. Liquid state

reactions end with solidification of α_{Al} dendritic network, eutectic (α_{Al} + β_{Si}) and α-$Al_{15}(FeMn)_3Si_2$ phase (Table 2.8) [255].

As indicated by previous reactions, the solidification of Fe-rich intermetallic phase can occur in different morphologies such as: needle-like, Chinese script and polyhedral or star-like morphology. The morphology of solidified phases is influenced by manganese/iron weight ratio (w (Mn/Fe)). The exact w (Mn/Fe) necessary for modifying effect of Mn and the transition of needle-like to Chinese script morphology is not fully established. With the w (Mn/Fe) at 0.35 the partial transformation of needle-like to Chinese script morphology was observed. At w (Mn/Fe) of 0.5 transformation of β-Al_5FeSi to α-$Al_{15}(FeMn)_3Si_2$ was fully achieved [257]. However, α-$Al_{15}(FeMn)_3Si_2$ with Chinese script morphology was also observed at w (Mn/Fe) as low as 0.17 [223]. Additional increase in the w (Mn/Fe) causes precipitation of α-$Al_{15}(FeMn)_3Si_2$ with polyhedral morphology. The solidification of α-$Al_{15}(FeMn)_3Si_2$ phase with polyhedral morphology occurs at w (Mn/Fe) of 0.65 [257]. The difference in morphology between α-$Al_{15}(FeMn)_3Si_2$ phase with Chinese script and polyhedral form in the AlSi12 alloy with w (Mn/Fe) of 0.99 is indicated in Figure 2.26. Since it is surrounded by a dendritic network of primary α_{Al}, it can be concluded that the branched α-$Al_{15}(FeMn)_3Si_2$ phase with Chinese script morphology occurs earlier in the solidification sequence (Figure 2.26 a). On the contrary, the compact α-$Al_{15}(FeMn)_3Si_2$ phase with polyhedral morphology is surrounded by the main eutectic (α_{Al} + β_{Si}) as one of the last phases appearing in the solidification sequence (Figure 2.26 b) [258]. The solidification of α-$Al_{15}(FeMn)_3Si_2$ phase with polyhedral morphology is avoided due to its negative effect on machinability [257]. Due to the similarities in atomic radius and Bravais lattice between Cr, Co and Mn, the similar effect on the modification of Fe-rich intermetallic phase morphology is expected. Though the Mn and Cr are two commonly used microstructure modifying elements, Co should have highest modifying effect on Fe containing phases due to its lower tendency towards segregation during solidification and non-reaction with Si [259]. By adding to the bulk of the liquid phase, both Cr and Co substitute Fe during solidification of Fe containing phases [260]. In Al-rich Al-Fe-Cr ternary system the Al_7Cr phase, solidified during peritectic reaction between liquid and Al_5Cr phase at 790.0 °C, can dissolve up to 4.0 wt% Fe. On the other hand, 4.0 wt% Cr is dissolved by Al_3Fe phase solidified at 645.5 °C during eutectic reaction. The Al_3Fe and Al_9Co_2 are two intermetallic phases solidifying during eutectic reaction at 675.0 °C. The phase Al_3Fe contains from 25.9 wt% to 37.0 wt% Fe and dissolves up to 12.4 wt% Co corresponding to the formula $Al_3(FeCo)$. The Al_9Co_2 phase can contain between 20.3 wt% and 33.2 wt% Co and up to 10.8 wt% Fe and can be described as $Al_9(FeCo)_2$. The Al-Fe-Cr and Al-Fe-Co systems do not recognize formation

of ternary phases [255]. In the alloying systems containing Si, the negative impact of β-Al_5FeSi phase is suppressed by the formation of complex $Al_5(Fe_x,Cr_{1-x})Si$ and $Al_5(Fe_x,Co_{1-x})Si$ intermetallic phases with branched or Chinese script morphology [260].

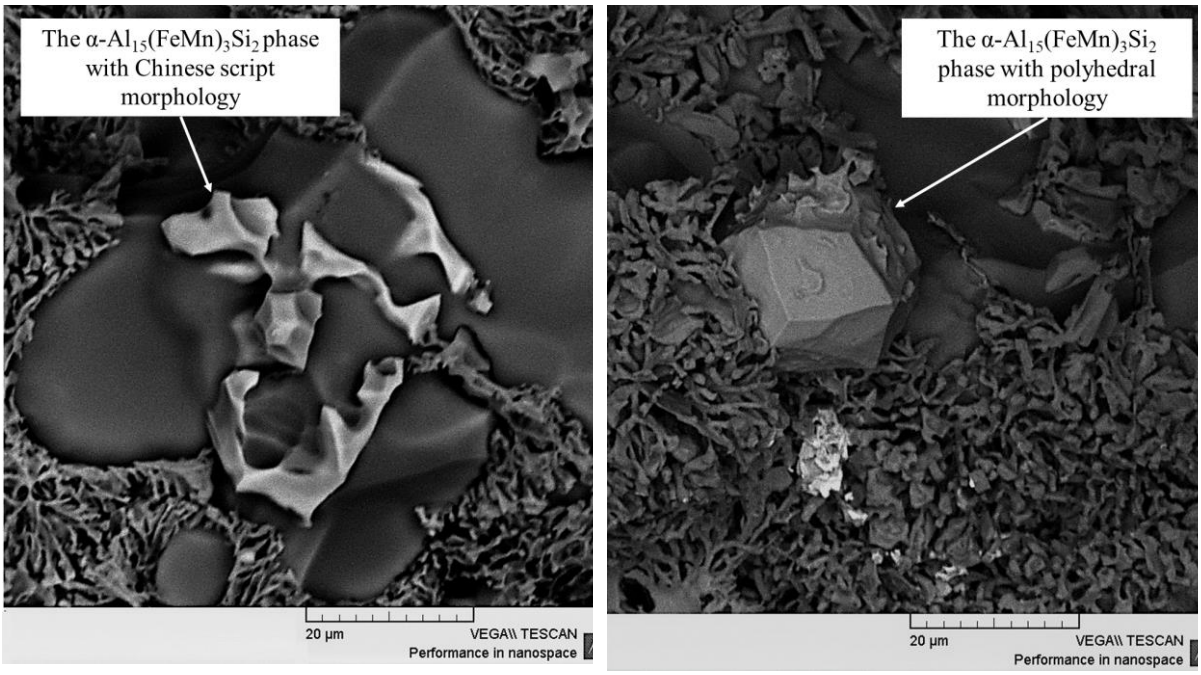

a) **b)**

Figure 2.26. The iron-rich intermetallic phases with: a) Chinese script morphology, b) polyhedral morphology [258]

In the alloying systems containing both Si and Mg the beneficial influence of Co is manifested through the decrease in size and increase in volume fraction of β-Al_5FeSi phase. The transformation of needle-like to Chinese script or skeleton-like morphology depends on Fe/Co ratio. The full transition of β-Al_5FeSi phase to α-$Al_{15}(FeMn)_3Si_2$ and π-$Al_8Mg_3FeSi_6$ phase is obtained at Fe/Co = 1.0 to 2.0 [259]. Apart from the modification of eutectic ($\alpha_{Al} + \beta_{Si}$) microstructure, the addition of Sr affects the solidification of Fe-rich intermetallic phase. Modifying effect of Sr originates from its influence on Fe segregation. By promoting local segregation of Fe, Sr assures Fe/Si ratio > 1.0 required for preferred solidification of α-$Al_{15}(FeMn)_3Si_2$ phase. Strontium additions lower the volume fraction of Fe-rich intermetallic compounds and refine the needle-like morphology of β-Al_5FeSi making it shorter and thinner [261]. A combined addition of Mg and Sr is required to enable transformation of β-Al_5FeSi to π-$Al_8Mg_3FeSi_6$ phase with skeletal morphology. In wrought Al alloys of the 6xxx series, addition of Sr promotes the formation of α-$Al_{15}(FeMn)_3Si_2$ phase leaving excess Si available for precipitation of Mg_2Si during aging [262]. The microstructure modifying effect of Be manifests through the refinement of β-Al_5FeSi phase size, transformation of β-Al_5FeSi phase

needle-like morphology to globular morphology and solidification of ternary $Al_4Fe_2Be_5$ [255] and quaternary Al_8Fe_2BeSi phase with script-like morphology [263].

2.3. Utilization of lithium as alloying element

Right from the inception of space program, aircraft designers, engineers, and manufacturers required materials with high specific properties in order to increase payload capabilities. The Li-containing Al alloys have drawn a lot of attention specifically for their usage in stiffness- and weight-critical structures for military, space, and commercial applications. Aluminum-lithium alloys are distinguished from the commercially available 2xxx and 7xxx series of Al alloys by exhibiting a low density, increased specific strength and a high stiffness [264]. Since Al is a metal with low density (2.7 g/cm^3 [265]) only a few alloying elements can be used to achieve further weight reduction. Silicone (2.3 g/cm^3 [265]), Be (1.8 g/cm^3 [265]), Mg (1.7 g/cm^3 [265]), and Li (0.5 g/cm^3 [265]) are the only elements of the periodic table less dense then Al that can be used for that purpose. In addition to being the lightest metal and a least dens solid element [266], it has been found that each 1.0 wt% of Li added to Al alloys:

- Decreases density by 3.0 %,
- Increase modulus of elasticity by 6.0 %,
- Increases stiffness by 5.0 % for the additions up to 4.2 wt% Li [14].

However, increasing Li content above 1.3 wt% will result in yield and tensile strength decrease, respectively. The highest strength values were obtained in the range of 1.1 wt% to 1.3 wt% Li [264].

The increase in Al-Li alloy's modulus of elasticity is an exception to the general rule of alloying [15]. Usually, in Al alloys this is accomplished by the addition of elements with modulus of elasticity greater than that of α_{Al} matrix. Since Li is alkaline metal with low melting point of 165.8 °C and maximum modulus of elasticity of 5.2 GPa [16], this atypical effect can be attributed to electron redistribution between the compounds (Al-Li) in the α_{Al} solid solution and to the elastic modulus of the secondary phase precipitates [17].

The solid solubility of Li in α_{Al} solid solution decreases from 4.0 wt% at the eutectic temperature of 603.0 °C to less than 1.0 wt% at 100.0 °C enabling formation of strengthening precipitates. The primary strengthening precipitate in Al-Li alloys is the metastable Al_3Li (δ') phase. With maximum solvus temperature between 300.0 and 350.0 °C at 4.0 wt% Li, the Al_3Li (δ') phase precipitates coherent to the α_{Al} matrix leading to order hardening. Usually, the Al-Li alloys are hardened by quenching and subsequent aging during which the Al_3Li (δ') precipitates

from super saturated solid solution (SSS) of α_{Al} as intermediate phase during total decomposition indicated by Equation 5 [267].

$$\alpha_{Al} \rightarrow \delta'(Al_3Li) \rightarrow \delta(AlLi) \quad (5)$$

The degree of hardening and the obtained mechanical properties are also influenced by the presence of other alloying elements such as Cu, Mg, Zn, Zr, Ag and rare earth metals. Unfortunately, Al-Li alloys are also characterized by decreased ductility, formability, fracture toughness and anisotropic mechanical properties originating from Li additions. These shortcomings made Al-Li alloy inappropriate for a variety of commercial applications [266].

2.3.1. The development of Al-Li alloys through history

Since solid solubility of Li in α_{Al} solid solution is impacted by temperature, it is not surprising that the early development of Al-Li alloys is associated with discoveries related to age hardening. While the investigations performed on *Duralumin* alloy in the period between 1919 and 1921 concluded that the age hardening was a result of phase precipitation from supersaturated solid solution (SSS), the first Li containing Al alloy *Scleron* was developed in 1924. With nominal composition of Al-12Zn-3Cu-0.6Mn-0.1Li the alloy was described as superior to other Al alloys because it could be worked in variety of forms with high resistance to wear, tensile strength and resistance to corrosion and oxidation (Figure 2.27). Unfortunately, the production of *Scleron* was discontinued due to the inconclusive research results on the strengthening effect of Li and development of other types of Al alloys with superior properties [268]. Development of modern Al-Li alloys is connected to the discovery that Li can be used as a major strengthening element in Al-Cu alloys. Despite research resulting in a patent for the Al-Cu-Li-Mn-Cd alloy in 1945, the introduction of AA 7075 established dominance of Al-Zn-Mg-Cu system for high-strength applications thereby hindering further development of Li containing Al alloys [269]. The interest in the use of Li as an alloying element peaked after the Li containing strengthening precipitates were identified in Al-Li-Cu alloying system [270]. As indicated by Table 2.8 the key historical Al-Li alloys are divided into three generations. The first generation of Al-Li alloys initiated in 1957 with the development of AA 2020 alloy by Alcoa Company (Table 2.9). Development of this alloy was preceded by the U.S. patent in 1950 related to stiffness improvement by Li additions (Figure 2.27). The AA 2020 possessed a high strength and creep resistance in temperature range between 150.0 °C and 200.0 °C and it was commercially utilized in manufacturing of the United State Navy's RA-5C Vigilante aircraft.

The aircraft was in use for more than 20 years without a single documented failure (crack or corrosion issues) [271]. In 1960 the AA 2020 was recalled from the commercial use due to the high brittleness and poor ductility stemming from high level of Fe and Si impurities (Figure 2.23). The course particles of α-$Al_{12}(FeMn)_3$ and ω-Al_7Cu_2Fe phase caused non-uniform strain distribution and acted as a crack initiation sites during processing [266].

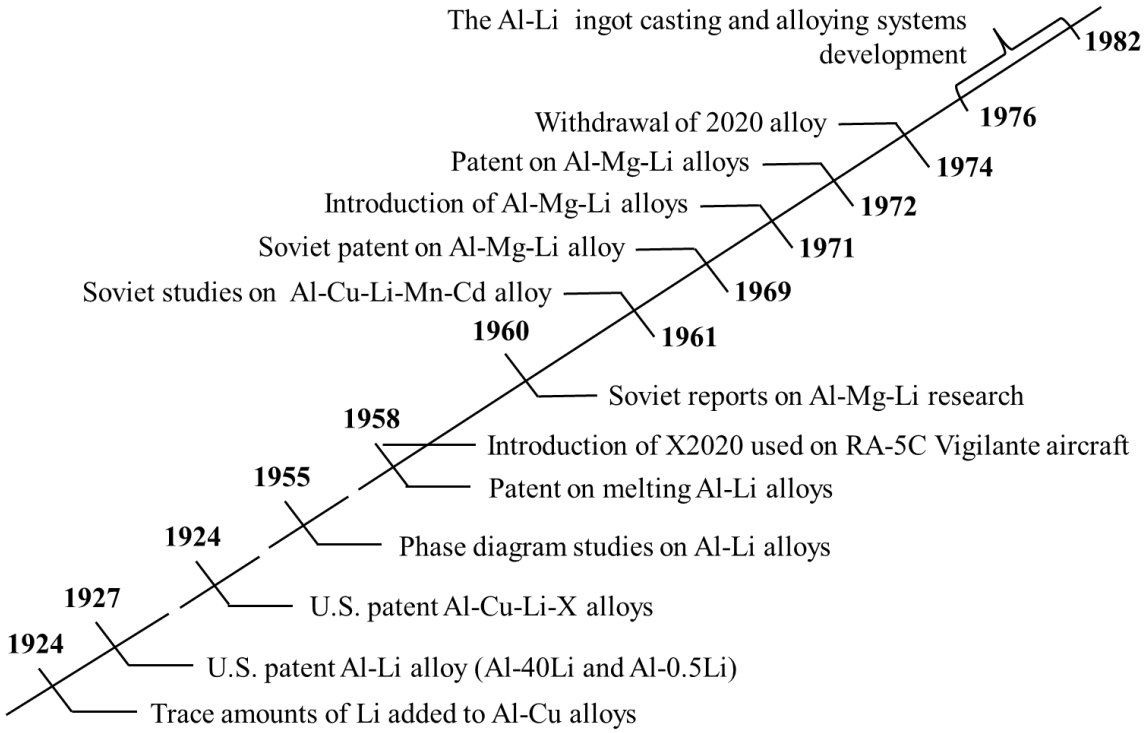

Figure 2.27. The early development and use of Li in Al alloys [268]

In the early 1960s further investigations and development in the former Soviet Union resulted in an improvement of sheets, plates, forgings, and extrusions from VAD23, AA 1420 and AA 1421 alloys (Table 2.9). The improvements in the AA 1420 weldability and solid solution strengthening were obtained through the combined additions of 5.2 wt% Mg and 2.0 wt% Li (Figure 2.27). Moreover, the 0.11 wt% Zr was added to impact grain growth and enable recrystallization (Table 2.9). In 1971, the vertical take-off and landing aircrafts Ak36 and Ak38 were produced using AA 1420 alloy. Although it had lowest density compared to the other commercially available alloys, its strength and toughness were not sufficient to meet the requirements of modern aircraft industry. The main reason for lower mechanical properties was shearing of Al_3Li (δ') phase and planar slip formation. As a consequence, further investigations covered different chemical compositions to optimize microstructure development and enable precipitation of other non-shareable phases that can decrease the planar slip tendency and enable further hardening [272].

Table 2.9. Historical development of the key Al-Li alloys [268]

Alloy	Chemical composition, wt%									Density, g/cm^3
	Li	Cu	Mg	Ag	Zr	Sc	Mn	Zn	Al	
First generation										
2020	1.2	4.5							Balance	2.71
1420	2.1		5.2							2.47
1421	2.1		5.2		0.11	0.17				2.47
Second generation										
2090	2.1	2.7			0.11					2.59
2091	2.0	2.0	1.3		0.11					2.58
8090	2.4	1.2	0.8		0.11					2.54
1430	1.7	1.6	2.7		0.11	0.17				2.57
1431	1.9	1.65	0.9		0.11					2.55
1450	2.1	2.9			0.11					2.60
1460	2.25	2.9			0.11					2.60
Third generation										
2195	1.0	4.0	0.4	0.4	0.11					2.71
2196	1.75	2.9	0.5	0.4	0.11		0.35	0.35		2.63
2297	1.4	2.8	0.25		0.11		0.3	0.5		2.65
2397	1.4	2.8	0.25		0.11		0.3	0.5		2.65
2098	1.05	3.5	0.53	0.43	0.11		0.35	0.35		2.70
2198	1.0	3.2	0.5	0.4	0.11		0.5	0.35		269
2099	1.8	2.7	0.3		0.09		0.3	0.7	Balance	2.63
2199	1.6	2.6	0.2		0.09		0.3	0.6		2.64
2050	1.0	3.6	0.4	0.4	0.11		0.35	0.25		2.70
2296	1.6	2.45	0.6	0.43	0.11		0.28	0.25		2.63
2060	0.75	3.95	0.85	0.25	0.11		0.3	0.4		2.72
2055	1.15	3.7	0.4	0.4	0.11		0.3	0.5		2.70
2065	1.2	4.2	0.5	0.30	0.11		0.4	0.2		2.70
2076	1.5	2.35	0.5	0.28	0.11		0.33	0.30		2.64

The optimization of chemical composition enabled second-generation Al-Li alloys to be lighter (8.0 to 10.0 %) and stiffer compared to other materials traditionally used for aerospace and aircraft applications. In the 1970s and 1980s various researchers focused on reducing the content of Si and Fe impurities to the amounts required for a high ductility and toughness. To enable grain refinement and precipitation of Al_3Zr particles, the Mn was replaced by Zr. This had an excellent effect on void nucleation, as well as ductility and toughness increase. Furthermore, the Cd was abandoned as an alloying element because it had no beneficial effect on the prevention of the intergranular fracture in AA 2020 alloy [273]. There were two different approaches in the production of second-generation Al-Li alloys:

- Powder metallurgy (P/M),

- Ingot metallurgy (I/M).

The P/M process offered wider composition range, microstructural flexibility and several different production process like rapid solidification and mechanical alloying [268]. The rapid solidification processing (RSP) was developed to produce Al-Li alloys with homogeneous chemical composition without the need for additional homogenization heat treatment. The unform chemical composition was obtained by rapidly progressing solid/liquid interface preventing microsegregation or segregation of solute elements [274]. Due to its complexity and limitations the RSP is more suitable for the production of thin films and powders [275]. The mechanical alloying fabrication technique was primarily used to produce dispersoid-strengthened Al and Ni alloys. It is a fully solid-state process that consists of rapid cold welding and fracturing of powder particles. The strengthening of mechanically alloyed Al-Li alloys derived from the finely dispersed oxide and carbide particles as well as ultrafine grain size [276]. The main goal of P/M process was to produce an Al-Li-X alloy with an increase of 30.0 % in stiffness and 20.0 % in specific strength compared to the AA 7075-T76. Unfortunately, the goal was not met due to the manufacturing difficulties primarily concerning small production capabilities resulting in small ingot size [268]. In contrast, I/M was used to produce large ingot sizes using mostly preexisting production equipment. The utilization of I/M enabled replacement of AA 7075-T6 and AA 2024-T3 sheets and light gauge products with alloys containing approximately 2.0 % or more Li, around 2.0 % Cu, as well as the additions of Mg and Zr. One of major issues that needed to be initially addressed was the cost of I/M alloy manufacturing, referring to the cost of special casting technology associated with the reactivity of Li-containing Al alloys [268]. The main advantages and disadvantages of second-generation Al-Li alloys are summarized in Table 2.10. Despite commercial application of AA 2090-T86, AA 2090-T83 and AA 2090-T84 in United States as well as AA 0145, AA 0146 and AA 0143 in former Soviet Union, the second-generation Al-Li alloys had a few characteristics that were viewed as unsuitable by airframe designers and manufacturers (Table 2.10) [266].

The physical and mechanical properties of third generation Al-Li alloys were designed to fulfil the requirements of the future aircraft industry. The development of third generation Al-Li alloys initiated in late 1980s with the idea to produce weldable Al based alloy with low density for use in aerospace launching vehicles and cryogenic tankage. Since it had good cryogenic properties, the AA 2019 was used as a base. Lithium was added until the strength peaked at 1.3 wt%. Silver and Mg were added to promote preferred precipitation of Al_2CuLi (T_1) phase while Zr was added as grain refiner and to prevent grain coarsening in the weld zone.

The *Weldalite™* alloy with nominal composition of Al-(4.6-6.3)Cu-1.3Li-0.4Mg-0.14Zr-0.06Fe-0.03Si (Table 2.8) could reach a yield strength of 700.0 MPa through the uniform distribution of Al_2CuLi (T_1) phase [265]. To improve corrosion resistance, subsequent versions of the *Weldalite™* alloy contained Zn additions. The improvement of the static and dynamic corrosion properties was obtained through the reduction of difference in electrochemical potential between the grains and grain boundaries. The third generation AA 2195 was used in the production of the super lightweight thank of the space shuttle that was first flown in 1998. The newly developed alloy and some design changes reduced the thank weight by 3175.0 kg and provided a significant increase in the performance required for the shuttle to reach the International space station [268].

Table 2.10. Advantages and disadvantages of second-generation Al-Li alloys [277]

2^{nd} generation Al-Li alloys (Li ≥ 2 wt% and Cu ≤ 3 wt%)	
Advantages	Disadvantages
Lower density for 7.0 % to 10.0 %	Lower short-transverse fracture toughness
Modulus of elasticity higher for 10.0 % to 15.0 %	Lower plane stress fracture toughness/residual strength in sheet
Lower fatigue growth rate	Higher anisotropy of tensile properties

A more contemporary approach to Al-Li alloy development comprehended production of AA 2055 and AA 2060 (Table 2.10) in 2012. These alloys replaced AA 2024-T3 and AA7075-T6 in the production of fuselage, upper and lower wing structures because of their excellent corrosion resistance, high thermal stability and a synergy of high strength and toughness. The utilization of these alloys enabled between 17.0 % and 24.0 % weight savings, respectively [266].

2.3.2. The shortcomings of historical aluminum-lithium alloys

The shortcomings of second and third generation Al-Li alloys mainly concern:

- High anisotropy of mechanical properties,
- Crack deviation,
- Low fracture toughness,
- Microcracking during manufacturing,
- Poor corrosion resistance,
- Poor thermal stability resulting in loss of toughness after thermal exposure [277].

2.3.2.1. High anisotropy of mechanical properties

Second generation Al-Li alloys as uncrystallized plates or sheets exhibit significantly lower strength at 45° angle compared to the strength in rolling direction. Furthermore, there was a high difference in strength through the thickness. During fabrication, the Al-Li alloys have a tendency to form pronounced texture with high gradient leading to the anisotropy of mechanical properties representing the obstacle in design, forming and machining. Texture development in fcc materials is a function of stacking fault energy (SF). As a material with high SF energy, Al is prone to development of Copper-type, Brass-type and S-type texture components [278]. Annealing heat treatment is needed to prevent recrystallization during solutionizing treatment. This enables formation of final unrecrystallized microstructure with a moderate level of hot-deformation texture, as indicated in Figure 2.28 for AA 2099 extrusions, AA 2099, and AA 2199 plate products. Although the microstructure remains uncrystallized, the reduction in the through-thickness anisotropy is obtained as a result of reduction in Brass texture [279]. The Brass texture is a single-component {110}<112> type texture attributed to the suppression of cross sliding due to the splitting of dislocations and planar slip formation [280]. It develops during thermo-mechanical processing and in combination with highly oriented precipitates lowers yield strength at 45° and 60° to the rolling direction. For optimal mechanical properties the extrusion and plate products needed to be uncrystallized (Figure 2.28, extrusions and plates) while sheet products typically have recrystallized structure with elongated grain morphology (Figure 2.28, sheet).

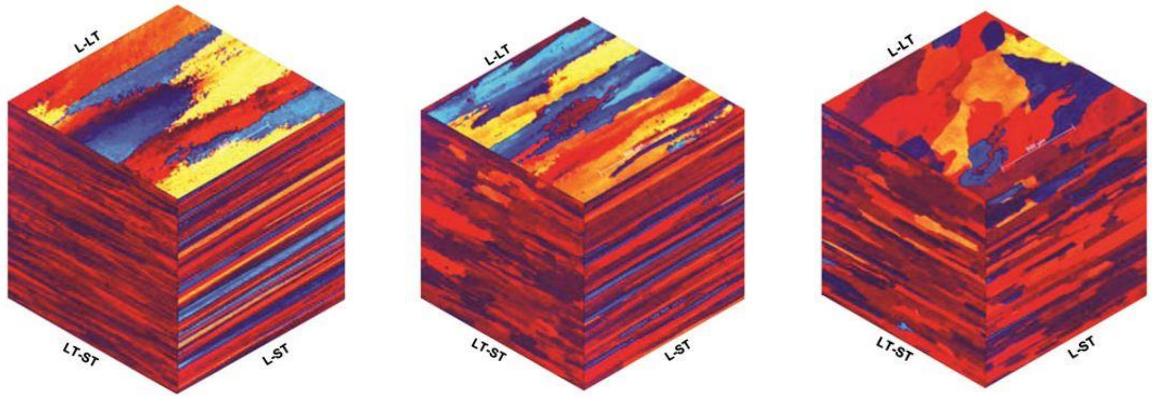

AA 2099 extrusion **AA 2099 and AA 2199 plate** **AA 2199 sheet**

Figure 2.28. The microstructure of AA 2099 extrusions with thin elongated unrecrystallized grain, AA 2099 and AA 2199 plate products with elongated unrecrystallized grains, AA 2199 sheet products with recrystallized grains (longitudinal direction (L), long transverse direction (LT), short transverse direction (ST)) [277]

The in-plane and through-thickness anisotropy of mechanical properties originates from the interaction between crystallographic texture, grain size and shape, cold deformation and the precipitates developed during aging [267]. By subjecting Al alloys with and without Li content to the same thermo-mechanical processing it was concluded that the underlying mechanism during thermo-mechanical processing is responsible for the strong Brass texture component and not the chemical composition. Therefore, control of the texture by introducing suitable steps in overall processing is likely to reduce anisotropy of mechanical properties [278]. The solutions have been developed combining chemical composition optimization and innovative thermo-mechanical processing [277].

2.3.2.2. The deviation in the crack propagation direction

Crack deviation represents further difficulty in structural design. Deviation from the expected direction of the crack propagation makes it difficult to define locations for inspection or for the placement of crack arresters (Figure 2.29 a) [277]. Deviation in crack propagation initiates after reaching a certain value of the stress intensity coefficient. This creates difficulties not only for strength engineers who have to determine specific values of fatigue crack growth rate as a function of the stress intensity coefficient, but also for aircraft designers who use the principle of "permissible damage" in their computations [281].

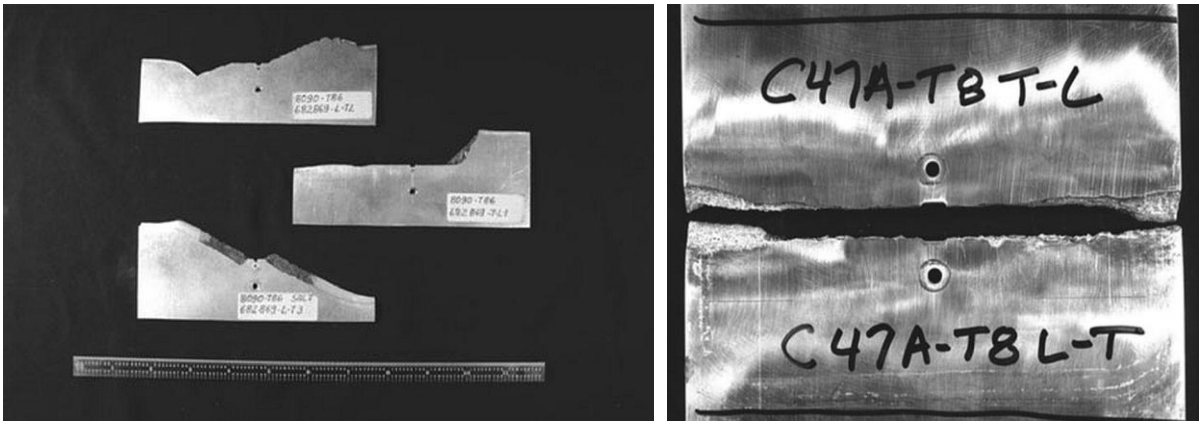

a) **b)**

Figure 2.29. Fatigue crack growth test specimens: a) second generation AA 8090 showing crack deviation, b) third generation AA 2199 showing straight crack path perpendicular to the stress axis [277]

Successful mitigation of crack deviation and anisotropy of mechanical properties required chemical composition optimization, control of crystallographic texture, grain size and shape, cold deformation as well as the amount and type of precipitates as reflected by the crack propagation of third generation AA 2199 (Figure 2.29 b) [266].

2.3.2.3. Low fracture toughness

The fracture toughness of second-generation AA 8090-T86 was lower compared to AA 2024 products for damage tolerance applications [277]. The investigations into short transverse fracture toughness, ductility, and associated occurrence of brittle intergranular fracture of AA 8090 refer to the following grain boundary phenomenon [282]:

- Planar slip band formation,
- Large area fraction of grain boundary precipitates and soft PFZ,
- The presence of alkaline-metal impurities [283],
- Segregation of impurity elements,
- High level of H_2 segregation,
- Segregation of Li.

The slip on the same slip plane is facilitated by shearing of Al_3Li (δ') phase by dislocations. The dislocations in planar slip bands pile up at grain boundaries producing large stress concentrations and promoting intergranular fracture. Furthermore, the intergranular fracture is facilitated by the presence of grain boundary precipitates and soft PFZ adjacent to grain boundaries. In the absence of segregations, crack growth often involves strain localization in soft PFZ, nucleation of voids by separation at precipitate/matrix interface and coalescence of voids. Voids generally nucleate at lower strains around large closely spaced precipitates. Although, less plasticity may be required for void coalescence when the soft PFZ are narrower, the fracture behavior will be primarily determined by the size and spacing of grain boundary precipitates. However, it has been suggested that the size and area fraction of grain boundary precipitates for Al-Li alloys can be higher compared to the other types of Al alloys since the matrix precipitation is more sluggish and requires higher aging temperatures and longer aging times to obtain high strength. Also, there is a grater difference between the solubility of phases precipitating at the grain boundaries and inside of the grains [282].

Although, the preferential reaction between Li and alkaline-metal impurities results in precipitation of discrete liquid Na-K phases [283], the number of investigations indicated that the liquid-metal embrittlement is not a significant cause of low fracture toughness in AA 8090 [282]. Similarly, it is very unlikely that the brittle intergranular fracture is caused by the segregation of impurity elements such as Na, K, Ca and S at the grain boundaries. They are most frequently present as discrete phases [284].

Since the Al-Li alloys often contain 10 times more hydrogen than other conventionally used Al alloys, it is not surprising that some studies suggested that embrittlement is a consequence of increased hydrogen content. However, the form and distribution of H_2 in Al-Li alloy is not well established. Hydrogen can be present as an embrittling segregant at the grain boundaries or in the less deleterious forms of solute element within the grains, entrapped gas or as a discrete hydrogen phase. It has also been suggested that sodium and potassium hydrates can be present in over aged condition when sufficient hydrogen has diffused to preexisting stable Na- and K-rich phases [282].

Like impurity elements, the segregation of Li at grain boundaries is another process that could result in weakening of intermetallic bounds and intergranular fracture. It has been proposed that segregation of some alloying elements could result in precipitation of embrittling two-dimensional grain boundary precipitates with polyhedral structure [285]. Theoretical considerations and thermodynamic calculations suggest that Li and Mg grain boundary segregation should weaken intermetallic bounds. Moreover, the activation energy necessary for embrittlement is roughly equal to the energy of Li segregation. An abrupt increase in aging temperature for a short period of time could produce a large increase in the amount of solute that diffuses along the grain boundaries, with only a relatively small increase in the amount of solute arriving at the grain boundaries from the matrix. This could occur because grain boundary diffusion distances are increased to much greater extent compared to volume diffusion distances, and to the significant distance of solute rich region near the edge of the PFZ [282]. However, the investigations into ductile-to-brittle fracture transformation of AA 8090 in underaged condition linked decrease in brittleness due to the Li segregation with increase in aging time. The results of the same investigation indicated that the appearance of low-energy intergranular fracture in AA 8090 in peak aged condition is also influenced by other factors such as strain localization in PFZ and around grain boundary precipitates (Figure 2.30) [286]. The transmission electron micrographs of peak aged AA 8090-T8771 plate fracture surface replicas indicate the presence of both ductile fracture surface with clearly defined dimples (Figure 2.30 a), as well as brittle areas formed as a consequence of strain localization in PFZ (Figure 2.30 b). Furthermore, other previously proposed explanations, such as occurrence of planar slip, excessive grain boundary precipitation and liquid-metal embrittlement were not identified during microstructural investigations of AA 8090 in underaged or peak aged condition [282].

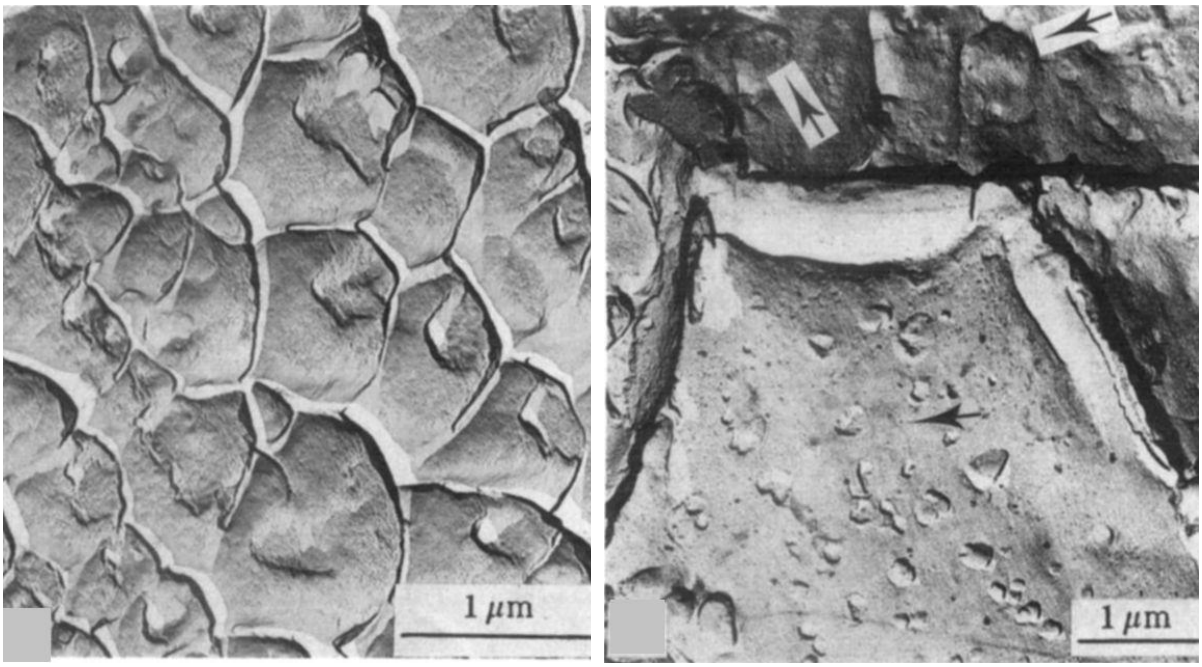

a) **b)**

Figure 2.30. The transmission electron micrograph of AA 8090-T8771 45 mm plate intergranular fracture surface showing: a) region of well-defined dimples, b) brittle regions with shallow poorly defined dimples [282]

2.3.2.4. The microcracking induced by manufacturing

Microcracking during manufacturing refers to the microcracks developed in the short transverse direction during insertion of interference fit fasteners. This problem becomes more complex when the product enters post-buckling stage, due to the interactions of geometric nonlinearity and different failure models. The buckling failure performance of thin-walled structures is a major concern for aircraft designers. The fatigue failure process and failure models for 1.2 mm thick AA 2A97 panels are shown in Figure 2.31. The load control was selected for fatigue test to make the skin buckle repeatedly under the shear cyclic load. A sinusoidal fatigue load with the frequency of 2.0 Hz was applied with the load rate of 0.1 [287]. As indicated by Figure 2.31 the fatigue failure of stiffened panel is complex and involves prolapse of the fasteners/rivets, nucleation of microcracks near the fasteners/rivets and skin tearing. The fatigue test results indicate two typical fatigue models:

- The first failure model is the prolapse of the fastener/rivet that was detected at panels 3, 4 and 5 (Figure 2.31). The prolapse of the fastener caused a decrease in structural stiffness and formation of microcracks at the fastener hole.

- The second failure model refers to the crack near the fastener. The crack nucleated near the fastener in the diagonal region of the tension field and grew parallel to the stiffener boundary (Figure 2.31 panel 4) [287].

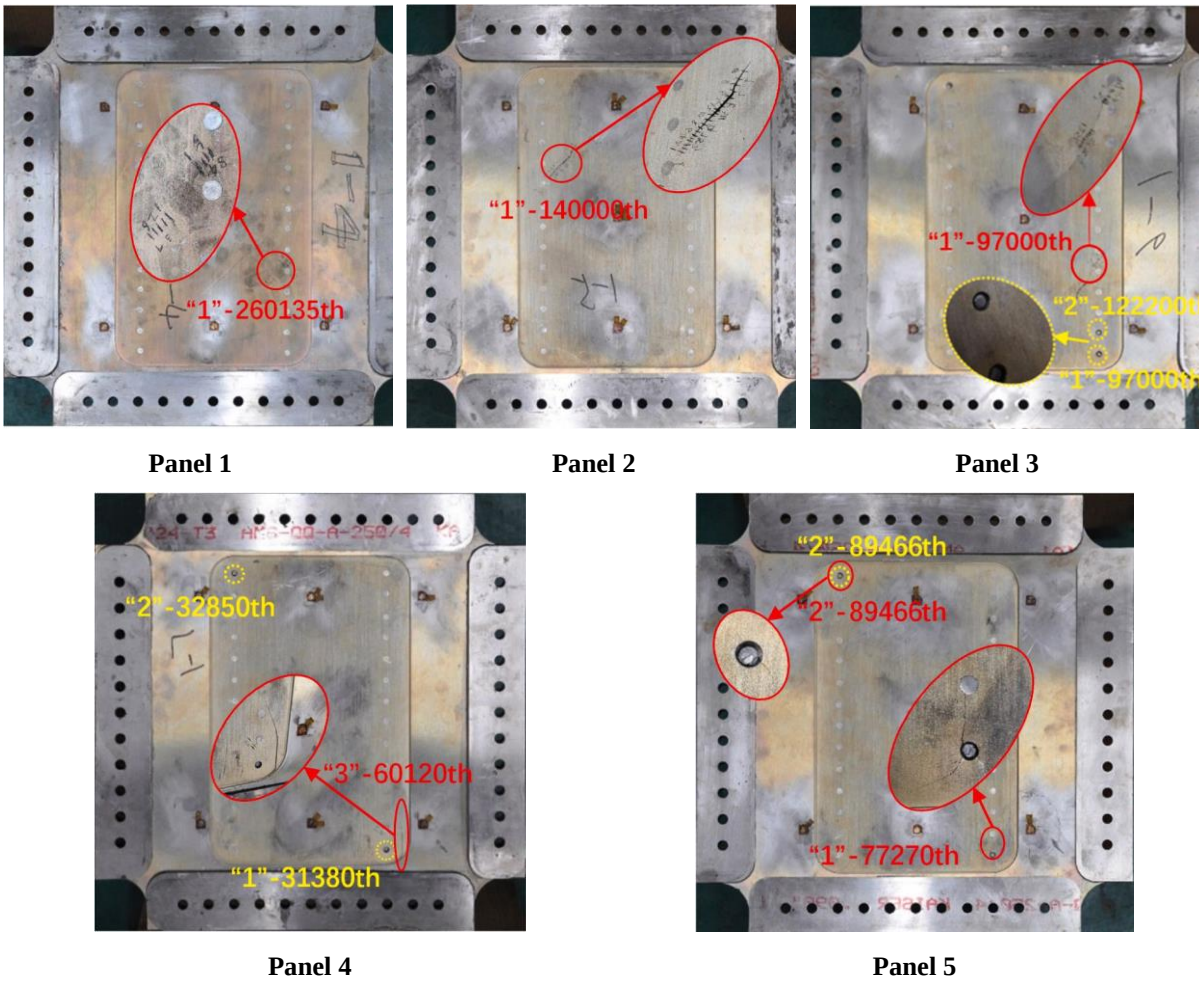

Panel 1 **Panel 2** **Panel 3**

Panel 4 **Panel 5**

Figure 2.31. Failure model of 1.2 mm tick AA 2A98 panels (solid line – crack initiation, dotted line – fastener prolapse) [287]

The cracking originated from low elongation and work hardening ability of the product. In order to increase elongation and obtain higher work hardening it is necessary to lower the amount of cold deformation/stretching prior to aging and to perform artificial aging at the temperatures with a longer separation between tensile yield strength and ultimate tensile strength [288].

2.3.2.5. Low corrosion resistance

The corrosion resistance of Al-Li alloys is usually determined using two different types of tests:

1. Laboratory test type,
2. Environment exposure test type.

The laboratory test types include exfoliation corrosion susceptibility test (EXCO), salt spray test (MASTMAASIS) and sulfur dioxide (SO_2) salt fog tests. The environmental test type involves exposing the testing material to various environments over a long period of time. Usually, this type of test is performed aboard a ship or near a coastal area for a period of one year.

The most extensive evaluation of Al-Li alloy corrosion resistance was presented by the Thompson experiment that comprehended the use of both laboratory and environmental exposure tests. To compare corrosion resistance of Al-Li alloys with conventionally used Al alloys, Thompson experiment was performed on AA 2090-T8E41, AA 8090-T851, AA 7075-T651 and 7075-T7351. The testing was performed on samples with uniform dimensions and step geometry. The environmental test type was performed on two different aircraft carriers and in two different environments. Weather reports measuring temperature and relative humidity were taken hourly on both ships. The laboratory test type included EXCO, MASTMAASIS and SO_2 salt fog corrosion tests. Although, the EXCO corrosion tests is the quickest, it does not imitate any typical environment. It involved total immersion of the sample in the solution acidified by nitric acid (NH_4) for 48 hours. The MASTMAASIS was performed by intermittent spraying of solution containing acetic acid (CH_3COOH) and NaCl. The samples were tested for four weeks with weekly sample imaging. The characteristics of laboratory and carrier environments are given in Table 2.11, while the results of corrosion testing are represented in Table 2.12.

Table 2.11. The characteristics of laboratory and environmental tests [289]

Test	Conditions	Acidifying agent	pH	Temperature, °C	Relative humidity, %
EXCO	Total immersion	NH_4	0.4-3.0	25	100
MASTMAASIS	Cyclic salt spray	CH_3COOH	2.8-3.0	49	65-95
SO_2 salt fog	Continuous salt spray	SO_2	2.5-3.2	35	95
Carrier	Cyclic salt spray	SO_X, NO_X, jet exhausts, stack gases	2.4-4.0	23-29	71-87

The severity of corrosion and corresponding rating were in accordance with the ASTM standard. As indicated by Table 2.11 the SO_2 salt fog corrosion test is the closest imitation of a shipboard environment. The SO_2 mimics the exhaust from fuel-burning ships and the salt spray represents the ocean water spray. The Al-Li test materials aboard the aircraft carriers did not corrode above moderate exfoliation level (Table 2.12, EB). The samples on the *U.S.S. Constellation* exhibited more pronounced corrosion compared to the samples aboard *U.S.S. John F. Kennedy*, demonstrating that monsoon conditions including rough sea, high temperature and humidity (Table 2.11) have more pronounced effect on the corrosion degradation (Table 2.12). It should be noted that on both ships AA 2090-T8E41 and AA 80901-T851 exhibited less corrosion degradation compared to AA 7075-T651, as indicated by Figure 2.32 a and b.

Table 2.12. The results of Thompson experiment [289]

Alloy	Plane	*U.S.S. Constellation Aircraft carrier*	*U.S.S. John F. Kennedy Aircraft carrier*	EXCO	MAST	SO_2
7075-T651	T/10	EA[3]	N[1]-P[2]	ED[6]	ED	ED
	T/2	EC[5]	EB[4]	ED	ED	ED
7075-	T/10	P	P	EA	P	EA
T7351	T/2	P	P	EA	P	EA
2090-	T/10	P	P	ED	P	P
T8E41	T/2	P	P	ED	P	P
8090-T851	T/10	P-EA		ED	P	P
	T/2	P-EA		ED	P	P

[1]N- no attack, [2]P- pitting, [3]EA- slight exfoliation, [4]EB- moderate exfoliation, [5]EC- severe exfoliation, [6]ED- very severe exfoliation

The results of laboratory corrosion testing indicated that the EXCO test had a most severe impact on sample degradation, during which all the tasted samples, except AA 7075 T7351, exhibited very severe exfoliation corrosion (Table 2.12). However, the results of this test gave no significant conclusions, since no difference between the samples could be determined. In contrast, the MASTMAASIS test resulted in a pitting corrosion of all samples except the AA 7075 T651 that showed a very severe exfoliation (Table 2.12).

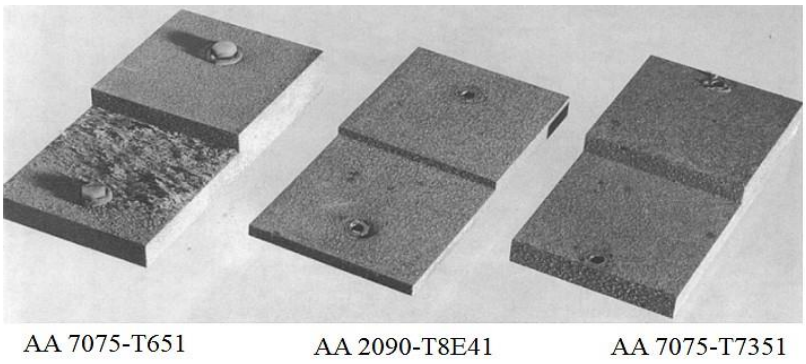

a)

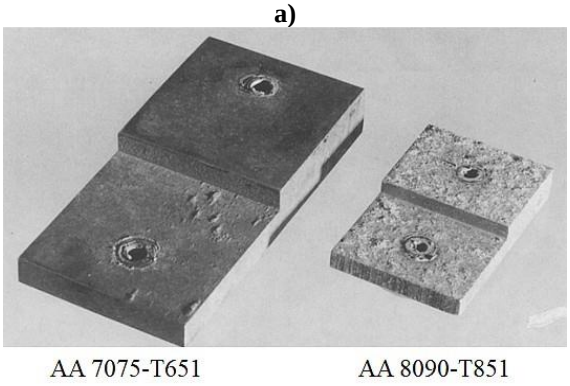

b)

Figure 2.32. The Al alloy step samples after the exposure abord the: a) *U.S.S. Constellation, b) U.S.S. John F. Kennedy* [289]

Under the most realistic laboratory testing conditions, the Al-Li alloys clearly outperformed the conventionally used AA 7075. While during SO_2 testing the AA 7075 T651 and AA 7075 T7351 exhibited different degrees of exfoliation corrosion, neither of Al-Li alloys degraded beyond the stage of pitting corrosion (Table 2.12, Figure 2.32).

Although, the results of Thompson experiment indicated that second-generation of Al-Li alloys exhibited higher corrosion resistance compared to commercially used Al alloys, they were still prone to microstructure degradation through pitting and exfoliation in certain environments [289]. The second-generation products from AA 2091 and AA 8090 as recrystallized sheet exhibit lower resistance to long transverse SCC, while recrystallize AA 8090 and AA 2090 plate product show susceptibility to short transverse SCC [266]. The SCC appears in a particular crack promoting environment when the alloy is subjected to a tensile stress above some minimum threshold value. The joined effect of stress and the aggressive medium results in ductility loss and a brittle fracture [277]. The initial thought on the pitting and intergranular corrosion susceptibility of AA 2090 T8E51 was based on a proposal that intergranular corrosion attacks are strongly associated with dissolution of Cu-depleted zones formed adjacent to grain and subgrain boundaries. This proposal was countered by the suggestion that continuous subgrain boundary dissolution occurs by the localized galvanic

attack on active precipitates. This hypothesis was later supported by the observations that the local corrosion for AA 2090 T8E51 was significantly greater in comparison to AA 2090 T8E41. This higher corrosion resistance was explained by the fact that AA 2090 T8E41 was subjected to the 6.0 % stretching before aging which simultaneously promoted precipitation of Al_2CuLi (T_1) phases within the grains and retarded its precipitation at the grain and subgrain boundaries. Further experimental work established dissolution characteristics and electrochemical behavior concerning Al_2CuLi (T_1). The Al_2CuLi (T_1) intermetallic compounds are involved in rapid anodic and cathodic reactions leading to de-alloying of α_{Al} solid solution through Li^+, Mg^{2+} and Al^{3+} cation release and formation of 10.0-100.0 nm tick Cu-rich clusters. These clusters are often unstable and detach facilitating Cu liberation and its local surface redistribution in corrosion products [278].

Besides heat treatment, chemical composition is crucial in obtaining a product with good corrosion performance. The second-generation Al-Li-Cu alloys developed in United Kingdom contained Mg additions to stimulate co-precipitation of The Al_2CuLi (T_1), Al_3Li (δ') and Al_6CuMg_4 (T_2) phase. Magnesium additions in combination with stretching after solution heat treatment established dominance of Al_6CuMg_4 (T_2) phase precipitation during subsequent aging. In addition to its beneficial effect on corrosion resistance, it enabled exploitation of Al_2CuLi (T_1) phase hardening effect and prevention of planar slip formation [279]. Several Al-Li products incorporated Zn additions to obtain higher exfoliation corrosion and SCC resistance [280]. The improvement in localized corrosion resistance through Zn addition is a consequence of the reduced electrochemical potential between the α_{Al} matrix and the potentially active precipitates. Furthermore, when present as a solute in α_{Al} solid solution, Zn will increase its passive current, but when incorporated into intermetallic phases it will reduce their electrochemical potential [277].

2.3.2.6. Low thermal stability

In aircraft industry, thermal stability is understood as the capacity of heat-treated semi-product to preserve its functional properties at elevated temperatures corresponding to solar or operational heating. It is defined as the stability of supersaturated solid solution (SSS) or intermetallic phases at elevated temperatures. The instability of intermetallic phases is the consequence of supersaturated solid solution (SSS) depletion. The problem of thermal stability is very important because the solid solution in Al-Li alloys is not stable and it easily decomposes even at the low saturation remaining after hardening and artificial aging. Moreover, the thermal

stability requirements for structural materials used in aircraft production are more stringent [281]. Though there is no universal test to simulate all types of thermal exposures that commercial aircraft may experience in the wings and fuselage structures, the exposure for $500.0 \cdot 10^2$ s to $1000.0 \cdot 10^2$ s in the temperature range between 70.0 °C and 85.0 °C is considered sufficient [277]. The significant reduction in fracture toughness during simulated thermal exposure at the 85.0 °C for $1000.0 \cdot 10^2$ s was characteristic for second generation Al-Li products (AA 2090, AA 8090, and AA 2190) [290]. Thermal stability needs to be considered during alloy design and thermo-mechanical processing development. The degree of alloying needs to be sufficient to reach targeted properties at peak strength with no remaining solute elements in solid solution that can later precipitate as intermetallic phases and impact alloy properties. The maximum thermal stability is achieved in semi-products with recrystallized structure or unrecrystallized structure with insignificant polygonization process [281]. The influence of recovery degree on the fracture surface of AA 1450 plate is given in Figure 2.33. The fracture of the deformed unrecrystallized sample occurs at the angle to the plane of the main fracture propagation with the formation of smooth ridges on the fracture surface (Figure 2.33, unrecrystallized). This tape of fracture is characterized as intergranular. The fracture surface in a sample with a well-developed polygonised structure is of a brittle type. The brittle fracture is a result of the crack propagation along subgrain boundaries (Figure 2.33, polygonised) [291]. The polygonization process refers to the formation of large number of differently oriented fine subgrains within the grain structure [292]. During heat treatment polygonization leads to a coarsening and increase in misorientation between the subgrain structure and formation of high-angle grain boundaries. The appearance of these boundaries indicates the occurrence of *in situ* recrystallization or transformation of growing subgrains into a recrystallized grain. In plates with a coarse elongated grain structure the polygonization process occurs more rapidly due to the high specific area of the deformed grain boundaries. Contrarily, the probability of polygonization process occurring in the fine elongated microstructure is lesser [291]. The fracture of the sample in recrystallized condition is of a ductile type with dimple formation (Figure 2.33, recrystallized) [291].

From a tempering perspective, the aging to reach peak strength needs to be performed with a final aging step as close as possible to the service temperature. The under aging or over aging heat treatment will result in reduced thermal stability. Slow cooling rate from the aging temperature enables additional depletion from the supersaturated solid solution (SSS) and has a beneficial influence on thermal stability [277].

Better understanding of chemical composition and microstructure development on mechanical properties and corrosion behavior led to the simultaneous optimization of alloying additions and thermo-mechanical processing [266].

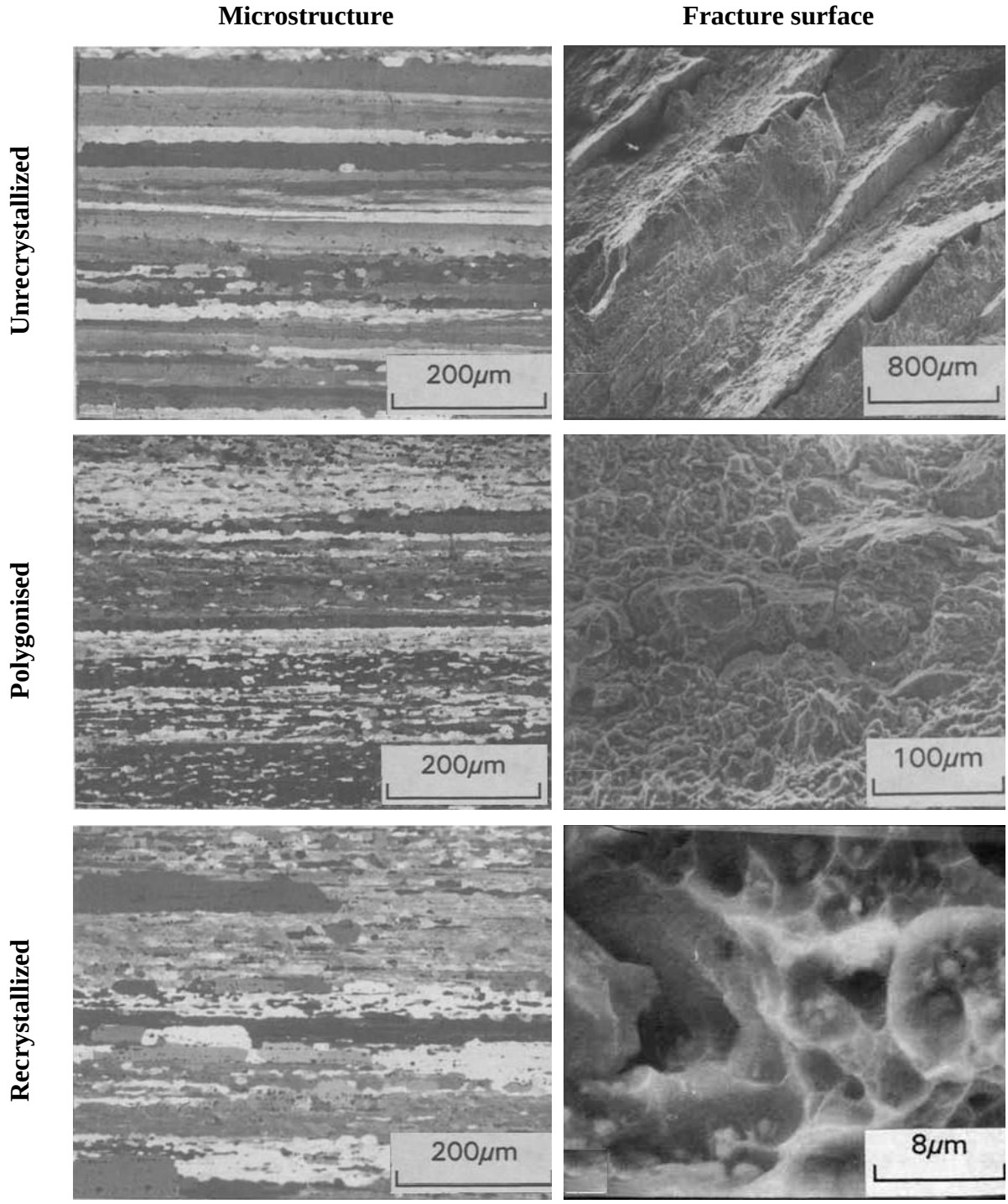

Figure 2.33. The microstructure and fracture surface of AA 1450 plate in: unrecrystallized condition, polygonised condition, recrystallized condition [292]

2.3.3. The key alloy design principles of the third generation aluminum-lithium alloys

Development of last generation of Al-Li alloys is based on the following alloying principles [277]:

- Li and Mg to decrease density and solutionizing and precipitation strengthening,
- Cu and Ag for solutionizing and precipitation strengthening,
- Zn for solid solutionizing and corrosion improvements,
- Zr and Mn for recrystallization and texture control,
- Ti as a grain refiner during solidification of ingots,
- Fe and Si as impurities affecting fracture toughness, fatigue, and corrosion resistance,
- Na and K as impurities affecting fracture toughness.

Figure 2.34 schematically indicates the difference in microstructure development between second and third generation Al-Li alloys as a result of difference in alloying principles. The strengthening of second generation Al-Li alloys was achieved through the precipitation of large volume fraction of the Al_3Li (δ') phase (Figure 2.34 a). Strengthening through the Al_3Li (δ') phase precipitation was caused by the coherency, surface, modulus, and order hardening [280]. Although the strengthening effect of modulus and order hardening is higher compared to the strengthening effect of coherency and surface hardening, the increase in mechanical properties can vary with the aging conditions. In the early stages of age hardening the strengthening is caused by the synergy of modulus hardening, coherency hardening and hardening from the interfacial energy, while in the peak-aged condition strengthening is affected by modulus and order hardening [293].

Other alloying elements such as Cu and Mg were added to second generation Al-Li alloys to influence phase precipitation by altering the solid solubility of principal alloying elements and form Cu- and Mg-based co-precipitates [294]. In ternary Al-Li-Cu systems the strengthening was obtained by co-precipitation of Al_2CuLi (T_1) and Al_6CuLi_3 (T_2) Cu-based intermetallic phases (Figure 2.34 a). The addition of Mg lead to the precipitation of Al_2LiMg (T) phase near the grain boundaries that reduced or fully eliminated precipitation free zone (PFZ) formation. Reduction in PFZ had a beneficial effect on strength properties and early failure prevention [266]. Zirconium additions were found to be effective in inhibiting recrystallization and improving toughness and resistance to stress corrosion cracking (SCC). The property improvement is a consequence of spherical and coherent Al_3Zr (β') phases

precipitation (Figure 2.34 a) and its interaction with grain boundaries and Al_3Li (δ') phase. Due to low solid solubility of Zr in α_{Al} solid solution, small Al_3Zr (β')/α_{Al} misfit strains of approximately 0.8 % and sluggish diffusion of Zr from α_{Al} solid solution, Al_3Zr (β') precipitates are effective in pinning grain and subgrain boundaries during thermo-mechanical processing [295].

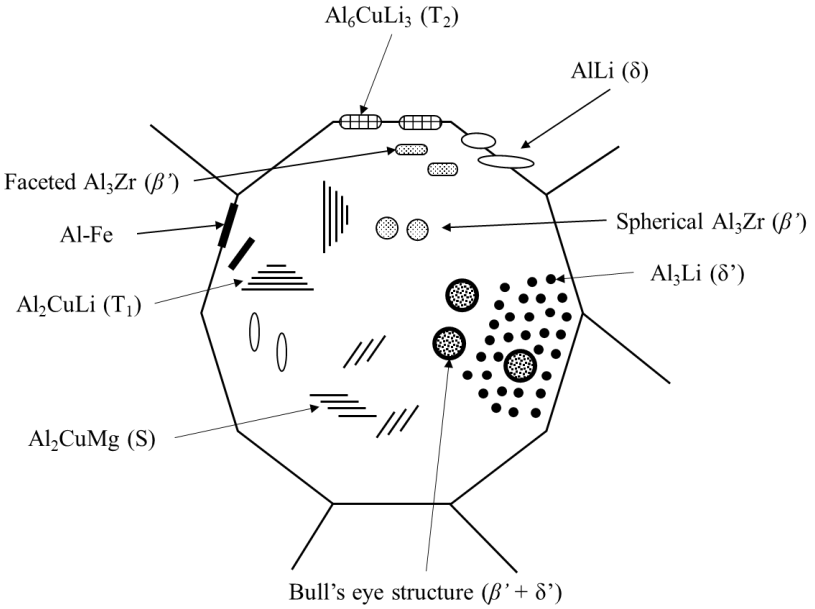

a)

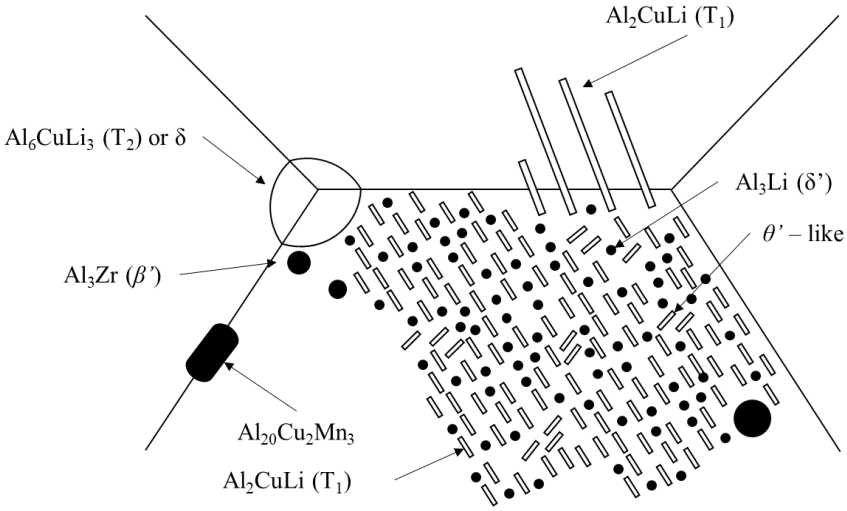

b)

Figure 2.34. The schematics of typical microstructural features in: a) second-generation, b) third generation Al-Li alloys [294]

Moreover, Al_3Zr (β') precipitates provide heterogeneous nucleation sites for Al_3Li (δ') phase precipitation. However, its heterogeneous nucleation potential is affected by Al_3Zr (β')/α_{Al} orientation relationship. If Al_3Zr (β') phase is dissolved at the migrating grain boundary and

reprecipitated with faceted morphology (Figure 2.34 a), it is no longer suitable for the Al_3Li (δ') phase nucleation. Instead, faceted Al_3Zr (β') phase enables heterogeneous nucleation of Al_6CuLi_3 (T_2) and $MgZn_2$ phases [296]. The formation of Bull's eye structure is characteristic for Al-Li alloys containing small additions of Zr, Scandium (Sc) and Ytterbium (Yb) (Figure 2.34 a). The Bull's eye structure is a compound phase consisting of Al_3(Zr, Sc, Yb) core surrounded by a Al_3Li shell that develops during double-aging of quenched alloy. Two important features of these composite structures are a nearly uniform size dispersion and considerably improved strength [297].

The strengthening effect in third generation Al-Li alloys is achieved through the precipitation of Al_2CuLi (T_1), Al_3Li (δ') and Al_2Cu (θ')-type phases. The Al_2CuLi (T_1) phase precipitates simultaneously at the grain boundaries and inside the grains (Figure 2.34 b). Though, it is not entirely clear whether the Al_2CuLi (T_1) phase is formed by the mechanism of intrinsic stacking fault (SF) [298], T_1' precursor (Figure 2.34 b) [299] or GPT_1 zone nucleation [300], it requires pre-deformation before artificial aging. Furthermore, precipitation kinetic of Al_2CuLi (T_1) phase is also determined by the alloy composition, mostly the presence of minor solute elements such as Mg, Zn and Ag. Silver additions improve the precipitation strengthening of Al-Cu-Li alloys by trapping vacancies to inhibit precipitation of Al_2Cu (θ') and increase the density of Al_2CuLi (T_1) phase. Furthermore, the addition of Ag in conjunction with Mg reduces the SF energy and facilitates the formation of dislocations during pre-deformation, subsequently benefiting the precipitation of Al_2CuLi (T_1) phase [301] and significantly improving the aging response. Although, the Al_2CuLi (T_1) precipitates were described as strong non-shareable [302], the recent investigations have indicated that the aging condition will affect the interaction between dislocations and Al_2CuLi (T_1) precipitates, influencing strength properties and plastic behavior [303]. The single-layer Al_2CuLi (T_1) precipitates that form during early stages of aging can be shared by dislocations. The formation of planar slip and localization of plasticity on a microscopic scale is prevented by the fact that single-layer Al_2CuLi (T_1) can be sheared once in the same place. However, the formation of slip lines is not affected. The transition between shearing and by-passing is progressive and correlated to the increase of the Al_2CuLi (T_1) plate thickness occurring at the over aged condition [304]. When Ag atoms substitute Cu atomic positions and Mg atoms substitute Li atomic positions in the Al_2CuLi (T_1) structure, the Al_2(Cu,Ag)(Li,Mg) (Ω) phase precipitates. Although currently the exact mechanism of Al_2(Cu,Ag)(Li,Mg) (Ω) phase nucleation is not clear, it has been associated with the existence of precursor phase (Ω') [305], formation of Ag and Mg co-clusters [306], as well as the newly discovered type of GP zones [307]. Regardless,

the $Al_2(Cu,Ag)(Li,Mg)$ (**Ω**) phase grows isomorphous and isostructural to the Al_2CuLi (T_1) phase through the segregation of Mg and Ag atoms at the α_{Al}/ $Al_2(Cu,Ag)(Li,Mg)$ (**Ω**) interface. The similarities in the structure between Al_2CuLi (T_1) and $Al_2(Cu,Ag)(Li,Mg)$ (**Ω**) phase result in the similar interaction with dislocations. Previous investigations have correlated the precipitation sequence of Al-Cu-Li-X alloys with Cu/Li ratio and suggested that the peak aged microstructure is dominated by Al_2CuLi (T_1) phase. However, the recent investigations indicated the precipitation of several metastable phases, including Al_2Cu (θ') [308]. It is also postulated that Li atoms could substitute into the defect sites of the Al_2Cu (θ') structure leading to the precipitation of Al_2Cu (*θ'*)-type phases that are thought to be isomorphous and isostructural to Al_2Cu (θ') precipitates [309]. To control the recrystallization and texture development, the dispersoids that form in most third generation wrought products are Al_3Zr and $Al_{20}Cu_2Mn_3$. The $Al_{20}Cu_2Mn_3$ phase is the main strengthening precipitate in Al-Cu(-Mg), Al-Zn-Mg(-Cu), Al-Mn and Al-Li-Cu alloys that are generally formed during homogenization. Due to its complicated structure containing anti-phase boundary (ABP) and twin boundaries, the $Al_{20}Cu_2Mn_3$ phase exerts an effect of grain boundary and dislocation pinning which promotes both grain refinement and dispersion strengthening [310].

The optimization of thermo-mechanical processing refers to the beneficial influence of cold deformation prior to the artificial aging on strength and fracture toughness. This property improvement is a consequence of refinement of the precipitates and discouragement of grain boundary precipitation during aging. The pronounced effect of cold deformation prior to aging on strength and toughness in Al-Cu-Li alloys is caused by the high tendency of Al_2CuLi (T_1) phase to nucleate on dislocations increasing its number by approximately two orders of magnitude [277]. Introduction of dislocations prior to artificial aging enhances diffusion of substitutional solute providing heterogeneous nucleation sites and facilitating the optimum distribution of Al_2CuLi (T_1) phase. The pre-deformation is also beneficial for preferential precipitation of Al_2CuLi (T_1) phase in competition to the Al_2Cu (θ') and Al_3Li (δ') phases during aging [311].

2.4. The microstructure development in aluminum-lithium based alloys

Besides chronological development, the Al-Li alloys can be further classified based on the chemical composition as:

- Al-Cu-Li with additions of Mn and Cd (AA 2020, VAD 23),

- Al-Li-Mg with additions of Zr, Mn and Sc (AA 1420, AA 1421, and AA 1423),
- Al-Li-Cu-Mg-Zr with additions of Ag (AA 2091, AA 8090, Weldalite 049).

The nature, structure, size, and distribution of the intermetallic phases as well as the properties of the precipitate/matrix interfaces are influenced by chemical composition, processing, and thermodynamic parameters. In turn, all microstructural constituents have a pronounced effect on functional properties of the alloy. This emphasizes the need for extensive and detailed studies of phase equilibria and mechanisms of nucleation and growth. Furthermore, the presence of the impurities in Al alloys and minor alloying additions can lead to the formation of intermetallic phases with desirable and detrimental effect on alloy's properties. The schematic representation of microstructural constituent development in Al-Li based alloys is given in Figure 2.35. The intermetallic phases in Al-Li based alloys can be divided into three categories:

- Intermetallic constituent particles,
- Dispersoid particles,
- Precipitate particles.

Intermetallic constituent particles form during solidification of the molten alloy at relatively high temperatures. Some of these intermetallic particles like Al_2Cu (θ), Al_3Zr (β') and Al_2CuLi (T_1) may dissolve during subsequent heat treatment, while the others, such as Al_7Cu_2Fe, $AlFe_3$, $Al_{12}Fe_3Si$, remain relatively unaffected. The coarse insoluble constituent particles have minor effect on strength properties but adversely affect ductility and fracture toughness. Dispersoid particles are usually Mn-, Zr-, or Cr-containing particles that predominantly form during ingot homogenization. Dispersoid particles such as Al_3Zr (β'), $Al_{20}Cu_2Mn_3$ and $Al_{12}Mg_2Cr$ have a strong influence on grain size by retarding recrystallization and grain growth.

While fine grain size beneficially influences strength properties, the partition between solute elements (Li, Mg) from the matrix and dispersoid particles results in improved ductility. Precipitate particles and their nature depend on the type and the amount of present alloying elements as well as the conditions of heat treatment. Precipitate particles form during aging at room or elevated temperatures in the alloying systems that are characterized by decreasing solid solubility with respect to temperature [84]. Therefore, it is necessary to consider the equilibrium phase diagrams of various systems and to examine the possibility of metastable phase formation.

2.4.1. The aluminum-lithium binary system

The binary Al-Li diagram is given in Figure 2.36. The Al-Li phase diagram has been carefully analyzed in the past from the experimental perspective in order to ascertain the precipitation sequence and the optimum heat treatment. It is characterized by the eutectic reaction at 600.0 °C in the Al rich corner leading to the formation of α_{Al} solid solution and AlLi (δ) phase. The solid solubility of Li in α_{Al} solid solution varies from 4.0 at% at the eutectic temperature to less than 1.0 at% at 100.0 °C. The precipitation of the equilibrium AlLi (δ) phase is preceded by the solidification of Al_3Li (δ') with solvus line between 150.0 to 250.0 °C for the alloys of practical interest [312]. The similarities in the structure and lattice parameters of α_{Al} and Al_3Li (δ') phase result in the small lattice mismatch and reduced strain effect. Consequently, the Al_3Li (δ') phase forms as coherent spherical particle that retains its shape up to the size of 0.3 μm. The surface energy of the α_{Al}/ Al_3Li (δ') interface is very small (< 30.0 mJ/m^2) and the antiphase boundary energy of Al_3Li (δ') is low (180.0 mJ/m^2) resulting in strain localization during deformation [313].

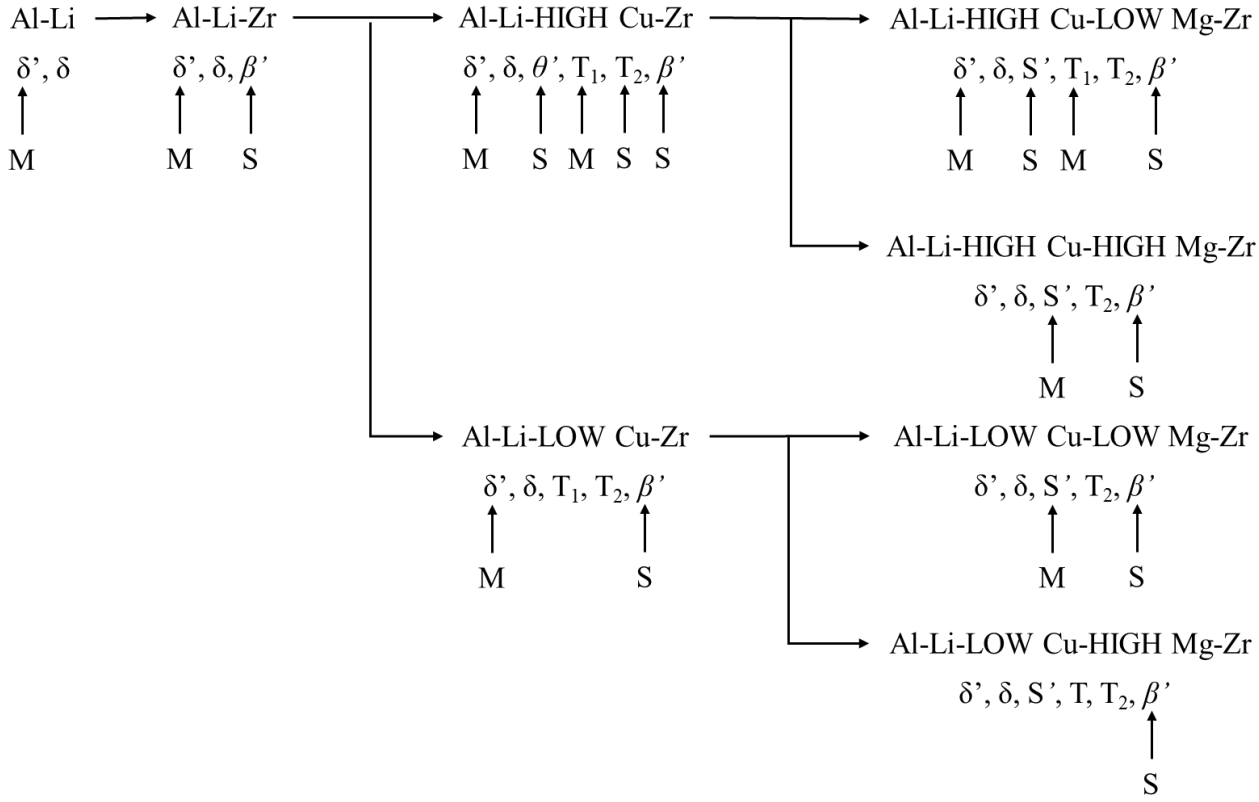

Figure 2.35. The schematic representation of microstructure constituents in Al-Li based alloys, M-major, S – minor constituents [266]

Despite its simplicity, there are several controversial issues in Al-Li phase diagram concerning:

- The appearance of GP zones prior to the Al_3Li (δ') formation and the type of their structure [314],
- The precise path for the formation of Al_3Li (δ') phase as a function of Li content and temperature [315],
- Classification of Al_3Li (δ') phase as metastable [316].

These issues are not likely to be verified experimentally due to the uncertainties associated with the kinetics of phase transformations. The wide variation in phase transformation kinetics for the low and high Li content is mainly due to the slow precipitation kinetics in low Li alloys and competing formation of AlLi (δ) at high Li concentrations. These uncertainties also affect the currently accepted version of the Al-Li phase diagram constructed using the computation of phase diagrams (CALPHAD) methodology from approximate analytical expressions of free energy of the different processes that are obtained from the available experimental and theoretical results [317].

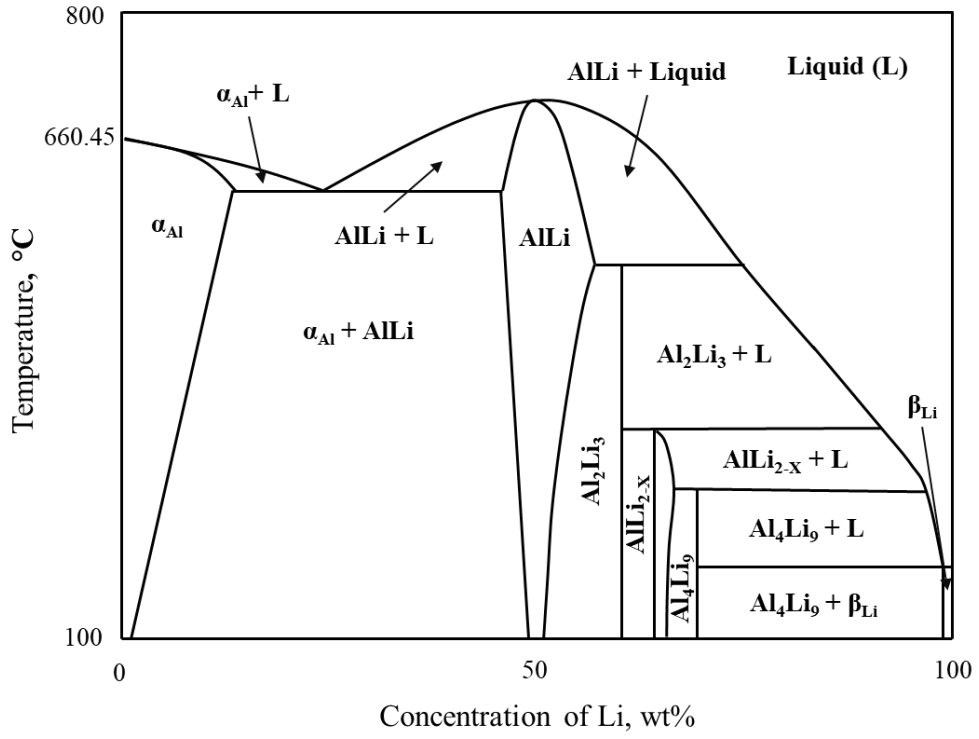

Figure 2.36. The Al-Li binary phase diagram [313]

2.4.2. The aluminum-lithium-copper ternary system

The additions of Cu to Al-Li binary system decrease the maximum solubility of Li in α_{Al} solid solution at all temperatures. The sections of Al-rich corner at 500.0 °C and 350.0 °C are given in Figure 2.37 a and b. The phases formed under equilibrium conditions are Al_2Cu (θ), AlLi (δ), Al_2CuLi (T_1), Al_6CuLi_3 (T_2), and $Al_{7.5}Cu_4Li$ (T_B). The Guinier-Preston (GP) zones, Al_3Cu (θ''), Al_2Cu (θ') and Al_3Li (δ') metastable phases characteristic for Al-Cu and Al-Li systems are also found in ternary Al-Cu-Li alloys during aging at elevated temperatures. Based on the results of several investigations, the precipitation reactions in the Al-Cu-Li ternary system can be summarized as a function of Cu/Li ratio [312]:

For Cu/Li > 4 $\alpha_{Al} \rightarrow$ GP zones$\rightarrow \theta'' \rightarrow \theta'$ (6)

For Cu/Li = 2.5 to 4 $\alpha_{Al} \rightarrow$ GP zones$\rightarrow$ GP zones + $\delta' \rightarrow \theta'' + \theta' + \delta' \rightarrow \delta' + T_1 \rightarrow T_1$ (7)

For Cu/Li = 1 to 2.5 $\alpha_{Al} \rightarrow$ GP zones + $\delta' \rightarrow \theta' + \delta' \rightarrow \delta' + T_1 \rightarrow T_1$ (8)

For Cu/Li < 1 $\alpha_{Al} \rightarrow \delta' + T_1 \rightarrow T_1$ (9)

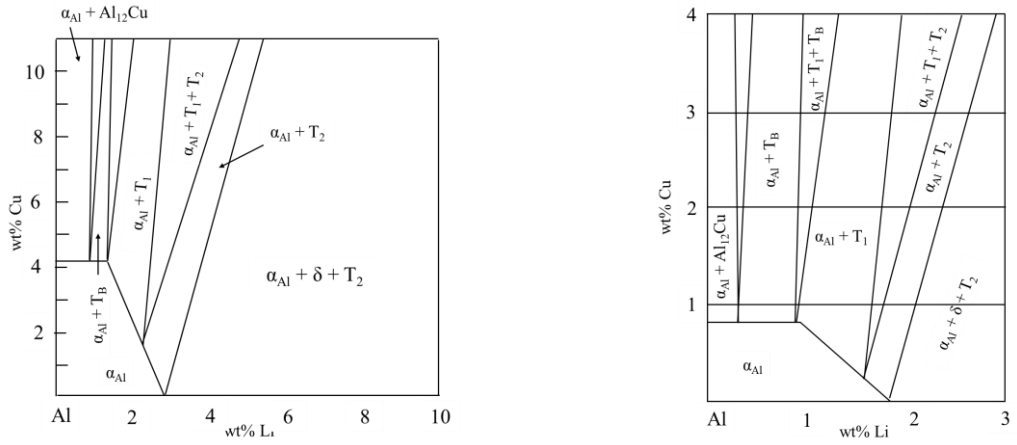

a) **b)**

Figure 2.37. Isothermal sections of Al-Li-Cu system at: a) 500.0 °C, b) 350.0 °C [312]

Although, the Cu additions have no effect on the position of α_{Al}/Al_3Li (δ') solvus boundary, there are some inconsistencies about the effect of Cu in the α_{Al} solid solution on the precipitation of Al_3Li (δ'). Earlier investigations indicated that the Al_3Li (δ') phase precipitation is not affected by the presence of Cu, while the recent research postulates that the kinetics of Al_3Li (δ') phase precipitation are accelerated by the formation of GP zones that act as heterogeneous nucleation sites [318]. At the high Cu/Li rations the Al_3Li (δ') phase can grow on the facets of Al_2Cu (θ') phase (Equation 6) followed by the competitive growth of Al_2CuLi (T_1) phase (Equation 7). The presence of Al_2CuLi (T_1) phase at the grain boundaries leads to

the formation of precipitation free zones (PFZ). These zones are characteristic for the Al-Li-Cu alloys with high Cu/Li ratio, as well as the coarsening and the transition of Al_3Li (δ') to AlLi (δ) phase [319]. The Al_2Cu (θ') phase can also be replaced by the Al_2Cu (θ) phase at high aging temperatures. However, transformation from Al_2Cu (θ') to Al_2Cu (θ) is associated with a large reduction in the yield strength because the large Al_2Cu (θ) precipitates do not represent strong obstacles for dislocation movement [320]. The most relevant precipitate in the Al-rich region of the ternary Al-Li-Cu system is the Al_2CuLi (T_1) phase with hexagonal structure. In the alloys with the higher Cu and lower Li the Al_2CuLi (T_1) phase nucleates on the GP zones. On the other hand, in the alloys with higher Li and lower Cu the Al_2CuLi (T_1) phase nucleates heterogeneously on the stacking faults (SF) formed by the dissociation of dislocations into Shockly partials. Depending on the alloy composition and processing conditions, other minor phases, such as Al_6CuLi_3 (T_2) and Al_7Cu_4Li (T_B) have been reported [309]. The T_2 phase with Al_6CuLi_3 or Al_5CuLi_3 stoichiometry is characterized by its large size. The stoichiometry of the T_B phase is assumed to be Al_7Cu_4Li and is always considered as a metastable phase that can be dissolved during heat treatment at high temperatures. The appearance of Al_7Cu_4Li (T_B) phase at lower temperatures was explained by the influence of strain on the precipitation at high-angle grain boundaries [275].

2.4.3. The aluminum-lithium-zirconium ternary system

As previously indicated, the small amounts of Zr have an important effect on the functional properties of commercially used Al-Li alloys due to its influence on grain growth and crystallographic texture [312].

At the Al-rich corner of the Al-Li-Zr system, two binary phases AlLi (δ) and Al_3Zr (β') exist in the equilibrium with α_{Al} solid solution [321]. Although the solubility of Zr in AlLi (δ) phase is negligible, the Al_3Zr (β') phase can absorb up to 1.3 at% of Li and lead to the formation of $Al_3(Li_xZr_{1-x})$ phase. The similarity in the structure type and lattice parameters, enables heterogeneous nucleation of $A_{l3}Li$ (δ') phase on the $Al_3(Li_xZr_{1-x})$ and formation of Bull's eye structure during aging (Figure 2.34 a). The precursor to the Al_3Zr (β) phase precipitation is the formation of β_0 with the same stoichiometry of Al_3Zr but with $L1_2$ structure [322]. This precursor phase is resistant to the dislocation shearing during thermo-mechanical processing and also plays an important role in retarding recrystallization and grain growth by pinning the migrating grain boundaries [323].

2.4.4. The aluminum-lithium-magnesium ternary system

The Al-rich corner of ternary Al-Li-Mg system at 500.0 °C and 200.0 °C is shown in Figure 2.38. The first solid phases to form from the melt are α_{Al} solid solution, AlLi (δ) and Al_8Mg_5 (β). Later, these phases participate in the peritectic reaction to form Al_2LiMg (T) and $Al_{12}Mg_{17}$ phase. It should be emphasized that the high solid solubility of Mg in α_{Al} solid solution is unaffected by the presence of Li. However, the Mg reduces solubility of Li in α_{Al} solid solution resulting in the formation of high-volume fraction of Al_3Li (δ') phase [312].

Based on the chemical composition the solidification sequence can be described by following equations [324]:

For high Li/Mg ratio $\alpha_{Al} \rightarrow Al_3Li\ (\delta') \rightarrow AlLi\ (\delta)$ (10)

For low Li/Mg ratio $\alpha_{Al} \rightarrow Al_3Li\ (\delta') \rightarrow Al_2LiMg\ (T)$ (11)

The strengthening in Al-Li-Mg alloys is mainly achieved by the precipitation of metastable Al_3Li (δ') phase. Increasing the Mg amount above 2.0 wt% increases the likelihood of ternary Al_2LiMg (T) phase formation. Thus, the Mg has an indirect impact on the strengthening improvement through the:

- Enhancing the solid solution strengthening,
- Partially substation of Li in the Al_3Li (δ') phase precipitates,
- Reduction the solid solubility of Li in α_{Al} solid solution.

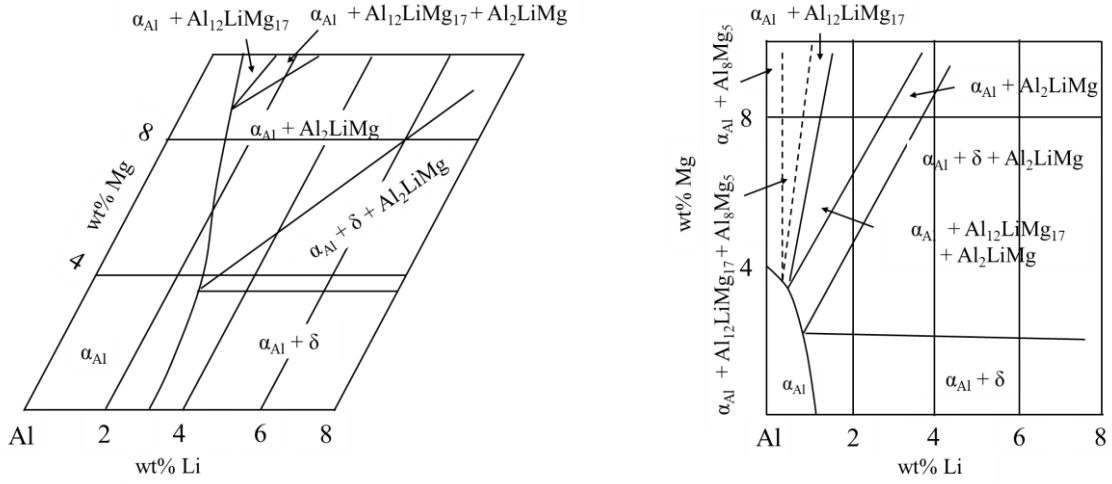

a) **b)**

Figure 2.38. Isothermal sections of the Al-Li-Mg system at: a) 500.0 °C, b) 200.0 °C [312]

Although the precipitation in Al-Li and Al-Li-Mg alloys seems very similar as far as the formation of Al_3Li (δ') and AlLi (δ) phases is concern (Equation 10), it has been proposed that the addition of Mg changes the solubility of Li in α_{Al} solid solution enhancing the precipitation of Al_3Li (δ') phase. It is not clear whether the addition of Mg changes the diffusion rate of Li in α_{Al} solid solution. The kinetic studies indicate that such a change would be small [78]. Moreover, the distribution of Mg atoms in between the α_{Al} solid solution and Al_3Li (δ') particles is not known, although some research results indicate that the Al_3Li (δ') phase contains a significant concentration of Mg [325]. It is also not known if the enhancement of precipitation due to Mg atoms is mainly controlled by the phase stability, by changes in interfacial energy, or by the changes in the diffusion coefficient. Solving these issues is not simple due to the precipitation during quenching and development of high volume of precipitates [326].

2.4.5. The minor alloying additions to aluminum-lithium alloys

Minor alloying additions have been suggested to improve the mechanical properties of Al-Li-based alloys. These additions include Co, Ti, Mn, Ni, Sc, Cr, Cd, Ge, Indium (In), Sn. Minor element additions influence grain size and precipitation processes through:

- Grain refinement by the addition of Ti, B, C,
- Grain refinement and retardation of recrystallization and grain growth by low additions of Zr, Cr, Sc, Lanthanum (La),
- Strong binding between quenched-in vacancies and solute additions leading to the reduced nucleation of GP zones and reduced widths of PFZ,
- Increasing the GP zones solvus line and changing the phase stability regions,
- Segregating at the nucleating particle/matrix interface and reducing the surface energy thereby facilitating easier nucleation of phases and contributing to the finer dispersion of the precipitates,
- Enabling the formation of new phases,
- Forming the clusters in the initial stages of the aging process and contributing to the heterogeneous nucleation,
- Decreasing the solubility of the major elements in the matrix resulting in higher supersaturation in the quenched alloy [312].

The increase in strength of 15.0 to 20.0 % in Al-Li-Cu alloys can be achieved through the addition of Cd, In and Sn. These elements suppress the formation of GP zones and Al_3Cu

(θ'') and promote fine and uniform distribution of Al_2Cu (θ') phase [327]. Furthermore, the additions of 0.5 % In to Al-Li-Cu alloys increase the homogeneity of two major strengthening precipitates Al_2CuLi (T_1) and Al_2Cu (θ') [266]. Combined additions of Sc and Ytterbium (Yb) prevent over-aging by the formation of coherent clusters consisting of Al_3Yb core and Al_3Sc shell [328].

2.5. Solidification in pure metals and alloys

The melting and solidification processes represent transformations between crystallographic and non-crystallographic conditions of the metal or alloying system. They have a crucial application in ingot, foundry or continuous casting, single-crystal growth for semiconductors, directionally solidified, composite alloys as well as rapidly solidified alloys and gasses. The understanding of solidification mechanism and its relation to the processing parameters such as temperature distribution and cooling rate, is important to achieve appropriate mechanical properties of cast metals and fusion welds [329].

2.5.1. The nucleation

When a liquid is cooled below its equilibrium melting temperature (T_m) there is a solidification driving force implying that the liquid phase would solidify. However, spontaneous solidification does not always occur. This behavior is caused by the formation of very small sold particles or nuclei. In the foundry practice the walls of the mold and the presence of solid impurity particles represent the suitable locations for the nucleation of solid at low undercoolings (~ 1.0 °C). This solidification is initiated by heterogeneous nucleation. On the other hand, when heterogeneous nucleation sites are unavailable, the large undercoolings (~ 250.0 °C) are required for homogeneous nucleation [329].

2.5.1.1. The homogeneous nucleation

Figure 2.39 a represents the free energy G_1 during the homogeneous nucleation of a defined volume of the liquid at a temperature (ΔT) below T_m. The free energy of this system is represented by Equation 12:

$$G_1=(V_s+V_L)\cdot G_V^L \tag{12}$$

If the atoms of liquid cluster formulate a small sphere of the solid (Figure 2.39 b), the changes in free energy of the system (G_2) will occur according to Equation 13:

$$G_2=V_sG_V^s+V_LG_V^L+A_{SL}\gamma_{SL} \tag{13}$$

where V_s is the volume of the solid sphere, V_L the volume of the remaining liquid, A_{SL} is the solid/liquid interface area, γ_{SL} is the solid/liquid interface energy, G_V^s and G_V^L are the free energies per unit volume of solid and liquid respectively.

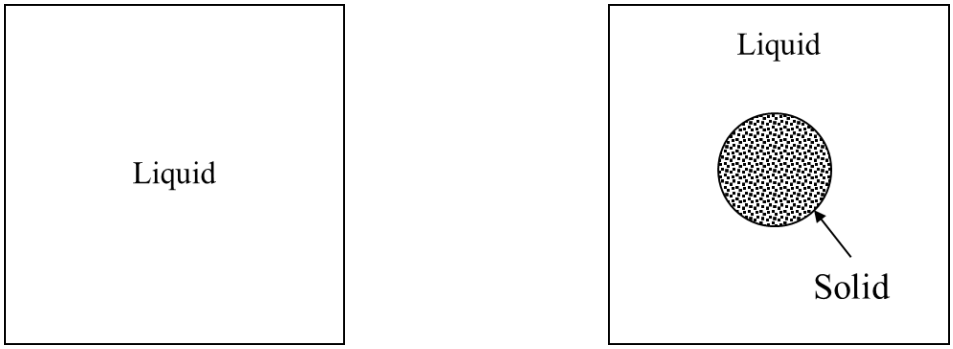

Figure 2.39. Schematic representation of homogeneous nucleation: a) liquid phase, b) clustering of atoms and formation of solid sphere [329]

The formation of solid phase is accompanied by the free energy change $\Delta G=G_2-G_1$ where:

$$\Delta G=-V_S\Delta G_V+A_{SL}\gamma_{SL} \tag{14}$$

and

$$\Delta G_V=G_V^L-G_V^s \tag{15}$$

For the ΔT undercooling the free energy ΔG_V is determined by the Equation 16.

$$\Delta G_V=\frac{L_V\Delta T}{T_m} \tag{16}$$

where L_V represents the latent heat of fusion per unit volume. Below the considered temperature of T_m the free energy per volume unit ΔG_V is positive so that the change in energy related to the formation of small volume of solid has a negative contribution as a consequence of lowered solid's free energy. However, the contribution is positive due to the formation of solid/liquid interface [330]. The excess free energy of the solid can be minimized by the correct choice of particle shape. If γ_{SL} is isotropic, which is characteristic for a sphere with radius r, the Equation 14 translates to:

$$\Delta G_r=-\frac{4}{3}\pi r^3\Delta G_V+4\pi r^2\gamma_{SL} \tag{17}$$

The changes in free energy related to homogeneous nucleation of a sphere with a radius r are represented in Figure 2.40.

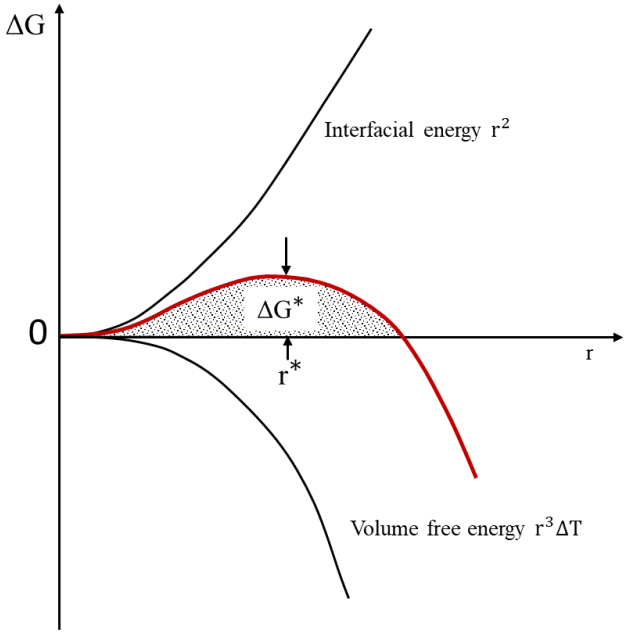

Figure 2.40. The changes in free energy associated with homogeneous nucleation of a sphere with a radius r [329]

While the interferential part of the equation 16 increases as r^2, the released volume free energy only increases as r^3. This increase in free energy allows the liquid to remain in the metastable condition almost indefinitely at the temperatures below T_m. Figure 2.40 indicates that for a given undercooling of ΔT there is a certain radius r^* associated with a maximum excess free energy. The growth behaviour of the system can be defined by following Equations:

$$r < r^* \tag{18}$$

$$r > r^* \tag{19}$$

If $r < r^*$ the system can lower its free energy by dissolution of the solid phase, whereas $r > r^*$ the free energy of the system decreases with increase of solid fraction. The unstable solid particles mentioned in the Equation 18 are identified as clusters or embryos, while stable particles mentioned in Equation 19 are considered as nuclei. The r^* is known as the critical nucleus size. Under conditions of $r=r^*$ and $dG=0$ the critical nucleus is effectively in equilibrium with the surrounding liquid fraction. Differentiation of Equation 17 describes the critical radius as follows:

$$r^* = \frac{2\gamma_{SL}}{\Delta G_V} \tag{20}$$

and

$$\Delta G^* = \frac{16\pi\gamma_{SL}^3}{3(\Delta G_V)^2} \tag{21}$$

By substituting Equation 16 for ΔG_V in Equation 20 gives:

$$r^* = \left(\frac{2\gamma_{SL} T_m}{L_V}\right)\frac{1}{\Delta T} \tag{22}$$

and

$$\Delta G^* = \left(\frac{16\pi\gamma_{SL}^3 T_m^2}{3L_V^2}\right)\frac{1}{(\Delta T)^2} \tag{23}$$

The Figure 3.41 a illustrates the volume free energy as a function of temperature for solid and liquid phase defining the quality of free energy as:

$$\Delta G_V = \frac{2\gamma_{SL}}{r^*} \tag{24}$$

Which is identical to Equation 20.

To understand the possibility of the formation of homogeneous solid nucleus it is necessary to understand the atomic structure of the liquid. At the melting point the liquid phase has a volume 2.0–4.0 % grater compared to the solid. This enables atoms to have greater freedom of movement in the liquid. The movement of atoms appears completely random. However, the small close-packed clusters of atoms are present in the liquid phase. The number of clusters that are temporarily in the same crystalline array is defined as:

$$n_r = n_0^{\left(-\frac{\Delta G_r}{kT}\right)} \tag{25}$$

where n_r is the total number of atoms in the system, ΔG_r is the excess free energy associated with the cluster and k is the Boltzmann's constant. For a liquid above T_m Equation 25 applies for all the values of r. At the temperatures below T_m the Equation 25 applies only for $r \leq r^*$ because clusters greater than the critical size appear to be stable nuclei of solid phase and are no longer a part of the liquid phase.

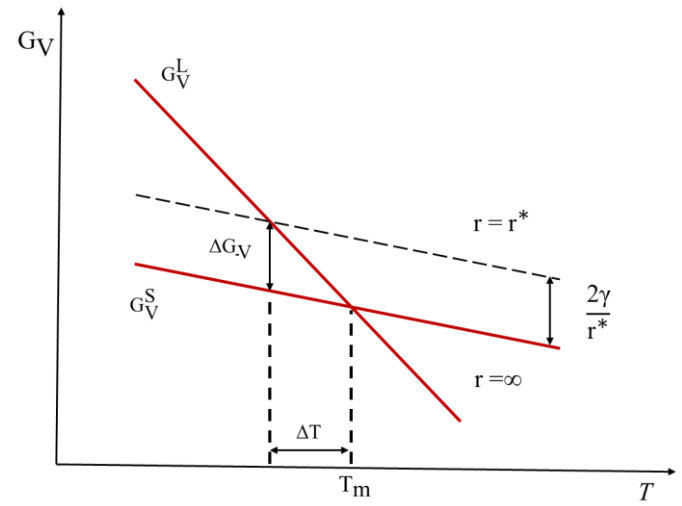

a)

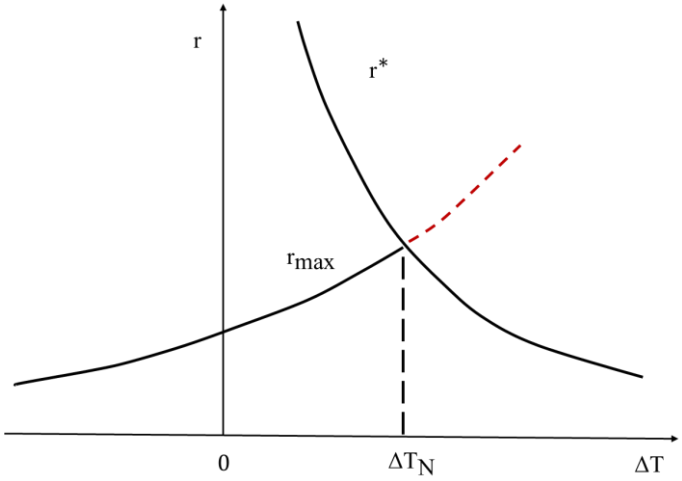

b)

Figure 2.41. The impact of undercooling on: a) volume free energy of solid and liquid phase, b) variation in particle radius [329]

Since n_r decreases exponentially with ΔG_r the possibility of finding a given cluster decreases with the increase in cluster size. Below T_m there is an increasing contribution from ΔG_V as the solid becomes progressively more stable increasing the maximum cluster size. The Figure 2.41 b schematically shows how r_{max} varies with the undercooling ΔT. The formation of clusters larger than r_{max} is possible in large enough systems or in sufficient time, but the possibility of finding clusters only slightly larger than r_{max} is extremely small. The Figure 2.42 also indicates that at low undercoolings r^* is so large that there will be no chance of forming a stable nucleus. On the other hand, at the supercooling of ΔT_N, there is a very good chance of clusters reaching r^* and growing into the stable solid particles [329].

If the liquid contains C_0 atoms per unit volume, the number of clusters reaching the critical size (C^*) can be calculated by the following Equation:

$$C^* = C_0^{\left(-\frac{\Delta G^*_{hom}}{kT}\right)} \left[\frac{clusters}{m^{-3}}\right] \tag{26}$$

The addition of one more atom to each of these clusters will convert them into stable nuclei. If this addition happens with a frequency of f_0, the homogeneous nucleation rate will be determined as:

$$N_{hom} = f_0 C_0^{\left(-\frac{\Delta G^*_{hom}}{kT}\right)} \left[\frac{nuclei}{m^3 s}\right] \tag{27}$$

where f_0 is a complex function that depends on the vibration frequency of the atoms, the activation energy for diffusion in the liquid, and the surface area of the critical nuclei. The exact nature of f_0 is not crucial in understanding the rate of homogeneous nucleation, and it is enough to consider it as a constant equal to ~ 10^{11}. Moreover, since the atomic jumps from the liquid to the solid clusters are thermally activated, the f_0 will diminish with the decrease in the temperature. In some alloying systems the liquid can be rapidly cooled to the temperatures below the so-called glass transition temperature without the formation of crystalline solid. In these instances, the f_0 is very small and the supercooled liquid is referred to as stable metallic gass or amorphous metal [331]. Since C_0 is typically ~ 10^{29} atoms/m^3 a normal nucleation rate (1/cm s) is achieved with $\Delta G^* \sim 78\ kT$.

$$N_{hom} = f_0 C_0^{\left\{-\frac{A}{(\Delta T)^2}\right\}} \tag{28}$$

where A is relatively insensitive to temperature and is quantified as:

$$A = \frac{16\pi\gamma_{SL}^3 T_m^2}{3L_v^2 kT} \tag{29}$$

In Figure 2.42 the N_{hom} is plotted as a function of temperature change. The $(\Delta T)^2$ term indicated in exponential part of the Equation 28, the N_{hom} changes by orders of magnitude from zero to very high values over a very narrow temperature range. This implies that there is a critical undercooling for nucleation ΔT_N.

In industrial practice homogeneous nucleation is rarely encountered during solidification of the castings. Instead, the heterogeneous nucleation occurs at the crevices in the mold walls, or at the impurity particles present in the liquid [329].

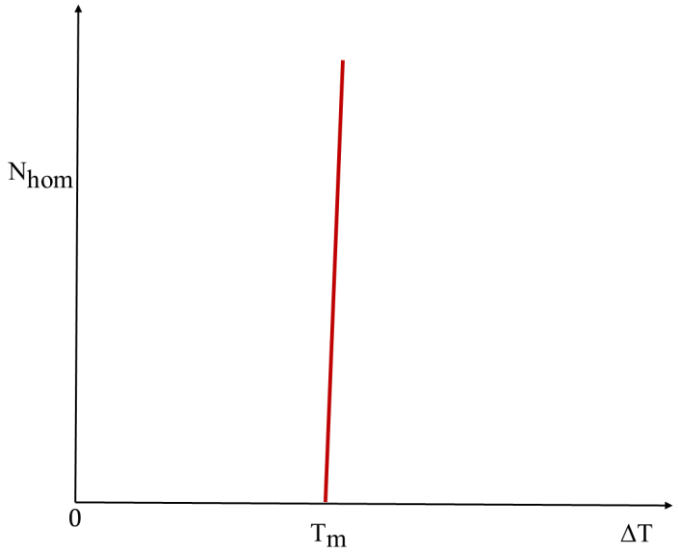

Figure 2.42. The homogeneous nucleation rate as a function of undercooling [329]

2.5.1.2. The heterogeneous nucleation

Based on Equation 23 it can be observed that nucleation is easier at small undercoolings if the interfacial energy relation is reduced. This is most effectively achieved if nuclei form in contact with the mold walls. Figure 2.43 illustrates the forming of embryo in contact with a perfectly flat mold wall. If γ_{SL} is isotropic it can be shown that for a given volume of solid the total interfacial energy of the system is minimized if the embryo has the shape of a spherical cap with a wetting angle θ. Given by the condition that the interfacial tension γ_{ML}, γ_{SM} and γ_{SL} balance in the plane of mould walls [329]:

$$\gamma_{ML} = \gamma_{SM} + \gamma_{SL} cos\theta \tag{30}$$

or

$$cos\theta = \frac{(\gamma_{ML} - \gamma_{SM})}{\gamma_{SL}} \tag{31}$$

As indicated by the Equations 30 and 31 the vertical component of γ_{SL} remains unbalanced. In time, this force would pull the mould surface upwards until the surface tension forces balance in all directions.

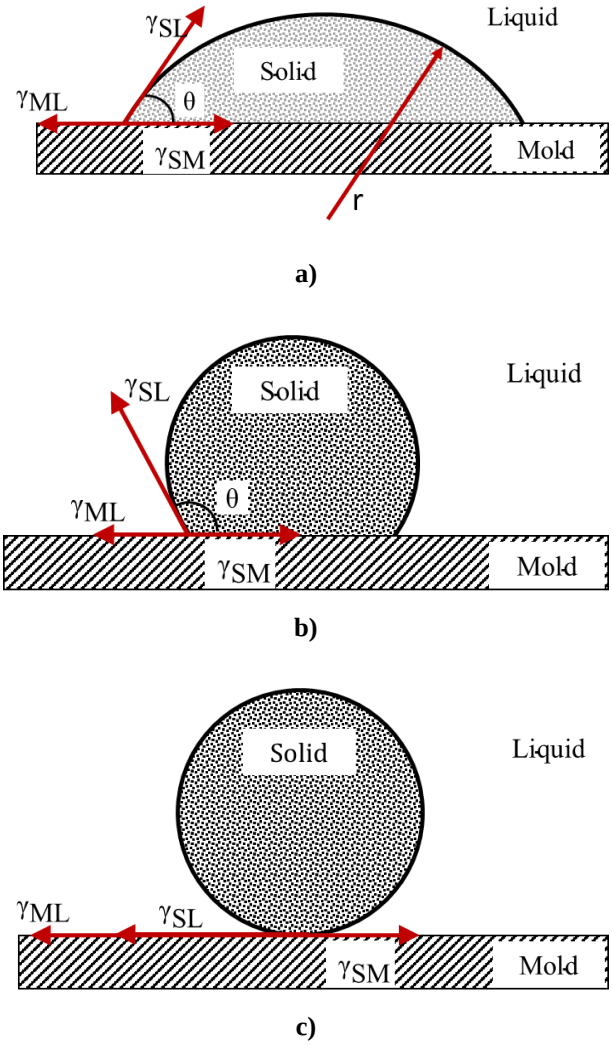

Figure 2.43. The heterogeneous nucleation of cap on a flat mold wall: a) favourable nucleus-surface interaction results in $\theta < 90$ °, b) unfavourable nucleus-surface interactions results in $90° < \theta < 180°$, c) complete absence of wetting results in $\theta = 180°$ [332]

Therefore, Equation 31 only determines the optimal shape of the embryo with the condition that the mold walls remain planar. The formation of that type of embryo will be associated with an excess free energy defined by following Equation 32:

$$\Delta G_{het} = -V_S \Delta G_V + A_{SL}\gamma_{SL} + A_{SM}\gamma_{SM} - A_{SL}\gamma_{ML} \quad (32)$$

where V_S is the volume of spherical cap, A_{SL} and A_{SM} are the areas of the solid/liquid and solid/mould interfaces, and γ_{ML}, γ_{SM} and γ_{SL} are the free energies of the solid/liquid, solid/mould and mould/liquid interfaces respectively. Equation 32 indicates three interfacial energy conditions concerning heterogeneous nucleation. The first two conditions are positive since they originate from interfaces created during the nucleation process, while the third has negative energy contribution due to the dissolution of the interface under the spherical cap [333]. If the

Equation 32 is considered with respect to the wetting angle (θ) and the cap radius (r), the free energy can be shown as:

$$\Delta G_{het} = \left\{ -\frac{4}{3}\pi r^3 \Delta G_V + 4\pi r^2 \gamma_{SL} \right\} S(\theta) \tag{33}$$

where $S(\theta)$ is defined as:

$$S(\theta) = \frac{(2+\cos\theta)(1-\cos\theta)^2}{4} \tag{34}$$

Apart from the factor $S(\theta)$, Equation 33 is identical to homogeneous nucleation relation. The Equation 34 has the numerical value ≤1 dependent only on the shape of nucleus $S(\theta)$. Therefore, the $S(\theta)$ is referred to as shape factor. The differentiation of Equation 34 results in:

$$r^* = \frac{\gamma_{SL}}{\Delta G_V} \tag{35}$$

and

$$\Delta G^* = \frac{16\pi\gamma_{SL}^3}{3\Delta G_V^2} S(\theta) \tag{36}$$

The activation energy barrier against heterogeneous nucleation ΔG_{het}^* is reduced by shape factor $S(\theta)$ compared to ΔG_{hom}^* (Figure 2.39). Additionally, the critical nucleation radius (r^*) is unaffected by the mould walls and only depends on the undercooling.

Combining the Equations 23 and 36 results in the following relation:

$$\Delta G_{het}^* = S(\theta)\Delta G_{hom}^* \tag{37}$$

The Figure 2.44 schematically shows the effect of undercooling on ΔG_{het}^* and ΔG_{hom}^*. If n_1 is the number of atoms in contact with the mould walls, the number of nuclei is determined by Equation 38:

$$n^* = n_1 \left(-\frac{\Delta G^*_{het}}{kT} \right) \tag{38}$$

Therefore, the heterogeneous nucleation is enabled by ΔG^*_{het} becoming sufficiently small with the critical value similar to the critical value of ΔG^*_{hom}.

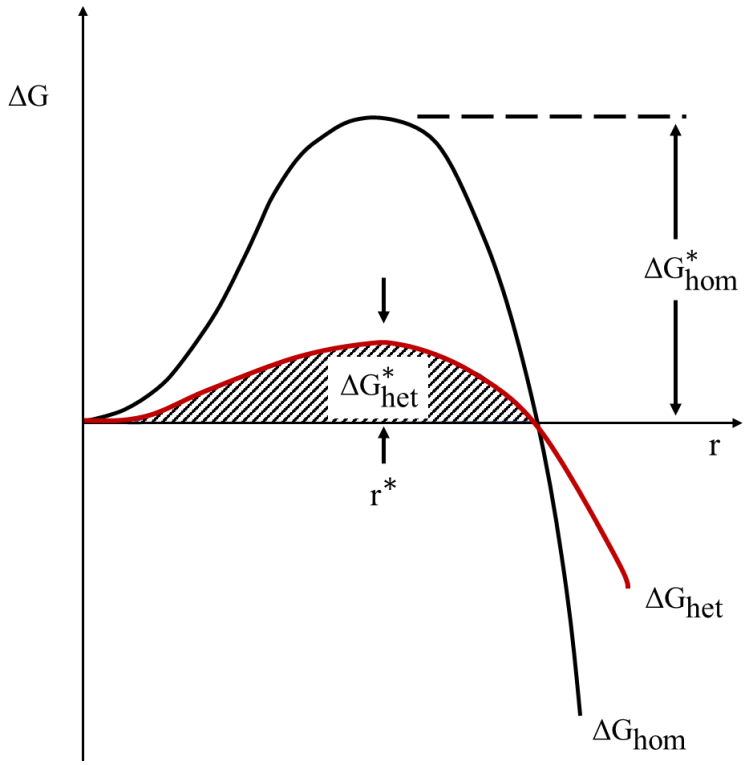

Figure 2.44. The excess free energy of solid clusters necessary for homogeneous and heterogeneous nucleation [334]

In Equation 38 it mainly depends on the magnitude of n_1. The volume rate of heterogeneous nucleation is determined by the following relation:

$$N_{het} = f_1 C_1 \left(-\frac{\Delta G^*_{het}}{kT} \right) \tag{39}$$

where f_1 is frequency factor similar to f_0 in Equation 28, C_1 is the number of atoms in contact with heterogeneous sites per unit volume of liquid.

So far nucleation has been considered under the assumption that the mould walls are microscopically flat. However, in foundry practice it is likely to contain many microscopic cracks or crevices. The Equation 45 is used to define the nucleation in such a condition:

$$\Delta G^* = \frac{1}{2} V^* \Delta G_V \tag{40}$$

where V^* is the volume of a critical nucleus (sphere or cap). Equation 40, as well as the Equation 22, are generally applicable for any nucleus geometry [335].

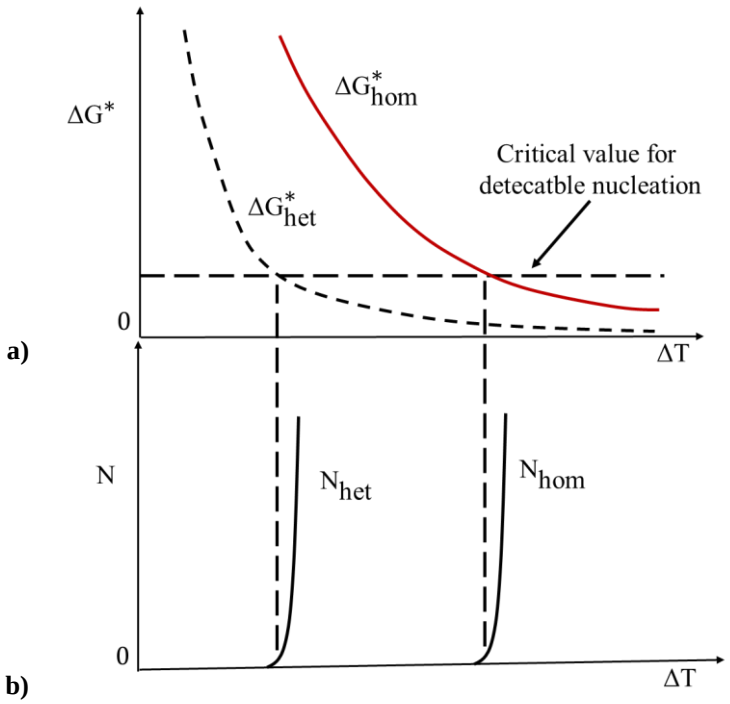

Figure 2.45. The variation of ΔG^*_{het} with: a) undercooling (ΔT) for homogeneous and heterogeneous nucleation, b) the corresponding nucleation rates assuming the same critical value of ΔG^* [329]

Besides heterogeneous nucleation on the mold walls, heterogeneous nucleation in commercial practice is further enabled by the addition of inoculants or grain refiners. The inoculant forms a solid component with one of the components acting as a nucleation site. The effectiveness of the grain refinement depends on the wetting angle and the surface roughness. The low value of θ is favoured by a low-energy interface between the inoculant and solid nucleus (γ_{SM}) that should in turn be preferred by good lattice matching between the inoculant and solid. However, the lattice matching alone is not sufficient for effective grain refinement. Other contributions include chemical effects, as well as surface segregation and roughness. In practice the aim of inoculant additions is not to reduce the undercooling but to achieve a fine grain structure [336].

2.5.2. The nucleation and growth of pure solid

There are two types of atomic structures for solid/liquid interfaces:

- Atomically flat or sharply defined interfaces concerning non-metals,
- Atomically rough or diffuse interface concerning metallic systems.

Due to the differences in atomic structures these two types of interfaces migrate in different ways. The atomically rough interface migrates by a continuous growth process while flat interface migrates by a lateral growth process involving ledges. Thus, solid to liquid transition occurs over a narrow transition zone with the thickness of approximately one atom layer. Such interface is often described as smooth, faceted, or sharp (Figure 2.46 a). In the atomically rough interface transition from liquid to solid occurs over several atom layers (Figure 2.46 b) leading to the weakening of the intermetallic bonds and an increasing disorder. Figure 2.46 c illustrates the changes in enthalpy and entropy from bulk solid to bulk liquid phase across the interface. When solid and liquid are in equilibrium (T_m) the high enthalpy of the liquid is balanced by a high entropy so that both phases have the same free energy. However, in the interface the balance is disturbed thereby giving rise to an excess free energy (γ_{SL}). The type of structure characteristic for individual systems will be determined by the minimization of the interfacial free energy.

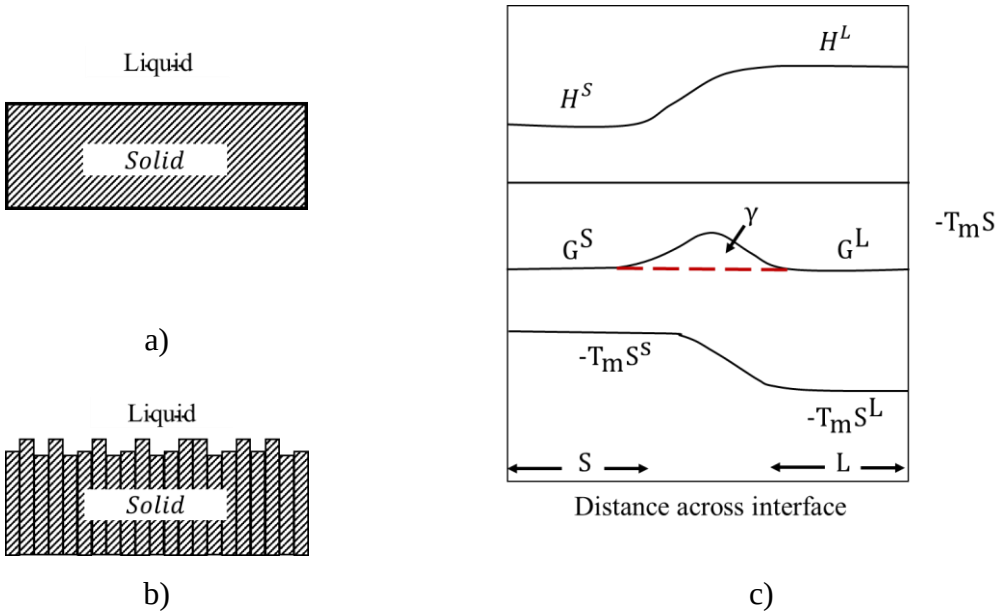

Figure 2.46. Solid/liquid interface: a) atomically smooth, b) atomically rough, c) the variation in H, $-T_mS$ and G across the solid/liquid interface at the equilibrium temperature T_m with indicated origin of solid/liquid interface energy γ [329]

The broken-bond model assumes that the optimal atomic arrangement mainly depends on the latent heat of fusion (L_t) relative to the melting temperature T_m. In this respect, there is a critical value of $^{L_t}/_{T_m} \cong 4R$ above which the interface should be flat and below which it should be atomically rough. Most metals have $^{L_t}/_{T_m} \cong R$ and are predicted to have rough interfaces.

If the broken-bond model is used to calculate the energy of a solid/liquid interface it can be argued that the atoms in the interface are roughly half-bonded to the solid and half-bonded to the liquid so that the interfacial enthalpy should be defined as $\sim 0.5\, ^{L_t}/_{T_m}$ per atom [329].

2.5.2.1. Continuous growth

The migration of a diffuse solid/liquid interface can be compared to the movement of a random high-angle grain boundary. The free energy of an atom migrating through the solid/liquid interface will vary (Figure 2.47).

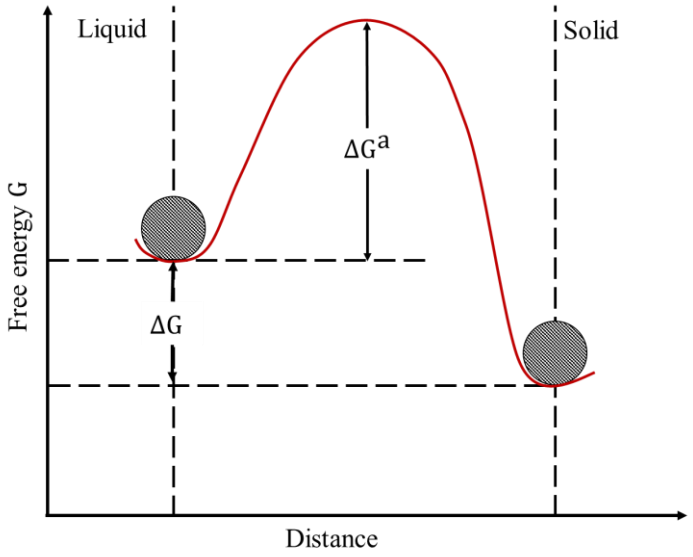

Figure 2.47. The free energy of the atom crossing the solid/liquid interface [329]

The activation energy barrier ΔG^a should be approximately the same as that for diffusion in the liquid phase, while the driving force for solidification will be defined as:

$$\Delta G = \frac{L}{T_m}\Delta T_i \tag{41}$$

where L is the latent heat of melting and ΔT_i is the undercooling of the interface below the equilibrium melting temperature T_m. The rate of solidification is defined by following Equation 42:

$$v = k_1 \Delta T_i \tag{42}$$

where k_1 determines the properties of boundary mobility. Since theoretically k_1 has high value, the normal rates of solidification can be achieved with interfacial undercoolings of only fraction of the degree. For most purposes the ΔT_i can be neglected, and the solid/liquid interface is assumed to be at the equilibrium melting temperature. In other words, the solidification of the melt is usually a diffusion-controlled process. For pure metals growth occurs at the rates controlled by the heat conduction, while the alloy solidification is controlled by solute diffusion [337].

2.5.2.2. Lateral growth

Materials with high melting entropy tend to form atomically smooth, close-packed interfaces. In that instance the minimal free energy also corresponds to the minimal internal energy or minimal number of broken solid bonds. If the single atom migrates from the liquid and attaches itself to the flat solid surface (Figure 2.48 a), the number of broken bonds corresponding to the interface will grow. There is a low possibility of atom remaining attached to the solid. Since there is a high likelihood of atom jumping back into the liquid, atomically smooth interfaces are characterized by inherently low accommodation factor [337].

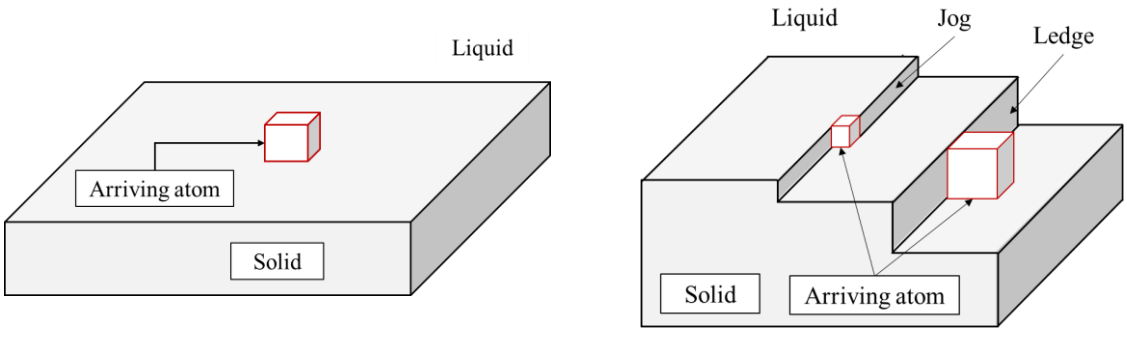

a) **b)**

Figure 2.48. Atomically smooth solid/liquid interface with: a) addition of a single atom onto a flat interface increasing the number of broken bonds by four, b) addition to a ledge (increasing the number of broken bonds by two) and jog (with no increase in number of broken bonds) [338]

If there are ledges present at the interface (Figure 2.48 b), the atom from the liquid will join the ledges with much lower increase in interfacial energy. If the ledges contain a jog (J),

atoms from the liquid can join the solid without any increase in the number of broken bonds with interfacial energy remaining the same (Figure 48 b). Therefore, the probability of an atom remaining attached to the solid at these positions is much higher compared to the atom joining the facet. Smooth solid/liquid interface can advance by the lateral growth of ledges. Since the ledges and jogs are non-equilibrium features of the interface, growth will depend on how they are supplied. They can be supplied in three different ways [329]:

- Repeated surface nucleation (Figure 2.49 a),
- Twin boundaries (Figure 2.49 b),
- Spiral growth (Figure 2.49 c).

As previously mentioned, a single atom migrating on to a flat solid surface will be unstable and tend to rejoin the liquid. However, if the sufficient number of atoms comes together to form a disc-shape layer as indicated in Figure 2.44, it is possible for the arrangement to become self-stabilized and continue to grow [339].

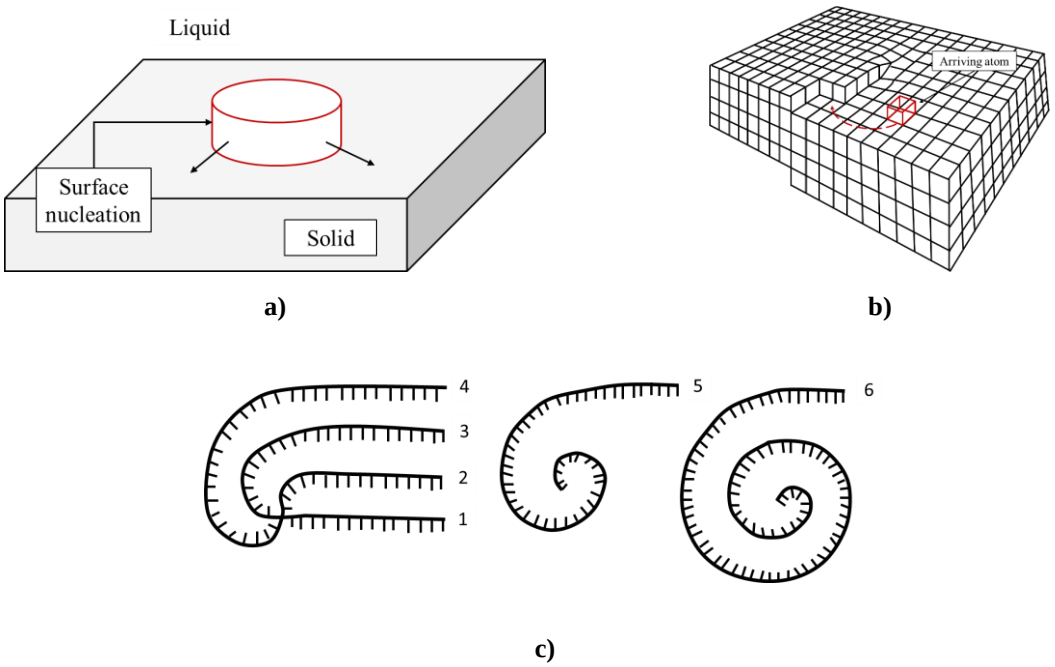

Figure 2.49. Ledge creation through the: a) surface nucleation, b) screw dislocation, c) addition of the atoms at the ledge [339]

The problem of disc-shape layer formation is similar to the cluster formation during homogeneous nucleation. In this instance the edges of the disc contribute a positive energy that needs to be balanced by the volume free energy released during growth. There will be a critical radius (r^*) associated with the particle geometry, decreasing with the increase in interface

undercooling. Once nucleated the disc will spread rapidly over the surface with the growth rate governed by surface nucleation rate given in Equation 43:

$$v^{\left(\frac{-k_2}{\Delta T_i}\right)} \tag{43}$$

where k_2 is roughly constant. This type of growth is not effective at small undercoolings where critical radius is very large [329].

Introduction of the screw dislocation will result in creation of a step or ledge in the surface of the crystal as indicated by Figure 2.49 b. Further addition of atoms will lead to the ledge rotation above the point of dislocation emergence. Consequently, the ledge will never run out of the interface. If the atoms are added at an equal rate to all points along the step, the angular velocity of the step will decrease with the increase in the distance from the dislocation center. Therefore, as growth proceeds the ledge will develop into a growth spiral as shown by Figure 2.49 c. The growth spiral tightens till it reaches a minimum radius of curvature (r^*) at which it is in equilibrium with the surrounding liquid and cannot decrease further. Eventually a state is reached when the spiral appears to rotate with a constant angular velocity [340]. The theoretical considerations indicate that the spiral growth rate v and the undercooling of the interface ΔT_i are connected by the following expression:

$$v = k_3(\Delta T_i)^2 \tag{44}$$

where k_3 is a material constant. This variation is indicated in Figure 2.50 together with the variation for continuous growth and two-dimensional nucleation.

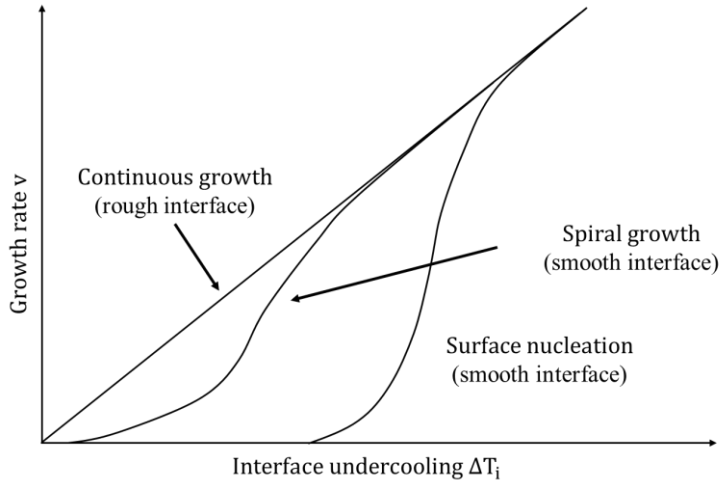

Figure 2.50. The influence of interface undercooling on growth rate for atomically rough and smooth interface [331]

For the given solid growth rate, the necessary undercooling at the interface is lowest for the continuous growth of rough interface. For a given undercooling, faceted interface is less mobile, and it is to be expected that the spiral growth mechanism will normally be more important than repeated nucleation [331].

During solidification it is frequent for faceted crystals to solidify as two crystals in twin orientation. Interfacial facets will intersect at the twin boundaries acting as a permanent source of new steps providing an easy growth mechanism similar to the spiral growth mechanism.

2.5.2.3. Heat flow and interface stability in pure metals

The solidification in pure metals is dictated by the latent heat of solidification rate that is taken away from the solid/liquid interface. The heat can be conducted through the solid or the liquid phase depending on the temperature gradient at the interface. Figure 2.51 illustrates the solid growth at a rate v with a planar interface into a superheated liquid. The heat is conducted away from the interface through the solid and must be in balance with the heat from the liquid and the latent heat gradient at the interface, as indicated by Equation 45.

$$K_s T_s' = K_L T_L' + v L_V \tag{45}$$

where K is the thermal conductivity, T' is the temperature gradient $\left({}^{dT}/_{dx}\right)$ of solid and liquid phase, v is the rate of growth of the solid, and L_V is the latent heat of fusion per unit volume. The Equation 45 is general for a planar interface and can be used to describe the heat conduction through the liquid (Figure 2.51) [329].

When the solid grows into a superheated liquid, a planar solid/liquid interface is stable. If it is assumed that the local increase in rate v will lead to the formation of a small protrusion (Figure 2.51 protrusion formation), its curvature will influence the Gibbs-Thomson effect. Since Gibbs-Thompson relation refers to the observation that small crystals are in equilibrium with the liquid at a lower temperature compared to the large crystals [341], the large radius of the protrusion will enable the solid/liquid interface to remain isothermal at T_m .

The temperature gradient in the liquid ahead of the protrusion will increase. Consequently, more heat will be conducted into the protruding solid so that the growth rate will decrease below that of the planar regions. Under these conditions the protrusion will disappear. This situation is different for a solid growing into supercooled liquid, Figure 2.51 b. If a

protrusion forms on the solid the negative temperature gradient in the liquid becomes even more negative, so the heat is removed more effectively from the tip of the protrusion compared to the surrounding regions allowing it to grow preferentially.

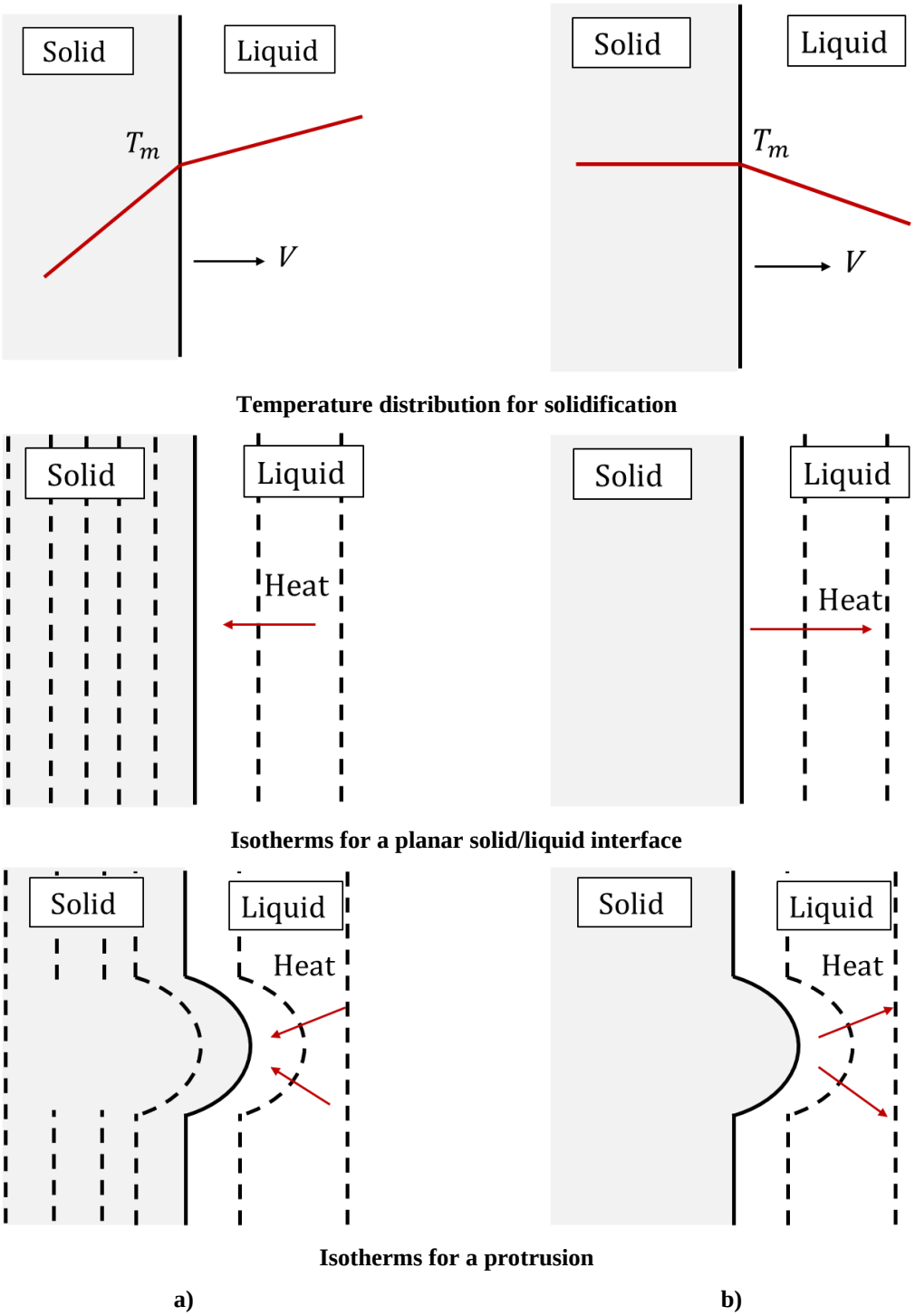

Figure 2.51. The temperature distribution during solidification and isotherms for: a) planar, b) protruded interface [329]

A solid/liquid interface advancing into supercooled liquid is thus inherently unstable. This situation, as described by Figure 2.51 a, occurs when solidification initiates at the mold walls which are cooler than the melt. On the other hand, heat flow into the liquid (Figure 2.51 b), can only occur if the liquid is supercooled below T_m. Such an occurrence can start at the beginning of solidification if nucleation initiates at impurity particles in the bulk liquid. Since a certain supercooling is required before nucleation can occur, the first solid particles will grow into supercooled liquid and the latent heat of solidification will be conducted into the liquid [329]. An initially spherical solid particle will therefore develop arms into many directions, as shown in Figure 2.52.

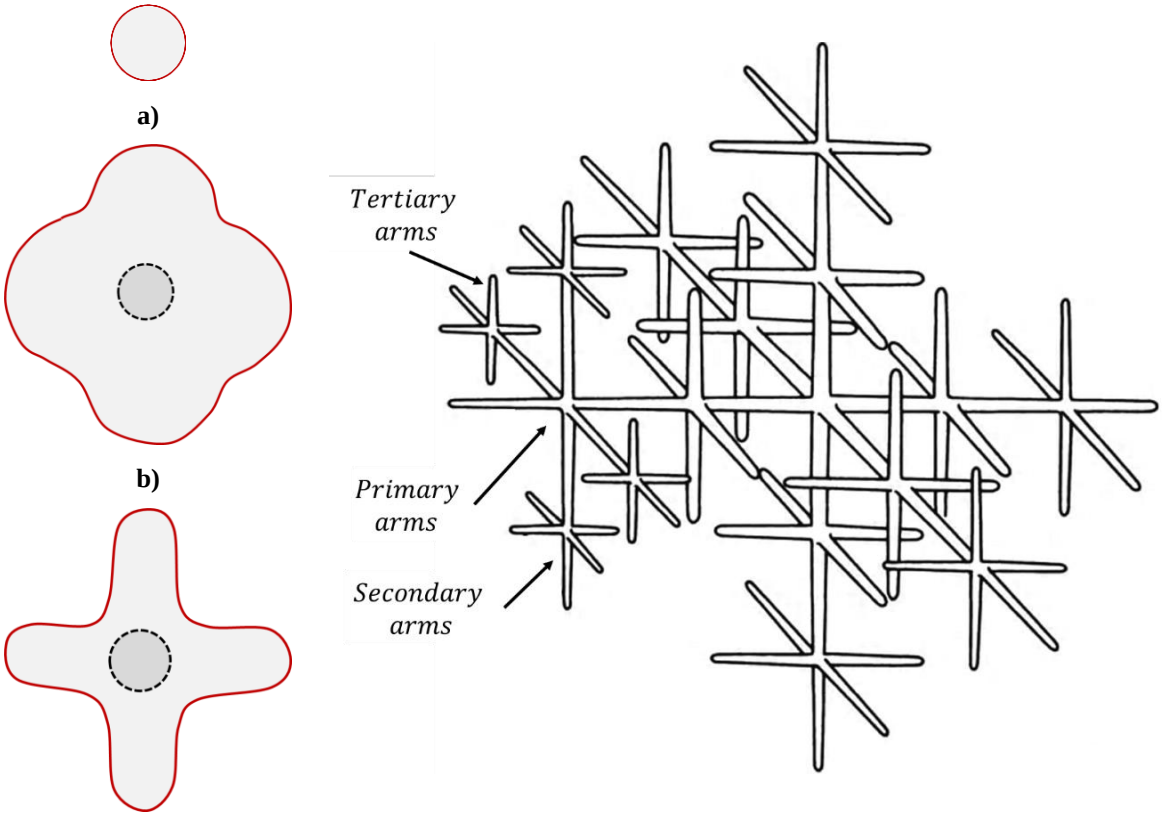

Figure 2.52. The development of thermal dendrites: a) spherical nucleus, b) the interface becoming unstable, c) primary arms development, d) secondary and tertiary arm development [329]

When the length of primary arms increases their surface becomes unstable and deviates into secondary and even tertiary arms. This shape of solid is referred to as a dendrite. In pure metals, dendrites are also known as thermal dendrites to distinguish them from the dendrites in alloys.

Since the heat can be conducted in three different directions, the situation at the tip of the dendrite differs from the planar one. If it is assumed that the solid is isothermal ($T_S' = 0$)

the growth rate of the tip v will be determined by the equation similar to the Equation 45, provided T_L' is measured in the direction of v. The solution to the heat-flow equations for hemispherical tip shows that the negative temperature gradient T_L' is approximately given by $\Delta T_c/r$ where ΔT_c is difference between the interface temperature (T_i) and the temperature of the supercooled liquid far from the dendrite (T_∞). Based on the Figure 2.53 the growth rate is defined by the Equation 46:

$$v = \frac{-K_L T_L'}{L_V} \cong \frac{K_L}{L_V} \cdot \frac{\Delta T}{r} \tag{45}$$

Thus, for a given ΔT, rapid growth will be favoured by the small values of r due to the increasing effectiveness of heat conduction as r diminishes. As a result of the Gibbs-Thomson effect equilibrium across a curved interface occurs at an undercooling ΔT_r below T_m given by the following relation:

$$\Delta T_r = \frac{2\gamma T_m}{L_V r} \tag{46}$$

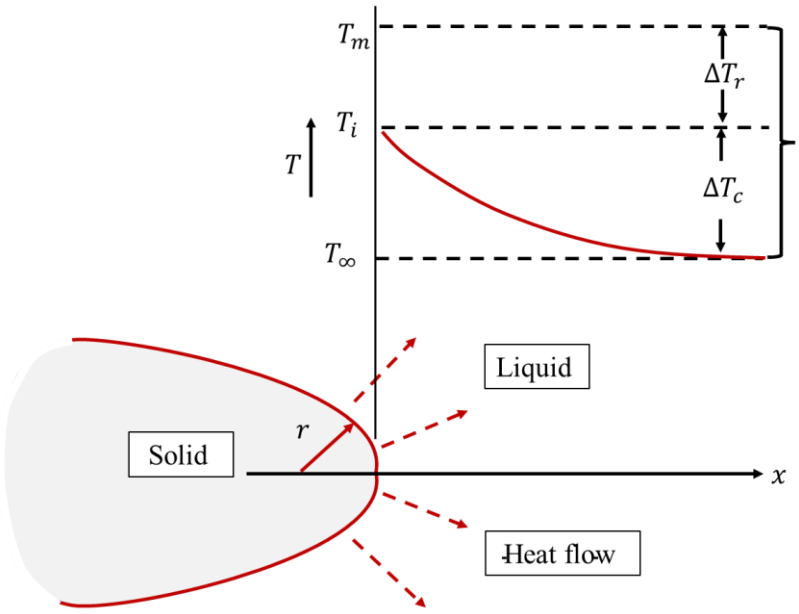

Figure 2.53. Temperature at the tip of a growing thermal dendrite [329]

At the minimum possible radius of curvature of the thermal dendrite the ΔT_r equals the total undercooling $\Delta T_0 = T_m - T_\infty$. This is known as a critical nucleus radius r^* given by $\left(2\gamma T_m/L_V \Delta T_0\right)$. Generally, the ΔT_r is defined as $\Delta T_0 r^*/r$. If $\Delta T_0 = \Delta T_c + \Delta T_r$ the Equation 45 becomes:

$$v \cong \frac{K_L}{L_V} \cdot \frac{1}{r} \cdot \left(1 - \frac{r^*}{r}\right) \tag{47}$$

Conclusively, the tip velocity tends to zero as $r \to r^*$ due to the Gibbs-Thomson effect and as $r \to \infty$ due to slower heat conduction. The maximum velocity is obtained when $r = 2r^*$ [329].

2.5.3. The solidification of alloys

The solidification of pure metal is rarely encountered in industrial practice. Even commercially pure metals contain sufficient amount of impurities to change the characteristics of solidification from pure metal to alloys solidification.

2.5.3.1. Solidification of the single-phase alloys

In the hypothetical phase diagram represented in Figure 2.54, the single-phase alloy marked as X_0 with partition coefficient k is defined by Equation 48:

$$k = \frac{X_S}{X_L} \tag{48}$$

where X_S and X_L are mole fractions of solute in the solid and liquid in equilibrium at a given temperature. In the hypothetical instance (Figure 2.54), k is independent of the temperature. Since the solidification of single-phase alloys in industrial practice is complex and depends on temperature gradient, cooling rate and growth rate, the simplest way is to consider three limiting factors [342]:

1. Equilibrium solidification with infinitively slow diffusion rate,
2. Solidification without diffusion in the solid phase but with perfect mixing in the liquid phase,
3. Solidification without diffusion in the solid phase and diffusion-based mixing in the liquid.

During equilibrium solidification, the alloy X_0 from Figure 2.49 begins to solidify at T_1 with the formation of small amount of solid with composition kX_0. The amount of solid increases with the decrease in temperature. The solid and liquid phase will remain homogeneous till the end of the solidification if the slow enough cooling is provided to allow extensive solid-state

diffusion. At T_3 the last drop of liquid will have a composition equal to $\frac{X_0}{k}$, while the solid phase will have a composition X_0.

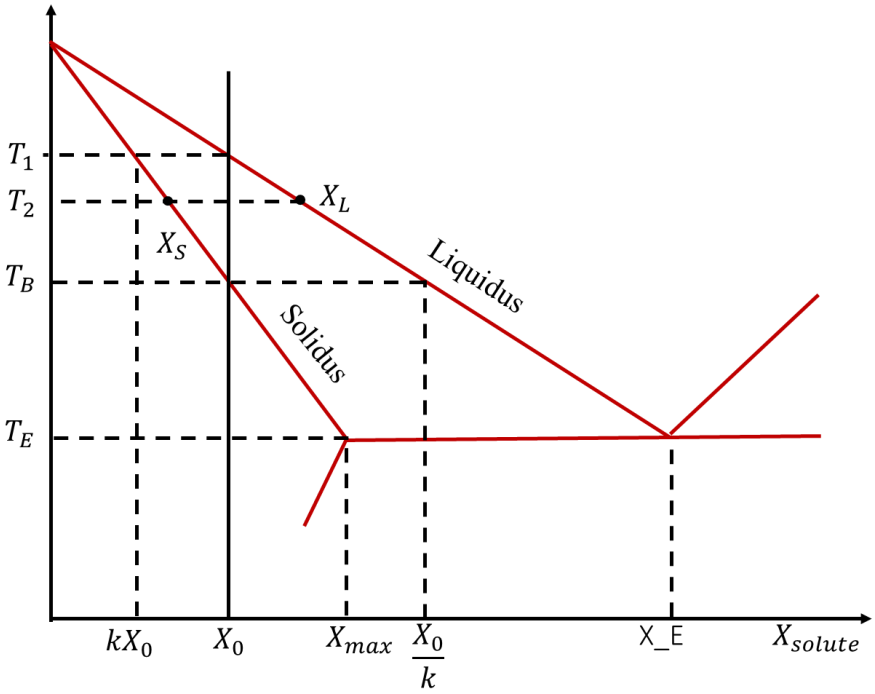

Figure 2.54. The hypothetical phase diagram with $k = \frac{X_S}{X_L}$ [329]

Very often in industrial practice the cooling rate will be too fast to allow substitutional diffusion in the solid state and solidification under equilibrium conditions. If it is assumed that no diffusion takes place in the solid but that the liquid composition is kept homogeneous, the first solid phase will appear when the alloy reaches temperature T_1 (Figure 2.54). At this stage, the solid containing kX_0 mol of solute forms. Since $kX_0 < X_0$ the first solid will be more pure compared to the liquid. Since solute is rejected from the solid, its concentration in liquid raises above X_0. Consequently, the temperature of the interface needs to decrease below T_1 before further solidification can occur, and the next layer of solute will be slightly richer in solute compared to the first. As the solidification sequence continues the liquid becomes richer in solute and solidification occurs at progressively lower temperatures. It follows that the liquid can become much richer in solute than $\frac{X_0}{k}$ and it may even reach the eutectic composition X_E. Solidification will then terminate closer to T_E with the formation of the eutectic structure $(\alpha + \beta)$. Ignoring the difference in molar volume between the solid and liquid gives:

$$(X_L - X_S)df_s = (1 - f_s)dX_L \tag{49}$$

where f_s is a volume fraction of solid. Integrating the Equation 49 using boundary condition $X_S = kX_0$ when $f_s = 0$ gives:

$$X_S = kX_0(1 - f_s)^{(k-1)} \tag{50}$$

and

$$X_L = X_0 {f_L}^{(k-1)} \tag{51}$$

These equations are known as the non-equilibrium lever rule or the Scheil equations. When $k < 1$ these Equations 50 and 51 predict that when there is no diffusion in the solid there will always be some eutectic present in the last drop of liquid. The Scheil Equations are generally applicable even for non-planar solid/liquid interfaces provided the liquid composition is uniform and that the Gibbs-Thomson effect is negligible [343].

If there is no stirring or convection in the liquid the solute rejected from the solid will only be transported away by diffusion (Figure 2.54 X_B). As a consequence, there will be a rapid buildup of solute ahead of the solid and correspondingly fast increase in the composition of the solid formed. This is known as initial transient. If the solidification occurs at the constant rate v it can be shown that the steady state is finally obtained when the interface temperature reaches T_3 (Figure 2.49). Then, the liquid adjacent to the solid has a composition $\frac{X_0}{k}$ and the solid forms with the bulk composition of X_0. The rate at which solute diffuses down the concentration gradient away from the interface is balanced by the rate at which solute is rejected from the solidifying liquid, as indicated by the Equation 52.

$$-DC_L' = v(C_L - C_S) \tag{52}$$

where D is diffusivity in the liquid, C_L' stands for ${dC_L}/{dx}$ at the inface, C_L and C_S are the solute concentration of liquid and solid in the equilibrium. If the diffusion Equation 53 is solved for steady-state solidification, it can be shown that the concentration profile in the liquid is given by:

$$X_L = X_0 \left\{ 1 + \frac{1 - k\left[-\frac{x}{(D/v)}\right]}{k} \right\} \tag{53}$$

When the solid/liquid interface is within $\sim D/v$ the solute is compressed onto a very small volume and the interface composition rises rapidly leading to a final transient and eutectic formation [329].

In the industrial practice the alloy solidification will possess features from all three of the cases. Solidification will usually include some stirring either due to liquid turbulence caused by pouring, convection occurrence or gravity effects. However, the stirring will not be sufficient to prevent the formation of a boundary layer and some liquid diffusion will be expected. In some cases, diffusion in the solid must also be taken into account. When interstitial atoms are involved, solute can diffuse away from the solidifying interface back into the solid as well as into the liquid increasing the homogeneity of the alloy. Unidirectional solidification has commercial application in the production of creep resistant aligned microstructure for gas turbine blades, as well as in the production of extremely pure metals (zone refining) [329].

Since diffusion of solute into the liquid during solidification of an alloy is analogous to the conduction of latent heat into the liquid during solidification of a pure metal, it would seem that the planar front should break up into dendrites. However, the analogy is complicated by the possibility of temperature gradients in the liquid. As the result of the varying solute concentration ahead of the solidification front there is a corresponding variation of the equilibrium liquidus temperature (Figure 2.55 line T_e). Apart from interface temperature, the actual liquidus temperature can follow any line such as T_L. When the temperature gradient is lower than the critical value indicated in Figure 2.55 the liquid ahead of the solidification front exists below its equilibrium freezing temperature. Since supercooling arises from compositional or constitutional effects it is known as constitutional supercooling. A necessary condition for the formation of stable protrusions on a planar interface is the existence of a constitutional supercooling region in the liquid. Assuming the T_L (Figure 2.55) is the temperature at the tip of any protrusion that forms, it will be higher than that of the surrounding interface. However, providing the tip remains below the local liquidus temperature T_e solidification is still possible, and the protrusion can further develop. Otherwise, if the temperature gradient ahead of the interface is steeper than the critical gradient in Figure 2.55 the tip will be raised above the liquidus temperature, and the protrusion will melt back into the liquid [329]. The critical growth gradient illustrated in Figure 2.55 can be defined as $(T_1 - T_3)/(D/v)$ where T_1 and T_3 are liquidus and solidus temperature for the bulk composition X_0.

The condition for a stable planar interface is defined as is defined by Equation 54:

$$T_L' > \frac{(T_1 - T_3)}{(D/v)} \tag{54}$$

Where T_L' substitutes (dT_L/dx) at the interface. The condition for no constitutional supercooling is defined by Equation 55:

$$\left(\frac{T_L'}{v}\right) > \frac{(T_1 - T_3)}{D} \tag{55}$$

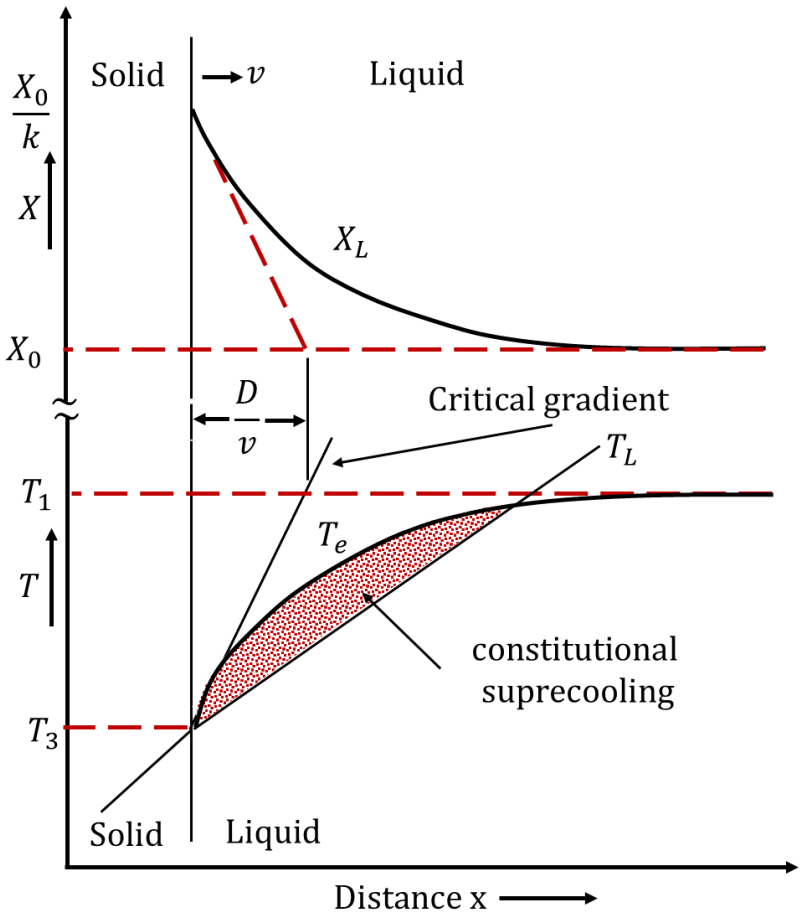

Figure 2.55. The origin of constitutional supercooling ahead of a planar solidification front [329]

The $(T_1 - T_3)$ is identified as the equilibrium freezing range of the alloy. The planar solidification is most difficult for alloys with a wide solidification range and high solidification rates. Apart from experimental conditions, alloys rarely solidify with planar solid/liquid interface. Under normal solidification conditions, the temperature gradients and growth rates are not distinguishable, but are determined by the rate of heat conductivity. If the temperature gradient ahead of an initially planar interface is gradually reduced below the critical value, the first stage in the breakdown of the interface is the formation of cellular structure (Figure 2.56).

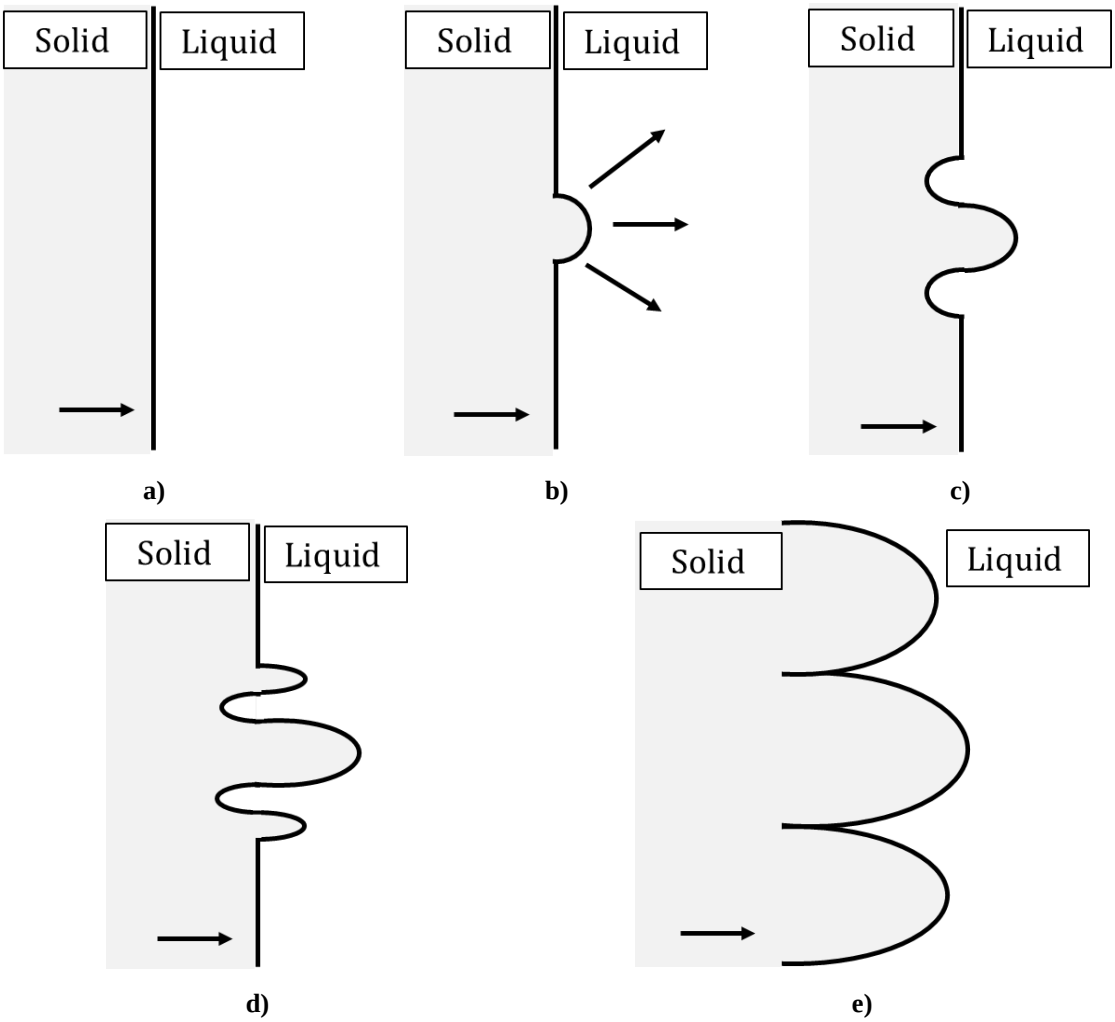

Figure 2.56. The breakdown of the planar solidification front into cells [329]

The formation of the first protrusion causes solute to be rejected laterally and pile up at the root of the protrusion (Figure 2.56 b). This lowers the equilibrium solidification temperature causing recession to form (Figure 2.56 c), that in turn enables the formation of other protrusions (Figure 2.56 d). In time, the protrusions transition to long arms or cells that progress parallel to the direction of heat flow (Figure 2.56 e). The solute rejected from the solidifying liquid concentrates into the cell walls that solidify at the lowest temperatures. On the other hand, the tip of the cell grows into the hottest liquid and contains the least amount of solute. Even if $X_0 \ll X_{max}$ (Figure 2.54) the liquid between the cells can reach the eutectic composition resulting in second phase development [329].

The stability of cellular microstructure is determined by the range of temperature gradients. If the temperature gradient is sufficiently low, the primary arms of solid start to develop secondary and tertiary arms (Figure 2.52). In general, the tendency to form dendrites increases with the increase in the solidification range. Although the reason for the transition from cellular to dendritic solidification is not fully understood, it is associated with the

supercooling in the liquid between the cells leading to the interface instabilities. The cell and dendrite arm spacing decrease with increase in colling rate (Figure 2.57). Higher cooling rates allow less time for lateral diffusion of the rejected solute and therefore require smaller cell or dendrite arm spacing to avoid constitutional supercooling [344].

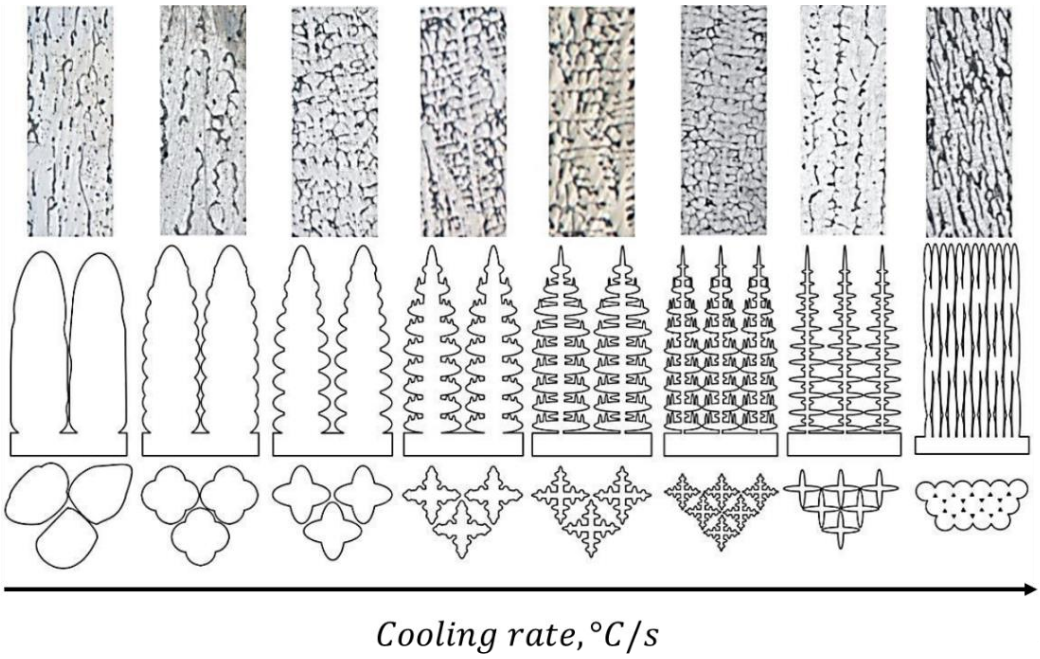

Figure 2.57. Schematic progression of α_{Al} morphology transition in Al-3wt% Mg-1 wt.% Si alloy as a function of cooling rate [344]

Figure 2.57 gives the schematical representation of the complete cycle of morphological transition for Al-3wt% Mg-1 wt.% Si alloy. Besides the cellular to dendritic transition typical for diluted alloys and lower cooling rates, Figure 2.57 illustrates the reverse dendritic to cellular shift known as the high-speed cells that occurs at very high growth rates [344].

2.5.3.2. Solidification of alloys with eutectic composition

The eutectic, peritectic and monotectic solidification involve the freezing of an alloy at or near a special liquid composition. This characteristic composition is defined thermodynamically as the liquid composition that can simultaneously be in equilibrium with two other phases. In the eutectic and peritectic case, the liquid is in the equilibrium with two solid phases, while in monotectic reaction the liquid is in equilibrium with a solid phase and another liquid phase.

Eutectic solidification of eutectic alloys comprehends conversion of a liquid into two solid phases in proximity. Alloys with near eutectic compositions are important in the casting industry due to:

- Lower liquidus temperature compared to the melting temperature of pure component simplifying the melting and casting operations,
- Zero or small freezing range that effectively eliminates the dendritic mushy zone and reduces macrosegregations and shrinkage porosity while promoting possibility of excellent mold filling,
- The possibility of forming "*in situ*" composites.

Among the most frequently used eutectic or near-eutectic alloys of industrial importance are cast iron, Al-Si alloys, wear-resistant alloys, and solders. In numerous other practically used alloys that freeze dendritically, secondary phases are formed near the end of freezing by eutectic solidification [329].

The eutectic solidification involves the following stages:

1. Eutectic liquid is supercooled and one of the solid phases nucleates leading to the solute enrichment in the surrounding liquid and sympathetic nucleation of the second solid phase,
2. Repeated nucleation and/or overgrowth of one solid phase by the other produces a growth center that defines an individual eutectic grain,
3. Simultaneous growth of two interspersed solid phases at a common solid/liquid interface.

The solute rejected into the liquid by either phase is taken up by the adjacent phase particle. As solidification progresses the spatial and crystallographic rotation of the solid phase together with competitive overgrowth of adjacent eutectic grains cause stabilization of the solidification front [345].

When the eutectic liquid solidifies, the resulting material generally consists of a dispersed two-phase microstructure that is approximately 10 times finer compared to cellular or dendritic microstructure solidifying under similar conditions. The exact redistribution of the two phases in the eutectic microstructure depends on the particular alloy and solidification conditions [346]. The eutectic structures can be classified with respect to the entropy of fusion

of the components, representing the difference between the entropy of liquid and solid phase at the melting point. Type of the eutectic solidification can be evaluated based on the Jackson's factor:

$$a = \frac{\eta}{v}\frac{\Delta H_F}{RT_M} = \xi\frac{\Delta S_F}{R} \tag{56}$$

where ξ is the orientation factor defined as the ratio between the number of nearest neighbours for a growth unit at the solid/liquid interface of the crystal (η) and the coordination number (v), ΔH_F the entropy of fusion (or latent heat of fusion), T_M the melting temperature and $\frac{\Delta S_F}{R}$ the dimensionless entropy of fusion [347]. According to this factor phases with $a > 2$ (high entropy of fusion) grow in a faceted manner with an atomically smooth interface, while phases with $a < 2$ (low entropy of fusion) grow isotropically showing no facets and atomically rough interface. Consequently, eutectic structure can be classified as regular (or normal) and irregular (or anomalous). Regular eutectics are formed by two nonfaceted phases, while irregular eutectics consist of one faceted phase with high entropy of fusion. Furthermore, regular eutectics occur for symmetric phase diagrams with symmetric eutectic coupled zone (Figure 2.58 a). The coupled zone represents the solidification conditions under which two eutectic phases can grow together with similar velocities. For two nonfaceted phases that have similar undercooling, the coupled zone is symmetric. To the contrary, in an irregular eutectic where one phase is faceted, the dendrites of nonfaceted phase can grow faster and can even grow at the eutectic composition. Because of this reason, pure eutectic microstructure can be obtained only at hypereutectic composition forming an asymmetric coupled zone (Figure 2.58 b) [334]. Further classification can be obtained if the volume fraction of the solute V_F is considered (Table 2.13). Based on the solute fraction of minor phase, regular eutectics can have rod-like ($V_F < 30$) or lamellar ($V_F > 30$) structure, while the structure of the irregular eutectic is classified as rod-like (fibre) ($V_F < 30$) or branched flakes (acicular structures) ($V_F > 30$).

Figure 2.59 gives schematic representation of the eutectic classification considering Jackson's factor and volume factor of solute phase. Generally, rod-like of fibre structure is characteristic for small V_F because the solid/liquid interfacial area decreases with decreasing volume of solute component. The criteria indicated in Table 2.13 are approximated, and lamellae can also form for lower V_F if specific interfacial energy is strongly anisotropic. This is the case for irregular Al-Si system, where the Si phase represents only about 11.0 % of the eutectic structure, but still forms a plate-like silicone phase. The irregular eutectics can have a

wide range of morphologies, depending on the solidification conditions. In comparison, the Jack's factor has a considerable success in predicting whether the eutectic structure will grow in normal or anomalous manner.

Table 2.13. Eutectic classification based on volume fraction of solid [348]

Type of eutectic	Volume fraction of solute phase, %	Structure type
Regular eutectic	$V_F < 30$	Rod-like structure
	$V_F > 30$	Lamellar structure
Irregular eutectic	$V_F < 30$	Faceted phase grows with rod-like or fiber morphology
	$V_F > 30$	Branched flakes or acicular structures

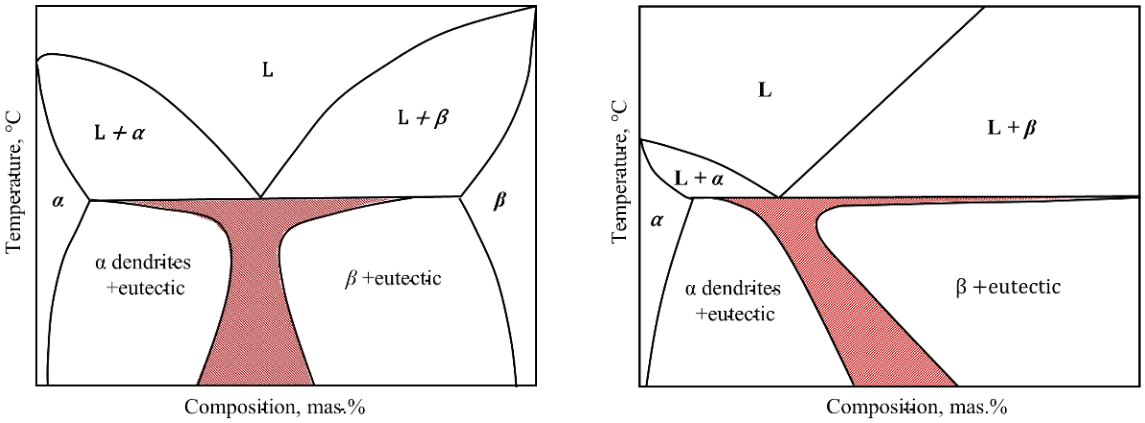

Figure 2.58. Schematic representation of the coupled zone for: a) eutectic system with regular eutectic, b) eutectic system with irregular structure [345]

However, since the eutectic structure grows from solution at a considerably lower temperature than the meting point of its pure components, the tendency to consider may be higher. In that instance, the Jackson's factor can be recalculated for the growth from solution by replacing the latent heat of fusion of the separate components with the latent heat of fusion of the solid solution, and the melting temperature with the eutectic temperature. This enabled more detailed classification of the eutectic structure. In this approach, an entropy of solution of 23.0 J/(mol·K) was determined as the transition value between nonfaceted and faceted behaviour. Due to the difficulty in calculating the orientation factor $\left(\frac{\eta}{\nu}\right)$ for complex structures, it is advantageous to use this entropy of solution instead of the Jackson's factor. Eutectic systems with the entropy of solution $\Delta S < 23\,J/(mol \cdot K)$ present a normal growth, while

$\Delta S > 23\,J/(mol \cdot K)$ are considered irregular. The structure in each group, particularly the anomalous, depend on V_F and the growth velocity [345].

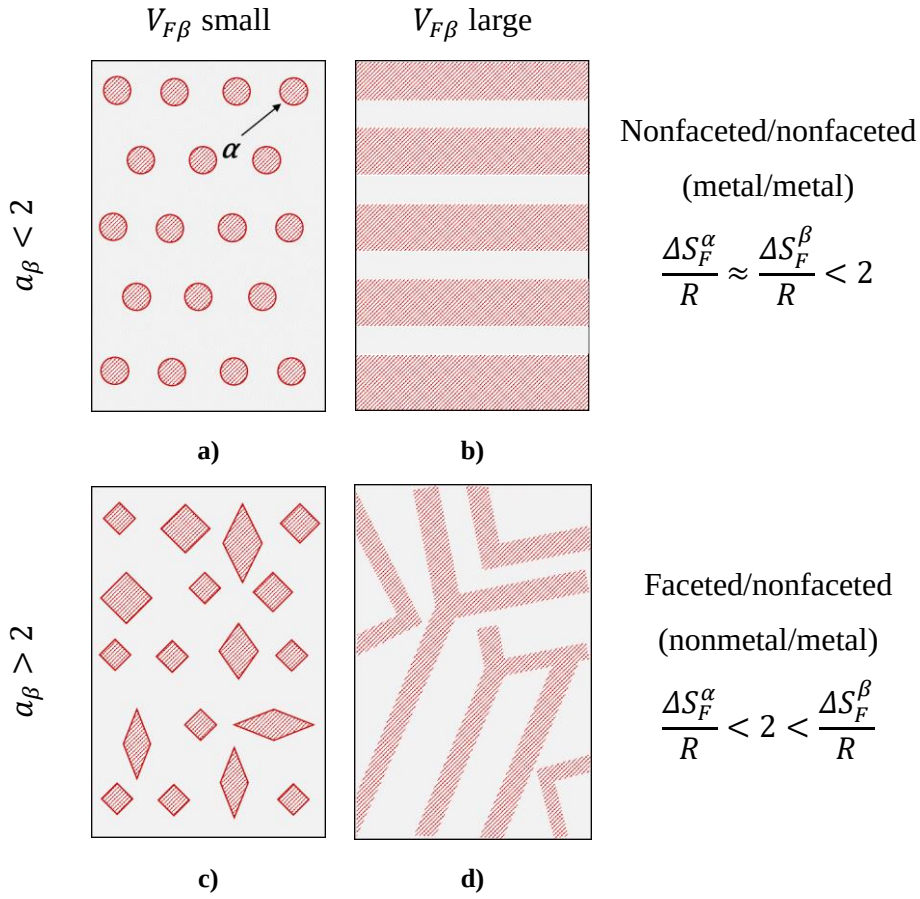

Figure 2.59. The schematic illustration of four broad eutectic categories based on Jackson's factor and volume of solute: a) regular eutectic with rod morphology, b) regular eutectic with lamellar morphology, c) irregular eutectic with acicular morphology, d) irregular eutectic with fibres morphology [348]

The mixture of two nonfaceted phases tends to form regular eutectic microstructures consisting of either rods (Figure 2.59 a) or alternate lamellae (Figure 2.59 b). In lamellar or rod eutectic solidification two phases solidify side by side with an approximately planar and isothermal solid/liquid interface. During solidification of hypothetical A-B system, the A-rich α phase rejects B atoms into the liquid, while B-rich β phase rejects atoms A. The interaction of the diffusion fields in the liquid in front of the two phases enables coupled growth during eutectic solidification. At the given solidification rate, the spacing between the lamellae or rods and the undercooling below the eutectic temperature are the consequence of:

- The lateral diffusion of excess A and B in the liquid just ahead of the solid/liquid interface,
- The necessity to create α/β interfacial area that favour large spacing between the lamellae or rods.

Figure 2.60 illustrates the lamellar or rod growth at the slow solidification velocities. In this system the interface temperature at each interface point is composed of three contributions (Equation 57) controlled by the velocity on the interface at each point, the composition of the liquid at the interface at each point and the curvature of the interface at each point:

1. The interface attachment kinetic supercooling (ΔT_K) that is usually neglected when compared to the other contributions,
2. The supercooling below the eutectic temperature (ΔT_D) due to the local deviation from the eutectic composition,
3. The supercooling due to the interface curvature (ΔT_C) or Gibbs-Thomson effect.

$$\Delta T = \Delta T_K + \Delta T_D + \Delta T_C \quad (57)$$

The total supercooling ΔT defined by the Equation 57 is constant across the interface. The assumption that the interface is isothermal indicates that any variation in ΔT_D must be balanced by the variation in ΔT_C at each point of the interface. Since the solution of diffusion equation indicates that ΔT_D has a minimum value near the α-β-Liquid groove, while ΔT_C has the maximum value [346] the radius of interface curvature of each solid phase is smallest near the triple junction and leads to an interface shape similar to that illustrated in Figure 2.60.

The modeling of nonfaceted-faceted eutectics is important given the fact that the eutectic of technological importance such as Al-Si and Fe-C belong to this class. The main features of nonfaceted-faceted eutectic growth can be summarized as [346]:

- The degree of structural regularity is much lower and a wide distribution of local spacing is observed,
- At the predetermined growth rate and fraction of phases, the average spacing and the average interface supercooling below the eutectic composition are much larger compared to nonfaceted-nonfaceted eutectic,
- At the predetermined solidification rate, the supercooling and the spacing for nonfaceted-faceted eutectic decreases as the temperature gradient increases.

To understand the increased average supercooling below the eutectic temperature, early investigations considered interface attachment supercooling. However, it was indicated

that the kinetic supercooling of Si in Al-Si eutectics is too small to explain the increased supercooling of eutectic front.

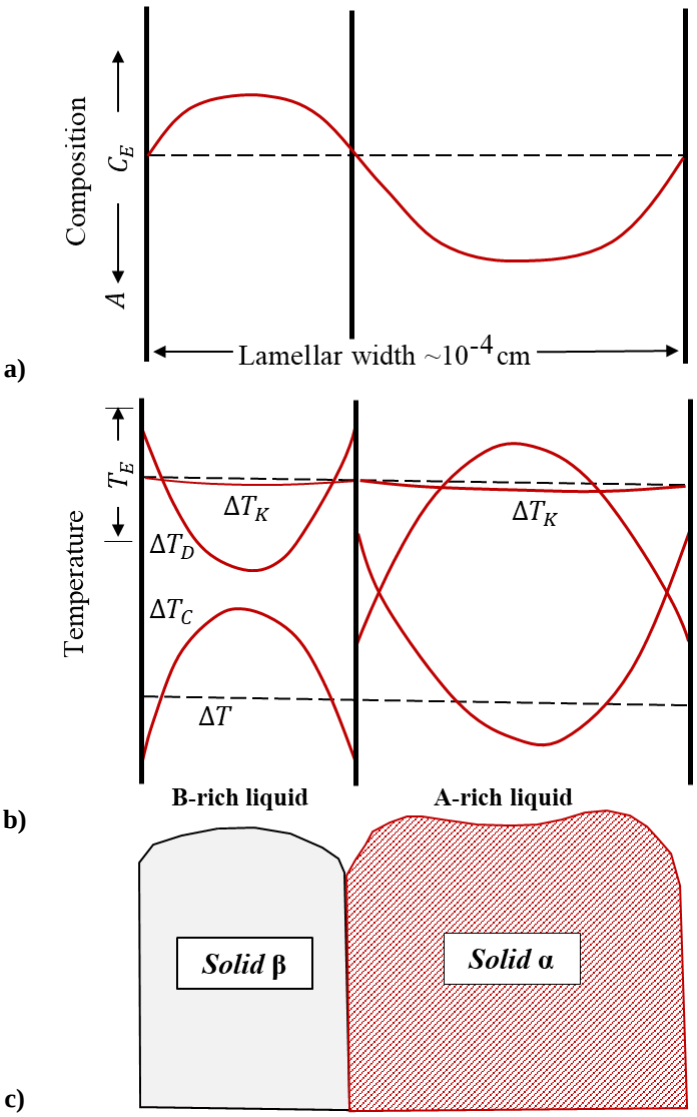

Figure 2.60. Illustration of the lamellar or rod eutectic growth at the slow solidification rates: a) liquid composition (%B) across an α/β interface, b) contribution to the total supercooling existing at the solid/liquid interface, c) shape of the lamellar solid-liquid interface [346]

The growth plates of Si phase in Al-Si and the graphite phase in Fe-C contain defects that are parallel to the plate growth direction enabling easier growth. These planes refer to the twin formation in Al-Si alloys and boundary rotation in graphite. Instead, the supercooling originates from the hindrance of minimizing of diffusion distances. These difficulties are related to the anisotropy of growth of the faceted phase. For irregular eutectics the growth direction of different lamellae is not parallel. So, as growth proceeds the local spacing decreases between converging lamellae and increases between diverging lamellae. For converging lamellae, when their spacing decreases below the extremum value, one of the lamellae is pinched off. For

diverging lamellae, when the local spacing increases beyond the critical value, faceted phase branches into two diverging lamellae. The formation of new lamellae decreases the local spacing. The anisotropic growth kinetics of the faceted phase is referred to as branching-limited growth [349].

2.5.3.3. Monotectic solidification

In some metallic systems, before any solidification occurs the liquid separates into two distinct liquid phases with different compositions. On the phase diagram, the range of temperature and average composition where this separation occurs, as well as the composition of both phases are represented by a dome-shape curve that defines the miscibility gap. The maximum temperature of the miscibility gap is called the critical temperature. Even for the alloy compositions outside the miscibility gap, its consideration is important in developing and understanding of microstructure development.

From the technical standpoint the monotectic solidification is important for understanding the sulfide and silicate inclusion formation in commercial steels. Also, free-machining Cu alloys containing Pb involve the monotectic reactions. Application of the directional solidification in monotectic systems enables production of composites, thin fibers or films [346].

2.5.3.4. Peritectic solidification

The typical phase diagram exhibiting peritectic reaction is given in Figure 2.61. During equilibrium solidification solid α with composition (a) and liquid with composition (c) react at the temperature of peritectic reaction T_p resulting in the solid β with the composition (b). If the solidification of an alloy X_0 at the finite velocity with a shallow temperature gradient (Figure 2.61 b and c) is considered, the first phase to solidify is α with the composition kX_0 at a temperature close to T_1. This phase grows in form of dendrites with layers solidifying with the composition determined by the local temperature and the α solidus. Since the solid state diffusion in dendrites is slow, the liquid will eventually reach the point c (Figure 2.61). Further cooling will cause it to react with α to produce the layer of β. However, the α dendrites are often effectively isolated from future reactions and are retained to lower temperatures [329].

Meanwhile, the β phase continues to solidify from the liquid at compositions following the *bd* line. If there is no diffusion in the solid the liquid will reach the point *e* and solidify as the $(\beta + \gamma)$ eutectic. Finally, the solidified microstructure will consist of cored α dendrites

surrounded by a layer of β and islands of $\beta + \gamma$ eutectic, or divorced eutectic. Alloys between the *a* and *b* line (Figure 2.61) tend to solidify with the "eutectic-like" $\alpha + \beta$ structure. This type of structure is better described as composite. Between the *b* and *d* line the single- phase β forms, and beyond the *d* line $\beta + \gamma$ eutectic structure can be expected.

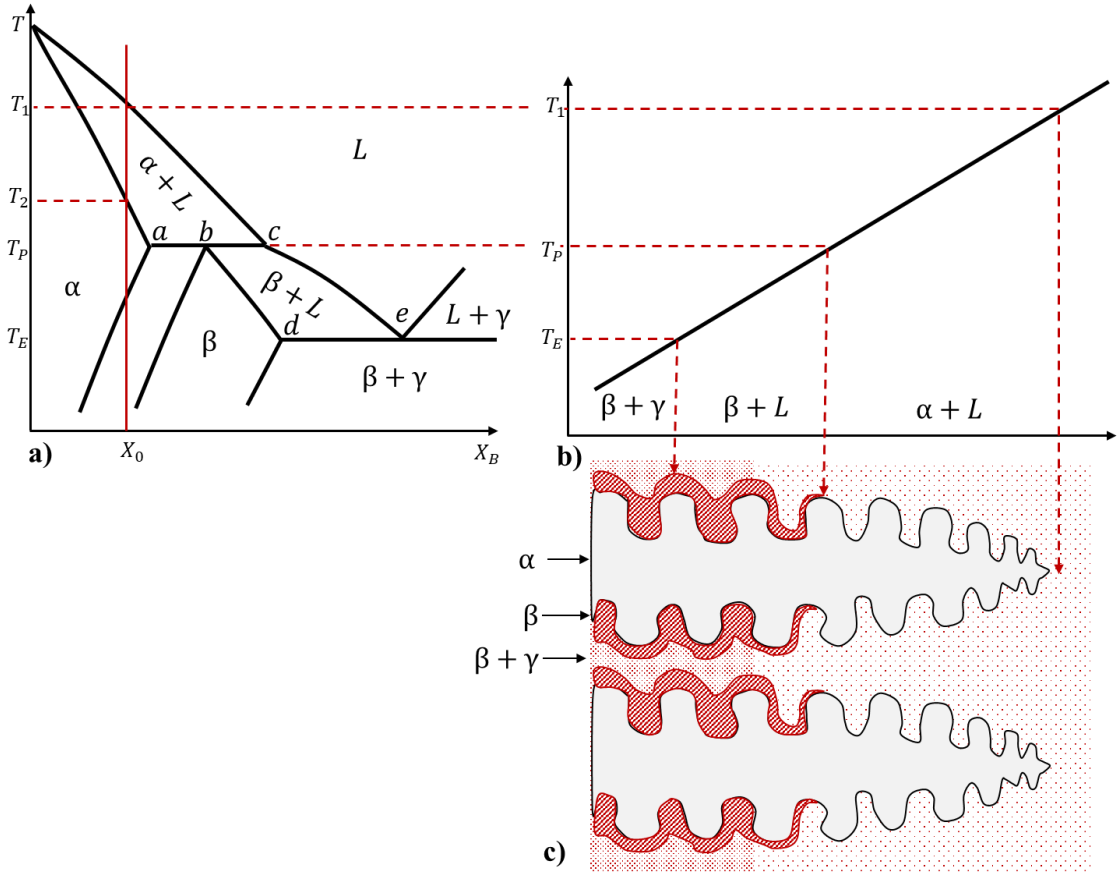

Figure 2.61. Peritectic solidification in temperature gradient: a) peritectic phase diagram for A-B system, b) temperature gradient across solidification front, c) microstructure development [329]

In the technical application the peritectic solidification is encountered in Fe-C phase diagram. However due to the high diffusivity of C at high temperatures the peritectic reaction is very fast and can fully convert primary (δ) dendrites into the more stable austenite [329].

2.6.Solidification of ingots

Most engineering alloys initiate by being cast into a mold. Afterword's, if the as cast pieces retain their shape or are processed by machining, they are referred to as castings. If they are intended for further processing, the pieces are called ingots or blanks. In eater instance, the principles of solidification and the requirements for high density and strength are the same.

The classical representation of ingot microstructure shows three distinct zones (Figure 2.62) [346]:

- The chill zone that is a peripheral region near the mold surface composed of small equiaxed grains,
- The columnar zone composed of grains elongated in the heat flow direction,
- Central equiaxed zone.

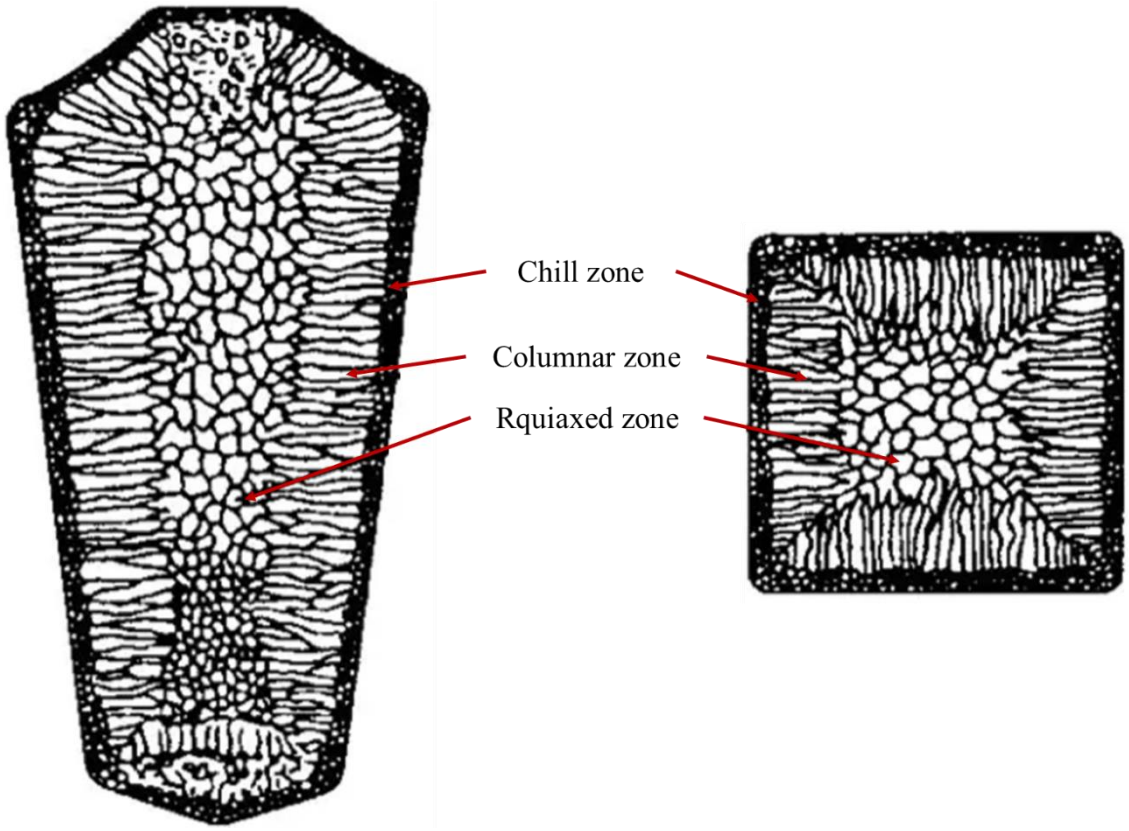

Figure 2.62. The schematic representation of structural zones developed during ingot solidification [346]

Inside each grain a substructure of cells, dendrites and/or eutectic exists. The origin and development of the three zones is affected by the fluid flow. There are many aspects of molten metal or alloy flow that can occur during solidification [346]:

- Residual flow due to the mold filing,
- Thermal and solute-driven buoyancy convection,
- Convection due to the expansion or contraction of alloy upon solidification,
- Convection driven by the variation of free surface energy with temperature and concentration,
- Effect of external forces (rotation, magnetic fields),
- Floating or settling of free crystals because of density differences,
- Dendritic braking and transport,
- Pushing of equiaxed crystals and/or inclusions by the columnar solidification front.

Convection has the largest effect on the thermal transport and macrostructure when solid/liquid interface or the position of dendrite tip is parallel to the gravity vector. During welding the fluid flow makes a large change in the heat flow [350]. The capillary flow on the free surface of a weld puddle can reverse the circulation direction depending on surface active additions and significantly alter the penetration depth [351]. The flow can be reduced by the application of magnetic field resulting in an induced eddy current that exerts a body force in the fluid. Similarly, the rotation of the ingots exerts the Coriolis force that deflects the particles of fluid in the direction normal to the axis of rotation, and normal to the direction of fluid motion. Since molten alloys have a viscosity similar to water, the flow is rapid. Turbulent flow occurs quite frequently during rapid mold filling increasing the possibility of inclusion entrapping and mold erosion. Thus the smooth transition between different mold segments is needed to reduce turbulence [352].

2.6.1. The zone of chill crystals

The chill zone structure formation involves complex interactions of molten metal flow, metal-mold heat transfer, heterogeneous nucleation and dendritic flow. When a molten metal is rapidly cooled in the vicinity of a cold mold, heterogeneous nucleation on the mold walls or on other heterogeneous sites occurs producing a large number of initiation sites (Figure 2.63). The growth from this site is limited by impingement with neighboring crystals formed at similar times. As a consequence, the size of these grains is usually very small and uniform with random orientation. Furthermore, the dendritic substructure in chill zone and establishment of grain multiplication or fragmentation mechanism is induced by melt turbulence during pouring [346].

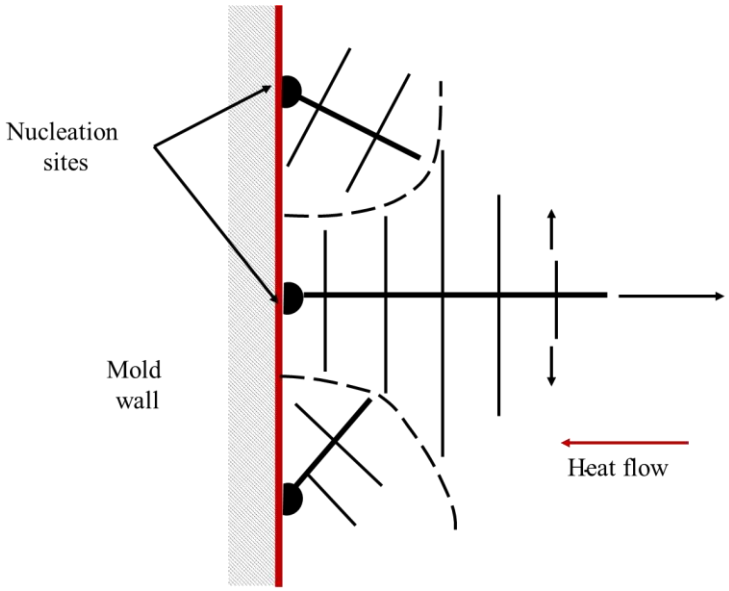

Figure 2.63. The initiation of competitive growth immediately after pouring [329]

2.6.2. The zone of columnar crystals

At the distance from the mold surface, the morphology of the crystals transitions into the columnar that grows opposite to the heat flow direction. Each columnar grain consists of many primary dendrite stalks. The crystallographic texture is a consequence of competitive growth mechanism through which favorably oriented grains eliminate less favorable grains. In ingots frequently used in industrial practice, columnar growth does not need to be perpendicular to the mold walls if convection sweeps past solid/liquid interface because of the horizontal temperature gradient. The Figure 2.64 illustrates competitive columnar growth of three grains. The columnar grains on the left and right contain dendrites with crystallographic orientation that is nearly perpendicular to the liquidus isotherm. These dendrites grow with the velocity (v_L) that is equal to the isotherms. When the growth kinetic model of the dendrite tip is considered, the faster growing dendrites are characterized by a large tip undercooling. As a consequence, the central misoriented grains are pinched off by the left and right grains. Figure 2.64 also illustrates how the left grain boundary is parallel to the nominal heat flow direction while the right grain boundary is tilted because of the tertiary arm formation. The orientation disruption of the columnar grains narrows and the grain size increases as the distance from the mold surface increases [353]. When the structure is mainly single-phase, the secondary and tertiary arms of adjacent dendrites can link to form walls of solid containing many primary dendrite arms. The region between the tip of the dendrites and the point where the last drop of liquid solidifies is known as mushy or pasty zone. The length of this zone depends on the temperature gradient and the non-equilibrium freezing region of the alloy [329].

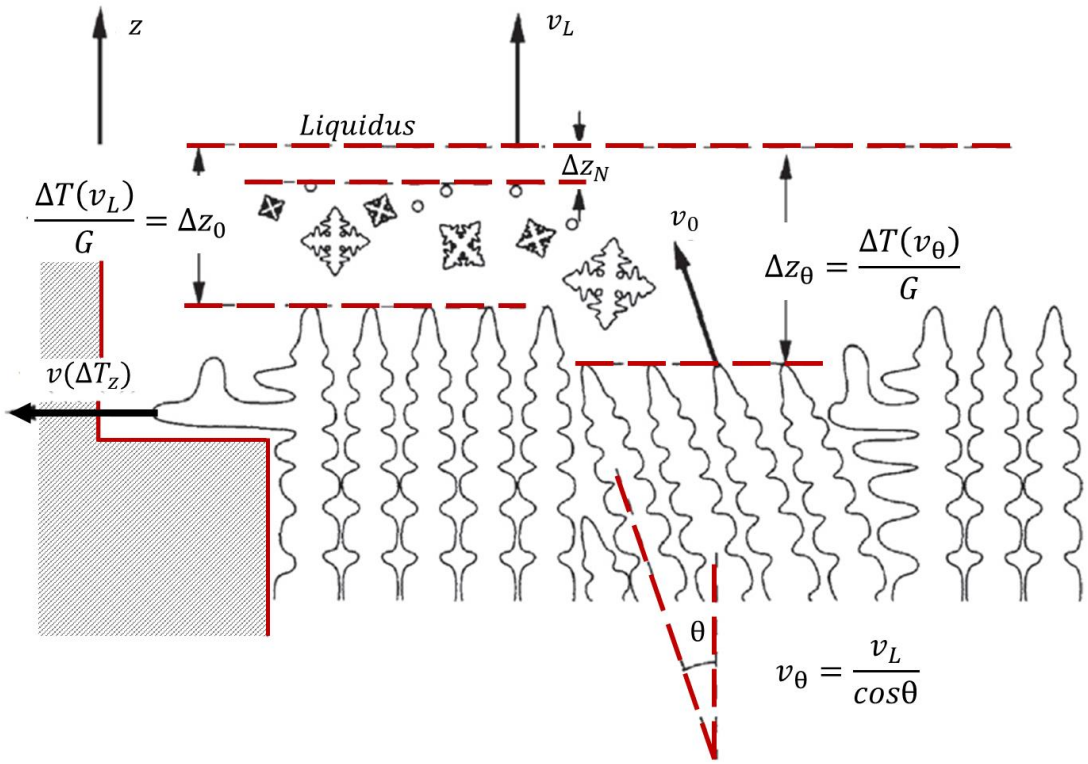

Figure 2.64. The competition process during dendritic growth, the development of preferred orientation in the columnar region and the formation of equiaxed grains ahead of the columnar front [354]

2.6.3. The central zone of equiaxed crystals

In many ingots the central zone of equiaxed grains can be found. Typically, this type of microstructure is more desirable than the columnar structure due to its beneficial influence on mechanical properties. As indicated by Figure 2.64 the equiaxed grains grow in front of the columnar dendrites. The columnar to equiaxed grain transition occurs when nuclei can survive and grow to occupy sufficient spaces to hinder the development of columnar front. The major challenges in predicting the columnar to equiaxed grain transition and size of equiaxed zone, refer to the accurate description of the nuclei source and competing growth rates of individual zones under the given conditions. The three sources of growth sites for equiaxed grains in the bulk liquid zone of a castings are [346]:

- Constitutional supercooling enabling heterogeneous nucleation,
- Big-Bang mechanism,
- Dendritic fragments are produced and transported from the columnar zone.

Because the tips of the columnar dendrites are at a temperature below the bulked alloy's liquidus, a region of liquid exists where heterogeneous nuclei may become active. The

Big-Bang mechanism comprehends equiaxed grain growth from the predendritic shaped crystals formed during pouring at or near the mold walls. These crystals are carried into the bulk by fluid flow with some surviving until the superheat stops. The dendritic fragmentation occurs from the columnar grains or dendritic crystals nucleated at the top of the ingot as a result of the radiation cooling occurred in that region [331].

2.6.4. Transition from columnar to equiaxed zone

The crystal structure of the ingot will be fully equiaxed or fully columnar depending on whether the liquid temperature gradient is smaller or higher compared to the critical value indicated in Equation 58:

$$G_L = 0.617 N_0^{1/2} \left[1 - \left(\frac{\Delta T_n}{\Delta T_C}\right)^3\right] \Delta T_C \tag{58}$$

where N_0 is the density of nucleating sites, ΔT_n supercooling required for heterogeneous nucleation and ΔT_C is supercooling of the dendritic tip below the liquidus temperature of the columnar front. In accordance with Equation 58, the factors that promote columnar to equiaxed grain transition are [355]:

- Low temperature gradient that increases the size of the constitutionally supercooled region in front of the dendritic tips,
- Large solute content that increases the value of ΔT_C for fixed growth speed,
- A large number of nuclei.

Hunt's model based on the Equation 58, ignores many complexities of the dendritic growth of equiaxed grains and nucleation was assumed to take place at single temperature rather than over a temperature range. So, it is not suitable for predicting the effect of solidification conditions on equiaxed grain size.

The impact of chemical composition and cooling rate on columnar to equiaxed grain transition in Al-Si alloys is given in Figure 2.65. The two-dimensional micrographs were obtained using computational methods based on various laws for nucleation in the bulk and at the surface of the casting. Comparison among the three simulations (Figure 2.65 a, b and c) indicates that the physical blocking of the columnar front by equiaxed grains causes the zone transition. However, around every dendrite there is a boundary layer of solute that interacts with equiaxed grains and the advancing columnar front [356].

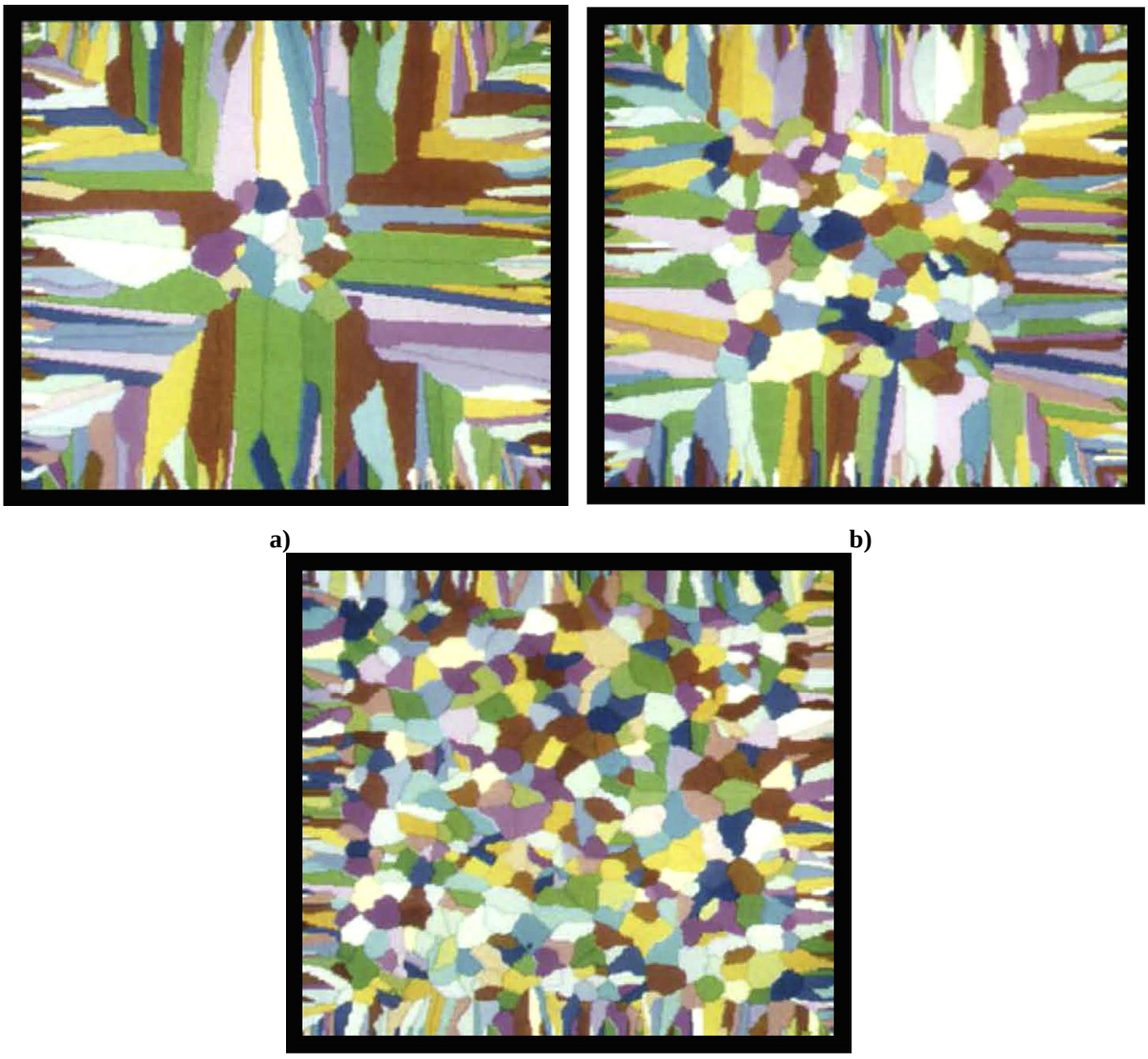

a) **b)**

c)

Figure 2.65. Simulation of columnar and equiaxed structure for: a) Al-5wt%Si with solidification rate of 2.2 K/s, b) Al-7wt%Si with solidification rate of 2.2 K/s, c) Al-7wt%Si with solidification rate of 7.0 K/s [354]

The micrographs given in Figure 2.65 a and b represent the alloys with different Si content solidifying under similar solidification conditions. As it can be seen, the average distance D_c over which the columnar dendrites can grow before getting stopped by the equiaxed grains is larger in the alloy containing lower Si amount (2.65 a). Besides the chemical composition, the difference in the equiaxed zone width between the Al-5Si and Al-7Si is a consequence of the growth kinetics. The micrograph shown in Figure 2.65 c corresponds to the same Al-7Si alloy but after the solidification at a three times higher cooling rate. While there is no significant difference in the size of equiaxed grains between micrographs in Figure 2.64 b and c, the drastic reduction of columnar grain zone can be seen. The absence of difference in the grain size is a consequence of narrow nucleation site distribution. Therefore, all the nucleation sites become active giving the same final grain size [354].

3. EXPERIMENTAL

Since the aim of this thesis is to design, synthesize and characterize the light-weight Al-Mg-Li alloy with improved mechanical properties in as-cast condition, it is necessary to devise the experimental procedure to establish the influence of chemical composition, thermodynamic and processing parameters on solidification sequence and microstructure development. The schematic representation of experimental procedure is given in Figure 3.1.

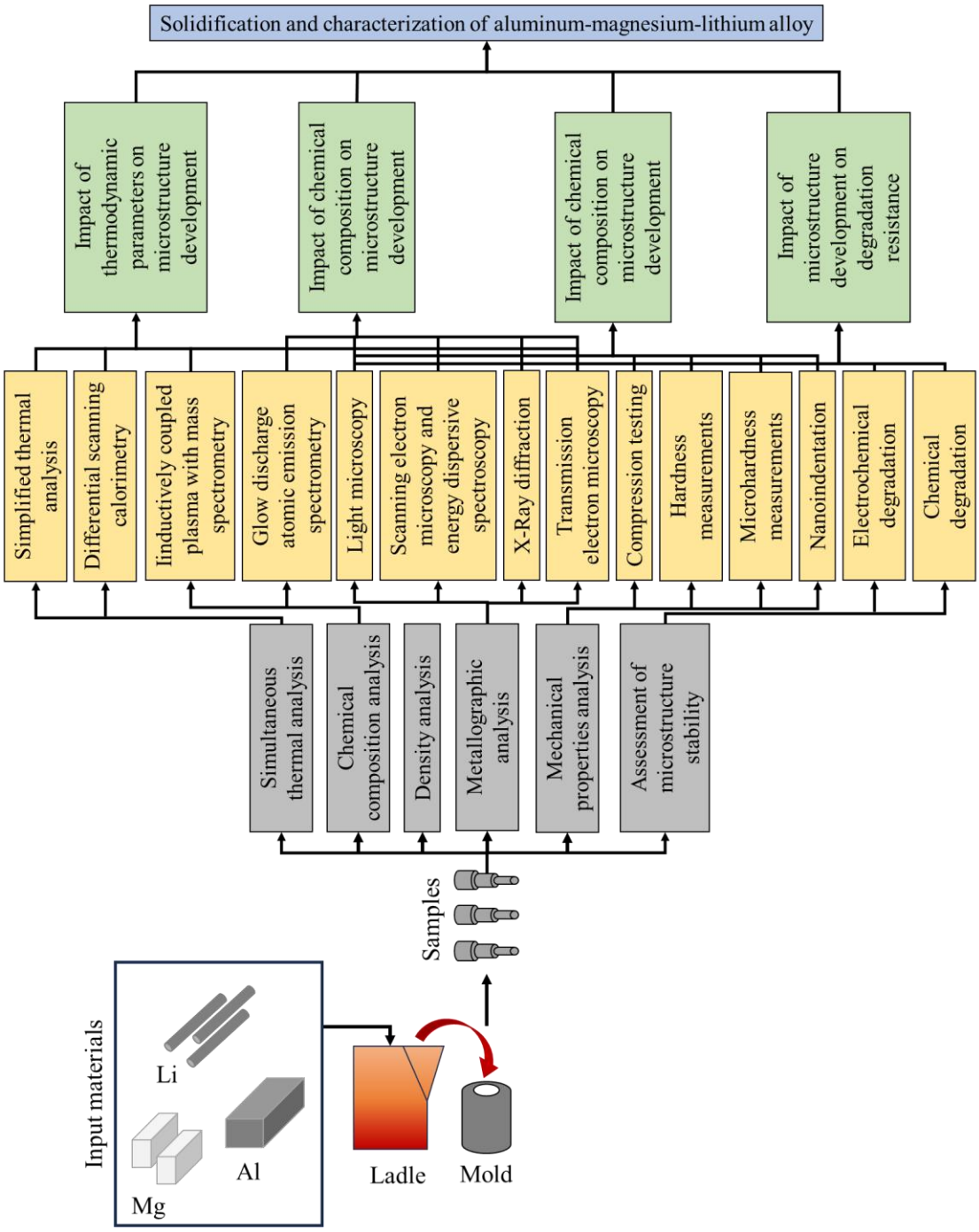

Figure 3.1. The schematic representation of experimental procedure

3.1. Sample synthesis

To successfully synthesize Al-Mg-Li alloys the reactivity of Li and Mg with furnace atmosphere and refractory materials must be considered. Table 3.1 indicates the possible oxidation reactions at 526.9 °C and 726.9 °C during production of commercial Al-Li alloys. Despite the higher thermodynamic stability of magnesium oxide (MgO), the oxidation reactions will result in the earlier formation of lithium oxide (Li_2O). As a consequence of higher mobility and atomic fraction of Li, the formation of Li_2O in dry oxygen will already initiate at 100 °C.

Table 3.1. The changes in free energy per mol of gaseous reactants for surface reactions at 800 K and 1000 K [345, 346]

Reaction No.	Reaction	ΔG, kJ/mol	
		800 K	1 000 K
1	$2Mg + O_2 \rightarrow 2MgO$	-1029	-986.9
2	$Li + Al + O_2 \rightarrow LiAlO_2$	-1018.4	-974.5
3	$4\ Li + O_2 \rightarrow 2Li_2O$	-988.4	-930.2
4	$Li + 5\ Al + 4\ O_2 \rightarrow LiAl_5O_8$	-962.0	--
5	$1.33\ Al + O_2 \rightarrow 0.66\ Al_2O_3$	-950	-907.6
6	$4\ LiH + O_2 \rightarrow 2\ Li_2O + 2\ H_2$	-879.5	-880.2
7	$Li + Al + CO_2 \rightarrow LiAlO_2 + C$	-622.8	578.6
8	$4\ Li + CO_2 \rightarrow 2Li_2O + C$	-592.8	-534.3
9	$4\ Li + Li_2CO_3 \rightarrow 3Li_2O + C$	-494.4	-466.8
10	$2.5\ Li + 0.5\ Al + H_2O \rightarrow 0.5\ LiAlO_2 + 2\ LiH$	-360.2	-318.3
11	$4\ Li + H_2O \rightarrow Li_2O + 2LiH$	-345.2	-297.5
12	$0.5\ Li + 0.5\ Al + H_2O \rightarrow 0.5\ LiAlO_2 + H_2$	-305.7	-294.6
13	$2\ Li + H_2O \rightarrow Li_2O + H_2$	-290.7	-273.7
14	$2LiH + H_2O \rightarrow Li_2O + H_2$	-290.7	-249.9
15	$0.66\ Al + H_2O \rightarrow 0.33\ Al_2O_3 + H_2$	-271.5	-255.8
16	$1.32\ Li + CO_2 \rightarrow 0.66\ Li_2CO_3 + 0.33\ C$	-263.2	-225.8
17	$2\ Li + H_2O \rightarrow LiOH + LiH$	-185.1	-155.7
18	$Li_2O + CO_2 \rightarrow Li_2CO_3$	-98.4	-71.5
19	$Li_2O + H_2O \rightarrow 2LiOH$	-25.1	-13.8

Equally, Li will react with $H_2O_{(g)}$ present in furnace atmosphere and crucible material to form Li_2O and hydrogen (H_2). The formation of lithium hydroxide (LiOH) and lithium

hydroxide monohydrate ($LiOH \cdot H_2O$) in minor quantities is expected when both $H_2O_{(g)}$ and carbon dioxide (CO_2) are present. The metallic Li will quickly react with nitrogen (N_2) to from black hydroscopic lithium nitride (Li_3N). In the temperature range between 500.0 and 800.0 °C metallic Li can also react with H_2 leading to the formation of stable lithium hydrate (LiH) and lithium aluminum hydride (Li_3AlH_6). While Li_2O, Li_3N, LiH and Li_3AlH_6 are in solid state the LiOH remains in liquid state during melting and processing. To ensure sound cast billets suitable for further processing, the products of aforementioned reactions need to be removed through the addition of fluxes, degassing and filtration [358].

The refractory materials commonly used in the melting of industrial Al alloys cannot be used to synthesize the Al-Li alloys. The pure Fe crucibles have an excellent resistance to Li attacks. However, their resistance to chemical attacks decreases under thermal stresses limiting their practical application. Moreover, melting Al in pure Fe crucible will result in the Fe pickup as a consequence of high solubility of Fe in liquid Al [24]. The special grades of stainless steel have been reported to have a good resistance to Li attacks. The excellent service life of 304L, 321L and 347L stainless steel crucibles can be obtained if nitrogen concentration in the melt is less than 100.0 ppm [359]. Tantalum can be used as refractory material due to its good resistance to both molten Al and Li. However, tantalum is highly susceptible to Li attacks when oxygen concentration in refractory material exceeds 100.0 ppm [24]. Graphite is widely used as a refractory material for Al-Li alloy synthesis under inert atmosphere. In the presence of oxygen, Li will react with carbon containing materials. Clay bonded graphite crucibles have been found compatible with alloys containing up to 1.5 wt.% Li. The use of Al, Mg or Si carbide refractory materials is not recommended due to the risk of melt contamination and crucible shattering [24].

Since there is no single crucible material compatible with both Al and Li it is necessary to adopt a melting and casting sequence to avoid long holding times after Li addition, to reduce the crucible attack and melt contamination.

To reduce the loss of Li and Mg, prevent crucible attacks and melt contamination samples were synthesized using:

- Protective atmosphere of Ar,
- Protective atmosphere of Ar and partial crucible cover,
- Melting under vacuum,
- Protective atmosphere of Ar and full crucible cover.

3.1.1. The initial procedure of sample synthesis

The experimental setup for the initial sample synthesis is represented in Figure 3.2.

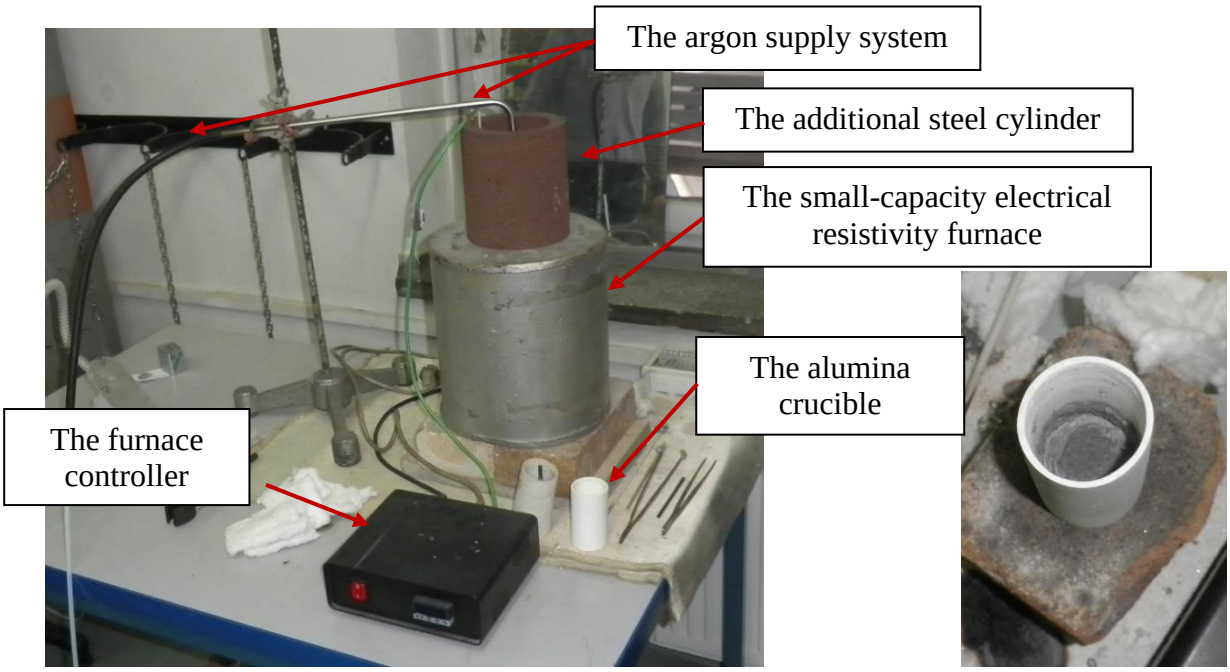

Figure 3.2. The initial procedure for sample synthesis: a) experimental setup, b) sample

The initial sample synthesis comprehended the use of small-capacity electrical resistivity furnace and the protective atmosphere of Ar (Figure 3.2 a). The compressed Ar UN 1006 designation was introduced under the pressure of 10.0 MPa. Considering that Ar has a higher relative density compared to air, good protection of the melt was ensured by increasing the furnace volume above the crucible. This was accomplished by placing an additional steel cylinder on top of the furnace opening (Figure 3.2 a). The input materials consisted of:

- 96.4 g of Al granules,
- 1.9 g of Li,
- 1.7 g of Mg.

Aluminum granules with 2.0 mm diameter and technical purity of 99.8 % were placed in the alumina crucible of 0.1 l capacity and invested in the electrical resistivity furnace. For easier manipulation and alloying Mg rod of 99.9 % purity and Li rod of 99.99 % purity were wrapped in the Al foil of commercial purity. Although Al melting initiated at 690.0 °C, the melt was heated to 745.0 °C before alloying. The additional heating was necessary to break the oxide layer formed on the melt surface and to prevent alloying induced undercooling. However,

despite the temperature increase the addition of alloying elements caused instant melt solidification. The rapid solidification prevented melt stirring and melt homogenization resulting in unrepresentative sample (Figure 3.2 b).

3.1.2. Synthesis under the protective atmosphere of argon and partial crucible cover

Based on the failure of previous experimental setup and synthesis, the processing parameters needed to be reconsidered. Firstly, the melting unit was changed to the induction melting furnace with the capacity of 10.0 kg. This enabled the synthesis of a larger amount of the melt, the easier addition of alloying elements, better melt stirring and homogeneous redistribution of alloying elements in the melt. Secondly, the alumina crucible was substituted by the graphite crucible with a 0.5 l capacity. To prevent the chemical attacks and formation of Li-C based compounds, the graphite crucible was coated with boron-nitrite. Boron-nitride coating is a ceramic compound that is chemically inert and stable up to 1800.0 °C in inert gas atmosphere. Its good separation and lubrication properties protect the crucible surface from oxidation and create non-wetting, non-adhesive dry lubricating layer. Since the oxidation of melt surface required additional increase in temperature, Al granules were substituted by Al block. Given that the Al block has a more favorable ratio between volume and surface, reduced oxidation is expected. Further reduction in the thickness of oxide layer was ensured through the crucible cover.

The experimental setup with modified processing parameters is given in Figure 3.3. The input materials consisted of:

- 118.9 g Al block,
- 2.8 g Li rod,
- 2.5 g Mg rod.

The Al block of technical purity (99.8 %) was mechanically cleaned using wire brush and placed into the graphite crucible coated with boron-nitride (Figure 3.3 b). The crucible was invested in the induction melting furnace and temporarily covered (Figure 3.3 c). The protective atmosphere was established using compressed Ar with 99.999 % purity and UN 1006 designation. The Ar was introduced under the pressure of 10.0 MPa (Figure 3.3 c). The Mg and Li rod were wrapped in Al foil of commercial purity and placed into a steel bell. The steel bell, previously coated with boron-nitride, was used for easier alloying, and melt homogenization.

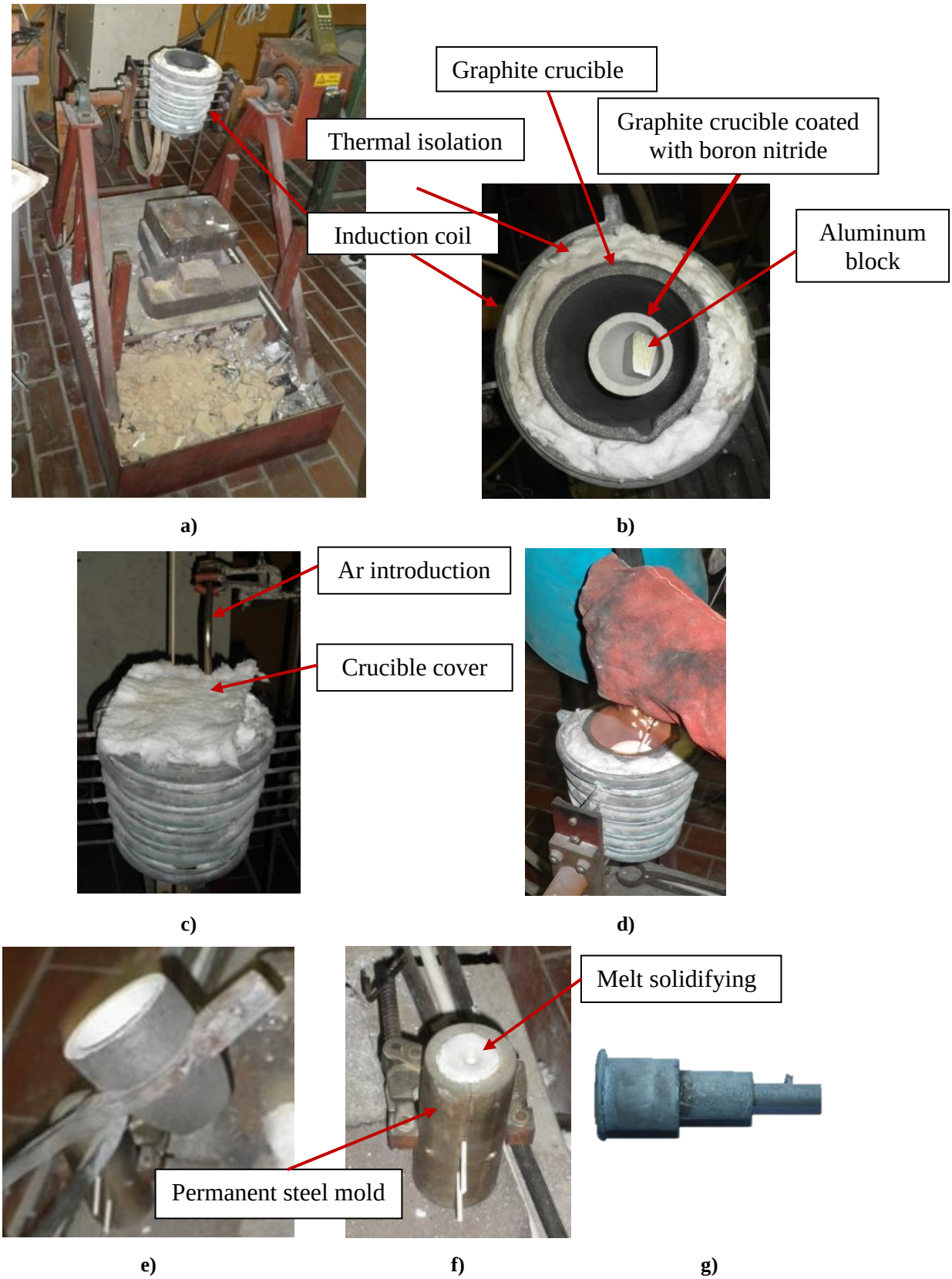

Figure 3.3. The experimental setup for sample synthesis under protective atmosphere of Ar and partial crucible cover: a) induction melting furnace, b) the positioning of graphite crucible and Al block, c) initiation of synthesis, d) alloying, e) casting, f) the solidification in permanent metal mould, g) sample

The melting of aluminum block initiated at 680.0 °C. Before alloying the melt was additionally heated to the temperature of 710.0 °C and kept for 2 min. Alloying, by immersing a steel bell into a molten Al block (Figure 3.3 d), caused the temperature decrease to 690.0 °C. To prevent the appearance of casting defects, the melt was reheated to 720.0 °C and kept for 2.0 min. The small amount of oxides formed on the surface of the melt were mechanically collected using steel bell, and the melt was cast into the permanent steel mold (Figure 3.3 e). After solidification the mold was opened (Figure 3.3 f), and the sample was obtained (Figure 3.3 g).

3.1.3. Synthesis under vacuum

Melting under vacuum was established as an attempt to achieve maximum adsorption of Li in the melt. The experimental procedure given in Figure 3.4 was used to synthesize two samples. The input materials used for sample synthesis are given in Table 3.2.

Table 3.2. The composition of input materials used for sample synthesis under vacuum

Sample	Input material addition, g			
	Al	Mg	Li	AlTi5B1
1st	112.1	2.8	2.7	/
2nd	113.8	3.9	4.0	1.5

As indicated in Table 3.2, in addition to the changes in the type of protective atmosphere, melting under vacuum also comprehended the grain refinement through the addition of AlTi5B1 master alloy (Table 3.2). The grain refinement was performed to reduce grain size and obtain more compact microstructure.

Before synthesis, the Al block of technical purity (99.8 %) was mechanically cleaned using wire brush and placed into the graphite crucible coated with ferric oxide (Figure 3.4 a). The crucible was invested in the chamber of induction melting furnace (Figure 3.4 a). The Mg rod and Li rod were wrapped in the Al foil of commercial purity and placed into the steel bell coated with boron nitride. The steel bell was pulled through the opening for alloying element addition (Figure 3.4 a and b). After the chamber doors were closed and secured, the vacuum of $1.0 \cdot 10^{-4}$ MPa was reached. The Al block melted at the temperature of 690.0 °C. The alloying was performed at 720.0 °C by lowering the steel bell into the melt and stirring. After a holding time of 2.0 min, the melt was heated to the temperature of 740.0 °C. The additional increase in temperature was necessary to prevent solidification of the melt in the crucible during

equalization of the pressures and opening the furnace chamber. The vacuum braking was necessary to cast the sample (Figure 3.4 c). The sample was cast into a permanent steel mold (Figure 3.4 e).

The synthesis of the second sample was performed identically apart from the addition of AlTi5B1 master alloy during alloying.

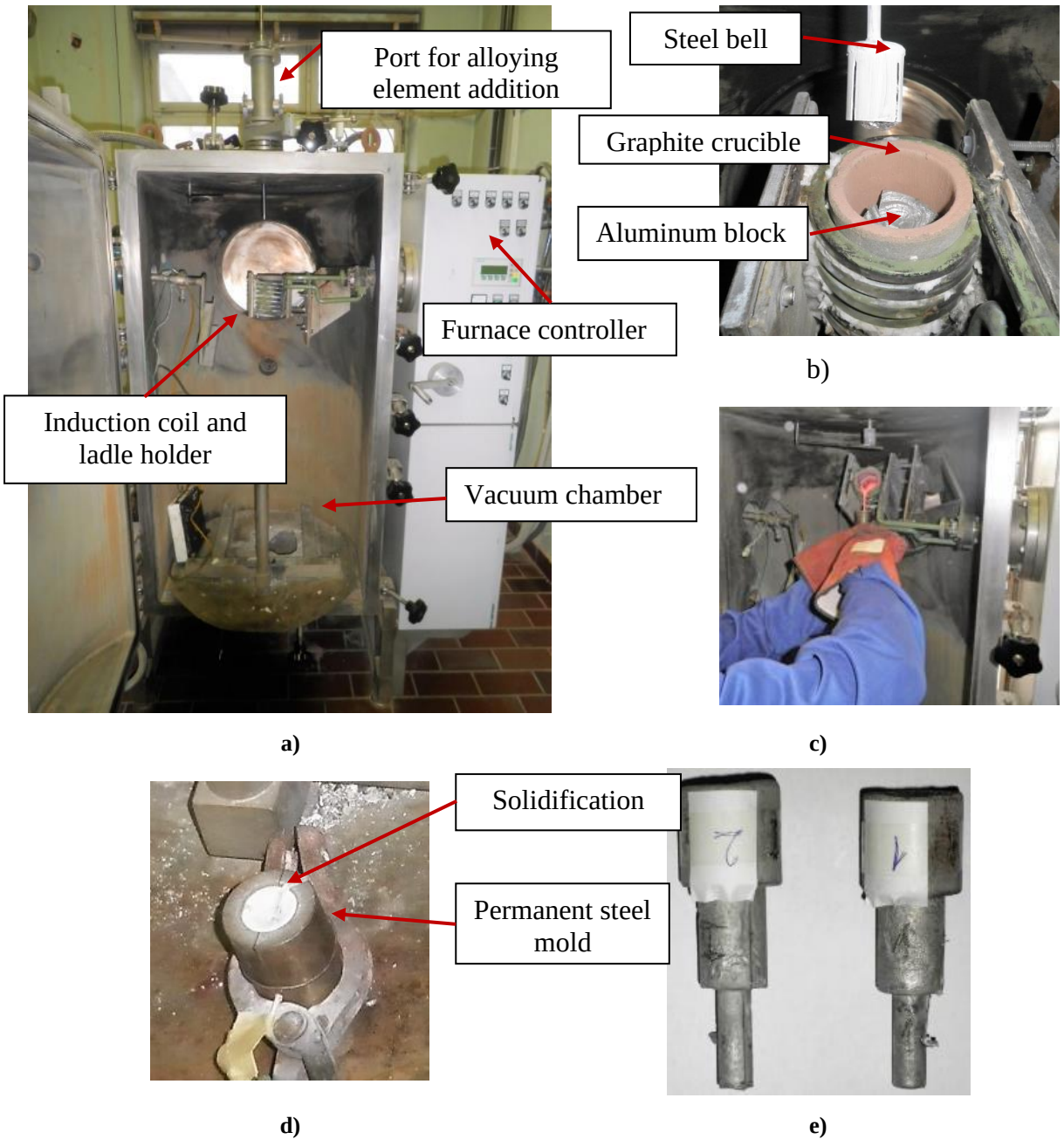

Figure 3.4. The experimental setup for melting under vacuum: a) vacuum furnace, b) the positioning of graphite crucible containing Al block, c) casting, d) permanent steel mold after casting, e) samples

3.1.4. Synthesis under protective atmosphere of Ar and full crucible cover

The experimental setup for synthesis under protective atmosphere of Ar and full crucible cover is represented in Figure 3.5.

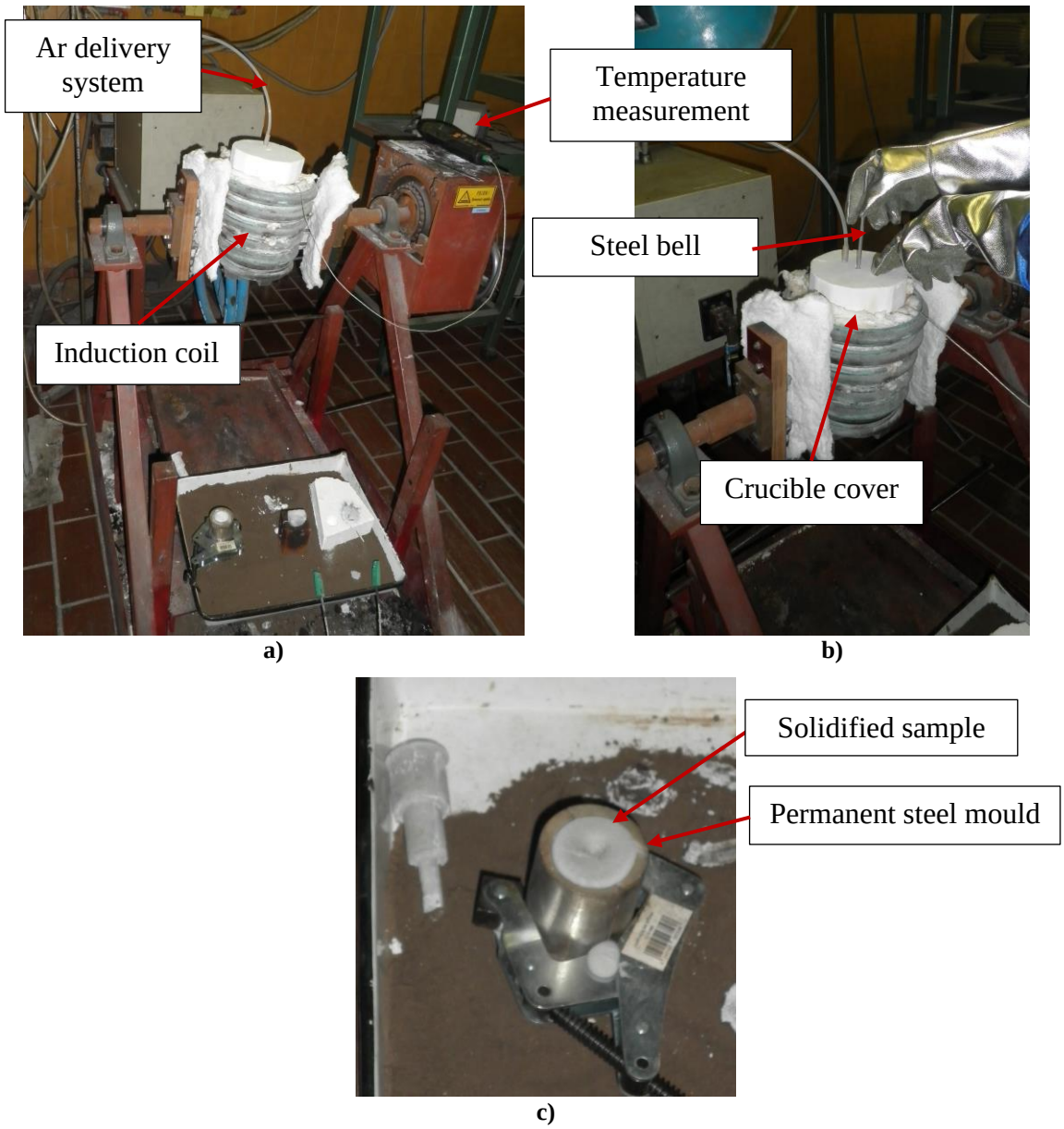

Figure 3.5. The experimental setup for synthesis under protective atmosphere of Ar and full crucible cover: a) preparation for synthesis, b) addition of alloying elements, c) alloy solidifying in permanent steel mold

Unlike synthesis under protective atmosphere of Ar and partial crucible cover, this experimental setup comprehended the modification of the cover to completely fit the crucible and include the ports for Ar introduction and alloying (Figure 3.5). Thusly, the effect of protective atmosphere was increased. This experimental setup was used to synthesize two

samples, one with and one without the addition of grain refiners. The input materials consisted of:

- 256.0 g Al block,
- 6.4 g Li rod,
- 6.4 g Mg rod,
- 1.4 g Ti5B1.

The Al block of technical purity (99.8 %) was mechanically cleaned using wire brush and placed into a graphite crucible coated with boron-nitride (Figure 3.5 a). The crucible was invested in the induction melting furnace and fully covered (Figure 3.3 a). The protective atmosphere was established using compressed Ar with UN 1006 designation. The Ar was introduced under the pressure of 10.0 MPa (Figure 3.5 b). The Mg and Li rod were wrapped in Al foil of commercial purity and placed into a steel bell coated with boron nitride (Figure 3.5 b). The melting of aluminum block initiated at approximately 690.0 °C. The alloying was performed at 720.0 °C by immersing the steel bell (Figure 3.5 b). To compensate for the temperature drop during alloying, the melt was additionally heated and kept at 720.0 °C for 2.0 min. The small amount of oxides formed on the surface of the melt were mechanically collected using steel rode and the first half of the melt was cast into the permanent steel mold (Figure 3.5 c). Afterwords, the rest of the melt was reheated and AlTi5B1 master alloy was added. The processed melt was kept for approximately one minute at 720.0 °C and cast into the permanent steel mold. Before it was cast, the previous casting was removed from the mold.

3.1.5. Designation of synthesized samples

The geometry of the synthesized samples is given in Figure 3.6 with the number of synthesized samples and their designation indicated in Table 3.3. The samples were obtained by casting into a permanent steel mold with corresponding geometry.

The permanent steel mold has a simple configuration consisting of three mold cavities with different diameters and 30.0 mm in length. Since the mold does not possess the gating system, the widest mold cavity with ø 30.0 mm diameter was used as a pouring basin. The second cavity located in the middle of the mold is ø 20.0 mm in diameter, while the last mold cavity is the smallest and has a diameter of ø 10.0 mm.

The experimental procedure comprehended synthesis of three sets of samples using different melting and processing techniques. Considering that only one sample was obtained by the synthesis procedure under protective atmosphere of Ar and the partial crucible cover, the 1st set of samples has two-digit designation. The first digit refers to the sample set while the second indicates the cavity diameter (Table 3.3). The 2nd and 3rd sample set have three-digit designations. The first digit referees to the sample set, second digit indicated the lack off (number 1) or the addition of grain refinement (number 2), while the third digit points to the cavity diameter (Table 3.3).

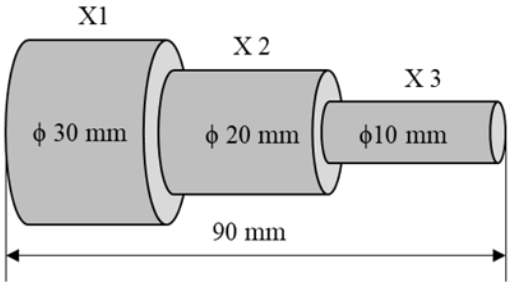

Figure 3.6. The geometry of synthesized samples

Table 3.3. The number of synthesized samples and their designation

Sample set	Designation	Cavity diameter, mm	Description
1	11	30.0	The sample synthesized using protective atmosphere of Ar and partial crucible cover
	12	20.0	
	13	10.0	
2	211	30.0	Sample synthesized under vacuum
	212	20.0	
	213	10.0	
	221	30.0	Sample synthesized under vacuum with the addition of AlTi5B1 inoculant
	222	20.0	
	223	10.0	
3	311	30.0	The sample synthesized using protective atmosphere of Ar and full crucible cover
	312	20.0	
	313	10.0	
	321	30.0	The sample synthesized using protective atmosphere of Ar and full crucible cover with the addition of AlTi5B1 inoculant
	322	20.0	
	323	10.0	

3.2. Chemical composition analysis

The chemical composition of the synthesized alloys was determined using the inductively coupled plasma with mass spectrometry (ICP-MS) on the Agilent Technologies inductively coupled plasma-mass spectrometer and glow discharge atomic emission spectrometer Leco GDS900. Considering that it can only detect predetermined elements, ICP-MS was used to determine the amount of Mg and Li. On the other hand, the emission spectrometer was used to determine the presence of other elements and impurities.

The ICP-MS is a type of mass spectrometry that uses an inductively coupled plasma to ionize the sample. During analysis it atomizes the sample creating atomic and small polyatomic ions, which are later detected. Before analysis, the standard solution is added to solid samples. This allows samples to decompose into atoms and ions when exposed to Ar plasma. Electron excitation to higher energy levels occurs in plasma. After the return of excited atoms and ions to the ground state or lower excited states, they emit electromagnetic radiation in the ultraviolet and visible part of the spectrum. Each excited element emits radiation of a certain wavelength enabling its identification. The concentration of the identified element is proportional to its intensity.

The sampling for ICP-MS analysis is indicated in Figure 3.7 a. The sampling was performed by cutting the tips of the smallest sections of the cast samples (Figure 3.7 a, section X 3). This section was chosen because it first encounters mold, has the highest solidification rate, and does not solidify in open atmosphere. From the samples with 5.0 mm × ø 10.0 mm dimensions, shavings were extracted and dissolved in standard solutions. Before initiating measurements, the spectrometer was calibrated using standardized calibrating solutions. Due to the high reactivity of Li, the ICP-MS was additionally calibrated using solutions containing 1.0, 10.0, 50.0, 100.0 mg/m^3 of Li.

The glow discharge spectrometry utilizes a low-pressure, non-thermal process during which material is uniformly sputtered from the sample surface by a stream of Ar. The sputtered material is then atomized and excited in a low-pressure plasma discharge. While, the identification of the elements is based on the wavelength of the emitted radiation, their concentration is determined by radiation intensity. The accuracy of the measurements depends on the calibration methods and the availability of standards. The device was calibrated with about thirty different standards starting with the pure aluminum method.

As indicated by Figure 3.7 b, the sampling for chemical analysis using Leco GDS900 atomic emission spectrometer was performed by cutting the 5.0 mm × ø 20.0 mm piece from the middle section of the cast samples (Figure 3.7 b, section X2). The sampling was performed differently because atomic emission spectrometer requires a larger contact surface to provide relevant results. The surface of the sample was prepared for analysis by fine grinding. Before the measurements were initiated, the spectrometer was calibrated using reference material for Al alloys. The chemical composition of each sample was measured three times, and a mean value was calculated. The surface of the sample was grinded before each measurement in order to remove traces from previous sputtering.

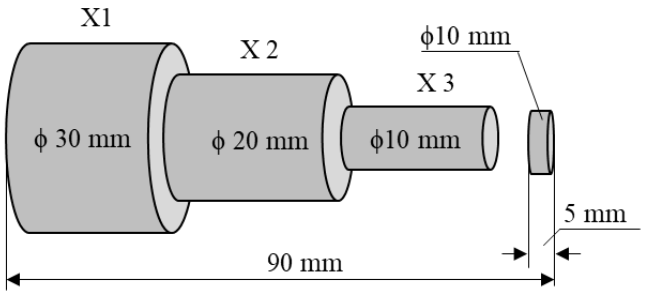

a)

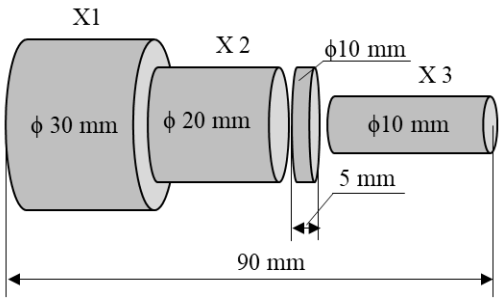

b)

Figure 3.7. The schematic representation of the sampling for determining chemical composition using: a) ICP-MS, b) emission spectrometer

3.3. Density calculation

The experimental setup for density calculation is illustrated in Figure 3.7. Density measurements were based on the Archimedes' principle stating that the upward buoyant force exerted on a body immersed in a fluid is equal to the weight of the fluid displaced by the body. Hance, the density calculation expression is shown in Equation 59:

$$\rho = \frac{m_x}{V_x} \tag{59}$$

where ρ is samples density (g/cm^3), m_x is the samples' mass (g), and V_x is a volume of the sample (mL).

To calculate density using Equation 59 the mass and the volume of the whole sample were measured (Figure 3.8 a). The mass of the sample (m_x) was measured using analytical scale Mettler Toledo, while the volume of the sample (V_x) was measured by its immersion in a measuring beaker filled with water (Figure 3.8 b). Afterwords, the sample was cut into specific sections (Figure 3.8 a) and their physical properties were measured (Figure 3.8 c).

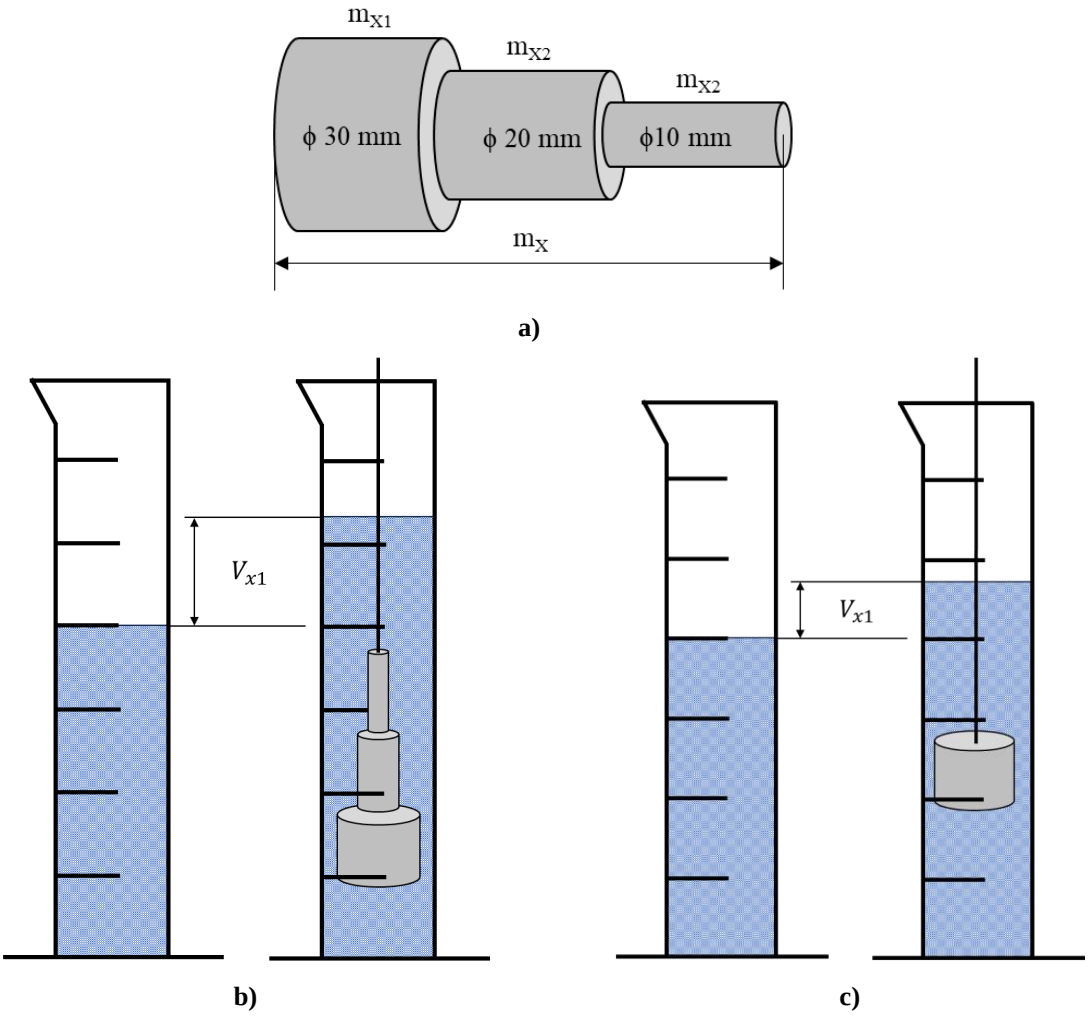

Figure 3.8. The experimental setup for density measurements: a) the schematic representation of the sample with indicated mass measurements, b) measuring the volume of the whole samples, c) measurement of the volume of the specific sample sections

The impact of alloying elements, primarily Li and Mg, on the physical properties of the alloy was evaluated by comparing the density values of the whole samples. The influence of the cooling rate on the segregation of Li and Mg was evaluated by comparing the density

values of the specific sample sections. This assumption is based on the fact that the difference in the amount of Li and Mg between specific sample sections will result in a lower density.

3.4. Calculation of phase diagrams using Thermo-Calc software support

The CALculation of PHAse Diagrams (CALPHAD) is a phenomenological approach to calculating/predicting thermodynamic, kinetic, and other properties of multicomponent systems. It is based on describing the properties of the intermetallic phases starting with pure elements, binary and ternary systems. The properties of higher-order alloys are predicted through extrapolation from the previously defined systems. As a phase-based approach, the properties for the individual phases are modeled as a function of composition, temperature, and pressure. In this thesis, the use of Thermo-Calc software support enabled prediction of equilibrium and non-equilibrium solidification sequence.

After determining the chemical composition of the synthesized samples, the Thermo-Calc software support was used to calculate phase equilibria and determine the solidification sequence under equilibrium and non-equilibrium conditions. The Thermo-Calc 2022a software support enabled calculation of the thermodynamic stability of particular phases related to the chosen initial conditions, such as 720.0 °C temperature, 1×10^5 pressure and individual chemical composition of the samples. The TCAL68: Al-Alloys v8.1 technical sheet for Al was used as a basis for thermodynamic calculations. Figure 3.9 shows schematic representation of thermodynamic calculations performed with the help of Thermo-Calc software support.

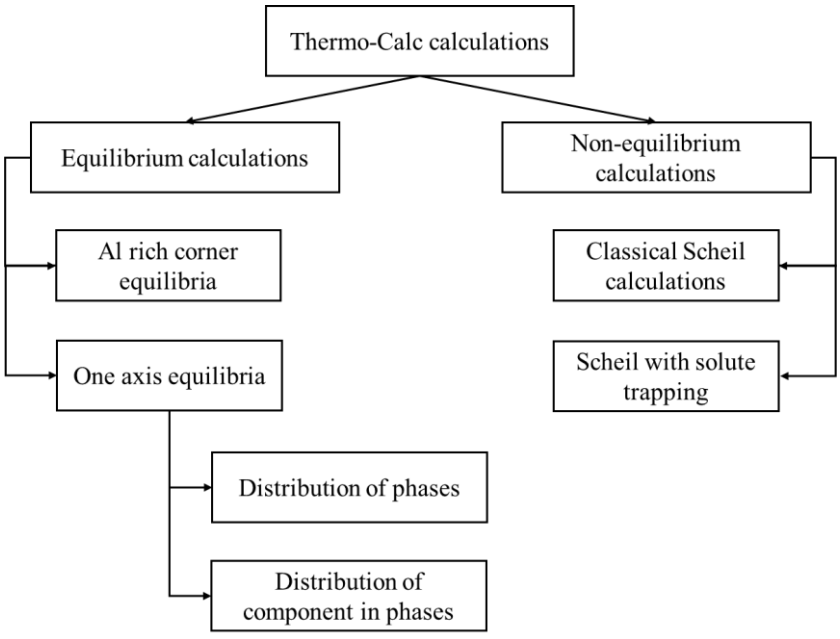

Figure 3.9. The schematic representation of thermodynamic calculations

3.4.1. Equilibrium solidification sequence

The thermodynamic calculation under equilibrium conditions resulted in the construction of equilibrium phase diagram and the list of all thermodynamically stable phases present at the predetermined conditions in relation to the temperature (Figure 3.9). The constructed equilibrium phase diagram as well as the list of stable phases were further used as an input parameter for evaluating the behavior of all components in the individua phases using One axis equilibrium calculator (Figure 3.9).

3.4.2. Non - equilibrium solidification sequence

The prediction of non-equilibrium solidification sequence was based on the Classical Scheil-Gulliver model (Figure 3.9) assuming that:

- Diffusion in the liquid state is infinitely fast,
- Diffusion in solid state is equal to zero,
- The liquid/solid interface is in thermodynamic equilibrium.

The Classical Scheil calculations were performed under the initial conditions of 720.0 °C temperature and temperature step of 1.0 °C. These conditions are only valid for systems without fast diffuser components or solute trapping. While fast diffuser components can be ignored because they are mostly characteristic for steels, solute trapping needs to be considered. Since the basic assumption of solute trapping is the formation of only one phase with dendritic morphology, which is in accordance with the solidification sequence of Al-Li-Mg alloys available in the literature, the Scheil with solute trapping model (Figure 3.9) needs to be considered. This model further assumes:

- The only phase forming dendrites is not necessarily the first solid phase,
- The dendrite forming phase is the only solute trapping phase, while the other solid phases have equilibrium composition corresponding to the Classical Scheil model,
- Amount of solid phase is dependent on solute trapping and solidification speed,
- Dynamic liquidus for primary solid phase is dependent on solute trapping and solidification speed,
- Dynamic solidus is calculated as complete solidification.

This consideration is important because solute trapping can affect composition and the amount of other solid phases. The Scheil with solute trapping calculations were performed under the initial conditions of 720.0 °C temperature, temperature step of 1.0 °C, scanning speed of 1.0 m/s, the angle between solid/liquid boundary and scanning direction of 45 °, solidification speed of 0.7071 m/s and α_{Al} solid solution as primary phase with dendritic morphology. The solidification speed was calculated automatically according to the following Equation 58:

$$V_s = V_{scanning} \cdot \cos \alpha \tag{60}$$

where V_s is calculated solidification speed (m/s), $V_{scanning}$ scanning speed (m/s), α angle between solid/liquid boundary and scanning direction (°).

The utilization of Scheil calculator allows for estimation of the solidification range of an alloy, depression of the solidus temperature due to segregation, composition of the last liquid to solidify in the interdendritic region as well as phases formed during final solidification in segregating pockets.

3.5. Characterization of Al-Mg-Li alloy using thermal analysis

Thermal analysis is a classical method of determining phase diagrams. The liquidus temperature for the alloy of known chemical composition can be obtained by registering the temperature-time curve during melting and cooling of an alloy. Since it enables study of any process that could be activated thermally, the thermal analysis will enable determination of fusion temperature, latent heat of fusion, allotropic transformation, diffusion-based solid-state precipitation, transformation changes, changes in magnetic behavior, behavior with respect to oxidation at high temperature, the variation in thermal expansion coefficient, the variation in the specific heat as well as thermal stability.

This investigation comprehended the use of simplified thermal analysis and differential scanning calorimetry to estimate the Al-Mg-Li alloy's behavior during heating and cooling above the liquidus temperature and determine the solidification sequence and microstructure development.

3.5.1. Application of simplified thermal analysis during sample casting

As indicated by Figure 3.10 a, simplified thermal analysis comprehended placement of Ni-CrNi thermo-couples in the casting cavity of the permanent steel mold. The cooling curves were obtained by the instrument for data acquisition equipped with measuring card DAQ Pad-MI0-16XE-50 and corresponding LabView 7.0 software support (Figure 3.10 b).

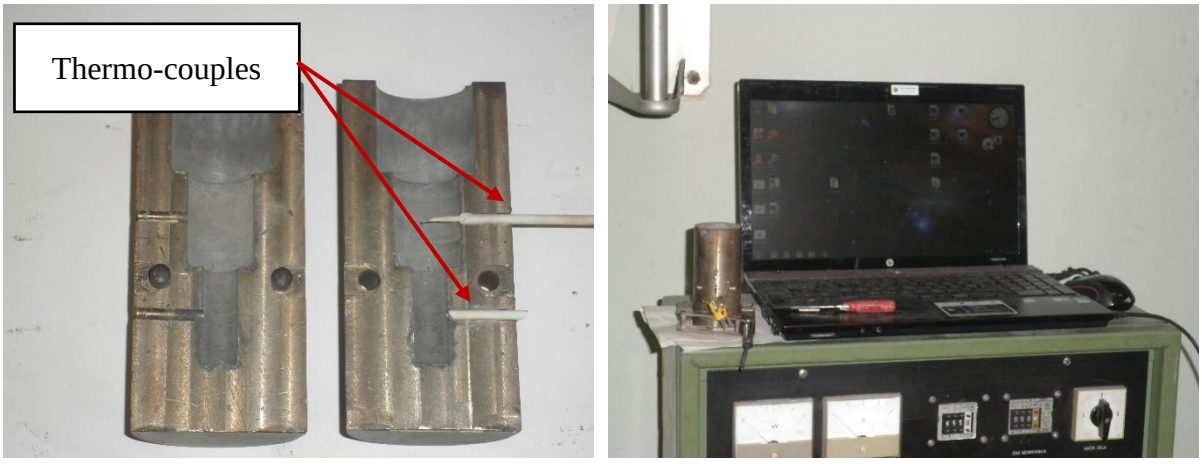

a) **b)**

Figure 3.10. Experimental setup for Simplified Thermal Analysis: a) placement of thermo-couple in mold cavity, b) data acquisition instrument

Cooling curves were later processed using Origin 2017 software support enabling determination of characteristic temperatures and temperature deviations induced by phase

formation. The list of characteristic temperatures and additional parameters obtained from cooling curve interpretation is given in Table 3.4. Furthermore, in combination with CALPHAD calculations and microstructural investigations, it will help in understanding solidification sequence of synthesized Al-Li-Mg alloys.

Table 3.4. The characteristic temperatures and additional parameters obtained from cooling curve interpretation

Symbol	Description	Calculation	Units
T_p	Pouring temperature		°C
T_n	Nucleation temperature		°C
T_L^{min}	Minimum liquidus temperature		°C
T_L^{max}	Maximum liquidus temperature		°C
T_{EDS}	Eutectic reaction starting temperature		°C
T_{EDE}	Eutectic reaction ending temperature		°C
T_S	Solidus temperature		°C
Δt_{L-S}	Time solidification interval	$\Delta t_{L-S} = t_L - t_S$	s
ΔT_{L-S}	Temperature solidification interval	$\Delta T_{L-S} = T_L - T_S$	°C
ΔT_{Lr}	Liquidus recalescence	$\Delta T_{Lr} = T_L^{max} - T_L^{min}$	°C

3.5.2. Identification of characteristic temperatures using Simultaneous Thermal Analysis

The simultaneous thermal analysis (STA) involved the application of differential scanning calorimetry (DSC) method using NETZSCH 449 Jupiter simultaneous thermal analyzer. The sampling for DSC analysis was performed by cutting the sample of cube geometry with 4.0 × 4.0 × 4.0 mm dimensions from the smallest sections of the sample 1 (Figure 3.11).

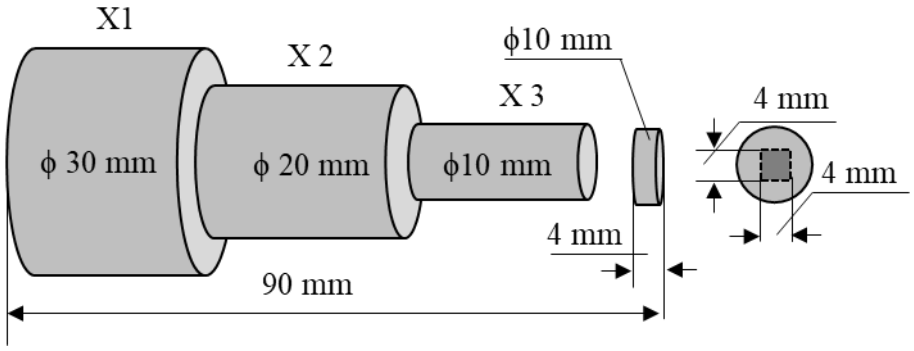

Figure 3.11. The sampling for differential scanning calorimetry

The solidification interval as well as temperatures and enthalpies of phase solidification and precipitation were determined using techniques of heating and cooling from room temperature to the temperature of 720.0 °C with the rates of 2.0, 10.0, 20.0, 30.0, 40.0 and 50.0 K/min in the protective atmosphere of Ar. The measurements were performed by placing the crucible with a sample in one of the measuring cells, while the other measuring cell remained empty. The empty measuring cell was used as a reference. Both cells were heated identically over time. The difference in the input energy required to match the temperature of both measuring and reference cell, represents the amount of excess heat absorbed or released by the sample. This enables determination of the characteristic temperatures and changes in heat flow associated with material transitions as a function of time and temperature.

3.6.Metallographic analysis and microstructure characterization

Metallography as a scientific discipline focuses on examining and determining the constitution and underlying structure of the constituents in metals, alloys, and materials. The structural examination may be performed over a wide range of length scales or magnification levels, ranging from visual or low magnification examination to very high magnifications obtained through the use of electron microscopy. This wide range of magnifications stemming from macroscopic to microscopic levels, enables detection of various important microstructural features such as solidification structure in cast products, flow lines in wrought products, characterization of failure surface as well as determination of grain size, twins and type, size, shape and redistribution of intermetallic phase particles. These microstructural constituents are crucial in determining the properties and behavior of most metals and alloys.

Since the properties of Al alloys depend on the complex interaction between chemical composition, microstructural constituents developed during solidification, heat treatment and deformation processes, microstructural characterization of Al alloys comprehends grain size and morphology determination, size, shape and distribution of intermetallic phases as well as the presence of macrostructural and microstructural defects.

In order to fully characterize the impact of chemical composition and cooling rate on microstructure development of synthesized alloys the techniques of light microscopy, scanning electron microscopy (SEM) with energy dispersive spectroscopy (EDS) and transmission electron microscopy (TEM) were employed. This enabled qualitative and quantitate microstructure constituent analysis.

3.6.1. Light microscopy

The light optical microscope remains the most important tool for the study of microstructure, despite the evolution of sophisticated electron metallographic instruments such as the SEM and TEM. In general, all microstructural studies should start with light microscopy and lower magnification. Most microstructures can be observed using light microscope and identified on the bases of their characteristics. Identification of unknown constituents may be assisted by observation of their hardness relative to the matrix, by their naturally occurring color, by their response to polarized light as well as their reaction to selective etchants. These observations are compared to known details about the physical metallurgy of the material being

examined. If doubt still remains concerning the unknown constituents, more sophisticated techniques of microscopy must be implemented.

To identify the macrostructural and microstructural constituents in synthesized alloys the Olympus SZ-CTV macroscope with Quick PHOTO Camera 3.2 software support and inverted metallographic microscope Olympus GX51 with motorized sample holding table and Stream Motion software support were used. While macroscope was used for microstructural observation of the etched sample up to the magnification of 55 X, the utilization of inverted metallographic microscope enabled qualitative and quantitative sample analysis at higher magnifications. The quantitative microstructural analysis comprehended identification of intermetallic phases present in the matrix of etched samples based on their morphology. The quantitative microstructural analysis evolved grain size determination in accordance with the intercept method described in ASTM E-112 standard.

3.6.2. The scanning electron microscopy with energy dispersive spectroscopy

Scanning electron microscope is one of the most versatile instruments used in microstructure investigations. Under electron bombardment a variety of different signals are generated, including secondary electrons, backscattered electrons, characteristic X-rays as well as the long-wave radiation in the ultraviolet and visible region of the spectrum. Using secondary electrons, SEM expands the resolution gap between optical and TEM microscopy. Scanning electron microscopy offers possibilities for image acquisition that is usually easy to interpret and will reveal clear images of as-polished and etched cross sections as well as rough surfaces and particles.

When an electron is ejected from the electron shell of an atom, an empty spot remains, which is filled with an electron from another electron shell of higher energy. During this electron jump, one quantum of energy or X-ray is emitted. The energy of the resulting radiation is characteristic for each chemical element. This type of radiation is detected by the EDS detector. This detector is used to determine the chemical composition of the sample based on X-rays emitted by the sample under the electron beam of the microscope.

The use of SEM and EDS analysis enabled closer observation of intermetallic phases identified by light microscopy, as well as distribution of chemical composition components within the microstructural constituents. Since Li is too light of an element to be detected, the EDS analysis mostly comprehended detection of Al, Mg and impurity elements. For that

purpose, the TESCAN VEGA 5136MM Scanning electron microscope (SEM) and energy dispersive spectrometer (EDX) were used.

3.6.3. The transmission electron microscopy

The conventional TEM comprehends irradiation of a thin sample with an electron beam of unmodified current density. The electrons are emitted in electron gun by thermic, Schottky or field emission. The field emission is used when high gun brightness and coherence are needed. Since electrons interact strongly with atoms by elastic and inelastic scattering, the sample must be very thin (5.0 - 100.0 nm) requiring special preparation techniques. This enabled TEM to emerge as one of the preeminent characterization tools for materials science. It can characterize materials on length scales ranging from macroscopic (grain boundaries, inclusions) to atomic (interfaces, dopants, individual atomic columns or even atoms). In characterization of functional materials and development of innovative materials with improved properties, a deep understanding of the relation between the properties and the crystal structure is the key to design new materials and improve existing ones. Transmission electron microscopy provides unique opportunities for crystal structure analysis at a very local scale.

The application of TEM microscopy provided additional insight into the solidification sequence and microstructural characterization of the synthesized alloys. In doing so, emphasis was placed on the solidification of metastable or precursor phases in the early stages of solidification, and the possibility of their retention in the microstructure. The TEM microscopy was performed using JEOL JEM-2100 with a thermionic emission filament LaB6 at an accelerating voltage of 200.0 kV. A conventional bright-field observation technique was used to render the image.

3.6.4. The X-ray diffraction

The X-ray diffraction (XRD) is a technique used in materials science to determine the atomic and molecular structure of the material. This is done by irradiating a given sample with incident X-rays followed by measuring the intensities and scattering angles of the X-rays scattered by the material. The intensity of the scattered X-rays is plotted as a function of the scattering angle, and the structure of the material is determined from the analysis of the location, in angle, and the intensities of scattered peaks. Beyond being able to measure the average positions of the atoms in the crystal, it can also provide information on how the actual structure deviates from the ideal due to the presence of internal stresses or defects. The diffraction of the

X-rays, that is central to the XRD method, is a subset of the general X-ray scattering phenomena. The term XRD usually refers to the wide-angle X-ray diffraction (WAXD) and represents one of the several methods that use the elastically scattered X-ray waves. Other X-ray techniques include small angle X-ray scattering (SAXS), where the X-rays are incident on the sample over the small angular range of 0.1 - 100.0.

Similar to the TEM microscopy technique, the main goal of XRD method was to further the knowledge on microstructure development during solidification under conditions defined by experiment. For that purpose, a PANalytical X'Pert PRO X-ray diffractometer with an Empyrean X-ray tube and Cu-target was used. The voltage and current in the X-ray tube were 45 kV and 40 mA, respectively. The wavelength of the X-ray light was K_α = 15418.0 nm (without using a monochromator). Recording took place in the range of 2.0 θ angles from 20.0 ° to 80.0 °.

3.6.5. The standard metallographic sample preparation

To meet the requirements necessary for metallographic analysis, the surface of the sample was subjected to the standard metallographic preparation of grinding and polishing. Grinding removes damage and deformed surface material without introducing additional changes to the sample surface. When a flat surface of certain quality is achieved, the remaining discontinuities can be removed quickly by polishing. The metallographic preparation varies depending on the applied method as well as the device.

3.6.5.1. The sampling and sample preparation for light microscopy, scanning electron microscopy and X-ray diffraction

As illustrated in Figure 3.12 the sampling for light and scanning electron microscopy was performed with respect to the specific sample sections. The sample section with ø 30.0 mm diameter was cut parallel to the length of the sample, while ø 20.0 mm and ø 10.0 mm sections were cut perpendicular to its length.

The sampling for XRD was performed by cutting the plate with 5.0 mm thickness from the ø 10.0 mm sample section. This type of sampling was performed in accordance with the X-ray diffractometer specifications.

The sample preparation for both types of analysis consisted of cutting using Abrasive cutter Buhler ABRASIMET 2 and grinding and polishing on Struers Tegramin-30 Automatic, microprocessor-controlled machine for grinding and polishing. It is important to emphasize that

during cutting the samples were continuously cooled with emulsion to prevent the influence of heat release on the analysis results. The grinding and polishing were performed using silicon-carbide based grinding papers and appropriate polishing cloths and suspensions.

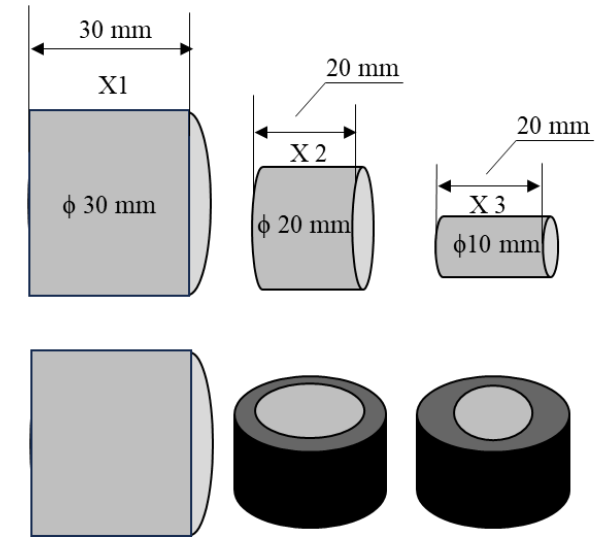

a)

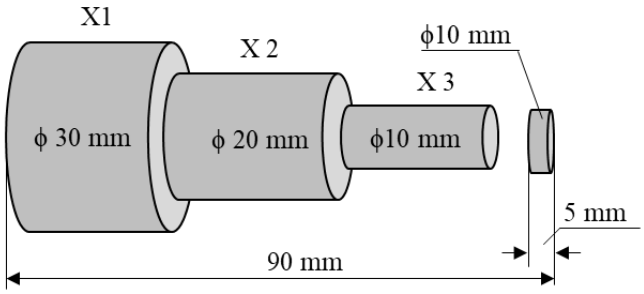

b)

Figure 3.12. The sampling for: a) light, scanning electron microscopy, and transmission electron microscopy, b) X-ray diffraction

The sample for X-ray diffraction was analyzed after polishing, while light and SEM analysis required additional etching. To fully comprehend the microstructure constituents in the alloy, the etching was performed as follows:

1. **CHEMICAL ETCHING:**

   a. 0.5 % aqueous solution of hydrochloric acid,

   b. Poulton's etching solution (60 mL hydrochloric acid, 30 mL nitric acid, 5 mL hydrofluoric acid, 5 mL water),

c. Keller's etching solution (95 mL water, 2.5 mL nitric acid, 1.0 mL hydrofluoric acid, 1.5 mL hydrochloric acid).

2. COLOR ETCHING:

a. Weck's etching solution (4 g potassium permanganate, 1 g sodium hydroxide, 100 mL water).

While Poulton's etching solution was used to reveal the macrostructure and grain structure, the rest of the solutions were used for intermetallic phase identification. Intermetallic phases were identified based on the position, color, and shape with respect to the data available in the literature.

3.6.5.2. The sampling and sample preparation for transmission electron microscopy

Considering that TEM analysis is based on electron interaction with atoms by elastic and inelastic scattering, the sample must be very thin (5.0-100.0 nm) requiring special preparation techniques. The samples for TEM analysis were prepared as follows:

1. Cutting of a thin plate of 0.5 mm thickness using a Buehler Isomet Low Speed Saw,
2. Cutting out cylinders with a diameter of ø 3.0 mm (thickness 0.5 mm) from this thin plate with the help of an ultrasonic cutter Ultrasonic Cutter 380, Sonicut,
3. Polishing of thin rolls on cylindrical supports for controlled thinning using a TEM disc grinder TEM Disc Grinder 623, Gatan. The samples were ground on fine sandpaper to a thickness of 70.0 to 90.0 μm,
4. Sample dimpling of about 20.0 μm in the centre, with a device for thinning dimple samples Dimple Grinder 656, Gatan.
5. Making a hole in the middle of the sample with a precision ion polishing system PIPS, Gatan. Initial voltage 4.5 keV - place (when hole appears) 2.0 keV.

3.7. The characterization of alloys' mechanical properties

To finalize the material for an engineering product or application, it is important to understand its mechanical properties. The mechanical properties affect the mechanical strength and ability of a material to be molded in suitable shape. This means that the mechanical properties imply a material's reaction to an applied load. The mechanical properties of metals determine the range of usefulness and service life expectance. Mechanical properties are also used to help classify and identify material. The most common properties considered are strength, ductility, hardness, impact toughness, and fracture toughness.

To determine the mechanical properties of the synthesized alloys, compression testing and hardness measurements at macro-, micro-, and nano- scale were used.

3.7.1. The compression testing

There is an increasing number of engineering and technical applications in which it is desirable to know the compressive behaviour of materials. The engineering materials subjected to nominally compressive loadings may develop local tensile and/or shear fields resulting in fracture after considerable amounts of strain. This may be considered as material's load carrying capacity. So, it is important to identify these conditions of strain and stress that immediately preceded the fracture nucleation in an environment that is different from standard tensile testing.

However, it is important to acknowledge the existence of two complicating factors concerning compression testing. The first one refers to the ununiform and complex states of stress and strain within the barrelled sample. These states change as the deformation precedes. The other complicated factor concerns the different fracture patterns exhibited by different materials.

The compression testing was performed on the samples in as cast and solution hardened condition using Gleeble 1500D thermo-mechanical simulator. The sample was solution hardened at 520.0 °C for 4 h and quenched in water. The sample in as cast condition was compressed at the room temperature, while the solution hardened sample was compressed at the temperature of 190.0 °C. The testing temperature was achieved in 50 s. However, to obtain even distribution of the heat, the sample was kept at the testing temperature for 5 min before initiating the compression testing. The samples with initial length of 9.0 mm and diameter of ø 6.0 mm, were compressed using Gleeble 1500D thermo-mechanical simulator. The sampling for compression testing is illustrated in Figure 3.13. Samples were obtained by

circularly cutting into a cylinder from the thickest specific section of the sample. Such a sampling method was implemented as a compromise between ensuring the equal testing conditions and the minimum dimensions of the sample required for testing.

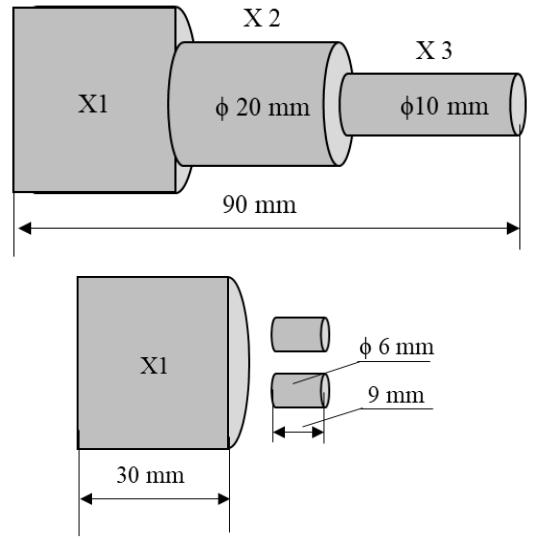

a)

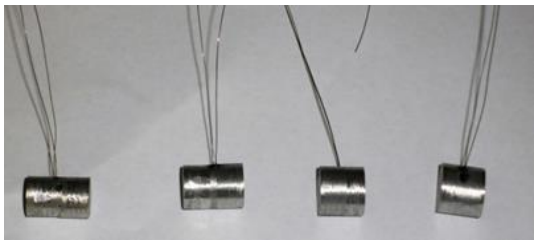

b)

Figure 3.13. The sampling for compression testing: a) schematic representation of the sampling position, b) samples for testing with welded thermocouples

During compression testing the force was increased from 0 N to almost 30 000.0 N with the strain rate of 25 1/s. The strain rate was constant during the testing. The compression was conducted with the data acquisition rate of 10 000.0 Hz during testing without any additional corrections of obtained data after testing. The influence of friction was limited by using tantalum foil and nickel-based paste between sample and Gleeble working jaws (Figure 3.14 a). To determine the strength properties, the samples were compressed till 0.7 deformation was reached (Figure 3.14 b). The obtained engineering stress-strain curves were used to determine yield strength, upper yield point, lower yield point, compression strength and ultimate point. At the yield strength point the engineering strain starts to increase faster than engineering stress because of the initiation of inelastic deformation. After reaching the yield strength the samples start to exhibit plastic behavior. At the upper yield, the maximum loading is required to initiate the plastic deformation causing the engineering stress increase. After

reaching its maximum, the plastic deformation of the material requires minimum loading. This drop in engineering stress is registered as a lower yield point. The compressive strength represents the maximum engineering stress till 0.7 deformation is reached. The ultimate point represents the engineering stress at which the 0.7 deformation is reached or the sample fractures. Measuring the sample before and after compression testing enabled calculation of sample height reduction. Surface temperature change was monitored during compression testing.

a)

b)

Figure 3.14. The Gleeble working jaws: a) sample positioning at the beginning of deformation, b) end of deformation

3.7.2. The hardness measurement

Hardness as a mechanical property represents the resistance of a material to localized plastic deformation. It can be determined using a number of techniques including indentation, scratch and rebound measurements. Hardness is used in numerous engineering and design applications because it directly correlates to the material performance and suitability.

To estimate the impact of chemical composition and cooling rate (specific sample section) on hardness property, the hardness measurements were performed using the Mitutoyo Hardness Testing Machine HV. The sampling for hardness measurements was conducted in accordance with sampling for light and SEM analysis indicated in Figure 3.12. The testing was performed on the samples after standard metallographic preparation and analysis using Vickers method with a loading of 1 N and indenting time of 10 s. The indentation was performed in the central part of the cross-section.

3.7.3. The microhardness measurement

Microhardness testing is used to determine the hardness of a material surface at the microscopic level. For some metals and alloys, there are empirical correlations between hardness, strength, and modulus of elasticity. In microhardness testing, a diamond indenter of a specific geometry is impressed into the surface of a sample with predetermined test load and loading time and produces an indentation with lengths measured in tens of microns. The hardness number is based on measurements made on the indentation mark formed on the surface of the specimen. The applied indentation force is divided by the surface area of the indentation mark. Microhardness testing can be conducted using a Vickers or Knoop indenter. In the Vickers hardness tests, both diagonals of the indentation are measured, and the average value is used to compute the Vickers hardness number (HV). In the Knoop hardness tests, only the longer diagonal is measured and the Knoop hardness is calculated based on the projected area of the indent divided by the applied force.

The sampling for microhardness testing was performed in accordance with sampling for light and SEM analysis indicated in Figure 3.12. Moreover, the locations for microhardness measurements were chosen based on the results of light microscopy enabling the assessment of microstructure development on the hardness at more local levels. The microhardness measurements were performed on the Microhardness tester LEICA VMHT using Vickers

testing method. The indentations were performed under the load force of 0.980 N and loading time of 15 s.

3.7.4. The nanoindentation

The scale of materials and machined components continues to decrease with advantages in material science and technology making traditional test systems increasingly more difficult to use for determining the mechanical properties. Consequently, instrumented indentation testing or depth sensing indentation testing is becoming the preferred technique for mechanical properties determination. Instrumented indentation testing is similar to hardness measurements concerning the indentation of rigid probe into the surface of a tested material. However, instrumented indentation testing does not require measurement of residual impression area and it results in Young's modulus and hardness values. Young's modulus can be considered as stiffness of a material or the material's resistance to elastic deformation. It is an intrinsic property meaning that Young's modulus can only be changed by changing the atomic structure of the material. Hardness is directly proportional to the yield stress and is generally reduced by the factor of approximately 3. Elastic modulus and hardness are important to design engineers because they deliver information on material's behavior under various types of stress and strain.

To determine the impact of Li and Mg additions on intrinsic properties of Al, the nanoindentation measurements were performed using Agilent Nano Indenter G200. The indentations were performed using Berkovich indentation tip on samples prepared using standard metallographic preparation (Figure 3.12). The measurements were performed using contact stiffness mode (CSM) which allows the contact stiffness to be determined at every interval of load-displacement curve. Indentations were made using a contact nominal strain rate of 0.05 1/s. Indentations were made with depth control and the indentation depth ranged from 0.0 to 14000.0 nm.

3.8. Assessment of the alloy's microstructure stability in corrosive environment

To simulate the material degradation in various types of outdoor services, especially in marine and automotive applications, accelerated degradation processes based on chemical and electrochemical reactions were applied. Both chemical and electrochemical microstructure degradation was estimated by exposing the sample 31 (Al-2.18Mg-1.92Li) alloy in as-cast and solutionized condition to EXCO solution. The solution hardening was performed under the assumption that the dissolution of cathodic and anodic microstructure constituents will result in greater degradation resistance. The EXCO solution was obtained by dissolving 234.0 g of sodium chloride (NaCl) and 50.0 g of potassium nitrate (KNO_3) in water. Afterwards, 6.3 ml of HNO_3 was added and the solution was diluted to 1.0 L bay adding distilled water. The obtained solution had an initial pH value of 0.4. To avoid the influence of degradation products on the bulk solution chemistry, approximately 250.0 mL of solution per sample was used. The sampling for degradation testing is illustrated by Figure 3.15.

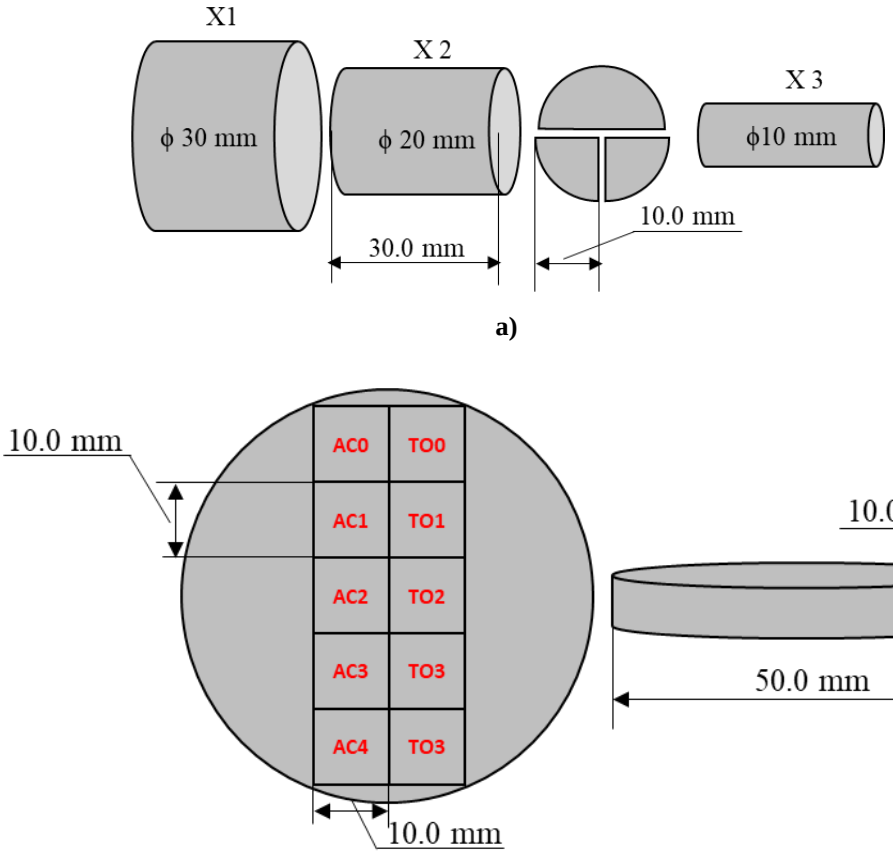

Figure 3.15. The sampling for: a) electrochemical degradation testing, b) chemical degradation testing

The samples for electrochemical degradation testing were taken from the middle cylinder of the cast sample with the diameter of ø 20.0 mm and the length of 30.0 mm. The cylinder was cut into quarters (Figure 3.15). One quarter was used to estimate the degradation in as-cast condition, while the other was first solution hardened and then subjected to degradation conditions. The sampling for chemical degradation testing was performed by cutting the sample of circular geometry with diameter of ø 50.0 mm and thickness of 10.0 mm into 10 samples (Figure 3.15). Before testing, the samples were mounted in a conductive mass at elevated temperatures and pressure using Buhler SimpliMet ® 1000 hot mounting machine. The samples were primarily mounted to ensure the effect of the degradation environment on only one analyzed surface of the sample. Afterwards, the samples were prepared by standard metallographic preparation techniques of grinding and polishing.

3.8.1. The electrochemical degradation testing

The experimental setup for electrochemical microstructure degradation testing is illustrated in Figure 3.16.

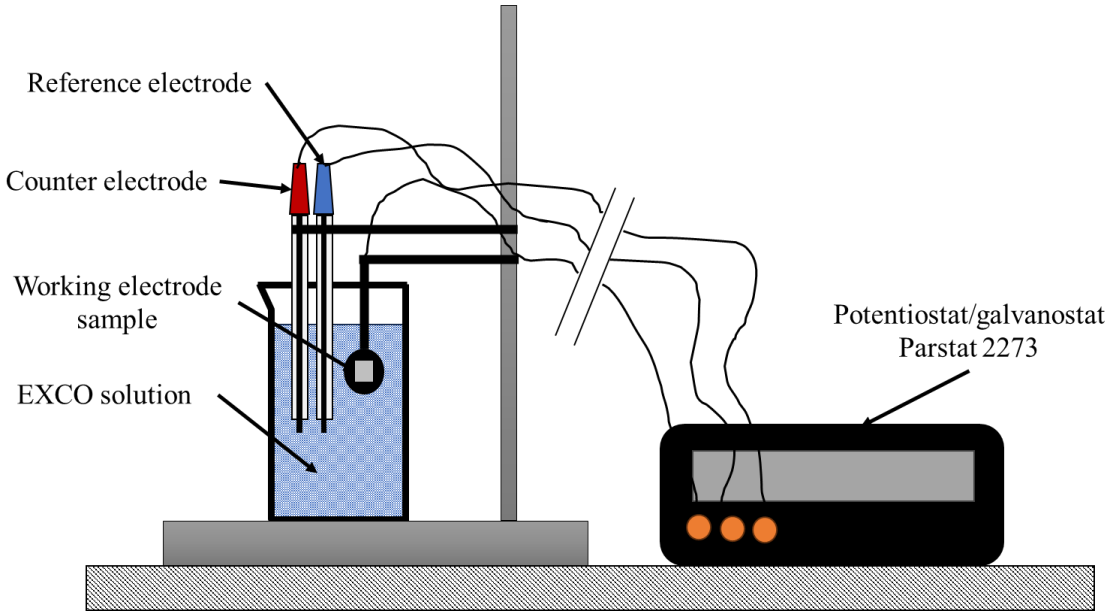

Figure 3.16. The experimental setup for electrochemical degradation testing

The electrochemical measurements were performed using standard three-electrode cell with a saturated calomel reference electrode (SEC), a platinum counter electrode and a 1.0 cm^3 exposed surface of a working electrode-sample. The electrochemical degradation was based on the electrochemical measurements performed using potentiostat/galvanostat Parstat 2273 at the room temperature (19.0 ± 2.0 °C) with a 0.5 mV/s scan rate. Before initiating the corrosion

measurements, the open circuit potential (E_{opc}) was stabilized for 600 s. The Tafel extrapolation method was performed using potentiodynamic polarization in the potential range from – 250.0 mV to +250.0 mV vs corrosion potential (E_{corr}) with a scan rate of 0.5 mV/s.

3.8.2. The chemical degradation testing

The chemical degradation was performed by exposing the previously prepared samples to the EXCO solution for a corresponding period of time. The sample designation in relation to exposure time is indicated in Table 3.5.

Table 3.5. The sample designation in relation to immersion time

Exposure time, h		5	24	48	72
Sample designation	As-cast	AC1	AC2	AC3	AC4
	Solution hardened	TO1	TO2	TO3	TO4

As indicated in Table 3.5 the samples were exposed to corrosive environment for 5, 24, 48 and 72 h without any additional rinsing of the sample surface, stirring or addition of EXCO solution. After the exposure time ended, each sample was individually rinsed in distilled water, immersed in a concentrated HCl acid for 5 s, rinsed in distilled water, alcohol and dried in hot air. The concentrated acid dipping was performed to neutralize residual EXCO solution and prevent subsequent degradation.

3.8.3. The key parameters of microstructural degradation assessment

The chemical and electrochemical microstructure degradation testing enabled determination of different physical, chemical, and electrochemical parameters indicated in Table 3.6.

After hot mounting and standard metallographic preparation of the exposure surface, the samples were weighed to determine the mass of the samples before degradation (m_S). The mass of degraded samples (m_E) was measured after neutralization, rinsing, and drying (Table 3.6). The starting and final pH values of EXCO solution were determined using laboratory pH meter and conductometer infoLab LeV1.

For chemically degraded samples, the corrosion rate was calculated using following Equation 61:

$$v_{corr} = \frac{\Delta m}{t_{exp}}, \frac{g}{s} \quad (61)$$

where Δm is difference between initial and fine mass of the sample and t_{exp} is exposure time. In this way, it was possible to estimate the corrosion rate depending on the changes in pH value of EXCO solution. The influence of degradation environment on the loss of alloy's components (Al, Mg, Li) was evaluated by measuring the chemical composition of the EXCO solution at the end of exposure time using ICP-MS methodology. The inductively coupled plasma with mass spectrometry analysis was performed on the Agilent Technologies inductively coupled plasma-mass spectrometer. Before chemical composition measurements, each sample of the EXCO solution was diluted using standardized solutions to reduce the influence of high sodium and chlorine content on the result accuracy.

Table 3.6. The parameters of microstructure degradation testing

Parameter	Definition
Chemical testing	
m_S, g	Mass of the samples before degradation
m_E, g	Mass of degraded samples
t_{exp}, s	Exposure time
v_{corr}, g/s	Corrosion rate
Electrochemical corrosion	
E_{corr}, mV	Corrosion potential
i_c, μA/cm^2	Corrosion current density
B_a, mV/dec	Anode slope
B_c, mV/dec	Cathode slope
v_{corr}, mm/year	Corrosion rate

The utilization of electrochemical measurements enabled determination of electrochemical parameters (Table 3.6). These parameters were extrapolated from Tafel's polarization curves using PowerCorrTM software support. The Corrosion potential or rest potential is a mixed potential at which the rate of andic dissolution of the electrode equals the rate of cathodic reactions without changes in net current. The corrosion current density is the dissolution current at the given corrosion potential. While corrosion potential indicates the state of sample surface, the corrosion current reflects the corrosion rate at the time of the measurement. The anode and cathode slope of Tafel's polarization curve indicate preferential dissolution of the sample or electrode.

To estimate the impact of electrochemical and chemical degradation on microstructure of the samples, metallographic analysis was performed. After electrochemical and chemical

degradation, macrostructure and microstructure of the exposed surface were analysed without previous standard metallographic preparation (Figure 3.17 a). Afterword's, samples were cut and cross-section of the sample was prepared using standard metallographic techniques of grinding, coarse polishing and polishing (Figure 3.17 b), as described in the Section 3.6.5.1. The cross-section surface of electrochemically tested samples was analysed in polished and etched condition, while the chemical etched sample was analysed without previous etching.

To assess the impact of degradation on the mechanical properties of the exposed samples, the microhardness on the previously prepared cross-section surface of the samples was measured. The microhardness measurements were performed as described in the Section 3.7.3. The microhardness was measured near the exposed surface in the areas affected by degradation (Figure 3.17 b).

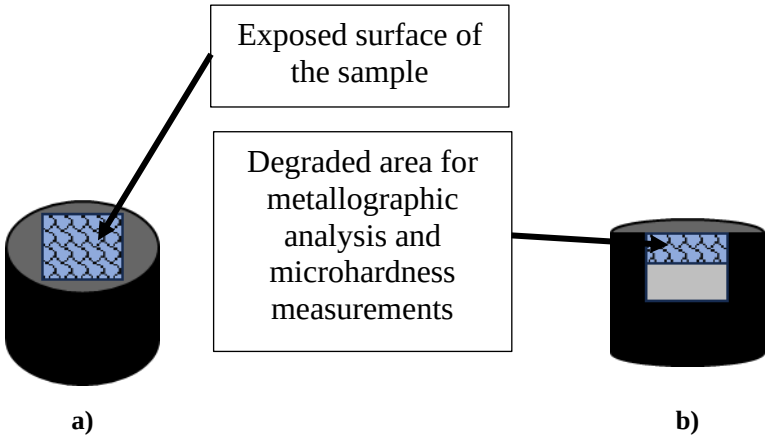

Figure 3.17. The sampling for metallographic analysis of the samples after electrochemical and chemical degradation: a) exposed surface, b) cross-section of the sample

4. RESULTS AND DISCUSSION

The results of chemical composition, calculation of equilibrium and non-equilibrium phase diagrams, thermodynamic and structural analysis were used to determine the solidification sequence of synthesized Al-Mg-Li alloys. The impact of identified microstructure constituents on mechanical properties and degradation susceptibility were analyzed.

4.1. The results of chemical composition analysis

The chemical composition of the synthesized samples determined using the ICP-MS as well as the composition of input material are given in Table 4.1.

Table 4.1. The results of ICP-MS chemical composition analysis

Sample	Chemical composition, wt.%			Composition of input material, wt.%			Material loss, %	
	Li	Mg	Li/Mg	Al	Li	Mg	Li	Mg
1	2.16	0.38	5.68	98.97	2.21	1.97	2.26	80.71
21	2.09	2.24	0.93	95.29	2.33	2.38	10.30	5.88
22	2.58	2.57	1.0	92.4	3.25	3.16	20.61	18.67
31	1.92	2.18	0.88	95.12	2.38	2.37	13.60	8.02
32	1.73	1.92	0.90				27.31	18.99

The results of chemical composition analysis indicate successful alloy synthesis using all three procedures. The least amount of alloying elements was lost during the synthesis of sample 21 under vacuum (Table 4.1). Even dough the sample 22 was obtained under similar circumstances, significant loss of alloying elements can be observed (Table 4.1). This loss of both Li and Mg is the result of the longer time required for the vacuum breaking and casting in an open atmosphere. The most Li and Mg was lost during the production of sample 32 using protective atmosphere of Ar and full ladle cover. This loss is not surprising given that the melt was exposed to the open atmosphere during casting of sample 31 and remained exposed during processing with the addition of grain refiners and melt homogenization. All samples, except for sample 1, are characterized by the grater loss of Li compared to Mg (Table 4.1). This behavior is a consequence of higher reactivity and atomic mobility of Li. The deviation from this behavior in alloy Al-0.38Mg-2.16Li remains unclear.

High Li/Mg ratio recorded in alloys Al-0.38Mg-2.16Li and Al-2.57Mg-2.58Li indicates that the solidification sequence will proceed based on the Equation 10. This means that the samples will solidify with the excess of Li and implies the development of final microstructure containing α_{Al} + AlLi (δ) with the formation of Al_3Li (δ') as a transitional phase. On the other hand, lower Li/Mg ratio characteristic for alloys Al-2.24Mg-2.09Li, Al-2.18Mg-1.92Li and Al-1.92Mg-1.73Li indicates solidification with excess Mg and the formation of α_{Al} + Al_2LiMg (T) as the final microstructure. Due to the complex nature of Li and Mg behavior during solidification, the solidification of metastable Al_3Li (δ') phase is expected.

The results of atomic emission spectrometry are represented in Table 4.2.

Table 4.2. The results of atomic emission spectrometry

Sample	Chemical composition, wt%							
	Cr	Cu	Fe	Mn	Ni	Si	Ti	Al
1	0.0002	0.0004	0.0038	0.0006	0.0003	0.0101	0.0004	balance
21	0.0006	0.0000	0.1585	0.0053	0.0057	0.0285	0.0070	balance
22	0.0041	0.0271	0.1380	0.0052	0.0140	0.0532	0.0478	balance
31	0.0010	0.0004	0.0000	0.0043	0.0033	0.0000	0.0013	balance
32	0.0012	0.0004	0.0000	0.0046	0.0054	0.0000	0.0457	balance

In all samples, except for alloys Al-2.24Mg-2.09Li and Al-2.57Mg-2.58Li, the amount of impurities is acceptable and their influence on the solidification sequence and microstructure development is not expected. In alloys Al-2.24Mg-2.09Li and Al-2.57Mg-2.58Li the increased amount of Fe impurities can be seen (Table 4.2). This is a consequence of the crucible attack and melt contamination due to the reaction between melt and iron-oxide coating. Based on the data available in the literature, this amount of Fe-pickup will result in the solidification of Fe-based intermetallic phases. Since both samples have Mn/Fe ratio < 0.5, the solidification of β-Al_5FeSi intermetallic phase with needle-like morphology is presumed (as indicated in chapter 2.2.4.3). Due to the detection limitations of the spectrometer and limited number of calibration methods, the amount of other impurity elements is low enough not to impact the microstructure development of synthesized samples (Table 4.2).

4.2. The results of density calculations

The physical properties of synthesized samples are given in Table 4.3.

Table 4.3. The physical properties of the synthesized samples

Sample	m, g	V, cm^3	ρ, g/cm^3
1	84.62	34.00	2.49
21	69.99	30.00	2.33
22	77.08	34.00	2.27
31	81.59	34.80	2.34
32	91.67	38.70	2.37

As indicated in Table 4.3 the lowest density of 2.27 g/cm^3 was obtained in alloy Al-2.57Mg-2.58Li, while the highest density of 2.49 g/cm^3 was obtained in alloy Al-0.38Mg-2.16Li. Alloys Al-2.24Mg-2.09Li, Al-2.18Mg-1.92Li, and Al-1.92Mg-1.73Li exhibit similar values of density ranging from 2.33 g/cm^3 for alloy Al-2.24Mg-2.09Li to 2.37 g/cm^3 for alloy Al-1.92Mg-1.73Li. By correlating the results of density calculations with the results of chemical composition analysis (Figure 4.1) it can be concluded that the low density of alloy Al-2.57Mg-2.58Li is a consequence of highest content of Li (2.58 wt.%) and Mg (2.57 wt.%). Furthermore, Figure 4.1 indicates that decrease in Li and Mg content increases density of the samples. However, despite Li content of 2.16 wt.%, alloy Al-0.38Mg-2.16Li has the highest density. High density of sample 1 can be related to a low Mg content (0.38 wt.%). This indicates the need to consider the influence of Li/Mg ratio on density.

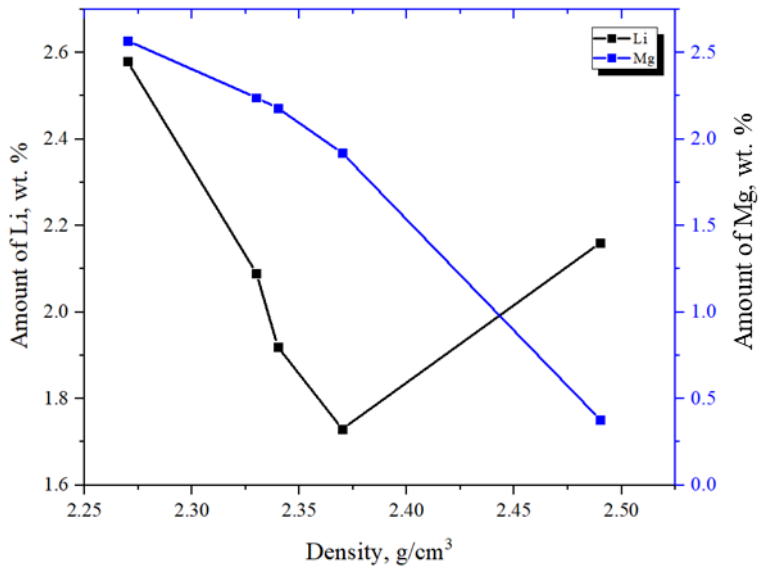

Figure 4.1. The dependence of density on Li/Mg ratio

Correlating the density of the samples with Li/Mg ratio, it can be concluded that closer the ratio is to one (1), lower the density. Therefore, lowest density of sample 22 is a consequence of Li/Mg = 1, while Li/Mg = 5.68 in sample 1 resulted in highest density. The deviation in density of sample 32 can result from the higher amount of impurity elements such as Cr, Mn and Ni compared to sample 31 (Table 4.1). The physical properties of specific sample sections are given in Table 4.4 with the relation between the section thickness and density shown in Figure 4.2.

Table 4.4. The physical properties of the sample sections

Sample section	m, g	ΔV, cm^3	ρ, g/cm^3
11	56.30	22.0	2.56
12	22.07	9.0	2.45
13	5.43	2.2	2.47
211	42.67	20.0	2.13
212	20.73	10	2.07
213	5.10	2.0	2.55
221	49.02	19.5	2.51
222	21.19	9.0	2.35
223	5.29	2.2	2.41
311	54.95	20.0	2.75
312	21.20	10.0	2.12
313	4.30	2.0	2.16
321	64.22	25.0	2.57
322	21.99	10.0	2.20
323	4.65	2.0	2.33

The lowest density of 2.07 g/cm^3 was measured in central section (ø 20.0 mm thickness) of the sample 21, while the highest density of 2.57 g/cm^3 was measured in thickest sections (ø 30.0 mm thickness) of the sample 31 (Table 4.5). The lowest density value of 2.12 g/cm^3 for the ø 10.0 mm thick section was measured in sample 31. The highest density of 2.55 g/cm^3 for thinnest section was measured in sample 21. Sample 21 also exhibited the lowest density in ø 20.0 mm and ø 30.0 mm thick sections. The highest density of 2.45 g/cm^3 in central section was measured in sample 1, while the highest density of 2.75 g/cm^3 in ø 30.0 mm thick section was measured in sample 31 (Table 4.5). In samples 1, 22, 31, and 32 the lowest density values were measured in the central section (ø 20.0 mm thickness), while the highest density

was calculated for the thickest sections (ø 30.0 mm). In sample 21 the highest density value of 2.55 g/cm^3 was measured in the thinnest section of the sample, and the lowest density of 2.07 g/cm^3 was calculated for the central section (Table 4.4 and Figure 4.2).

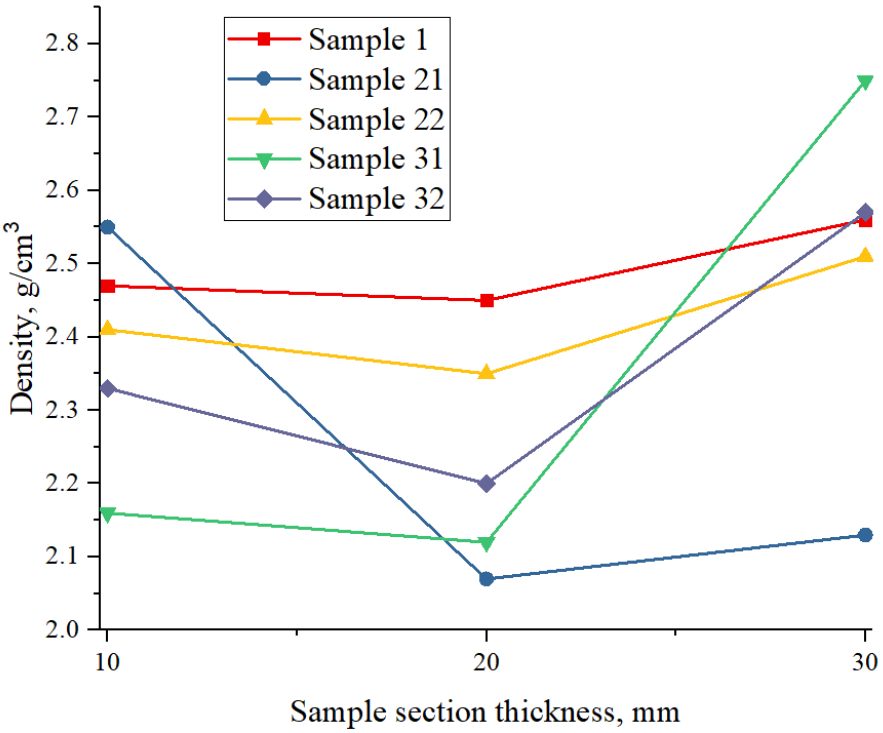

Figure 4.2. The dependence of density on section thickness

Lower density of central section of the samples can be considered as a consequence of Li and Mg segregation during solidification, while increase in density of thickest section of the samples can be associated with Li and Mg oxidation loss. The lower density of the thickest section of sample 21 is a consequence of the gas porosity shown in Figure 4.3.

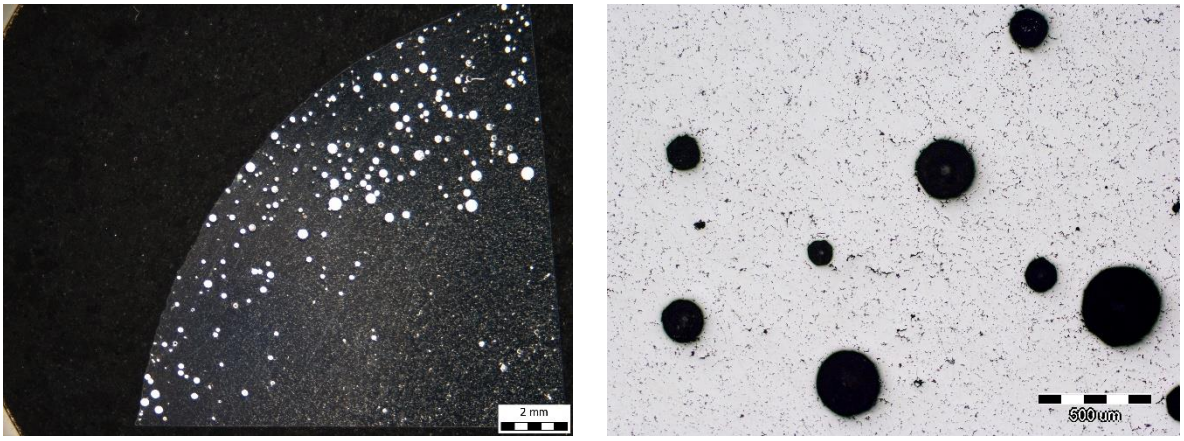

a) **b)**

Figure 4.3. The gas porosity in samples 21: a) macrostructure, b) microstructure

4.3. The results of thermodynamic modelling of solidification sequence using Thermo-Calc software support

The influence of chemical composition on the solidification sequence and microstructure development is given in Figure 4.4 and Table 4.5. The Al-rich corners of the equilibrium phase diagrams were calculated under initial conditions of 720.0 °C temperature and 1.0×10^5 MPa pressure for the following Li/Mg ratios:

- Li/Mg > 1– sample 1 with Li/Mg = 5.68 (Figure 4.4 a),
- Li/Mg = 1 – sample 22 with Li/Mg = 1.0 (Figure 4.4 b),
- Li/Mg < 1 – sample 31 with Li/Mg = 0.88 (Figure 4.4 c).

The invariant reactions indicated in Table 4.5 were calculated using Thermo-Calc's One axis equilibrium calculator. This enabled thermodynamic calculations of particular phase development in relation to the temperature, pressure and chemical composition. While the conditions of temperature and pressure remained identical to the equilibrium phase diagram calculations, the chemical composition was considered for individual samples.

Thermodynamic calculations of the equilibrium solidification sequence for all three characteristic Li/Mg ratios imply solidification of α_{Al} matrix and precipitation of AlLi (δ), Al_2LiMg (T), Al_8Mg_5 (β) and Al_3Mg_2 intermetallic phases.

According to the equilibrium phase diagram given in Figure 4.4 a, the microstructure development in Li/Mg > 1 system initiates with solidification of α_{Al} solid solution at 658.7 °C, followed by the precipitation of Al_2LiMg (T) and AlLi (δ) at 153.5 °C from α_{Al} solid solution. The second reaction occurred at 128.6 °C resulting in the precipitation of Al_8Mg_5 (β) and Al_2LiMg (T) phases from α_{Al} solid solution. These phases together with α_{Al} participate in reaction at 89.1 °C resulting in the formation of Al_8Mg_5 (β) and AlLi (δ) phases. The last reaction in this system involves the precipitation of Al_3Mg_2 and Al_2LiMg (T) intermetallic phase at 16.5 °C from Al_8Mg_5 (β) and α_{Al} solid solution.

The solidification sequence for Li/Mg = 1 (Figure 4.4 b) also initiates with solidification of α_{Al} solid solution at 649.8 °C, followed by three reactions. The first reaction occurs at 328.8 °C during which Al_2LiMg (T) phase precipitates. The second reaction involves precipitation of Al_8Mg_5 (β) and Al_2LiMg (T) phases at 233.8 °C, while the third reaction comprehends precipitation of Al_3Mg_2 and Al_8Mg_5 (β) at 169.5 °C.

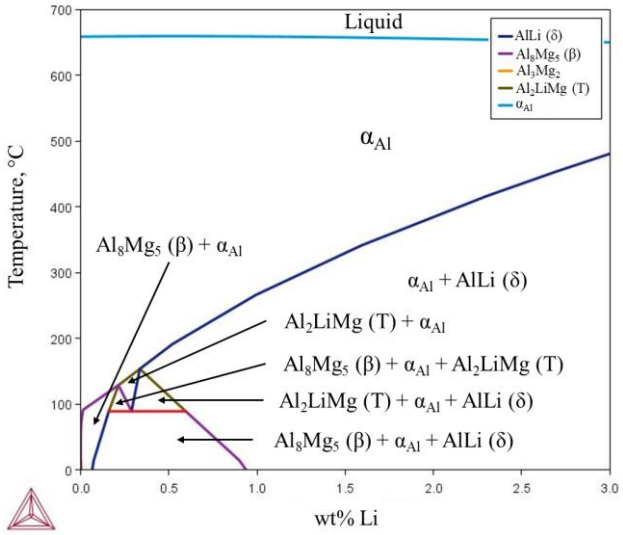

a)

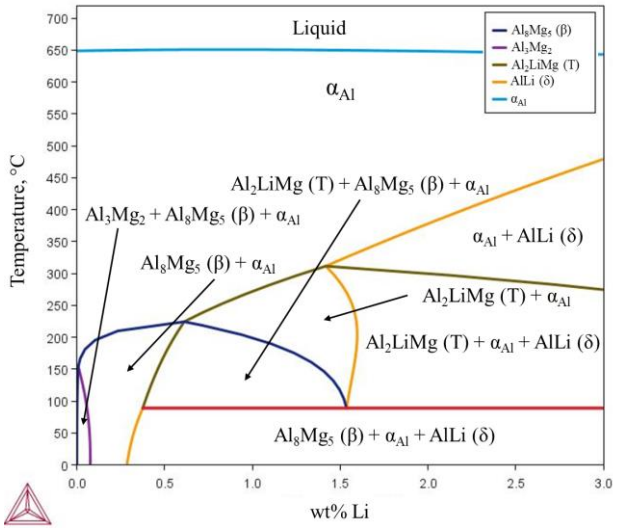

b)

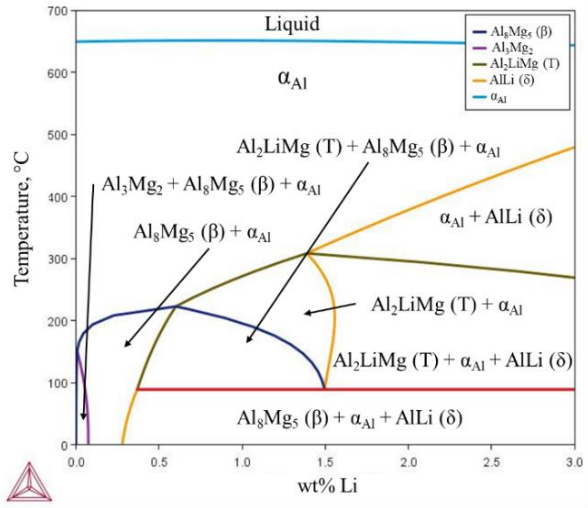

c)

Figure 4.4. The Al-rich corner of equilibrium phase diagrams for:
a) Li/Mg =5.68, b) Li/Mg = 1, c) Li/Mg =0.88

The last reaction involves precipitation of Al_8Mg_5 (β) and AlLi (δ) phase at 89.1 °C from Al_2LiMg (T) phase and α_{Al} solid solution.

The solidification sequence of Li/Mg < 1 system (Figure 4.4 c) implies the same reactions as the previous one. The microstructure development initiates with solidification of α_{Al} matrix at 650.9 °C followed by the reactions first of which begins at 308.2 °C resulting in precipitation of Al_2LiMg (T) phase. The second reaction occurs at 222.7 °C leading to the precipitation of Al_8Mg_5 (β) and Al_2LiMg (T) phases. The third reaction involves precipitation of Al_3Mg_2 and Al_8Mg_5 (β) phases at 151.4 °C. The last reaction in this system concerns the precipitation of Al_8Mg_5 (β) and AlLi (δ) phases at 89.1 °C.

Table 4.5. The invariant reactions obtained using Thermo-Calc's One axis equilibrium calculations

Sample	Reaction	Temperature, °C	Amount of components, g		
			Al	Li	Mg
1	$L \rightarrow \alpha_{Al}$	654.5	0.7153	0.0140	0.0020
	$\alpha_{Al} \rightarrow AlLi(\delta)$	402.0	0.0010	0.0002	$8.6963 \cdot 10^{-6}$
21	$L \rightarrow \alpha_{Al}$	647.9	0.6495	0.0122	0.0106
	$\alpha_{Al} \rightarrow AlLi(\delta)$	387.7	0.0037	0.0008	0.0002
	$\alpha_{Al} + AlLi(\delta) \rightarrow Al_2LiMg(T)$	298.0	0.0066	0.0010	0.0015
	$\alpha_{Al} \rightarrow Al_8Mg_5(\beta) + AlLi(\delta)$	89.1	0.0136	0.0014	0.0122
22	$L \rightarrow \alpha_{Al}$	644.3	0.3390	0.0068	0.0049
	$\alpha_{Al} \rightarrow AlLi(\delta)$	438.3	0.0044	0.0009	0.0002
	$\alpha_{Al} + AlLi(\delta) \rightarrow Al_2LiMg(T)$	310.6	0.0006	$9.7841 \cdot 10^{-5}$	0.0001
	$\alpha_{Al} \rightarrow Al_8Mg_5(\beta) + AlLi(\delta)$	89.1	0.0147	0.0015	0.0132
31	$L \rightarrow \alpha_{Al}$	648.8	0.0838	0.0011	0.0007
	$\alpha_{Al} \rightarrow AlLi(\delta)$	369.3	0.0041	0.0008	0.0002
	$\alpha_{Al} + AlLi(\delta) \rightarrow Al_2LiMg(T)$	297.5	0.0022	0.0003	0.0005
	$\alpha_{Al} \rightarrow Al_8Mg_5(\beta) + AlLi(\delta)$	89.1	0.0119	0.0012	0.0107
32	$L \rightarrow \alpha_{Al}$	650.5	0.0838	0.0011	0.0007
	$\alpha_{Al} \rightarrow AlLi(\delta)$	348.9	0.0041	0.0008	0.0002
	$\alpha_{Al} + AlLi(\delta) \rightarrow Al_2LiMg(T)$	282.9	0.0022	0.0003	0.0005
	$\alpha_{Al} \rightarrow Al_8Mg_5(\beta) + AlLi(\delta)$	89.1	0.0119	0.0012	0.0107

While the results of the thermodynamic calculations of equilibrium solidification sequence indicate significant difference in microstructure development between the Li/Mg > 1 and Li/Mg ≤ 1 the difference between Li/Mg = 1 and Li/Mg < 1 mostly concerns the reaction

temperatures (Figure 4.4). The solidification of systems with high Li/Mg ratio is characterized by the preferred precipitation of binary AlLi (δ) and ternary Al_2LiMg (T) phases. The solidification sequence of the systems with Li/Mg ≤ 1 ratio is initiated by the formation of ternary Al_2LiMg (T) phase, followed by the precipitation of Mg-containing Al_8Mg_5 (β) and Al_3Mg_2 phases.

The difference in solidification sequence and microstructure development between sample 1 and the other samples is additionally confirmed by the results of One axis equilibrium calculation. While the invariant equilibrium reactions are given in Table 4.5, the amounts of individual phases in relation to the temperature are indicated in Figure 4.5. The solidification sequence of sample 1 containing 0.38 wt.% Mg and 2.16 wt.% Li involves two reactions. The first reaction referees to the solidification of α_{Al} solid solution at 654.5 °C (Table 4.5 sample 1 and Figure 4.5 a), while the second reaction comprehends precipitation of AlLi (δ) phase from α_{Al} solid solution at 402.0 °C (Table 4.5 sample 1, Figure 4.5 b). The amount of AlLi (δ) phase increases till the end of solidification sequence, as indicated by Figure 4.5 b. Similarly, the microstructure development in samples 21, 22, 31, 32 initiates with solidification of α_{Al} matrix (Table 4.5. and Figure 4.5 a) followed by precipitation of AlLi (δ) phase from α_{Al} solid solution (Table 4.5 and Figure 4.5 b). The temperature of this reaction depends on the weight percent of Li (Table 4.5). The highest temperature of 438.3 °C was recorded for sample 22 containing 2.58 wt.% Li, while the lowest temperatures of 369.3 °C and 348.9 °C were observed in samples 31 and 32 containing 1.92 wt.% Li and 1.73 wt.% Li, respectively. The AlLi (δ) phase precipitates continuously until the precipitation of Al_2LiMg (T) phase (Table 4.5 and Figure 4.5 b and c). Since Al_2LiMg (T) is a complex intermetallic phase containing Al, Li and Mg, the precipitation temperature is determined by Li/Mg ratio. The highest temperature of 310.6 °C was observed in sample 22 with Li/Mg = 1(Table 4.5), while the lowest temperatures were observed in samples 21, 31 and 32 with Li/Mg < 1 (Table 4.5). The sample with Li/Mg > 1 is characterized by the lack of Al_2LiMg (T) phase precipitation (Table 4.5 sample 1). The last reaction comprehends precipitation of Al_8Mg_5 (β) phase from α_{Al} solid solution at 89.1 °C. Furthermore, the results of thermodynamic calculations given in Figure 4.5 b to d indicate that the amount of AlLi (δ) phase increases with the increase in Al_8Mg_5 (β) phase, while content of Al_2LiMg (T) phase remains constant (Figure 4.5 c).

The results of component distribution in phases obtained using One axis equilibrium calculator are given in Figure 4.6. During the solidification of sample 1 with high Li/Mg ratio the amounts of both Li and Mg in α_{Al} solid solution begin to decrease with the precipitation of AlLi (δ) phase (Figure 4.6).

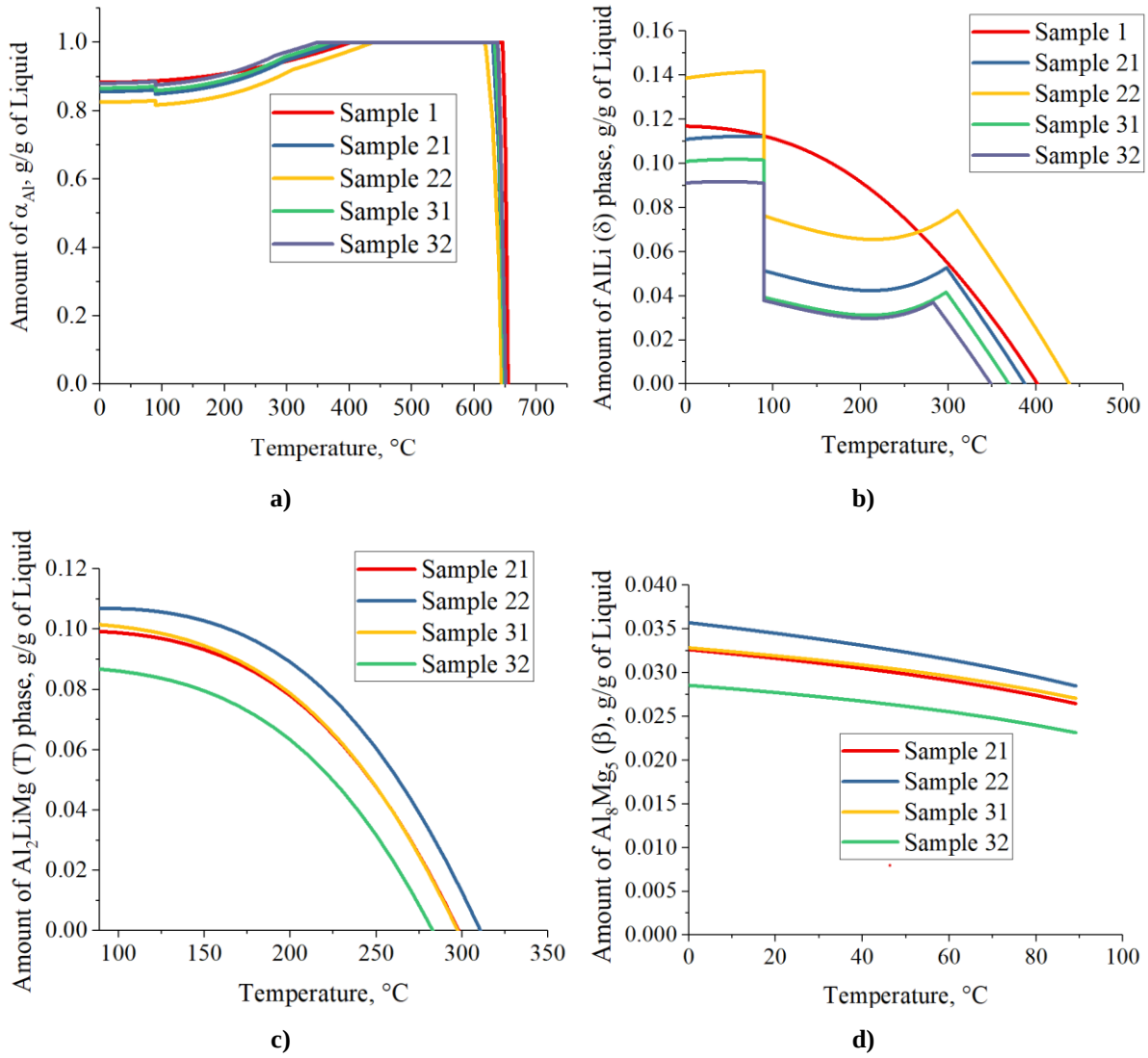

Figure 4.5. The results of phase distribution using Thermo-Calc's One axis equilibrium calculation: a) α_{Al}, b) AlLi (δ), c) Al_2LiMg (T), d) Al_8Mg_5

The samples 21, 31 and 32 with Li/Mg < 1 exhibit similar component distribution during solidification (Figure 4.6). For example, in sample 21 precipitation of AlLi (δ) phase leads to the reduction in Li and Mg content in α_{Al} solid solution from 0.0209 g Li per 1.0 g of liquid and 0.0224 g Mg per 1.0 g of liquid at 380.0 °C to 0.0115 g Li per 1.0 g of liquid and 0.0190 g Mg per 1.0 g of liquid at 290.0 °C (Figure 4.6 sample 21). At this temperature the amount of AlLi (δ) phase reaches the value of 0.0527 g per 1.0 g of liquid (Figure 4.5 b) when Al_2LiMg (T) phase begins to precipitate. The Al_2LiMg (T) phase reaches the maximum value of 0.0992 g per 1.0 g of liquid at 89.0 °C (Figure 4.5 c) reducing the amount of Li and Mg in AlLi (δ) phase to 0.0084 g Li per 1.0 g of liquid and 0.0043 g Mg per 1.0 g of liquid (Figure 4.6). After reaching its maximum value, the Al_2LiMg (T) phase stops to precipitate. Instead, Al_8Mg_5 (β) phase begins to precipitate. Parallelly, the value of AlLi (δ) phase increases from 0.0514 g per 1.0 g of liquid at 89.0 °C to 0.1109 g per 1.0 g of liquid at the end of solidification

(Figure 4.5 b). It is important to note that the amount of Li in AlLi (δ) phase increases from 0.0084 g per 1.0 g of liquid to 0.0190 g per 1.0 g of liquid, while the amount of Mg decreases from 0.0091 g per 1.0 g of liquid to 0.0077 g per 1.0 g of liquid. The decrease in Mg content is a consequence of Al_8Mg_5 (β) phase precipitation. At the end of solidification sequence microstructure of the sample 21 contains 0.8564 g of α_{Al} matrix per 1.0 g of liquid, 0.1109 g AlLi (δ) phase per 1.0 g of liquid, 0.0992 g Al_2LiMg (T) phase per 1.0 g of liquid and 0.0326 g of Al_8Mg_5 (β) phase per 1.0 g of liquid. Similarly, the microstructure of the sample 31 contains 0.8662 g of α_{Al} matrix per 1.0 g of liquid, 0.1009 g AlLi (δ) phase per 1.0 g of liquid, 0.1015 g Al_2LiMg (T) phase per 1.0 g of liquid and 0.0385 g of Al_8Mg_5 (β) phase per 1.0 g of liquid, while the final microstructure of sample 32 consists of 0.8803 g α_{Al} matrix per 1.0 g of liquid, 0.0911 g AlLi (δ) phase per 1.0 g of liquid, 0.0868 g Al_2LiMg (T) phase per 1.0 g of liquid and 0.0286 g of Al_8Mg_5 (β) phase per 1.0 g of liquid.

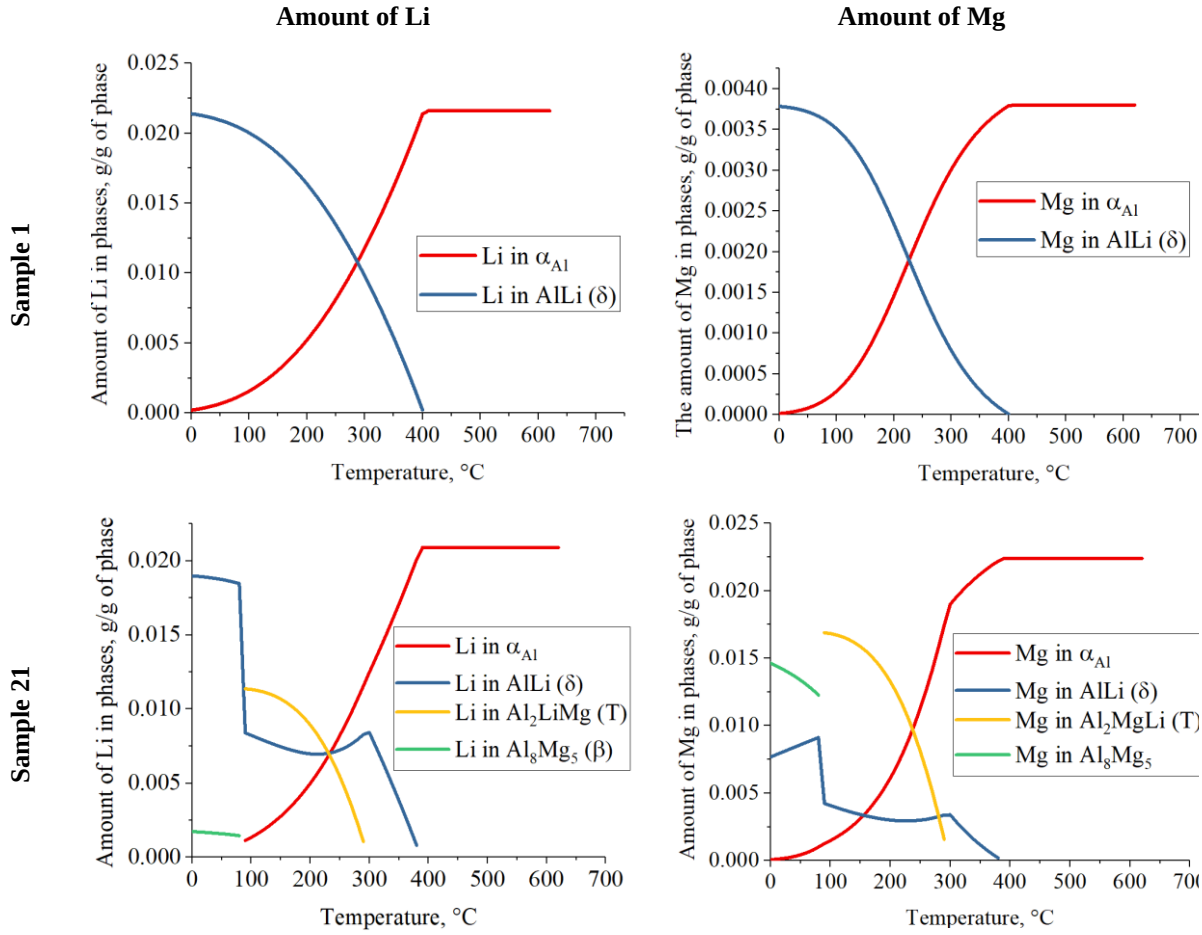

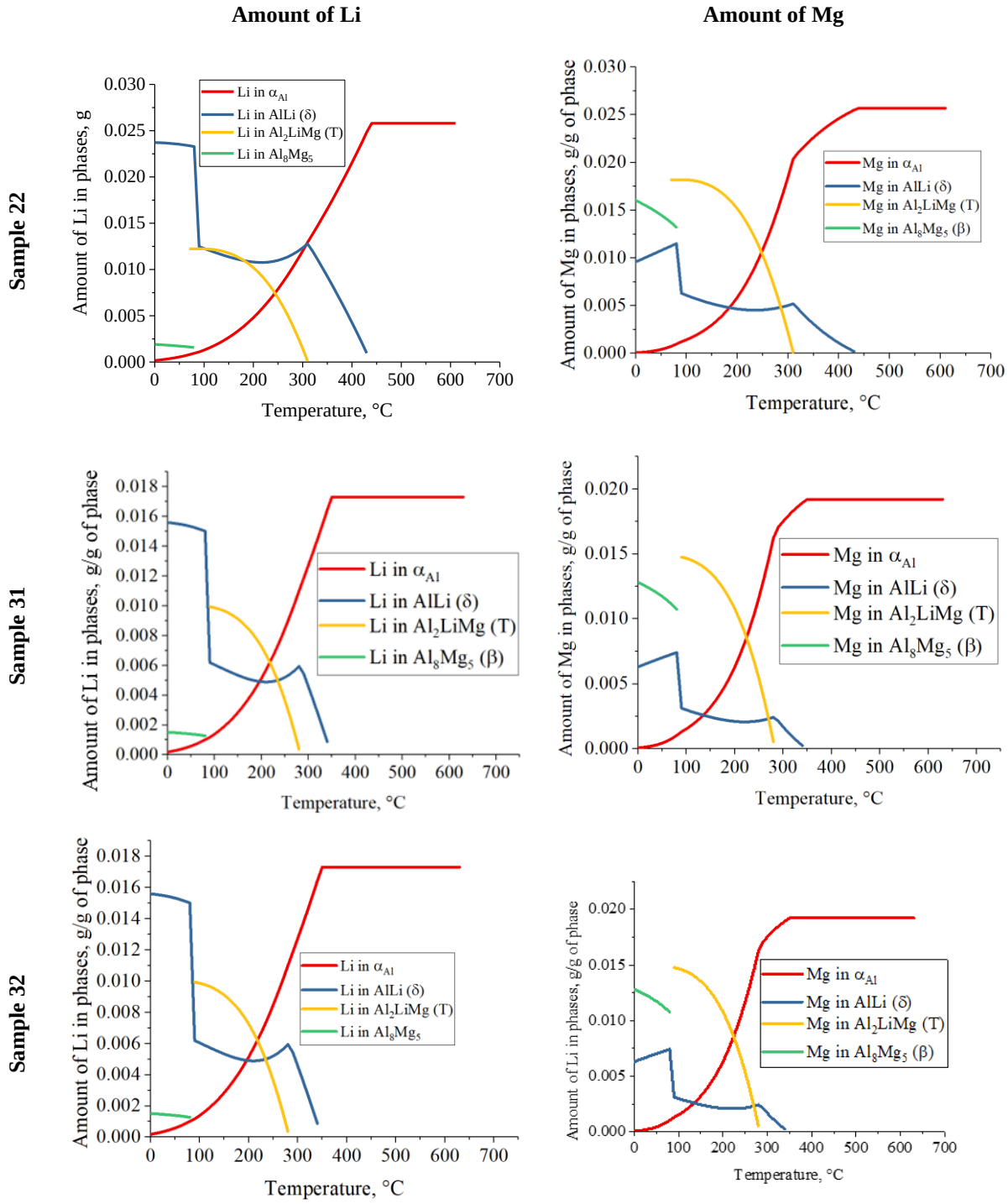

Figure 4.6. The results of component distribution in phases using Thermo-Calc's One axis equilibrium calculation

A slight difference in the component distribution can be observed during the solidification of sample 22, when in temperature range from 180.0 °C to 100.0 °C there is an almost equal distribution of Li between AlLi (δ) and Al_2LiMg (T) phase (Figure 4.6). Consequently, there is a higher amount of AlLi (δ) phase (0.1386 g per 1 g of liquid) in the final microstructure of sample 22 compared to the other samples.

Since the results of atomic emission spectrometry detected higher levels of impurity elements in samples 21 and 22, it was necessary to perform additional thermodynamic calculations to estimate their impact on solidification sequence and microstructure development. The calculations were performed under initial conditions of 720.0 °C temperature, 1.0×10^5 MPa pressure and chemical composition including Al, Mg, Li, Fe, Mn, and Si contents. The Al-rich corner of Al-Mg-Li-impurity element phase diagram is given in Figure 4.7 with invariant reactions indicated in Table 4.6.

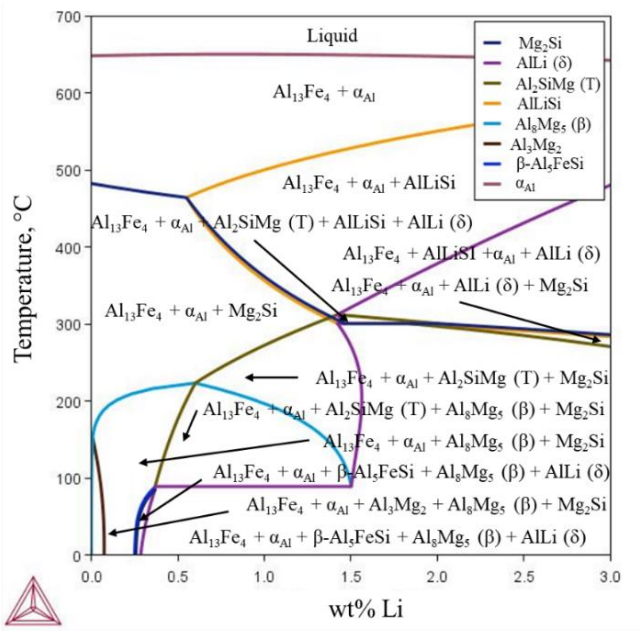

Figure 4.7. The Al-rich corner of Al-Mg-Li-impurity element equilibrium phase diagram

The results of equilibrium phase diagram calculations (Figure 4.7), indicate that the presence of Fe and Si impurities caused the formation of new phases such as Mg_2Si, $Al_{13}Fe_4$, AlLiSi and β-Al_5FeSi. The calculation results also implied that the Mn content was too low to affect the solidification sequence, therefore its influence was not considered further.

As indicated by reactions in Table 4.6, the microstructure development in Al-rich corner starts with solidification of α_{Al} solid solution and $Al_{13}Fe_4$ phase at 640.3 °C. The last reaction involving Liquid (L) is the solidification of AlLiSi phase at the temperature of 585.7 °C. All other reactions result from solid state precipitation, starting with Mg_2Si at 463.9 °C. The formation of phases characteristic for Al-Li-Mg alloys beging with precipitation of Al_2LiMg (T) phase at 312.3 °C followed by AlLi (δ) phase at 300.8 °C. A high solid solubility of Mg in α_{Al} solid solution results in the precipitation of Al_3Mg_2 and Al_8Mg_5 (β) phase at later stages of solidification sequence. The microstructure development ends with precipitatin of β-Al_5FeSi phase at 88.5 °C.

Table 4.6. The invariant reactions in Al-rich corner of Al-Mg-Li-impurity element phase diagram

Reaction	Temperature, °C
$L \rightarrow L + \alpha_{Al} + Al_{13}Fe_4$	640.3
$L + \alpha_{Al} + Al_{13}Fe_4 \rightarrow \alpha_{Al} + Al_{13}Fe_4 + AlLiSi$	585.7
$\alpha_{Al} + Al_{13}Fe_4 \rightarrow Mg_2Si + \alpha_{Al} + Al_{13}Fe_4$	463.9
$\alpha_{Al} + Al_{13}Fe_4 + AlLiSi \rightarrow \alpha_{Al} + Al_{13}Fe_4 + AlLiSi + Al_2LiMg(T)$	312.3
$\alpha_{Al} + Al_{13}Fe_4 + AlLiSi + Al_2LiMg(T) \rightarrow \alpha_{Al} + Al_{13}Fe_4 + Mg_2Si + AlLi(\delta)$	300.8
$\alpha_{Al} + Al_{13}Fe_4 + Mg_2Si \rightarrow \alpha_{Al} + Al_{13}Fe_4 + Mg_2Si + Al_8Mg_5(\beta)$	223.9
$\alpha_{Al} + Al_{13}Fe_4 + Mg_2Si \rightarrow \alpha_{Al} + Al_{13}Fe_4 + Mg_2Si + Al_3Mg_2$	152.6
$\alpha_{Al} + Al_{13}Fe_4 + Mg_2Si + Al_2LiMg(T) \rightarrow \alpha_{Al} + Al_{13}Fe_4 + Mg_2Si + Al_8Mg_5(\beta) + AlLi(\delta)$	89.4
$\alpha_{Al} + Al_{13}Fe_4 + Mg_2Si + Al_8Mg_5(\beta) \rightarrow \alpha_{Al} + Al_{13}Fe_4 + Al_8Mg_5(\beta) + Mg_2Si + \beta - Al_5FeSi$	88.5

The influence of Fe and Si impurities on reactions in liquid and solid state obtained using Thermo-Calc's One axis equilibrium calculation are shown in Figure 4.8 with invariant reactions given in Table 4.6. The calculation results indicate the difference in solidification sequence between samples 21 and 22 referring to the formation of Al_2LiMg (T) and Mg_2Si phases. According to the calculations the microstructure development in both samples starts with the solidification of α_{Al} solid solution followed by solidification of $Al_{13}Fe_4$ phase (Figure 4.8 liquid state reactions). The solidification temperatures of both phases are slightly higher in sample 21 (Table 4.7). The solid state reactions initiate at 553.6 °C for sample 21 and 593.9 °C for sample 22 (Table 4.7) with precipitation of AlLiSi phase (Figure 4.8 solid state precipitations). In both samples, the AlLiSi phase precipitates continuously until it reaches maximum value of 0.00627 g per 1 g of solid at 299.0 °C in sample 21 and 0.00117 g per 1 g of solid at 300.6 °C in sample 22 and stops. The end of AlLiSi phase precipitation is caused by the appearance of Mg_2Si phase (Figure 4.8 solid state precipitation). However, their precipitation is preceded by the formation of AlLi (δ). Unlike the equilibrium state diagram (Figure 4.7, Table 4.6), formation of phases characteristic for Al-Li-Mg system initiates with precipitation of AlLi (δ) phase at 388.0 °C in sample 21 and 438.0 °C in sample 22. The amount of AlLi (δ) phase increases till it reaches the value of 0.0547 per 1 g of solid at 295.0 °C in sample 21 and 0.0811 g per 1 g of solid at 311.4 °C in sample 22. The decrease in the AlLi (δ)

phase precipitation is caused by the formation of ternary Al_2LiMg (T) phase. The amount of Al_2LiMg (T) phase increases up to the temperature of 89.1 °C (Table 4.7) when it reaches maximum value of 0.0948 g per 1 g of solid in sample 21 and 0.0986 °C in sample 22 (Figure 4.8). The formation of Al_8Mg_5 (β) phase begins with the end of Al_2LiMg (T) phase precipitation. At this temperature, the AlLi (δ) phase precipitation is initiated again (Figure 4.8). Both Al_8Mg_5 (β) and AlLi (δ) phase precipitate continuously till the end of solidification (Figure 4.8). In this consideration, the Li/Mg ratio influences the precipitation of Al_2LiMg (T) and Mg_2Si phases. Although sample 22 has higher amount of Mg and Si compared to sample 21 (Table 4.4 and Table 4.7), the Li/Mg causes the precipitation of Al_2LiMg (T) phase at higher temperatures (Table 4.7). The microstructure development in both samples ends with precipitation of β-Al_5FeSi phase at 88.3 °C.

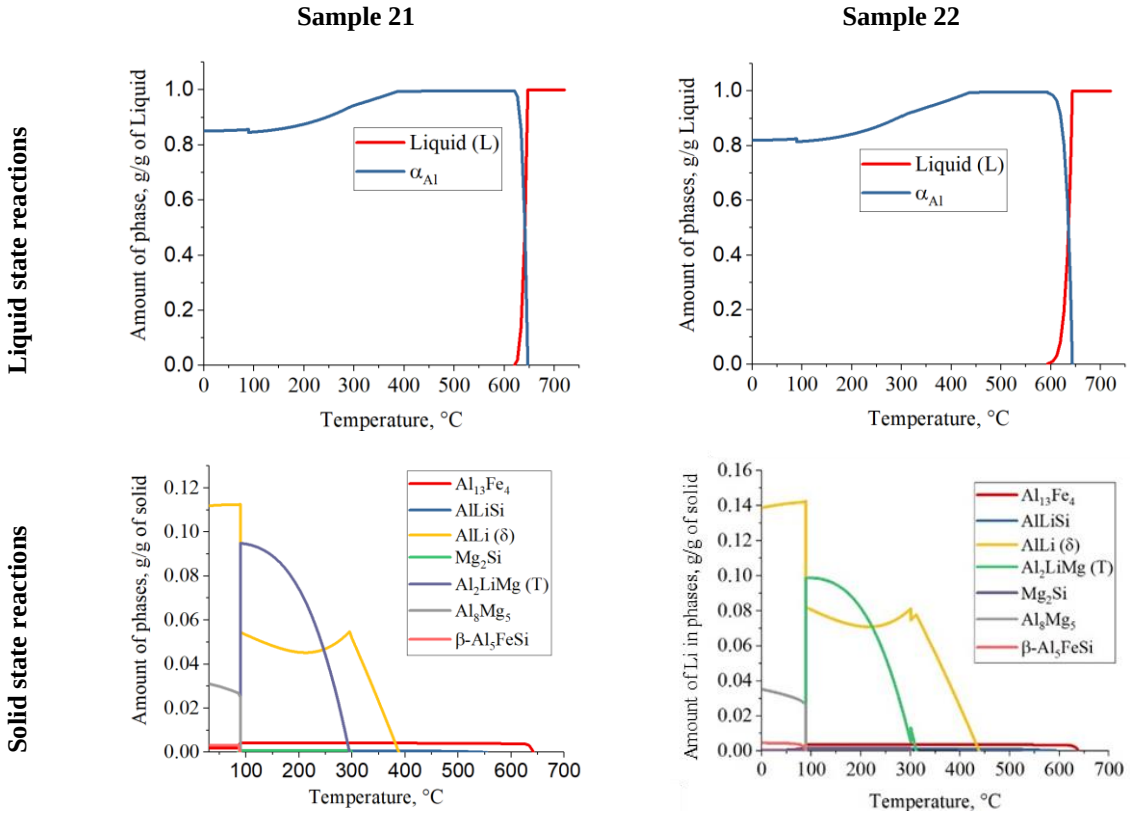

Figure 4.8. The influence of Fe and Si impurities on reactions in liquid and solid state

According to the results of thermodynamic calculations, the final microstructure of the sample 21 cosists of 0.8512 g α_{Al} solid solution per 1 g of solid, 0,002 g $Al_{13}Fe_4$ per 1 g of solid, 0,1109 g AlLi (δ) per 1 g of solid, 0.0326 g Al_8Mg_5 (β) per 1 g of solid, and 0.0032 g β-Al_5FeSi per 1 g of solid, while the microstructure of sample 22 contains 0.8205 g α_{Al} solid solution per 1 g of solid, 0.1388 g AlLi (δ) per 1 g of solid, 0.0352 g Al_8Mg_5 (β) per 1 g of solid, and 0.0043 g β-Al_5FeSi per 1 g of solid (Figure 4.8, Table 4.7).

Table 4.7. The invariant reactions of Fe and Si impurity influence on solidification sequence and microstructure development in sample 21 and 22

Sample number	Reaction	Temperature, °C
21	$L \rightarrow \alpha_{Al}$	647.0
	$L \rightarrow \alpha_{Al} + Al_{13}Fe_4$	641.6
	$\alpha_{Al} \rightarrow Al_{13}Fe_4 + AlLiSi$	553.6
	$\alpha_{Al} \rightarrow Al_{13}Fe_4 + AlLiSi + AlLi(\delta)$	388.0
	$\alpha_{Al} \rightarrow Al_{13}Fe_4 + AlLi(\delta) + Mg_2Si$	297.0
	$\alpha_{Al} + AlLi(\delta) \rightarrow Al_{13}Fe_4 + AlFeSi + Al_2LiMg(T)$	295.0
	$\alpha_{Al} \rightarrow Al_{13}Fe_4 + AlLi(\delta) + Al_8Mg_5(\beta)$	89.1
	$\alpha_{Al} + Al_{13}Fe_4 \rightarrow AlLi(\delta) + Al_8Mg_5(\beta) + \beta - Al_5FeSi$	88.3
22	$L \rightarrow \alpha_{Al}$	643.3
	$L \rightarrow \alpha_{Al} + Al_{13}Fe_4$	639.0
	$\alpha_{Al} \rightarrow Al_{13}Fe_4 + AlFeSi$	593.9
	$\alpha_{Al} \rightarrow Al_{13}Fe_4 + AlFeSi + AlLi(\delta)$	438.3
	$\alpha_{Al} + AlLi(\delta) \rightarrow Al_{13}Fe_4 + AlFeSi + Al_2LiMg(T)$	311.5
	$\alpha_{Al} + AlFeSi \rightarrow Al_{13}Fe_4 + AlFeSi + Mg_2Si$	300.4
	$\alpha_{Al} + Al_2LiMg(T) \rightarrow Al_{13}Fe_4 + AlLi(\delta) + Al_8Mg_5(\beta)$	89.1
	$\alpha_{Al} + Al_{13}Fe_4 \rightarrow AlLi(\delta) + Al_8Mg_5(\beta) + \beta - Al_5FeSi$	88.0

The results of Thermo-Calc's One axis equilibrium calculations of Li, Mg, Fe and Si distribution in phases for samples 21 and 22 are given in Figure 4.9. The results indicate that Fe and Si impurities do not significantly affect solidification of α_{Al} solid solution and precipitation of AlLi (δ), Al_2LiMg (T) and Al_8Mg_5 (β) phases. By comparing the values of the temperatures of the invariant reactions given in Tables 4.5 and Table 4.7 it can be observed that impurities present in sample 21 slightly increase temperature of AlLi (δ) phase formation and decrease temperature of Al_2LiMg (T) phase precipitation. In sample 22, Fe and Si impurities have an opposite effect on the precipitation of those phases. By comparing the behavior of components in phases shown in Figures 4.9 with Figure 4.6 and the amount of components in

Table 4.5 it can be seen that the presence of impurities does not affect the behavior of Al, Li and Mg in AlLi (δ), Al_2LiMg (T) and Al_8Mg_5 (β) phases.

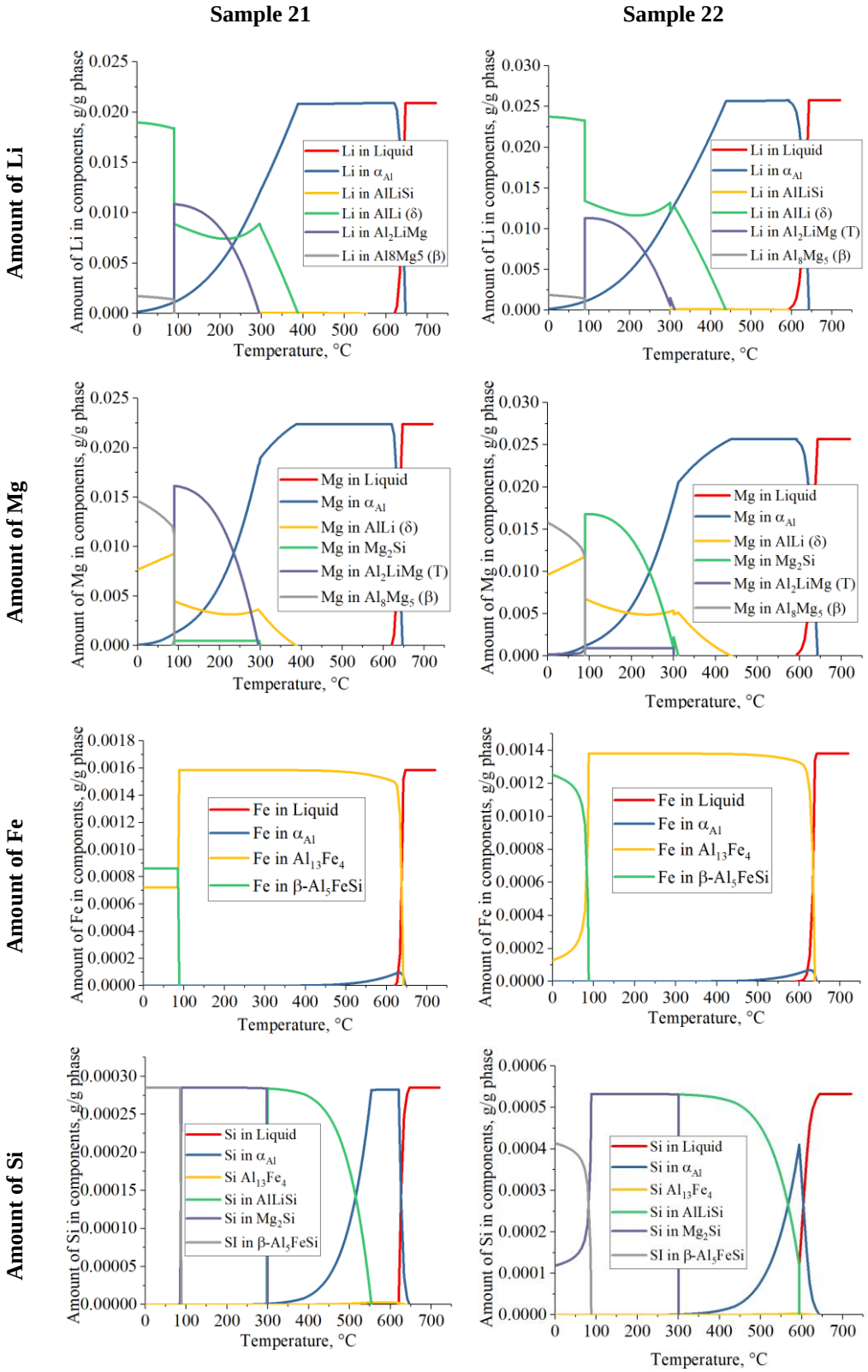

Figure 4.9. The results of component distribution in phases for samples 21 and 22 using Thermo-Calc's One axis equilibrium calculation

The effect of impurities is strictly related to the formation and behavior of $Al_{13}Fe_4$, AlLiSi, Mg_2Si and β-Al_5FeSi. The amount of Fe in Liquid (L) of sample 21 decreases from 0.00158 g per 1 g of liquid at initial temperature of 720.0 °C to 0.00151 g per 1 g of liquid at 641.0 °C due to the solidification of α_{Al} solid solution. The subsequent loss of Fe in Liquid (L) is a consequence of $Al_{13}Fe_4$ phase precipitation when the Fe content decreases from 0.00126 g per 1 g of liquid at 641.0 °C to 0 at the end of solid-state reactions. The maximum solid solubility of Fe in α_{Al} solid solution of 9.76×10^{-5} g per 1 g of solid at 633.6 °C and decreases continuously to 7.22×10^{-7} g per 1 g of solid at the end of solidification sequence. The maximum amount of Fe in $Al_{13}Fe_4$ increases till it reaches the value of 0.00158 g per 1 g of solid at 115.2 °C. Afterword, the amount of Fe remains constant until β-Al_5FeSi begins to precipitate at temperature of 88.39 °C when it decreases to 0.00072 g per 1 g of solid and remains unchanged to the end of solidification sequence. The amount of Fe in β-Al_5FeSi phase increases from 0.000647 g per 1 g of solid at the beginning of precipitation to 0.000862 g per 1 g of solid at the end of solidification. Similarly, the solubility of Si in Liquid (L) decreases from 0.00028 g per 1 g of liquid at the initial temperature of 720.0 °C to 0.000277 g per 1 g of liquid at 647.0 °C and reaches 0 value at the end of liquid state reactions (620.4 °C). The solid solubility of Si in α_{Al} increases from 7.646×10^{-6} g per 1 g of solid at 641.6 °C and reaches maximum value of 0.000283 g per 1 g of solid at 620.4 °C. At this temperature the amount of Si begins to decrease, firstly due to the precipitation of AlSiLi to the value of 8.28×10^{-6} g per 1 g of solid, secondly due to the formation of Mg_2Si to the value of 3.142×10^{-12} g per 1 g of solid, and lastly due to the precipitation of β-Al_5FeSi to the value of 8.867×10^{-13} g per 1 g of solid. The amount of Si in AlSiLi increases continuously from 3.0×10^{-5} g per 1 g of solid to 0.000284 g per 1 g of solid at the temperature of 297.0 °C. At this temperature, precipitation of AlSiLi stops due to the formation of Mg_2Si. The maximum solubility of Si in Mg_2Si of 0.000285 g per 1 g of solid is obtained at the temperature of 136.8 °C. Afterwords the amount of Si remains constant till the temperature of 86.4 °C when it sharply decreasing to the value of 7.123×10^{-5} g per 1 g of solid due to the β-Al_5FeSi phase precipitation.

The impurity elements in sample 22 behave similarly to sample 21. However, due to the higher amounts of Li, Mg and Si, the invariant reactions are shifted towards the higher temperatures with Al_2LiMg (T) phase precipitation preceding the formation of Mg_2Si phase (Table 4.7). The amount of Si in Liquid (L) decreases from 0.00053 g per 1 g of liquid at initial temperature of 720.0 °C to 0.00052 g per 1 g of liquid at 639.0 °C due to the solidification of α_{Al} solid solution. Further decrease in Si content is a consequence of $Al_{13}Fe_4$ phase solidification decreasing its amount to 0.0012 g per 1 g of liquid. The liquid state reactions end at the

temperature of 593.9 °C with solidification of AlLiSi phase. The solid solubility of Si in α_{Al} solid solution increases from 3.773×10^{-6} g per 1 g of solid at 643.8 °C and reaches maximum value of 0.00041 g per 1 g of solid at 593.9 °C. At this temperature the amount of Si begins to decrease, firstly due to the precipitation of AlLiSi, secondly due to the formation of Mg_2Si, and lastly due to the precipitation of β-Al_5FeSi. The amount of Si in AlLiSi increases continuously to 0.000531 g per 1 g of solid at the temperature of 300.4 °C. At this temperature, precipitation of AlLiSi stops due to the formation of Mg_2Si. The maximum solubility of Si in Mg_2Si of 0.00053 g per 1 g of solid is obtained at the temperature of 144.0 °C. Afterword, the amount of Si remains constant till the temperature of 88.0 °C when it sharply decreases to the value of 0.00012 g per 1 g of solid due to the β-Al_5FeSi phase precipitation.

The results of Classical Scheil and Scheil with solute trapping calculations are given in Figure 4.10 with phase equilibria indicated in Table 4.8. Both calculations were performed under initial conditions of 720.0 °C temperature and temperature step of 1.0 °C.

Table 4.8. The phase equilibria according to Classical Scheil and Scheil with solute trapping calculations

Sample	Phase equilibria	Classical Scheil	Scheil with solute trapping
		Temperature, °C	Temperature, °C
1	$L + \alpha_{Al}$	654.55	654.23
	$L + \alpha_{Al} + AlLi\ (\delta)$	585.54	586.0
21	$L + \alpha_{Al}$	647.83	647.45
	$L + \alpha_{Al} + AlLi\ (\delta)$	547.83	549.45
	$L + \alpha_{Al} + Al_2LiMg\ (T)$	524.03	524.03
22	$L + \alpha_{Al}$	644.34	643.90
	$L + \alpha_{Al} + AlLi\ (\delta)$	550.34	551.89
	$L + \alpha_{Al} + Al_2LiMg\ (T)$	524.48	524.29
	$L + \alpha_{Al} + Al_8Mg_5\ (\beta)$	474.97	/
31	$L + \alpha_{Al}$	648.75	648.84
	$L + \alpha_{Al} + AlLi\ (\delta)$	548.75	550.21
	$L + \alpha_{Al} + Al_2LiMg\ (T)$	524.05	524.18
32	$L + \alpha_{Al}$	650.56	650.20
	$L + \alpha_{Al} + AlLi\ (\delta)$	540.34	542.47
	$L + \alpha_{Al} + Al_2LiMg\ (T)$	524.30	524.03

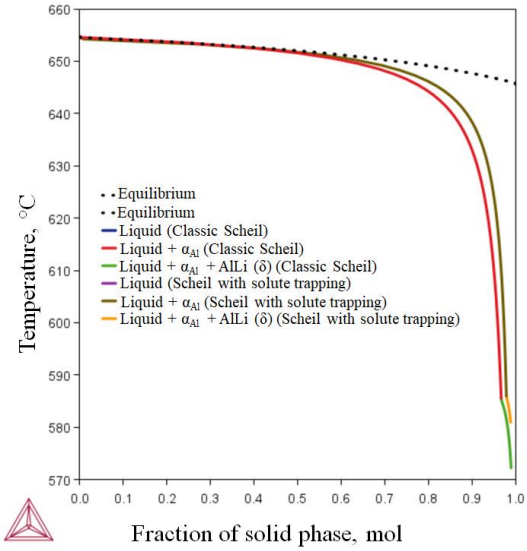

Sample 1

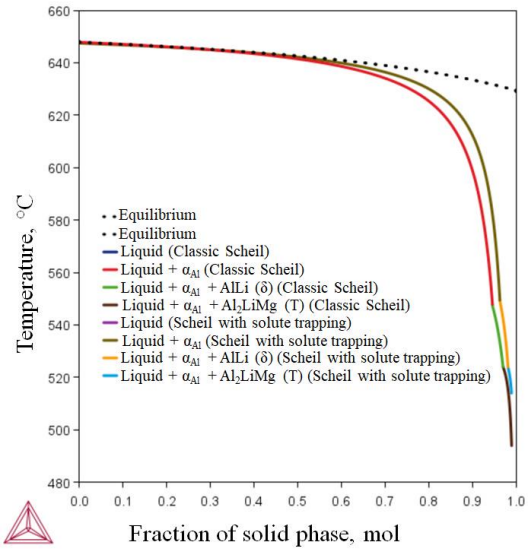

Sample 21

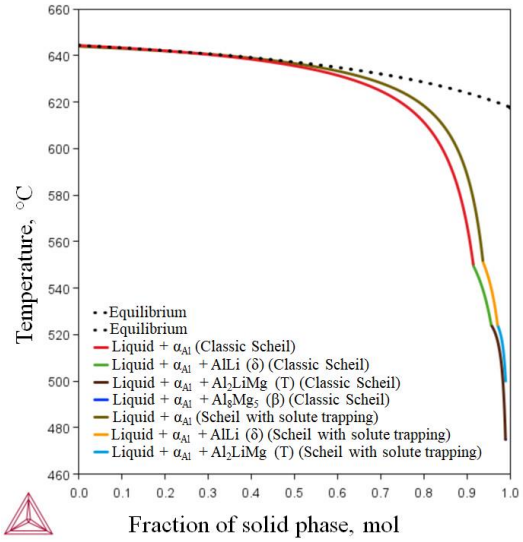

Sample 22

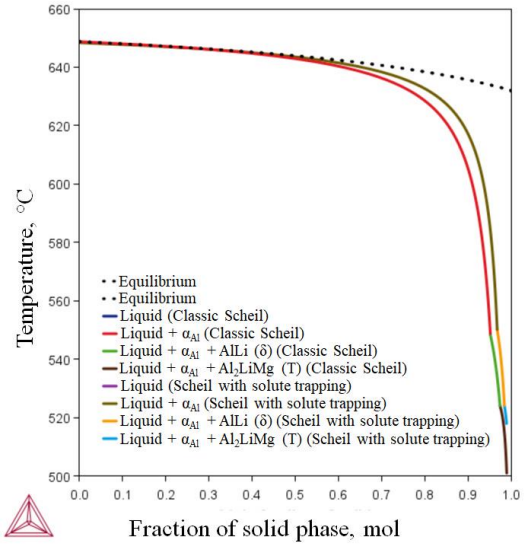

Sample 31

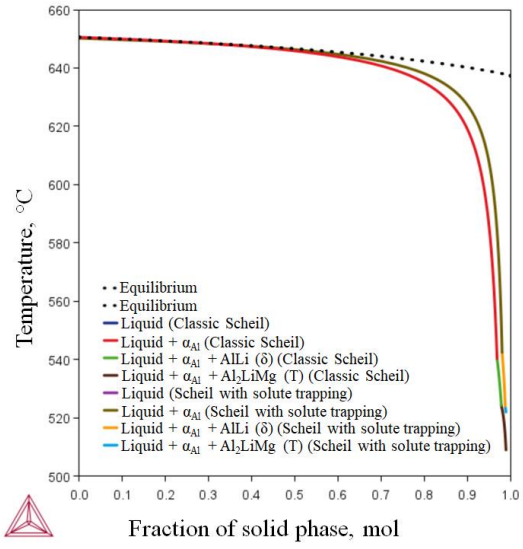

Sample 32

Figure 4.10. The results of Classical Scheil and Scheil with solute trapping calculations

To perform Scheil with solute trapping calculations the scanning speed of 1.0 m/s, the angle between the solid/liquid boundary and scanning direction (α) of 45.0 °, solidification speed of 0.7071 m/s and α_{Al} as primary phase were defined additionally.

Unlike equilibrium phase diagram and One axis phase equilibria, Classical Scheil and Scheil with solute trapping calculations stop with complete solidification of liquid phase (Figure 4.10). Aa a consequence, in Classic Scheil calculations, each infinitively small volume element of solid phase retains the same chemical composition during the whole solidification process. Neglecting the solid-state diffusion results in non-homogeneous chemical composition and microsegregations. Defining solidification rate as an initial condition during Scheil calculations with solute trapping allows the solid-liquid interface to deviate from local equilibria increasing the solute concentration in solid phase and reducing the segregations in the liquid side of interface. This enables prediction of very fine structure with uniform properties.

The results of Classical Scheil and Scheil with solute trapping calculations are in accordance with the results of equilibrium phase and One axis phase equilibrium calculations concerning development of α_{Al} solid solution, AlLi (δ) and Al_2LiMg (T) phases (Figure 4.8). The solidification of Al_8Mg_5 (β) phase is only predicted by the Classical Scheil calculation for sample 22 (Figure 4.10), while the formation of Al_3Mg_2 phase is only recognized by the equilibrium phase calculations (Figure 4.4). Similar to the previous calculations, the solidification sequence and microstructure development simulated using both types of Scheil calculations depend on the Li/Mg ratio. By comparing the simulation results for sample 1 with Li/Mg > 1, a significant difference is observed between the equilibrium phase diagram calculation and other three calculation results (One axis equilibrium calculation, Classical Scheil calculation and Scheil with solute trapping). While equilibrium phase diagram calculation recognize formation of α_{Al} solid solution, AlLi (δ), Al_2LiMg (T), Al_8Mg_5 (β) and Al_3Mg_2 phases, other three calculations comprehend formation of α_{Al} solid solution followed by the precipitation of AlLi (δ) phase. This difference can be explained by the fact that the equilibrium phase diagram calculations also include solid-state reactions. The highest solidification temperature of α_{Al} solid solution of 658.7 °C (Figure 4.4 a) was predicted by equilibrium phase diagram calculation. The other three calculations resulted in lower but almost similar solidification temperature (Table 4.5, Table 4.8). A more significant difference between the solidification sequence calculations is observed during formation of AlLi (δ) phase. While the formation of AlLi (δ) phase in the equilibrium solidification sequence results from eutectoid

reaction at 153.5 °C (Figure 4.4 a), its precipitation in One axis phase calculation is a consequence of solid-state reaction at 402.0 °C (Table 4.5). The highest temperature of AlLi (δ) phase solidification is predicted by both types of Scheil calculations (Table 4.8). Comparison of the simulation results for sample 22 with Li/Mg = 1 indicates good correlation in phase development between equilibrium phase diagram, One axis equilibrium and Classical Scheil calculations. Scheil with solute trapping deviates from other types of models regarding development of Al_8Mg_5 (β). Similar to the previous model, the highest solidification temperature of α_{Al} solid solution of 649.8 °C (Figure 4.4 a) was predicted by equilibrium phase diagram calculation, while in the other three types of calculations the solidification temperature of α_{Al} solid solution differs slightly (Table 4.5, Table 4.7, and Table 4.8). Furthermore, according to the equilibrium phase calculations the second phase to precipitate is Al_2LiMg (T). According to the other three calculations development of α_{Al} solid solution is followed by the formation of AlLi (δ). The temperature of AlLi (δ) phase precipitation is higher according to Scheil calculations with respect to the One axis phase equilibria (Table 4.5, Table 4.7). Scheil calculations also indicate development of Al_2LiMg (T) and Al_8Mg_5 (β) phases at higher temperatures in comparison to the equilibrium phase and One axis phase equilibrium calculations (Table 4.5, Table 4.7). Difference between the results of Classical Scheil and Scheil with solute trapping concerning Al_8Mg_5 (β) phase development can be explained by the high solubility of Li and Mg in α_{Al} solid solution as well as the influence of Mg on diffusion and redistribution of Li atoms, as indicated by Figure 4.9. Classical Scheil and Scheil with solute trapping calculations are given in Figure 4.11.

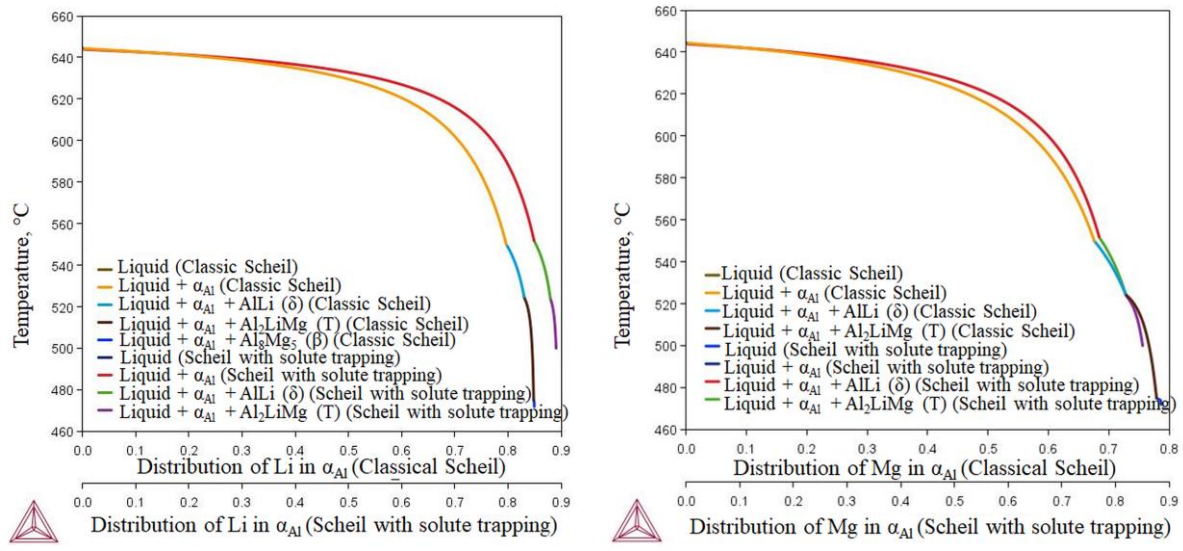

a) **b)**

Figure 4.11. The results of Classical Scheil and Scheil with solute trapping calculations concerning: a) distribution of Li, b) distribution of Mg

Comparing the results of Scheil's calculation of Li distribution in α_{Al} solid solution, it can be observed that during solidification Li diffuses towards the solid/liquid interface and has a grater tendency towards segregation (Figure 4.11). In contrast, Mg exhibits grater solid solubility in α_{Al} solid solution and lower segregation tendency (Figure 4.11 b). As a result of Mg interaction, the solubility of Li in α_{Al} solid solution decreases leading to the solidification of AlLi (δ) at slightly higher temperature compared to the Classical Scheil calculation. High solubility of Mg in α_{Al} solid solution prevents its diffusion to solid/liquid interface resulting in the formation of Mg bulk α_{Al} solid solution. Comparison of the simulation results for samples 21, 31 and 32 with Li/Mg < 1 indicates good correlation concerning development of the α_{Al} solid solution, AlLi (δ), Al_2LiMg (T) phase between equilibrium phase diagram, One axis equilibrium and Classical Scheil calculations. Unlike Scheil's calculations, the One axis equilibrium calculation implies the precipitation of Al_8Mg_5 (β), while the equilibrium phase calculations indicate formation of Al_8Mg_5 (β) and Al_3Mg_2 phases. Higher content of Mg in relation to Li results in preferred precipitation of the Al_2LiMg (T) following the development of α_{Al} solid solution (Figure 4.4). According to the other three models, development of α_{Al} solid solution is followed by the formation of AlLi (δ) phase. The temperature of AlLi (δ) phase precipitation is higher according to Scheil calculations with respect to the One axis phase equilibria (Table 4.5, Table 4.7). Furthermore, Scheil calculations also indicate development of Al_2LiMg (T) phase at higher temperatures in comparison to the equilibrium phase and One axis phase equilibrium calculations (Table 4.5, Table 4.7, and Table 4.8). When comparing the results of solidification sequence calculations with respect to the chemical composition, the difference in One axis and Scheil calculations is observed. Based on the results of One axis equilibrium calculation, the highest reaction temperatures were observed in sample 21 with Li/Mg = 0.93. Contrarily, according to both types of Scheil calculations the highest temperature of AlLi (δ) phase solidification were predicted for sample 31 with lowest Li/Mg = 0.98 ratio. The results of Classical Scheil calculation regarding Li and Mg distribution in samples 21 and 31 are indicated in Figure 4.12. Comparing the results of Scheil's calculation of Li and Mg distribution in α_{Al} solid solution with respect tom Li/Mg, it can be concluded that α_{Al} solid solution remains bulked with both Li and Mg forcing reactions to occur at higher concentrations of these elements (Figure 4.12). Furthermore, higher Mg content and its pronounced influence on Li distribution enables earlier solidification of AlLi (δ) phase. The temperature of Al_2LiMg (T) phase solidification is not significantly impacted by chemical composition. The results of Classical Scheil and Scheil with solute trapping calculation for samples 21 and 22 are in

accordance with the results of equilibrium phase and One axis phase equilibrium calculation regarding the type of Fe- and Si-containing intermetallic phases.

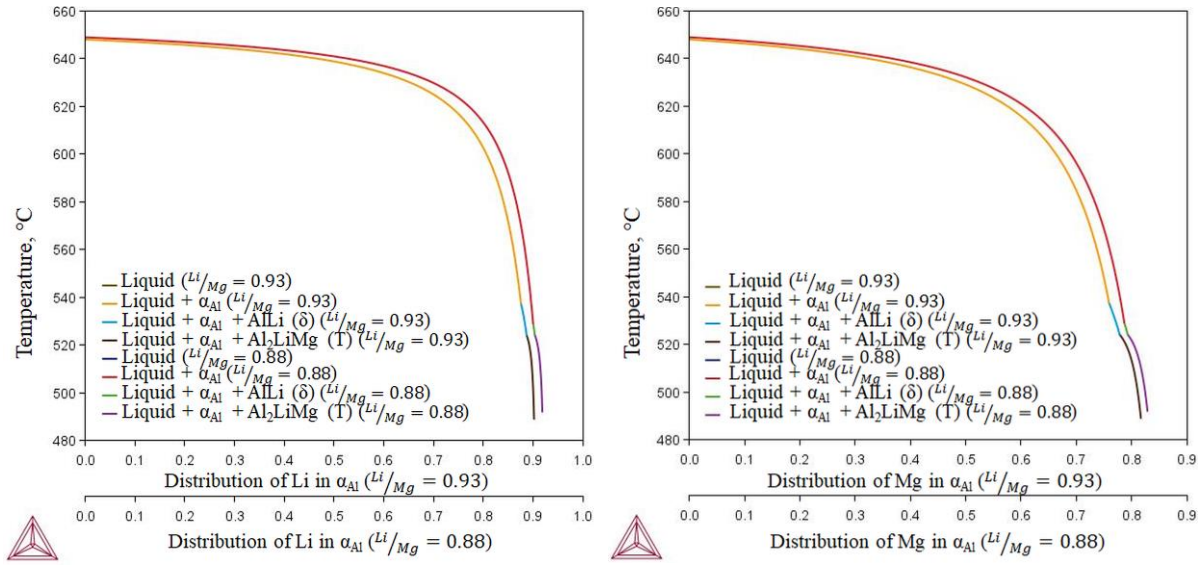

a) **b)**

Figure 4.12. The results of Classical Scheil calculations concerning: a) distribution of Li, b) distribution of Mg

The results of Classical Scheil and Scheil with solute trapping calculations for samples 21 and 22 including impurity elements are given in Figure 4.13 with phase equilibria in Table 4.9.

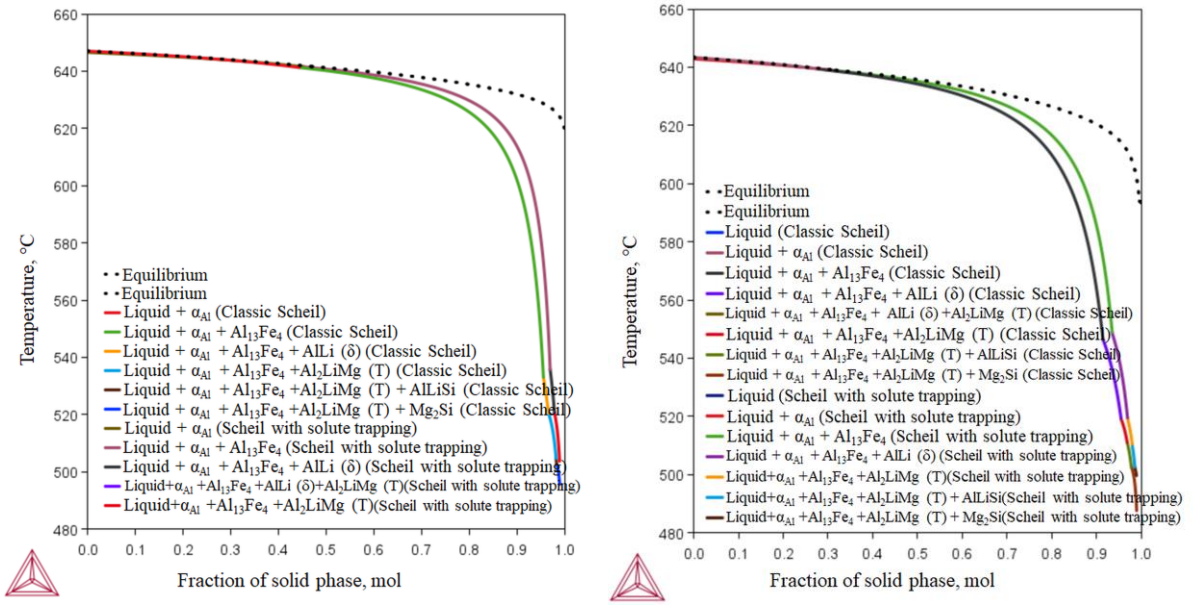

a) **b)**

Figure 4.13. The results of Classical Scheil and Scheil with solute trapping including impurity elements for: a) sample 21, b) sample 22

Table 4.9. The influence of Fe and Si impurity elements on Classical Scheil and Scheil with solute trapping calculations for samples 21 and 22

Sample	Phase equilibria	Classical Scheil	Scheil with solute trapping
		Temperature, °C	Temperature, °C
21	$L + \alpha_{Al}$	647.10	647.10
	$L + \alpha_{Al} + Al_{13}Fe_4$	641.27	641.56
	$L + \alpha_{Al} + Al_{13}Fe_4 + AlLi(\delta)$	533.80	535.86
	$L + \alpha_{Al} + Al_{13}Fe_4 + Al_2LiMg(T)$	520.74	/
	$L + \alpha_{Al} + Al_{13}Fe_4 + AlLi(\delta) + Al_2LiMg(T)$	/	520.85
	$L + \alpha_{Al} + Al_{13}Fe_4 + Al_2LiMg(T) + AlLiSi$	504.74	/
	$L + \alpha_{Al} + Al_{13}Fe_4 + Al_2LiMg(T)$	/	520.79
	$L + \alpha_{Al} + Al_{13}Fe_4 + Al_2LiMg(T) + Mg_2Si$	502.68	/
22	$L + \alpha_{Al}$	643.44	643.44
	$L + \alpha_{Al} + Al_{13}Fe_4$	639.34	638.91
	$L + \alpha_{Al} + Al_{13}Fe_4 + AlLi(\delta)$	546.45	548.88
	$L + \alpha_{Al} + Al_{13}Fe_4 + AlLi(\delta) + Al_2LiMg(T)$	519.42	/
	$L + \alpha_{Al} + Al_{13}Fe_4 + Al_2LiMg(T)$	519.07	519.50
	$L + \alpha_{Al} + Al_{13}Fe_4 + Al_2LiMg(T) + AlLiSi$	510.46	511.04
	$L + \alpha_{Al} + Al_{13}Fe_4 + Al_2LiMg(T) + Mg_2Si$	502.65	502.68

However, all four predictions differ in phase equilibria and solidification sequence. In contrast to both types of Scheil calculations, the equilibrium phase diagram calculations imply primary development of Fe- and Si-containing phases such as $Al_{13}Fe_4$, AlLiSi, Mg_2Si, followed by Al_2LiMg (T), AlLi (δ) and Al_8Mg_5 (β) phases (Figure 4.6, Table 4.6). Similar to the equilibrium diagram, One axis equilibrium calculation first predicts formation of α_{Al} solid solution, $Al_{13}Fe_4$ and AlLiSi phases, while Mg_2Si phase precipitates between the formation of AlLi (δ) and Al_2LiMg (T). In both calculations, β-Al_5FeSi is the last precipitating phase (Table

4.6, Table 4.7). When interpreting the results of Scheil's calculation, it is necessary to consider solubility of alloying elements in Liquid (L) phase (Figure 4.14) as well as the diffusion of Li and Mg in α_{Al} solid solution. The significant difference between Classical Scheil and Scheil with solute trapping calculation is observed for Si distribution (Figure 4.14 sample 21 and sample 22). According to the Classical Scheil calculations the amount of Si in Liquid (L) phase remains unchanged till the solidification of AlLiSi phase at the temperature of 504.7 °C for sample 21 and 510.4 °C for sample 22. Scheil with solute trapping calculations indicate that the amount of Si in Liquid phase begins to decrease already with solidification of α_{Al} solid solution (Figure 4.12).

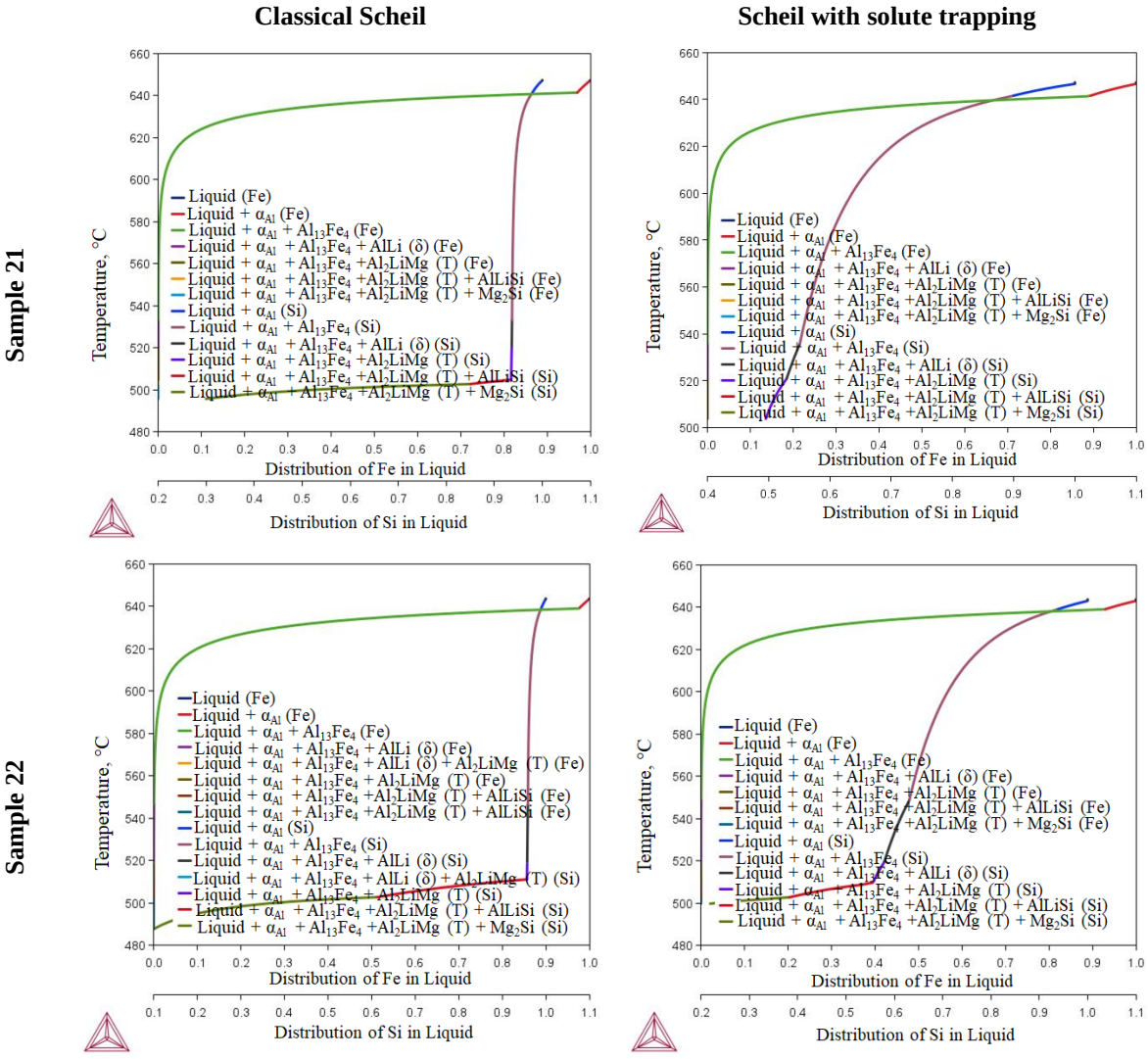

Figure 4.14. Distribution of Fe and Si in Liquid phase

Both types of Scheil calculations are in accordance concerning the distribution of Fe in Liquid phase (Figure 4.14). In both predictions, the reduction in Fe content is a consequence of $Al_{13}Fe_4$ phase solidification.

The difference between Classical Scheil and Scheil with solute trapping calculations can be observed. During the microstructure development of sample 21, Classical Scheil calculations predict separate solidification of AlLi (δ) and Al_2LiMg (T) phases, followed by the formation of AlLiSi and Mg_2Si phases. Contrarily, Scheil with solute trapping indicates parallel solidification of AlLi (δ) and Al_2LiMg (T) phases in temperature interval from 520.8 °C to 520.7 °C. Moreover, the Scheil with solute trapping does not recognize solidification of AlLiSi and Mg_2Si phases (Table 4.7).

The results of solidification sequence calculations for sample 22 differ in terms of AlLi (δ) and Al_2LiMg (T) phase solidification. While Classical Scheil solidification indicates AlLi (δ) and Al_2LiMg (T) phase equilibria at 519.4 °C, according to the Scheil with solute trapping calculation solidification of AlLi (δ) is followed by the formation of Al_2LiMg (T) phase (Table 4.8).

4.4. The results of simplified thermal analysis

The cooling curve obtained during casting of the Al-0.38Mg-2.16Li alloy in permanent steel mold is given in Figure 4.15 a and b. The interpretation of cooling curve resulted in identification of characteristic temperatures given in Table 4.10.

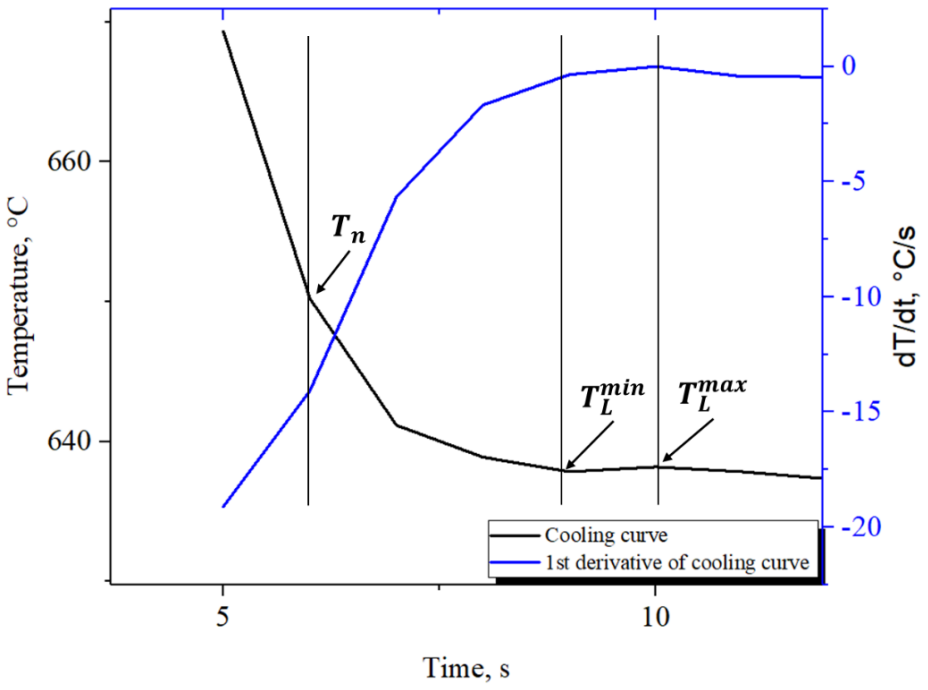

a)

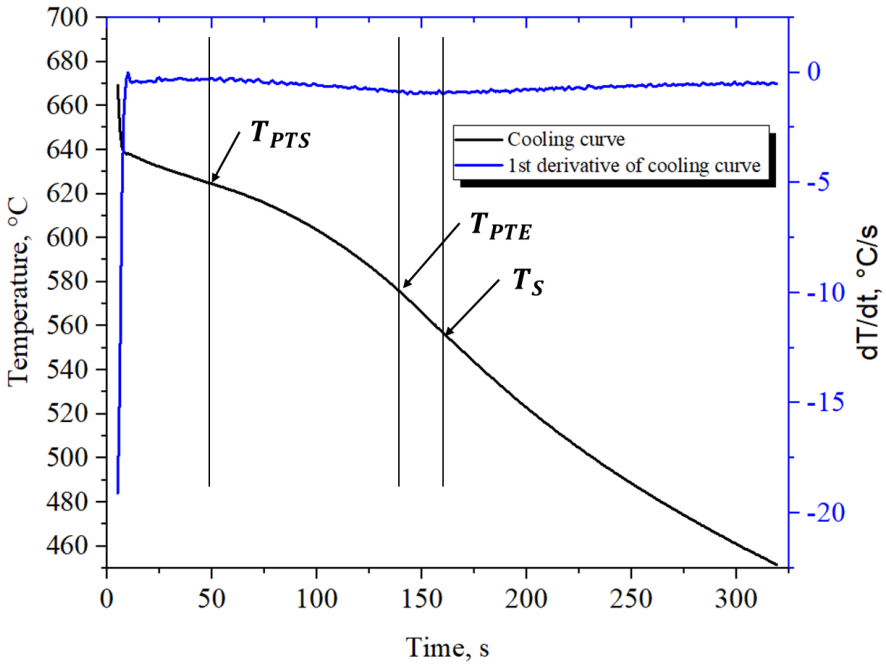

b)

Figure 4.15. The results of Simplified thermal analysis: a) initial part of the cooling curve, b) complete cooling curve

Table 4.10. The characteristic temperatures and additional parameters resulting from sample 1 (Al-0.38Mg-2.16Li) cooling curve interpretation

Characteristic temperature	Results	Additional parameters	Results
T_n	650.2 °C	Δt_{L-S}	187 s
T_L^{min}	637.94 °C	ΔT_{L-S}	121.97 °C
T_L^{max}	638.28 °C	ΔT_{Lr}	0.34 °C
T_{PTS}	625.0 °C		
T_{PTE}	578.0 °C		
T_S	528.03 °C		

The cooling curve obtained during casting of sample 1 (Al-0.38Mg-2.16Li alloy) in permanent steel mold is laid with no distinct peaks related to phase solidification. The lack of characteristic temperature peaks can be considered as a consequence of the relatively slow cooling rate of ~ 0.6 °C/s. The cooling curve in combination with the first derivative enabled identification of nucleation temperature, liquidus, peritectic and solidus temperature. Relatively high nucleation temperature (T_n) of 650.2 °C in combination with low undercooling (ΔT_{Lr}) of 0.34 °C indicate sufficient number of nuclei (Figure 4.15). The peritectic solidification according to the reaction $L + \alpha_{Al} \rightarrow \delta(AlLi)$ occurs in the temperature interval from 625.0 °C to 578.0 °C. However, the first derivative of the cooling curve indicates solidification of high temperature phase at 632.4 °C, as given in Figure 4.16. Based on the data available in literature, it can be assumed that this high temperature phase is metastable δ'(Al_3Li) phase that serves as a precursor for the latter solidification of stable δ (AlLi) phase explaining the low undercooling of the melt.

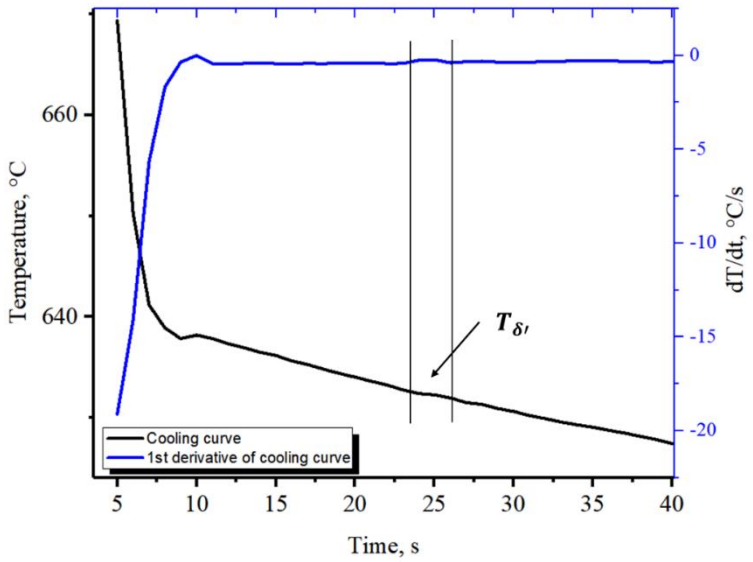

Figure 4.16. High temperature phase solidification identified by cooling curve derivative

4.5. The results of differential scanning calorimetry

Differential scanning calorimetry was performed on the sample 1 (Al-2.16Li-0.38Mg) using heating and cooling rates of 2, 10, 20, 30, 40, and 50 K/min to estimate the impact of chemical composition and thermodynamic parameters on solidification sequence and microstructure development. The recorded and analyzed heating and cooling curves are given in Appendix 1. The characteristic temperatures of phase solidification and precipitation obtained from heating and cooling curves are given in Table 4.11.

Table 4.11. The results of differential scanning calorimetry

Registered parameters		Characteristic temperatures, °C			
		T_L	T_S	Liquid state reactions	Solid state reactions
Heating rates, K/min	2.0	651.0	605.8	620.0	533.0 - 452.0 418.0 - 319.0
	10.0	666.0	608.1	647.3	356.8 332.2 - 313.6
	20.0	698.4	649.1	671.4	442.9 - 397.8
	30.0	704.0	645.1	672.7	/
	40.0	698.0	642.1	659.9	434.0 - 416.8
	50.0	/	612.7	659.9	/
Cooling rates, K/min	2.0	643.8	617.8	635.1	546.1
	10.0	643.1	594.2	638.8	/
	20.0	655.3	602.3	638.4	/
	30.0	656.1	585.2	628.5	696.0
	40.0	654.5	558.6	622.6	/
	50.0	639.7	540.0	588.4	/

As indicated in Table 4.11 interpretation of heating and cooling curves enabled identification of liquidus temperature (T_L), solidus temperature (T_S) as well as temperatures and temperature intervals related to liquid and solid state reactions. The lack of certain characteristic temperatures, mostly temperatures of the solid state reactions related from the lack of characteristic peaks. This lack of characteristic peaks at higher heating and cooling rates is caused by the absence of phase precipitation or growth due to the slow solid state diffusion. Increase in heating and cooling rate indicates the possibility of Mg and Li bulked solid solution

formation (Table 4.11). This is also confirmed by the dependance of T_L and T_S on the heating and cooling rates (Figure 4.17). Increasing the heating rate from 2.0 to 40.0 K/min increases T_L with maxima of the peaks shifting towards higher temperatures (Appendix 1). Increase in the solidification enthalpy with the increase in heating rate from 20.0 to 50.0 K/min reduces the solidus temperature (Figure 4.17).

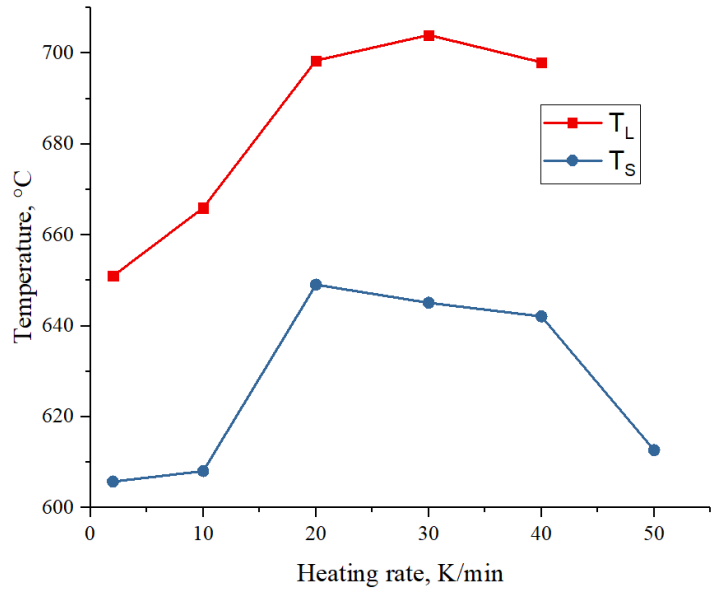

a)

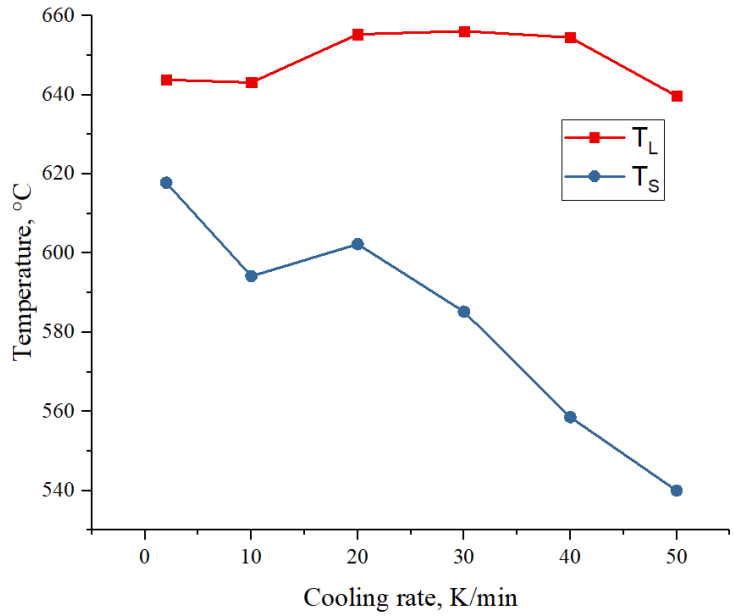

b)

Figure 4.17. Dependence of characteristic temperatures on the: a) heating rates, b) cooling rates

Similar behavior was exhibited by the liquidus temperature when the cooling rate increased from 10.0 to 40.0 K/min. A further increase in cooling rate to 50.0 K/min resulted in a decrease in the T_L. The increase in T_S is observed in the cooling rate range between 10.0 and

20.0 K/min, after which T_S continuously decreases. This indicates widening in the solidification range at the cooling rates of 20.0 to 50.0 K/min. Widening of solidification interval reduces the possibility of casting defect occurrence and enables segregation of alloying elements in the last solidifying areas (Table 4.11). Due to the high solid solubility of Mg in α_{Al} matrix and its influence on the solubility of Li in Liquid and solid solution, the segregation of alloying elements is not expected. This assumption is also confirmed by the dependance of liquid state reaction temperatures on the heating and cooling rates given in Figure 4.18.

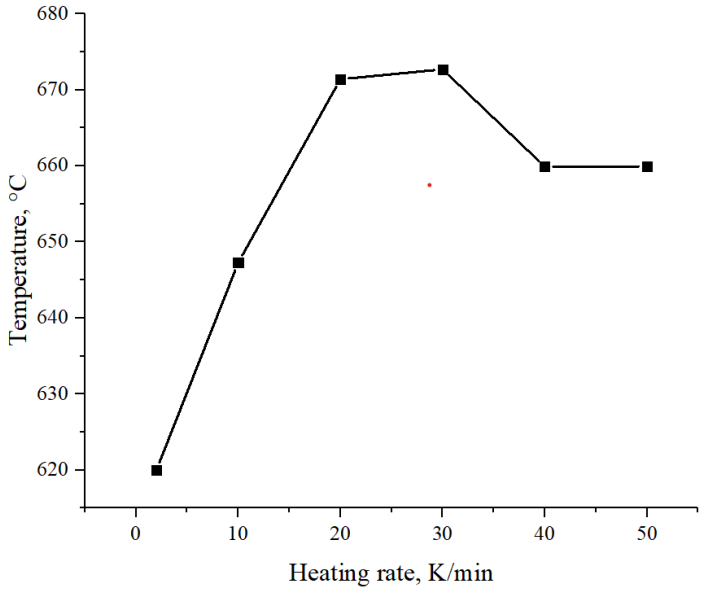

a)

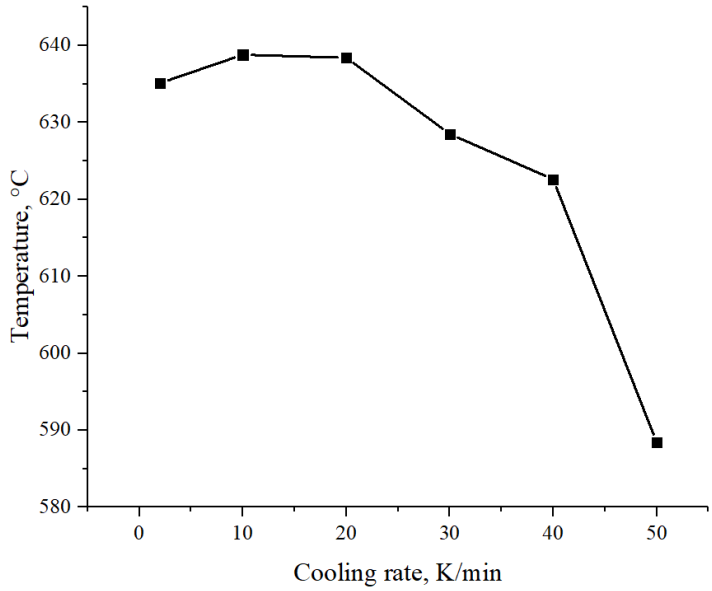

b)

Figure 4.18. Dependence of temperatures of the liquid state reactions on the: a) heating rates, b) cooling rates

Increasing the heating rate from 2.0 to 30.0 K/min increases the temperature of liquid state reactions, while the increase in cooling rate from 20.0 to 50.0 K/min decrease it. The change in liquid state reaction temperatures with the increase in heating/cooling rate is a consequence of changes in enthalpies and shifting of peak maxima (Appendix 1).

4.5.1. Correlation of differential scanning calorimetry results with the result of thermodynamic modelling

The interpretation of heating and cooling curves indicated a significant deviation in the solidification sequence compared to the results of the thermodynamic calculations for Al-rich corner and One axis equilibrium. While according to thermodynamic calculations for Al-rich corner, solidification sequence begins with solidification of α_{Al} matrix followed by the solid state precipitation of Al_2LiMg (T), AlLi (δ) and Al_8Mg_5 (β) phases (Figure 4.4 and Table 4.5), DSC results indicate the solidification of at least one more phase (Table 4.11).

Better correlation of the results can be achieved with Classical Scheil and Scheil with solute trapping calculations (Figure 4.10 and Table 4.8). In that instance the microstructure development begins with the solidification of α_{Al} dendritic network at T_L, followed by the eutectic reaction $L \rightarrow \alpha_{Al}$ + AlLi (δ) at the liquid state reaction temperatures. Considering that the development of other phases is not recognized by the non-equilibrium solidification calculations, reactions in the solid state may indicate the growth and coarsening of AlLi (δ) phase.

4.6. The results of metallographic analysis and microstructure characterization

The metallographic analysis and microstructure characterization were performed in order to fully understand the impact of chemical composition and cooling rate (specific sample section) on microstructure development of synthesized alloys. The metallographic analysis comprehended utilization of light microscopy, scanning electron microscopy (SEM) with energy dispersive spectroscopy (EDS) and transmission electron microscopy (TEM). This enabled qualitative and quantitate microstructure constituent analysis.

4.6.1. The results of light and electron microscopy analysis

The macrostructure of the samples in as-cast condition, given in Figures 4.19, 4.20 and 4.21 respectively. The samples exhibit macrostructure typical for alloy solidification with visible chill, columnar and equiaxed crystal zones. The thickness of individual crystal zones measured on the macrographs are given in Table 4.12

Table 4.12. Thickness of different crystal zones

Sample	Sample section, mm	Crystal zone thickness, mm		
		Chill	Columnar	Equiaxed
1	ø 30.0 mm	0.56	5.08	9.36
	ø 20.0 mm	0.98	5.53	3.49
	ø 10.0 mm	0.84	1.3	2.86
21	ø 30.0 mm	0.25	0.93	13.82
	ø 20.0 mm	0.25	1.72	8.03
	ø 10.0 mm	0.25	0.73	4.02
22	ø 30.0 mm ø 20.0 mm ø 10.0 mm	Homogeneous microstructure without distinguishable crystal zones		
31	ø 30.0 mm	0.23	1.09	13.68
	ø 20.0 mm	0.53	1.03	8.44
	ø 10.0 mm	0.33	1.57	3.1
32	ø 30.0 mm	0.14	1.36	13.5
	ø 20.0 mm	0.51	0.69	8.8
	ø 10.0 mm	0.35	0.73	3.92

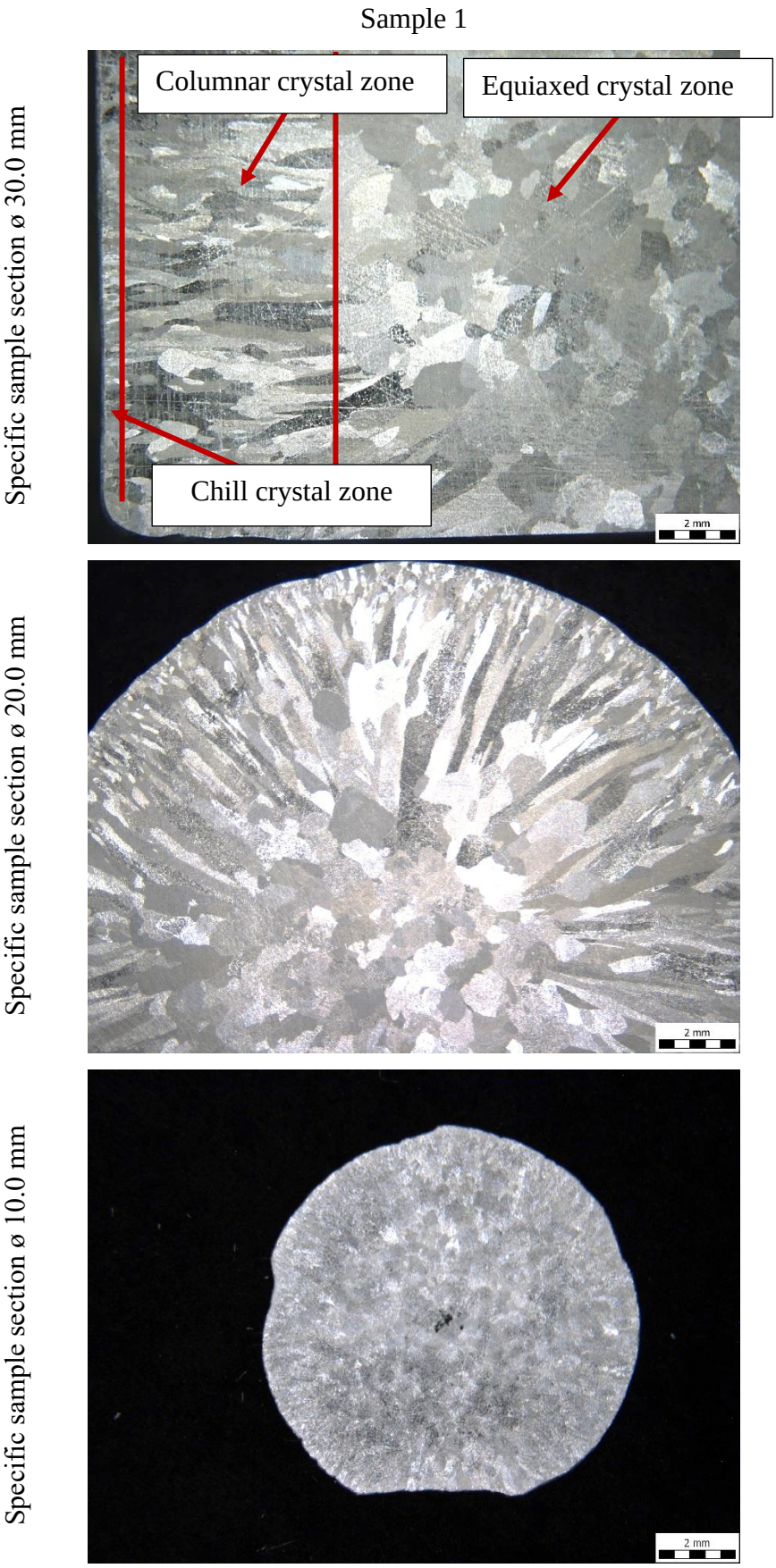

Figure 4.19. The macrostructure of the sample 1 in as-cast condition

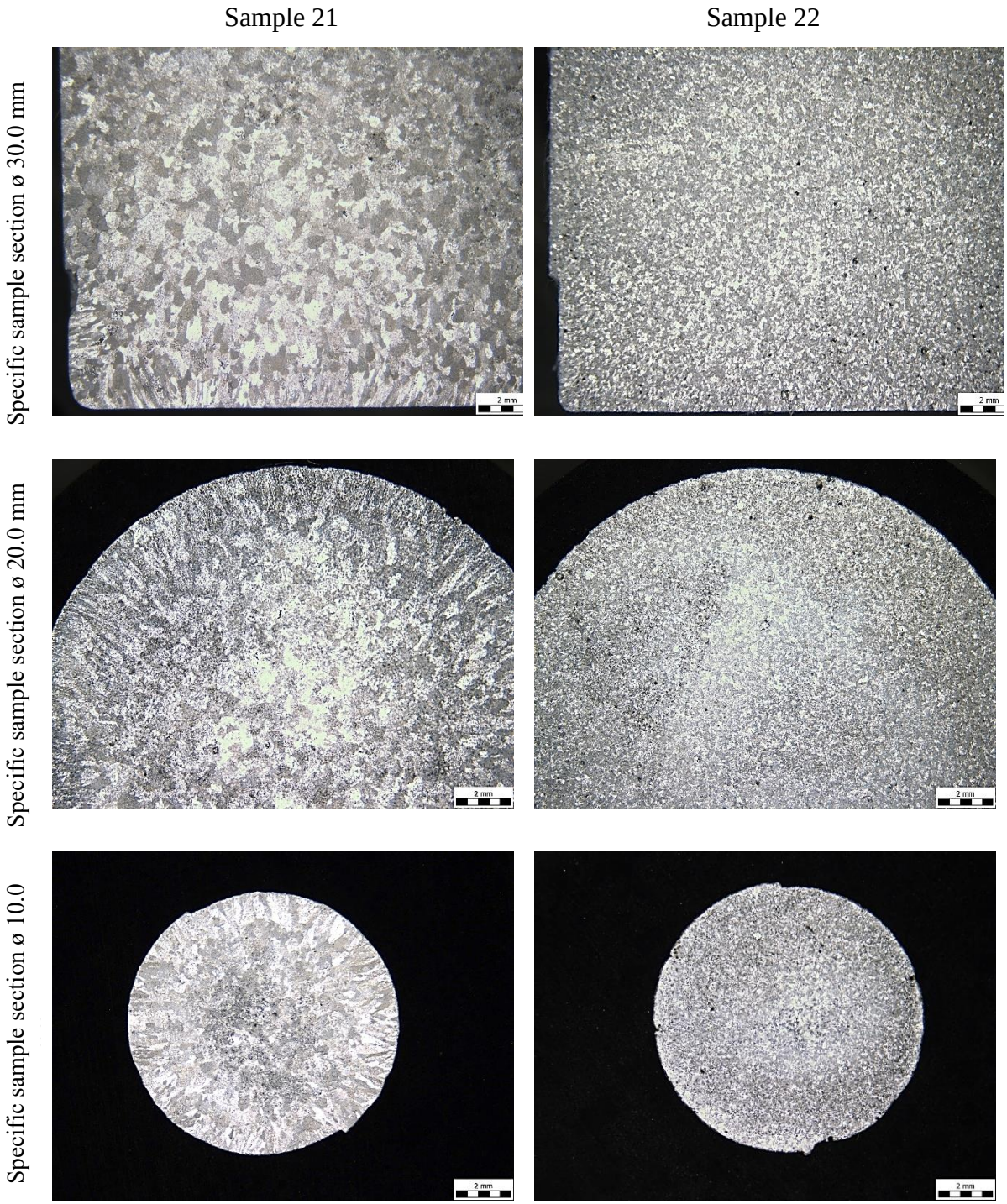

Figure 4.20. The macrostructure of the samples 21and 22 in as-cast condition

The thickness of the chill and columnar crystal zone was measured using the program package on the recorded images. The thickness of the equiaxed crystal zone was calculated by subtracting the measured values of the previous zones from the cross-section of the sample.

Based on the macrostructure and the measured values of individual crystal zones, it can be seen that the addition of the AlTi5B1 master alloy completely removed the casting

texture in sample 22. In sample 32 the AlTi5B1 master alloy addition reduced the thickness of chill and columnar crystal zones with respect to sample 31.

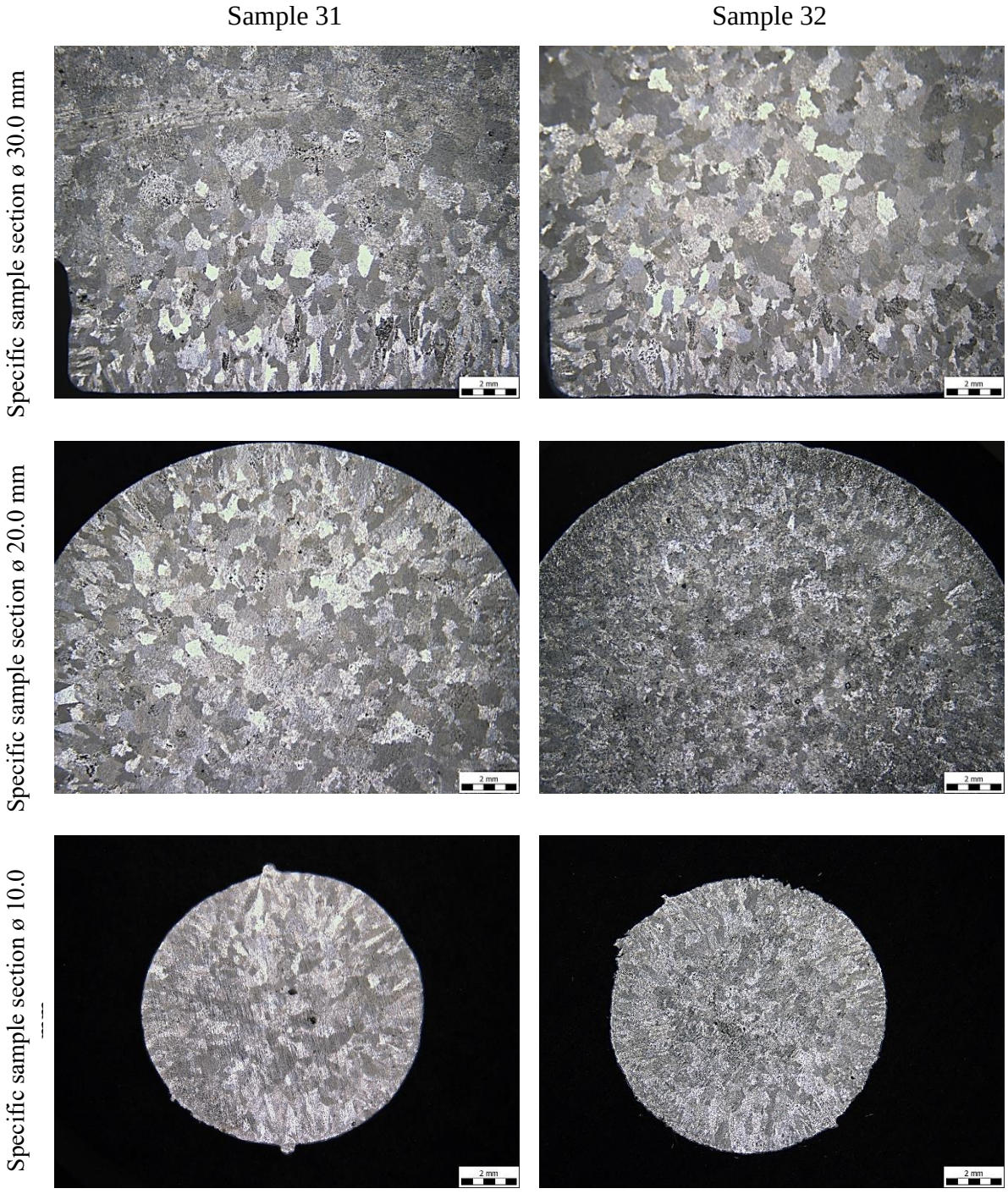

Figure 4.21. The macrostructure of the samples 31and 32 in as-cast condition

When considering the thickness of the chill and columnar crystal zones as a function of Li/Mg ratio, the thickness of crystallographic texture decreases with the decrease in the ratio. This is a consequence of Mg influence on reduced solid solubility of Li in α_{Al} matrix. Parallelly, there is an Li enrichment of the interdendritic area and the nucleation of intermetallic phases.

Given that the microstructural analysis indicated the development of equal intermetallic phases independent of the specific sample section, the Figures 4.22 shows the microstructures of the synthesized samples on a ø 10.0 mm sample section. The intermetallic phases were identified based on morphology and position in microstructure using data available in literature.

The utilization of light microscopy enabled identification of α_{Al} dendritic network, AlLi (δ), Al_2LiMg (T), (Al_8Mg_5 (β) + Al_2LiMg (T)) and Al_8Mg_5 (β) intermetallic phases (Figure 4.23). The intermetallic phases detected in all the samples, except AlLi (δ) in sample 1, show tendency to solidify in the interdendritic areas.

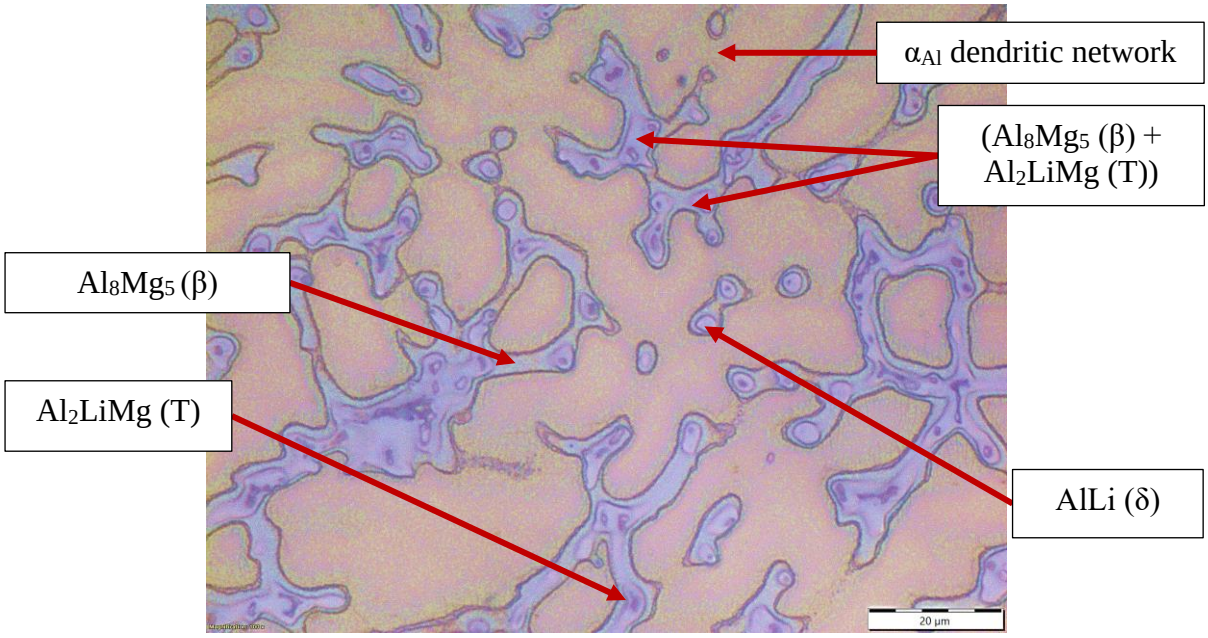

Sample 1

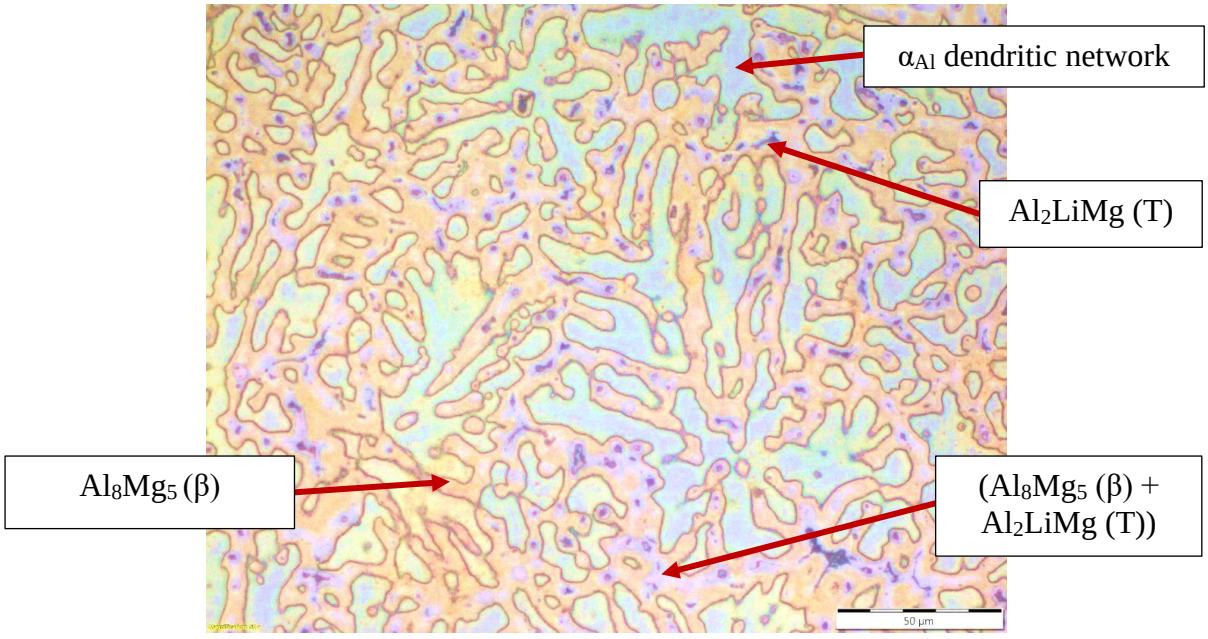

Sample 21

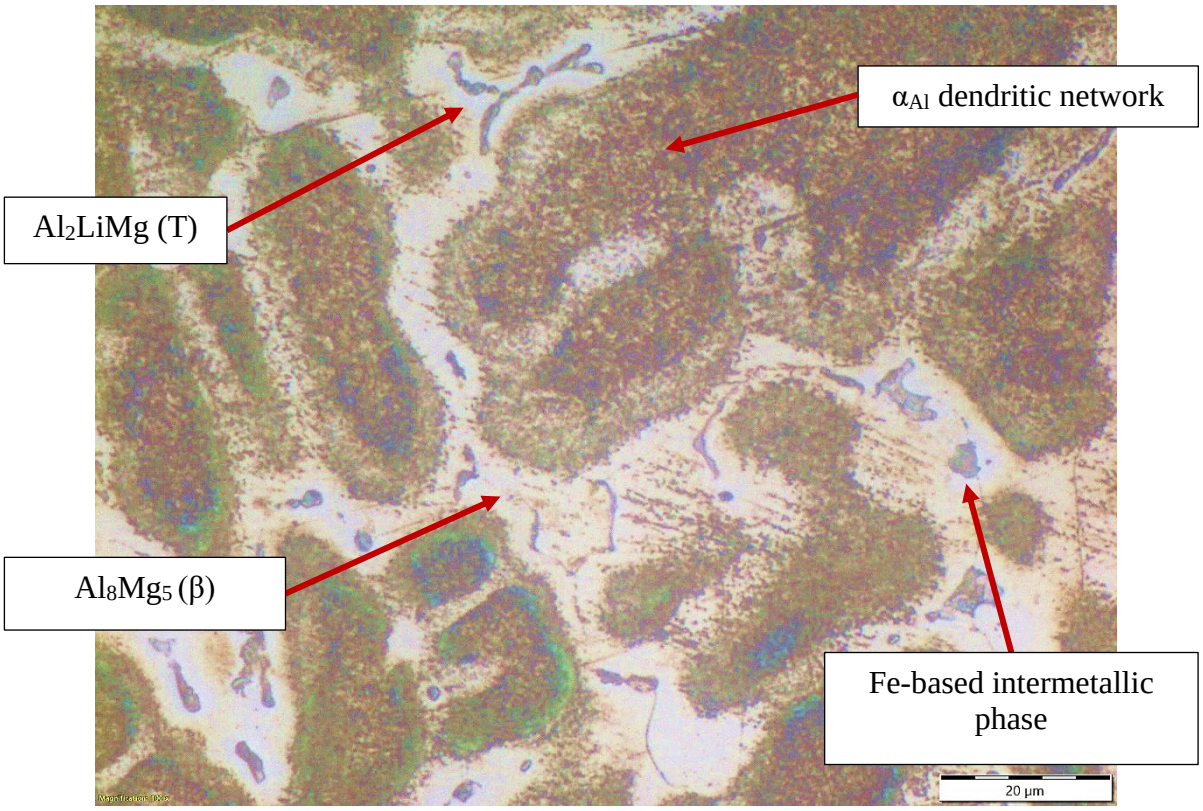

Sample 22

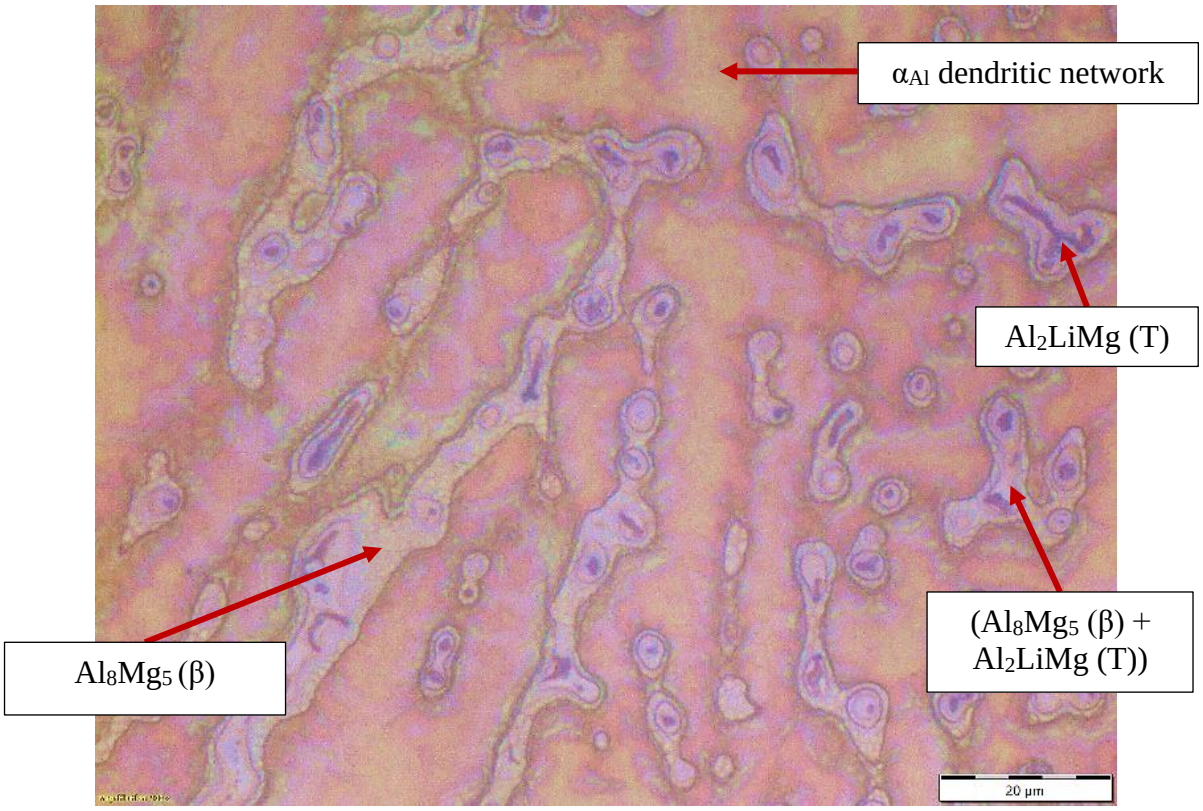

Sample 31

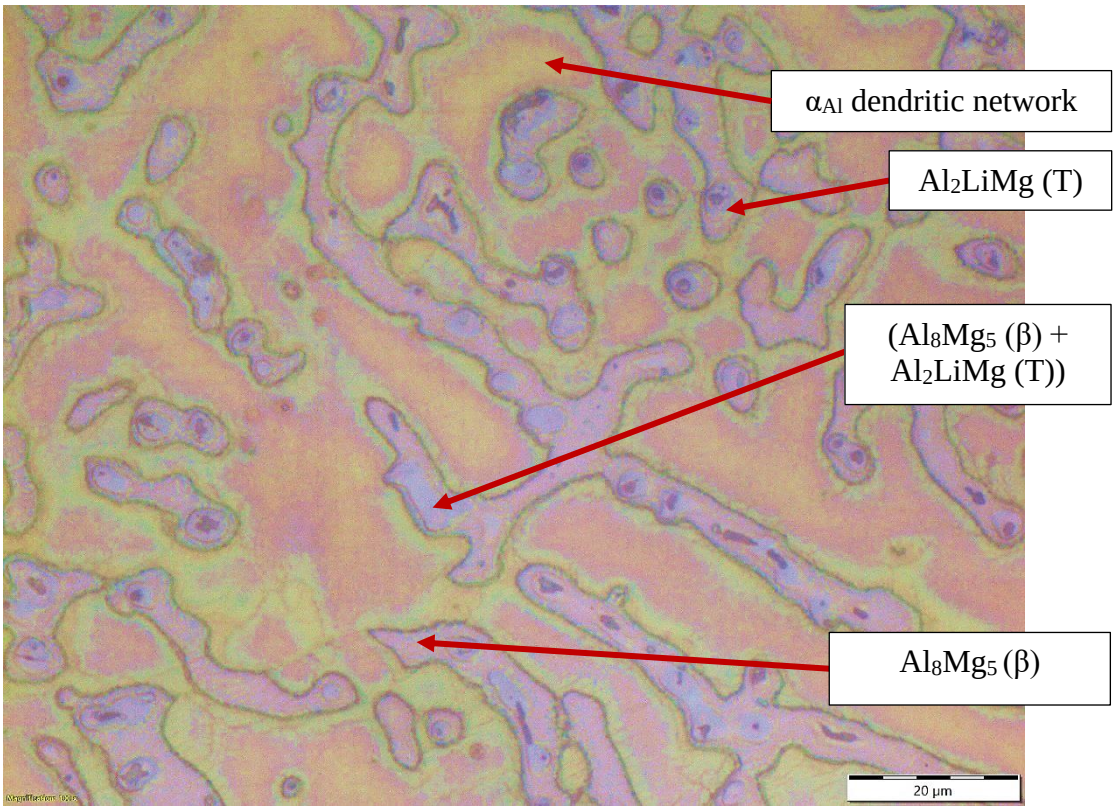

Sample 32

Figure 4.22. The light microstructure of the synthesized samples on the ø 10.0 mm section

The microstructure development in sample 1 comprehended solidification of primary α_{Al} dendritic network, followed by solidification of AlLi (δ) phase. Given that the nucleation and growth of this phase is based on the solidification of the precursor Al_3Li (δ') phase rather than the melt's bulking at the solidification front with Li and Mg, it is the only phase that solidifies within the α_{Al} dendritic network as well as along the grain boundaries (Figure 4.22). The results of SEM and linear EDS analysis performed on the phases located inside α_{Al} dendritic network and along the grain boundaries (Figure 4.23) indicated decrease in Al content at the intersection points. The Mg content remained constant.

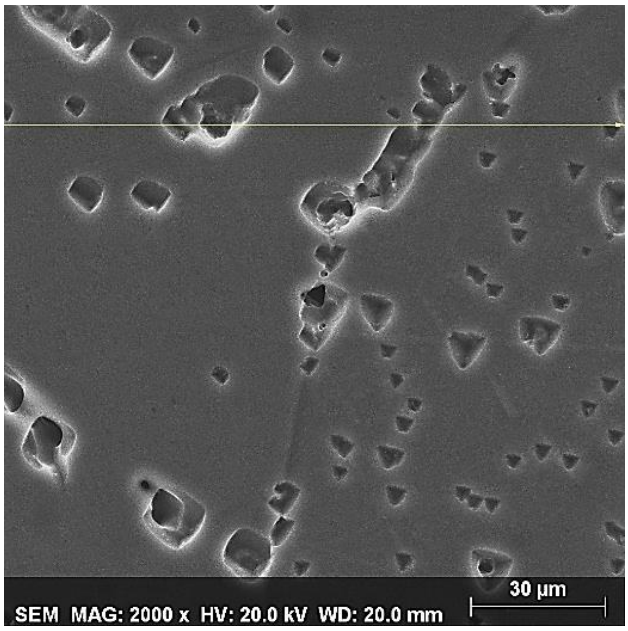

a)

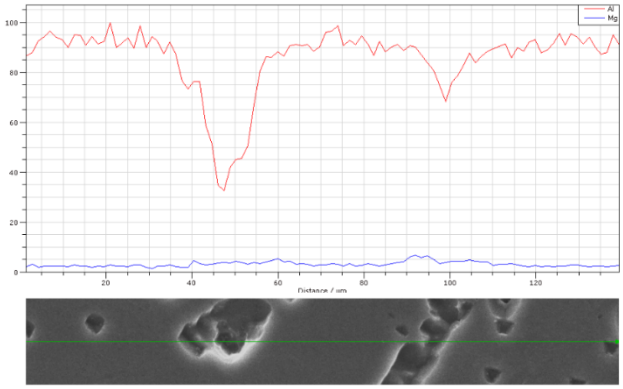

b)

Figure 4.23. The results of SEM and EDS analysis in sample 1: a) SEI with indicated area for linear analysis, b) EDS linear analysis

The solidification of remaining intermetallic phases is a consequence of reduced solid solubility of both Li and Mg in α_{Al} matrix. Consequently, the melt remaining between the branches of α_{Al} dendritic network is bulked with Li and Mg enabling solidification of Al_2LiMg (T), (Al_8Mg_5 (β) + Al_2LiMg (T)) and Al_8Mg_5 (β). The results of SEM and mapping EDS analysis performed on two different details in sample 1 are given in Figure 4.24. The results of additional quantitative EDS analysis performed on details from Figure 4.24 are given in Table 4.13. The results of EDS mapping analysis indicate occasional increase in Mg content in interdendritic area (Figure 4.24). These variations were confirmed by additional quantitative analysis that detected Mg content form minimal 3.23 wt.% to maximal 7.23 wt.% confirming the solidification of Al_2LiMg (T), (Al_8Mg_5 (β) + Al_2LiMg (T)) and Al_8Mg_5 (β) phases at different contents of Li and Mg.

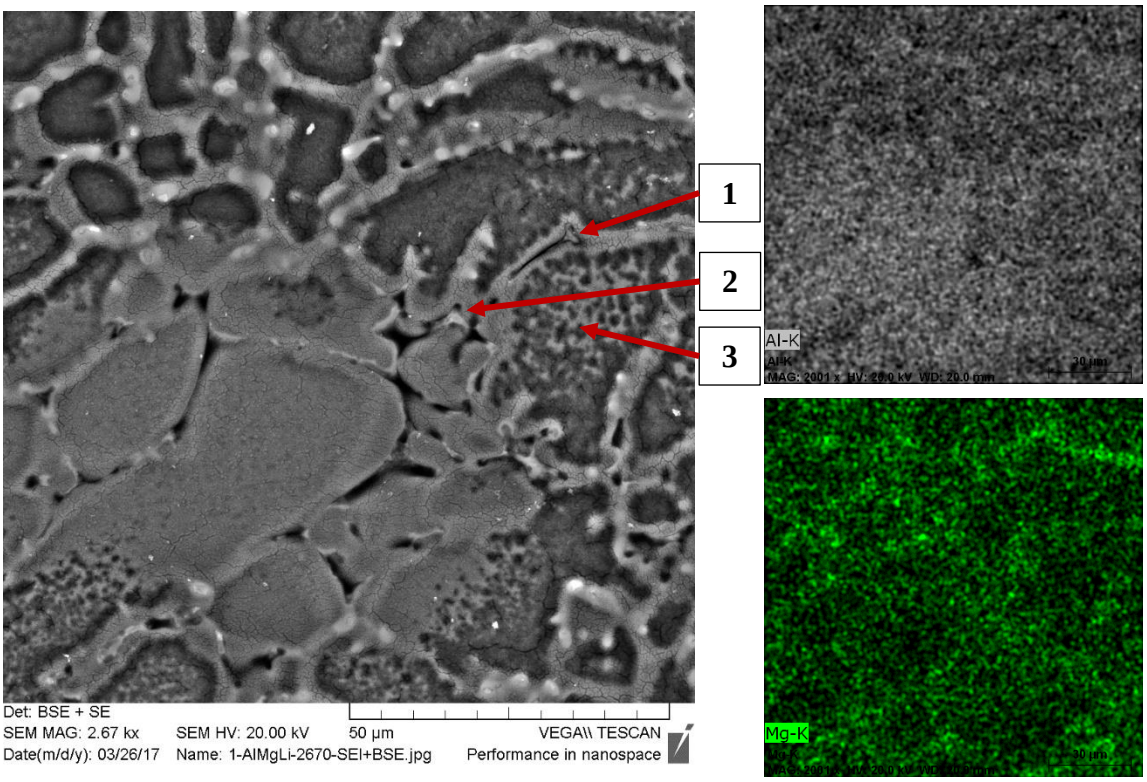

a)

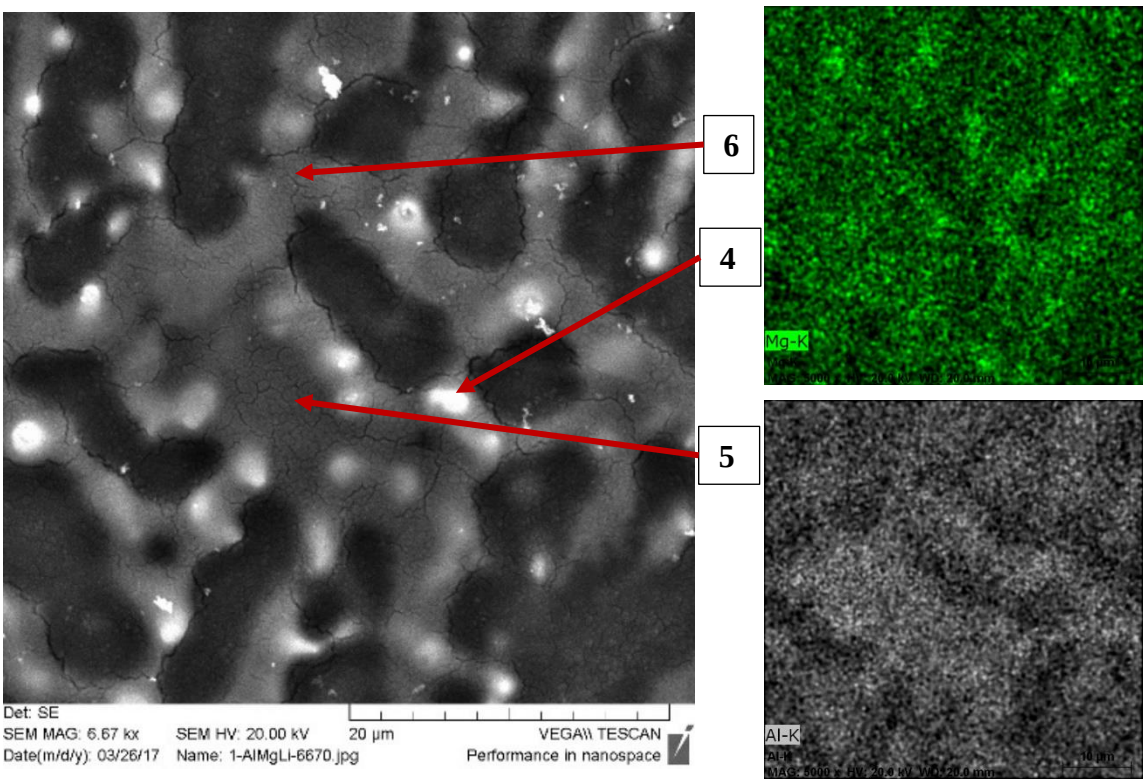

b)

Figure 4.24. The SEI with indicated locations for additional EDS analysis and the results of EDS mapping analysis in sample 1: a) detail 1, b) detail 2

Based on the Mg content it can be assumed that the first phase solidifying in interdendritic area is Al_2LiMg (T) (Figure 4.24, location 1) followed by the solidification of

two phase (Al_8Mg_5 (β) + Al_2LiMg (T)) region (Figure 4.24 locations 2 and 4) and Al_8Mg_5 (β) (Figure 4.24 locations 5 and 6). This assumption is in accordance with the results of thermodynamic modelling of solidification sequence and data available in literature.

Table 4.13. The results of quantitative EDS analysis performed on the locations indicated in Figure 4.24

Location from Figure 4.25	Amount of Al, wt.%	Amount of Mg, wt.%
1	96.4	3.28
2	95.0	4.99
3	97.82	2.18
4	92.77	7.23
5	96.42	3.58
6	96.77	3.23

The results of microstructural analysis performed on the samples 21, 22, 31 and 32 indicated similar microstructure development to sample 1. Since these samples have Li/Mg ≤ 1 the solidification of AlLi (δ) phase is not comprehended. Instead, microstructure development includes solidification of α_{Al} dendritic network and Al_2LiMg (T), (Al_8Mg_5 (β) + Al_2LiMg (T)) and Al_8Mg_5 (β) phases in interdendritic area. Additionally, the results of light microscopy indicated presence of Fe-based intermetallic phases in sample 22. The results of SEM and EDS analysis performed on samples 21 and 22 are given in Figure 4.25 with the results of quantitative EDS analysis performed on locations from Figure 4.25 given in Table 4.14.

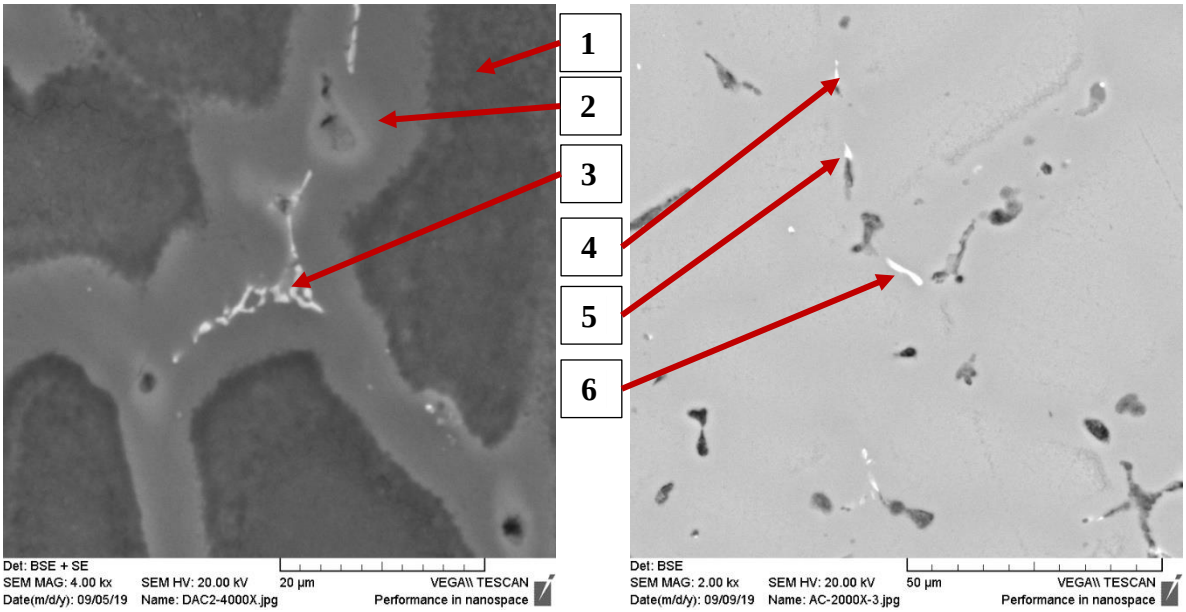

a) **b)**

Figure 4.25. The SEI with indicated locations for quantitative EDS analysis in: a) sample 21, b) sample 22

Table 4.14. The results of quantitative EDS analysis performed on the locations indicated in Figure 4.25

Location from Figure 4.26	Amount of Al, wt.%	Amount of Mg, wt.%	Amount of Fe, wt.%
1	93.12	2.63	0.34
2	94.03	5.20	0.52
3	83.36	3.96	12.27
4	91.88	7.08	1.04
5	92.66	4.31	3.02
6	90.43	3.97	5.60

The results of SEM and quantitative EDS analysis detected Fe-based intermetallic phases in sample 21 and 22. The phases with irregular globular/rode- like morphology were located in the interdendritic areas surrounded by Al_8Mg_5 (β) phases. Based on their morphology, location, and chemical composition these phases can be identified as $Al_{13}Fe_4$.

4.6.2. The results of X-ray diffraction

The microstructure analyses by X-ray diffraction were performed on the samples 1, 22 and 31 characterized by Li/Mg = 5.68, Li/Mg = 1.0, Li/Mg = 0.88. The XRD diffractograms for samples in as-cast condition are given in Figure 4.26.

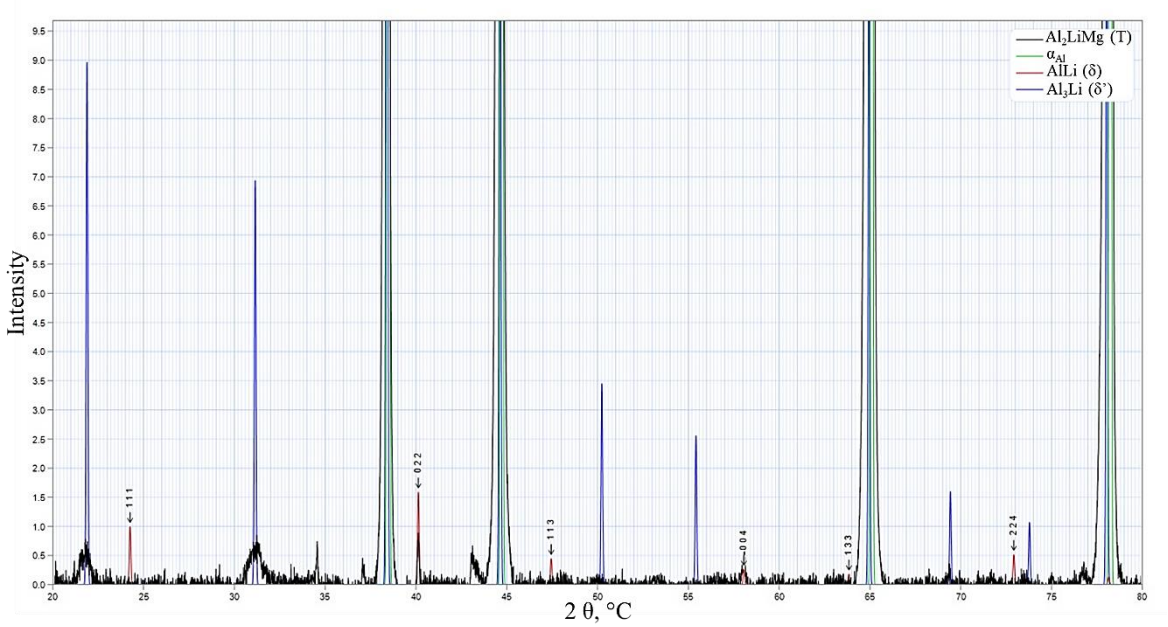

a)

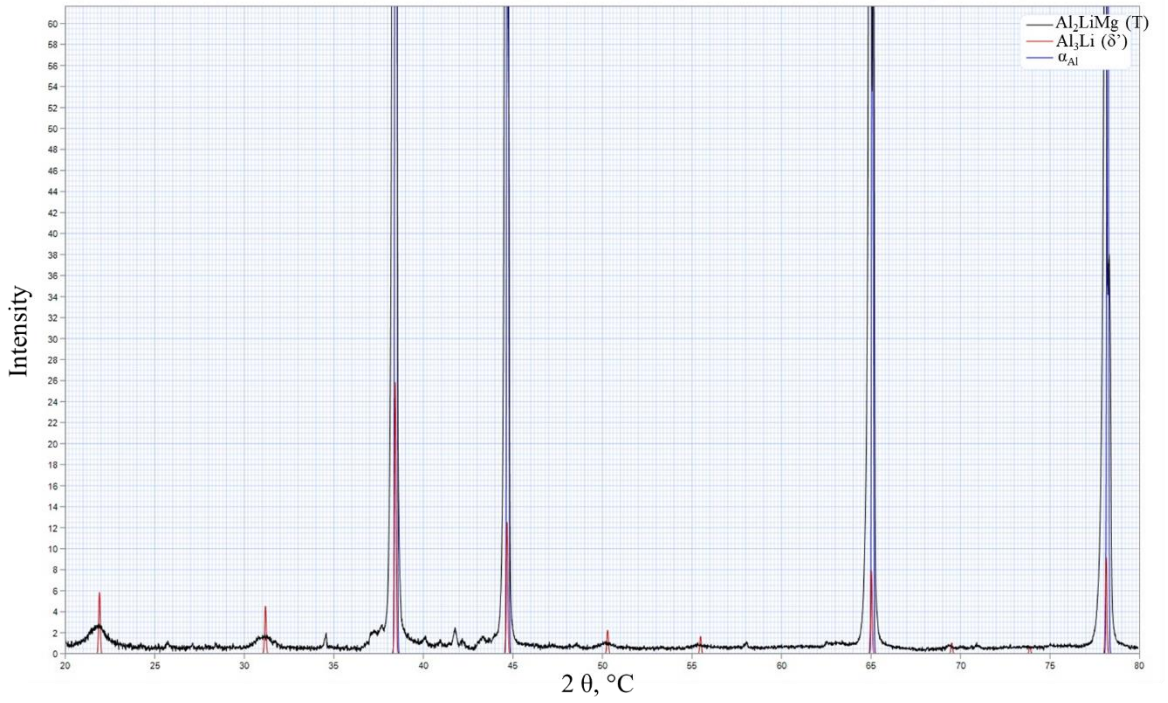

b)

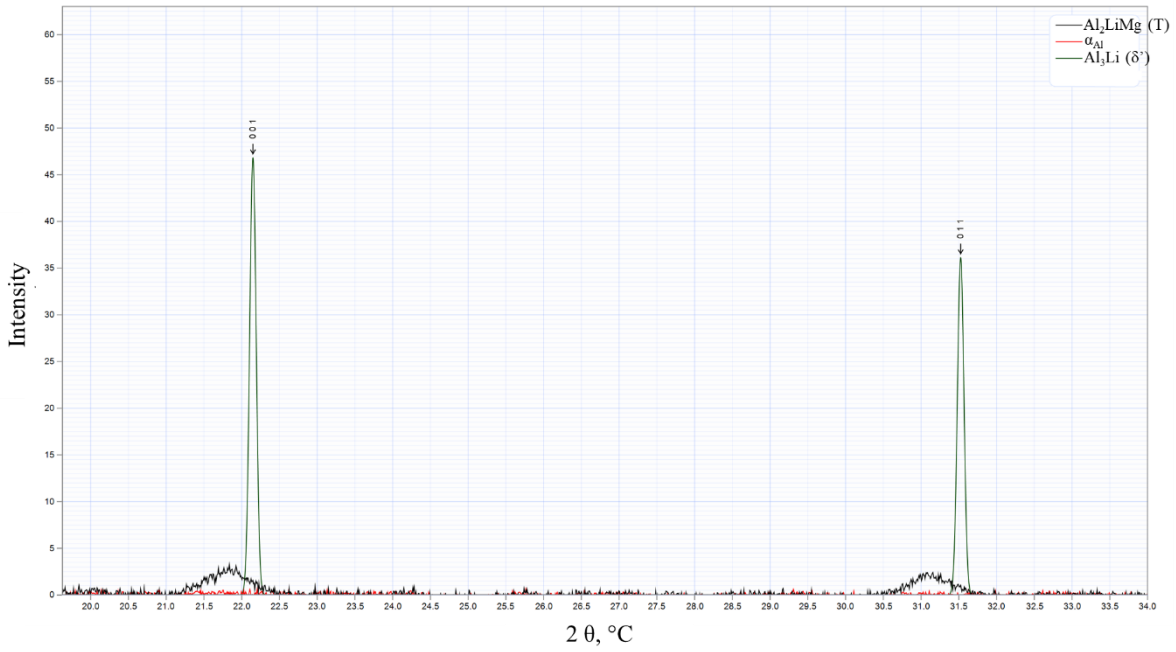

c)

Figure 4.26. The XRD diffractograms of: a) sample 1, b) sample 22, c) sample 31

The results of X-ray diffraction indicate the presence of Al_2LiMg (T) and Al_3Li (δ') intermetallic phases in α_{Al} matrix for all three samples. In sample 1 the presence of AlLi (δ) phase was detected additionally. Based on these results, it can be concluded that precursor Al_3Li (δ') phase solidified and is retained till the end of solidification sequence regardless of Li/Mg ratio. However, the intensity of Al_3Li (δ') phases characteristic peaks is highest for the sample 1 with Li/Mg = 5.68. Solidification and retention of the metastable phase at all Li/Mg ratios is important for achieving good mechanical properties. As the primary strengthening precipitate in Al-Li alloys, the metastable Al_3Li (δ') phase remains spherical and coherent to the α_{Al} matrix at significantly high temperatures and long aging times enabling residual stress removal and increase in stiffness and strength [18].

4.6.3. The results of transmission electron microscopy

The transmission electron microscopy (TEM) with selected area diffraction patterns (SAD) was performed on the samples with respect to Li/Mg ratios. The TEM bright field images and SAD pattern for sample 1 are given in Figure 4.27.

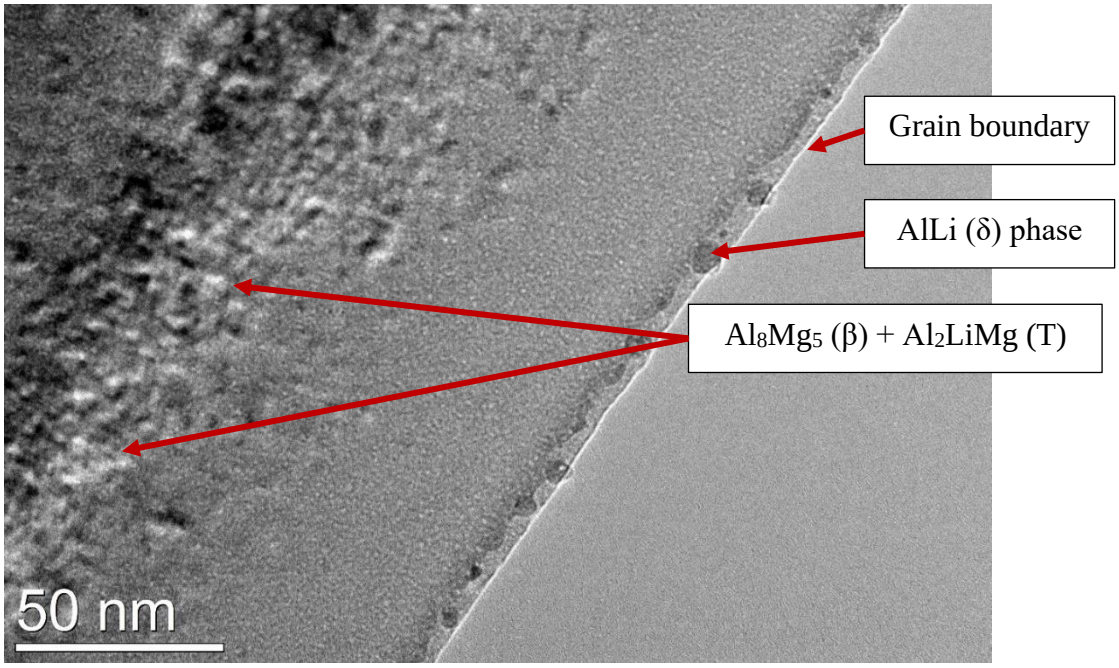

a)

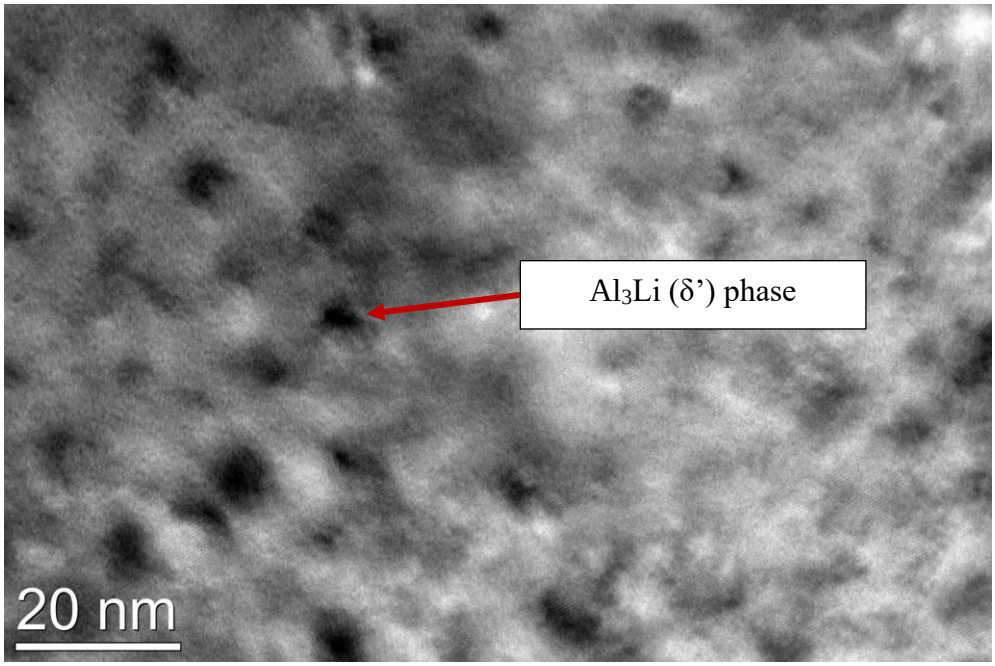

b)

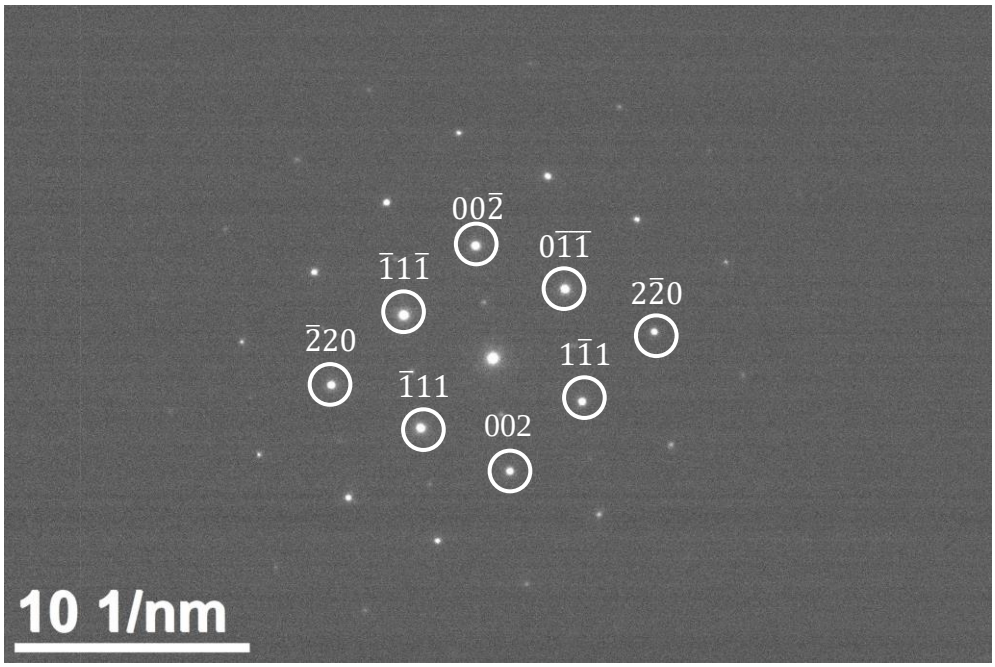

c)

Figure 4.27. TEM bright field images of sample 1: a) detail at lower magnification showing grain boundaries, b) higher magnification detail, c) SAD pattern identifying Al3Li(δ') phase

The TEM bright field images of sample 1 enabled identification of Al_3Li (δ'), AlLi (δ) and (Al_8Mg_5 (β) + Al_2LiMg (T)) intermetallic phases which is in accordance with the results of X-ray diffraction. The TEM bright field images and SAD patterns for sample 22 are given in Figure 4.28.

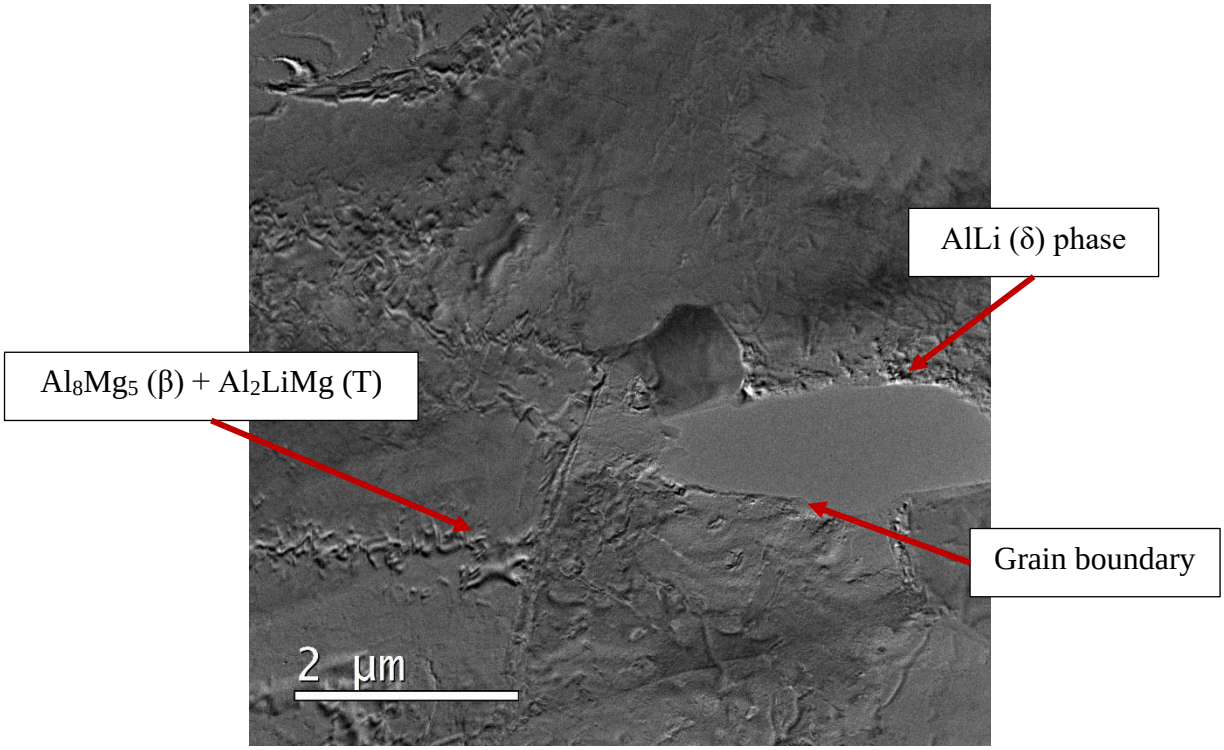

a)

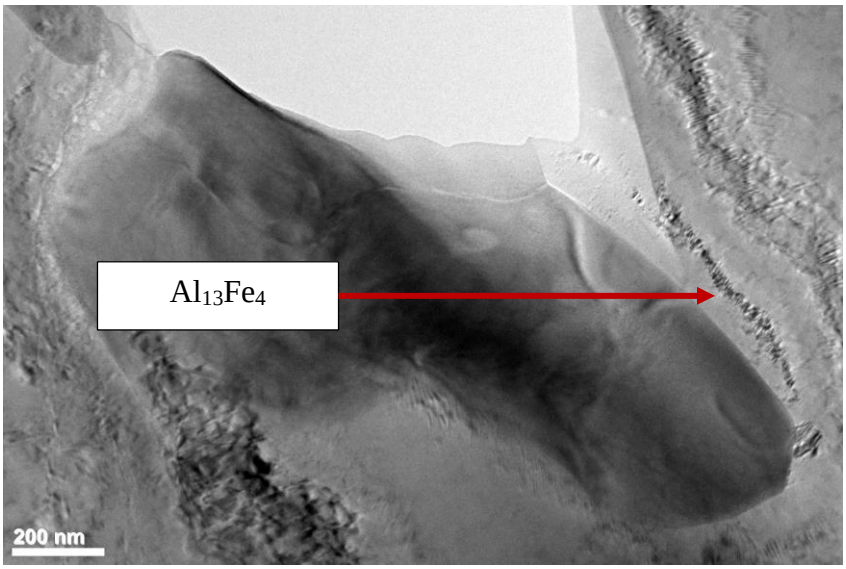

b)

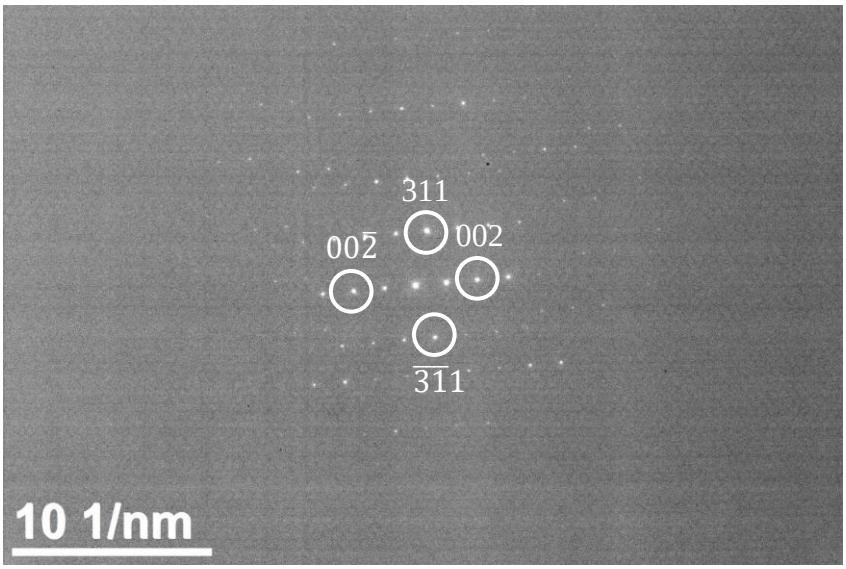

c)

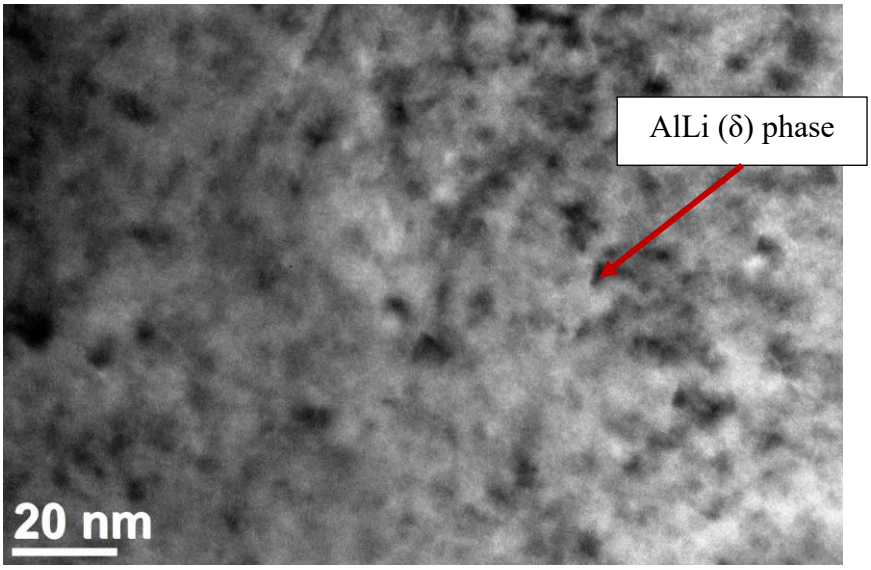

d)

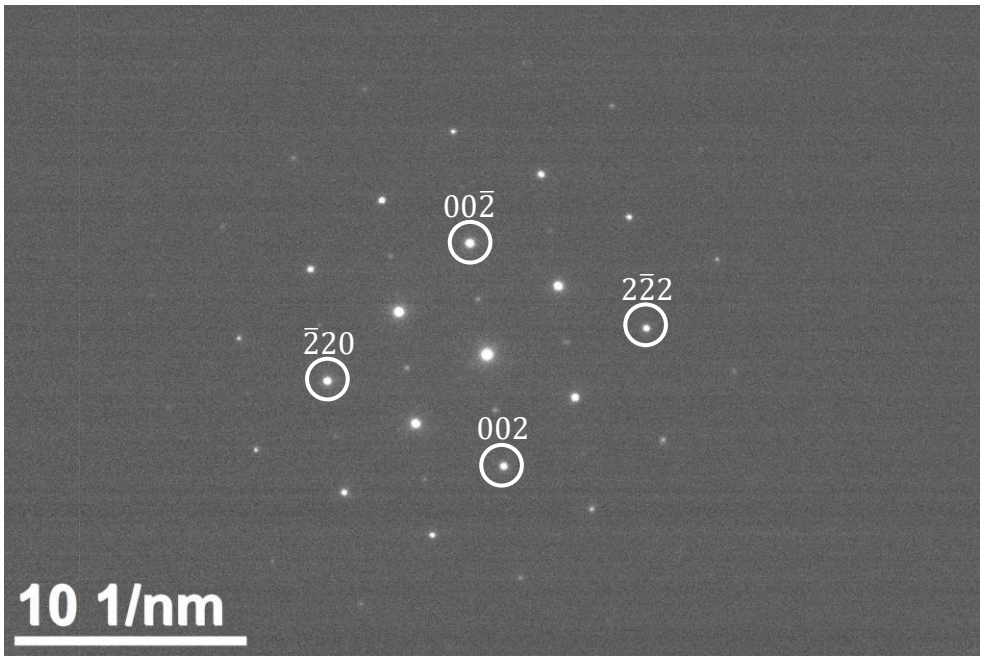

e)

Figure 4.28. TEM bright field images of sample 22: a) lower magnification TEM image, b) TEM image showing $Al_{13}Fe_4$ intermetallic phase, c) SAD pattern identifying $Al_{13}Fe_4$ intermetallic phase, d) TEM image showing Al_3Li (δ') intermetallic phase, e) SAD pattern identifying Al_3Li (δ') intermetallic phase

The results of TEM bright field imaging of sample 22 enabled identification of Al_3Li (δ'), AlLi (δ), (Al_8Mg_5 (β) + Al_2LiMg (T)) and $Al_{13}Fe_4$ intermetallic phases. The TEM bright field images and SAD patterns for sample 31 are given in Figure 4.29.

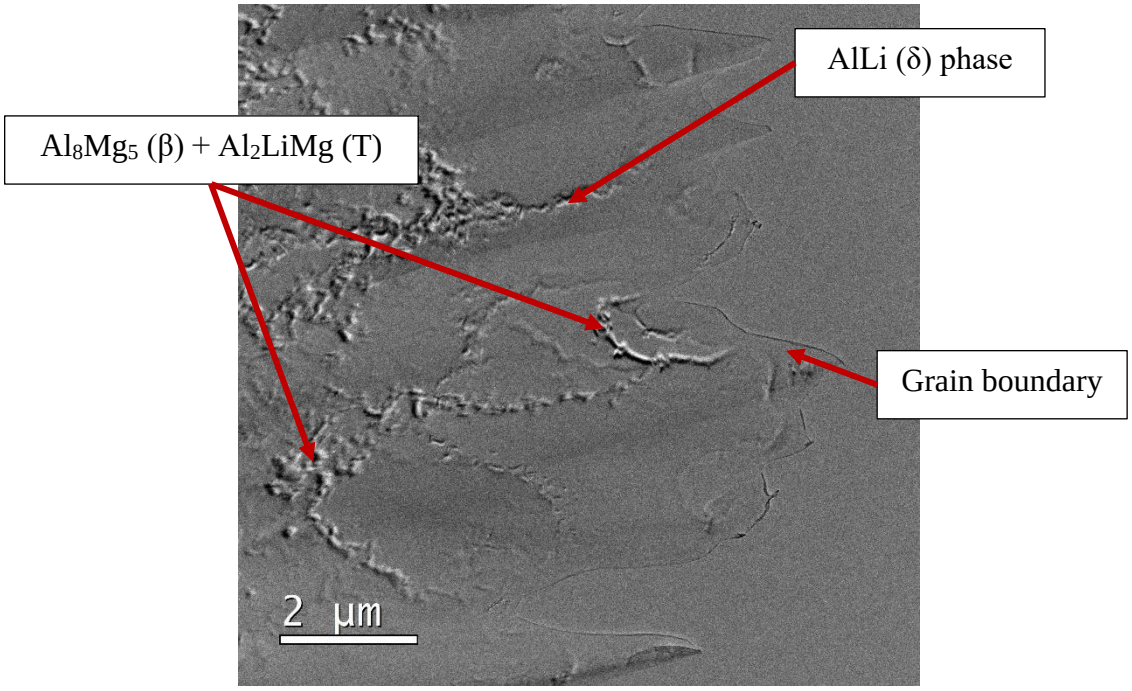

a)

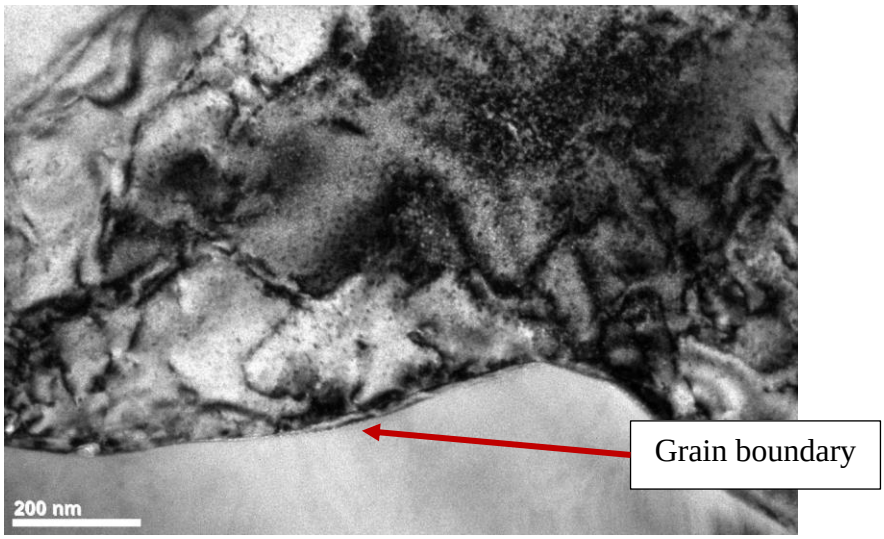

b)

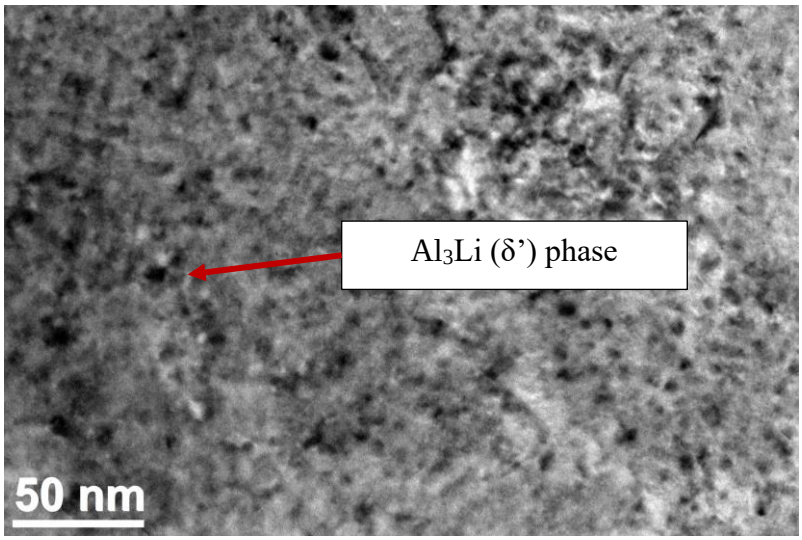

c)

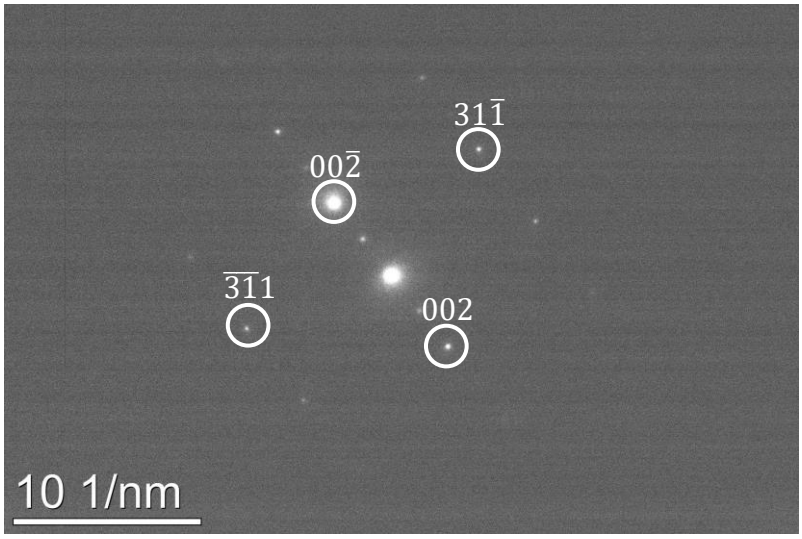

d)

Figure 4.29. TEM bright field images of sample 31: a) lower magnification TEM image, b) higher magnification TEM image, c) TEM image showing Al_3Li (δ') intermetallic phase, d) SAD pattern identifying image showing Al_3Li (δ')

The results of TEM bright field imaging of sample 31 enabled identification of Al_3Li (δ'), AlLi (δ) and (Al_8Mg_5 (β) + Al_2LiMg (T)) intermetallic phases.

4.7. The results of mechanical properties characterization

In order to assess the influence of microstructural constituents on mechanical properties of synthesized alloys, the compression testing as well as hardness, microhardness and nanoindentation measurements were utilized.

4.7.1. The results of compression testing

The results of compression testing are given in Table 4.15 with engineering strain – stress and engineering strain – temperature curves shown in Appendix 2. The engineering strain–stress curves show type A serrations indicating plastic instability behavior characterized by repeated nucleation and development of localized deformation areas.

The reduction of samples' initial length and increase in temperature during compression are indicated in Table 4.16.

Table 4.15. The results of compression testing

Sample	Metallurgical condition	Yield strength, MPa	Upper yield point, MPa	Lower yield point, MPa	Compression strength, MPa	Ultimate point, MPa
1	As cast	290.1	336.2	198.8	352.7	368.0
	Solutionized	230.7	279.2	118.0	239.3	242.9
21	As cast	233.9	293.0	116.3	338.1	341.0
	Solutionized	249.4	288.0	211.5	256.3	285.2
22	As cast	246.8	296.3	224.4	372.6	389.3
	Solutionized	230.7	279.2	118.0	237.5	249.2
31	As cast	235.5	245.5	53.7	235.7	242.5
	Solutionized	208.1	276.4	68.3	178.8	199.3
32	As cast	258.3	301.0	99.9	227.2	245.2
	Solutionized	208.4	299.8	82.1	221.8	232.7

The results of compression testing shown in Table 4.15 indicate a decrease in compression properties, primarily compression strength and ultimate point, due to the solutionizing heat treatment. Exceptions related to yield point, upper yield point and lower yield

point, can be seen in samples 22, 31 and 32. This indicates a later onset of samples' plastic deformation and a higher stress required for deformation to become permanent.

According to engineering strain – stress curves given in Appendix 2, sample 1 in as-cast condition exhibited the inelastic deformation behavior at 290.1 MPa (Table 4.15). The plastic deformation becomes permanent at the upper yield point of 336.2 MPa. Afterwards, the compression strength dropped to the lower yield point of 198.8 MPa. The as cast sample achieved the compression strength of 352.7 MPa with the end of sample yielding at engineering strain of 0.35. The compression testing stopped at ultimate point of 368.0 MPa when the sample was reduced by 60.0 % of its initial length followed by the increase in samples' temperature of 60.0 °C (Table 4.16). The solutionizing of sample 1 decreased all the characteristic compression testing points, leading to the earlier onset of permanent plastic deformation (Table 4.16). The compression testing was stopped at the ultimate point of 242.9 MPa with 40.0 % reduction of samples' initial length and temperature increase of 20.0 °C.

Table 4.16. The reduction of samples' area and increase in temperature induced by compression testing

Sample	Metallurgical condition	Area reduction, %	Temperature increase, °C
1	As cast	60.0	60.0
	Solutionized	40.0	20.0
21	As cast	50.0	50.0
	Solutionized	20.0	45.0
22	As cast	50.0	50.0
	Solutionized	50.0	20.0
31	As cast	60.0	50.0
	Solutionized	60.0	8.0
32	As cast	55.0	60.0
	Solutionized	50.0	40.0

According to engineering strain – stress curves, sample 21 in as-cast condition exhibited inelastic deformation behavior at 233.9 MPa (Appendix 2). The initial length of the sample started to reduce at the point of 293.0 MPa. After the compression strength dropped to the lower yield point of 116.3 MPa the initial length of the sample was reduced with a little increase in engineering stress. The as cast sample achieved the ultimate compression strength of 338.1 MPa with sample yielding recorded in the engineering strain range of 0.027-0.364. The compression testing stopped when the sample was reduced by 50.0 % of its initial length. The solutionizing of sample 21 increased the point of inelastic behavior to 249.4 MPa

(Appendix 2). The initial length of the sample started to reduce at the upper yield point of 288.0 MPa. The yielding of the solutionized sample started at a lower yield stress point of 211.5 MPa and ended at ultimate compression strength of 285.2 MPa. The compression testing stopped at 246.9 MPa after the sample broke. The temperature of both samples increased with the increase in engineering strain (Appendix 2). Both samples achieved their maximum temperature increase at the engineering strain of 0.74. The temperature of the sample in as cast condition increased by 50.0 °C at 338.6 MPa. The temperature of the solution hardened sample increased by 20.0 °C at the compression strength of 240.0 MPa (Appendix 2).

The grain refinement of sample 22 led to the increase in all the characteristic compression testing points in as-cast condition with respect to sample 21. Achieving a smaller grain size with a homogeneous equiaxial morphology increased the inelastic deformation point to 264.86 MPa with permanent plastic deformation onset at 296.38 MPa. The 50.0 % sample area reduction and 50.0 °C temperature increase was obtained at ultimate point of 389.32MPa.

Similar behavior was exhibited by samples 31 and 32 whereby grain refinement resulted in the increase of all characteristic compression points in sample 32 in as-cast condition (Table 4.15). In both samples, solutionizing caused a decrease in compression testing values except for upper yield point, indicating the need for higher stress in order for the plastic deformation to become permanent.

Dependance of yield strength, compression strength and ultimate point on Li/Mg ratio for samples in as-cast and solutionized condition is given in Figure 4.30. In as-cast samples the yield strength increases with increase in ratio from Li/Mg = 0.93 increase in compression strength of as-cast samples is observed with increase in ratio from Li/Mg = 0.90 to Li/Mg = 1.0, while ultimate point increases continuously with increase in ratio till Li/Mg = 1.0 (Figure 4.30 a). In solutionized condition all three characteristic compression values exhibit similar behavior increasing with the increase in ratio till Li/Mg = 1.0. Afterwards, ultimate point decreases with further increase in ratio (Figure 4.30 b). By comparing the influence of Li/Mg ratio on as-cast and solutionized samples, it can be concluded that intermetallic phases present in the sample will impact its behavior during compression testing. This mainly concerns yield strength and compression strength of as-cast samples with Li/Mg = 0.90 and Li/Mg =0.93 indicating that present intermetallic phases allowing for earlier onset of plastic deformation as well as the reduction in samples initial length.

These observations are in accordance with the results of metallographic analysis performed in the samples after compression testing.

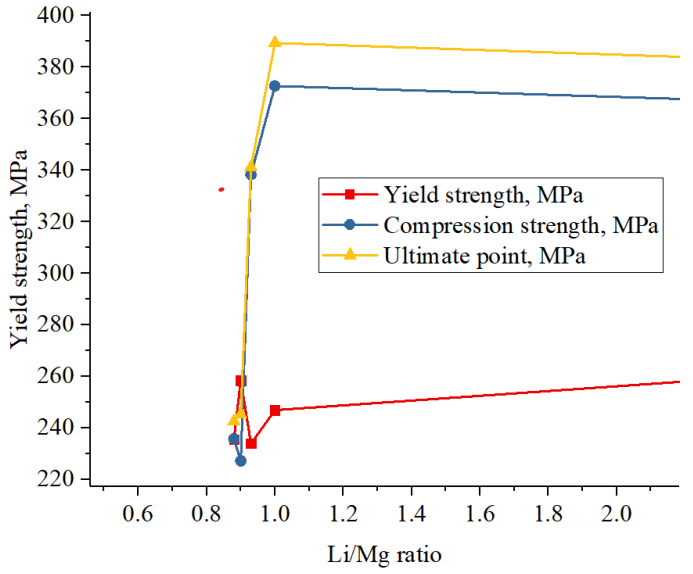

a)

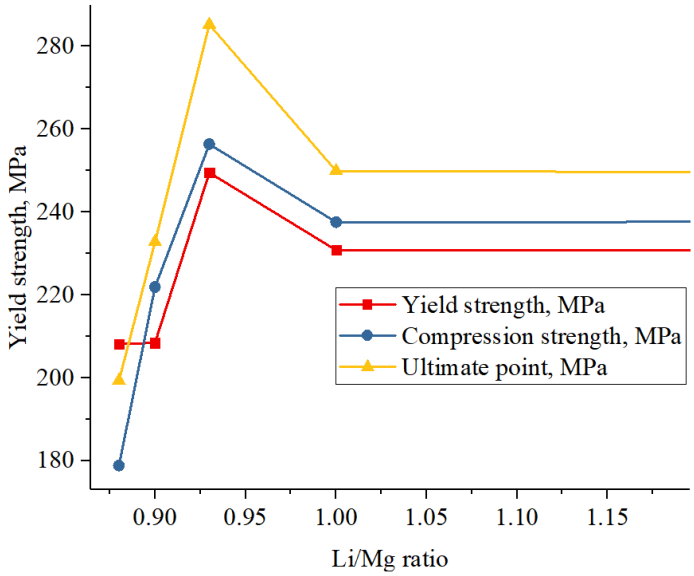

b)

Figure 4.30. Dependence of yield strength, compression strength and ultimate point on Li/Mg ratio: a) as-cast condition, b) solutionized condition

The results of the metallographic analysis indicate four typical behaviors exhibited by the samples during compression testing:

- Unequal deformation and barreling effect observed after testing samples 21, 22, 31 and 32 in as-cast condition,
- Formation of intergranular layering fracture in sample 1 in as-cast condition,
- Slip formation in solutionized samples 21 and 22,

- Formation of materials' flow lines and free movement of dislocations in solutionized samples 1, 31 and 32.

The cross-sectional microstructure of those typical behaviors is shown in Figure 4.31.

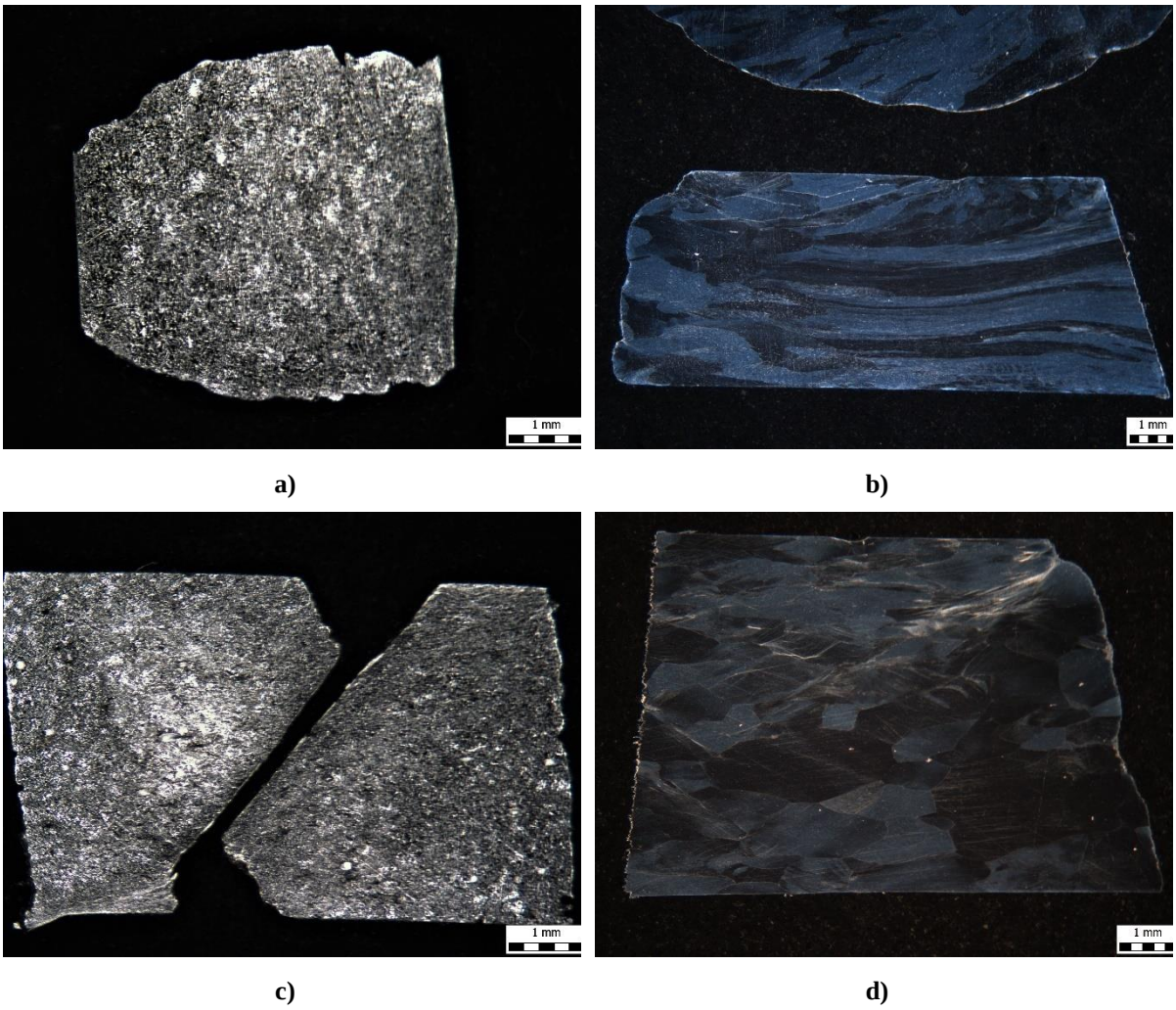

a) **b)**

c) **d)**

Figure 4.31. The cross-sectional microstructure of typical deformation behaviors: a) unequal deformation and barreling effect (sample 21 as-cast condition), b) layering fracture formation (sample 1 as-cast condition), c) slip formation (sample 2 solutionized condition), d) materials' flow line formation and free movement of dislocations (sample 1 solutionized condition)

The macrostructure of the compressed sample exhibiting barreling effect (Figure 4.31 a) is characterized by the unequal deformation between the surface area and the middle section of the sample. The measurements performed on the macrostructure indicate 49.6 % more deformation at the surface part of the sample compared to the sample's middle. This is also confirmed by the microstructural analysis given in Figure 4.32 pointing to more significant deformation of the α_{Al} dendrites near the surface of the sample. The elongation of α_{Al} dendrites perpendicular to the deformation direction resulted in the surface texture development. The α_{Al}

dendrites located near the middle part of the cross section show less deformation. The deformation had a similar effect on the Al_8Mg_5 (β) and two phase (Al_8Mg_5 (β) + Al_2LiMg (T)) area located between the branches of primary α_{Al} dendrites.

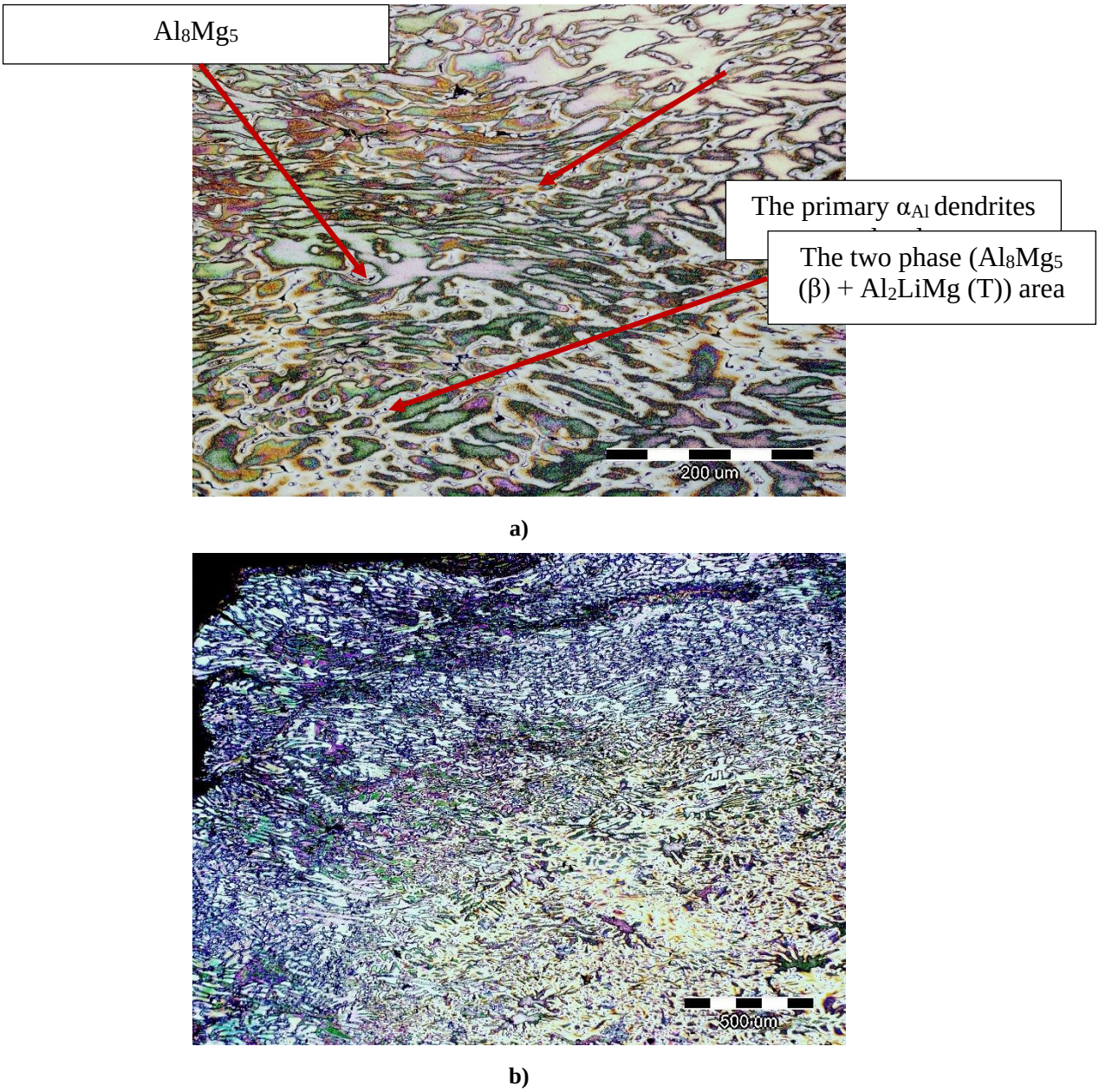

Figure 4.32. The microstructure of the sample with barrelling effect: a) surface of the sample, b) transition from the surface to the middle of the sample

The macrostructure of the samples with flow line, intergranular layering fracture and slip formation exhibit similar characteristics. In all three cases, the deformation starts at the surface of the sample and progresses towards its centre. Furthermore, the plastic deformation initiates at a 45 ° degree angle between the deformation phenomenon and the stress direction.

This indicates samples' tendency towards high shear stress zone (forging cross zone) formation. The microstructure of these typical deformation behaviours is given in Figure 4.33.

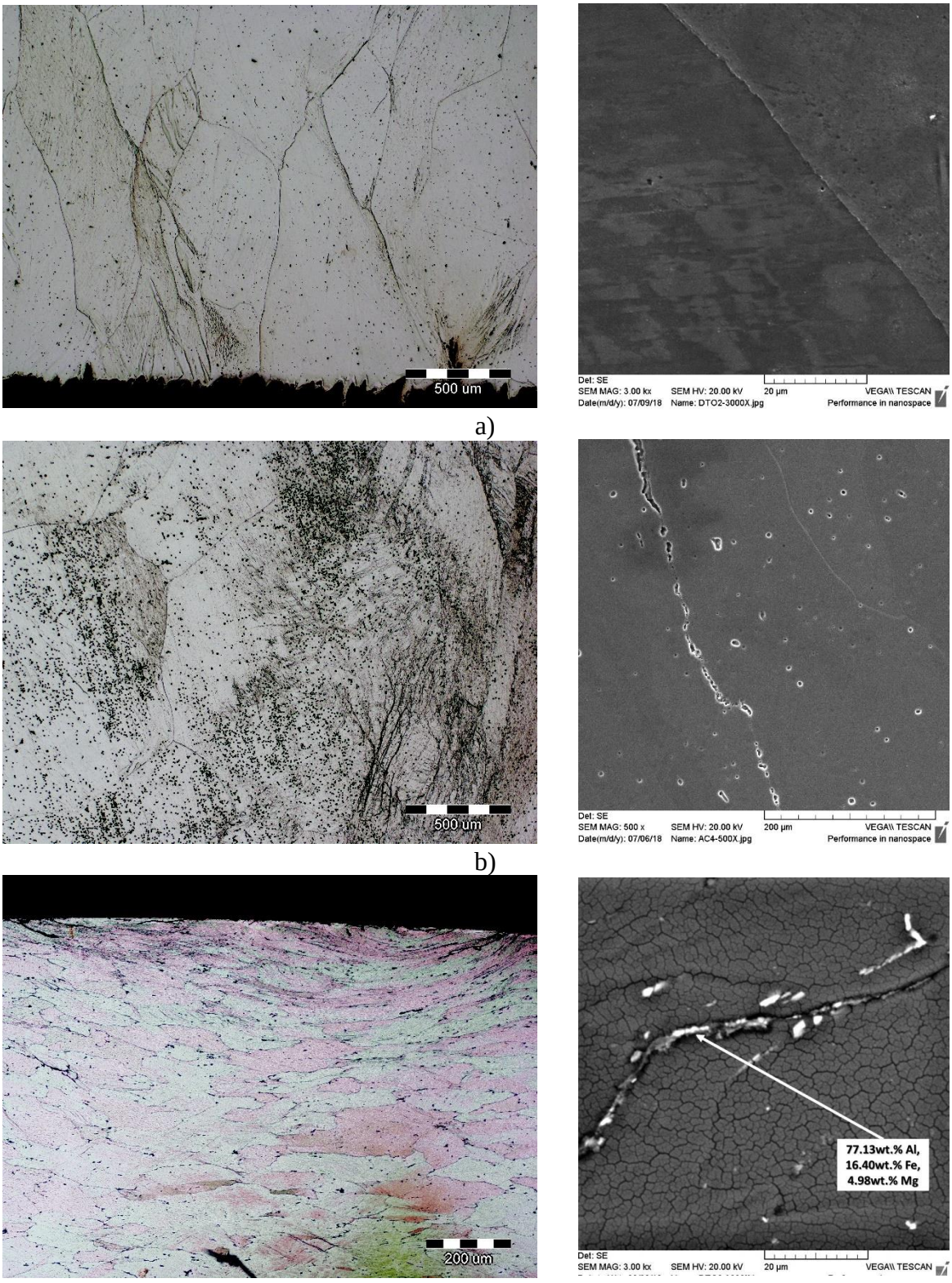

Figure 4.33. The light and SEM micrographs of typical deformation behaviours: a) flow line formation and free dislocation movements, b) intergranular layering fracture formation, c) slip formation

The results of microstructural analysis indicate that flow line formation is caused by the free movement of dislocations. The dislocation movement initiates at the grain boundaries and progresses toward the grain interior (Figure 4.33 a). Such behaviour was observed in solutionized samples due to the lack of intermetallic precipitates that would resist the movement of dislocations. The formation of intergranular layering fracture is initiated by the interaction between dislocations and intermetallic precipitates. Based on the results of light microscopy and X-ray diffraction, the intermetallic precipitates can be identified as AlLi (δ) phase. This can also explain the lack of this phenomenon in other samples because the solidification of the AlLi (δ) phase is a consequence of the high Li/Mg ratio. Finally, the slip formation is a consequence of Fe-based intermetallic phases presence. As a brittle intermetallic compound located at the grain boundary, they had a detrimental effect on compression properties and deformation behaviour of 21 and 22 samples.

4.7.2. The results of hardness measurements

The results of hardness measurements performed on the specific sections of samples in as-cast condition are given in Table 4.17 with dependence of hardness on Li/Mg ratio indicated in Figure 4.34.

Table 4.17. The results of hardness measurements

Sample	Hardness, HV		
	Number of measurements	Mean value ($\overline{HV}$)	Standard deviation (σ)
11	3	87.6	0.3
12	3	66.3	2.2
13	3	89.0	1.9
211	3	91.2	3.3
212	3	86.2	5.0
213	3	68.5	5.3
221	3	118.7	3.2
222	3	109.0	2.6
223	3	107.0	2.5
311	3	62.7	2.6
312	3	63.0	1.6
313	3	60.9	1.9
321	3	99.7	1.4
322	3	94.4	2.5
323	3	60.3	4.5

Based on the results given in Table 4.17, it can be concluded that hardness is affected by the Li/Mg ratio as well as the addition of AlTi5B1 master alloy (Figure 4.34). Consequently, the highest hardness was measured in samples 22 with Li/Mg = 1.0 and 32 with Li/Mg = 0.90 containing Ti5B1. The Li/Mg = 0.93 in sample 21 resulted in third highest hardness value, while the lowest hardness was measured in sample 31 with Li/Mg =0.88. The sample 1 with highest Li/Mg = 5.68 resulted in penultimate hardness value. Such behavior is consistent with the data available in the literature, according to which the addition of Li above a certain value (1.4 wt.%) will have a negative effect on mechanical properties [14].

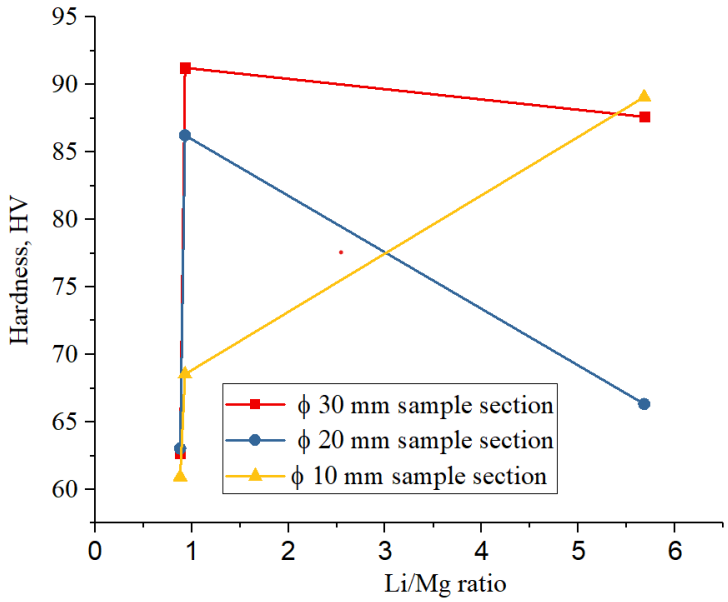

a)

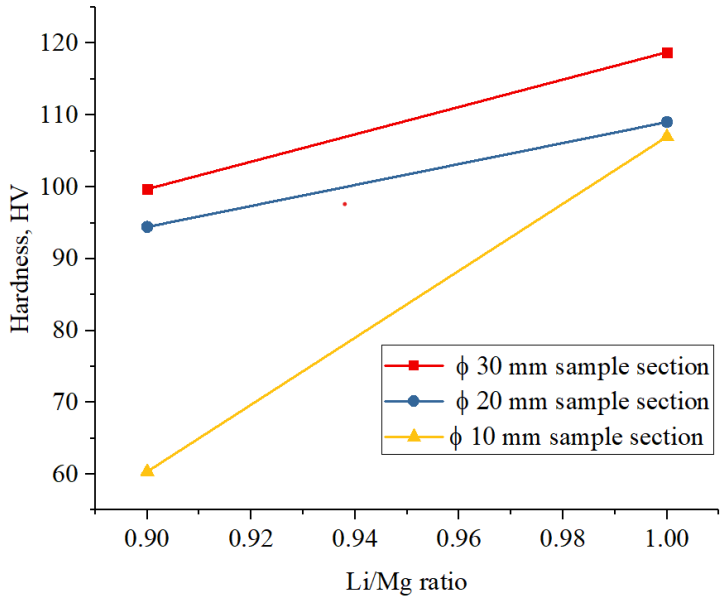

b)

Figure 4.34. Dependence of hardness on Li/Mg ratio and melt treatment: a) non grain refined samples, b) grain refined samples

Considering the influence of Li/Mg ration on hardness, it can be observed that in the grain refined samples hardness increases with increase in Li/Mg ratio in all three specific sample sections (Figure 4.34 b). In addition, the hardness values decrease with the reduction of the specific sample section. On the other hand, in the thinnest (ø 10.0 mm) section of non grain refined sample hardness increases with the increase in Li/Mg ratio (Figure 4.34 a). The impact of specific sample section on the hardness is shown in Figure 4.35.

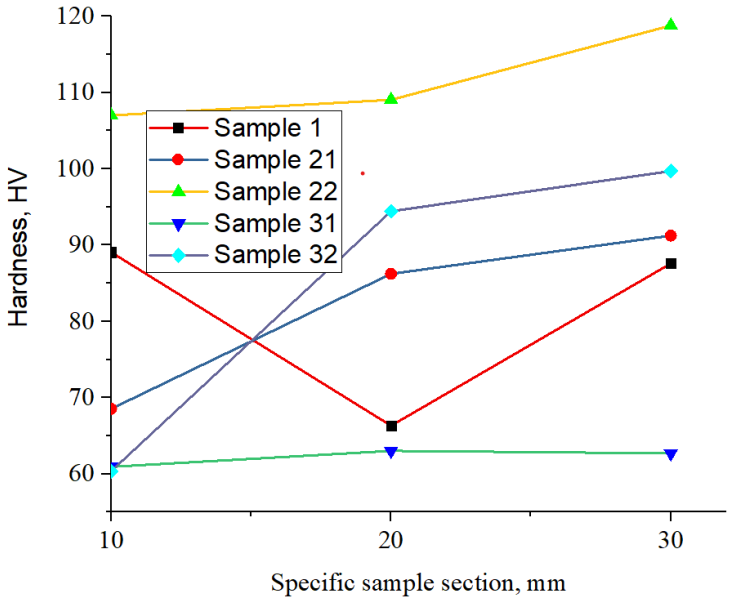

Figure 4.35. The impact of specific sample section on hardness

The graphic representation in Figure 4.35 indicates that deviation in hardness behavior occurred in sample 1. While in all other samples the hardness increases with the increase in the specific sample section, in sample 1 the lowest hardness value was measured in the central section of the sample (ø 20.0 mm) indicating the impact of crystal zone morphology on the hardness.

4.7.3. The results of microhardness measurements

The results of microhardness measurements performed on α_{Al} matrix and in the interdendritic areas of samples in as-cast condition are indicated in Table 4.18.

Higher hardness values were measured in the interdendritic areas of all samples. This indicates that intermetallic phases, mostly Al_8Mg_5 (β) and (Al_8Mg_5 (β) + Al_2LiMg (T)), solidified in the interdendritic areas have beneficial influence on hardness. The highest microhardness values of both α_{Al} matrix and interdendritic area were measured in sample 22 with Li/Mg = 1.0 processed with the addition of Ti5B1 master alloy. The following microhardness values of both areas were measured in sample 1 with a Li/Mg = 5.68, which is a consequence of the excess Li content and the solidification of precursor AlLi (δ') and Al_3Li (δ) phase within the dendritic branches of α_{Al} dendritic network. In other samples, a decrease in hardness is observed with a decrease in the Li/Mg ratio.

Table 4.18. The results of microhardness measurements

Sample	Number of measurements	α_{Al} matrix		Interdendritic area	
		Mean value ($\overline{HV}$)	Standard deviation (σ)	Mean value ($\overline{HV}$)	Standard deviation (σ)
11	3	93.90	1.13	134.50	3.63
12	3	136.07	7.90	167.73	5.81
13	3	160.87	8.44	160.53	2.81
211	3	87.137	3.12	183.90	13.0
212	3	90.97	2.60	123.80	10.31
213	3	110.33	4.80	138.13	13.79
221	3	158.23	2.63	174.50	4.45
222	3	130.87	2.49	192.50	2.19
223	3	104.40	6.15	180.13	9.46
311	3	81.43	1.02	134.40	3.90
312	3	71.57	5.80	115.33	2.30
313	3	90.70	4.25	137.63	8.58
321	3	88.83	7.14	130.46	2.80
322	3	88.50	1.57	185.06	4.42
323	3	82.63	1.01	134.40	3.90

The dependance of microstructure on specific sample section for α_{Al} matrix and interdendritic areas is shown in Figure 4.36. The given dependance indicates decrease in microhardness of α_{Al} matrix in samples 1, 21 and 31 with increase in specific sample section. On the other hand, in samples 22 and 32 the microhardness of α_{Al} matrix increases with the increase in specific sample section. These results indicate the α_{Al} matrix's dependance on grain size and morphology. Furthermore, higher microhardness values in smaller specific sample sections are a consequence of directional solidification and development of chill and columnar crystal zones, as indicated by the results of macrostructure analysis (Figure 4.36 a). Unlike α_A matrix, the microhardness of the interdendritic area does not show a clear dependence on the specific section of the sample. The highest values of interdendritic area's microhardness in samples 1, 22 and 32 were measured in a specific section of ø 20.0 mm, while the lowest values were measured in the section of ø 30.0 mm. Contrarily, for samples 21 and 31, the highest

microhardness of interdendritic area was measured in a specific section of ø 30.0 mm and the lowest in a section of ø 20.0 mm (Figure 4.36 b).

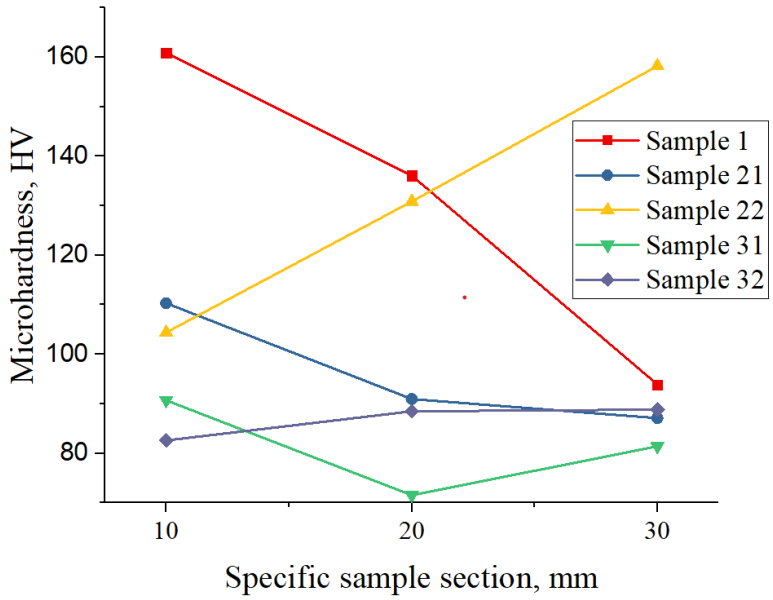

a)

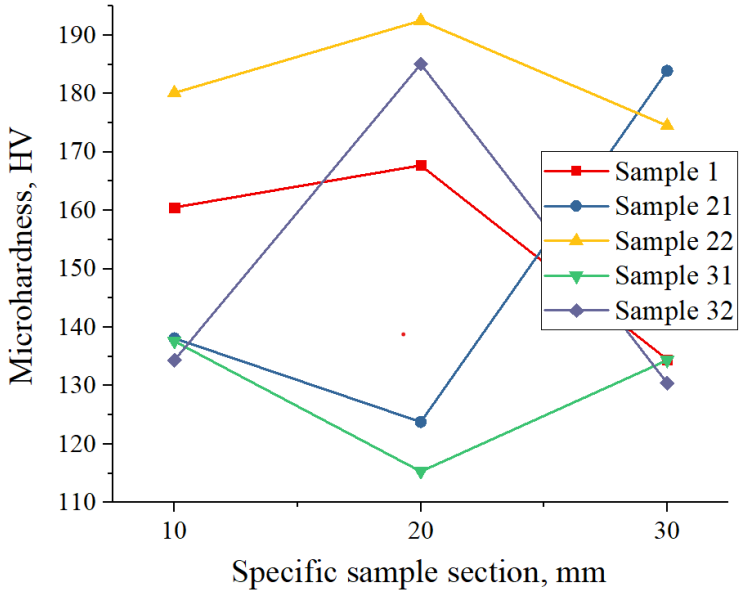

b)

Figure 4.36. Dependence of microhardness on specific sample section in: a) α_{Al} matrix, b) interdendritic areas

Dependance of microhardness of α_{Al} matrix and interdendritic area on Li/Mg ratio is given in Figure 4.37. The microhardness of α_{Al} matrix for specific sample sections of ø 20.0 mm and ø 30.0 mm increases with increase in Li/Mg ratio till the value of Li/Mg = 1.0. Further increase in Li/Mg ratio increases the microhardness of ø 20.0 mm specific section, while the microhardness of ø 30.0 mm specific section decreases sharply (Figure 2.37 a). The

microhardness of specific sample section of ø 10.0 mm decreases in the intervals between Li/Mg = 0.88 to Li/Mg = 0.90 and Li/Mg = 0.93 to Li/Mg = 1.0 (Figure 2.37 a).

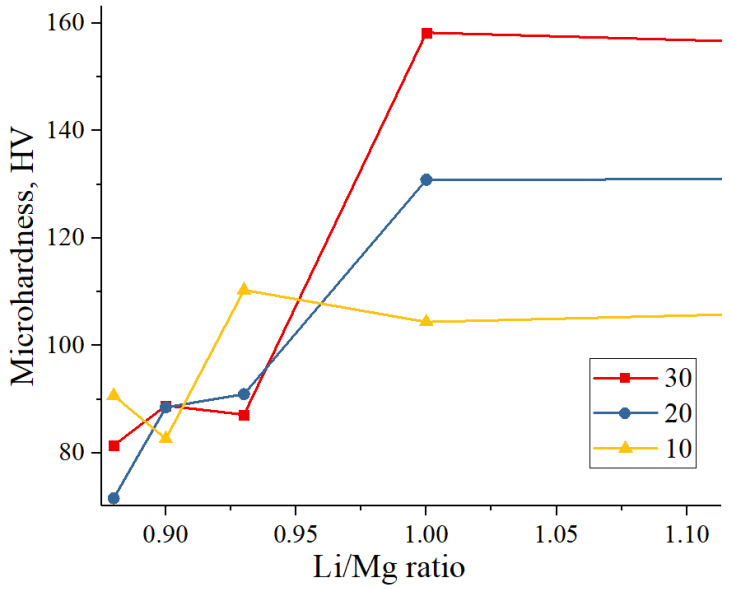

a)

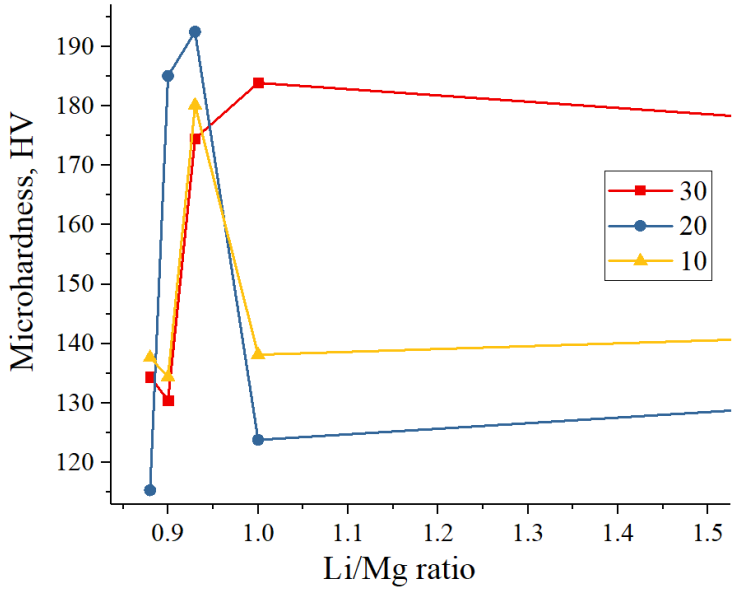

b)

Figure 4.37. Dependence of microhardness on Li/Mg ratio: a) α_{Al} matrix, b) interdendritic areas

In the range from Li/Mg = 0.88 to Li/Mg = 1.0, the specific sample sections ø 10.0 mm and ø 30.0 mm show the same behavior, with a decrease in the microhardness value of the interdendritic area at Li/Mg= 0.93. Afterwards, the microhardness of the interdendritic area in ø 10.0 mm specific section decreases at Li/Mg = 1.0 and increases with the further increase in the ratio. The specific section of ø 30.0 mm exhibits the opposite behavior. At a specific section

of ø 20.0 mm, the microhardness of interdendritic area increases till Li/Mg = 1.0 and at the ratio Li/Mg = 5.68.

The similar microhardness behavior of the α_{Al} matrix and the interdendritic area is observed only in the specific section of ø 10.0 mm. At a specific section of ø 20.0 mm, the microhardness of the interdendritic area and the α_{Al} matrix show the similar behavior up to Li/Mg =1.0, while the microhardness of ø 30.0 mm specific sections shows the completely opposite behavior. Based on this, it can be concluded that different specific sections (different cooling rates) differently affect solidification sequence and microstructure development for different Li/Mg ratios. If the increase in the microhardness value of both areas is taken into account, it can be concluded that Li/Mg = 1.0 is optimal for the ø 30.0 mm section, while the ratio Li/Mg = 0.93 is optimal for the ø 10.0 mm and ø 20.0 mm sections.

4.7.4. The results of nanoindentation

The results of nanoindentation measurements are given in Table 4.19. The measurements were performed on samples in as-cast and solutionized conditions. Both, hardness and modulus were determined till the surface displacement depth of 13 000 nm. The recorded hardness - and modulus – surface displacement curves are given in Appendix 3.

Table 4.19. The results of nanoindentation measurements

Sample	Condition	Hardness, GPa	Modulus of elasticity, GPa
1	As-cast	0.86	73.6
	Solutionized	0.96	75.0
21	As-cast	0.92	66.0
	Solutionized	0.95	73.3
22	As-cast	1.01	65.6
	Solutionized	1.0	73.0
31	As-cast	0.65	52.0
	Solutionized	0.9	84.0
32	As-cast	0.89	81.0
	Solutionized	0.70	82.0

The results of nanoindentation measurements indicate higher hardness and modulus values for samples in solutionized compared to the as-cast condition. The difference in the hardness and modulus behavior between these two metallurgical conditions can also be seen in the hardness- and modulus - surface displacement curves (Appendix 3). As a rule, for samples in the as-cast condition, the values of hardness and modulus increase from the initial position to a displacement depth of 1 000 nm, after which both values decrease. For samples in the solutionized condition, both values decrease after the initial displacement position. Deviation from this behavior was observed in sample 22 for both conditions. Achievement of higher modulus values in solutionized samples confirms that it is an intrinsic proportion of the alloy typically attributed to electron redistribution between the Al-Li bounds in the α_{Al} solid solution. These results differ from observations available in the literature [17] attributing the modulus increase to the development of intermetallic phases.

Considering that the increase in modulus of Al-Li-X alloys is primarily attributed to the addition of Li, the dependence of hardness and modulus on Li content for samples in as-cast and solutionized condition is given in Figure 4.38.

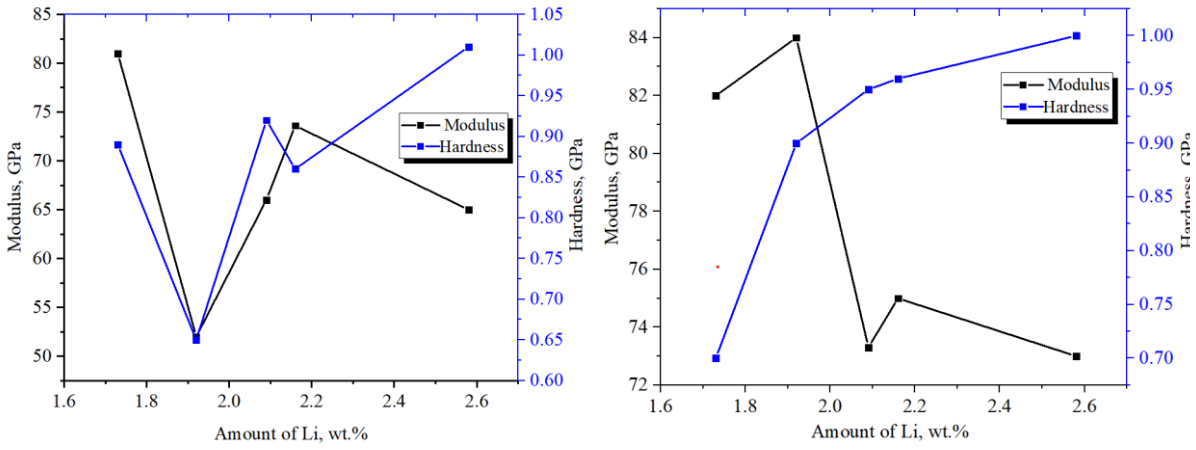

Figure 4.38. Dependence of hardness and modulus on Li content for samples in: a) as-cast condition, b) solutionized condition

For samples in the as-cast condition, the highest modulus was recorded for the sample with lowest Li content (1.73 wt.%). An increase in the Li content to 1.92 wt.% led to a drastic drop in the modulus value. A further increase in Li content to values of 2.09 wt.% and 2.16 wt.% increases the modulus. Ultimately, at the highest Li content, modulus dropped. In contrast, the hardness values increase with an increase in the Li content above 1.92 wt.%. If the Li/Mg ratio is taken into account when interpreting the modulus behavior of as-cast samples, it can be

observed that the lowest modulus of 52 GPa was measured at the lowest Li/Mg = 0.88 ratio, while higher values of the modulus were observed at higher Li/Mg ratio. These results indicate the influence of Mg on Li redistribution during solidification and formation of Li-enriched α_{Al} matrix.

In the solutionized samples the modulus decreases with an increase in Li content above 1.93 wt.%. These observations deviate from the data available in literature according to which each 1 wt.% of Li added increase modulus of elasticity by 6 % for the additions up to 4.2 wt.% Li [14].

4.8. The results of microstructure degradation assessment

The microstructure stability in corrosive environment was estimated using the methods of electrochemical and chemical degradation. Both methods were used in order to obtain more parameters and to better estimate the behavior of Al-2.18Mg-1.92Li alloy in various types of outdoor services, especially in marine and automotive applications.

4.8.1. Defining the initial microstructure in the as-cast and solution hardened condition

The macrostructure of the sample in as-cast and solution hardened condition at magnifications of 9 X and 50 X is given in Figure 4.39.

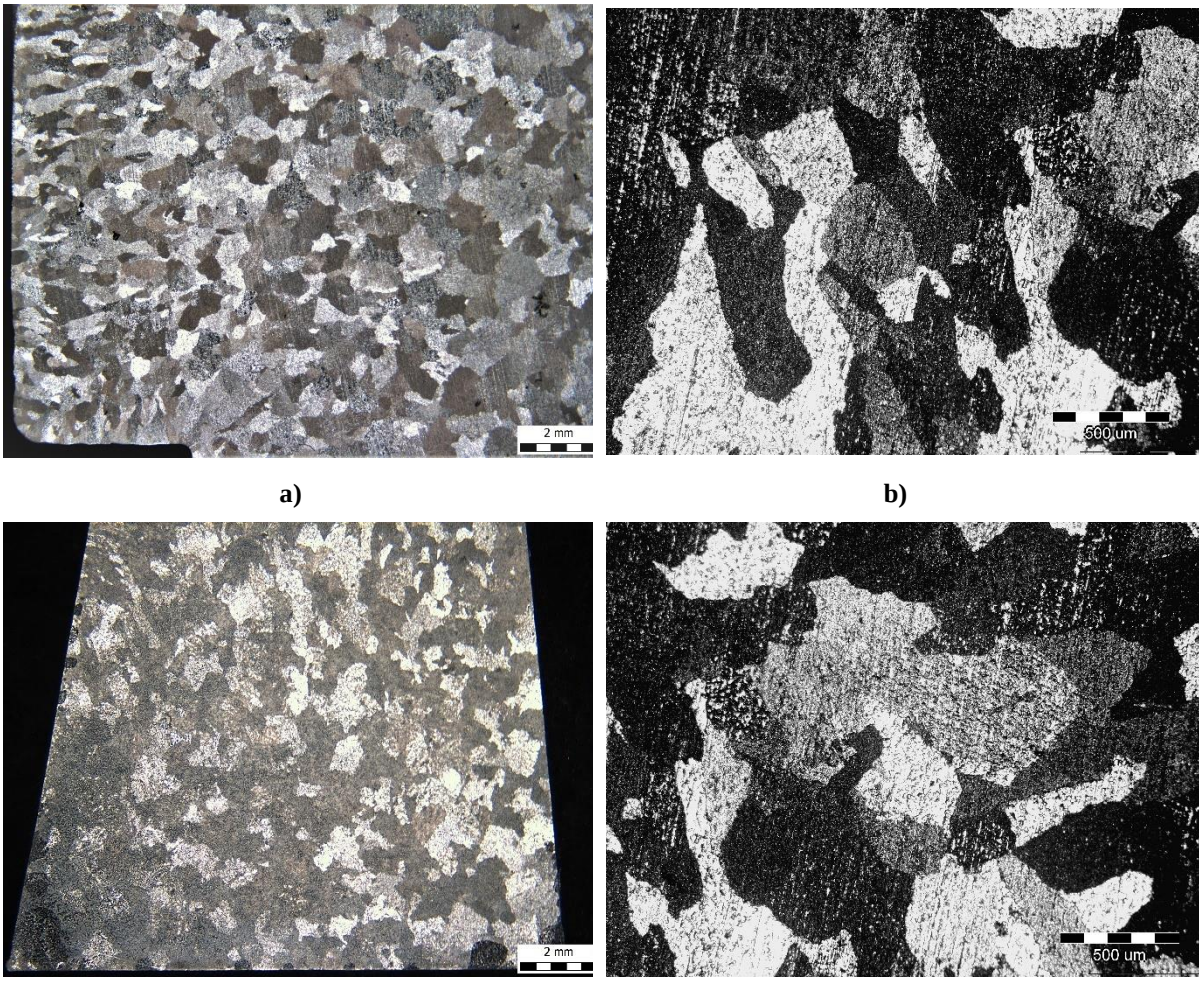

Figure 4.39. The macrostructure of the sample in: a) as-cast condition at magnification of 9 X, b) as-cast condition at magnification of 50 X, c) solution hardened condition at magnification of 9 X, d) solution hardened condition at magnification of 50 X

The macrostructure of the sample in as-cast condition has a heterogeneous grain morphology consisting of chill, columnar and equiaxed zones. A zone of chill crystals with a average thickness of 0.86 mm formed along the outer edge of the sample is followed by a zone of columnar crystals with an average thickness of 2.8 mm formed in the direction opposite to the heat flow, and zone of equiaxed crystals with average thickness of 11.69 mm occupying the central part of the sample (Figure 4.39 a and c). The solutionizing led to the homogenization of grain morphology (Figure 4.39 b). The macro and micro grain size values measured on five different details at magnification of 50 X are given in Table 4.20.

Table 4.20. The macroscopical and microscopical grain size according to ASTM E112-10

Sample	L, mm	P_i, intersections/mm	P_L, intersections/mm	Macro grain size	G
As-cast	1600	87	2.718	12.9	0
Solutionized	1800	112	3.5	13.6	0

The results of grain size measurements given in Table 4.20 indicate that solution hardening did not only affect the homogenization of the grain morphology, but also decreased macro grain size. However, correlating the measured values of the macro grain size with the data in the ASTM E112-10 standard, the average grain size (G) at the micro level remained 0.

The microstructure of the samples in as-cast and solution hardened conditions is given in Figure 4.40. The microstructure of the sample in as-cast condition consists of α_{Al} dendritic network and precipitates located between the branches of α_{Al} dendrites (Figure 4.40 a and b). The precipitates located between differently oriented primary α_{Al} dendritic branches have coarse morphology corresponding to Al_8Mg_5 (β) phase (Figure 4.40 a). The precipitates located between the secondary branches of α_{Al} dendrites have rod-like morphology and can be identified as Al_2LiMg (T) phase (Figure 4.40 a). Additionally, in the microstructure of as-cast sample, a two phase (Al_8Mg_5 (β) + Al_2LiMg (T)) region can be observed, where solidification of Al_8Mg_5 (β) occurred near the previously solidified globular Al_2LiMg (T) phase (Figure 4.40 b). The microstructural analysis of the solutionized sample revealed the α_{Al} grains (Figure 4.40 c) and residual phases precipitated inside and at the grain boundaries (Figure 4.40 c). The phase with globular morphology located inside the α_{Al} grains corresponding to AlLi (δ) phase (Figure 4.40 c and d), while phase with coarse morphology located at the α_{Al} grain boundaries coincides with c Al_8Mg_5 (β) phase. The AlLi (δ) phase is homogeneously distributed inside the grains of α_{Al} matrix with no Precipitation free zone (PFZ) near the grain boundaries (Figure 4.40 c and d).

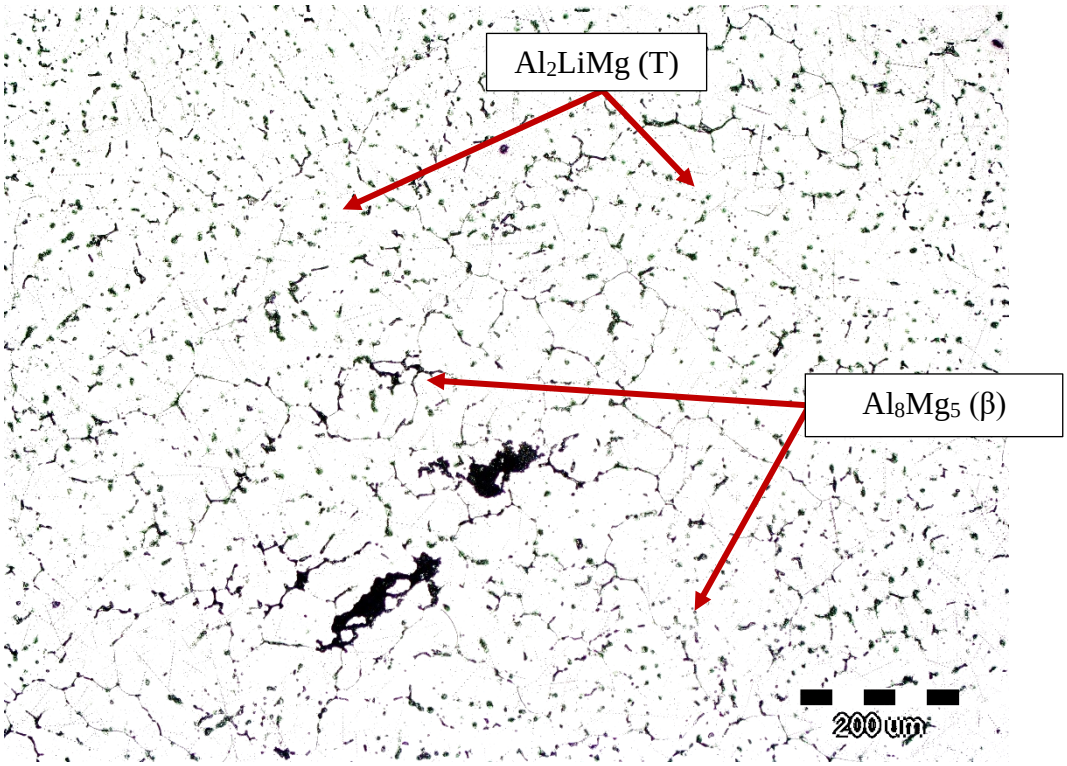
Al2LiMg (T)
Al8Mg5 (β)
200 um

a)

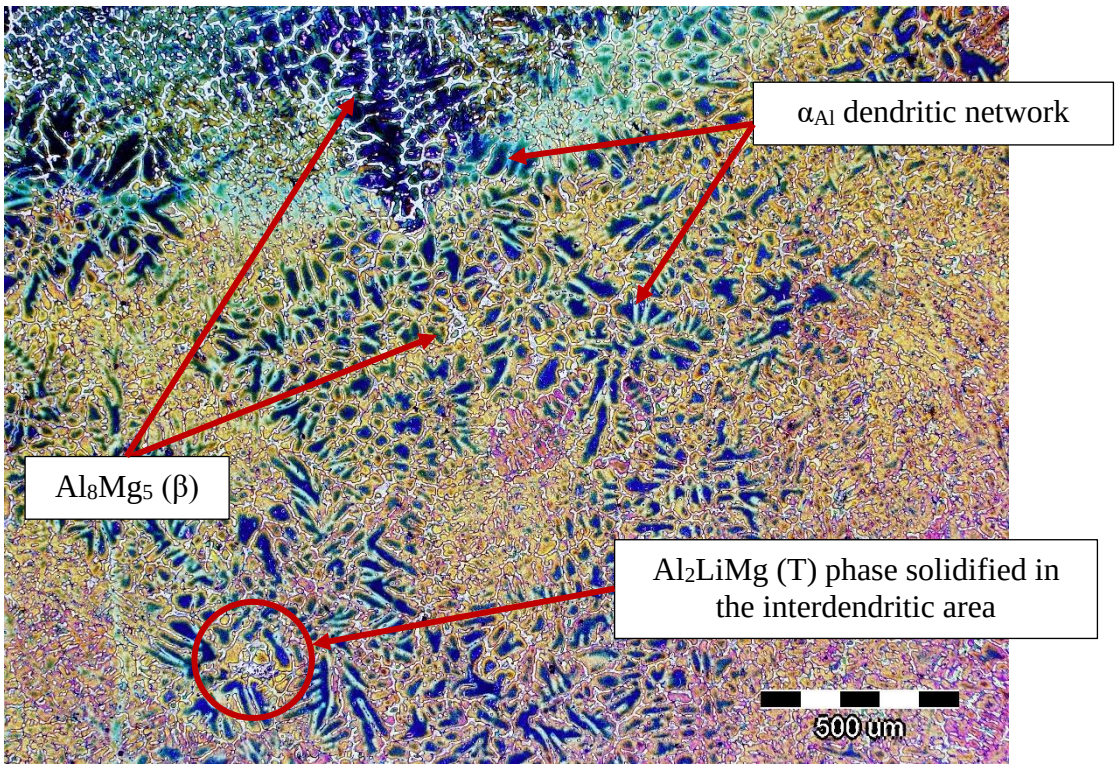
αAl dendritic network
Al8Mg5 (β)
Al2LiMg (T) phase solidified in the interdendritic area
500 um

b)

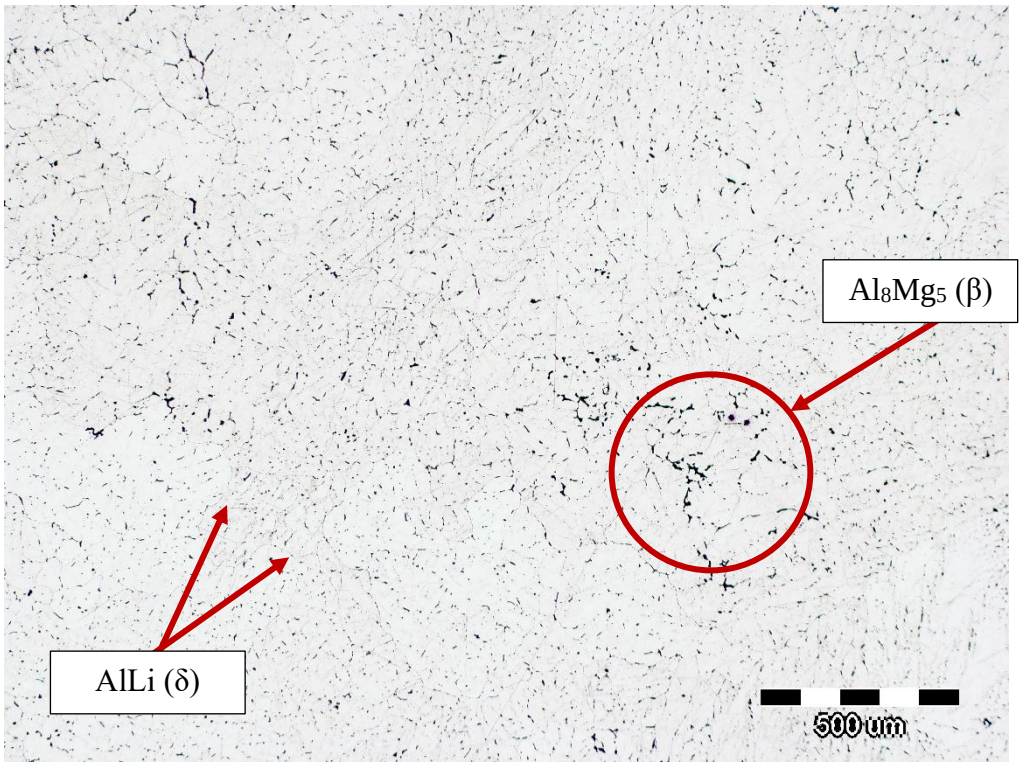

c)

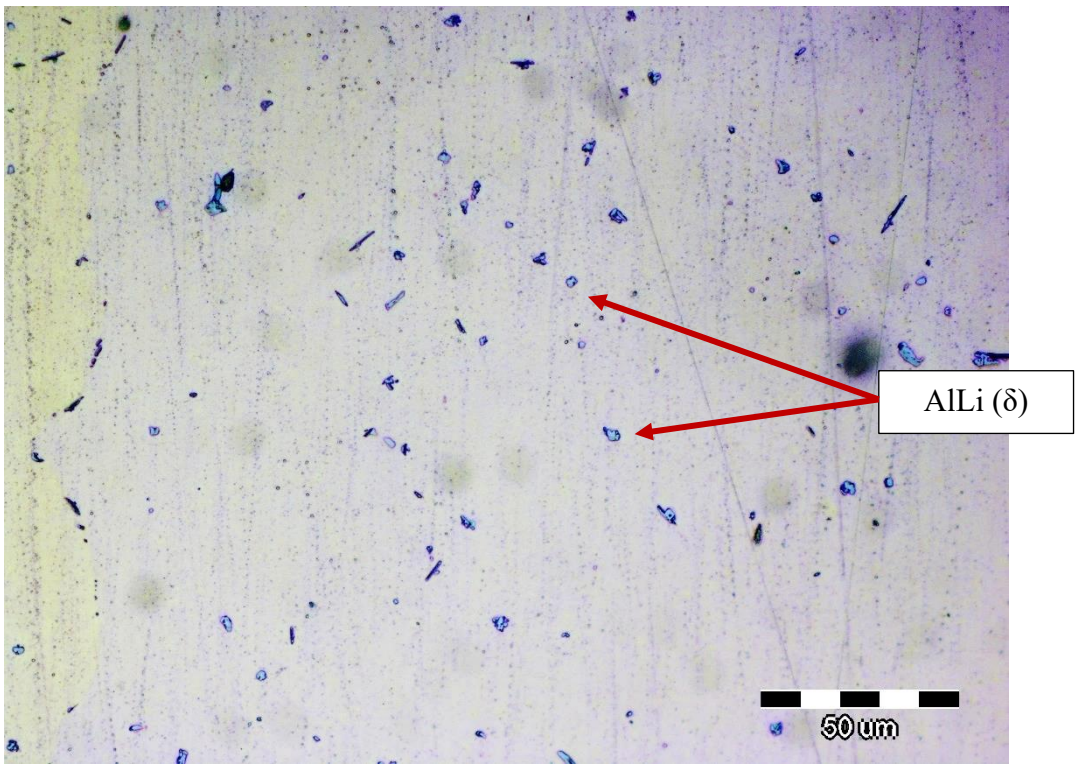

d)

Figure 4.40. The microstructure of the sample in: a) as-cast condition etched with Weck's etching solution, b) as-cast condition etched with Keller's etching solution, b) solutionized condition etched with Weck's etching solution, b) solutionized condition etched with Keller's etching solution

Comparing the results of microstructure analysis with the predicted solidification sequence for Li/Mg < 1 ratio based on the results of DSC analysis and thermodynamic

calculations, the absence of metastable Al_3Li (δ'), AlLi (δ) and Al_3Mg_2 phases was observed. This can be considered a consequence of non-equilibrium solidification under realistic conditions, where instead of the formation of two separate phases AlLi (δ) and Al_3Mg_2, the formation of two-phase region (Al_8Mg_5 (β) + Al_2LiMg (T)) occurred.

The temperature and holding time of solutionizing was calculated to dissolve all intermetallic phases and obtain bulked α_{Al} matrix. However, the temperature selection based on the predicted solidification sequence and holding time allowed for AlLi (δ) phase remnant. Although, it did not result in desired effect, the results of this research can be considered relevant due to the natural aging tendency of Al-Mg and Al-Mg-Li alloys.

4.8.2. Results of electrochemical degradation testing

The Time dependance of open circuit potential and Tafel polarization curves are given in Figure 4.41 with extrapolated results of electrochemical testing indicated in Table 4.21.

The negative corrosion potential (E_{corr}) recorded during Time dependance of open circuit potential measurements indicated instability of the samples and their dissolution during testing (Figure 4.41 a and Table 4.21). The sample in as-cast condition (AC) showed less negative potential (-755 mV) compared to the solutionized sample (-767 mV) indicating higher resistance to microstructure degradation (Table 4.20). However, the increase in corrosion potential of the solutionized sample (TO) during degradation pointed to spontaneous passivation (Figure 4.41 a). The Tafel polarization curves ratified higher degradation resistance of sample in as-cast condition. The extrapolation of obtained Tafel polarization curves indicated more negative corrosion potential (-752.52 mV), higher current density ($4.61 \cdot 103$ $\mu A.cm^2$), anode slope (174.76 mV/dec), cathode slope (742.96 mV/dec) and corrosion rate (51.24 mm/year) for solutionized sample. While current density and anode slope are a consequence of dealloying and dissolution of Al from the matrix, the higher cathode slope is attributed to changes in bulk solution chemistry and increase in pH value. However, the solution's pH value remained unimpacted by the electrochemical testing (pH 0.4), indicating that the increase in cathode slope is due to a local change in solution's chemistry. This led to the spontaneous passivation of the solution hardened sample and increase in corrosion potential (Figure 4.41 a and Table 4.21).

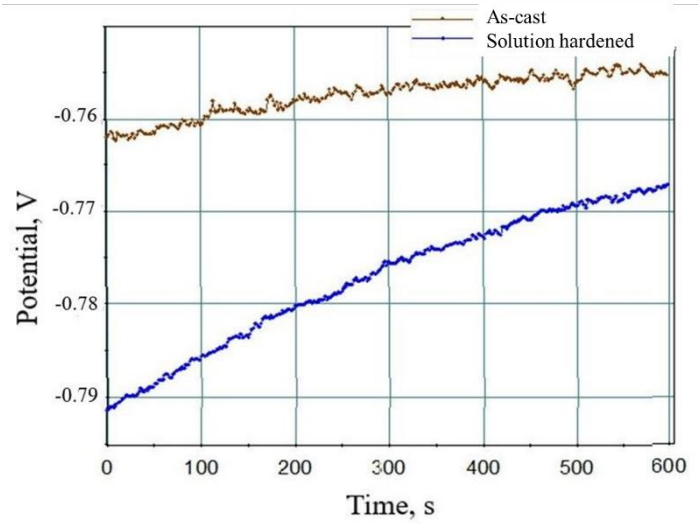

a)

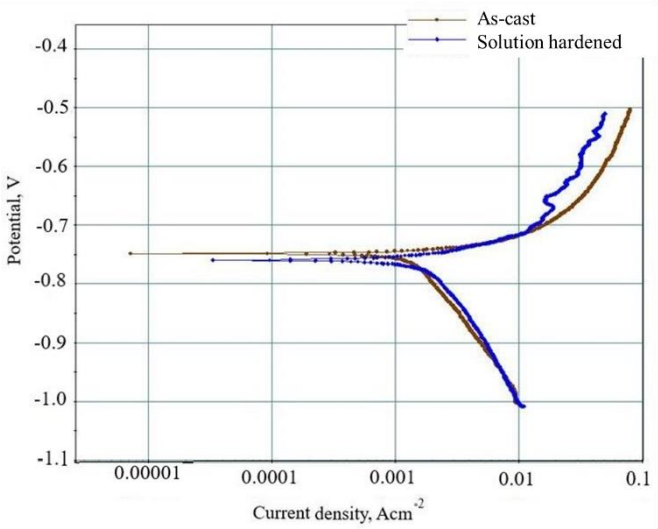

b)

Figure 4.41. The results of electrochemical testing: a) Time dependence of open circuit potential, b) Tafel polarization curves

Table 4.21. The results of electrochemical testing

Sample	E_{corr}, mV	i_{corr}, μA/cm^2	B_a, mV/dec	B_c, mV/dec	V_{corr}, mm/ year
As-cast	-749.84	1.52×10^3	38.60	296.26	17.01
Solutionized	-752.52	4.61×10^3	174.76	742.96	51.24

The macrostructure and microstructure of the samples after electrochemical testing are given in Figure 4.42. The macrostructure of the exposed surface of the sample in as-cast condition after degradation indicated the equally distributed cavities across the exposed surface (Figure 4.42 a and c). On the other hand, the pitting corrosion of the solutionized sample initiated and propagated at the grain boundaries (Figure 4.42 b) in proximity to the phases (Figure 4.42 d). The microstructural analysis of the cross-section of the sample indicated cavity

formation at the surface of both samples (Figure 4.42 e and f). In the as cast sample the degradation progressed by dissolution of the Al_8Mg_5 (β) and Al_2LiMg (T) phases located between the branches of the α_{Al} dendritic network (Figure 4.42 e and g). In the solution hardened sample degradation is manifested as intergranular and transgranular involving the grain boundaries and α_{Al} grains. The remnant of the AlLi (δ) phase inside the α_{Al} grains resulted in the cavity formation and sample surface layering (Figure 4.42 g and h).

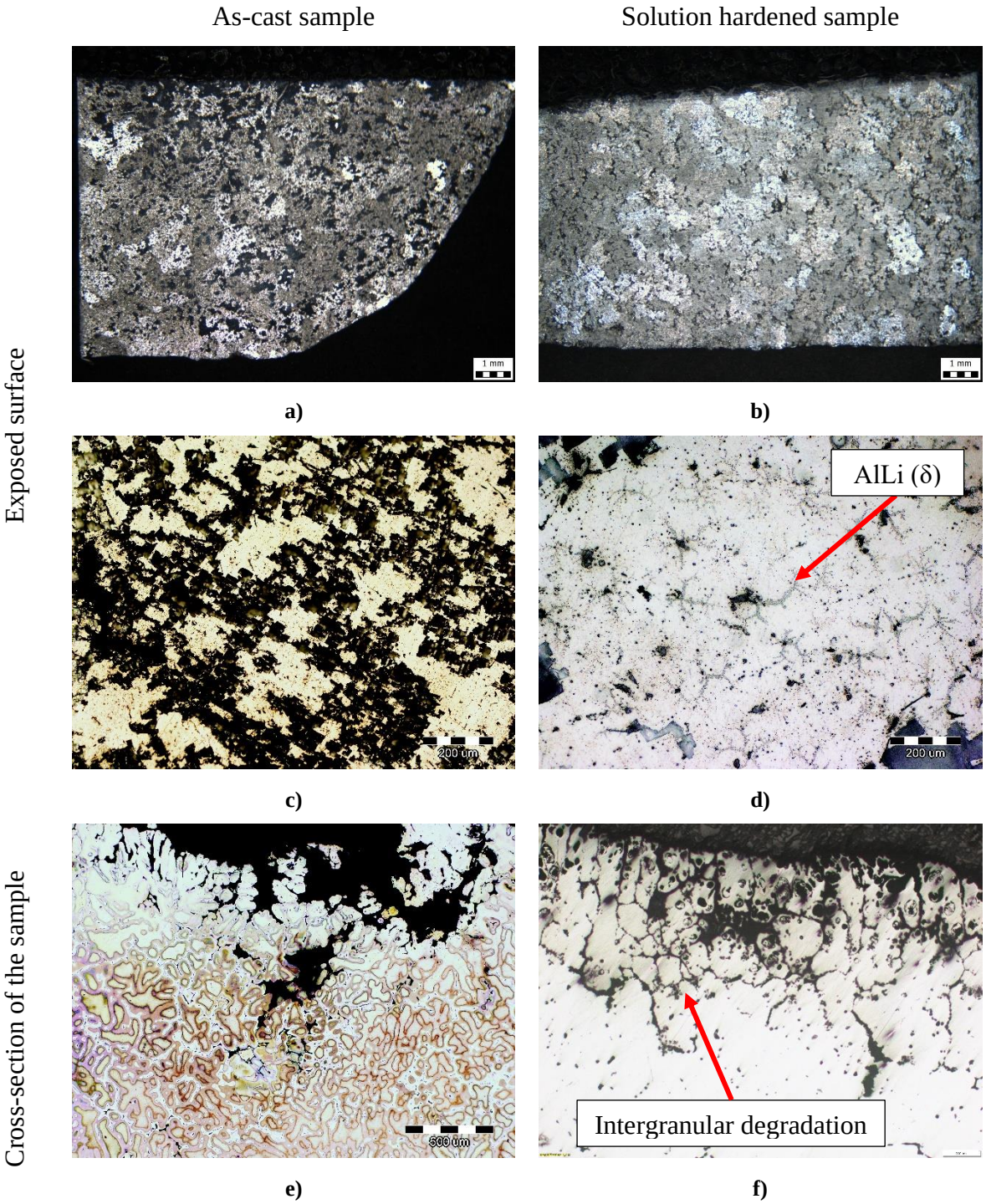

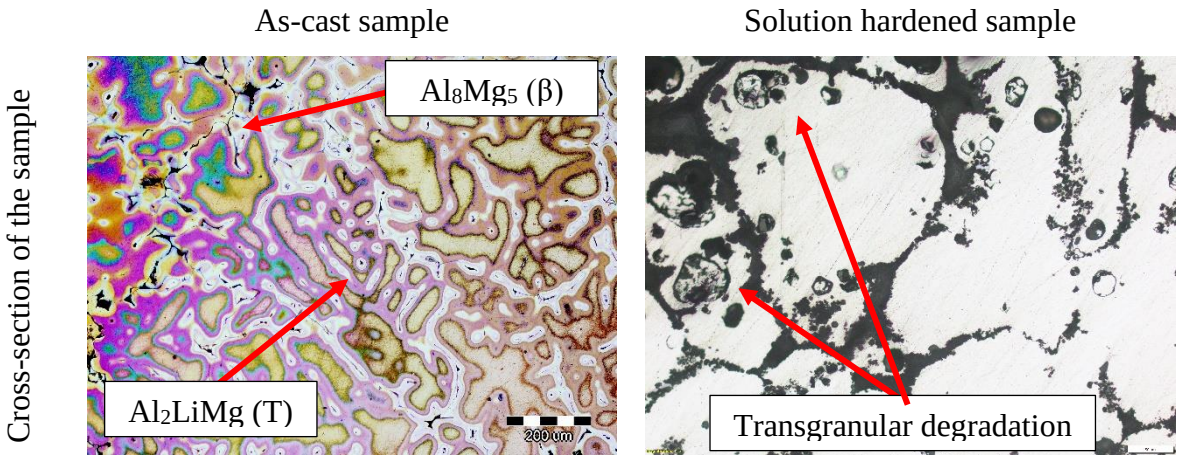

Figure 4.42. The structure of the samples after electrochemical testing: a) macrostructure of the exposed surface of the as-cast sample, b) macrostructure of the exposed surface of the solution hardened sample, c) microstructure of the exposed surface of the as cast sample, d)microstructure of the exposed surface of the solutionized sample, e) microstructure of the perpendicular surface of the as cast sample, f) microstructure of the perpendicular surface of the solutionized sample, g) phase involvement during degradation of as-cast sample, h) dissolution of the α_{Al} matrix in solutionized sample

4.8.3. Results of chemical testing

The impact of chemical degradation time on physical properties of the samples and calculated corrosion rate are given in Table 4.22.

Table 4.22. The impact of chemical degradation time on the physical properties of the sample

Sample	Exposure time, h	m_S, g	m_E, g	Δm, g	v_{corr}, 10^{-5} g/s
AC1	5	12.1	12.1	0.06	9.3
AC2	24	11.1	11.1	0.20	6.9
AC3	48	8.8	8.7	0.35	5.9
AC4	72	13.6	13.6	0.17	1.9
TO1	5	13.1	13.1	0.07	11.8
TO2	24	12.0	12.0	0.26	9.0
TO3	48	12.8	12.8	0.21	3.6
TO4	72	16.4	16.4	0.17	1.9

During degradation in corrosive environment the decrease in the mass of the as-cast and solutionized samples was observed (Table 4.22). The mass loss (Δm) increased with the increase in exposure time, up to a period of 72 h. The highest corrosion rate for both conditions was calculated for the exposure time of 5 h. Further increase in exposure time led to a decrease in corrosion rate. Higher corrosion rates were calculated for the solution hardened sample,

except for the degradation period of 48 h. The change in pH value and chemical composition of the EXCO solution with respect to the exposure time is shown in Table 4.23.

Table 4.23. The change in pH value and chemical composition of the EXCO solution with respect to the sample exposure time

Sample	Exposure time, h	Starting pH	Final pH	Chemical composition of the EXCO solution, mg/L		
				Al	Li	Mg
AC1	5	0.4	0.45	233	10.4	6.24
AC2	24	0.4	1.02	778	35.6	21.3
AC3	48	0.4	2.0	771	47.4	21.5
AC4	72	0.4	3.29	797	45.9	21.5
TO1	5	0.4	0.48	278	24.8	12
TO2	24	0.4	1.44	960	47.7	19.6
TO3	48	0.4	3.24	903	45.7	21.5
TO4	72	0.4	3.31	932	53.6	25.4

As indicated by Table 4.23, the solutions' pH values increase with the increase in exposure time. The pH value of ECXO solution remains acid for all exposure periods. A higher increase in pH value was observed for solutionized samples at all exposure times. Based on the dependence of the corrosion rate on the pH value of the solution, shown in Figure 4.43, it can be concluded that the corrosion rate decreases with the increase in the pH value. The obtained observations are in accordance with data from the literature [277, 289] indicating 0.4 pH value as critical for Al-Li alloys. The higher corrosion rate for the as-cast sample in the period of 48 h is explained by slower increase in solutions pH value (Figure 4.43).

The results of ICP-MS analysis of the solution after sample degradation indicate the occurrence of rapid anodic and cathodic reactions leading to dealloying of α_{Al} solid solution through Li^{+}, Mg^{2+} and Al^{3+} cation release (Table 4.23). In both conditions the Al release is highest, followed by Li and Mg. The solution used in degradation of solutionized samples exhibited higher amounts of all three components due to the α_{Al} solid solution bulking with Li and Mg. From the dependance of component dissolution on the pH value (Figure 4.44), formation of this bulked α_{Al} solid solution and dissolution of phases, except for AlLi (δ), resulted in the same behavior exhibited by Al, Li and Mg. On the other hand, in the as-cast sample Li shows different behavior during dealloying (Figure 4.44 a). While the amounts of Al and Mg in solution increase slowly after exposure time of 24 h, Li continues to grow till the

period of 48 h. This indicates occurrence of different degradation mechanisms during the exposure of as-cast samples.

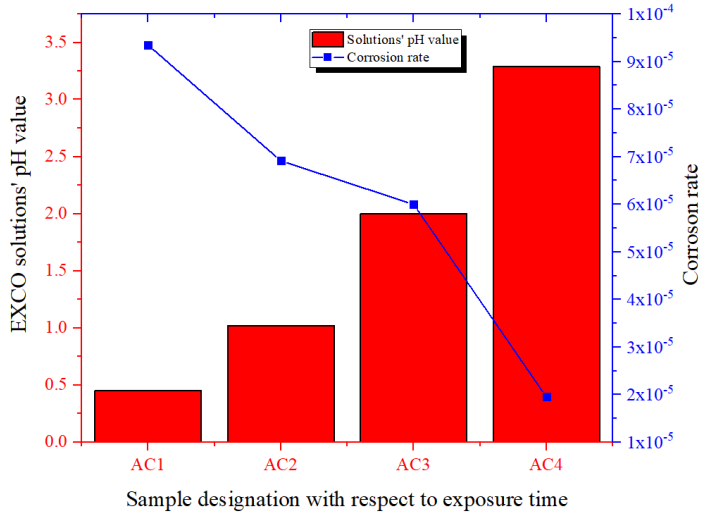

a)

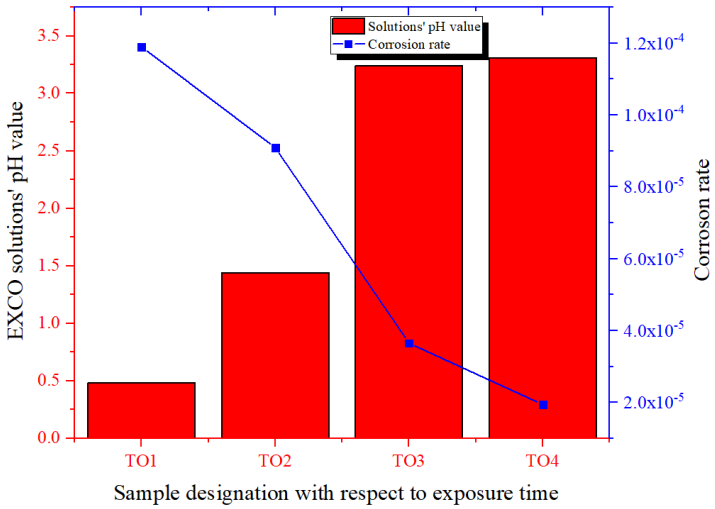

b)

Figure 4.43. Dependence of corrosion rate on EXCO solution pH value for: a) as-cast sample, b) solutionized sample

The results of metallographic analysis of the samples after degradation are given in Appendix 4. The metallographic analysis comprehended macrostructure and microstructure of the exposed surface without preparation, and microstructure of the samples' cross-section after standard metallographic preparation. The macrostructure and microstructure of the exposed surface indicate that the degradation initiated and progressed along the grain boundaries for both conditions. However, when analysing the microstructure of the cross-section of the samples in the as-cast condition, it can be seen that the degradation for a period between 5 and 24 h first affects the Al_8Mg_5 (β) and Al_2LiMg (T) resulting in the formation of cavities in the

interdendritic area. Further increase in exposure involved other intermetallic phases, mostly Al_2LiMg (T) and (Al_8Mg_5 (β) + Al_2LiMg (T)). The microstructure analysis of the solutionized samples' cross-section pointed out the degradation progression across the grain boundaries and AlLi (δ) phase in their proximity.

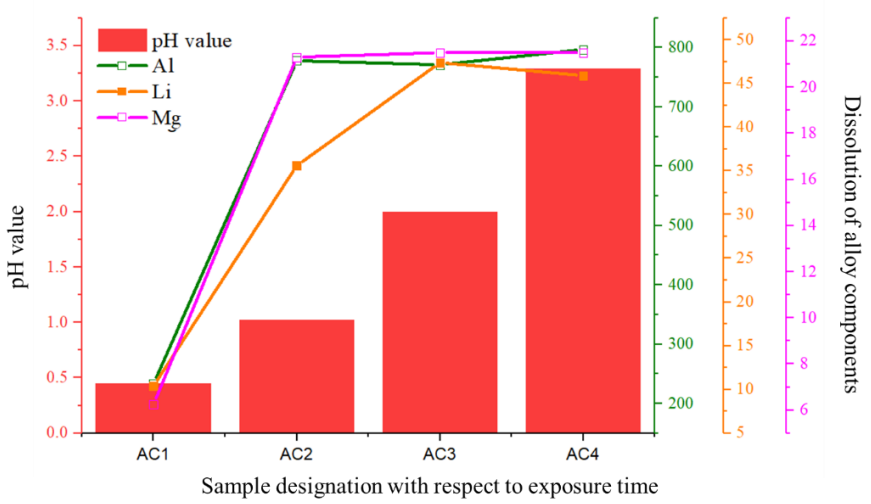

a)

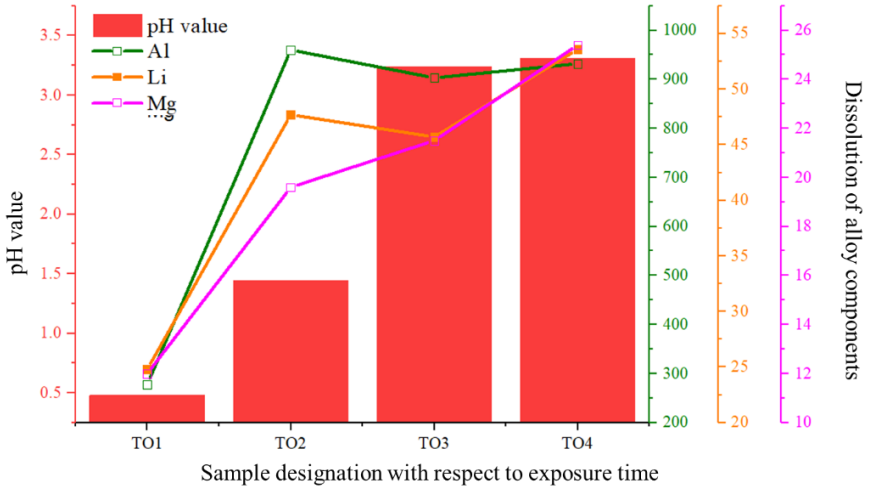

b)

Figure 4.44. The dependence of degradation with respect to pH value for: a) as-cast sample, b) solutionized sample

By comparing the results of microstructural analysis after electrochemical and chemical testing, the same pattern of degradation behavior can be observed for both conditions. This pattern for the sample in the as-cast condition implied degradation via phases in the interdendritic areas, while in the solutionized sample degradation occurs through intercrystalline and transcrystalline mechanisms.

4.8.4. Results of microhardness measurements after degradation

The results of microhardness measurements performed on the cross-section of the samples after electrochemical and chemical degradation are given in Table 4.24.

Table 4.24. The results of microhardness measurements after sample degradation

Sample	Number of measurements	Mean value ($\overline{HV}$)	Standard deviation (σ)
AC	3	63.07	1.45
AC1	3	73.137	5.52
AC2	3	75.737	1.66
AC3	3	72.67	3.15
AC4	3	75.767	6.71
TO	3	53.67	1.27
TO1	3	92.40	3.30
TO2	3	75.90	3.75
TO3	3	71.43	0.61
TO4	3	63.90	2.31

By comparing microhardness values of electrochemically (AC, TO) and chemically tested samples (AC1-AC4, TO1-TO4), significantly lower microhardness values were observed for electrochemically degraded samples. Furthermore, the microhardness values of as-cast samples remain unaffected by the increase in exposure time during chemical testing, while microhardness of solutionized samples decrease with increase in exposure time. This microhardness-exposure time dependance of solutionized sample is a consequence of α_{Al} solid solution dealloying through Li^{+} and Mg^{2+} cation loss weakening the hardening effect of solutionizing.

5. CONCLUSIONS

This study aimed to design and synthesize the light-weight Al-Mg-Li alloy with improved mechanical properties in as-cast condition by establishing the influence of chemical composition, thermodynamic and processing parameters on the solidification sequence and microstructure development. The application of different characterization techniques to determine chemical composition, thermodynamic behavior, microstructure development, as well as mechanical and corrosion properties resulted in following conclusions:

- The results of the chemical composition analysis showed that the synthesis of the samples was successful both in a protective Ar atmosphere and in a vacuum. The greatest loss of alloying elements was observed during synthesis under vacuum. A greater loss of alloying elements resulted from additional processing operations, such as the longer time required to equalize the pressure in the vacuum chamber and the loss of the protective atmosphere as a result of the consecutive casting of two samples. The inadequate choice of crucible coating led to crucible attack and melt contamination in some samples.

- The results of the density calculations showed the influence of the chemical composition on the physical properties of the synthesized samples. The lowest density was determined for the alloy Al-2.57Mg-5.58Li, while the highest density was calculated for sample 1 with 2.16 wt% Li and 0.38 wt% Mg. It can be seen that the closer the Li/Mg ratio is to 1, the lower the density. When comparing the density results as a function of section thickness, similar behavior was observed for all samples except for the sample with 2.09 wt% Li and 2.24 wt% Mg. This deviation is due to the gas porosities observed during the visual inspection of the cross-section. The lower density of the middle section (ø 20.0 mm) of all samples indicates segregation of Li and Mg during solidification, while the increase in density in the upper sections (ø 30.0 mm) indicates oxidation losses.

- On the basis of the results obtained, it was not possible to estimate the influence of section thickness and chemical composition on sample density. The lack of correlation is due to the presence of casting defects such as gas and shrinkage porosity. The occurrence of gas porosity can be avoided by synthesizing the alloy in a protective Ar atmosphere and full crucible cover.

- The results of Thermo-Calc software support indicated the appearance of following phases: α_{Al} solid solution, AlLi (δ), Al_2LiMg (T), Al_8Mg_5 (β) and Al_3Mg_2. Expanding the chemical composition to include impurity elements indicated the additional formation of $Al_{13}Fe_4$, AlLiSi and Mg_2Si. The results of Equilibrium phase diagram and One axis phase equilibria calculation indicated the influence of Li/Mg ratio on the equilibrium solidification sequence referring to the formation of AlLi (δ) and Al_2LiMg (T) phase. The results of non-equilibrium solidification sequence calculated using Classical Scheil and Scheil with solute trapping models indicated that the composition of last Liquid phase solidifying in the interdendritic region will not only depend on the Li/Mg ratio but also on the interaction between Li and Mg. While Li shows grater tendency towards segregation at the solid/liquid interface, Mg tends to bulk α_{Al} solid solution.

- The application of simplified thermal analysis during solidification of sample 1 (Al-0.38Mg-2.16Li alloy) indicated lack of characteristic peaks related to phase solidification due to low cooling rate. Cooling curve derivative enabled identification of nucleation temperature at 650.2 °C, liquidus interval (638.3°C to 637.9 °C) peritectic reaction interval (625.0 °C to 578.0 °C) and solidus temperature at 528.0 °C. The results of simplified thermal analysis also indicated low undercooling (0.34 °C) as a consequence of high temperature Al_3Li (δ') precursor phase solidification at 632.4 °C.

- The investigations using differential scanning calorimetry (DSC) made it possible to identify characteristic temperatures such as the liquidus temperature (T_L), the solidus temperature (T_S) and the temperatures of reactions in the liquid and solid state as a function of the heating and cooling rates. With increasing heating and cooling rates, a lack of characteristic peaks was found, which is due to the absence of phase precipitation or growth due to slow solid state diffusion. An increase in the heating and cooling rate indicates the possibility of the Mg and Li bulked solid solution formation. Increasing the heating rate from 2.0 to 40.0 K/min increases the T_L, with the maxima of the peaks shifting towards higher temperatures. The increase in the solidification enthalpy with the increase in the heating rate from 20.0 to 50.0 K/min reduces the solidus temperature. Extending the solidification interval reduces the possibility of casting defects occurring and enables the segregation of alloying elements in the areas that solidify last. Due to

the high solid solubility of Mg in the α_{Al} matrix and its influence on the solubility of Li in liquid and solid solution, segregation of alloying elements is not to be expected.

- The interpretation of heating and cooling curves indicated a significant deviation in the solidification sequence compared to the results of thermodynamic calculations for Al-rich corner and One axis equilibrium. Better correlation was achieved with Classical Scheil and Scheil with solute trapping calculations identifying solidification of α_{Al} dendritic network at T_L, followed by the eutectic reaction $L \rightarrow \alpha_{Al} + AlLi$ (δ) at the liquid state reaction temperatures, and growth and coarsening of AlLi (δ) phase at solid state reaction temperature.

- The samples exhibit macrostructure typical for alloy solidification with visible chill, columnar and equiaxed crystal zones. The additional processing through the addition of AlTi5B1 completely removed the casting texture in Al-2.57Mg-2.58Li alloy and reduced the thickness of chill and columnar crystal zones in Al-1.92Mg-1.73Li alloy. The thickness of crystallographic texture decreases with the decrease in the ratio Li/Mg. This is a consequence of Mg's influence on reduced solid solubility of Li in α_{Al} matrix. Parallelly, there is a Li enrichment of the interdendritic area and the nucleation of intermetallic phases.

- The utilization of light microscopy enabled identification of α_{Al} dendritic network, AlLi (δ), Al_2LiMg (T), (Al_8Mg_5 (β) + Al_2LiMg (T)) and Al_8Mg_5 (β) intermetallic phases. The intermetallic phases detected in all the alloys, except AlLi (δ) in Al-0.38Mg-2.16Li alloy, show tendency to solidify in the interdendritic areas. Since the nucleation and growth of AlLi (δ) phase are based on the solidification of the precursor Al_3Li (δ') phase rather than the melt's bulking at the solidification front, it is the only phase that solidifies within the α_{Al} dendritic network as well as along the grain boundaries.

- The solidification sequence in interdendritic area was identified using SEM and EDS analysis enabled. The first phase solidifying in interdendritic area is Al_2LiMg (T) followed by the solidification of two phase (Al_8Mg_5 (β) + Al_2LiMg (T)) region and Al_8Mg_5 (β). This assumption is in accordance with the results of thermodynamic modelling of solidification sequence and data available in literature. The results of SEM and EDS analysis indicated solidification of Fe-based intermetallic phases in Al-2.24Mg-2.09Li and Al-2.57Mg-2.58Li synthesized in the induction melting furnace

under vacuum. Based on their chemical composition, morphology and microstructural placement, the phases were identified as $Al_{13}Fe_4$.

- The results of X-ray diffraction indicate the development of Al_2LiMg (T) and Al_3Li (δ') intermetallic phases in α_{Al} matrix for all three alloys (Li/Mg = 0.88, Li/Mg = 1.0, Li/Mg = 5.68). In alloy with Li/Mg = 5.68 the presence of AlLi (δ) phase was detected additionally. Based on these results, it can be concluded that precursor Al_3Li (δ') phase solidified and is retained till the end of solidification sequence regardless of Li/Mg ratio. However, the intensity of Al_3Li (δ') phases characteristic peaks is the highest for Al-0.38Mg-2.16Li alloy with Li/Mg = 5.68. Solidification and retention of the metastable phase at all Li/Mg ratios is important for achieving good mechanical properties.

- The transmission electron microscopy with selected area diffraction patterns was performed on the samples with respect to Li/Mg ratios. The TEM and SAD analysis of samples 1, 22 and 31 enabled identification of Al_3Li (δ'), AlLi (δ) and (Al_8Mg_5 (β) + Al_2LiMg (T)) intermetallic phases. In the Al-2.57Mg-2.58Li alloy the $Al_{13}Fe_4$ phase was identified additionally.

- The results of compression testing indicate a decrease in compression properties, primarily compression strength and ultimate point, due to the solutionizing heat treatment. By comparing the influence of Li/Mg ratio on as-cast and solutionized samples, it can be concluded that intermetallic phases present in as-cast samples will impact their behavior. This mainly concerns yield strength and compression strength of as-cast samples with Li/Mg = 0.90 (Al-1.92Mg-1.73Li) and Li/Mg = 0.93 (Al-2.24Mg-2.09Li) indicating earlier onset of plastic deformation as well as the reduction of sample area.

- The results of the metallographic analysis performed on the samples after compression indicate four typical behaviors: unequal deformation and barreling effect, formation of intergranular layering fracture, slip formation, flow lines formation. The results of microstructural analysis indicated that flow line formation is linked to the lack of precipitates and free movement of dislocations. The formation of intergranular layering fracture is initiated by the interaction between dislocations AlLi (δ) phase precipitates, while the slip formation is a consequence of the presence of Fe-based intermetallic phases presence.

- The hardness values depend on the Li/Mg ratio and the addition of AlTi5B1. Consequently, the highest hardness was measured in alloy Al-2.57Mg-2.58Li with Li/Mg = 1.0 and Al-1.92Mg-1.73Li with Li/Mg = 0.90, which contain AlTi5B1. Furthermore, for all samples except sample 1 (Al-0.38Mg-2.16Li), where the lowest hardness value was measured in the central section of the sample (ø 20.0 mm), an increase in hardness was observed with the increase in the specific sample section, indicating the influence of crystal zone morphology on hardness.

- The results of microhardness measurements were higher in the interdendritic areas of all samples. This indicated that intermetallic phases, mostly Al_8Mg_5 (β) and (Al_8Mg_5 (β) + Al_2LiMg (T)), solidified in the interdendritic areas have beneficial influence on hardness. The highest microhardness values of both α_{Al} matrix and interdendritic area were measured in sample 22 (Al-2.57Mg-2.58Li) with Li/Mg = 1.0 containing the addition of AlTi5B1. The similar microhardness behavior of the α_{Al} matrix and the interdendritic area is observed only in the specific section of ø 10.0 mm. At a specific section of ø 20.0 mm, the microhardness of the interdendritic area and the α_{Al} matrix show similar behavior up to Li/Mg = 1.0 while the microhardness of ø 30.0 mm specific sections shows the completely opposite behavior. Based on this, it can be concluded that different specific sections (different cooling rates) differently affect solidification sequence and microstructure development for different Li/Mg ratios. If the increase in the microhardness value of both areas is considered, it can be concluded that Li/Mg = 1.0 is optimal for the ø 30.0 mm section, while the ratio Li/Mg = 0.93 is optimal for the ø 10.0 mm and ø 20.0 mm sections.

- The results of nanoindentation measurements indicate higher hardness and modulus of elasticity values for samples in solutionized compared to the as-cast condition. Achievement of higher modulus values in solutionized samples confirms that it is an intrinsic proportion of the alloy typically attributed to electron redistribution between the Al-Li bounds in the α_{Al} solid solution. These results differ from observations available in the literature attributing the modulus increase to the development of intermetallic phases. Moreover, decrease in the modulus of solutionized sample with increase in Li content above 1.93 wt.% deviates from the data available in literature according to which each 1 wt.% of Li added increase modulus of elasticity by 6 % for the additions up to 4.2 wt.% Li.

- The results of electrochemical testing, mainly Tafel polarization curves, indicated more negative corrosion potential, higher current density, anode slope, cathode slope and corrosion rate for solutionized sample. While, in the as-cast sample degradation progressed by dissolution of the Al_8Mg_5 (β) and Al_2LiMg (T) phases located between the branches of the α_{Al} dendritic network, the solutionized sample degraded through the grain boundary and α_{Al} grain involvement. The remnant of the AlLi (δ) phase inside the α_{Al} grains resulted in cavity formation and sample surface layering.

- The results of chemical degradation testing indicated that during degradation in corrosive environment mass of the as-cast and solutionized samples decreased. The mass loss increased with the increase in exposure time, up to a period of 72 h. The highest corrosion rate for both conditions was calculated for the exposure time of 5 h. Decrease in corrosion rate is a consequence of increase in pH value of the solution. The results of ICP-MS analysis of the solution after sample degradation indicate the occurrence of rapid anodic and cathodic reactions leading to dealloying of α_{Al} solid solution through Li^+, Mg^{2+} and Al^{3+} cation release. Combining the results of solutions' chemical composition with metallographic analysis it can be concluded that degradation of as-cast sample for a period between 5 and 24 h first affects the Al_8Mg_5 (β) and Al_2LiMg (T) resulting in the formation of cavities in the interdendritic area. Further increase in exposure time led to the involvement of other intermetallic phases, mostly Al_2LiMg (T) and (Al_8Mg_5 (β) + Al_2LiMg (T)). The microstructure analysis of the solutionized samples' cross-section pointed out the degradation progression across the grain boundaries and AlLi (δ) phase in their proximity.

- To assess the impact of degradation on the mechanical properties of the exposed samples, the microhardness was measured. Lower microhardness values were observed for electrochemically degraded samples. The microhardness values of as-cast samples remain unaffected by the increase in exposure time during chemical testing, while microhardness of solutionized samples decrease with increase in exposure time as a consequence of dealloying of α_{Al} solid solution through Li^+ and Mg^{2+} cation loss weakening the hardening effect of solutionizing.

5.1.Hypotheses

The hypotheses set in the Introduction section are revised in order to determine validity of initial assumptions.

The addition of Mg and Li will contribute to the density reduction of the alloy.

The first hypothesis was proven valid. The influence of chemical composition on physical properties of synthesized alloys was confirmed by density calculations based on Archimedes' law. The lowest density was obtained in sample 22 containing highest amounts of Li and Mg, while the highest density was calculated for the sample 1 containing lowest amount of Mg. It is noted that the closer the Li/Mg ratio is to 1, the lower the density.

The addition of Mg and Li will affect the development of strengthening intermetallic phase and improve mechanical properties of the Al-Mg-Li alloy.

The second hypothesis was proven valid by the results of microstructure and mechanical properties characterization. The results of hardness measurements and compression properties were higher for samples in as-cast with respect to solutionized condition indicating beneficial influence of intermetallic phases on alloys' properties. The deviation was noted in nanoindentation measurements that indicated higher hardness and modulus of elasticity values for samples in solutionized condition. This indicated that modulus is an intrinsic proportion of the alloy typically attributed to electron redistribution between the Al-Li bonds in the α_{Al} solid solution.

Correlation of chemical composition, thermodynamic and processing parameters will enable determination of Al-Mg-Li alloy solidification sequence.

The third hypothesis was proven valid by the results in this thesis. The characterization of thermodynamic, microstructural and mechanical properties of synthesized alloys enabled better understanding of its microstructural development. The correlation of chemical composition (Li/Mg ratio), thermodynamic modelling, simplified thermal analysis, differential scanning calorimetry and metallographic analysis allowed the Al-Mg-Li alloys' solidification sequence to be amended:

- Li/Mg > 1:

$$\alpha_{Al} \rightarrow Al_3Li\ (\delta') \rightarrow AlLi\ (\delta) \rightarrow (Al_8Mg_5\ (\beta) + Al_2LiMg\ (T)) \rightarrow Al_8Mg_5\ (\beta)$$

- Li/Mg ≤ 1:
  - $\alpha_{Al} \rightarrow Al_3Li\ (\delta') \rightarrow Al_2LiMg\ (T) \rightarrow (Al_8Mg_5\ (\beta) + Al_2LiMg\ (T)) \rightarrow Al_8Mg_5\ (\beta)$

It was proven that regardless of the Li/Mg ratio, the Al_3Li phase (δ') will serve as a precursor but also as one of the hardening phases.

5.2.Hypotheses Outlook and future work

Regardless of the fact that Al-Li and Al-Li-X alloys have a long history and application in the aerospace and space industry, this research provided new insights into the solidification sequence and microstructure development of Al-Li-Mg alloys that could prove important in solving the shortcomings of historically utilized alloys.

In order for synthesized alloy to be classified as foundry alloy, it is necessary to consider the influence of the casting's complexity on the solidification sequence, microstructure development and mechanical properties. It is also necessary to assess the tendency of synthesized samples to natural aging and its potential influence on mechanical properties and alloys' applicability. It is also crucial to find and adopt a heat treatment regime that would improve alloy's properties.

REFERENCES

[1] Jovičević-Klug P, Podgornik P. Review on the Effect of Deep Cryogenic Treatment of Metallic Materials in Automotive Applications. Metals (Basel). 2020;10(4):434.

[2] Salonitis K, Jolly M, Pagone E, Papanikolaou M. Life-cycle and energy assessment of automotive component manufacturing: The dilemma between aluminum and cast iron. Energies.2019;12(13):2557.

[3] Chatterjee B, Bhowmik S. Evolution of material selection in commercial aviation industry-a review. In: Sustainable Engineering Products and Manufacturing Technologies, Kumur K, Zindani D, Davim P. Academic Press. Elsevier; 2019., p. 199-219.

[4] Orłowicz AW, Mróz M, Tupaj M, Trytek A. Materials used in the automotive industry. Archives of Foundry Engineering. 2015;15(2):75-78.

[5] Jin L, Liu K, Chen X. G. Improved Elevated Temperature Properties in Al-13%Si Piston Alloys by Mo Addition. Journal of Materials Engineering and Performance. 2020;29(1):126-134.

[6] Yang H, Ji S, Yang W, Wang Y, Fan Z. Effect of Mg level on the microstructure and mechanical properties of die-cast Al-Si-Cu alloys. Materials Science and Engineering: A, 2017;642(November):340–350.15.

[7] Lia R. X, Lia RD, Zhao Y. H, He L. Z, Li CX, Guan HR,. Hu ZQ. Age-hardening behavior of cast Al-Si base alloy, Materials Letters, 2004;58(15):2096–2101.

[8] Zhang B, Zhang L, Wang Z, Gao A. Achievement of High Strength and Ductility in Al-Si-Cu-Mg Alloys by Intermediate Phase Optimization in As-Cast and Heat Treatment Conditions. Materials (Basel). 2020;13(3):647.

[9] Hughes AE, Parvizi R, Forsyth M. Microstructure and corrosion of AA2024. Corrosion Reviews. 2015;33(1-2):1–30.

[10] Kamp N, Gao N, Starink, MJ, Sinclair I. Influence of grain structure and slip planarity on fatigue crack growth in low alloying artificially aged 2xxx aluminium alloys. International Journal of Fatigue. 2007;29(5):869-878.

[11] Shu WX, Hou LG, Liu JC, Zhang C, Zhang F, Liu JT, Zhuang L. Z, Zhang JS. Solidification Paths and Phase Components at High Temperatures of High-Zn Al-Zn-Mg-Cu Alloys with Different Mg and Cu Contents. Metallurgical and Materials Transactions A. 2015;46(11):5375–5392.

[12] Liang H, Chen SL, Chang YA. A thermodynamic description of the Al-Mg-Zn system. Metallurgical and Materials Transactions A. 1997;28(9):1725–1734.

[13] Ghiaasiaan R, Zeng X, Shankar S. Controlled Diffusion Solidification (CDS) of $Al_3Zn_3Mg_3Cu$ (7050): Microstructure, heat treatment and mechanical properties. Materials Science and Engineering: A. 2014;594:260–277.

[14] Augustyn-Pieniążek J, Adrian H, Rzadkosz S, Choroszyński M. Structure and Mechanical Properties of Al-Li Alloys as Cast. Archives of Foundry Engineering. 2013;13(2):5-10.

[15] Kraposhin VS, Kolobnev IN, Ryabova EN, Everstov AA, Talis AL. Inhomogeneous Solid Solutions in Alloys of the Al – Cu – Li System: Possible Structure of Clusters. Metal Science and Heat Treatment. 2019;61(1-2):73-82.

[16] Fincher CD, Ojeda D, Zhang Y, Pharr GM, Pharr M. Mechanical properties of metallic lithium: from nano to bulk scales. Acta Materialia. 2019;186(December):215-222.

[17] Meric C. Investigation on the elastic modulus and density of vacuum casted aluminum alloy 2024 containing lithium additions. Journal of Materials Engineering and Performance. 2000;9(3):266-271.

[18] Kostrivas A, Lippold JC. Weldability of Li-bearing aluminum alloys. International Materials Reviews. 1999;44(6):217-237.

[19] Howard R, Bogh N, MacKenzie DS. Heat treating processes and equipment. In: Handbook of Aluminum: Vol. 1: Physical Metallurgy and Processes, editors. Totten G. E, MacKenzie D. S. Marcel Dekker; 2003., p. 881-971.

[20] Mallick A. Improvement of mechanical properties in light weight Mg-based materials. Procedia Engineering. 2016;149(June):283–287.

[21] Brodarac ZZ, Unkić F, Medved J, Mrvar P. Determination of solidification sequence of the AlMg9 alloy. Kovove Materialy. 2012;50(1):59–67.

[22] Gao Y, Guan W, Zhai Q, Xu K. Study on undercooling of metal droplet in rapid solidification. Science China Technological Sciences. 2005;48(6):632–637.

[23] Davydov VG, Ber LB, Kaputkin EY, Komov VI, Ukolova OG, Lukina EA. TTP and TTT diagrams for quench sensitivity and ageing of 1424 alloy. Materials Science and Engineering: A. 2000;280(1):76-82.

[24] Akhtar N, Akhtar W, Wu, SJ. Melting and casting of lithium containing aluminium alloys. International Journal of Cast Metals Research. 2015;28(1):1-8.

[25] Wang FY, Wang XJ, Sun W, Yu F, Cui JZ. Low Frequency Electromagnetic Casting of 2195 Aluminum–Lithium Alloy and Its Effects on Microstructure and Mechanical Properties. Acta Metallurgica Sinica. 2020;33(3).

[26] Sauermann R, Friedrich B, Grimmig T, Buenck M, Bührig-Polaczek A. Development of aluminum-lithium alloys processed by the rheo container process. Solid State Phenom. 2006;116-117:513-517.

[27] Webster D. The effect of low melting point impurities on the properties of al-li alloys. Le Journal de Physique Colloques. 1987;48(C3):C3-685-C3-691.

[28] Ashkenazi D. How aluminum changed the world: A metallurgical revolution through technological and cultural perspectives. Technological Forecasting and

Social Change. 2019;143:101-113

[29] Paparazzo E. Pliny the Elder on Metals: Philosophical and Scientific Issues. Classical Philology. 2008;103(1):40-54.

[30] Keaveney A. Notes on the First Mithridatic War in Macedonia and Greece. Syllecta Classica. 2018;29(1):29-65.

[31] Marmor M. On the art of building in ten books. Leon Battista Alberti, Joseph Rykwert, Neil Leach, Robert Tavernor. Art Documentation: Journal of the Art Libraries Society of North America. 1989;8(3):154-155.

[32] Johnson W. Historical Aspects of Fires, After Impact, in Vehicles of War. In: Grant C. E, Pagni P. J, editor. Fire safety science – Proceedings of the first international symposium; Bearkly, United States of America, 7.10.-11.10.1986. International Association for Fire Safety Science.

[33] Matyszak P. The mithridatic wars. In: Whidby M, Sidebottom H., editor. The Encyclopedia of Ancient Battles || The Mithridatic Wars, 89-66 BC. Wiley-Blackwell; 2017., p 1-13.

[34] Pliny the Eldar. The Natural History. Book XXXIII: The natural History of Metals.

http://www.perseus.tufts.edu/hopper/text?doc=Perseus%3Atext%3A1999.02.0137%3Abook%3D33%3Achapter%3D20 [cited 2023 Feb 6].

[35] Elnaggar A, Leona M, Nevin A, Heywood, A. The Characterization of Vegetable Tannins and Colouring Agents in Ancient Egyptian Leather from the Collection of the Metropolitan Museum of Art. Archaeometry. 2017;59(1):133-147.

[36] Photos-Jones E, Christidis G. E, Piochi M, Keane C, A. Mormone A, Balassone G, Perdikatsis V, Leanord A. Testing Greco-Roman medicinal minerals: The case of solfataric alum. Journal of Archaeological Science: Reports. 2016;10:82-95.

[37] Lopez R. The Earliest Chemical Industry: An Essay in the Historical Relations of Economics and Technology Illustrated from the Alum Trade. Journal of Economic History. 1948;10(1):66-68.

[38] Agrikola G. De Re Metallica translated from the first latin edition of 1556. New Yourk: Dover Publications, Inc.; 1950. Available from: https://www.gutenberg.org/files/38015/38015-h/38015-h.htm [cited 2022 Sep 29].

[39] Kite M, Thomson R. Conservation of Leather and Related Materials. London: Routledge; 2006.

[40] Holmes HN. Fifty years of industrial aluminum. The Scientific Monthly. 1936;42(3):236-239.

[41] Kvande H. Two hundred years of aluminum... or is it aluminium?. Jom. 2008;60(8):23-24.

[42] Hnll M, Gallitzin D. The discovery of the elements. XII. Other elements isolated with the aid of Potassium and Sodium: Beryllium, Boron, Silicon, and Aluminum.

Journal of chemical education. 1825;9(8):1836-1932.

[43] Weeks, M.E. Discovery of the Elements. Whitefish: Kessinger Publishing; 2010.

[44] Partington R. A history of chemistry. London: Macmilln & Coltd; 1970.

[45] Wisniak J. Henri Étienne Sainte-Claire Deville: A Physician Turned Metallurgist. Journal of Materials Engineering and Performance. 2004;13(2):117-128.

[46] Kvande H. The aluminum smelting process. Journal of Occupational and Environmental Medicine. 2014;56(5):2-4.

[47] Punge M. The metallurgy of anodizing aluminum: Connecting science to practice. Cham: Springer International Publishing; 2018.

[48] Lockwood J. Topping of the tip. National Archives. https://www.archives.gov/files/publications/prologue/2014/summer/aluminum.pdf [cited 2022 Mar 1].

[49] Houser M, Collier S, Cook R, Klein HB, Palmiero K. A History of Pittsburgh, in 50 Artifacts. https://www.pittsburghmagazine.com/a-history-of-pittsburgh-in-50-artifacts/ [cited 2022 Mar 1].

[50] Reverdy M, Potocnik V. History of Inventions and Innovations for Aluminum Production. In: Minerals, The Minerals, Metals & Materials Society, editor. TMS 2020 149th Annual Meeting & Exhibition Supplemental Proceedings 2020. The Minerals, Metals & Materials Series. Springer; 2020., p. 1895-1910.

[51] Haupin W. History of Electrical Energy Consumption By Hall-Heroult Cells. The Minerals, Metals & Materials Series. Springer; 2002.

[52] Hall-Hbroult Centennial First Century of Aluminum Process Technology 1886 – 1986. The Minerals, Metals & Materials Series. Springer; 2002.

[53] Tarcy G. P, Kvande H, Tabereaux A. Advancing the industrial aluminum process: 20th century breakthrough inventions and developments. Jom. 2011;63(8):101-108.

[54] Langlois S, Rappaz J, Martin O, Caratini Y, Flueck M, Masserey A, Steiner G. 3D coupled MHD and thermo-electrical modelling applied to AP technology pots. In: Chesonis C., editor. Light Metals The Minerals, Metals & Materials Series. Springer; 2015., p. 771-775.

[55] Haraldsson J, Johansson MJ. Effects on primary energy use, greenhouse gas emissions and related costs from improving energy end-use efficiency in the electrolysis in primary aluminium production. Energy Efficiency. 2020;13(7):1299-1314.

[56] Saevarsdottir G, Kvande H, Welch J. Aluminum Production in the Times of Climate Change: The Global Challenge to Reduce the Carbon Footprint and Prevent Carbon Leakage. Jom. 2020;72(1):296-308.

[57] Dubois C, Batista E, Espinoza-Nava L, Dubreuil A. Validation of pfc slope at alcoa canadian smelters with anode effect assessment and future implications to add low

voltage emissions into total pfc emissions. In: Chesonis C., editor. Light Metals 2019. The Minerals, Metals & Materials Series. Springer; 2019, p. 849-855.

[58] Pawlek RP. Inert Anodes: An Update. In: Schneider W., editor. Light Metals 2002. The Minerals, Metals & Materials Series. Springer; 2002., p. 1126-1133.

[59] Liang T., Chang G, Qing L, Zhang K, Li J. Effect of sintering atmosphere on corrosion resistance of Ni/(NiFe2O4–10NiO) cermet inert anode for aluminum electrolysis. Transactions of Nonferrous Metals Society of China. 2016;26(11):2925–2929.

[60] Kvande H, Drabløs A. The aluminum smelting process and innovative alternative technologies. Journal of Occupational and Environmental Medicine. 2014;56(5):23-32.

[61] Kvande H, Haupin W. Inert anodes for Al smelters: Energy balances and environmental impact. Jom. 2001;53(5):29–33.

[62] International Aluminium Institute. https://international-aluminium.org/. [cited 2022 Nov 19].

[63] International Aluminium Institute. Public Access – International Aluminium Institute. https://alucycle.world-aluminium.org/public-access/ [cited 2022 Nov 19].

[64] Sevigné-Itoiz E, Gasol M, Rieradevall J, Gabarrell X. Environmental consequences of recycling aluminum old scrap in a global market. Resources, Conservation & Recycling. 2014;89:94-103.

[65] Gaustad G, Olivetti E, Kirchain R. Improving aluminum recycling: A survey of sorting and impurity removal technologies. Resources, Conservation & Recycling. 2012;58:79-87.

[66] Modaresi R, Müller D. The role of automobiles for the future of aluminum recycling. Environmental Science & Technology. 2012;46(16):8587–8594.

[67] Capuzzi S, Timelli G. Preparation and melting of scrap in aluminum recycling: A review. Metals (Basel). 2018;8(4):1-24.

[68] Kaufman JG. Introduction to aluminum alloys and tempers. Materials Park: ASM International; 2000.

[69] Dokšanović T, Džeba I, Markulak D. Primjene aluminijskih legura u građevinarstvu. Tehnički Vjesnik. 2017;24(5):1609-1618.

[70] Al circle. What does the AlCircle's report on "Future of Aluminium in Transportation Sector - an industry analysis with forecasts to 2027" offer to you? https://www.alcircle.com/specialreport/1336/future-of-aluminium-in-transportation-sector-an-industry-analysis-with-forecasts-to-2027 [cited 2023 Mar 1]

[71] Li Y, Hu A, Fu Y, Liu S, Shen W, Hu H. Al Alloys and Casting Processes for Induction Motor Applications in Battery-Powered Electric Vehicles: A Review.

Metals (Basel). 2022;12(2): vol. 12, no. 2, 2022.

[72] Ghen K, Yan L, Zhang Y, Li X, Li Z, Gao G, Liu H, Xiong B. Microstructure, Texture, and Formability Control by Initial Hot-Rolling Temperature of Al–Mg–Si Alloy Sheets for Automotive Applications. Advanced Engineering Materials. 2022;24(9):1-14.

[73] Sun X, Han X, Dong C, Li X. Applications of Aluminum Alloys in Rail Transportation. In: Bobranski L., editor. Advanced aluminum composites adn alloys. Storres: IntechOpen; 2020.

[74] Pantelakis S. Historical Development of Aeronautical Materials. In: Pantelakis S, Tserpes K., editors. Revolutionizing Aircraft Materials and Processes. Storres: Springer; 2020.

[75] Zhou B, Liu B, Zhang S. The advancement of 7xxx series aluminum alloys for aircraft structures: A review. Metals (Basel). 2021;11(5).

[76] Bouzekova-Penkova A, Miteva A. Some Aerospace Applications of 7075 (B95) Aluminium Alloy. Aerospace Research in Bulgaria. 2022;34:165–179.

[77] Tiwary A, Kumar R, Chohan JS. A review on characteristics of composite and advanced materials used for aerospace applications. Materials Today: Proceedings. 2021;51:865–870.

[78] Mondolfo L. F. Aluminum Alloys: Structure and Properties. London: Butterworths; 1976.

[79] Frank W, Haupin W, Vogt H, Thonstad J, Dawless R, Kvande H, Taiwo O. Aluminum. In: Chadwick S., editor. Ullmann's encyclopedia of industrial chemistry. Reference Services Review; 1988.

[80] Kondo M, Maeda H, Mizuguchi M. The production of high-purity aluminum in Japan. Jom. 1990;42(11):36–37.

[81] Jadayil WA, Serhan D. The Effect of Heat Treatment and Alloying of Ni – Ti Alloy with Copper In: The Minerals, Metals & Materials Series, editor. TMS 2019 148th Annual Meeting & Exhibition Supplemental Proceedings. The Minerals, Metals & Materials Series. Springer; 2019.

[82] Pearson TG, Phillips H. The production and properties of super-purity aluminium. International Materials Reviews. 1957;2(8):305-360.

[83] Li J, Sun WJ. Magnetic moments of odd-Aaluminum isotopes in covariant density functional theory. Communications in Theoretical Physics. 2020;72(5): 055301.

[84] Sverdlin A. Properties of pure aluminum. In: Totten GE, MacKenzi DS, editors. Handbook of Aluminum: Volumen 1: Physical Metallurgy and Processes.

[85] Xu X, Feng Y, Fan H, Wang Q, Dong G, Li G, Ding H. The grain refinement of 1070 alloy by different Al-Ti-B mater alloys and its influence on the electrical conductivity. Results in physics, 2019;14: 02482.

[86] Smirnov AV, Shelton WA, Johnson DD. Importance of thermal disorder on the properties of alloys: Origin of paramagnetism and structural anomalies in bcc-based $Fe_{1-x}Al_x$. Physical Review B. 2005;71(6): 064408.

[87] Peled D, Pratt VR, Holzmann G. Partial Order Methods in Verification. Storres: AMS eBook Collections; 1997.

[88] Smith YD, Shiles E, Inokuti M. The optical properties of metallic aluminum. In: Palik ED., editor. Handbook of optical constants of solids. Academic press; 1997., p. 369-406.

[89] Zhao T, Munis A, Rehman AU, Zheng M. Corrosion behavior of aluminum in molten hydrated salt phase change materials for thermal energy storage. Materials Research Express. 2020;7(1):015529.

[90] Salas BV, Wiener MS. Corrosion Resistance of Aluminum and Magnesium Alloys Understanding, Performance and Testing. Corrosion Engineering, Science and Technology. 2011;46(1):1-2.

[91] González-Rovira L, González-Souto L, Astola PJ, Bravo-Benítez C, Botana FJ. Assessment of the corrosion resistance of self-ordered anodic aluminum oxide (AAO) obtained in tartaric-sulfuric acid (TSA). Surface and Coatings Technology. 2020;399:126131.

[92] Saravanakumar R, Ramachandran K, Padmanabhan PAV. Plasma Assisted Aluminothermic Reduction of Cr and Fe Oxides from Chromium Bearing Waste. Plasma Chemistry and Plasma Processing. 2021;41:155-169.

[93] Shen Z, Chen H, Lv Z, Wang D, Chen D, Huang F. Study on large-scale steam explosion of molten aluminum and water. Process Safety Progress. 2020;39(4):1-9

[94] May J, Dinkel M, Amberger D, Höppel HW, Göken M. Mechanical properties, dislocation density and grain structure of ultrafine-grained aluminum and aluminum-magnesium alloys. Metallurgical and Materials Transactions A. 2007;38(9):1941–1945.

[95] Kaufman JG. Introductio to aluminum alloys and tempers. Materials Park: ASM International :2000.

[96] Nathan AJ, Scobell A. How China sees America; The Sum of Beijing's Fears. Foreign Affairs. 2012;91(5):340.

[97] Cambel FC. Elements of Metallurgy and Engineering Alloys. Ohio: ASM International; 2008.

[98] Zhang J, Song B, Wei Q, Bourell D, Shi Y. A review of selective laser melting of aluminum alloys: Processing, microstructure, property and developing trends. Journal of Materials Science & Technology. 2019;35(2):270-284.

[99] Aboulkhair NT, Simonelli M, Parry L, Ashcroft I, Tuck C, Hague R. 3D printing of Aluminium alloys: Additive Manufacturing of Aluminium alloys using selective

laser melting. Progress in Materials Science. 2019;106:100578.

[100] Cavazos JL, Colás R. Precipitation in a heat-treatable aluminum alloy cooled at different rates. Materials Characterization. 2001;47(3-4):175–179.

[101] Vasudevan A, Doherty R. Aluminum Alloys--Contemporary Research and Applications. London: Academic Press; 1989.

[102] ASM International Handbook Committee. Heat treating of aluminum alloys. In: ASM International Handbook Committee. ASM Handbook Volume 04 - Heat Treating. Storrs: ASM International; 1991., 1861-1960.

[103] Ozesmi M, Patiroglu TE, Hillerdal G, Ozesmi C. Peritoneal mesothelioma and malignant lymphoma in mice caused by fibrous zeolite. British Journal of Industrial Medicine. 1985;42(11):746-749.

[104] Bai Z, Qiu F, Liu Y, Jiang Q. Superior strength and ductility of the Al-Cu alloys inoculated by Zr-based metallic glass at elevated temperatures. Materials Science and Engineering: A. 2015;645;357-360.

[105] Gao YH, Kuang J, Liu G, Sun J. Effect of minor Sc and Fe co-addition on the microstructure and mechanical properties of Al-Cu alloys during homogenization treatment. Materials Science and Engineering: A. 2019;746(September):11-26.

[106] He C, Yu W, Li Y, Wang Z, Wu D, Xu G. Gelationship between cooling rate, microstructure evolution, and performance improvement of an Al-Cu alloy prepared using different methods. Materials Research Express. 2020;7(11).

[107] Zuo L, Ye B, Feng J, Zhang H, Kong X, Jiang H. Effect of ε-Al3Ni phase on mechanical properties of Al–Si–Cu–Mg–Ni alloys at elevated temperature. Materials Science and Engineering: A. 2019;772(October):138794.

[108] McMahon ME, Haines RL, Steiner PJ, Schulte JM, Fakler SE, Burns JT. Beta phase distribution in Al-Mg alloys of varying composition and temper. Corrosion Science. 2020;169(March):108618.

[109] Zhao J, Liu, Bai S, Zeng D, Luo L, Wang J. Effects of natural aging on the formation and strengthening effect of G.P. zones in a retrogression and re-aged Al–Zn–Mg–Cu alloy. Journal of Alloys and Compounds. 2020;829:154469.

[110] Zhou B, Lu S, Xu K, Xu C, Wang Z, Wang B. Hot cracking tendency test and simulation of 7075 semi-solid aluminium alloy. Transactions of Nonferrous Metals Society of China. 2020:30(2);318-332.

[111] Jang JH, Nam DG, Park YH, Park MI. Effect of solution treatment and artificial aging on microstructure and mechanical properties of Al-Cu alloy. Transactions of Nonferrous Metals Society of China. 2013;23(3):631-635.

[112] Li X, Xia W, Yan H, Chen J, Li X. Improving strength and corrosion resistance of high Mg alloyed Al–Mg–Mn alloys through Ce addition. Corrosion Engineering, Science and Technology. 2020;55(5):381-391.

[113] Argade GR, Panigrahi SK, Mishra RS. Aging response on the stress corrosion cracking behavior of wrought precipitation-hardened magnesium alloy. Journal of Materials Science. 2020;55(3):1216-1230.

[114] Soboyejo W. Mechanical Properties of Engineered Materials. New York: CRC Press; 2002.

[115] Zhao K, Benton A, Xu F, Shi X, He J. Atomic size mismatch: What if it is too large?. Matter. 2021;4(8):2618–2619, Aug. 2021.

[116] Tsai AP. A test of Hume-Rothery rules for stable quasicrystals. Journal of Non-Crystalline Solids. 334-335 vol. 334–335, pp. 317–322, 2004, doi: 10.1016/j.jnoncrysol.2003.11.065.

[117] Tański T, Snopiński P. Effect of the Processing Conditions on the Microstructural Features and Mechanical Behavior of Aluminum Alloys. In: Sivasankaran, S. Aluminium Alloys-Recent Trends in Processing, Characterization, Mechanical behavior and Applications. Storrs: IntechOpen Book Series; 2017., p. 1196-1242.

[118] Ryen Ø, Nijs O, Sjölander E, Holmedal B, Ekström HE, Nes E. Strengthening mechanisms in solid solution aluminum alloys. Metallurgical and Materials Transactions A: Physical Metallurgy and Materials Science. 2006;37(6):1999–2006.

[119] Padilha AF, Plaut RL. Work hardening, Recovery, Recrystallization, and Graina Growth. In: Totten GE, MacKenzie DS., editors. Handbook of Aluminum: Volume 2: Alloy Production and Materials Manufacturing. Storrs: Taylor & Francis eBooks; 2004., p. 193-221.

[120] Liu G, Zhang GJ, Ding XD, Sun J, Chen KH. The influences of multiscale-sized second-phase particles on ductility of aged aluminum alloys. Metallurgical and Materials Transactions A: Physical Metallurgy and Materials Science. 2004;35(6):1725–1734.

[121] Ma Y, Huang Y, Zhang X. Precipitation thermodynamics and kinetics of the second phase of Al-Zn-Mg-Cu-Sc-Zr-Ti aluminum alloy. Journal of Materials Research and Technology. 2010;10: 445-452.

[122] Gladman T. Precipitation hardening in metals. Journal of Materials Science and Technology. 1999;15(1):30-36.

[123] Safara N, Golpayegani A, Engberg G, Ågren J. Study of the mean size and fraction of the second-phase particles in a 13% chromium steel at high temperature. Philosophical Magazine. 2020;100(20):217–233.

[124] Santos-Güemes R, Bellón B, Esteban-Manzanares G, Segurado J, Capolungo L, LLorca J “Multiscale modelling of precipitation hardening in Al–Cu alloys: Dislocation dynamics simulations and experimental validation. Acta Materialia. 2020;188:475-485.

[125] Guo Z, Sha W. Quantification of precipitation hardening and evolution of precipitates. Materials Transactions. 2002;43(6):1273–1282.

[126] Hatano T. Dynamics of a dislocation bypassing an impenetrable precipitate: The Hirsch mechanism revisited. Physical review. B, Condensed matterials. 2006;74(2):1-4.

[127] Courtney TH. Mechanical Behavior of Materials: Second Edition. Waveland Press; 2005.

[128] Ardell AJ. Precipitation hardening. Metallurgical and Materials Transactions A. 1985;16(12):2131–2165.

[129] Martin JW. Precipitation Hardening: Theory and Applications. Oxford: Butterworth Heinemann; 2021.

[130] Hirsch PB, Kelly A. Stacking-fault strengthening. Philosophical Magazine. 1965;12(119):881–900.

[131] Mlikota M, Schmauder S. A newly discovered relation between the critical resolved shear stress and the fatigue endurance limit for metallic materials. Metals (Basel). 2020;10(6):1–12, 2020.

[132] Liu J, Muraishi S. Dislocation dynamics simulations of dislocation-particle bypass mechanisms. Materials Science Forum. 2020;85:35–41.

[133] Shin CS, Fivel MC, Verdier M, Oh, KH Dislocation-impenetrable precipitate interaction: A three-dimensional discrete dislocation dynamics analysis. Philosophical Magazine. 2003;83(31-34):3691–3704.

[134] Lu L, Chen X, Huang X, Lu K. Revealing the maximum strength in nanotwinned copper. Science. 2009;323(5914):607–610.

[135] Haouala S, Alizadeh R, Bieler TR, Segurado J, LLorca J. Effect of slip transmission at grain boundaries in Al bicrystals. International Journal of Plasticity. 2020;126(March).

[136] Masoumi M, Ariza EA, Sinatora A, Goldenstein H. Role of crystallographic orientation and grain boundaries in fatigue crack propagation in used pearlitic rail steel. Materials Science and Engineering: A. 2018;722(May):147–155.

[137] Kumar D, Idapalapati S, Wang W, Narasimalu S. Effect of surface mechanical treatments on the microstructure-property-performance of engineering alloys. Materials (Basel). 2019;12(16).

[138] Wu XX, San XY, Liang XG, Gong YL, Zhu XK. Effect of stacking fault energy on mechanical behavior of cold-forging Cu and Cu alloys. Materials and Design. 2013;47:372-376.

[139] Valiev RZ, Estrin Y, Horita Z, Langdon TG, Zehetbauer JM, Zhu YT. Fundamentals of superior properties in bulk NanoSPD materials. Materials Research Letters. 2016;4(1);1-21.

[140] Fernández R, Bruno G, Garcés G, Nieto-Luis H, González-Doncel G. Fractional brownian motion of dislocations during creep deformation of metals. Materials

Science and Engineering: A. 2020;796(7).

[141] Babaniaris S, Ramajayam M, Jiang L, Varma R, Langan T, Dorin T. Effect of Al3(Sc,Zr) dispersoids on the hot deformation behaviour of 6xxx-series alloys: A physically based constitutive model. Materials Science and Engineering: A. 2020;793:139873.

[142] Alloying: Understanding the Basics. Materials Park: ASM International; 2001.

[143] Dorin T, Ramajayam M, Lamb J, Langan T. Effect of Sc and Zr additions on the microstructure/strength of Al-Cu binary alloys. Materials Science and Engineering: A. 2017;707(July):58–64.

[144] Roesler J, Harders H, Baeker M. Mechanical Behaviour of Engineering Materials: Metals, Ceramics, Polymers, and Composites. 1st ed. Braunschweig:SpringerLink; 2006.

[145] Muggerud AMF, Mørtsell EA, Li Y, Holmestad R. Dispersoid strengthening in AA3xxx alloys with varying Mn and Si content during annealing at low temperatures. Materials Science and Engineering: A. 2013;567(April):21–28.

[146] Li JCM, Feng CR, Rath BB. Emission of Dislocations from Grain Boundaries and Its Role in Nanomaterials. Crystals. 2020;11(1):41.

[147] Massalski TB, Okamoto H, Subramanian PR, Kacprzak L, editors. Binary Alloy Phase Diagrams. ASM International; 1990.

[148] WebElements Periodic Table. https://www.webelements.com/magnesium/atom_sizes.html [cited 2023 Feb 19]

[149] WebElements Periodic Table. https://www.webelements.com/aluminium/atom_sizes.html [cited 2023 Feb 19]

[150] Jang DH, Park YB, Kim WJ. Significant strengthening in superlight Al-Mg alloy with an exceptionally large amount of Mg (13 wt%) after cold rolling. Material Science and Engineering: A. 2019;744:36–44.

[151] Liu Z, Sun J, Yan Z, Lin Y, Liu M, Roven HJ, Dahle AK. Enhanced ductility and strength in a cast Al–Mg alloy with high Mg content. Material Science and Engineering: A. 2021;806:140806.

[152] Liu K, Chen XG. Development of Al–Mn–Mg 3004 alloy for applications at elevated temperature via dispersoid strengthening. Materials and Design. 2015;84:340-350.

[153] Han JK, Liss KD, Langdon TG, Jang JI, Kawasaki M. Mechanical properties and structural stability of a bulk nanostructured metastable aluminum-magnesium system. Materials Science and Engineering: A. 2020;796(June):140050.

[154] Encyclopedia of Aluminum and Its Alloys, Two-Volume Set. Boca Raton: CRC Press; 2019.

[155] Heat Treater's Guide: Practices and Procedures for Nonferrous Alloys. Materials Park: ASM International; 1996.

[156] Aluminum and Aluminum Alloys. Materials Park: ASM International; 2020.

[157] Mukhopadhyay AK. Guinier-preston zones in a high-purity Al-Zn-Mg alloy. Philosophical Magazine Letters. 1994;70(3):135-140.

[158] Esteban-Manzanares G, Martínez E, Segurado J, Capolungo L, LLorca J. An atomistic investigation of the interaction of dislocations with Guinier-Preston zones in Al-Cu alloys. Acta Materialia. 2019;162:189-201.

[159] Zhang X, Tang J, Li H, Liang X, Lu Y, Che Y, Tu W, Zhang Y. Effects of non-isothermal aging on mechanical properties, corrosion behavior and microstructures of Al-Cu-Mg-Si alloy. Journal of Alloys and Compounds. 2020;819; 152960

[160] Heat Treating of Aluminum Alloys. Materials Park: ASM International; 1991.

[161] Barbosa CR, Machado GH, Azevedo HM, Rocha FS, Filho JC, Pereira AA, Rocha OL. Tailoring of Processing Parameters, Dendritic Microstructure, Si/Intermetallic Particles and Microhardness in As-cast and Heat-Treated Samples of Al7Si0.3Mg Alloy. Metals and Materials International. 2020;26(3):370-383.

[162] Berlanga-Labari C, Biezma-Moraleda MV, Rivero PJ. Corrosion of cast aluminum alloys: A review. Metals (Basel). 2020;10(10):1-30.

[163] Zolotorevsky VS, Belov NA, Glazoff MV. Casting Aluminum Alloys. Oxford:Elsevier Ltd; 2007.

[164] Petter L, Øye HA. Removing impurities from secondary alumina. JOM. 1991:43(11): 41-45.

[165] Darlapudi A, McDonald SD, Terzi S, Prasad A, Felberbaum M, StJohn DH. The influence of ternary alloying elements on the Al-Si eutectic microstructure and the Si morphology. Journal of Crystal Growth. 2016;433:63–73.

[166] Skoko Ž, Popovic S, Štefanić G. Microstructure of Al-Zn and Zn-Al Alloys. Croatica Chemica Acta. 2009;82(2):405-420.

[167] Shin J, Kim T, Kim DE, Kim D, Kim K. Castability and mechanical properties of new 7xxx aluminum alloys for automotive chassis/body applications. Journal of Alloys and Compounds.2017;689:577–590.

[168] EngineeringToolBox.https://www.engineeringtoolbox.com/fusion-heat-metals-d_1266.html. [cited 2021 Feb 10].

[169] Wang M, Pang JC, Liu HQ, Li SX, Zhang MX, Zhang ZF, Effect of constraint factor on the thermo-mechanical fatigue behavior of an Al-Si eutectic alloy. Materials Science and Engineering: A. 2020;783(December):139279.

[170] Murray JL, McAlister AJ. The Al-Si (Aluminum-Silicon) system. Bulletin of alloy phase diagrams.1984;5(1):74–84.

[171] Barrirero J, Engstler M, Ghafoor N, De Jonge N, Odén M, Mücklich F. Comparison of segregations formed in unmodified and Sr-modified Al-Si alloys studied by atom probe tomography and transmission electron microscopy," Journal of Alloys and Compounds. 2014;611:410–421.

[172] Donadoni B, Gouveia GL, Garcia A, Spinelli JE. A comparison of experimental time-secondary dendritic spacing and coarsening models for Al-Si-Cu alloys. Journal of Manufacturing Processes. 2019;54(October):14–18.

[173] Hellawell A. The growth and structure of eutectics with silicon and germanium. Progress in Materials Science. 1970;15(1):3–78.

[174] Day MG, Hellawell. The microstructure and crystalography of aluminum-silicone eutectuc alloys. Proceedings of the Royal Society of London Series A: Mathematical, Physical and Engineering Sciences. 1938;165:372.

[175] Steent AHA, Hellawell A. Structure and properties of aluminium-silicon eutectic alloys. Acta Metallia. 1972;20(3):363–370., 1972.

[176] Silva CAP, Layo RML, Guimarães EC, Júnior PM, Moreira AL, Rocha OL, Silva AP. Influence of Thermal Parameters, Microstructure, and Morphology of Si on Machinability of an Al-7.0 wt.% Si Alloy Directionally Solidified Advances in Materials Science and Engineering. 2018.

[177] Nikanorov SP, Osipov VN, Regel LI. .Structural and Mechanical Properties of Directionally Solidified Al-Si Alloys. Journal of Materials Engineering and Performance. 2019;28(12);7302–7323.

[178] Sato T, Kojima Y, Takahashi T. Modulated structures and GP Zones in Al-Mg alloys. Metallurgical and Materials Transactions A: Physical Metallurgy and Materials Science. 1982;13(8):1373–1378.

[179] Czechowski M. Slow-strain-rate stress corrosion testing of welded joints of Al-Mg alloys. Journal of Achievements in Materials and Manufacturing Engineering. 2019;20(1-2):219–222.

[180] Murray J. The Al−Mg (Aluminum−Magnesium) system. Journal of Phase Equilibria. 1982;3(1):60–74.

[181] Hamana D, Baziz L, Bouchear M. Kinetics and mechanism of formation and transformation of metastable β′-phase in Al-Mg alloys. Materials Chemistry and Physics. 2004;84(1):112–119.

[182] Osamura K, Ogura T. Metastable phases in the early stage of precipitation in Al-Mg alloys. Metallurgical and Materials Transactions A: Physical Metallurgy and Materials Science. 1984;15(5):835–842.

[183] Tsao CS, Chen YC, Jeng US, Kuo TY. Precipitation kinetics and transformation of metastable phases in Al-Mg-Si alloys. Acta Materialia. 2006;54(17):4621–4631.

[184] Goodwin F, Guruswamy S, Kainer KU, Kammer C, Knabl W, Koethe A, Leichtfried G, Schlamp G, Stickler R, Warlimont H. Metals. In: MartienssenW, Warlimont H,

editors. Springer Handbook of Condensed Matter and Materials Dana. Storrs: Springer; 2005. p. 161–430.

[185] Zovko Brodarac Z, Unkić F, Medved J, Mrvar P. Determination of solidification sequence of the AlMg9 alloy. Kovove Materialy. 2013;50(January):59-67.

[186] Asghar G, Peng L, Fu P, Yuan L, Liu Y. Role of Mg_2Si precipitates size in determining the ductility of A357 cast alloy. Materials and Design.2020;186:108280.

[187] Zhang Y, Li R, Chen R, Li X, Liu Z. Microstructural evolution of Al_2Cu phase and mechanical properties of the large-scale Al alloy components under different consecutive manufacturing processes. Journal of Alloys and Compounds. 2019;808:151634.

[188] Stanić D, Zovko Brodarac Z, Li L. Influence of copper addition in AlSi7MgCu alloy on microstructure development and tensile strength improvement. Metals (Basel). 2020;10(12):1–16.

[189] Vončina M, Medved J, Bončina T, Zupanič F. Effect of Ce on morphology of α(Al)-Al2Cu eutectic in Al-Si-Cu alloy. Transactions of Nonferrous Metals Society of China. 2014;24(1):36–41.

[190] Mageto JM. Tem study of microstructure in relation to hardness and ductility in Al-Mg-Si (6xxx) alloys [MSc Thesis]. Torgarden: Department of Physics Faculty of Natural Sciences and Technology Norwegian University of Science and Technology; 2016.

[191] Wlverton C. First-principles prediction of equilibrium precipitate shapes in Al-Cu alloys. Philosophical Magazine Letters. 1999;79(9):683–690.

[192] Kim K, Zhou B, Wolverton C. Interfacial stability of θ ′ / Al in Al-Cu alloys. Scripta Materialia 2018;159:99–103.

[193] Kim K, Roy A, Gururajan MP, Wolverton C, Voorhees PW. First-principles / Phase-fi eld modeling of q 0 precipitation in Al-Cu alloys. Acta Materialia. 2017:140;344–354.

[194] Wolverton C, Ozoliņš V. Entropically favored ordering: The metallurgy of Al_2Cu revisited. Physical Review Letters. 2001;86(24):5518–5521.

[195] He H, Yi Y, Huang S, Zhang Y. Effects of cold predeformation on dissolution of second-phase Al_2Cu particles during solution treatment of 2219 Al-Cu alloy forgings. Materials Characterization. 2018;135(October):18–24.

[196] Murry JL. The Al-Zn (Aluminum-Zinc) System. Bulletin of Alloy Phase Diagrams. 1983;4(1):55-73.

[197] Ren YP, Qin GW, Pei WL, Hao SM. The (a 1 + a 2) miscibility gap of the Al – Zn – Cu system at 360°C. Scripta Materialia. 2009;61(1):36–39.

[198] Satyanarayana KG. Metastable solvus curves in Al-Zn alloys - Part 2 The transition

phase: Journal of Materials Science. 1981;16(5):1240–1248.

[199] Davey T, Tran ND, Saengdeejing A, Chen Y. First-principles-only CALPHAD phase diagram of the solid aluminium-nickel (Al-Ni) system. Calphad. 2020;71(June):102008.

[200] Novakovic R, Mohr M, Giuranno1 D, Ricci1 E, Brillo J, Wunderlich R, Egry I, Plevachuk Y,. Fecht HJ. Surface Properties of Liquid Al-Ni Alloys: Experiments Vs Theory. Microgravity Science and Technology. 2020;32(6):1049–1064.

[201] Rodrigues AV, Lima TS, Vida TA, Brito C, Garcia A,. Cheung N. Microstructure and Tensile/Corrosion Properties Relationships of Directionally Solidified Al–Cu–Ni Alloys. Metals and Materials International. 2018;24(5):1058–1076.

[202] Arthanari S, Jang JC, Shin KS. Corrosion studies of high pressure die-cast Al-Si-Ni and Al-Si-Ni-Cu alloys. Journal of Alloys and Compounds. 2018;749:146–154.

[203] Belov NA, Akopyan TK, Gershman IS, Stolyarova OO, Yakovleva AO. Effect of Si and Cu additions on the phase composition, microstructure and properties of Al-Sn alloys. Journal of Alloys and Compounds. 2017;695:2730–2739.

[204] Lu ZC, Gao Y, Zeng MQ, Zhu M. Improving wear performance of dual-scale Al-Sn alloys: The role of Mg addition in enhancing Sn distribution and tribolayer stability. Wear. 2014;309(1-2):216–225.

[205] Liu X, Zeng MQ, Ma Y, Zhu M. Promoting the high load-carrying capability of Al-20 wt% Sn bearing alloys through creating nanocomposite structure by mechanical alloying. Wear. 2012;294–295:387–394.

[206] Kong JC, Brown PD, Harris SJ, McCartney DG. The microstructures of a thermally sprayed and heat treated Al-20 wt.%Sn-3 wt.%Si alloy. Materials Science and Engineering: A. 2005;403(1-2):205–214.

[207] Raghavan V. Al-Mg-Sn (Aluminum-Magnesium-Tin). Journal of Phase Equilibria and Diffusion. 2011;32(1):57–60.

[208] Sadhukhan S, Kundu M, Ghosh M. Effect of trace added Sn on mechanical properties of Al- Zn-Mg alloy. Advanced Materials Research. 2016;828(October):73–80.

[209] Qian F, Zhao D, Mørtsell EA, Jin S, Wang J, Marioara CD, .Andersen SJ, Sha G, Li Y. Enhanced nucleation and precipitation hardening in Al–Mg–Si(–Cu) alloys with minor Cd additions. Materials Science and Engineering: A. 2020;792:139698.

[210] Zhu S, Yao J, Sweet L, Easton M, Taylor J, Robinson P, Parson N. Influences of nickel and vanadium impurities on microstructure of aluminum alloys. Jom. 2013;65(5);584-592.

[211] Mahfoud m, Rao AKP, Emadi D. The role of thermal analysis in detecting impurity levels during aluminum recycling. Journal of Thermal Analysis and Calorimetry. 2010;100(3):847-851.

[212] Prasad A, Taylor JA, Grandfield JF. Control and removal of impurities from Al melts: A review. Materials Science Forum. 2011;693:149-160.

[213] Khaliq A, Rhamdhani MA, Brooks GA, Grandfield JF. Removal of vanadium from molten aluminum-Part I. Analysis of VB2 formation. Metallurgical and Materials Transactions B: Process Metallurgy and Materials Processing Science. 2014;45(2):752-768.

[214] Khaliq A, Rhamdhani MA, Brooks GA, Grandfield JF. Removal of vanadium from molten aluminum-Part III. Analysis of industrial boron treatment practice. Metallurgical and Materials Transactions B: Process Metallurgy and Materials Processing Science. 2014;45(2):784-794.

[215] Cui X, Wu Y, Zhang G, Liu Y, Liu X. Study on the improvement of electrical conductivity and mechanical properties of low alloying electrical aluminum alloys. Composites Part B: Engineering. 2017;110:381-387.

[216] Khaliq A, AlghamdI AS, Rajhi W, Subhani T, Ramadan M, Abdel Halim KS, Qian MA. Thermodynamic and Kinetic Analyses of the Removal of Impurity Titanium and Vanadium from Molten Aluminum for Electrical Conductor Applications. Metallurgical and Materials Transactions B: Process Metallurgy and Materials Processing Science. 2021;52(2):3130-3141.

[217] Lindsay JS, Welch BJ. A Review: Understanding the Science and the Impacts of Impurities upon the Electrolytic Bath of Hall–Héroult Reduction Cells. Jom. 2021;73:1196–1209.

[218] Taylor JA, Stjohn DH, Easton MA. Case studies in aluminium casting alloys. In: Lomley R., editor. Fundamentals of Aluminium Metallurgy. Storrs: ScienceDirect; 2011, p. 185-214.

[219] Shi D, Wen B, Melnik R, Yao S, Li T. First-principles studies of Al-Ni intermetallic compounds. Journal of Solid State Chemistry. 2009;182(10):2664–2669.

[220] Ji S, Yang W, Gao F, Watson D, Fan Z. Effect of iron on the microstructure and mechanical property of Al-Mg-Si-Mn and Al-Mg-Si diecast alloys. Materials Science and Engineering: A. 2012;564:130-139.

[221] Ji S, Yang W, Gaol F, Watson D, Fan ZI. Effect of iron in AI-Mg-Si-Mn ductile die cast alloy. In: Sadler BA. Light Metals. Storrs: Springer Link; 2013, p. 317–322.

[222] Timpel M, Wanderka N, Grothausmann R, Banhart J. Distribution of Fe-rich phases in eutectic grains of Sr-modified Al-10 wt.% Si-0.1 wt.% Fe casting alloy. Journal of Alloys and Compounds. 2013;558:18–25.

[223] Cao X, Campbell J. Morphology of β-Al5FeSi phase in Al-Si cast alloy. Metallurgical and Materials Transactions A. 2006;47(5):1303–1312.

[224] Lu L, Dahle AK. Iron-rich intermetallic phases and their role in casting defect formation in hypoeutectic Al-Si alloys. Metallurgical and Materials Transactions A. 2005;36(13) 819–835.

[225] Roy N, Samuel MA, Samuel FH. Porosity formation in AI-9 Wt Pet Si-3 Wt Pet Cu alloy systems: Metallographic observations. Metallurgical and Materials Transactions A. 1996;27(2):415–429.

[226] Dinnis CM, Taylor JA, Dahle AK. Interactions between iron, manganese, and the Al-Si eutectic in hypoeutectic Al-Si alloys. Metallurgical and Materials Transactions A. 2006;37(11):3283–3291.

[227] Guan RG, Tie D. A review on grain refinement of aluminum alloys: Progresses, challenges and prospects. Acta Metallurgica Sinica (English Letters). 2017;30(5):409–432.

[228] Hansen N. Hall-Petch relation and boundary strengthening. Scripta Materialia. 2004;51(8);801–806.

[229] Friedman LH, Chrzan DC. Scaling Theory of the Hall-Petch Relation for Multilayers. Physical Review Letters. 1998;81(13):2715–2718.

[230] Legros M, Elliott BR, Rittner MN, Weertman JR, Hemker KJ. Microsample tensile testing of nanocrystalline metals. Philosophical Magazine A: Physics of Condensed Matter, Structure, Defects and Mechanical Properties. 2000;80(4): 1017–1026.

[231] Zhang MX, Kelly MP, Easton MA, Taylor JA. Crystallographic study of grain refinement in aluminum alloys using the edge-to-edge matching model. Acta Materialia. 2004;53(5):1427–1438.

[232] Easton M, Stjohn D. Grain refinement of aluminum alloys: Part I. The nucleant and solute paradigms - a review of the literature. Metallurgical and Materials Transactions A: Physical Metallurgy and Materials Science. 1999;30(6):1613–1623.

[233] Alamdari HD, Dubé D, Tessier P. Behavior of boron in molten aluminum and its grain refinement mechanism. Metallurgical and Materials Transactions A: Physical Metallurgy and Materials Science. 2013;44(1):388–394.

[234] Kashyap KT, Chandrashekar T. Effects and mechanisms of grain refinement in aluminium alloys. Bulletin of Materials Science. 2001;24(4):345–353

[235] Maxwell I, Hellawell A. A simple model for grain refinement during solidification. Acta Materialia. 1975;23(2):229–237.

[236] Hong QZ, Barmak K, Clevenger LA. Crystallization of amorphous Co-Si alloys. Journal of Applied Physics. 1992;72(8):3423–3430.

[237] Johnsson M. Grain refinement of aluminium studied by use of a thermal analytical technique. Thermochimica Acta. 1995;256(1):107–121.

[238] Wang F, Liu Z, Qiu D, Taylor JA, Easton MA, Zhang MX. Revisiting the role of peritectics in grain refinement of Al alloys. Acta Materialia. 2012;61(1):360–370.

[239] Easton M, StJohn D. Grain refinement of aluminum alloys: Part II. Confirmation of, and a mechanism for, the solute paradigm. Metallurgical and Materials Transactions A: Physical Metallurgy and Materials Science. 1999;30(6):1625–1633.

[240] Chandrashekar T, Muralidhara MK, Kashyap KT, Rao PR. Effect of growth restricting factor on grain refinement of aluminum alloys. The International Journal of Advanced Manufacturing Technology. 2009;40(3-4):234–241.

[241] Murty BS, Kori SA, Chakraborty M. Grain refinement of aluminium and its alloys by heterogeneous nucleation and alloying. International Materials Reviews. 2002;47(1):3–29.

[242] Nogita K, McDonald SD, Dahle AK. Eutectic Modification of Al-Si Alloys with Rare Earth Metals. Material Transaction. 204;45(2):323–326.

[243] Joseph S, Kumar S. A systematic investigation of fracture mechanisms in Al-Si based eutectic alloy-Effect of Si modification. Materials Science and Engineering A. 2013;588:111–124.

[244] Samuel MA, Elgallad EM, Doty HW, Valtierra S, Samuel FH. Effect of metallurgical parameters on the microstructure, hardness impact properties, and fractography of Al-(6.5-11.5) wt% Si based alloys. Materials and Design. 2016;107:426–439.

[245] Lu SZ, Hellawell A. The mechanism of silicon modification in aluminum-silicon alloys: Impurity induced twinning. Metallurgical and Materials Transactions A. 1987;18(10):1721–1733.

[246] Kozina F, Zovko Brodarac Z, Tubić B, Dolić N. The effect of sodium and strontium on modification of eutectic silicon. In: Mladenović S, Maluckov Č, editors. 51st International October Conference on Mining and Metallurgy; Borsko Jezero, Srbia, 16.10-19.10.2019. Bor: University of Belgrade Technical Faculty in Bor; 2019.

[247] Knuutinen A, Nogita K, McDonald SD, Dahle AK. Modification of Al-Si alloys with Ba, Ca, Y and Yb. Journal of Light Metals. 2001;1(4):229–240.

[248] Li J, Hage F, Wiessner M, Romaner L, Scheiber D, Sartory B, Ramasse Q, Schumacher P. The roles of Eu during the growth of eutectic Si in Al-Si alloys. Scientific Reports. 2015;5:1–10.

[249] Zarif M, McKay B, Schumacher P. Study of heterogeneous nucleation of eutectic Si in high-purity Al-Si alloys with Sr addition. Metallurgical and Materials Transactions A. 2011;42(6):1684–1691.

[250] Shamsuzzoha M, Hogan LM. The role of non-cozonal twinning in the growth of fibrous silicon in strontium-modified Al-Si eutectic. Journal of Materials Science. 1989;24(8):2849–2859.

[251] Giovanni MD, Warnett JM, Williams MA, Srirangam P. 3D imaging and quantification of porosity and intermetallic particles in strontium modified Al-Si alloys. Journal of Alloys and Compounds. 2017;727:353–361.

[252] Mcdonald SD, Dahle AK, Taylor JA,. St. John DH. Modification-related porosity formation in hypoeutectic aluminum-silicon alloys. Metallurgical and Materials Transactions B. 2004;35(6):1097–1106.

[253] Tiedje NS, Taylor JA, Easton MA, Feeding and distribution of porosity in cast Al-Si alloys as function of alloy composition and modification. Metallurgical and Materials Transactions A. 2012;43(12):4846–4858.

[243] Shabestari SG, Ghodrat S. Assessment of modification and formation of intermetallic compounds in aluminum alloy using thermal analysis. Materials Science and Engineering: A. 2007;467(1-2):150–158.

[254] GaoT, Hu K, Wang L, Zhang B, Liu X. Morphological evolution and strengthening behavior of α-Al(Fe,Mn)Si in Al–6Si–2Fe–xMn alloys. Results in Physics. 2017;7(March):1051–1054.

[255] Belov NA, Aksenov AA, Eskin DG. Iron in aluminum alloys : impurity and alloying element. London and New York: Taylor and Francis;2002.

[256] Gao T, Hu K, Wang L, Zhang B, Liu X. Morphological evolution and strengthening behavior of α-Al(Fe,Mn)Si in Al–6Si–2Fe–xMn alloys. Results in Physics. 2017;7(March):1051–1054.

[257] Zhang Z, Tezuka H, Kobayashi E, Sato T. Effects of the Mn/Fe ratio and cooling rate on the modification of Fe intermetallic compounds in cast A356 based alloy with different Fe contents. Materials Transactions. 2013;54(8);1484–1490.

[258] Kozina F, Zovko Brodarac Z, Drobnjak D, Jukić I. Investigation of iron containing intermetallics in AlSI12 alloy. In: Dolić N, Zovko Brodarac Z. Begić Hadžipašić A, editors. 18th international foundrymen conference entitled: Coexistence of material science and sustainable technology in economic growth; Sisak, Croatia, 15.05.-17.05.2019. Sisak:University of Zagreb Faculty of Metallurgy; 2019.

[259] Wu X, Zhanga H, Zhanga F, Ma Z, Jia L, Yang B, Tao T, Zhang H. Effect of cooling rate and Co content on the formation of Fe-rich intermetallics in hypoeutectic Al7Si0.3Mg alloy with 0.5%Fe. Materials Characterization. 2018;139(February)116–124.

[260] Mahta M, Emamy M, Daman A, Keyvani A, Campbell J. Precipitation of Fe rich intermetallics in Cr- and Co-modified A413 alloy. International Journal of Cast Metals Research. 2005;18(2):73–79.

[261] Timpel M, Wanderka N, Murty BS, Banhart J. Three-dimensional visualization of the microstructure development of Sr-modified Al-15Si casting alloy using FIB-EsB tomography. Acta Materialia. 2010:58(20):6600–6608.

[262] Samuel FH, Ouellet P, Samuel MA, Doty HW. Effect of Mg and Sr additions on the formation of intermetallics in AI-6 Wt Pet Si-3.5 Wt Pet Cu-(0.45) to (0.8) Wt Pet Fe 319-Type Alloys. Metallurgical and Materials Transactions A: Physical Metallurgy and Materials Science. 1998;29(12):2871–2884.

[263] Ibrahim MF, Alkahtani SA, Abuhasel KA, Samuel FH. Microstructural Characterization of Beryllium Treated Al-Si Alloys. Advances in Materials Science and Engineering. 2015:2015;673025.

[264] Gupta RK, Nayan N, Nagasireesha G, Sharma SC. Development and characterization of Al-Li alloys. Materials Science and Engineering: A. 2006;420(1-2):228–234, 2006.

[265] Density of Elements Chart – Angstrom Sciences Elements Density Table

https://www.angstromsciences.com/density-elements-chart [cited 2022 May 8]

[266] El-Aty AA, Xu Y, Guo X, Zhang SH, Ma Y, Chen D. Strengthening mechanisms, deformation behavior, and anisotropic mechanical properties of Al-Li alloys: A review. Journal of Advanced Research. 2018;10: 49–67.

[267] Elagin VI, Zakharov VV. Modern Al - Li alloys and prospects of their development. Metal Science and Heat Treatment. 2013;55(3-4):184–190.

[268] Starke EA. Historical Development and Present Status of Aluminum-Lithium Alloys. In:Prasad NE, Gokhale AA, Wanhill, editors. Aluminum-Lithium Alloys: Processing, Properties, and Applications. Storrs: ScienceDirect; 2013., p. 3–26.

[269] Kakauridze G, Kilosanidze B. Dynamic energy transfer in a polarization hologram at low intensity of working beams. Practical Holography XXV: Materials and Applications. 2011;7957(2):79570T.

[270] Gilmore DL, Starke EA. Trace element effects on precipitation processes and mechanical properties in an Al-Cu-Li alloy. Metallurgical and Materials Transactions A: Physical Metallurgy and Materials Science. 1997; 28(7):1399–1415.

[271] Lavernia JE, Srivatsan TS, Mohamed FA. Strength, deformation, fracture behaviour and ductility of aluminium-lithium alloys. Journal of Materials Science.1990;25(2):1137–1158.

[272] Starke EA, Lin FS. Influence of grain structure on the ductility of the Al-Cu-Li-Mn-Cd alloy 2020. Metallurgical and Materials Transactions A: Physical Metallurgy and Materials Science. 1982;13A(12):2259–2269.

[272] Miller WS, Zhuang L, Bottema J, Wittebrood AJ, Smet P, Haszler A, Vieregge A.Recent development in aluminium alloys for the automotive industry. Materials Science and Engineering: A. 2000;280(1):37–49.

[273] Heard DW, Boselli J, Rioja R, Marquis EA, Gauvin R, Brochu M. Interfacial morphology development and solute trapping behavior during rapid solidification of an Al-Li-Cu alloy. Acta Materialia. 2013;61(5):1571–1580.

[274] Heard DW, Boselli J, Rioja R, Marquis EA, Gauvin R, Brochu M. Interfacial morphology development and solute trapping behavior during rapid solidification of an Al-Li-Cu alloy. Acta Materiallia. 2013;61(5):1571–1580.

[275] Luo L, Luo L, Li Z, Xia H, Su Y, Wang L, Guo J, Fu H. Microstructural evolution of Al-Cu-Li alloys with different Li contents by coupling of near-rapid solidification and two-stage homogenization treatment. China Foundry. 2020;17(3):190-197.

[276] Chen RT, Starke EA. Microstructure and mechanical properties of mechanically alloyed, ingot metallurgy and powder metallurgy AlLiCuMg alloys. Materials Science and Engineering: A. 1984;67(2): 229–245.

[277] Rioja RJ, Liu J. The evolution of Al-Li base products for aerospace and space applications. Metallurgical and Materials Transactions A: Physical Metallurgy and Materials Science. 2012;43(9):3325–3337.

[278] More AM, Kalsar R, Shivashankar P, Lingam R, Reddy NV, Prakash O, Suwas S. Incremental Forming of the Al-Li Alloy AA2195: Role of Texture and Microstructure. Jom. 2020;72(4):1647-1655.

[279] Giummarra C, Rioja RJ, Bray GH, Magnusen PE, Moran JP. Al-Li alloys: Development of corrosion resistant, high toughness aluminum-lithium aerospace alloy. In: Hirsch J, Skrotzki B, Gottstein G, editors. Aluminium Alloys: The Physical and Mechanical Properties. Storrs: DGM; 2008., p.176-189.

[280] Betsofen YS, Antipov VV, Knyazev MI. Al–Cu–Li and Al–Mg–Li alloys: Phase composition, texture, and anisotropy of mechanical properties. Russian Metallurgy. vol. 2016;2016(4):326–341.

[281] Zakharov VV. Some problems of the use of aluminum-lithium alloys. Metal Science and Heat Treatment. 2003;45(1):49–54.

[282] Lynch SP. Fracture of 8090 AlLi plate I. Short transverse fracture toughness. Materials Science and Engineering A. 1991;136(C):25–43.

[283] Sweet ED, Lynch SP, Bennett CG, Nethercott RB, Musulin I. Effects of alkali-metal impurities on fracture toughness of 2090 Al-Li-Cu extrusions. Metallurgical and Materials Transactions A: Physical Metallurgy and Materials Science. 1996;27(11):3530–3541.

[284] Pasang T, Symonds N, Moutsos S, Wanhill RJH, Lynch SP. Low-energy intergranular fracture in Al-Li alloys. Engineering Failure Analysis. 2012;22: 166–178, 2012.

[285] Lynch SP, Wilson AR, Byrnes RT. Effects of ageing treatments on resistance to intergranular fracture of 8090 AlLi alloy plate. Materials Science and Engineering A. 1993;172(1-2): 9–93.

[286] Lynch SP, Muddle BC, Pasang T. Ductile-to-brittle fracture transitions in 8090 Al-Li alloys. Acta Materialia. 2001;49(15):2863–2874.

[287] Peng Y, Ma Y, Sun W, Zhang W, Wang Z, Yang Z. Buckling fatigue behavior of 2A97 Al-Li alloy stiffened panels under shear loading. Engineering Failure Analysis. 2021;128(March).

[288] Zhang L, Cao W, Zhang Y, Jiang R. Microstructure evolution and enhanced mechanical properties of additive manufacturing Al-Zn-Mg-Li alloy via forging and aging treatment. Journal of Materials Research and Technology. 2022;18:4965–4979.

[289] Thompson JJ. Exfoliation corrosion testing of aluminum-lithium alloys. In: Agarwala VS, Ugiansky GM, editors. New Methods for Corrosion Testing of Aluminum Alloys. Storrs:ASTM; 1992., p. 70-101.

[290] Han J, Zhu Z, Li H, Gao C. Microstructural evolution, mechanical property and thermal stability of Al-Li 2198-T8 alloy processed by high pressure torsion. Materials Science and Engineering A. 2015;651:435–441.

[291] Elagin VI, Rostova TD, Shoheglova NM. Structure and properties of ingots and plates of type 1450 high-strength aluminum-lithium alloy. Advanced Performance Materials. 1995;2(1):21–41.

[292] Oding IA, Zubarev PV, Fridman ZG. Polygonization in metals. Metal Science and Heat Treatment of Metals. 1961;3:1-5.

[293] Harris SJ, Noble B, Dinsdale K. Mechanical Behaviour of Aluminium Alloys Containing Lithium. Institution of Metallurgists. 1983;28(20):48–56.

[294] Prasad Rambabu VVK, Prasad EN, Wanhill RJH. Aluminum-lithium alloys. In: Prasad EN, Wanhill RJH, editors. Aerospace Materials and Material Technologies. Storres: Springer Singapore; 2017., p. 586.

[295] Saunders N. Calculated Stable and Metastable Phase Equilibria in Al-Li-Zr Alloys / Berechnung der stabilen und metastabilen Phasengleichgewichte in Al-Li-Zr-Legierungen. International Journal of Materials Research. 1989;80(12):894–903.

[296] Zhao X, Liu W, Xiao D, Ma Y, Huang L, Tang Y. A critical review: Crystal structure, evolution and interaction mechanism with dislocations of nano precipitates in Al-Li alloys. Materials & Design. 2022;217:110629.

[297] Sun Z, He B, Chen R, Wang H. Anomalous precipitation of Al3Sc dispersoids on deformation behavior of a novel Al-Cu-Li alloy fabricated by direct energy deposition. Materials Letters. 2022;318:132207.

[298] Rodgers BI, Prangnell PB. Quantification of the influence of increased pre-stretching on microstructure-strength relationships in the Al-Cu-Li alloy AA2195. Acta Materiallia. 2016;108:55–67.

[299] Ott N, Kairy SK, Yan Y, Birbilis N. Evolution of Grain Boundary Precipitates in an Al-Cu-Li Alloy During Aging. Metallurgical and Materials Transactions A: Physical Metallurgy and Materials Science. 2017;48(1):51–56.

[300] Deng Y, Bai J, Wu X, Huang G, Cao L, Huang L. Investigation on formation mechanism of T1 precipitate in an Al-Cu-Li alloy. Journal of Alloys and Compounds. 2017;723:661–666.

[301] Araullo-Peters V, Gault B, De Geuser F, Deschamps A, Cairney JM. Microstructural evolution during ageing of Al-Cu-Li-x alloys. Acta Materiallia. 2014;66:199–208.

[302] Blankenship CP, Hornbogen E, Starke EA. Predicting slip behavior in alloys containing shearable and strong particles. Materials Science and Engineering: A.

1993;169(1-2):33–41.

[303] Deschamps A, Decreus B, De Geuser F, Dorin T, Weyland M. The influence of precipitation on plastic deformation of Al-Cu-Li alloys. Acta Materiallia. 2013;61(11):4010–4021.

[304] Dorin T, De Geuser F, Lefebvre W, Sigli C, Deschamps A, Strengthening mechanisms of T1 precipitates and their influence on the plasticity of an Al-Cu-Li alloy. Materials Science and Engineering: A. 2014;605:119–126.

[305] Abis S, Mengucci P, Riontino G. A study of the high-temperature ageing of Al-Cu-Mg-Ag alloy 201. Philosophical Magazine B-Physics of Condensed Matter Statistical Mechanics Electronic Optical and Magnetic Properties. 1993:67(4):465–484.

[306] Murayama M, Hono K. Role of Ag and Mg on precipitation of T1 phase in an Al-Cu-Li-Mg-Ag alloy. Scripta Materialia. 2001;44(4):701–706.

[307] Itoh G, Cui Q, Kanno M. Effects of a small addition of magnesium and silver on the precipitation of T1 phase in an Al-4%Cu-1.1%Li-0.2%Zr alloy. Materials Science and Engineering: A. 1996;211(1-2):128–137.

[308] Chen Z, Zhao K,. Fan L. Combinative hardening effects of precipitation in a commercial aged Al-Cu-Li-X alloy. Materials Science and Engineering: A. 2013;588:59–64.

[309] Wang SC, Starink MJ. Precipitates and intermetallic phases in precipitation hardening Al-Cu-Mg-(Li) based alloys. International Materials Reviews. 2005;50(4):193–215.

[310] Chen YQ, Tang ZH, Pan SP, Liu HW, Song YF, Liu Y, Zhu BW, Zhou W, Shen FH. A new type of anti-phase boundaries in the T(Al20Cu2Mn3) phase and the pre-deformation effect on T phase precipitation. Intermetallics. 2020;127(September):106977.

[311] Duan S, Guo F, Wu D, Wang T, Tsuchiya T, Matsuda K, Zou Y. Influences of pre-rolling deformation on aging precipitates and mechanical properties for a novel Al–Cu–Li alloy. Journal of Materials Research and Technology. 2021;15:2379–2392.

[312] Rodríguez-Veiga A, Bellón B, Papadimitriou I, Esteban-Manzanares G, Sabirov I, LLorca J. A multidisciplinary approach to study precipitation kinetics and hardening in an Al-4Cu (wt. %) alloy. Journal of Alloys and Compounds. 2018;757:504–519.

[313] Okamoto H. Al-Li (Aluminum-Lithium). Journal of Phase Equilibria and Diffusion. 2012;33(6):500-501.

[314] Rodríguez-Veiga A, Bellón B, Papadimitriou I, Esteban-Manzanares G, Sabirov I, LLorca J. A multidisciplinary approach to study precipitation kinetics and hardening in an Al-4Cu (wt. %) alloy. Journal of Alloys and Compounds. 2018;757:504–519.

[315] Spowage AC, Bray S. Characterization of nanoprecipitation mechanisms during isochronal aging of a pseudo-binary Al-8.7 at. pct Li alloy. Metallurgical and

Materials Transactions A: Physical Metallurgy and Materials Science. 2011;42(1):227–230.

[316] Liu S, Esteban-Manzanares G, LLorca J. First Principles Prediction of the Al-Li Phase Diagram. Metallurgical and Materials Transactions A: Physical Metallurgy and Materials Science. 2021;52(10):4675–4690.

[317] Lukas HL, Fries SG, Sundman B. Computational thermodynamics: The Calphad method. Michigen: Cambridge University Press; 2007.

[318] Katsikis S, Noble B, Harris SJ. Microstructural stability during low temperature exposure of alloys within the Al – Li – Cu – Mg system. Materials Science and Engineering: A. 2008;485:613–620.

[319] Grushko O, Ovchinnikov V. Aluminum-Lithium Alloys: Process Metallurgy, Physical Metallurgy, and Welding. 1st ed. Boca Raton: CRC Press 2016.

[320] Wolverton C. Entropically Favored Ordering : The Metallurgy of Al_2Cu Revisited. Physical Review Letters. 2001;86(24):5518-5521.

[321] Long Z, Cui D, Hu H, Li Z, Yin F. Thermodynamic Modeling of the Al-Li-Zr Ternary System. Journal of Phase Equilibria and Diffusion. 2020;41(5):623-641.

[322] Gayle FW, Vandersande B. Phase transformations in the Al-Li-Zr system. Acta Metallurgica. 1989;37(4):1033–1046, 1989.

[323] Raghavan V. Al-Li-Zr (Aluminum-Lithium-Zirconium). Journal of Phase Equilibria and Diffusio. 2009;30(6):624–625.

[324] Goel NC, Cahoon JR. The Al-Li-Mg system (Aluminum-Lithium-Magnesium). Bulletin of alloy phase diagrams. 1990;11(6):528-546.

[325] Tsubakino H, Nozato R, Sakurai T, Hasegawa Y, Hayashi Y. Precipitation of metastable δ′ in Al–1·9Li–2·5Mg alloy. Materials Science and Technology. 1994;10(3):222–226.

[326] Deschamps A, Sigli C, Mourey T, De Geuser F, Lefebvre W, Davo B. Experimental and modelling assessment of precipitation kinetics in an Al-Li-Mg alloy. Acta Materialia. 2012;60(5):1917–1928.

[327] Wu L, Li Y, Li X, Ma N, Wang H. Interactions between cadmium and multiple precipitates in an Al-Li-Cu alloy: Improving aging kinetics and precipitation hardening. Journal of Materials Science and Technology. 2020;46:44–49.

[328] Krug ME, Seidman DN, Dunand DC. Creep properties and precipitate evolution in Al-Li alloys microalloyed with Sc and Yb. Materials Science and Engineering: A. 2012;550:300–311.

[329] Porter DA, Easterling KE, Easterling KE. Phase Transformations in Metals and Alloys. Revised ed. Hong Kong: Springer-Science and Business Media; 1992.

[330] Smallman RE, Ngan AHW. Solidification. In: Smallman RE, Ngan AHW, editors. Modern Physical Metallurgy. Storrs: Elsevier; 2014., p.93–119.

[331] Laughlin D, Hono K, editors. Physical Metallurgy. Storrs: Elsevier; 2014.

[332] Myerson AS, Erdemir D, Lee AY. Crystal nucleation. In: Myerson AS, Erdemir D, Lee AY, editors. Handbook of Industrial Crystallization. Storrs: Cambridge University Press; 2019., p.76-114.

[333] Greer AL. Overview: Application of heterogeneous nucleation in grain-refining of metals. The Journal of Chemical Physics. 2016;145(21).

[334] Stefanescu DM. Science and engineering of casting solidification. Columbus: Springer; 2015.

[335] Vander Voort GF. Applied Metallography. Storres: Springer New York; 1986.

[336] Apel M, Eiken J, Hecht U. Phase field models for heterogeneous nucleation: Application to inoculation in alpha-solidifying Ti-Al-B alloys. The European Physical Journal Special Topics. 2014;223(3):545–558.

[337] Smallman RE, Ngan AHW, editors. Modern Physical Metallurgy. Storrs: Elsevier; 2014.

[338] Biloni H, Boettinger WJ. Solidification. In: Stefanescu DM, editor. Thermodynamics of Solidification. Storrs: Springer; 1996., p. 670–830.

[339] Smereka P. Spiral crystal growth. Physica D: Nonlinear Phenomena. 2000;138(3-4):282–301.

[340] Hötzer J, Steinmetz P, Jainta M, Schulz S, Kellner M, Nestler B, Rüde U. Phase-field simulations of spiral growth during directional ternary eutectic solidification. Acta Materiallia. 2016;106: 249–259.

[341] Dias M, Rosiński M, Rodrigues PCR, Correia JB,. Carvalho PA. Gibbs-Thomson effect as driving force for liquid film migration: Converting metallic into ceramic fibers through intrinsic oxidation. Acta Materiallia. 2021;218.

[342] Perez N. Phase Transformation in Metals: Mathematics, Theory and Practice. Puerto Rico: Springer Nature; 2020.

[343] Torabi M, Beckermann C. A truncated-Scheil-type model for columnar solidification of binary alloys in the presence of melt convection. Acta Materialia. 2019;7(May).

[344] Brito C, Nguyen-Thi H, Mangelinck-Noël N, Cheung NSpinelli JE,. Garcia A. Cellular-to-Dendritic and Dendritic-to-Cellular Morphological Transitions in a Ternary Al-Mg-Si Alloy. OP Conference Series: Materials Science and Engineering. 2019;529(1).

[345] Barrirer J. Eutectic Modification of Al-Si casting alloys. Linkoping: Linkoping University; 2019.

[346] Boettinger WJ, Banerjee DK. Solidification. In: Laughlin DE, Hono K, editors. Physical Metallurgy. Storrs: Science Direct; 2014., p.639-850

[347] Jackson KA. Crystal growth kinetics. Materials Science and Engineering: A. 1984;65(1) 7–13.

[348] Stefanescu DM, Ruxanda R. Fundamentals of Solidification. In: Vander Voort GF, editor. Metallography and Microstructures. Storrs: ASM International; 2004., p.71–92.

[349] Magnin P, Trivedi R. Eutectic growth: A modification of the Jackson and Hunt theory. Acta Metallurgica et Materialia. 1991;39(4):453–467.

[350] Dutta B, Rettenmayr M. An experimental investigation on the kinetics of solute driven remelting. Metallurgical and Materials Transactions A: Physical Metallurgy and Materials Science. 2000;31(11): 2713–2720.

[351] Weinberg F. The casting of steel Metallurgical and Materials Transactions A: Physical Metallurgy and Materials Science. 1975;6(11):1971–1985.

[352] Campbell J. Castings. Birmingham: Elsevier; 2003.

[353] Gandin CA, Desbiolles JL, Rappaz M, Thévoz P. A three-dimensional cellular automaton-finite element model for the prediction of solidification grain structures. Metallurgical and Materials Transactions A: Physical Metallurgy and Materials Science. 1999;30(12):3153–3165.

[354] Rappaz M,. Gandin CA. Probabilistic modelling of microstructure formation in solidification processes. Acta Metallurgica et Materialia. 1993;21(2).

[355] Flood SC, Hunt JD. Columnar and equiaxed growth. I. A model of a columnar front with a temperature dependent velocity. Journal of Crystall Growth. 1987;82(3):543–551.

[356] Martorano MA, Beckermann C,. Gandin CA. A solutal interaction mechanism for the columnar-to-equiaxed transition in alloy solidification. Metallurgical and Materials Transactions A: Physical Metallurgy and Materials Science. 2003;34(8):1657–1674.

[357] Partridge PG. Oxidation of aluminium—lithium alloys in the solid and liquid states. International Materials Reviews. 1990;35(1):37–58.

[358] Singh V, Gokhale AA. Melting and casting of aluminum-lithium alloys. In: Prasad NE, Gokhale AA, Wanhill RJH, editors. Aluminum-Lithium Alloy. Processing, Properties, and Applications. Storres: Elsevire; 2013, p. 167–185.

[359] Composites M. Calculated Phase Relations in the Al–Li–O System at 1000 K with Implications for Refractories and Metal–Matrix Composites. Journal of the American ceramic society. 1992;89:1484–1489.

CURRICULUM VITAE

Franjo Kozina was born on 3rd of January 1989 in Sisak, Croatia. He has finished both the elementary and high school in Petrinja, Croatia. He enrolled in the study of metallurgical engineering at Faculty of Metallurgy University of Zagreb in 2007. He finished his study in 2013, earning Faculty Medals at both the undergraduate and graduate levels. In the period from 2013 to 2016 Franjo is employed in local steel mill where he starts his career as a support worker at ladle metallurgy and vacuum degassing. Soon afterwards he becomes laboratory engineer in Mechanical and metallographic laboratory where he discovers a tendency for metallographic sample preparation and analysis. Because of this tendency, Franjo applied for a position at the Faculty of Metallurgy University of Zagreb and is employed as associate in metallographic analysis and foundry technology. His interests include the application and development of metallographic preparation techniques, microstructure analysis with a focus on defect analysis as well as development of innovative engineering alloys. He is an author and co-author of 25 scientific articles, six of which were published in scientific journals (WoS CC).

LIST OF PUBLICATIONS:

1. Z. Glavaš, A. Štrkalj, F. Kozina. The assessment of the nodule count and nodularity in ductile iron castings by using thermal analysis. Tehnički glasnik, 6(2012) 2; 145-150

2. Z. Glavaš, A. Štrkalj, K. Maladini, F. Kozina. Effect of bismuth and rare earth elements on graphite structure in different section thicknesses of spheroidal graphite cast iron castings. Archives of metallurgy and materials, 63(2018) 3; 1547-1553.

3. J. Krolo, B. Lela, I. Dumanić, F. Kozina. Statistical analysis of the combined ECAP and heat treatment for recycling aluminum chips without remelting. Metals, 9(2019) 6; 660.

4. F. Kozina, Z. Zovko Brodarac, M. Petrič, A. Penko. The influence of iron impurities on the compression behavior of Al-2.24Mg-2.09Li alloy. Journal of mining and metallurgy. Section: B, Metallurgy, 56(2020) 3; 425-433.

5. F. Kozina, Z. Zovko Brodarac, S. Brajčinović, M. Petrič. Determination of Al-2.18Mg-1.92Li alloy's microstructure degradation in corrosive environment. Crystals, 11(2021) 4; 338.

6. F. Kozina, Z. Zovko Brodarac, Metallurgy development: Discovery and utilization of aluminum through history. Engineering power: bulletin of the Croatian Academy of Engineering, 17(2022) 3; 6-19.

7. F. Kozina, Z. Zovko Brodarac, M. Petrič. Thermodynamic evaluation of Al-2.5 wt.%Mg-0.7 wt.%Li. In: A. Rotaru, T. Lupascu, F. Paladi (editors). Book of Abstracts of 4th Central and European Conference on Thermal Analysis and Calorimetry, 2017: 124.

8. F. Kozina, Z. Zovko Brodarac, M. Petrič. Microstructure development in as-cast Al-Mg-Li alloy. In: A. Gajović, I. Weber, G. Kovačević, V. Čadež, S. Šegota, A. Vidoš (editor). Book of Abstracts, 13th Multinational Congress on Microscopy, 2017: 549-550.

9. F. Kozina, Z. Zovko Brodarac, M. Petrič. The Al-2.5wt%Mg-0.7wt%Li alloy mechanical properties. In: Križman, P. Mrvar, J. Medved, P. Schumacher, R. Deike, M. Jan-Blažič, M. Petrič (editors). Conference Proceedings of 57th International Foundry Conference, 2017., CD-ROM.

10. Z. Zovko Brodarac, D. Stanić, F. Kozina. Influence of Cu on the microstructure development of AlSi7MgCu. Livarski vestnik, 66(2019) 3; 177-190.

11. Z. Zovko Brodarac, T. Rupčić, F. Kozina, D. Mašinović. Influence of the AlSI12 alloy inoculation on the microstructure and mechanical properties development. Livarski vestnik, 68(2021) 1; 35-50.

12. F. Kozina, Z. Glavaš, F. Unkić. The assessment of the microstructural features of ductile iron by using thermal analysis. In: Ž. Alar, S. Jakovljević (editors). Zbornik savjetovanja o materijalima, tehnologijama, trenju i trošenju, 2012: 140-153.

13. F. Kozina, Z. Zovko Brodarac, P. Mrvar, M. Petrič. Solidification sequence of Al-2.5wt.%Mg-0.7wt.%Li alloy. In: N. Štrbac, I. Marković, Lj. Balanović (editors). Proceeding book of 49th International October Conference on Mining and Metallurgy, 2017: 556-559.

14. T. Rupčić, Z. Zovko Brodarac, K. Terzić, F Kozina, J. Lošić. Overview of casting defects in ductile cast iron. In: Z. Zovko Brodarac, N. Dolić, A. Begić Hadžipašić

(editors). Proceedings Book of 16th International Foundrymen Conference, Global Foundry Industry - Perspectives for the Future, 2017: 227-239.

15. F. Kozina, Z. Zovko Brodarac, M. Petrič. Microstructural evaluation of Al-2.5wt.%Mg-0.7wt.%Li in as cast condition. In: Z. Zovko Brodarac, N. Dolić, A. Begić Hadžipašić (editors). Proceedings Book of 16th International Foundrymen Conference, Global Foundry Industry - Perspectives for the Future, 2017: 128-138.

16. Z. Zovko Brodarac, D. Stanić, F. Kozina. Influence of Cu on the microstructure development of AlSi7MgCu alloy. In: A. Križman, P. Mrvar, J. Medved, A. Bührig-Polaczek, P. Schumacher, R. Deike, J. Suchy, M. Jan-Blažič, M. Petrič (editors). Conference Proceedings 58th IFC Portorož, 2018: CD: 24, 1-10 - rad je objavljen u Livarskom vjesniku pod brojem A.2.1.

17. F. Kozina, Z. Zovko Brodarac, M. Petrič. Influence of solution hardening on microstructure and mechanical properties of Al-2.5Mg-0.7Li alloy. The 73rd World Foundry Congress, Krakow: World Foundry Organization, 2018., Poljska, 48.

18. F. Kozina, Z. Zovko Brodarac, M. Petrič. Analysis of the low energy layering fracture in Al- 2.5Mg-0.7Li. In: N. Dolić, Z. Zovko Brodarac, A. Begić Hadžipašić (editors). Proceedings book of 17th International Foundrymen Conference, Hi-tech Casting Solution and Knowledge Based Engineering, 2018: 144-160.

19. N. Dolić, I. Bunjan, F. Kozina. Correlation of mechanical and microstructural properties in as-cast condition of EN AW-5083 aluminium alloy using statistical analysis. In: N. Dolić, Z. Zovko Brodarac, A. Begić Hadžipašić (editor). Proceedings book of 17th International Foundrymen Conference, Hi-tech Casting Solution and Knowledge Based Engineering, 2018: 206-219.

20. I. Gavranović, Z. Zovko Brodarac, F. Kozina, T. Rupčić. Utjecaj uvjeta skrućivanja i debljine stijenke na razvoj primarnog α-Al u AlSi7Mg leguri. In: Lj. Slokar Benić, Z. Zovko Brodarac (editor). Knjiga sažetaka, 18th International Foundrymen Conference, Coexistence of Material Science and Sustainable Technology in Economic Growth, Studentska sekcija; 2019: 206-219.

21. F. Kozina, Z. Zovko Brodarac, D. Drobnjak, I. Jukić. Investigation of iron containing intermetallics in AlSi12 alloy with w (Mn/Fe) = 0.99. In: N. Dolić, Z. Zovko Brodarac,

A. Begić Hadžipašić (editors). Proceedings Book of 18th International Foundrymen Conference, Coexistence of Material Science and Sustainable Technology in Economic Growth, 2019: 255-275.

22. Z. Zovko Brodarac, T. Rupčić, F. Kozina, D. Mašinović. Influence of the AlSi12 alloy inoculation on the microstructure and mechanical properties development. In: A. Križman, M. Jan-Blažić, A. Turner. Conference Proceedings of WFO-Technical Forum and 59th IFC Portorož, 2019: USB: 15, 1-12.

23. F. Kozina, Z. Zovko Brodarac, B. Tubić, N. Dolić. The effect of sodium and strontium on modification of eutectic silicon. In: S. Mladenović, Č. Maluckov (editors). 51st International October Conference on Mining and Metallurgy Proceedings. 2019: 48-51.

24. F. Kozina, Z. Zovko Brodarac, M. Petrič. Investigation of equilibrium and non-equilibrium solidification of Al-2.2Mg-2.1Li alloy. In: D. Glišić, B. Marković, V. Manojlović. MME SEE 2019 Metallurgical and Materials Engineering Congress of South-East Europe Book of Abstracts, 2019: 17.

25. N. Dolić, Z. Zovko Brodarac, F. Kozina. Evaluation of EN AW-5083 aluminum alloy ingot homogeneity by measuring hardness. In: D. Glišić, B. Marković, V. Manojlović. MME SEE 2019 Metallurgical and Materials Engineering Congress of South-East Europe Book of Abstracts. 2019; 18.

26. F. Kozina, Z. Zovko Brodarac. Influence of modification on microstructure degradation of AlSi12 alloy exposed to the corrosion environment. 29th International Conference on Metallurgy and Materials-METALS 2020. 2020: 994-999.

27. F. Kozina, Z. Zovko Brodarac, M. Petrič, A. Penko. The influence of solution hardening on microstructure and mechanical properties of Al- 2.2Mg-2.1Li alloy. In: A. Križman, M. Jan-Blažić, A. Turner (editors). Abstract Proceedings WFO - Technical Forum and 59th IFC Portorož. 2019; 194-195.

28. F. Kozina, Z. Zovko Brodarac, M. Petrič, B. Leskovar. Thermodynamic consideration of Al-2.2Mg-2.1Li alloy behavior. In: A. Rotaru, S. V. Ciprioti (editors). Book of Abstracts of the 5th Central and Eastern Conference on Thermal Analysis and Calorimetry (CEEC-TAC5) and 14th Mediterranean Conference on Calorimetry and Thermal Analysis (Medicta2019), 2019: 145-145.

29. I. Jandrlić, F. Kozina, T. Brlić, M. Vučenović. Influence of cold reduction on the structure and hardness of cold drawn copper wire. In: N. Dolić, Z. Zovko Brodarac, S. Brajčinović (editors). 19th International foundrymen conference Humans - Valuable Resource for Foundry Industry Development, 2021: 314-324.

30. F. Kozina, Z. Zovko Brodarac, I. Jandrlić, R. Jagustović. Analysis of the crack formation in ASIS M2 high- speed tool steel during utilization. In: N. Dolić, Z. Zovko Brodarac, S. Brajčinović (editors). 19th International foundrymen conference Humans - Valuable Resource for Foundry Industry Development, 2021: 345-361.

31. S. Brajčinović, A. Begić-Hadžipašić. Inhibitory effect of commercial inhibitor vci 379/611 on corrosion behaviour of X153CrMoV12 tool steel for cold work. In: N. Dolić, Z. Zovko Brodarac, S. Brajčinović (editors). 19th International foundrymen conference Humans - Valuable Resource for Foundry Industry Development, 2021: 260-268.

32. Z. Zovko Brodarac, D. Stanić, M. Folta, F. Kozina. Recycling potential of AlSi9Cu3(Fe) alloy. In: A. Križman, Alojz, P. Mrvar, J. Medved, R. Rudolf, M. Petrič, A: Bühring-Polaczek, P Schumacher, P. Murrell, J.J. Sobczak, S. Marković (editors). Conference Proceedings 61st IFC Portorož 2021: 24,8.

33. F. Kozina, Z. Zovko Brodarac, B. Tubić Bulat, F. Dominković. The impact of melt retention time on the strontium modification efficiency. In: S. Jozić, B. Lela, N. Gjeldum (editors). Conference Proceedings Mechanical Technologies and Structural Materials, 2021: 67-73.

34. F. Kozina, Z. Zovko Brodarac, M. Stjepanović. The solidification sequence and microstructure development of secondary EN AC 46100 alloy. In: S. Jozić, B. Lela, N. Gjeldum (editors). Conference Proceedings Mechanical Technologies and Structural Materials, 2022: 71-81.

35. I. Jandrlić, F. Kozina, T. Brlić, L. Mrkobrada. Changes in structure and properties of copper wire during the production and processing. In: M. Jan-Blažič (editor). Abstract Proceedings 62nd IFC Portorož 2022: 41,13.

36. F. Kozina, Z. Zovko Brodarac, L. Zeljko, B. Tubić Bulat, P. Mrvar, A. Mahmutović, S. Zeljko. Technological development of the casting process for the thin-walled gray cast

iron. In: A. Kostov, M. Ljubujev (editors). 53rd International October Conference on Mining and Metallurgy Proceedings, 2022: 131-134.

37. Z. Zovko Brodarac, F. Kozina, D. Stanić, M. Folta. Quality assessment of the AlSi9Cu3(Fe) alloy with regard to recycling ratio. In: M. Sokić, B. Marković, V. Manojlović (editors). CONGRESS PROCEEDINGS - MME SEE 2023 5th Metallurgical & Materials Engineering Congress of South-East Europe, 2023:251-256.

APPENDIX 1

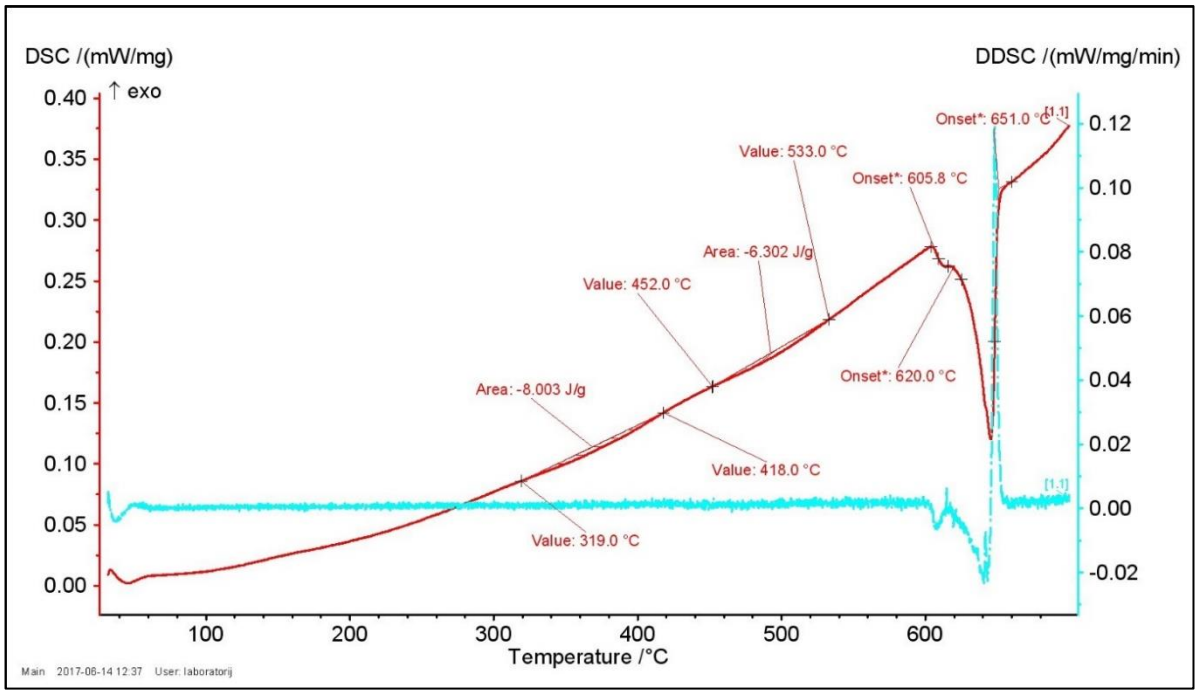

Heating with the rate of 2.0 K/min

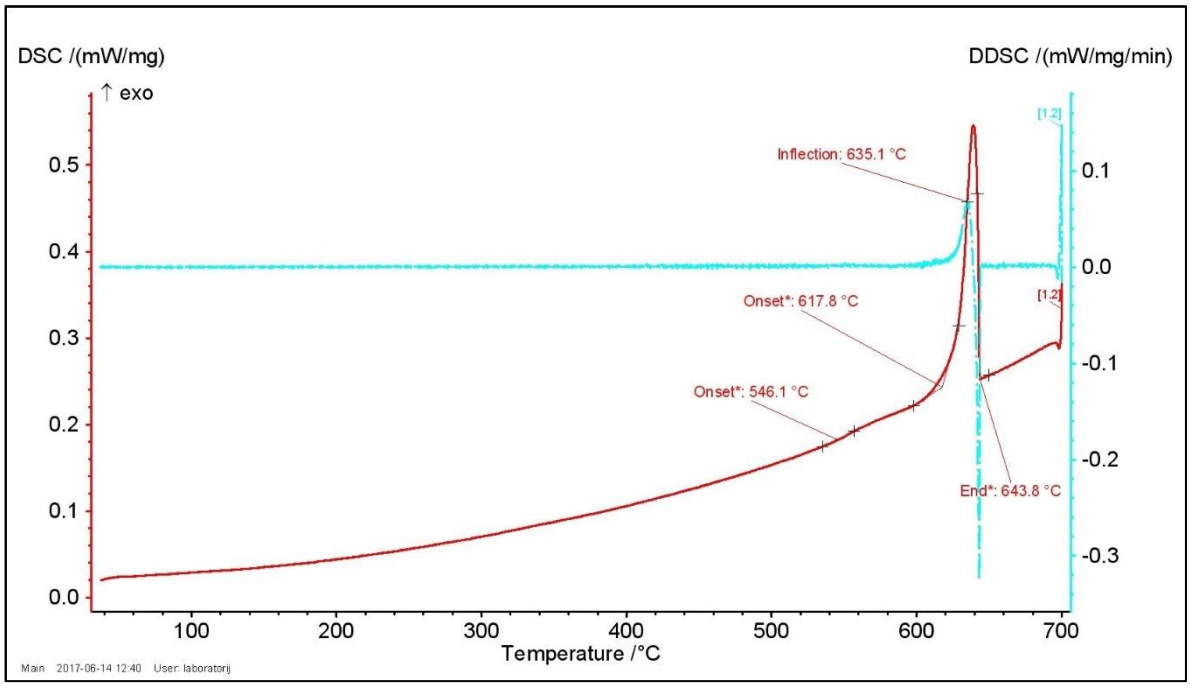

Cooling with the rate of 2.0 K/min

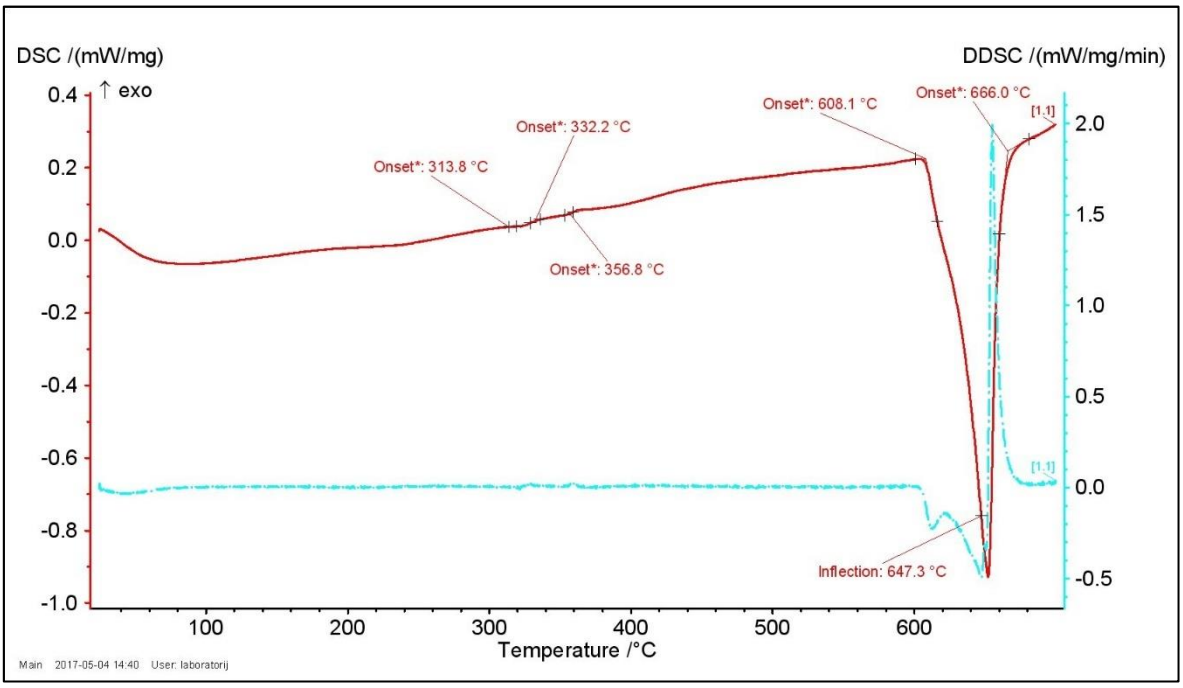

Heating with the rate of 10.0 K/min

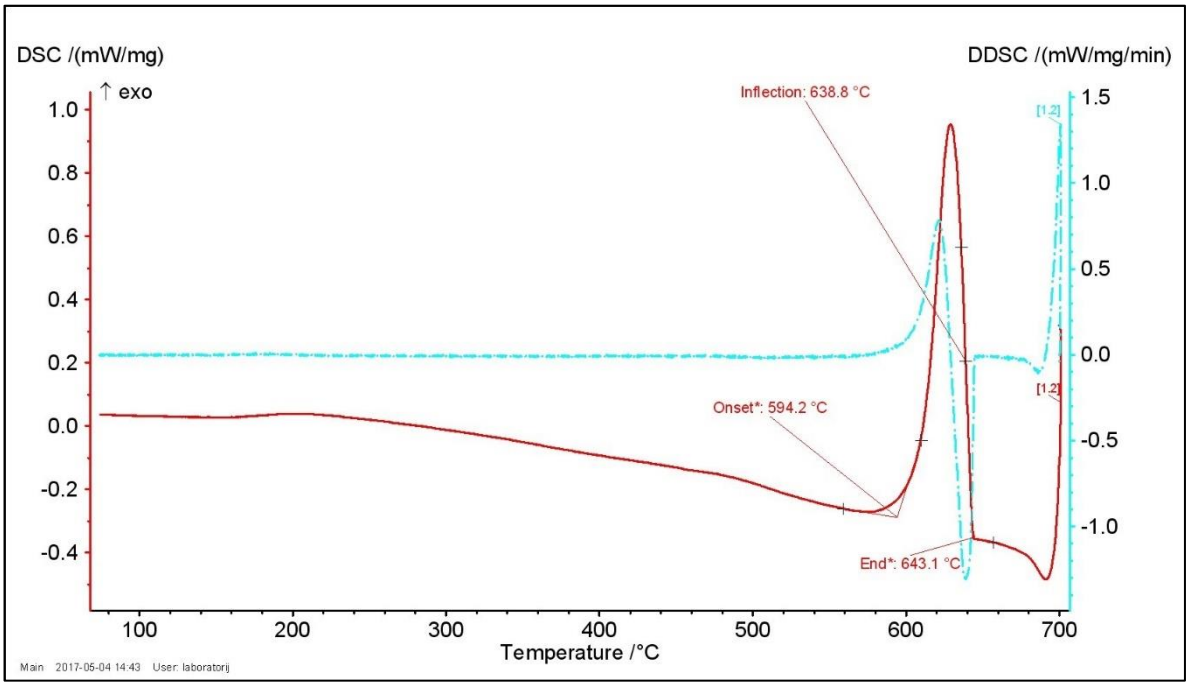

Cooling with the rate of 10.0 K/min

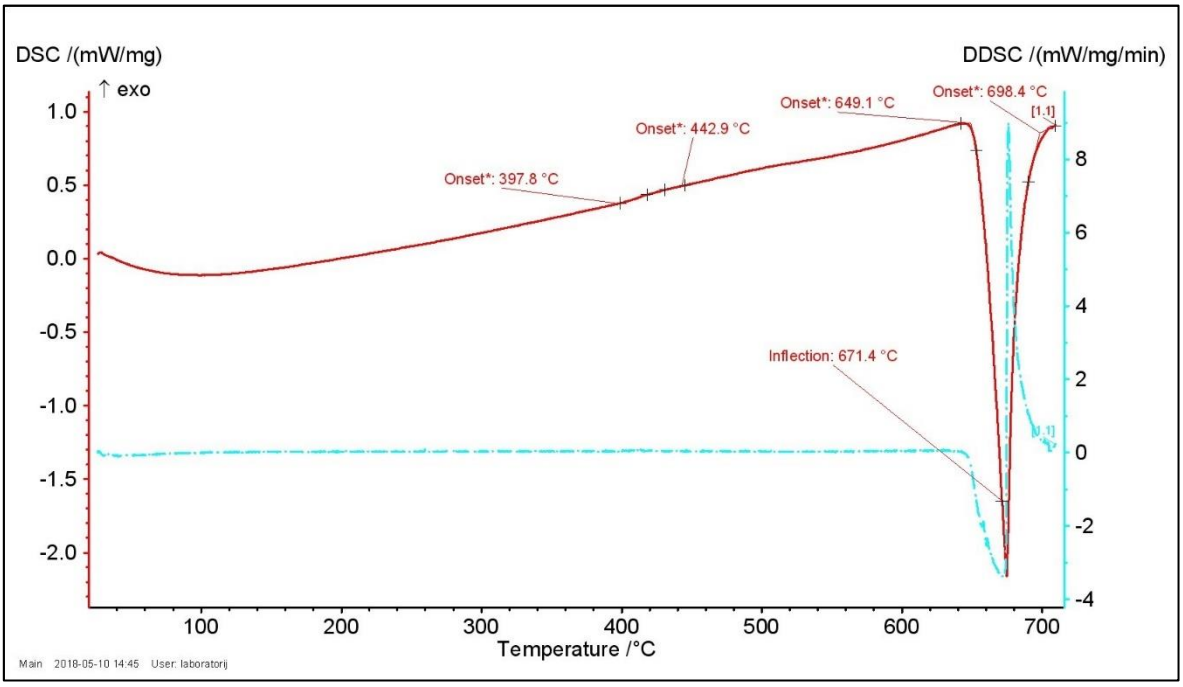

Heating with the rate of 20.0 K/min

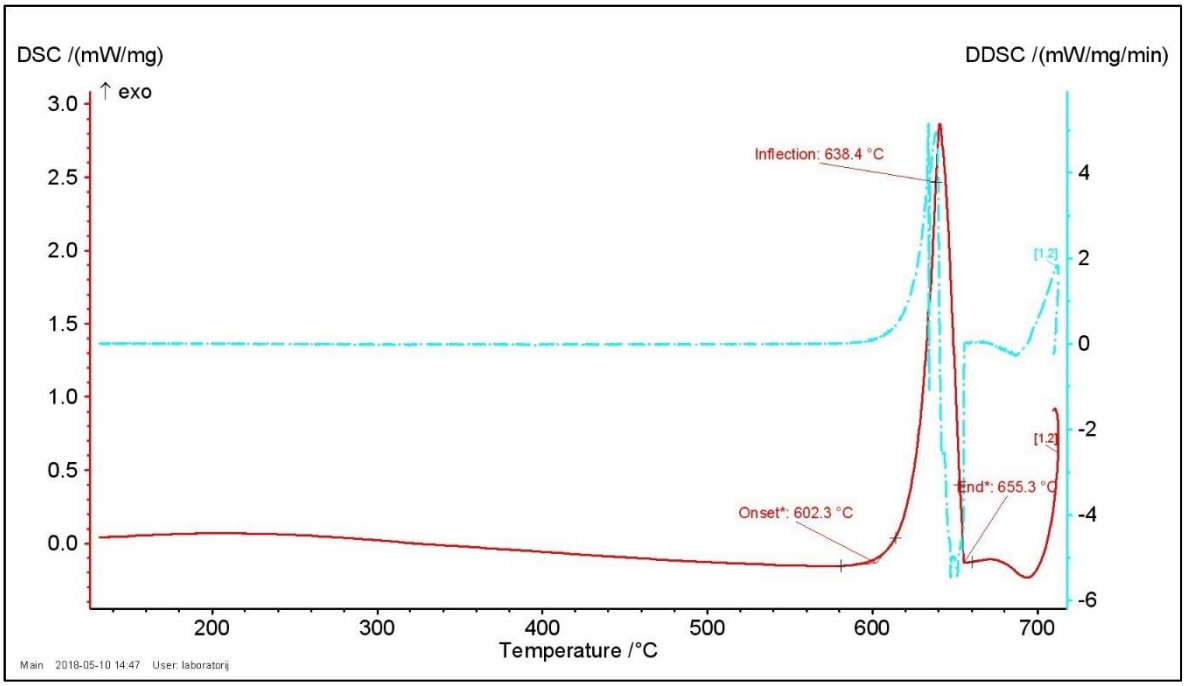

Cooling with the rate of 20.0 K/min

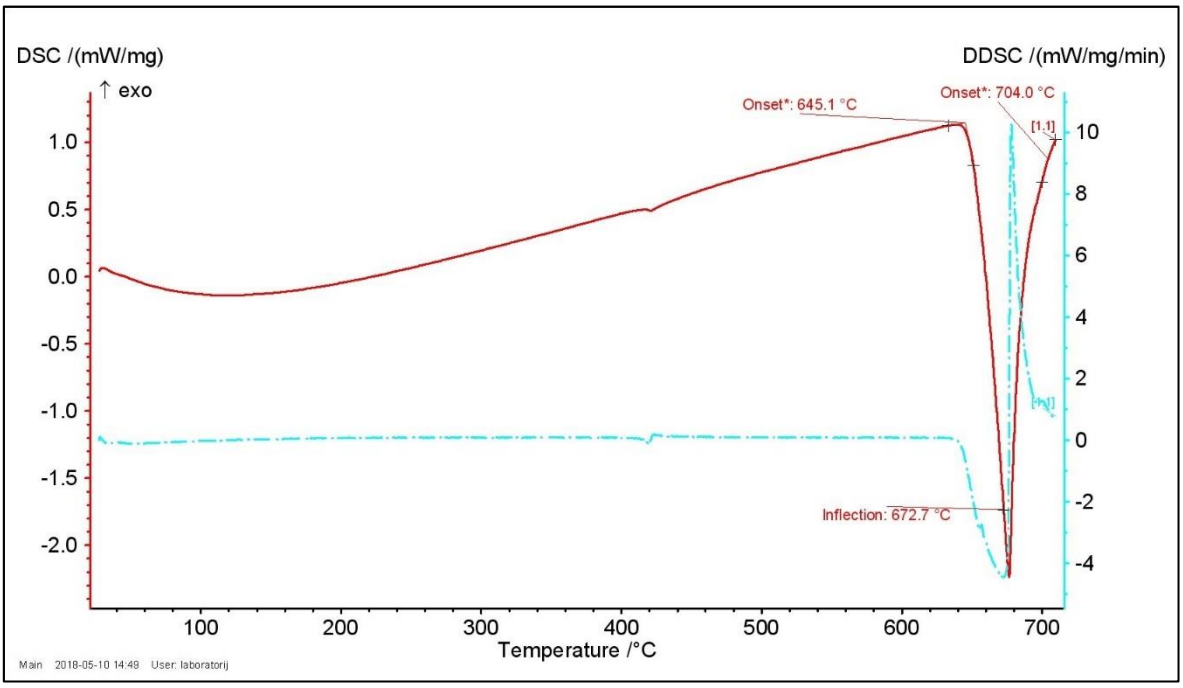

Heating with the rate of 30.0 K/min

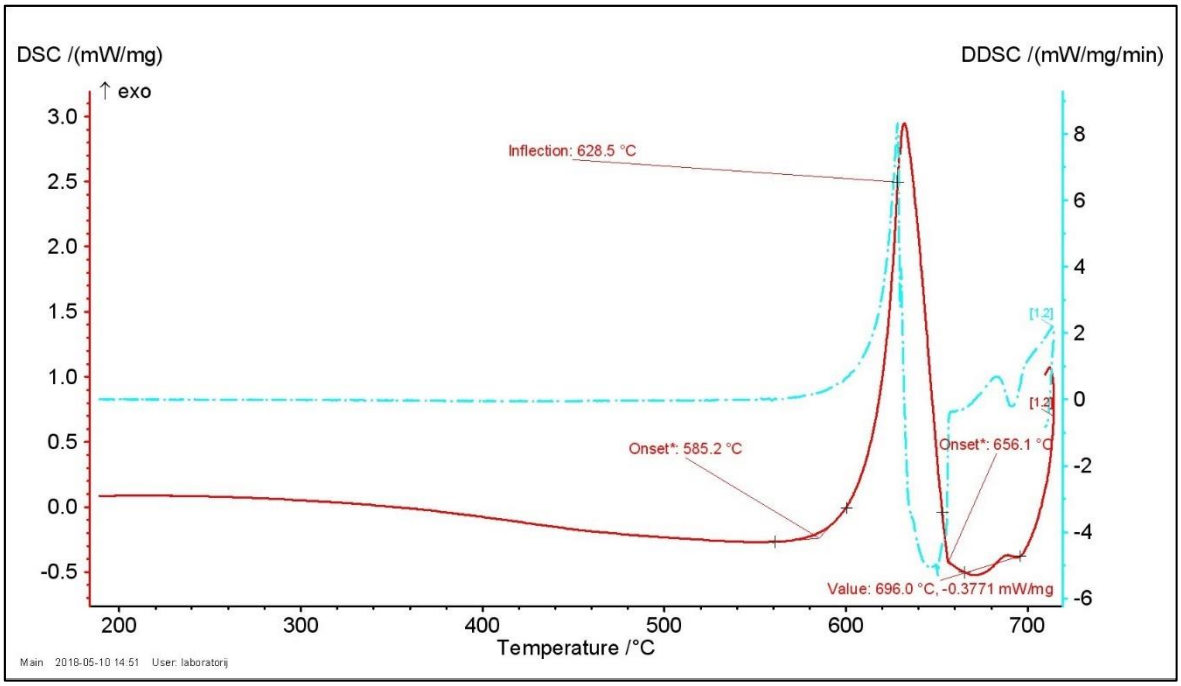

Cooling with the rate of 30.0 K/min

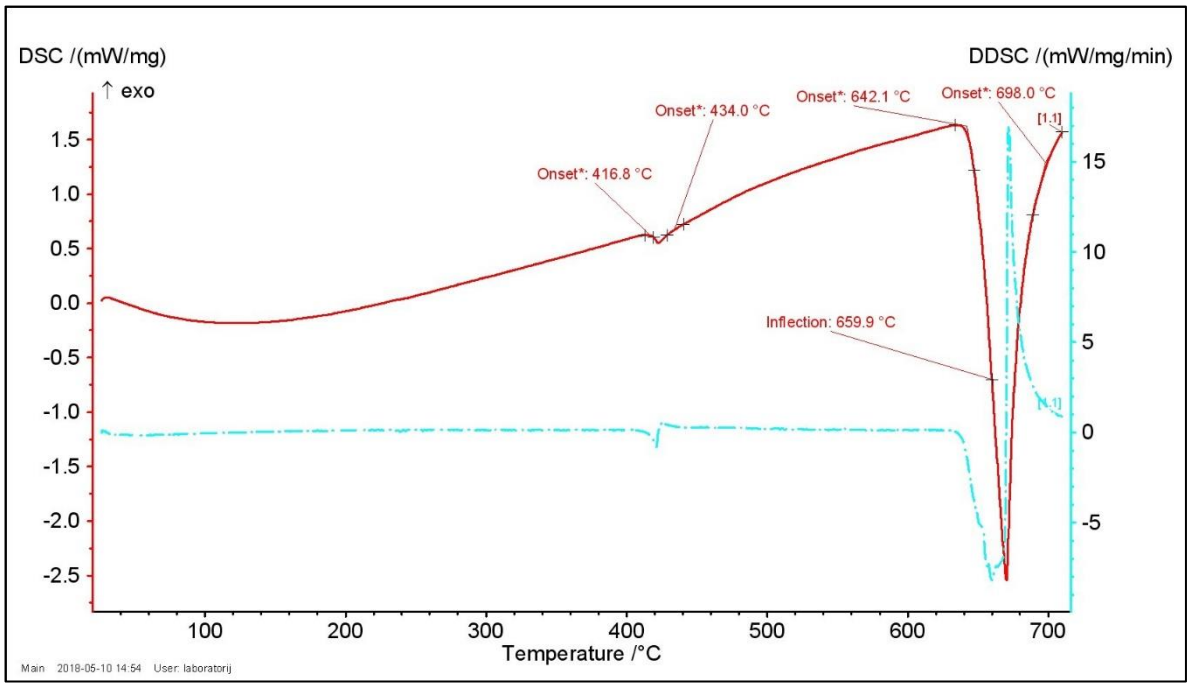

Heating with the rate of 40.0 K/min

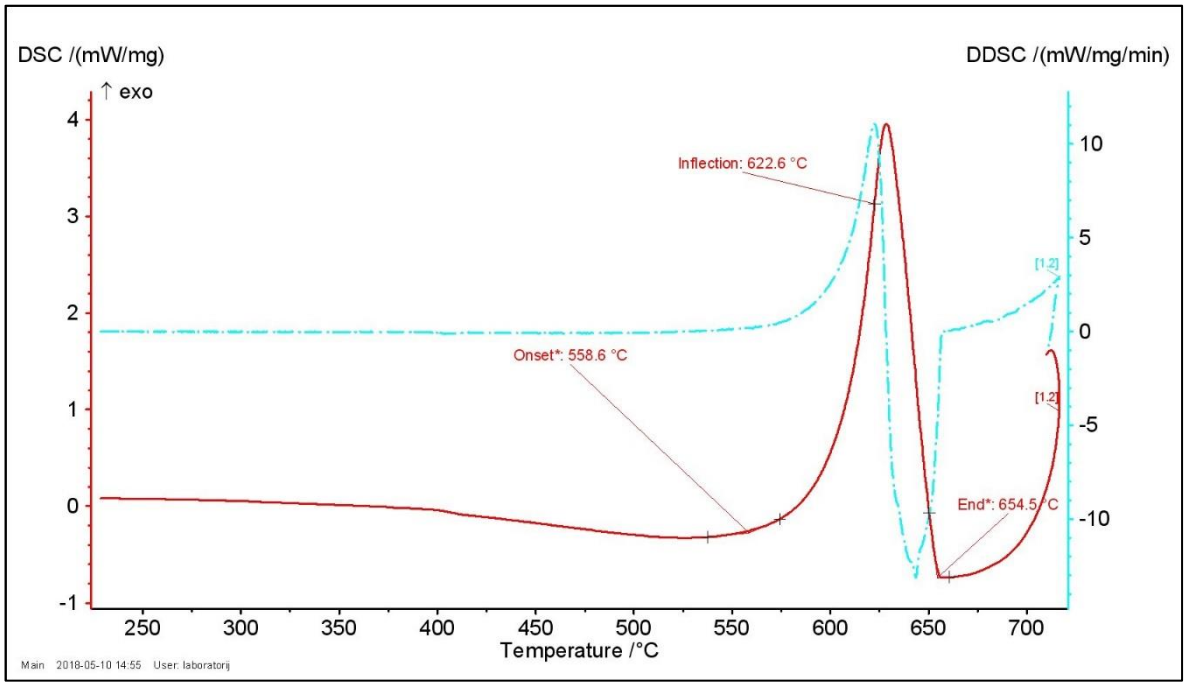

Cooling with the rate of 40.0 K/min

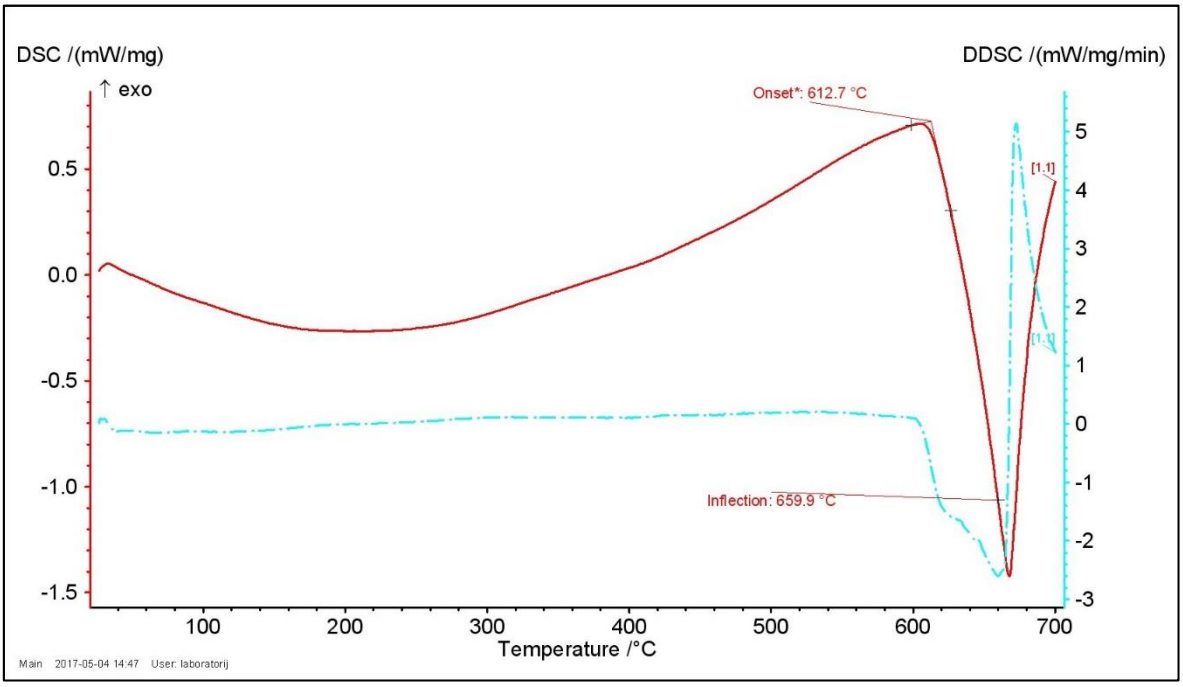

Heating with the rate of 50.0 K/min

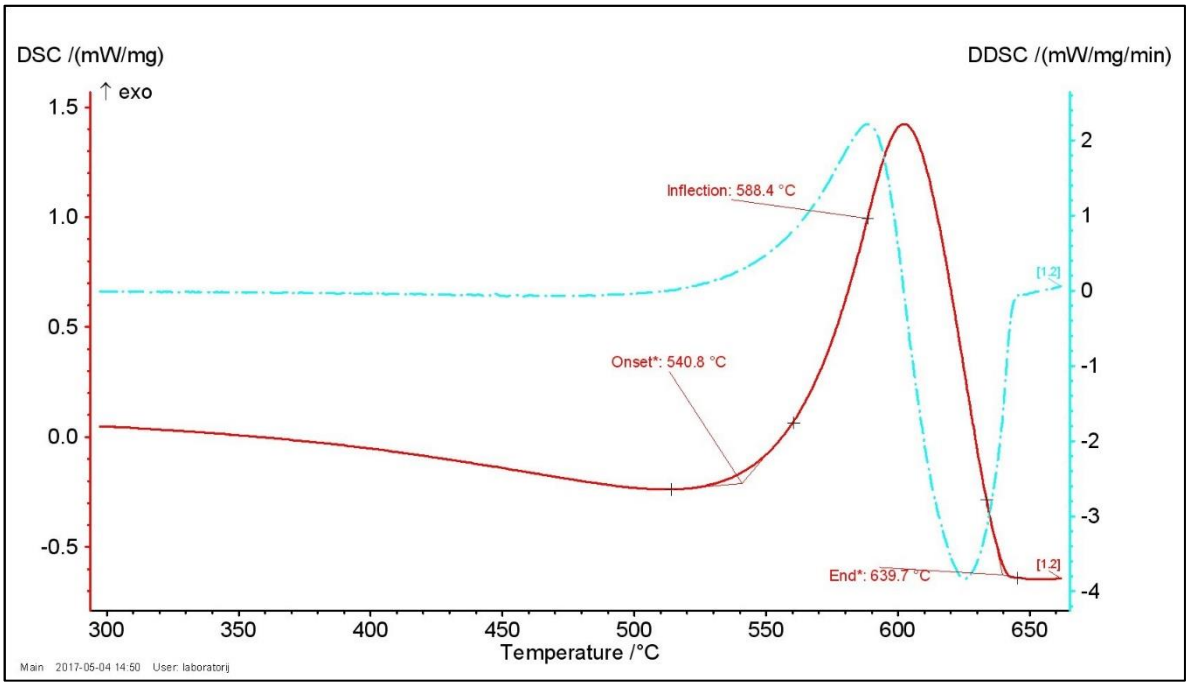

Cooling with the rate of 50.0 K/min

APPENDIX 2

The engineering strain-stress curves and engineering strain-temperature curves

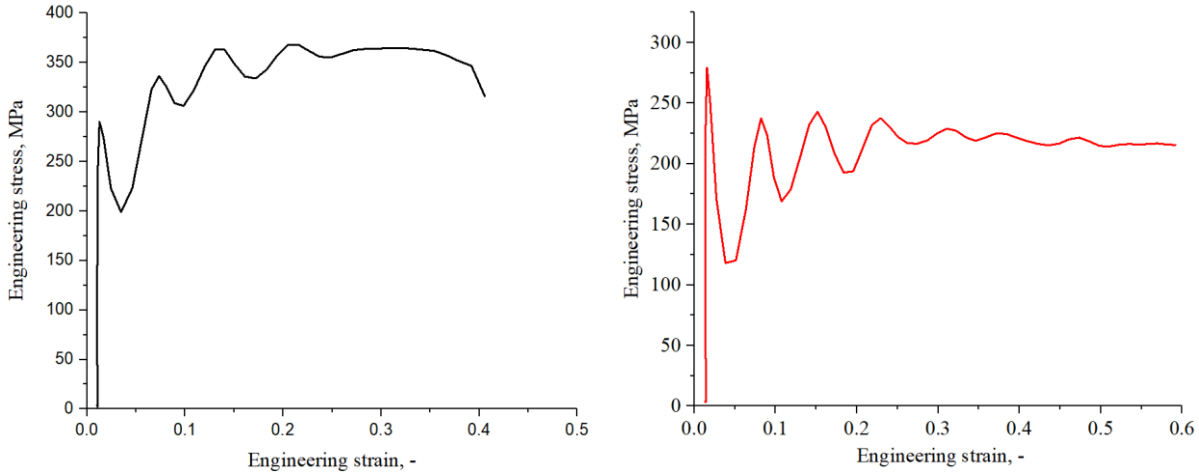

a) b)

The engineering strain-stress curve for sample 1 in:

a) as-cast condition, b) solutionized condition

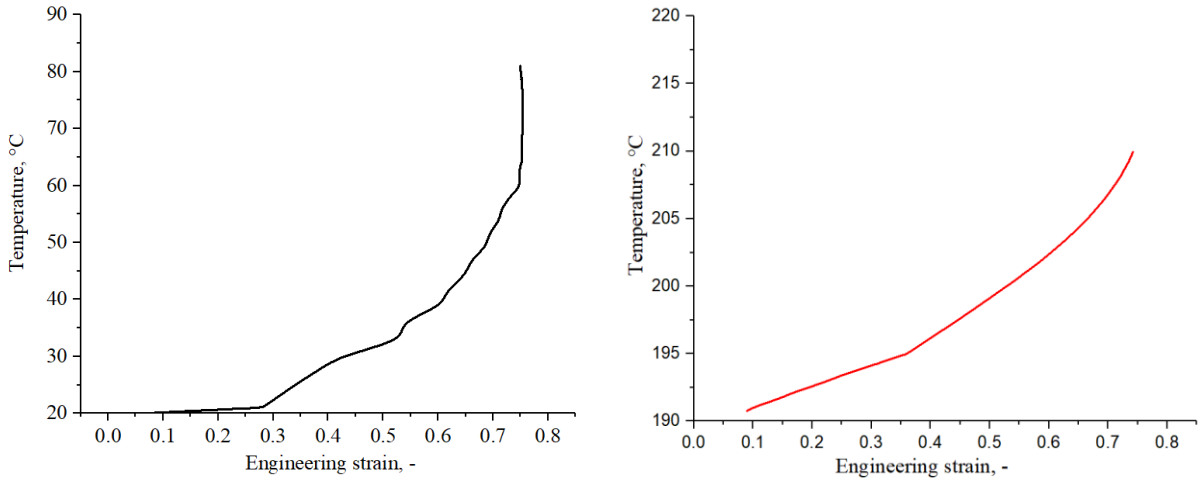

a) b)

The engineering strain-temperature curve for sample 1 in:

a) as-cast condition, b) solutionized condition

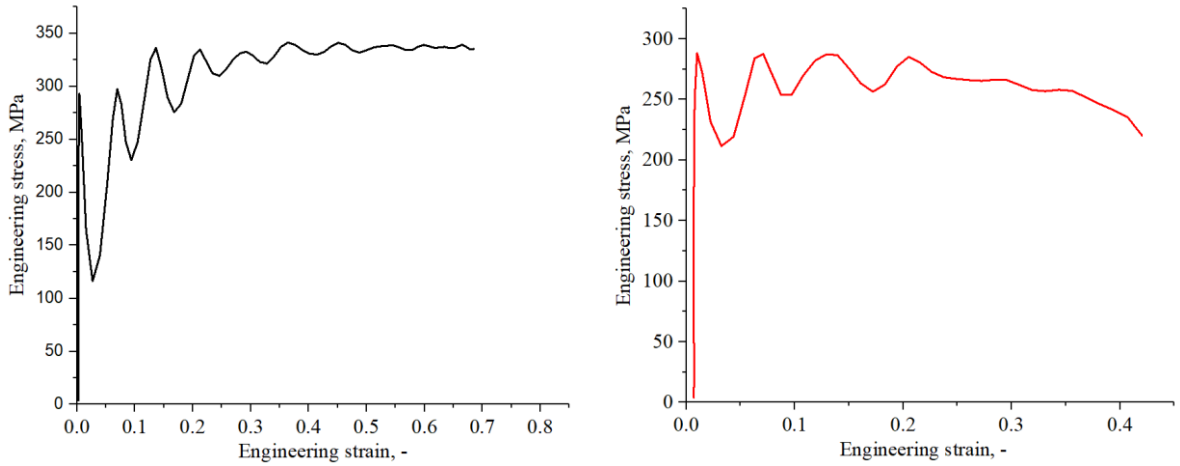

a) b)

The engineering strain-stress curve for sample 21 in:

a) as-cast condition, b) solutionized condition

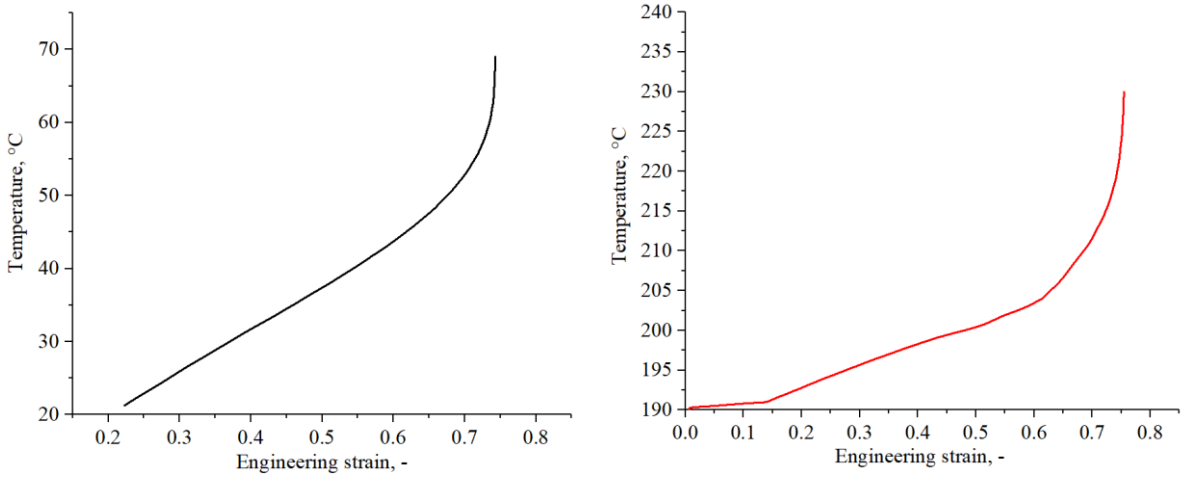

a) b)

The engineering strain-temperature curve for sample 21 in:

a) as-cast condition, b) solutionized condition

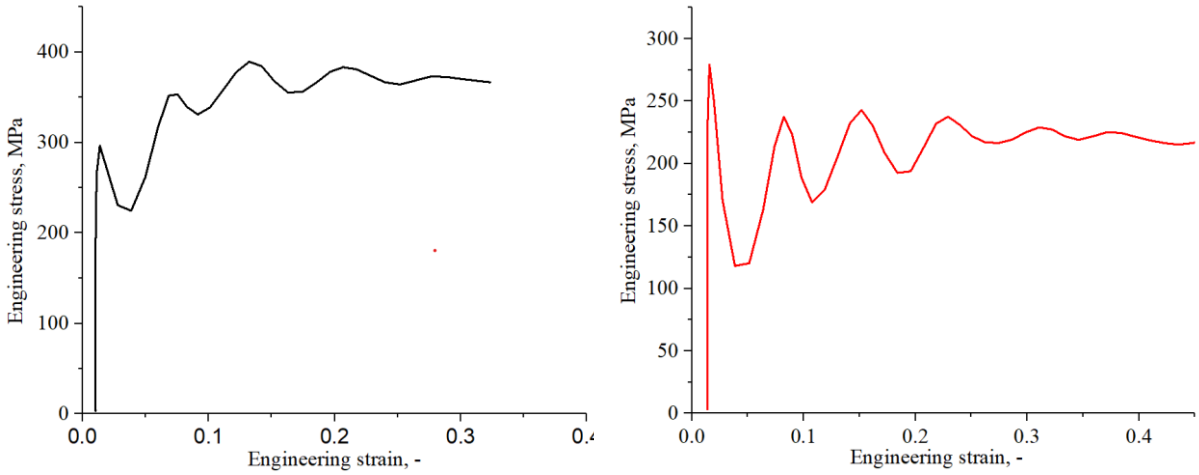

a) b)

The engineering strain-stress curve for sample 22 in:

a) as-cast condition, b) solutionized condition

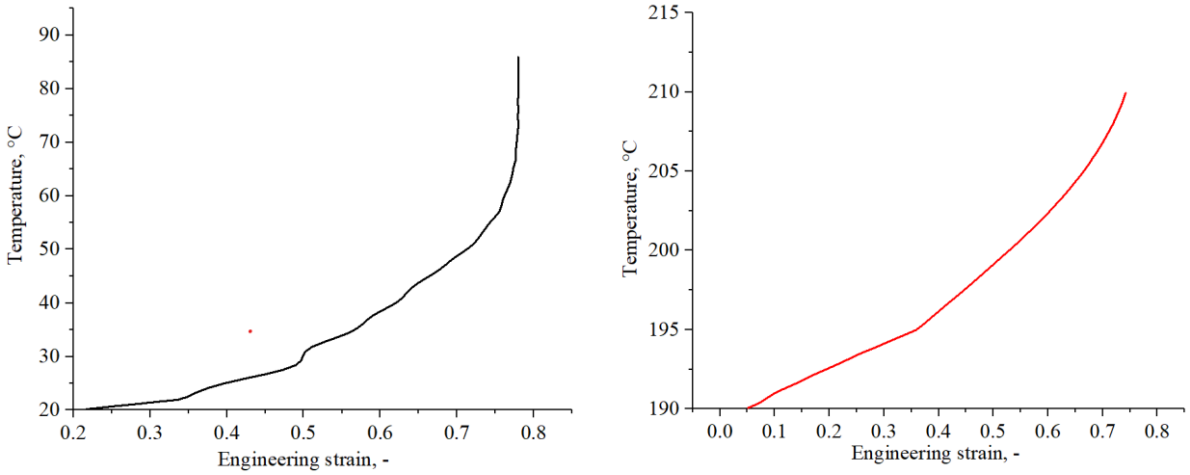

a) b)

The engineering strain-temperature curve for sample 22 in:

a) as-cast condition, b) solutionized condition

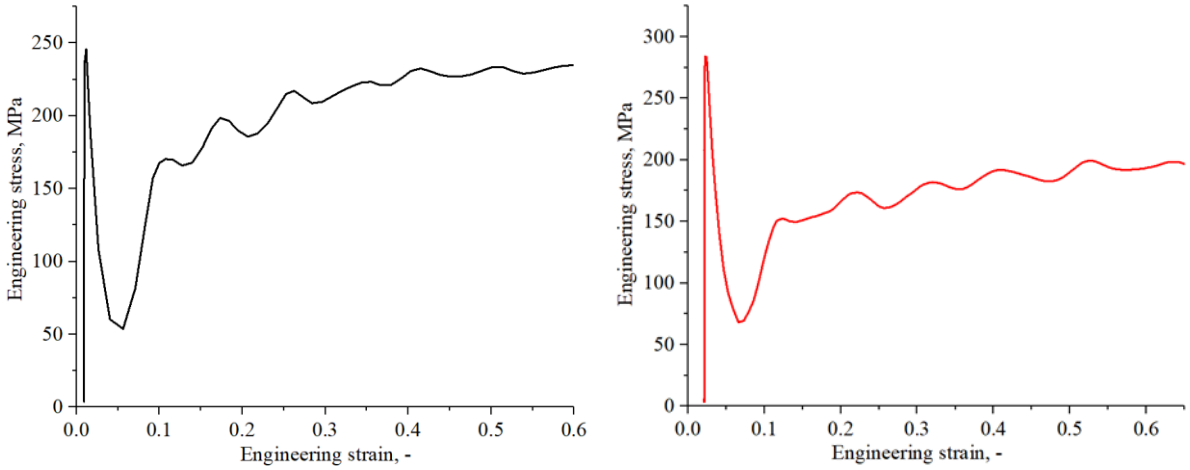

a) b)

The engineering strain-stress curve for sample 31 in:

a) as-cast condition, b) solutionized condition

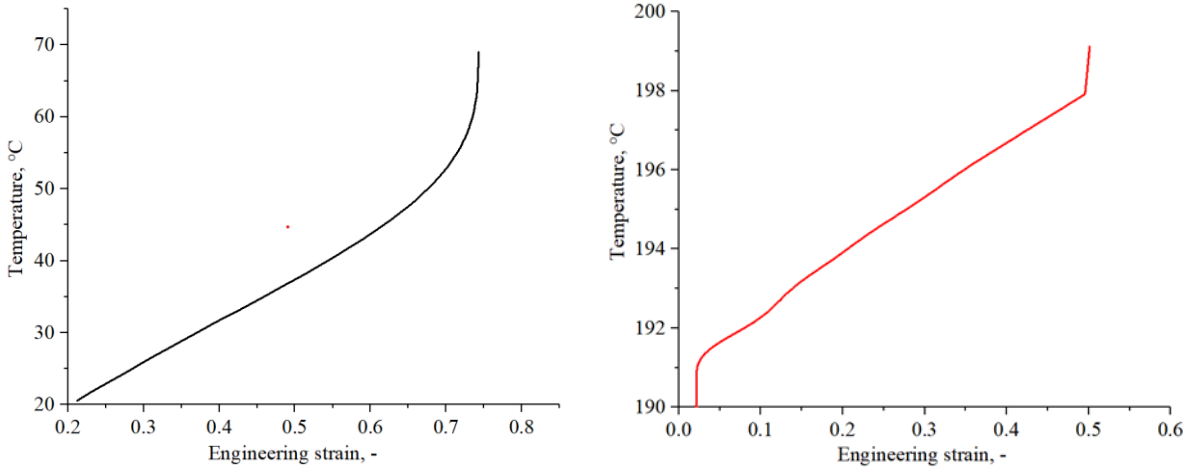

a) b)

The engineering strain-temperature curve for sample 31 in:

a) as-cast condition, b) solutionized condition

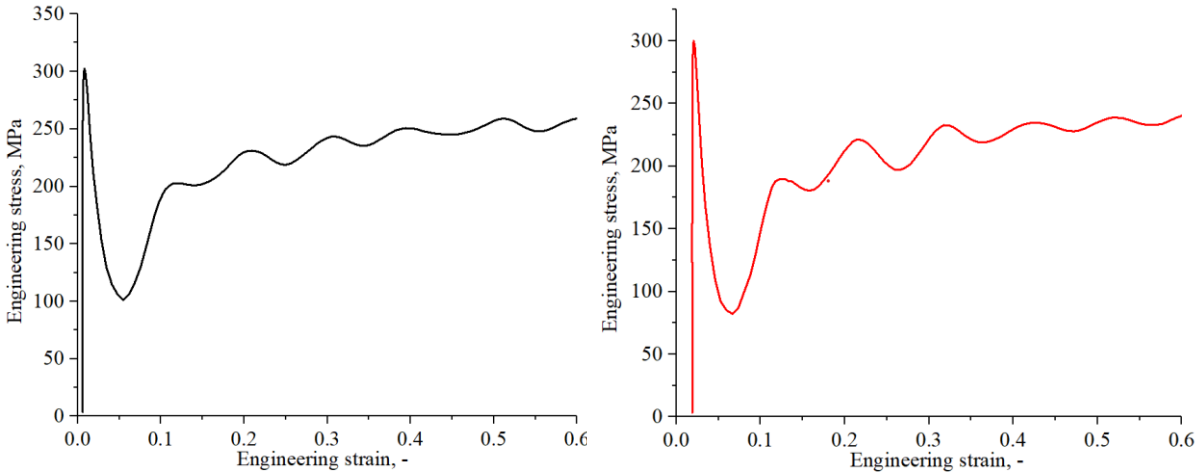

a) b)

The engineering strain-stress curve for sample 32 in:

a) as-cast condition, b) solutionized condition

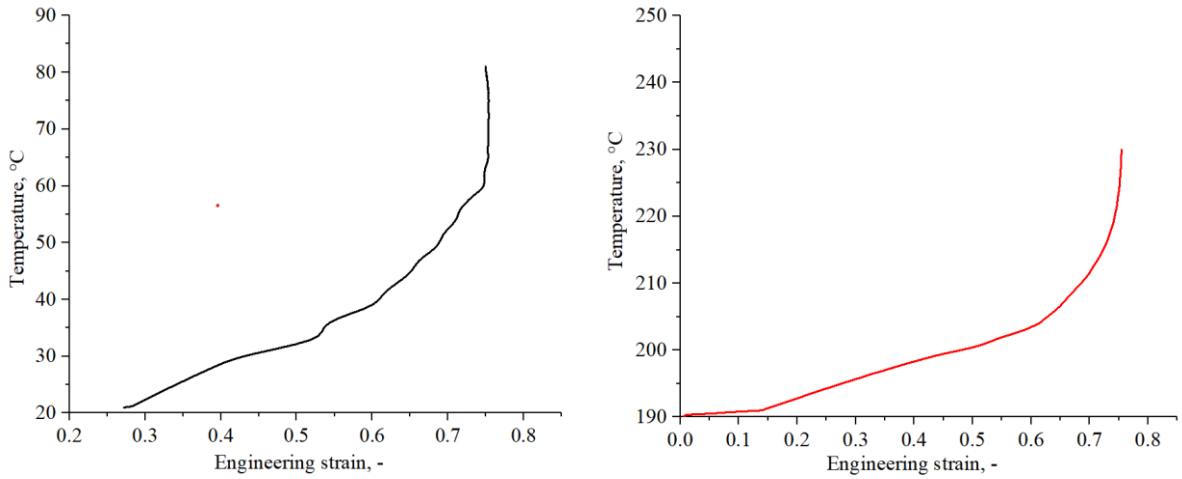

a) b)

The engineering strain-temperature curve for sample 32 in:

a) as-cast condition, b) solutionized condition

APPENDIX 3

The nanoindentation hardness - and modulus - displacement curves

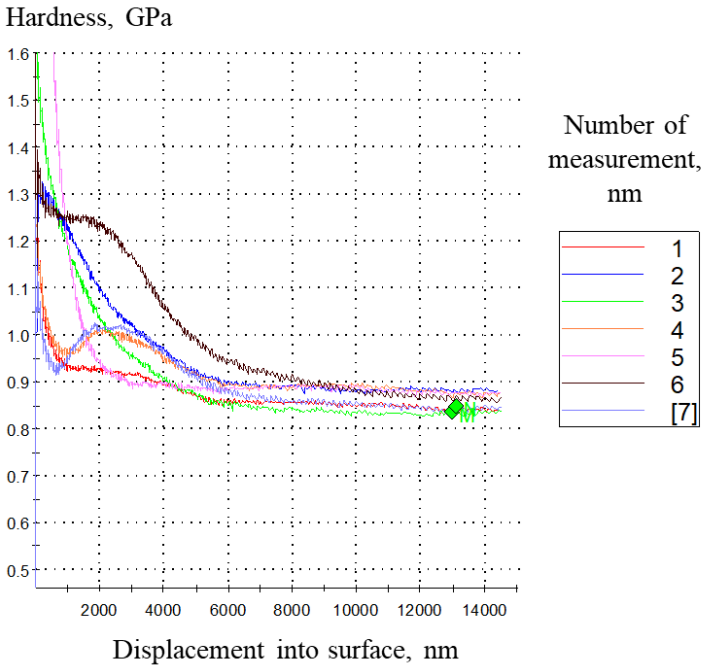

Dependence of hardness on displacement in sample 1 in as-cast condition

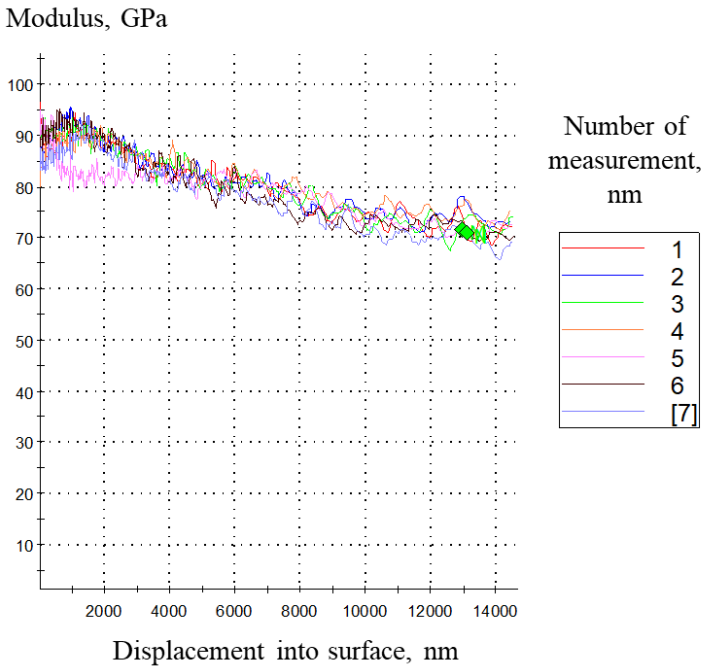

Dependence of modulus on displacement in sample 1 in as-cast condition

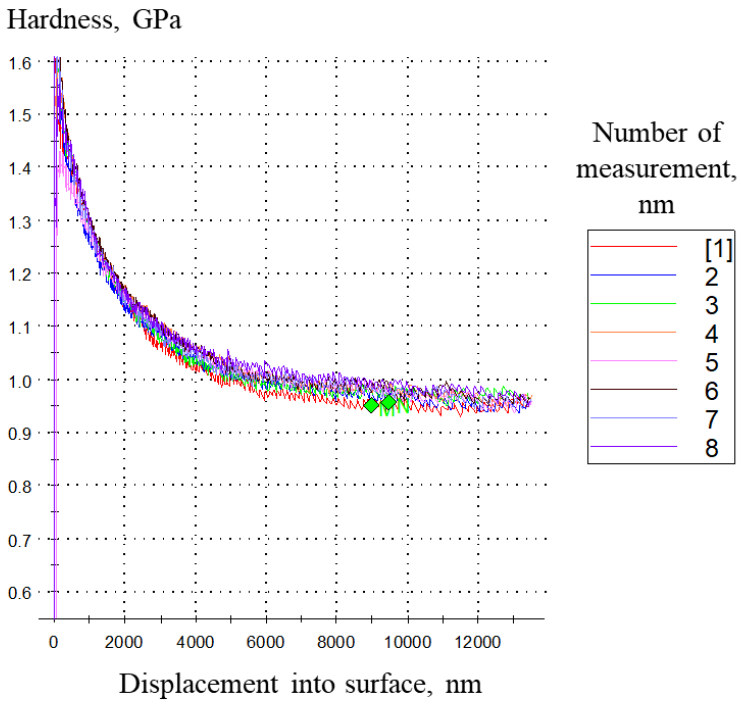

Dependence of hardness on displacement in sample 1 in solutionized condition

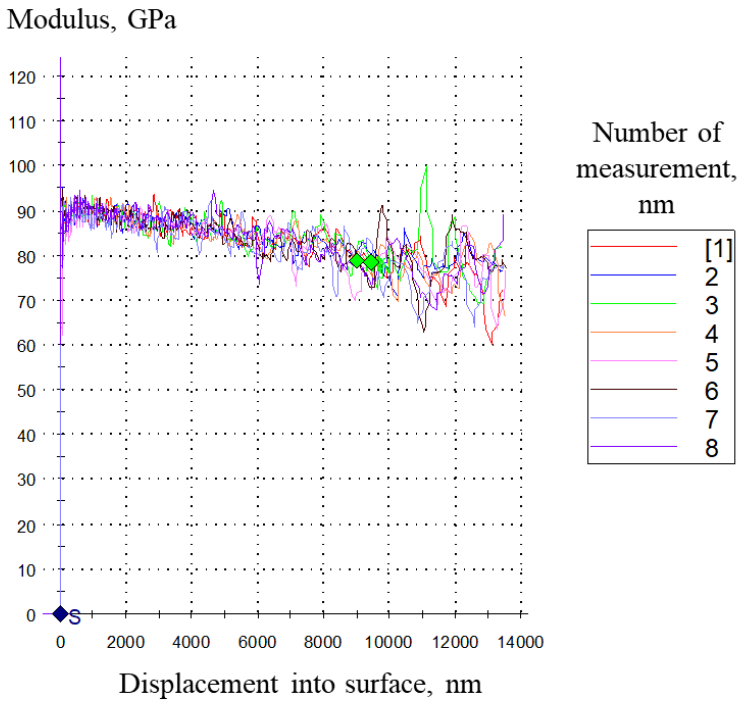

Dependence of modulus on displacement in sample 1 in solutionized condition

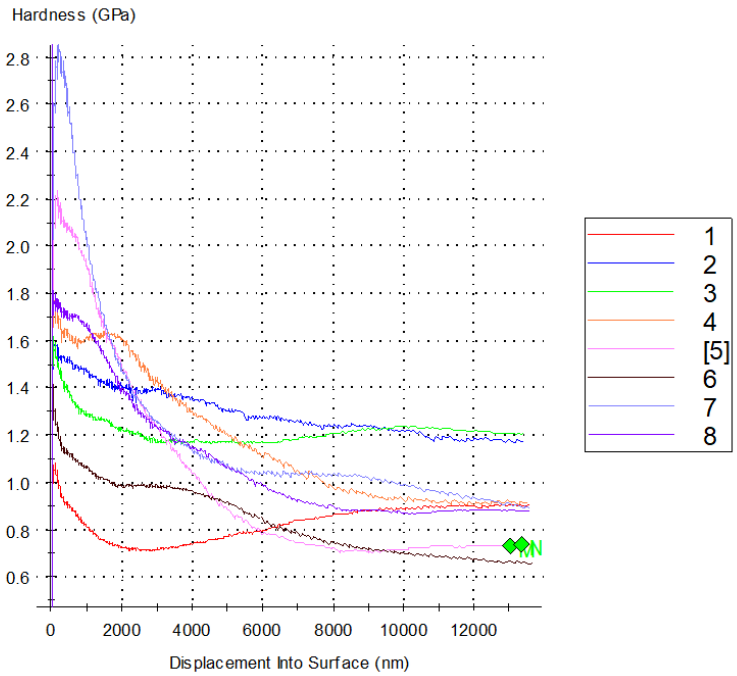

Dependence of hardness on displacement in sample 21 in as-cast condition

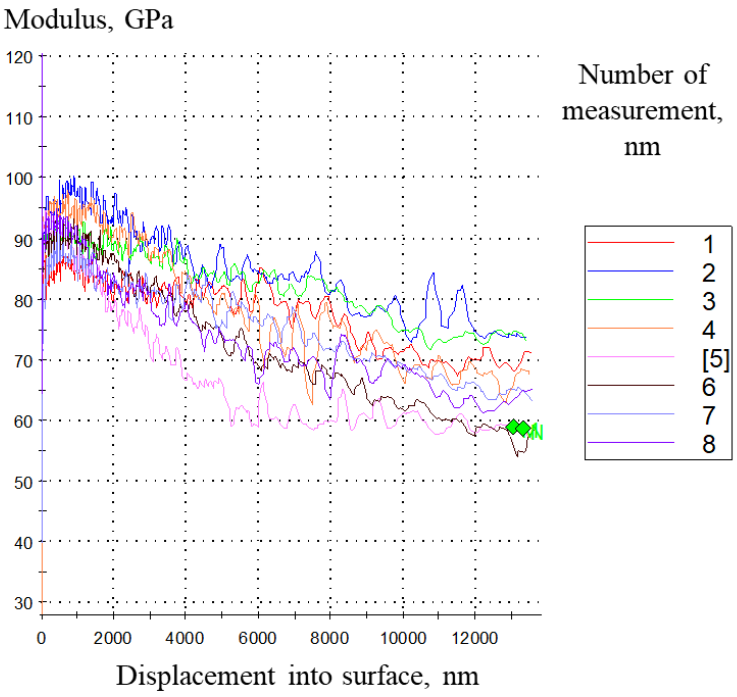

Dependence of modulus on displacement in sample 21 in as-cast condition

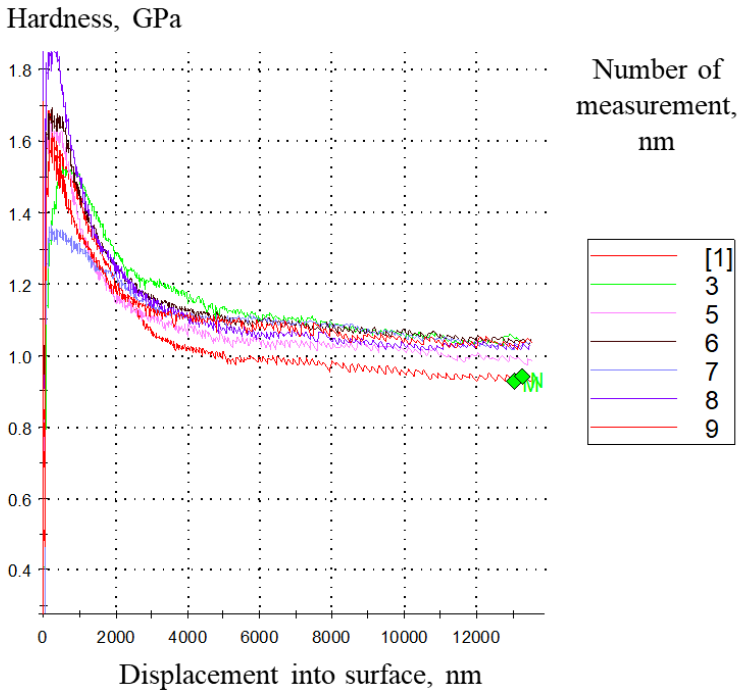

Dependence of hardness on displacement in sample 21 in solutionized condition

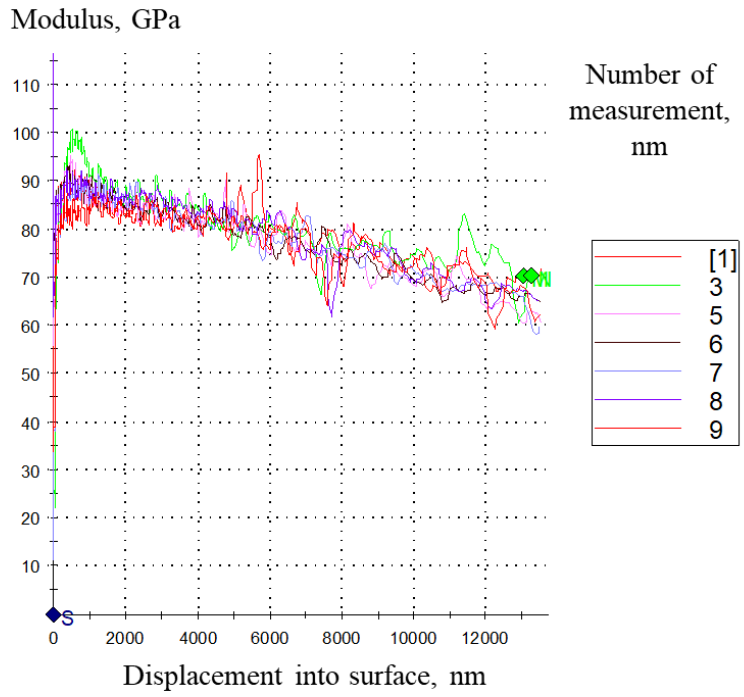

Dependence of modulus on displacement in sample 21 in solutionized condition

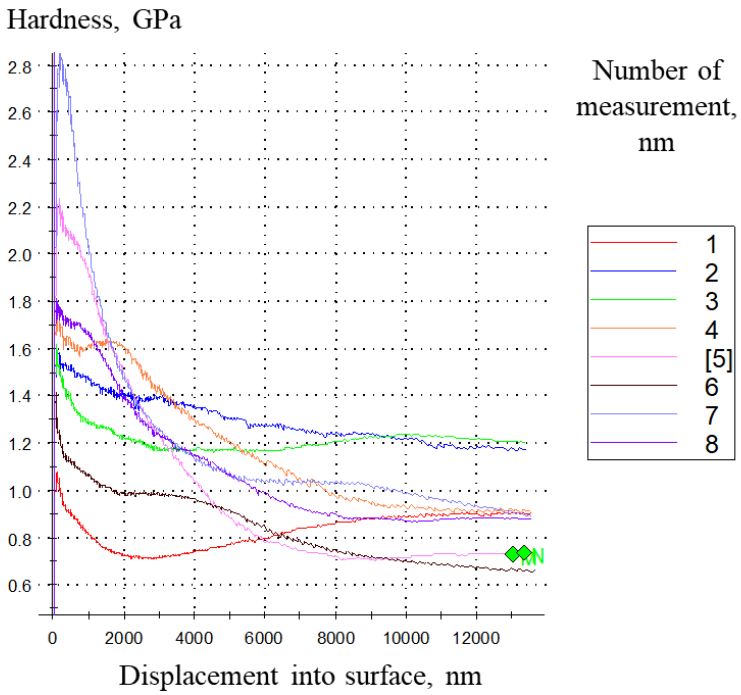

Dependence of hardness on displacement in sample 22 in as-cast condition

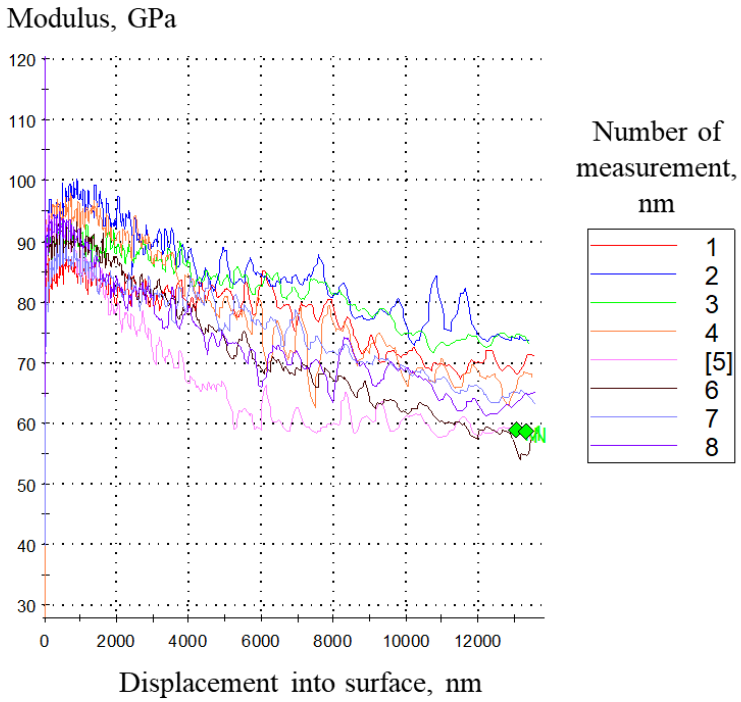

Dependence of modulus on displacement in sample 22 in as-cast condition

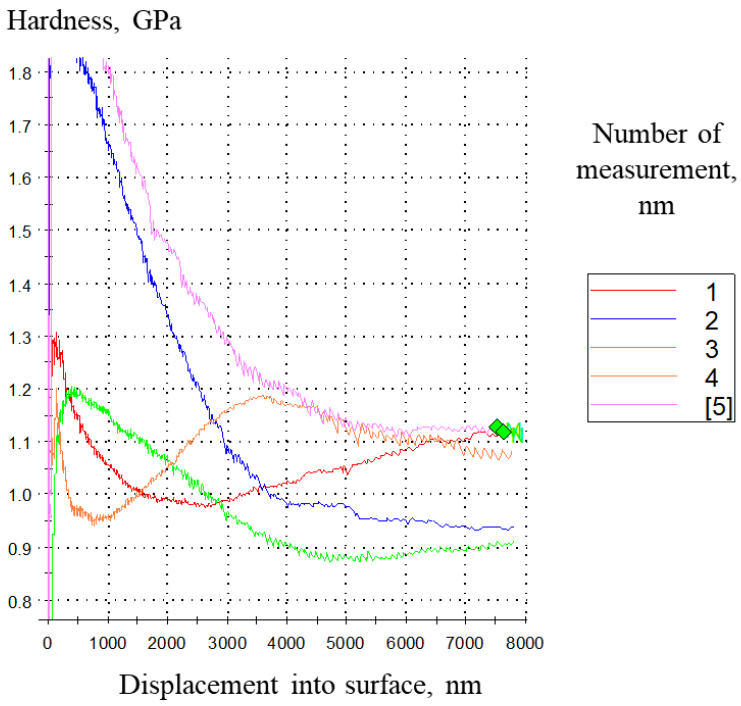

Dependence of hardness on displacement in sample 22 in solutionized condition

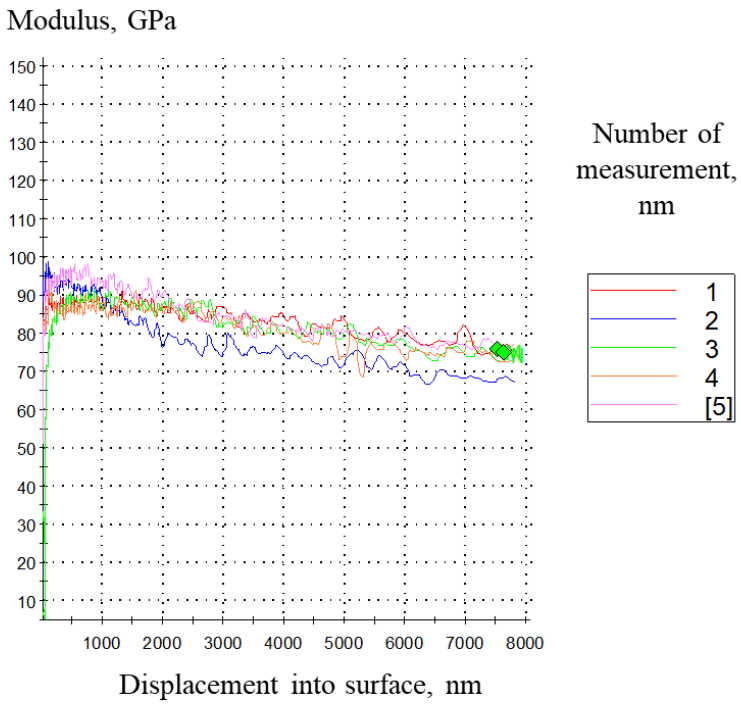

Dependence of modulus on displacement in sample 22 in solutionized condition

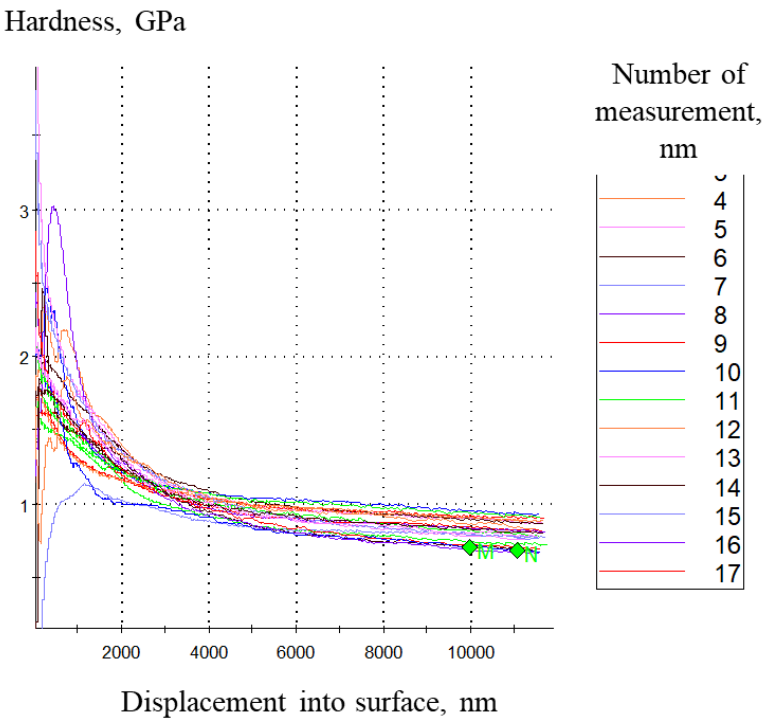

Dependence of hardness on displacement in sample 31 in as-cast condition

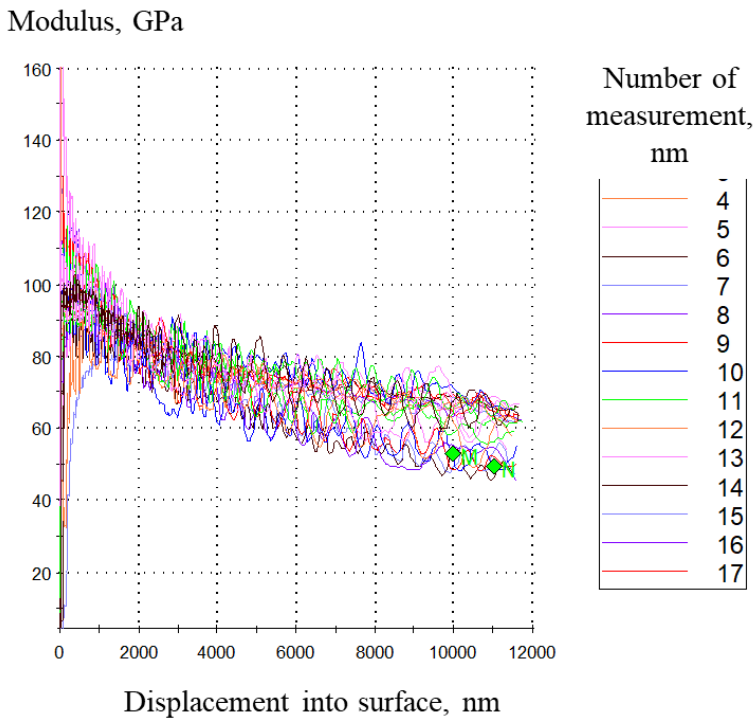

Dependence of modulus on displacement in sample 31 in as-cast condition

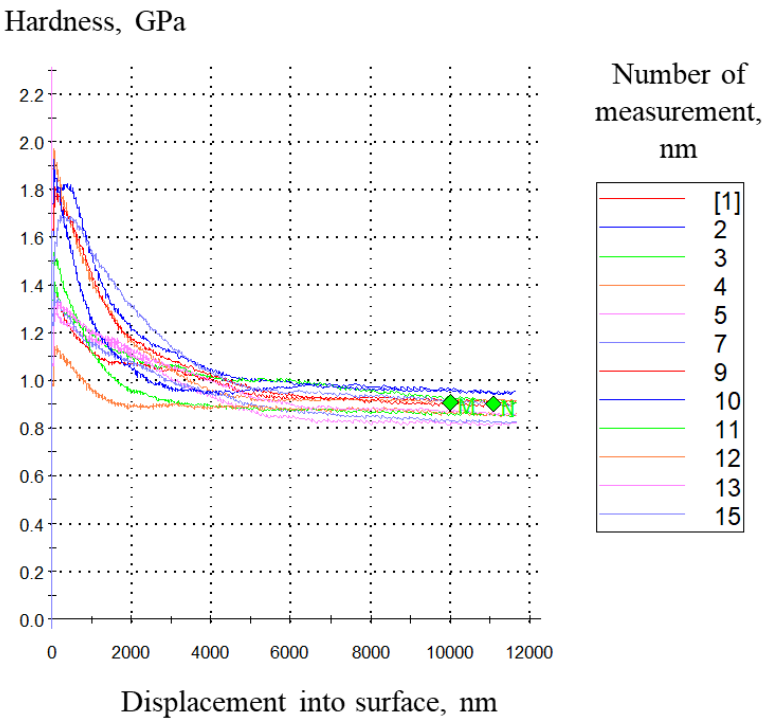

Dependence of hardness on displacement in sample 31 in solutionized condition

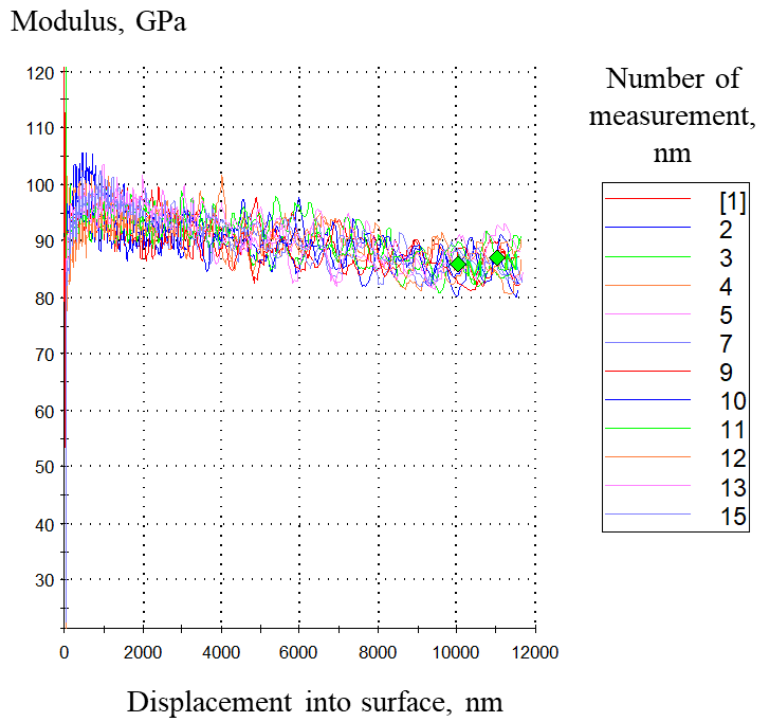

Dependence of modulus on displacement in sample 31 in solutionized condition

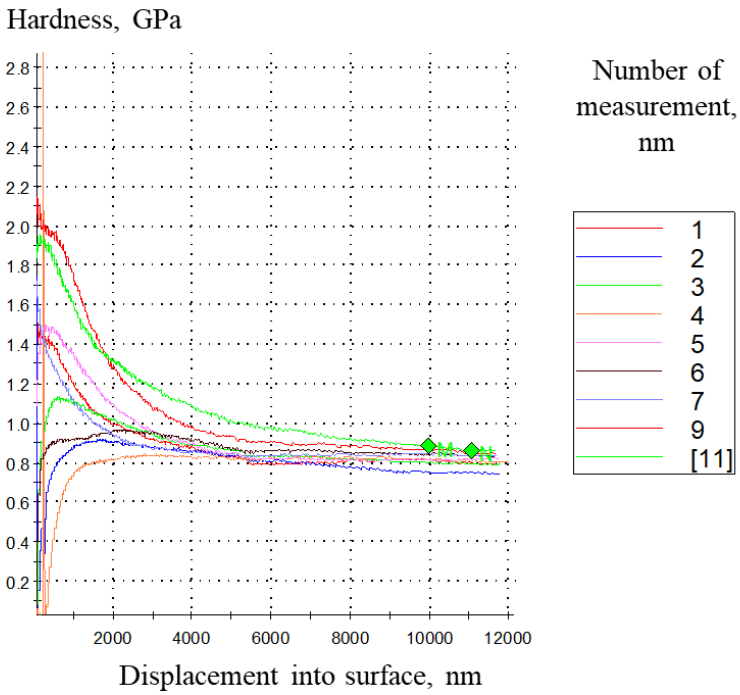

Dependence of hardness on displacement in sample 32 in as-cast condition

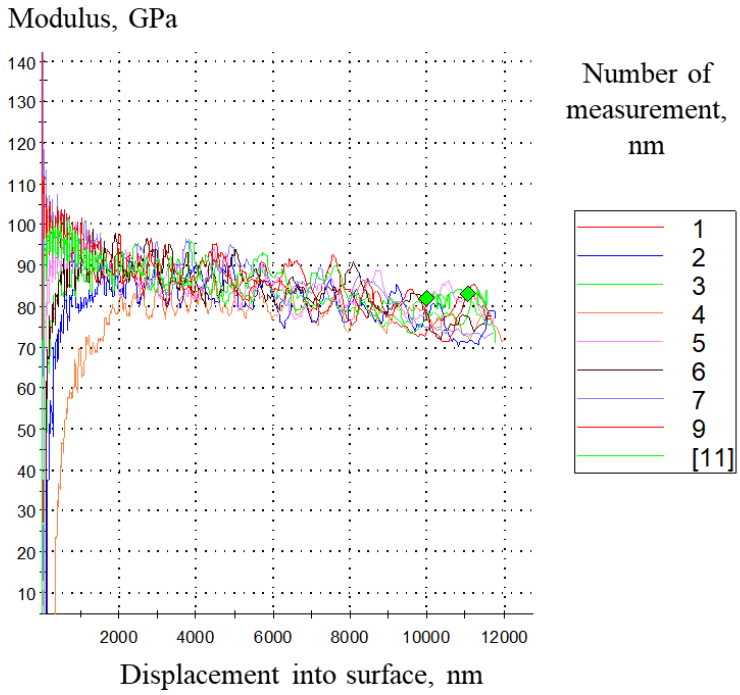

Dependence of modulus on displacement in sample 32 in as-cast condition

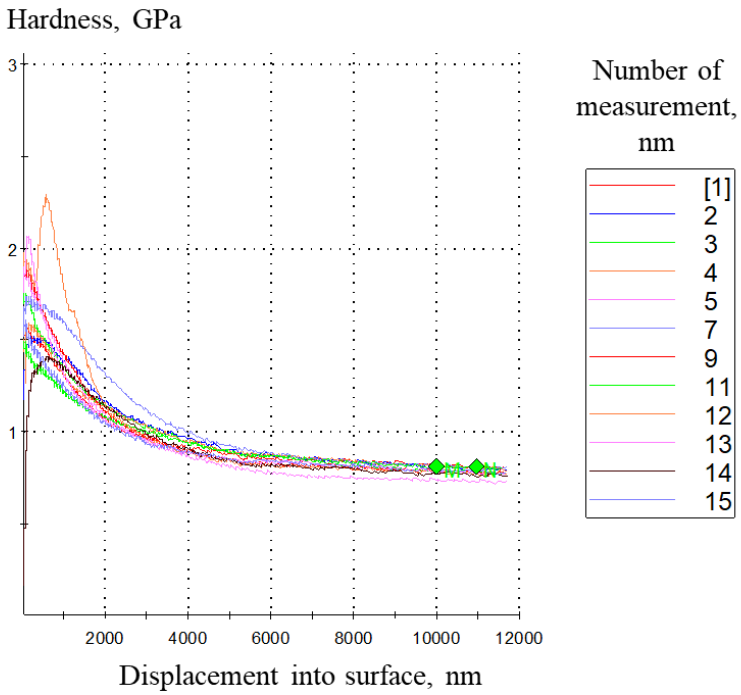

Dependence of hardness on displacement in sample 32 in solutionized condition

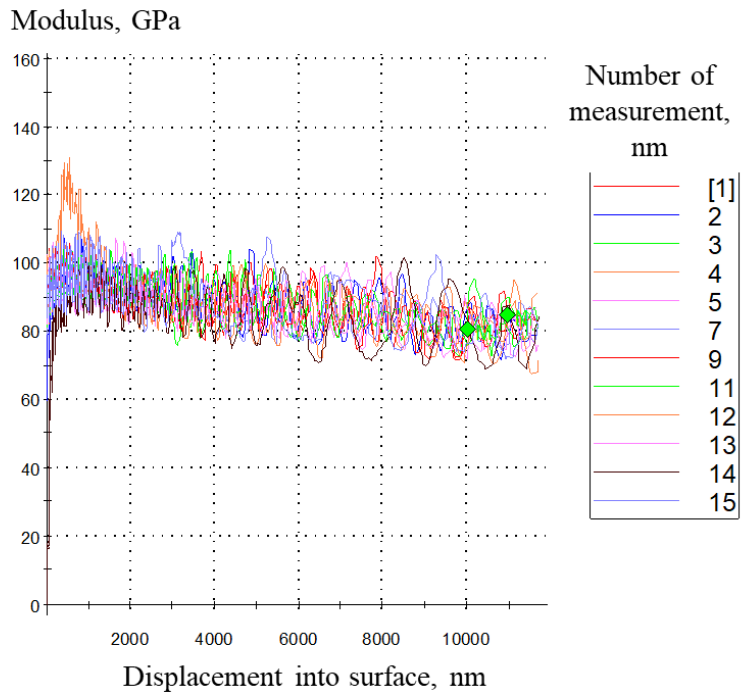

Dependence of modulus on displacement in sample 32 in solutionized condition

APPENDIX 4

The microstructure of chemically degraded samples

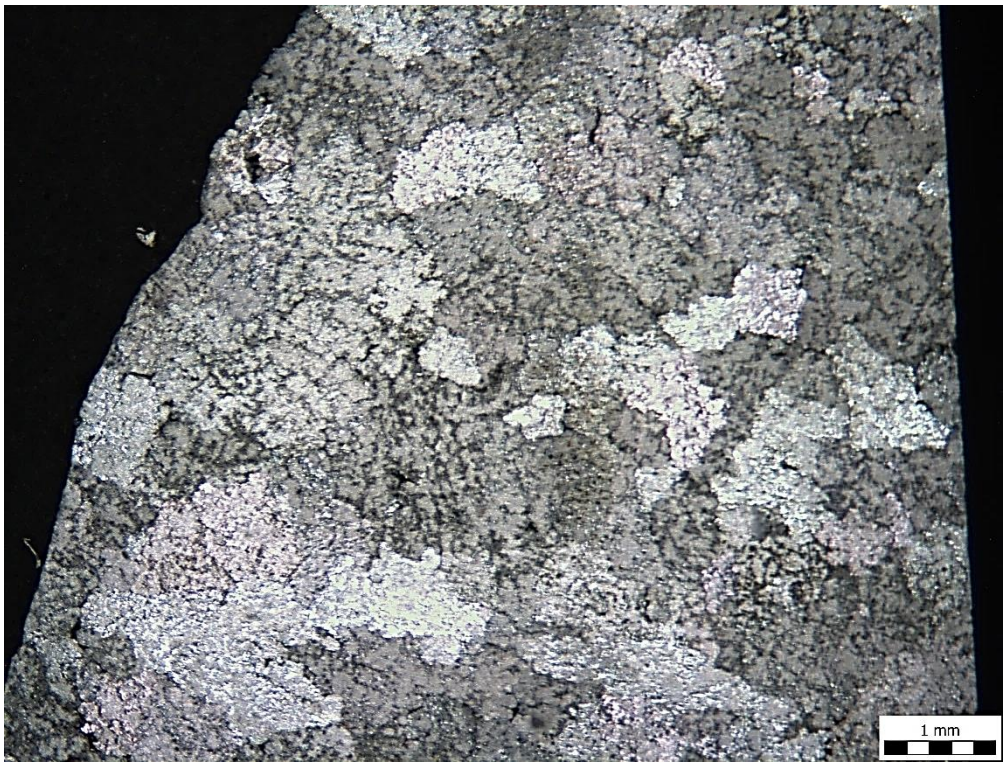

Macrostructure of the exposed surface of sample AC1 at a magnification of 17.5 X

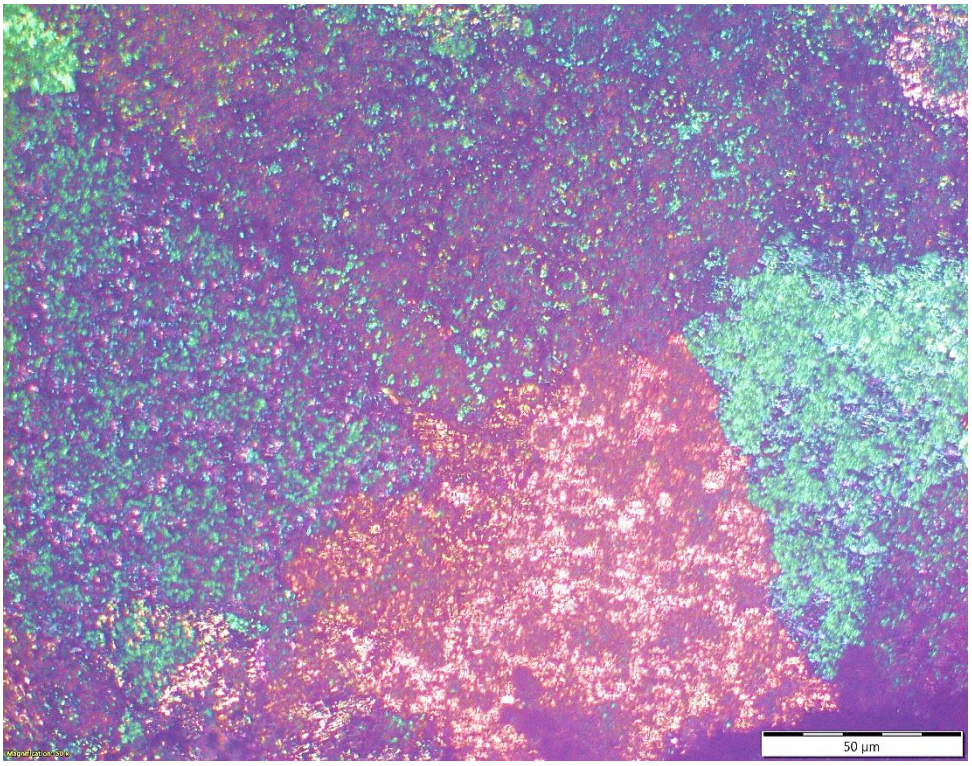

Microstructure of the exposed surface of sample AC1 at a magnification of 50 X

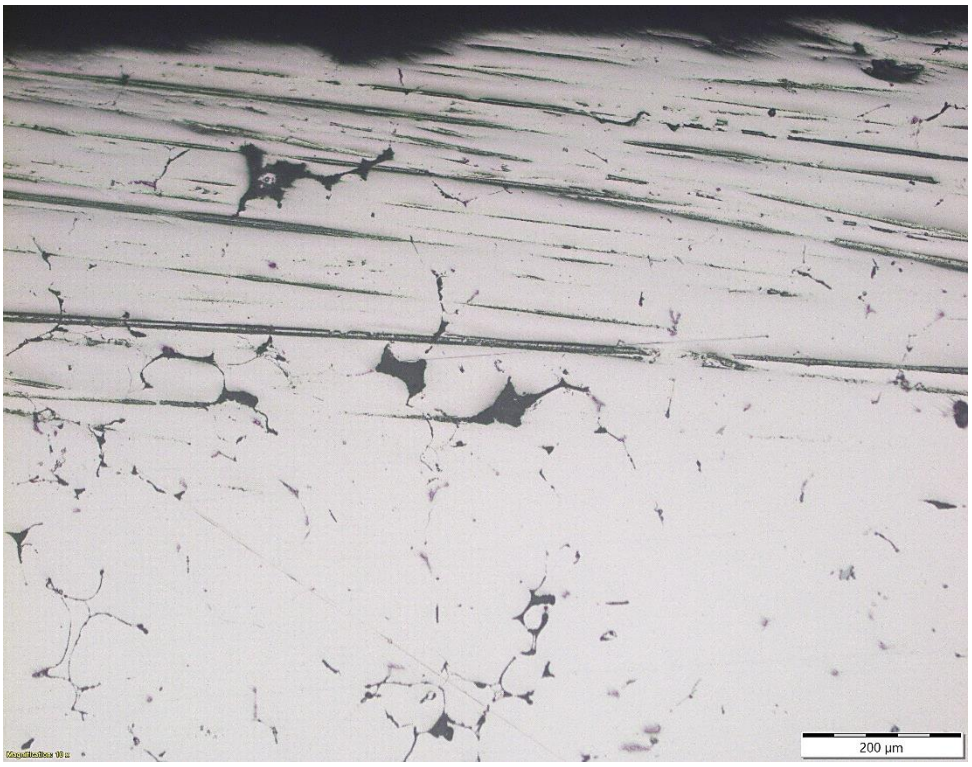

Microstructure of the cross-section of sample AC1 at a magnification of 100 X

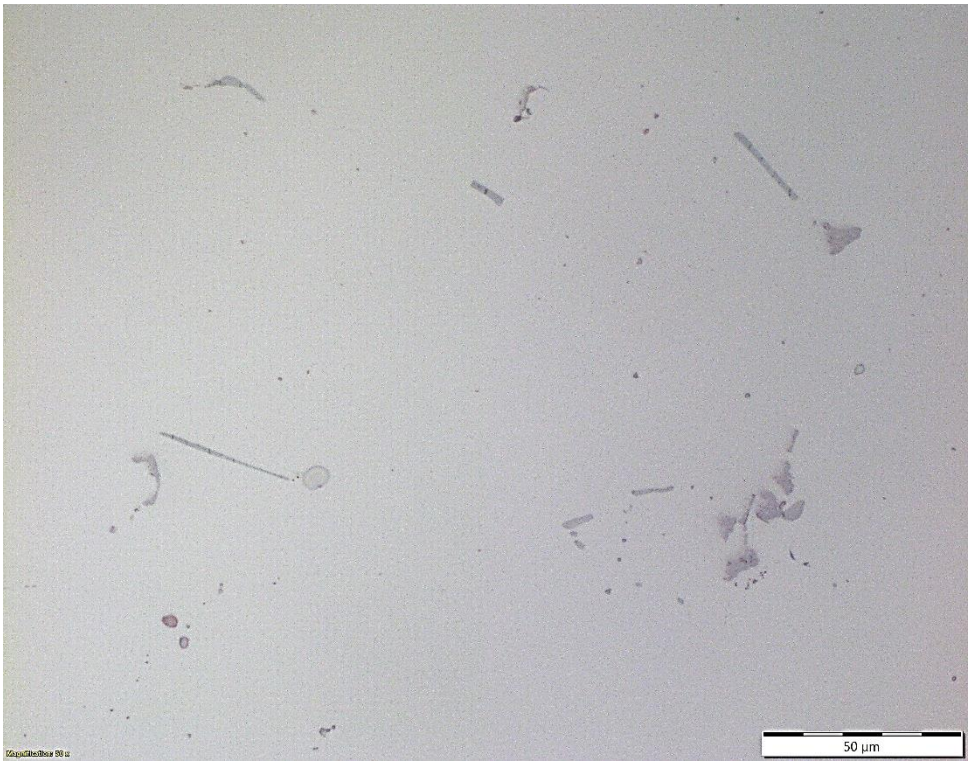

Microstructure of the cross-section of sample AC1 at a magnification of 500 X

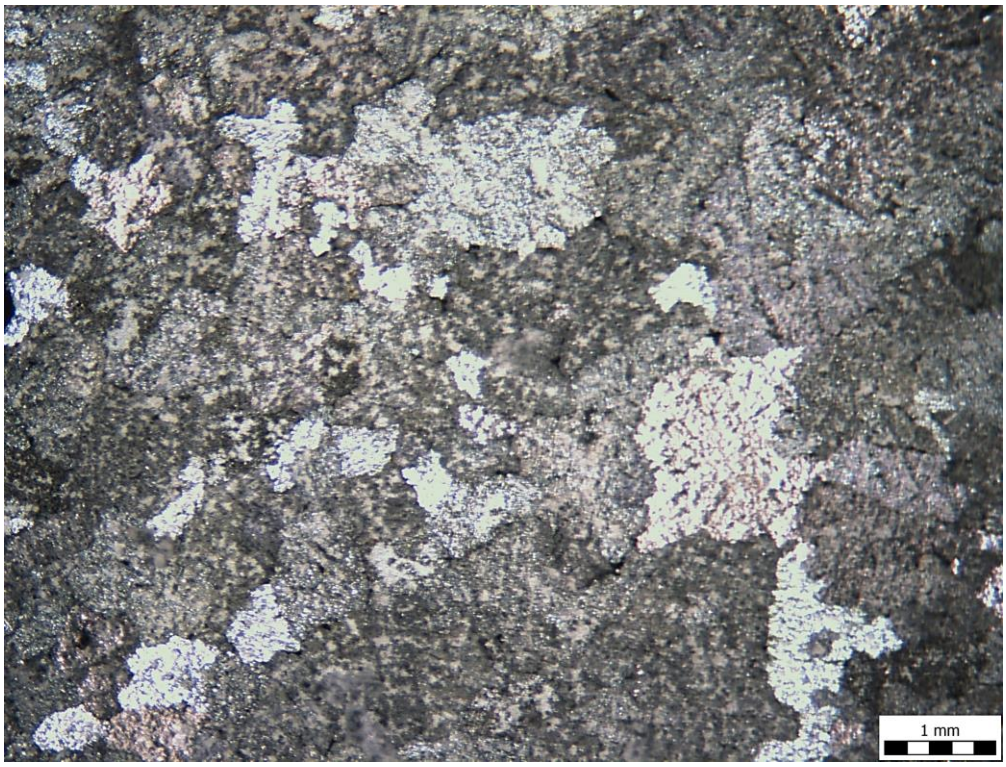

Macrostructure of the exposed surface of sample AC2 at a magnification of 17.5 X

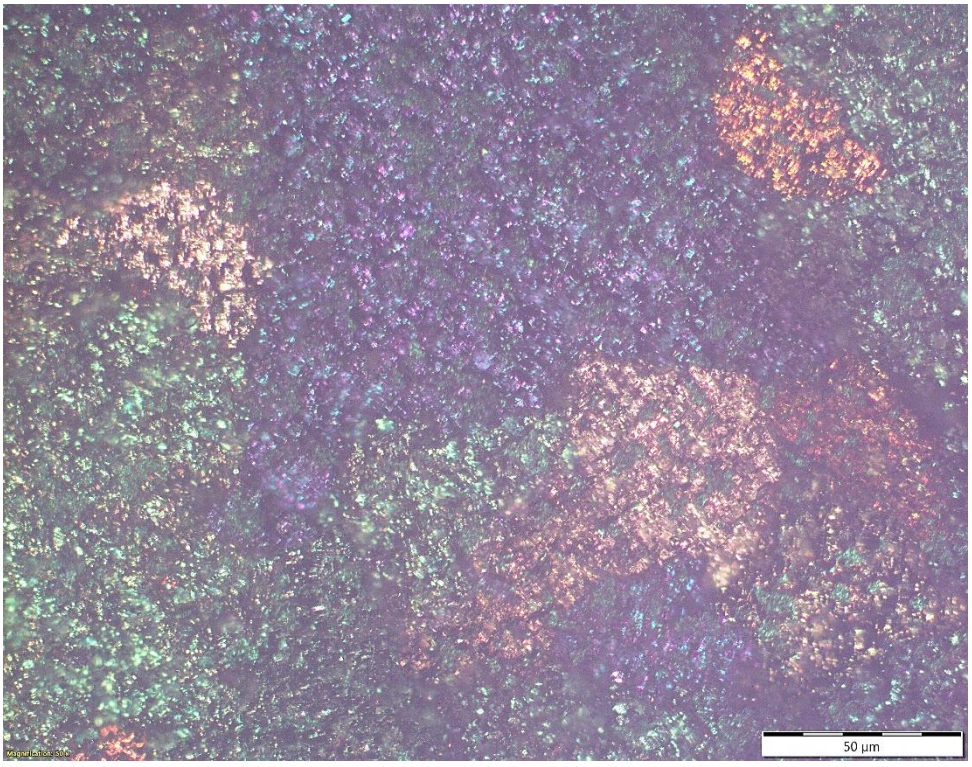

Microstructure of the exposed surface of sample AC2 at a magnification of 50 X

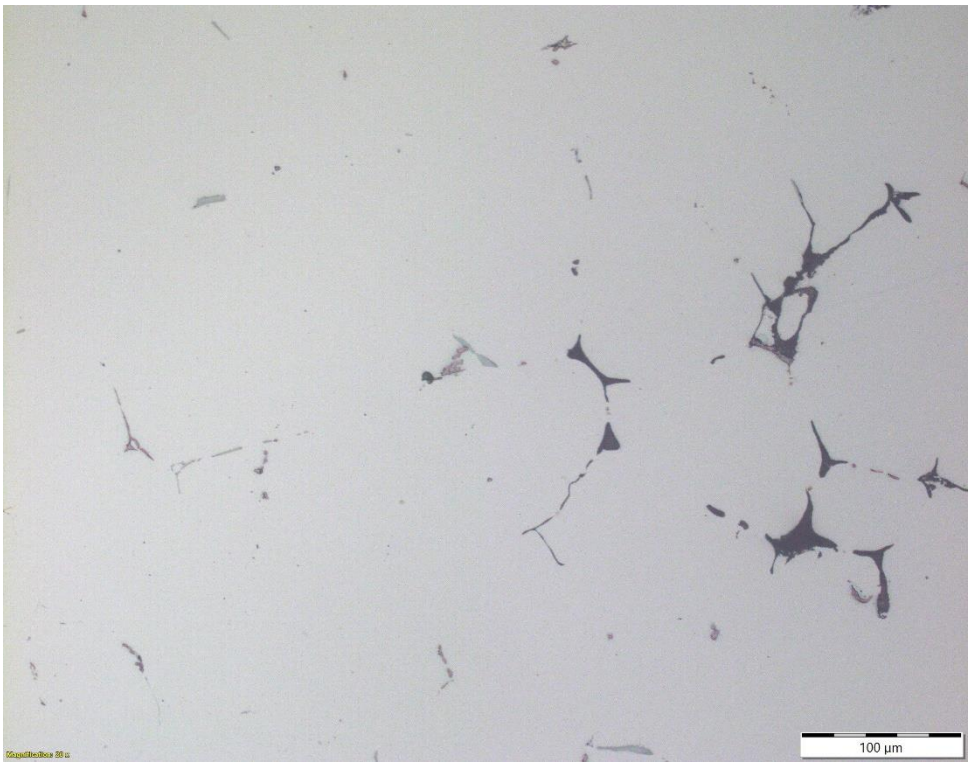

Microstructure of the cross-section of sample AC2 at a magnification of 100 X

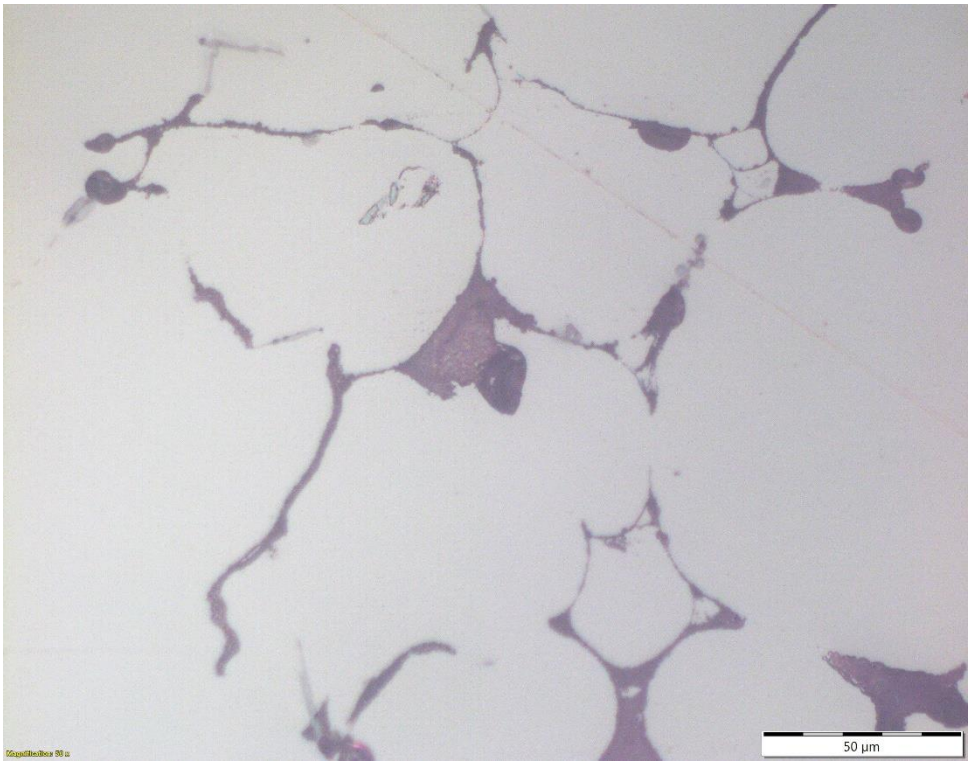

Microstructure of the cross-section of sample AC2 at a magnification of 500 X

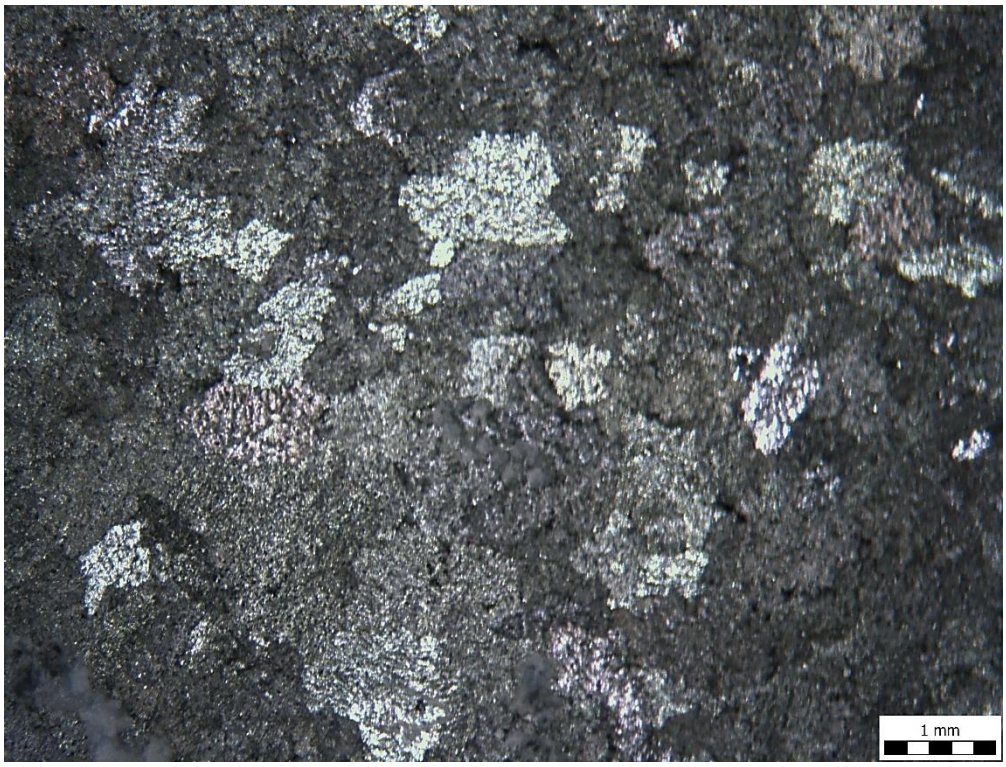

Macrostructure of the exposed surface of sample AC3 at a magnification of 17.5 X

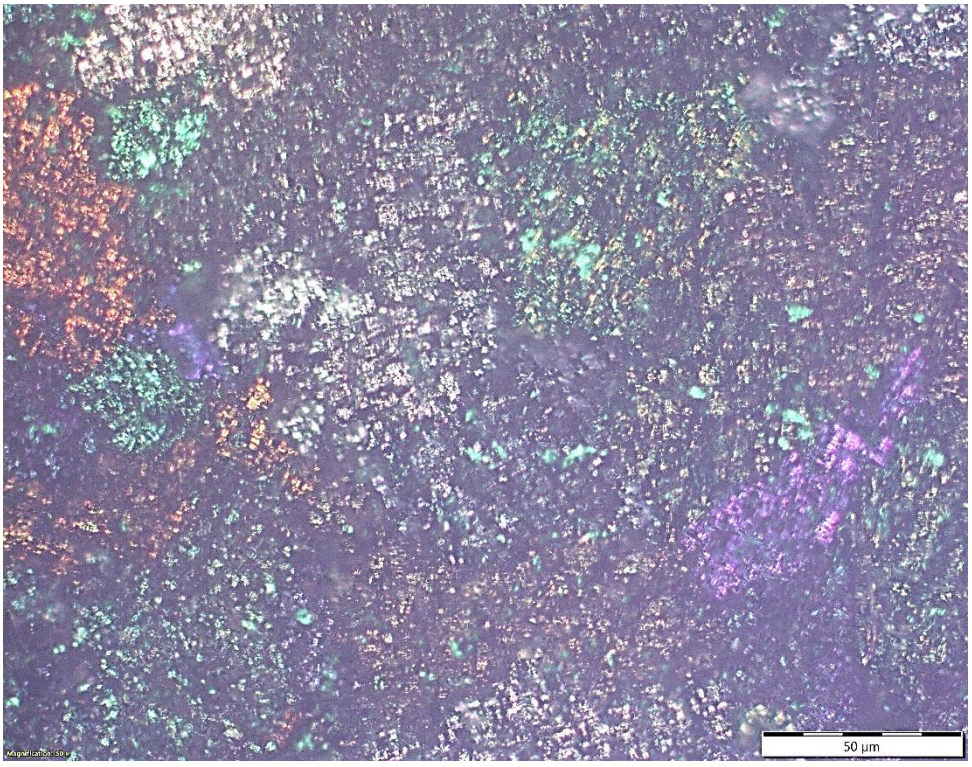

Microstructure of the exposed surface of sample AC3 at a magnification of 50 X

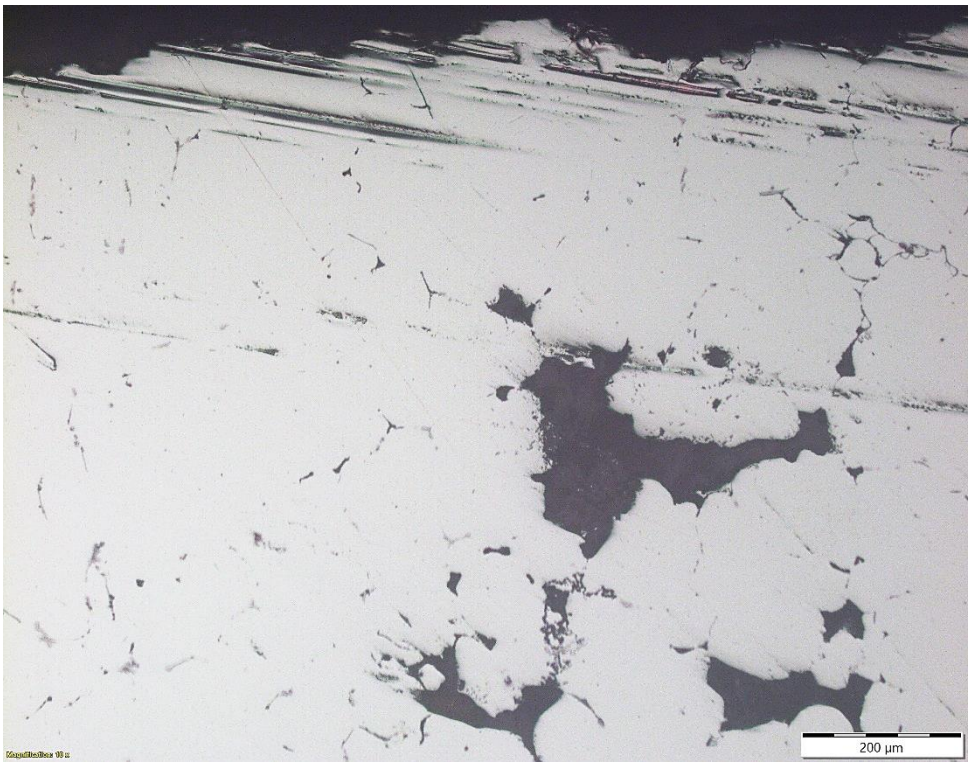

Microstructure of the cross-section of sample AC3 at a magnification of 100 X

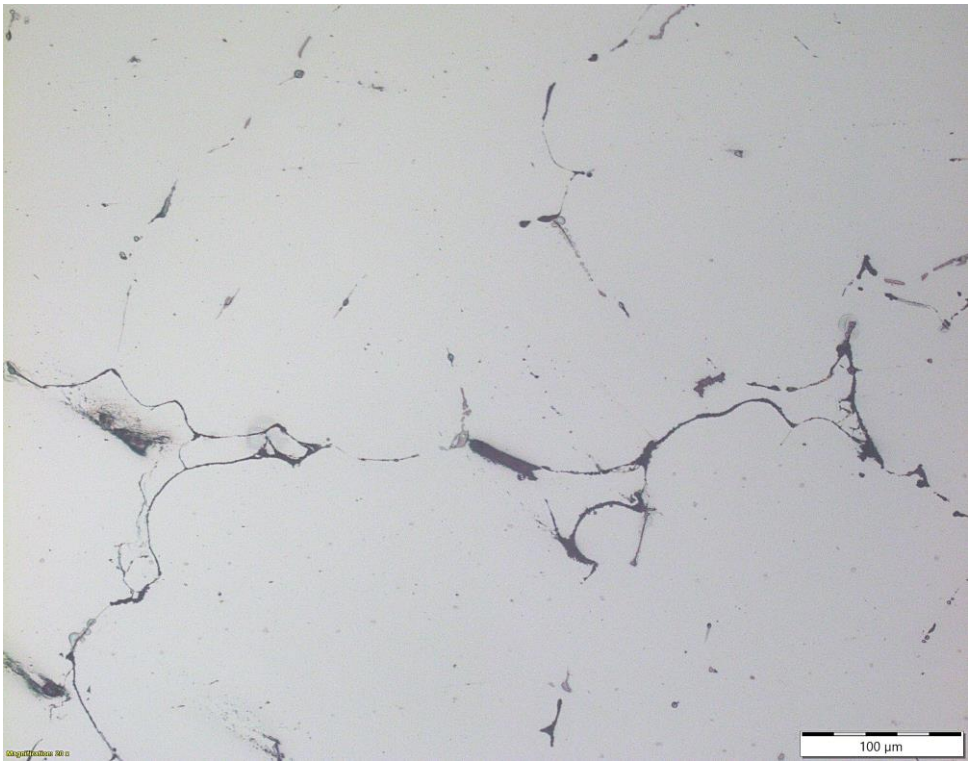

Microstructure of the cross-section of sample AC3 at a magnification of 500 X

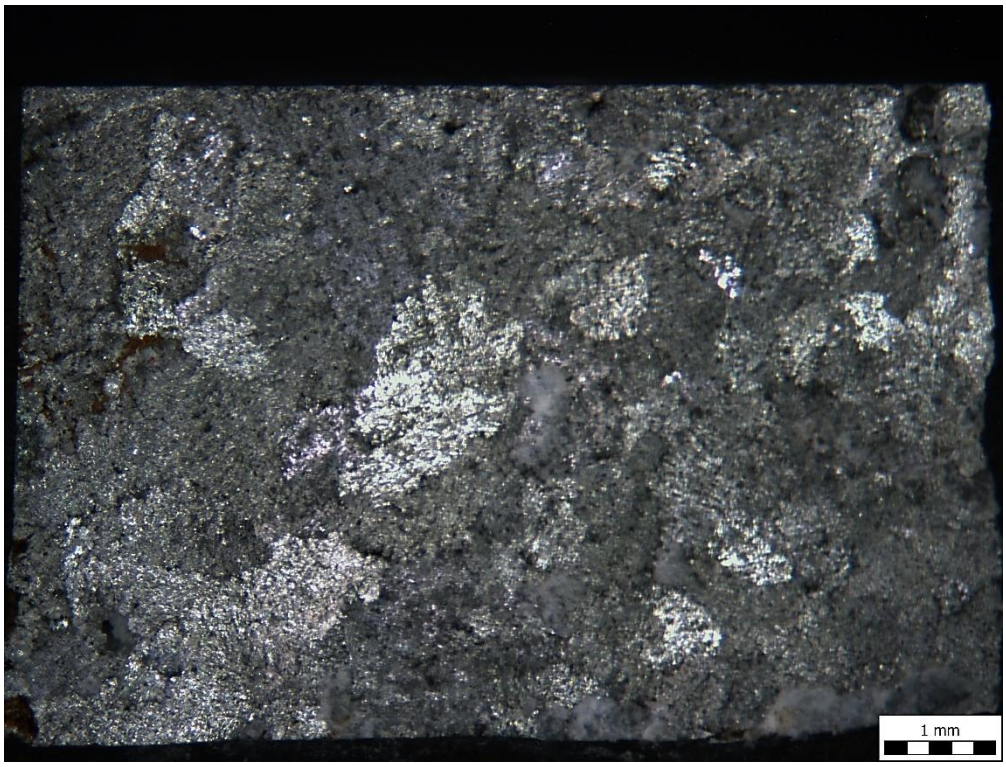

Macrostructure of the exposed surface of sample AC4 at a magnification of 17.5 X

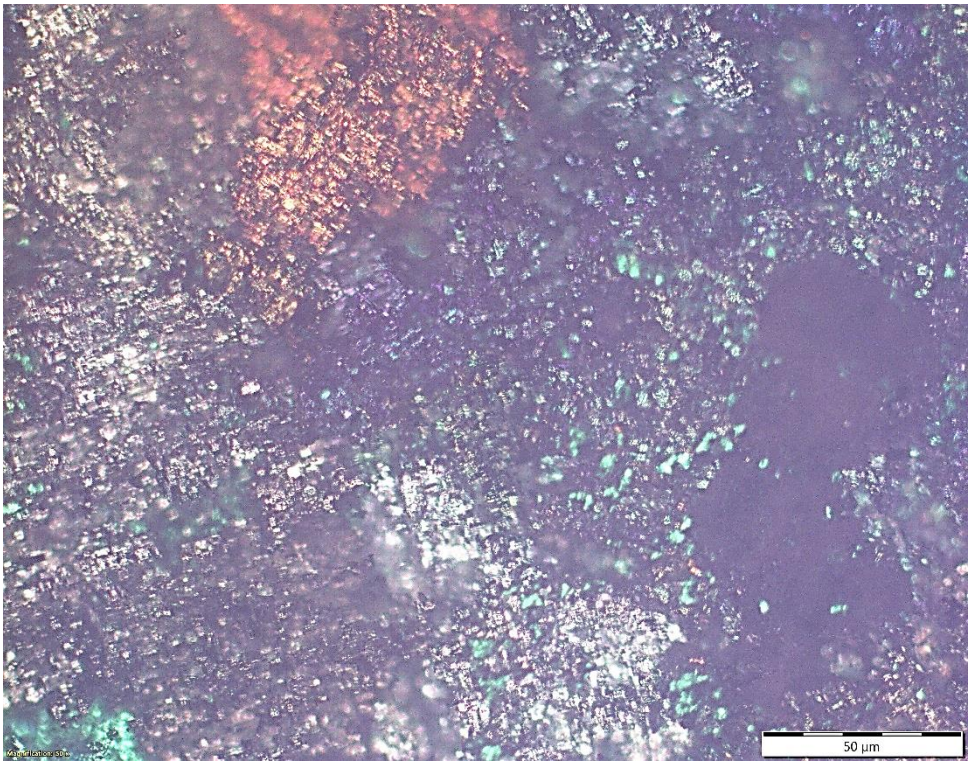

Microstructure of the exposed surface of sample AC4 at a magnification of 50 X

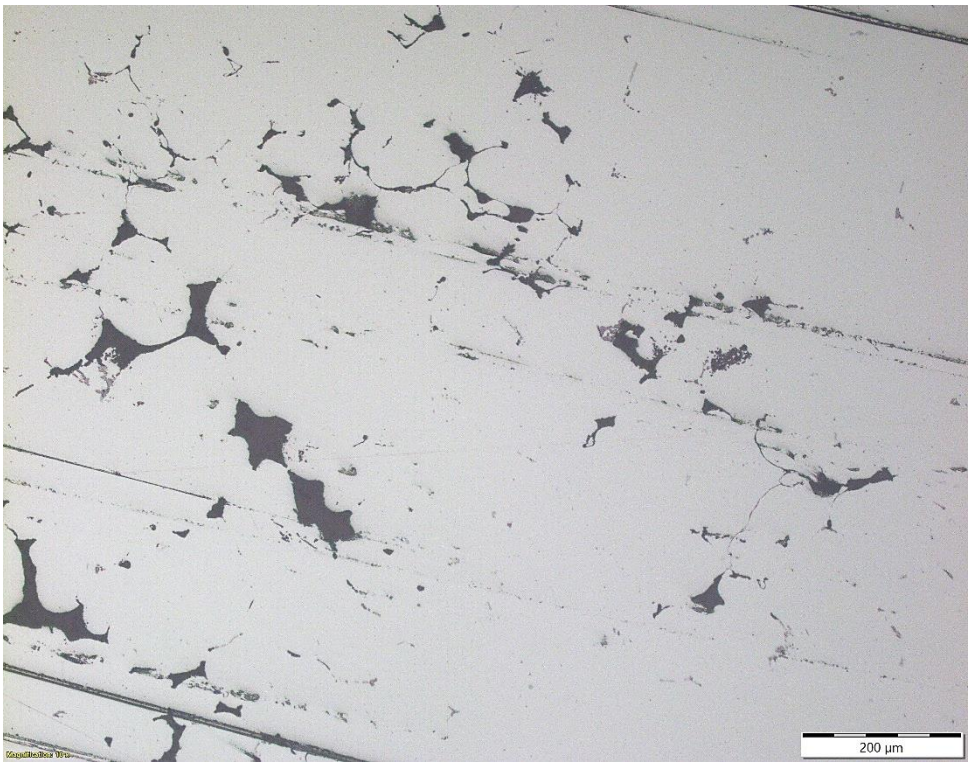

Microstructure of the cross-section of sample AC4 at a magnification of 100 X

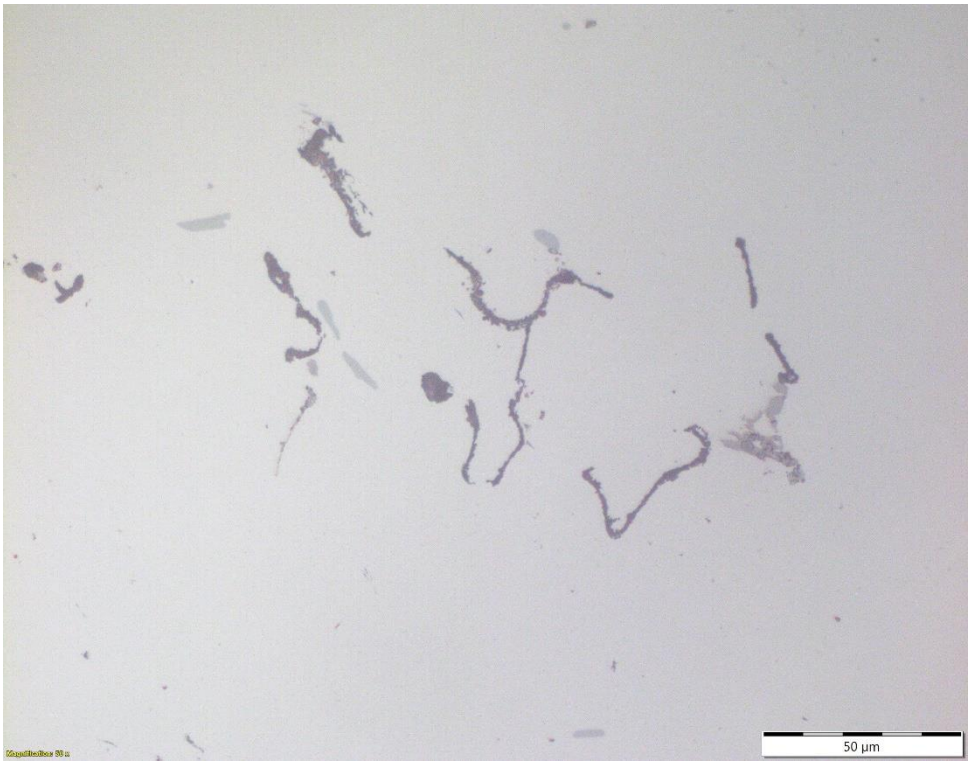

Microstructure of the cross-section of sample AC4 at a magnification of 500 X

Macrostructure of the exposed surface of sample TO1 at a magnification of 17.5 X

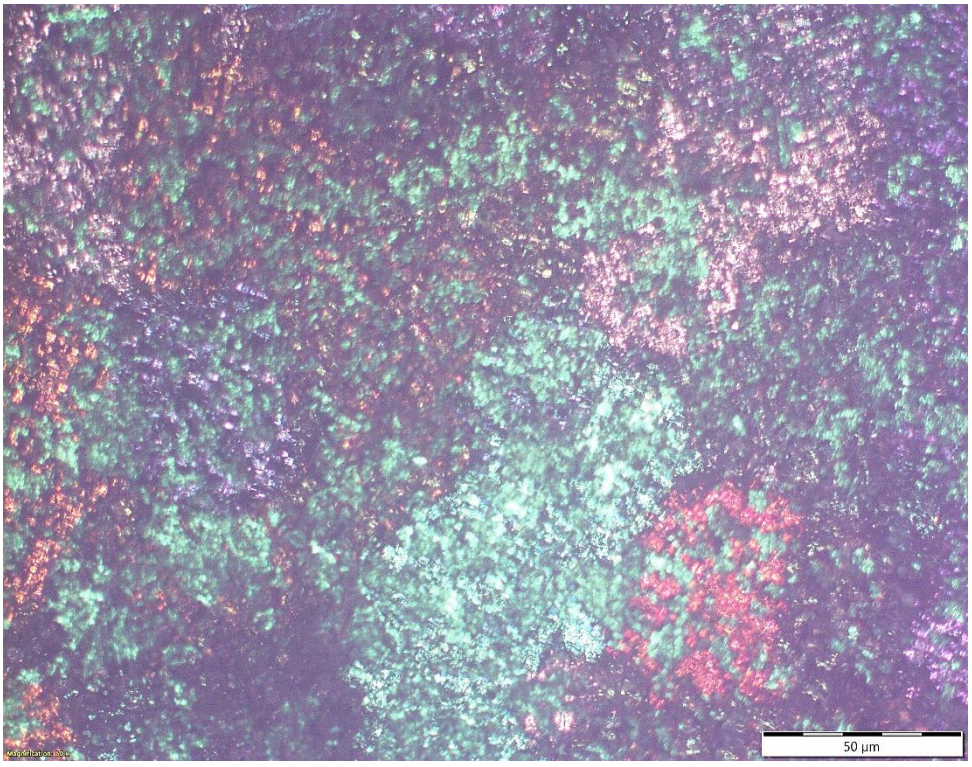

Microstructure of the exposed surface of sample TO1 at a magnification of 50 X

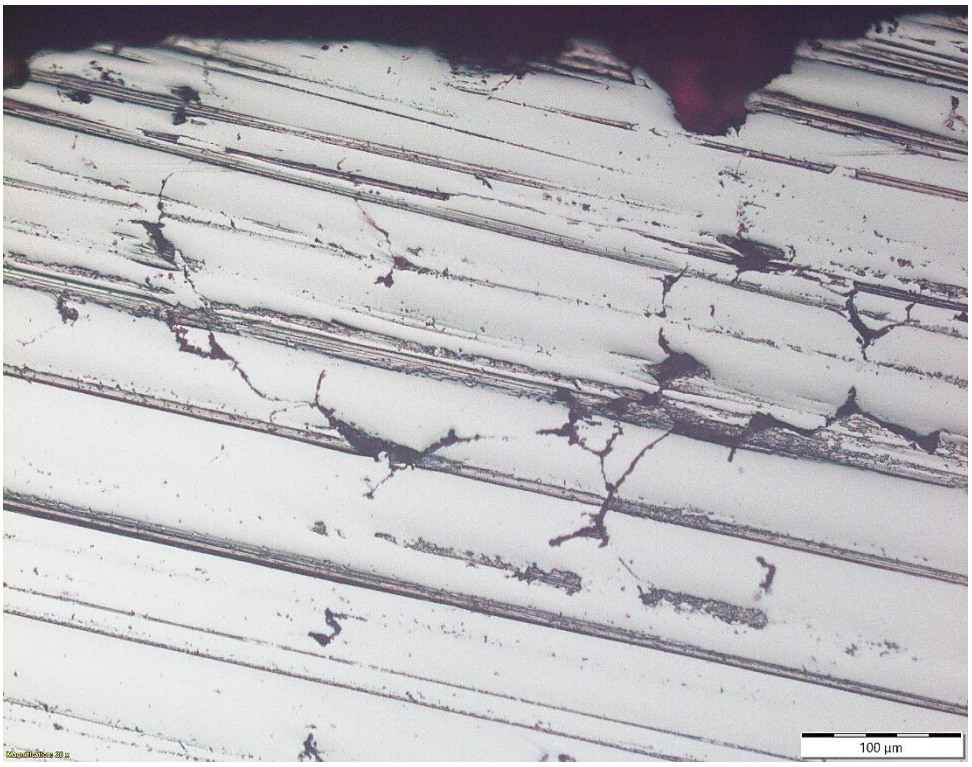

Microstructure of the cross-section of sample TO1 at a magnification of 100 X

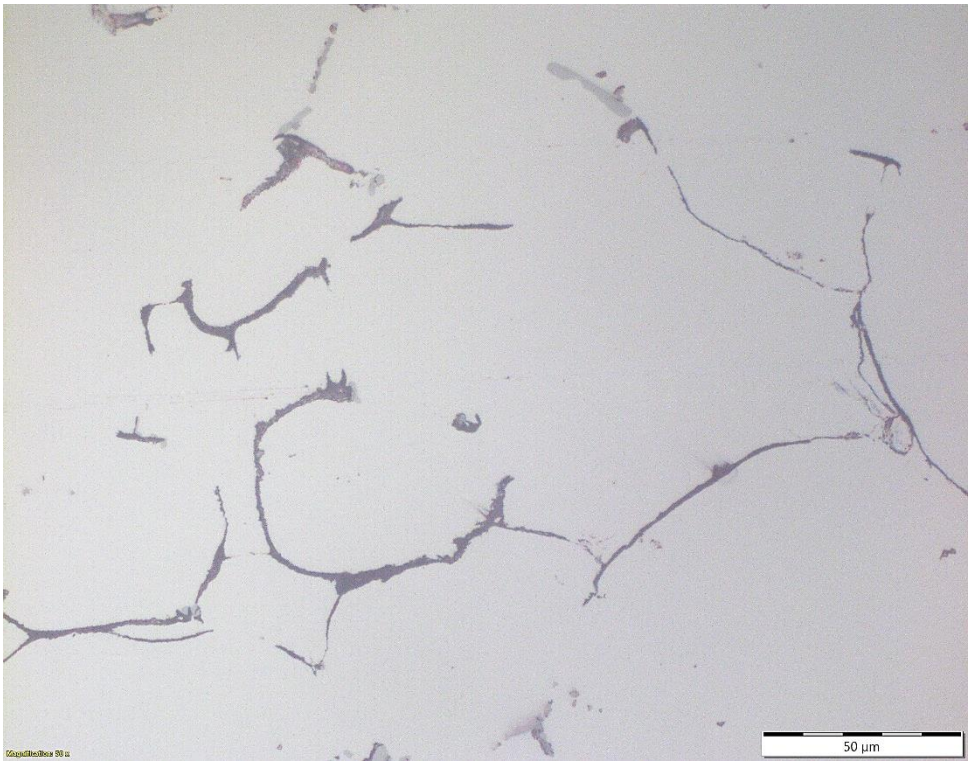

Microstructure of the cross-section of sample TO1 at a magnification of 500 X

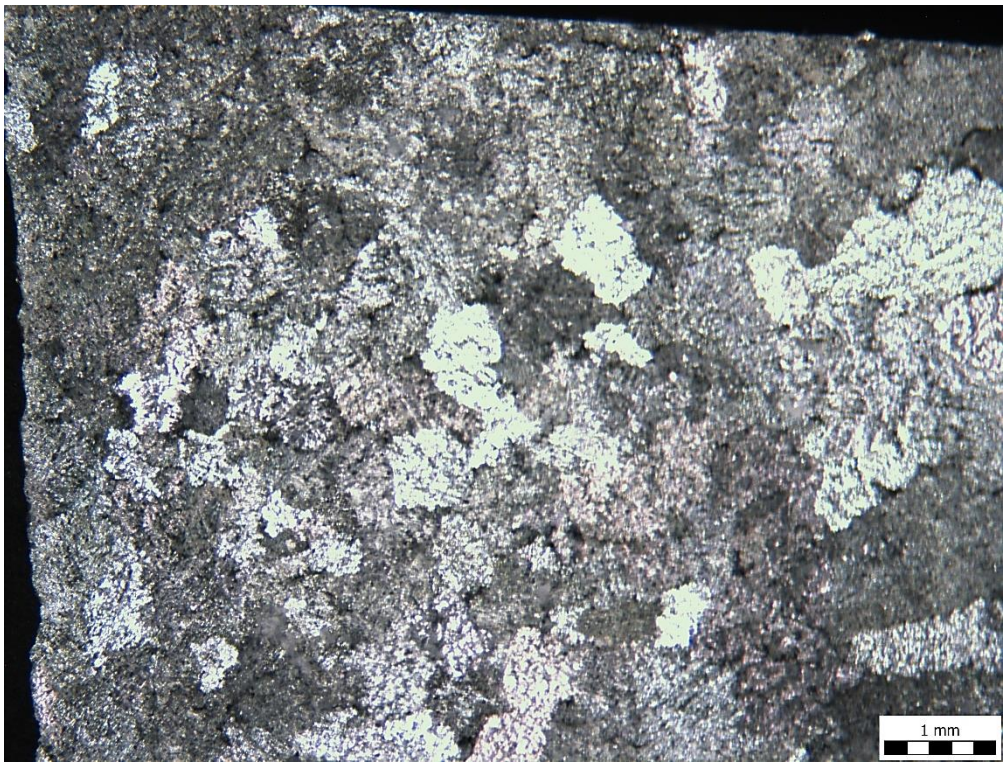

Macrostructure of the exposed surface of sample TO2 at a magnification of 17.5 X

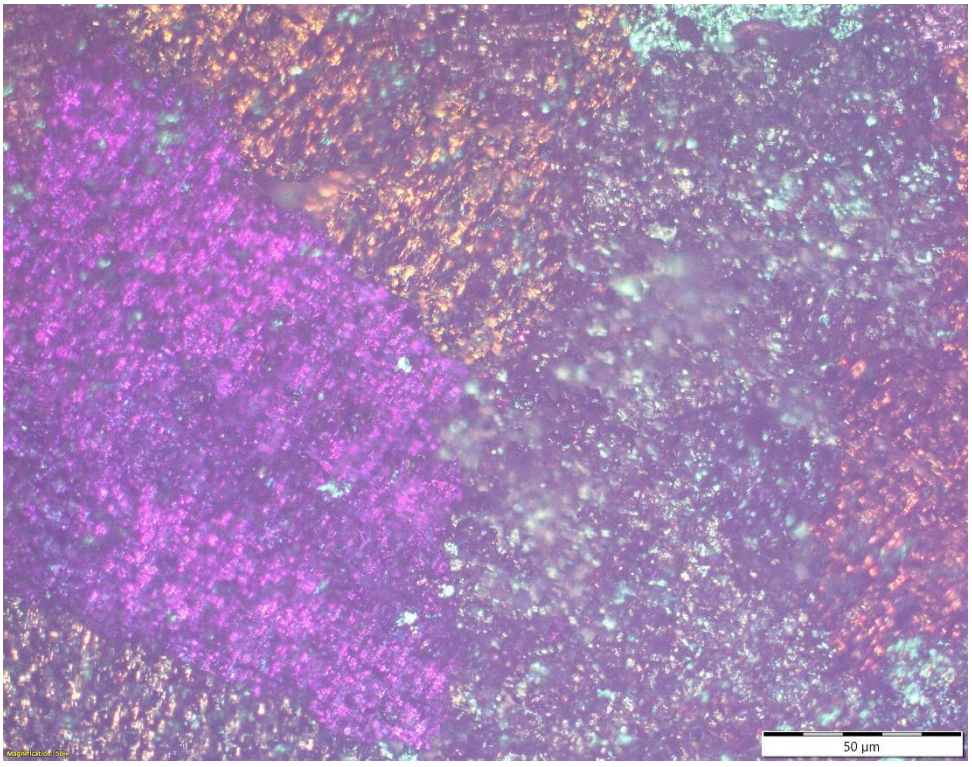

Microstructure of the exposed surface of sample TO2 at a magnification of 50 X

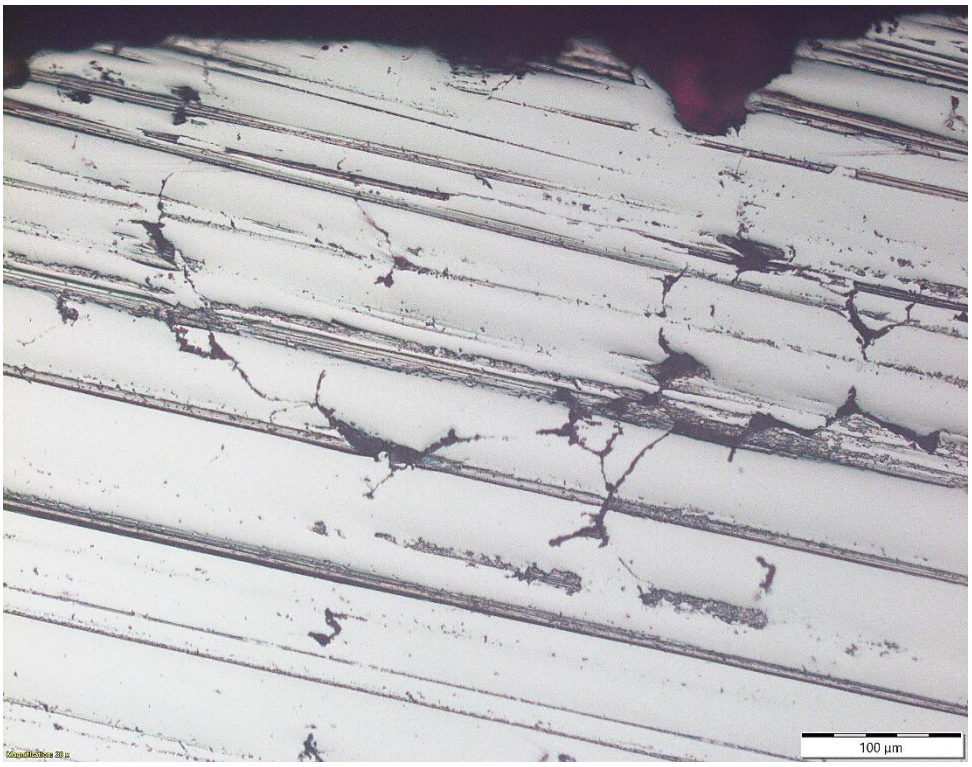

Microstructure of the cross-section of sample TO2 at a magnification of 100 X

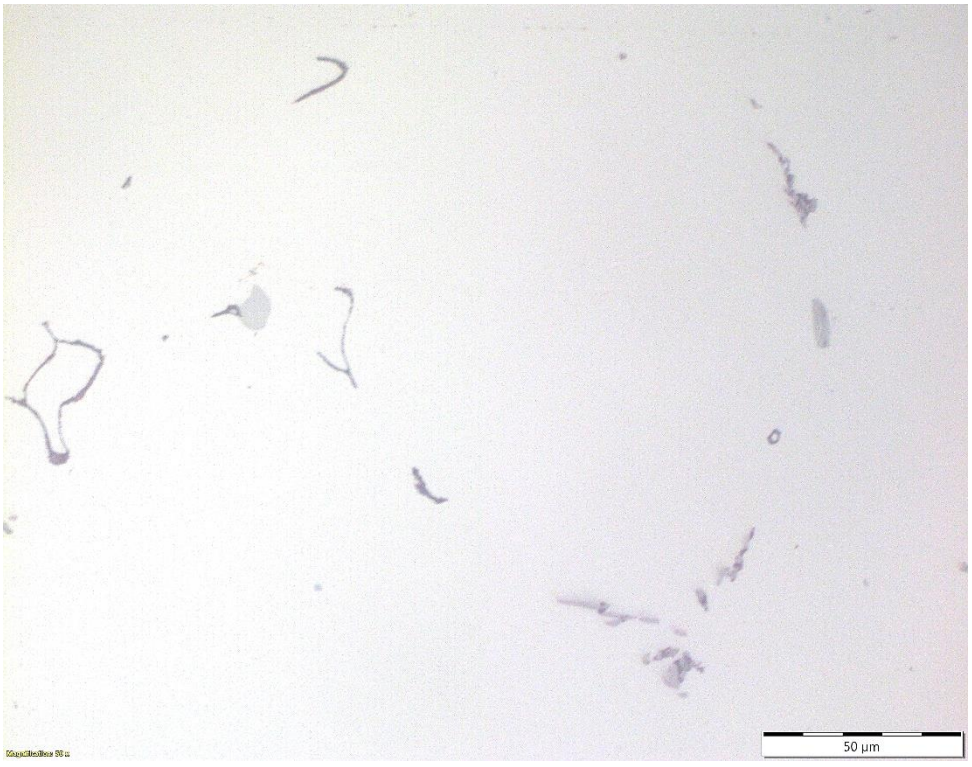

Microstructure of the cross-section of sample TO2 at a magnification of 500 X

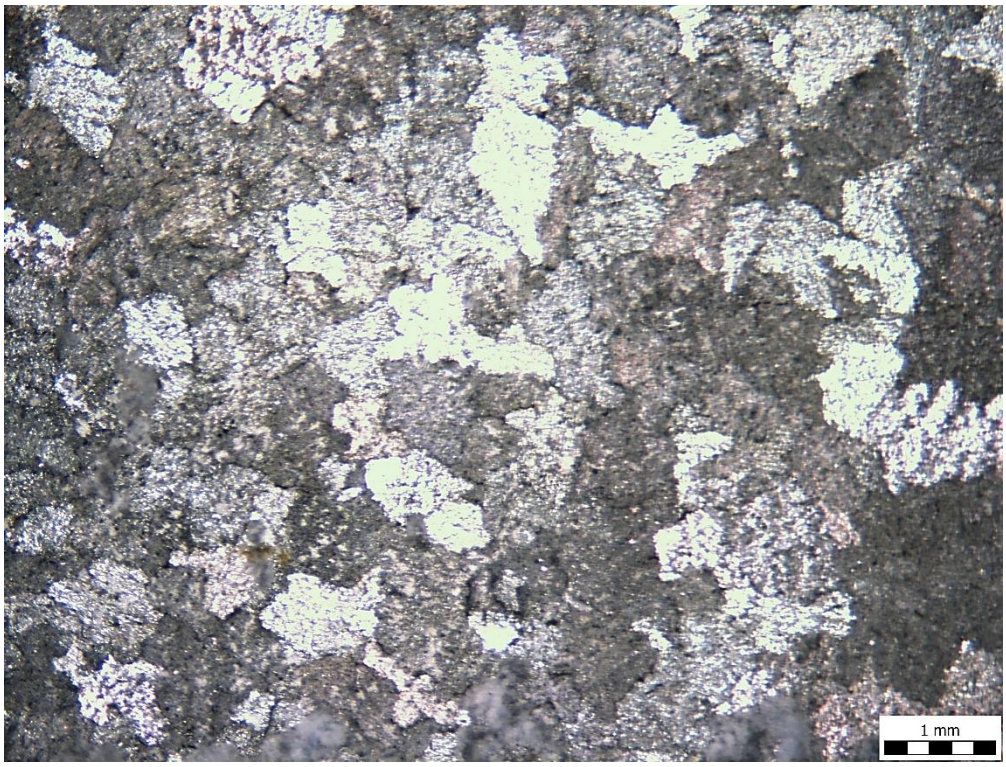

Macrostructure of the exposed surface of sample TO3 at a magnification of 17.5 X

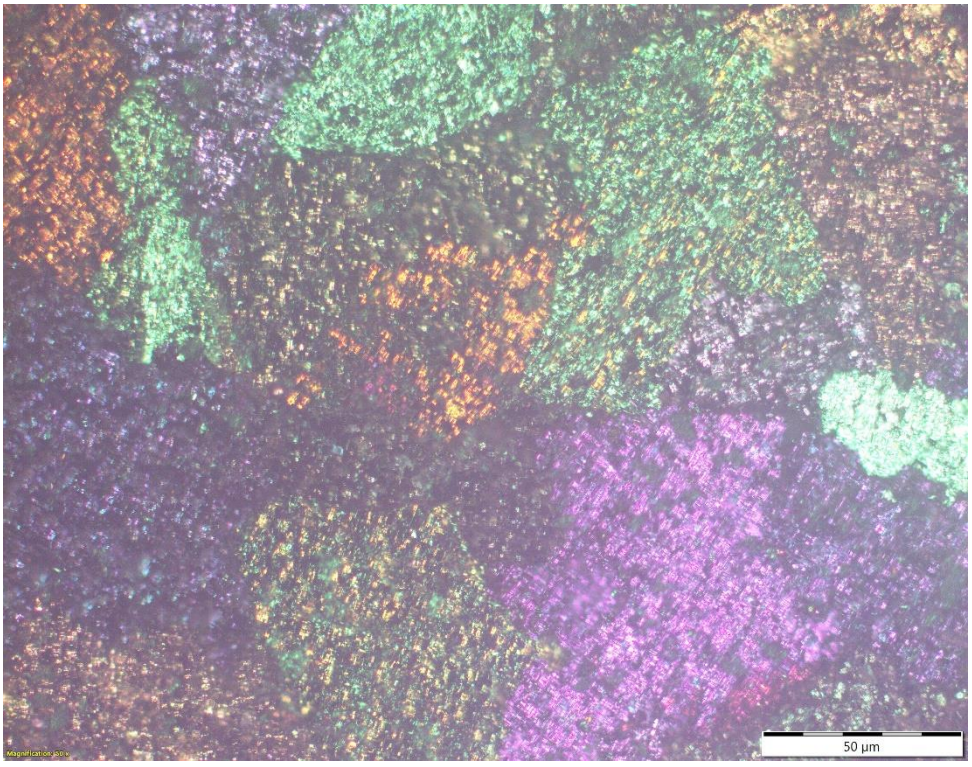

Microstructure of the exposed surface of sample TO3 at a magnification of 50 X

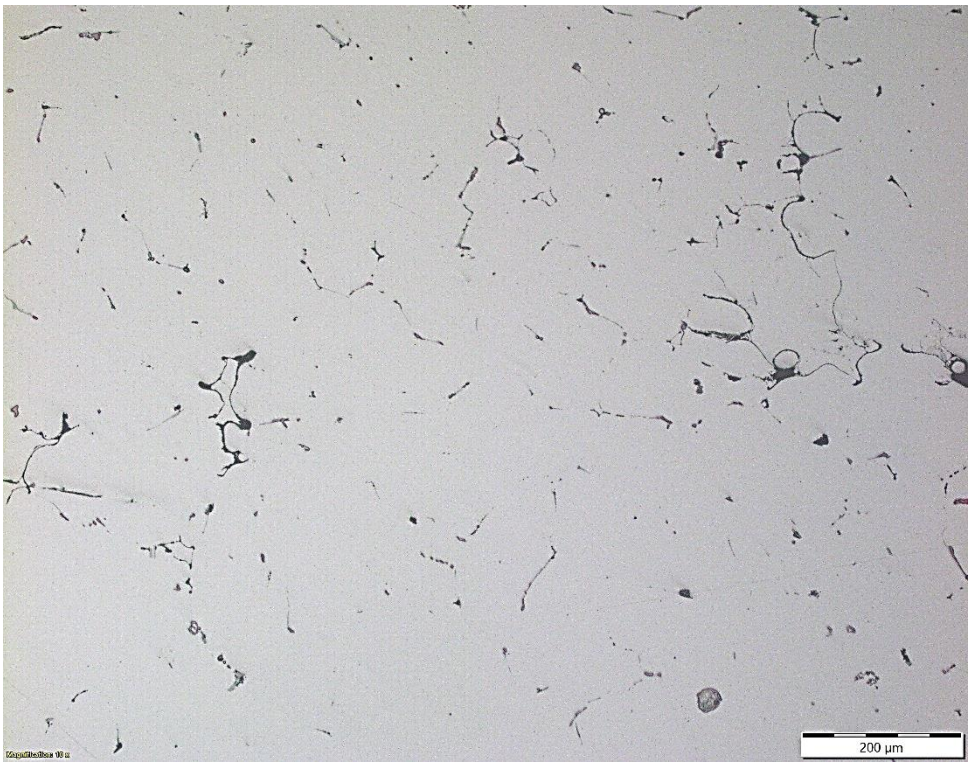

Microstructure of the cross-section of sample TO3 at a magnification of 100 X

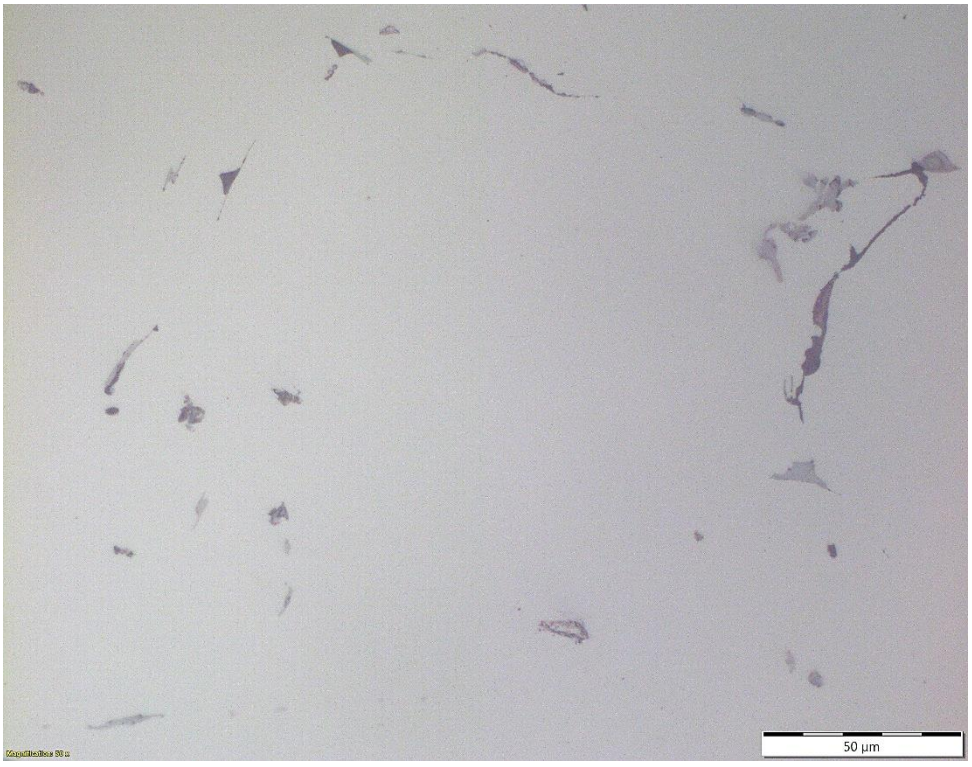

Microstructure of the cross-section of sample TO3 at a magnification of 500 X

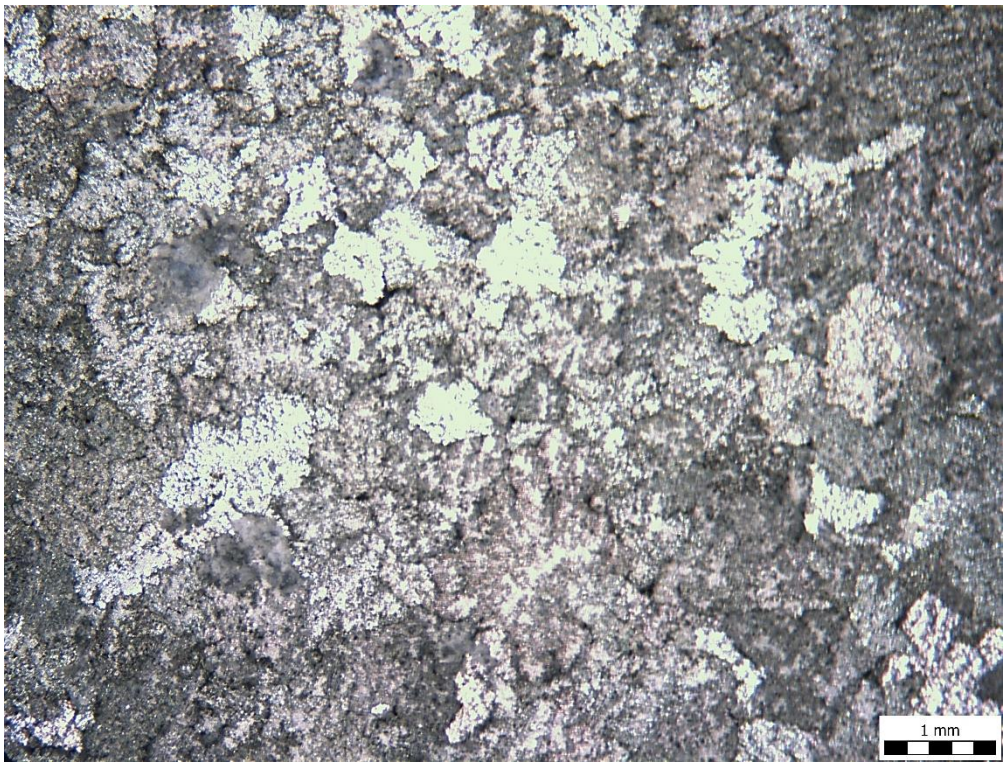

Macrostructure of the exposed surface of sample TO4 at a magnification of 17.5 X

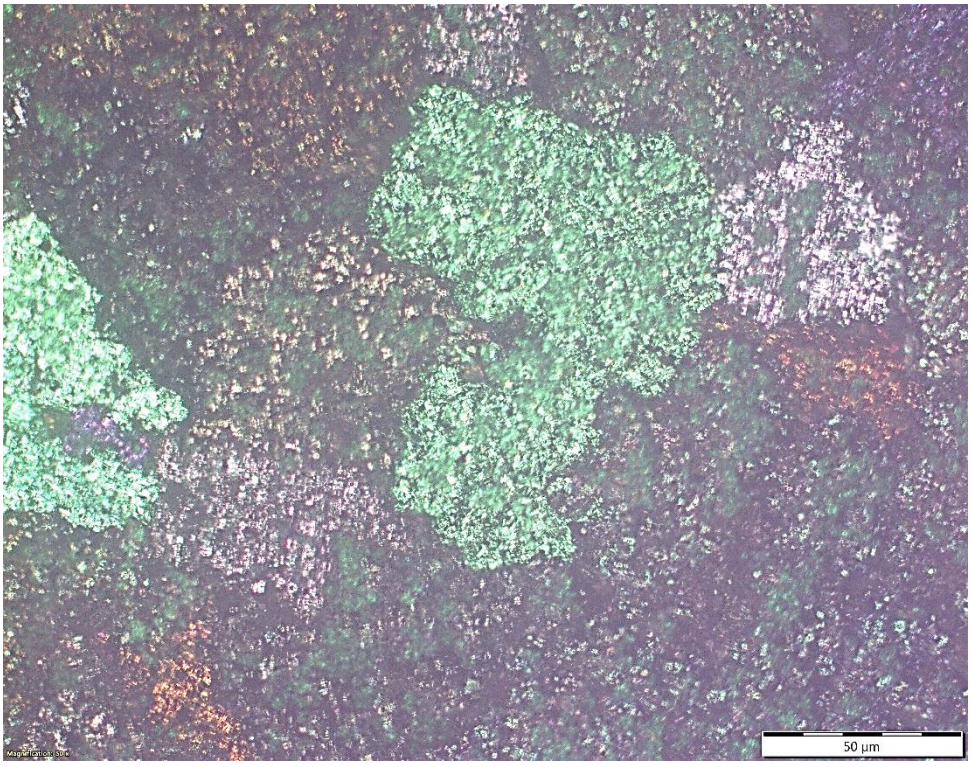

Microstructure of the exposed surface of sample TO4 at a magnification of 50 X

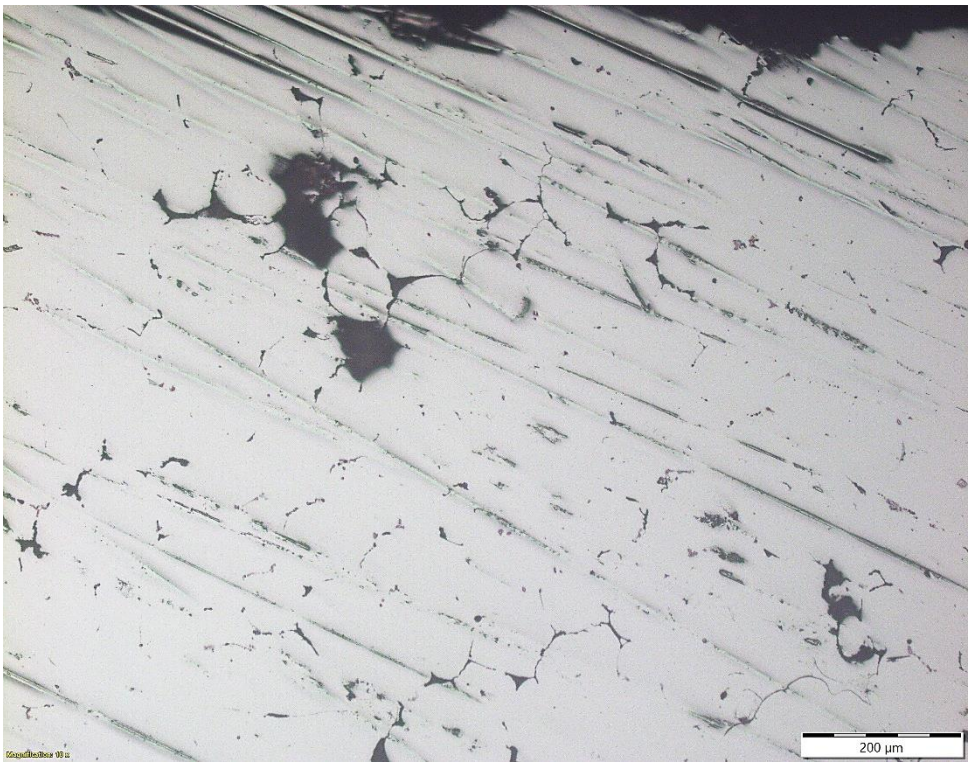

Microstructure of the cross-section of sample TO4 at a magnification of 100 X

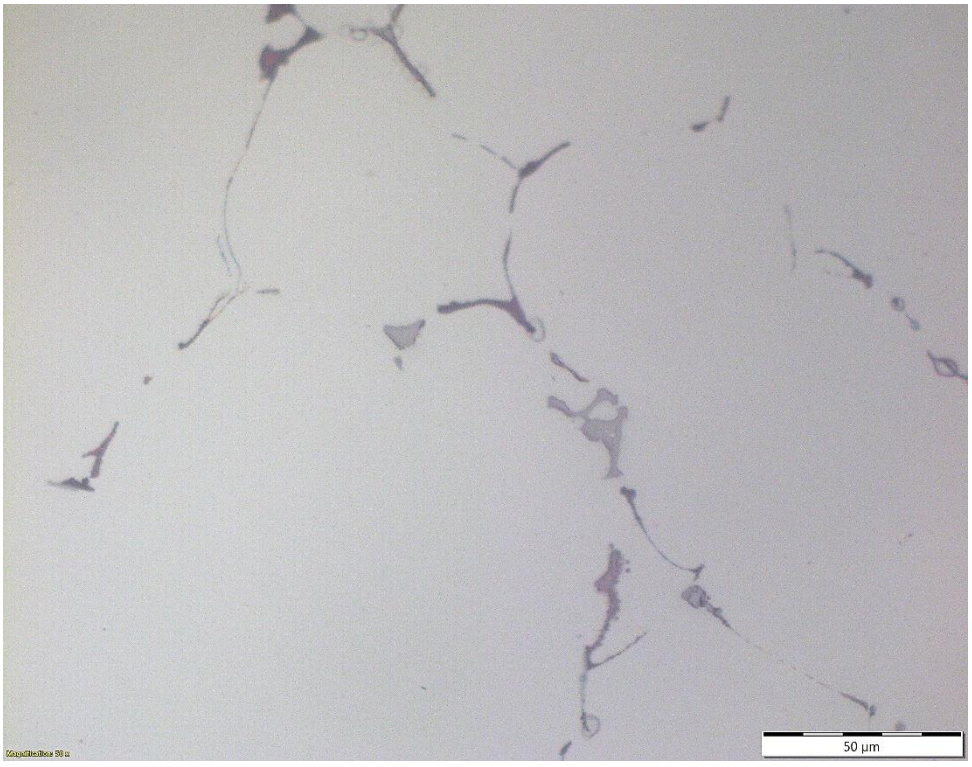

Microstructure of the cross-section of sample TO4 at a magnification of 500 X